

FLUID FLOW PHENOMENA IN METALS PROCESSING

Julian Szekely

DEPARTMENT OF MATERIALS SCIENCE AND ENGINEERING
MASSACHUSETTS INSTITUTE OF TECHNOLOGY
CAMBRIDGE, MASSACHUSETTS



1979

ACADEMIC PRESS

A Subsidiary of Harcourt Brace Jovanovich, Publishers

New York London Toronto Sydney San Francisco

**COPYRIGHT © 1979, BY ACADEMIC PRESS, INC.
ALL RIGHTS RESERVED.**

**NO PART OF THIS PUBLICATION MAY BE REPRODUCED OR
TRANSMITTED IN ANY FORM OR BY ANY MEANS, ELECTRONIC
OR MECHANICAL, INCLUDING PHOTOCOPY, RECORDING, OR ANY
INFORMATION STORAGE AND RETRIEVAL SYSTEM, WITHOUT
PERMISSION IN WRITING FROM THE PUBLISHER.**

**ACADEMIC PRESS, INC.
111 Fifth Avenue, New York, New York 10003**

United Kingdom Edition published by
ACADEMIC PRESS, INC. (LONDON) LTD.
24/28 Oval Road, London NW1 7DX

Library of Congress Cataloging in Publication Data

Main entry under title:

Fluid flow phenomena in metals processing.

Includes bibliographies.

1. Metallurgy. 2. Ore-dressing. 3. Fluid dynamics.

I. Szekely, Julian, Date

TN673.F62 669 78-67888

ISBN 0-12-680840-6

PRINTED IN THE UNITED STATES OF AMERICA

79 80 81 82 9 8 7 6 5 4 3 2 1

To David

Preface

Fluid flow phenomena play a very important role in the majority of metals extraction and refining operations, because the metals or ores that are being processed are in the molten state. During the past three decades major advances have been made in our understanding of the chemistry and particularly the thermodynamics of metals processing operations; however, our knowledge of the kinetics, that is, the rate of extraction and refining, has remained much less complete. The major stumbling block to our understanding of kinetics, particularly kinetics in the molten state, has been the insufficiency of information on the fluid flow phenomena in these systems.

When the fluid flow field is not known, the convective heat and mass transfer processes that take place within the system have to be represented in terms of empirical transport coefficients, which rather than being general are necessarily specific to given situations. This in turn may seriously hamper the fundamental understanding of the problems involved. The process metallurgist faced with these problems has been seriously handicapped by the fact that fluid mechanics per se has usually not been part of the metallurgical curriculum; furthermore, the basic physical situations encountered in metals processing operations (bubble stirring, impinging jets, turbulent recirculating flows in cavities, and the like) tended to be sufficiently different from the problem usually encountered in engineering practice to render such prior experience not immediately applicable.

Nonetheless, in recent years there has been a growing interest in the application of fluid flow concepts to metals processing operations, and we have seen a steady stream of useful papers that demonstrate the appropriateness of this approach to tackling a broad range of practical problems.

The purpose of this monograph is to outline the fundamentals of fluid flow theory, with emphasis on potential applications of fluid flow concepts illustrated by actual problems drawn from the metallurgical literature.

The first four chapters are devoted to the fundamentals while the following five chapters are concerned with the application of these basic concepts to specific systems, namely, electromagnetically driven flows, surface tension and natural convection driven flows, multiparticle systems, gas bubbles, and impinging jets. Finally, the last chapter covers flow measurements and also provides an introduction to physical modeling.

It should be stressed that fluid flow problems in metals processing can be tackled at various levels, depending on the specific task involved and on the mathematical skills of the investigator. In the presentation of the material care

has been taken to emphasize this possible diversity of approaches. While the fundamentals and applications are necessarily closely interrelated, an attempt has been made to make the applications chapters reasonably self-contained so that the reader, if he so desires, can obtain specific practical information (e.g., bubble rising velocity, jet penetration, minimum fluidization velocity, and the like) without the need to plough through all the fundamental material.

This volume would be suitable as the text for a one semester graduate level course given to students in metallurgy (materials engineering) or chemical engineering. Indeed, a good deal of this material has been presented by the author within this format to students in the Department of Materials Science and Engineering at the Massachusetts Institute of Technology, Cambridge.

It is hoped moreover that the book will appeal to a growing number of practicing engineers engaged in metallurgical process research and development.

The primary metals industry has had an impact on many of the vital problems faced by our society at present, such as shortages of energy and resources and pollution of the environment. A better understanding of fluid flow phenomena in metals processing could well provide an important component of the new process development effort that is needed in this area.

Acknowledgments

No book is ever the work of a single individual, but rather is a reflection of influences and experiences received from a broad range of sources. It is a pleasure to acknowledge the help and encouragement of Professor F. D. Richardson of Imperial College, London, who has drawn to my attention the fascinating field of process metallurgy as a rich source of problems in transport phenomena.

The main motivating force for writing this book has been provided by an extended period of research activity in this area with students and research associates, who included Drs. G. P. Martins, M. R. Todd, J. J. Poveromo, S. D. Fang, R. T. Yadoya, A. Jassal, M. Propster, C. W. Chang, V. Stanek, K. Nakanishi, S. Asai, A. H. Dilawari, Y. Yagi; Messrs. M. J. Mendrykowski, Y. Kajiwara, J. C. Wang, R. Metz, and others.

The manuscript itself was written while the author was a Guggenheim Fellow in the Department of Metallurgy at Imperial College, London. Sincere thanks are expressed to the John Simon Guggenheim Foundation for the support received during this period. During this time the author benefited appreciably from discussions with Professor A. V. Bradshaw and Dr. D. G. Robertson.

Many people have made helpful comments on the manuscript, and the author is particularly grateful to Professor R. I. L. Guthrie of McGill University, Montreal, and to Dr. J. Downing of Union Carbide Corporation, Niagara Falls, New York, for their very detailed comments and observations. Useful comments were also received from Professor J. W. Evans of the University of California at Berkeley.

However, the ultimate responsibility for the work rests with the author. Many colleagues have been very helpful in providing original figures and photographs; these are acknowledged in the text. The manuscript was ably typed and retyped by Mrs. Lucille Delmar and Mrs. Christine Jerome; additional substantial typing was done by Ms. Elizabeth Greene and Mrs. Marie McTighe. The drawings were prepared by Dr. R. Tai and Mr. J. Turlo.

Finally, I should like to thank the staff at Academic Press for their very competent and sympathetic approach to the trauma of getting a manuscript into the final book form.

List of Principal Symbols

a	acceleration Lt^{-2} (m s^{-2})
a_p	surface area per unit volume of packing L^{-1} (m^{-1})
A	surface area L^2 (m^2)
\mathbf{A}	vector potential (T/m); see Eq. (5.3.17)
A^*	area of the throat in a supersonic nozzle; see Table 2.6.2
B	magnetic flux density (T or Wb/m^2)
\hat{C}	coefficient; see Section 6.5.2
C	concentration ML^{-3} (kg moles/m^{-3})
C	constant; see Eq. (6.3.17)
\hat{C}_A	added mass coefficient; see Eq. (7.1.10)
C_A	concentration of species A ML^{-3} (kg m^{-3})
C_D	discharge coefficient
C_H	coefficient for the history term; see Chapter 7
C_p, C_v	specific heat at constant pressure and volume, respectively $\text{QM}^{-1}\text{T}^{-1}$, $\text{J kg}^{-1} \text{K}^{-1}$; see Eqs. (2.6.1–2)
D_e	effective diffusivity L^2t^{-1} (m^2s^{-1})
d_B	bubble diameter L (m)
$d_{b,\max}$	maximum stable bubble size in fluidized beds L (m, mm)
$d_{B,d}$	gas bubble diameter in liquid metals L (m)
$d_{b,i}$	inside nozzle diameter L (m)
d_c	pipe diameter L (m)
d_D	droplet diameter L (mm)
d_h	hydraulic mean diameter L (m); see 2.5.1
div	divergence operator; see Appendix 1
$d_{n,o}$	outside nozzle diameter L (m)
d_p	particle diameter L (m, mm)
\bar{d}_p	surface area mean diameter L (m, mm); see Eq. (7.2.4)
d_t	tube diameter L (m, mm)
$dy, \delta y$	infinitesimal increment in the y direction L (m, mm)
D	electric flux density C/m^2
D_{AB}	binary diffusivity L^2t^{-1} (m^2s^{-1} , cm^2s^{-1})
E	electric field (V/m)
E_f	rate of work done against frictional forces ML^2t^{-3}
E'_f	rate of work done against the frictional forces per unit mass flowing L^2t^{-2} (m^2s^{-2})

E_μ	activation energy for viscous flow (J/kg mole or kcal/mole)
f	frequency t^{-1} (s^{-1})
f_1, f_2	flow resistance parameters; see Eqs. (7.2.6–7)
f_f	friction factor; see Section 2.5
f_z	mean body force in z direction (N/m^3)
\mathbf{F}	force MLt^{-2} (N)
\mathbf{F}_b	body force MLt^{-2} (N)
F_{bx}	body force in x direction MLt^{-2} (N)
F_{by}	body force in y direction MLt^{-2} (N)
F_{bz}	body force in z direction MLt^{-2} (N)
F_d	drag force MLt^{-2} (N); see Eq. (7.1.1)
$F(\xi)$	dimensionless function; see Section 3.5.5
F_n	normal force component MLt^{-2} (N)
F_Σ	surface free energy QM^{-1} ($J\ kg^{-1}$)
F_x	force in the x, y, z direction F_x, F_y, F_z $ML\ t^{-2}$ (N)
$F_{x,p}$	force component in the x direction due to pressure $ML\ t^{-2}$ (N)
F_t	tangential force component $(ML\ t^{-2})\ N$
\mathbf{g}	acceleration due to gravity Lt^{-2} ($m\ s^{-2}$)
$G = u_m \rho,$	mass velocity $ML^{-2}t^{-1}$ ($kg\ m^{-2}\ s^{-2}$)
G_g	mass velocity of gas $ML^{-2}\ t^{-1}$ ($kg\ m^{-2}\ s^{-1}$)
$G(\xi)$	dimensionless function; see 3.5.5
G_L	mass velocity of liquid $ML^{-2}\ t^{-1}$ ($kg\ m^{-2}\ s^{-1}$)
G_s	mass velocity of the solids $ML^{-2}\ t^{-1}$ ($kg\ m^{-2}\ s^{-1}$)
h	height L (m)
H	enthalpy QM^{-1} ($J\ kg^{-1}$)
\mathbf{H}	magnetic field (A/m)
$H(\xi)$	dimensionless function; see 3.5.5
\mathbf{i}	unit vector
\mathbf{j}	unit vector
\mathbf{J}	current density (A/m^2)
J_A	molar flux of species A $ML^{-2}\ t^{-1}$ ($kg\ m^{-2}\ s^{-1}$); see Eqs. (6.2.11, 12)
J_o	Bessel function; see Chapter 3
J_z	momentum of a jet MLt^{-1} ($kg\ m\ s^{-1}$)
k	thermal conductivity $QL^{-1}T^{-1}t^{-1}$ ($J\ m^{-1}\ ^\circ K^{-1}\ t^{-1}$)
k	wave number (in Chapter 5)
\mathbf{k}	unit vector
k_E	elutriation constant t^{-1} (s^{-1})
K	turbulence energy per unit mass $L^2\ t^{-2}$ ($m^2\ s^{-2}$)
$K_{E,T}$	kinetic energy $L^2\ t^{-2}\ M$ ($m^2\ s^{-2}\ kg$)

L	length L (m)
L_r	macroscale L (m, mm); see Eq. (4.2.8)
l	length L (m)
\bar{l}	mean eddy size L (m, mm); see Eq. (6.5.10)
l_m	mixing length L (m)
m	mass M (kg)
M_T	total mass M (kg)
M_w	molecular weight M (kg)
n	frequency of fluctuations (s^{-1}); see Chapter 4
N_A	molar flux, fixed coordinate system $ML^{-2}t^{-1}$ (kg m $^{-2}s^{-1}$)
N_C	capacitance number; see Eq. (8.2.12)
N_{Eo}	Eotvos number; see Eq. (8.3.3)
N'_{Fr}	modified Froude number; see p. 386
N_{Gr}	Grashof number
N_{Ha}	Hartmann number; see Eq. (5.2.13)
N_{Ma}	$= u_m/u_s$ Mach number
N_{Mo}	Morton number; see Eq. (8.3.4)
N_{Pr}	$= \nu/\kappa$ Prandtl number; see Eq. (6.2.6)
$N_{Pr,m}$	magnetic Prandtl number; see Eq. (5.2.14)
N_{Ra}	$= N_{Gr} N_{Pr}$ Rayleigh number
N_{Re}	Reynolds number; see Eq. (2.5.5)
$N_{Re,b}$	bubble Reynolds number; see Eq. (8.3.1)
$N_{Re,m}$	magnetic Reynolds number; see Eq. (5.2.11)
$N_{Re,p}$	particle Reynolds number
N_{Sc}	$= \nu/D_{AB}$ Schmidt number
N_T	Nussell film thickness; see Eq. (4.4.14)
N_{We}	Weber number; see Eq. (8.3.2)
P	momentum per unit volume $ML^{-2} t^{-1}$ (kg m $^{-2}s^{-1}$)
p	pressure $ML^{-1} t^{-2}$ (N m $^{-2}$)
p_c	pressure in the critical state $ML^{-1} t^{-2}$ (N m $^{-2}$)
p_s	gas pressure at the sonic velocity $ML^{-1} t^{-2}$ (N m $^{-2}$)
$P_{x,G}$	pressure inside a bubble (N m $^{-2}$)
$P_{x,\infty}$	pressure in the fluid at the same level as bubble but at a large distance from the bubble
q	heat flux, $QL^{-2} t^{-1}$ (J m $^{-2}s^{-1}$)
Q	volumetric flow rate $L^3 t^{-1}$ (m $^3s^{-1}$)
\tilde{Q}	volumetric flow rate $L^3 t^{-1}$ (m $^3s^{-1}$)
r	radial coordinate L (m)
r'	radial distance from the wall L (m, mm)
\tilde{r}	dummy variable
R	radius L (m, mm)
R	universal gas constant; see Table 1.2.2

\dot{R}	= dR/dt radial velocity of a bubble surface $L t^{-1} (\text{m s}^{-1})$
\ddot{R}	= d^2R/dt^2 $L t^{-2} (\text{m s}^{-2})$
R_0	initial bubble radius $L (\text{m, mm})$
R_p	particle diameter $L (\text{m})$
R_r	correlation coefficient; see Eq. (4.2.7)
s	entropy $QM^{-1} T^{-1} (\text{J kg}^{-1} \text{ }^\circ\text{K}^{-1})$
t	time $t (\text{s})$
t_d	time needed for the detachment of a bubble $t (\text{s})$
T	temperature $T (\text{ }^\circ\text{K})$
T_b	boiling point $T (\text{ }^\circ\text{K})$
T_c	critical temperature $T (\text{ }^\circ\text{K})$
T_m	mean temperature $T (\text{ }^\circ\text{K})$
T_m	melting point $T (\text{ }^\circ\text{K})$
T_∞	temperature at an infinite distance from the wall $T (\text{ }^\circ\text{K})$
T_w	temperature of the wall $T (\text{ }^\circ\text{K})$
$U_{c,s}$	saltation velocity $L t^{-1} (\text{m s}^{-1})$
U_o	superficial velocity $L t^{-1} (\text{m s}^{-1})$
U_t	terminal falling velocity $L t^{-1} (\text{m s}^{-1})$
v	specific volume $L^3 M^{-1} (\text{m}^3 \text{ kg}^{-1})$
\tilde{v}	volume of filter cake deposited per unit volume of filtrate
V_B	bubble volume $L^3 (\text{m}^3, \text{mm}^3)$
V_c	Ante chamber volume $L^{-3} (\text{m}^3, \text{mm}^3)$
V_{v1}	volume of the float $L^3 (\text{m}^3); \text{ see Eq. (10.2.12)}$
\hat{V}_m	molar volume $L^3 M^{-1}$
w	mass flow rate $M t^{-1} (\text{kg s}^{-1})$
W	rate of work done on the surroundings $ML^2 t^{-2}$
W'	rate of work done on the surroundings per unit fluid flowing $L^2 t^{-2} (\text{m}^2 \text{ s}^{-2})$
x	coordinate $L (\text{m, mm})$
x_i, x_j	mole fraction
y	coordinate $L (\text{m, mm})$
y	distance in the y direction $L (\text{m, mm})$
y^+	dimensionless distance; see Eq. (4.2.15)
z	coordinate $L (\text{m})$
z	distance $L (\text{m})$
Z_T	potential energy $ML^2 t^{-2}$
\mathcal{Z}	complex number; see Eq. (3.4.1a)
\mathbf{u}	velocity $L t^{-1} (\text{m s}^{-1})$
u'	fluctuating velocity $L t^{-1} (\text{m s}^{-1})$
\bar{u}	time smoothed velocity $L t^{-1} (\text{m s}^{-1})$
u^+	dimensionless velocity; see Eq. (4.2.14)
u^*	friction velocity; see Eq. (4.2.13)

u_m	mean velocity Lt^{-1} ($m s^{-1}$)
u_r	radial velocity Lt^{-1} ($m s^{-1}$)
u_s	sonic velocity; see Eq. (2.6.24)
u_t	same random turbulent velocity Lt^{-1}
u_x, u_y, u_z	x, y , and z components of velocity Lt^{-1} ($m s^{-1}$)
U_b	fluid velocity in the bulk Lt^{-1} ($m s^{-1}$)
U	internal energy QM^{-1} ($J kg^{-1}$)
U_B	rising velocity of bubbles in fluidized beds Lt^{-1} ($m s^{-1}$)
$U_{B,m}$	mean bubble velocity Lt^{-1} ($m s^{-1}$); see Section 8.4
$U_{B,s}$	superficial gas velocity Lt^{-1} ($m s^{-1}$); see Section 8.4
α	angle formed between two planes (rad)
α	constant in Chapter 9
α_{spr}	spreading coefficient ($N m^{-1}$) $= C_p/C_v$
γ	
β	coefficient of thermal expansion T^{-1} ($^{\circ}K^{-1}$); see Chapter 6
β	dimensionless film thickness; see Eq. (4.4.9)
β	growth constant in Chapter 8; see Eq. (8.2.3)
δ_c	collision diameter; see p. 20
δ_j	half-width of the jet; see Eq. (9.1.31)
δ_t	thickness of the turbulent boundary layer
δ_T	thermal boundary layer thickness L (m, mm)
δ_w	boundary layer thickness for a rotating disk L (m, mm); see Eq. (3.5.86)
δ^*	displacement thickness of boundary layer; see Eq. (3.5.43)
δ, δ_u	velocity boundary layer thickness L (m, mm)
Δ	difference operator L^{-1}
ΔP	pressure drop ($N m^{-2}$)
∇	defined in Eq. (3.1.5)
∇^2	nabla operator; see Appendix 1
ϵ	permittivity (F/m); see Chapter 5
ϵ	energy parameter; see p. 20
ϵ_G	void fraction or gas hold-up in Section 8.4
ϵ_{mf}	bed voidage at minimum fluidization
ϵ_v	void fraction in packed beds
$\dot{\epsilon}$	rate of energy dissipation per unit volume ($Nms^{-1} L^{-3}$, Wm^{-3})
η	dimensionless distance; see Eq. (3.5.35)
η	microscale of turbulence L (m); see Eq. (4.2.12)
$\eta = r/z$	similarity variable in Chapter 9
η_m	$= 1/(\sigma_e \mu_m)$ magnetic diffusivity
$\bar{\eta}$	15.18 r/z in Chapter 9

θ	contact angle in Chapter 6 (rad)
θ	dimensionless temperature, Chapter 6, see Eq. (6.3.14)
θ	angle in cylindrical or in spherical coordinates (rad)
κ	Boltzmann's constant; see p. 20
μ	viscosity $ML^{-1}t^{-1}$ ($N\ s\ m^{-2}$)
μ_c	viscosity in the critical state $ML^{-1}\ t^{-1}$ ($N\ s\ m^{-2}$)
μ_{eff}	effective viscosity $ML^{-1}\ t^{-1}$ ($N\ s\ m^{-2}$)
μ_0	viscosity at a reference temperature $ML^{-1}\ t^{-1}$ ($N\ s\ m^{-2}$)
μ_m	magnetic permeability (H/m)
μ_t	turbulent viscosity $ML^{-1}\ t^{-1}$ ($N\ s\ m^{-2}$)
ξ	similarity variable; see Eq. (3.5.82)
ξ	defined in Section 9.1.17; see Chapter 9
Π	pressure energy/unit mass L^2t^2 (m^2s^{-2})
ρ_e	charge unit (C/m)
ρ_g	density of gas ML^{-3} ($kg\ m^{-3}$)
ρ_L	density of the liquid ML^{-3} ($kg\ m^{-3}$)
ρ_p	particle density ML^{-3} ($kg\ m^{-3}$)
ρ_s	gas density at the sonic velocity ML^{-3} ($kg\ m^{-3}$)
σ	surface $ML^{-1}\ t^{-1}$ ($N\ m^{-1}$)
σ_e'	electrical conductivity (ohm m^{-1})
σ_K	constant in the K-w turbulence model ≈ 0.9
σ_w	constant in the K-w model ≈ 0.9
σ_{equiv}	$ML^{-1}\ t^{-1}$ ($N\ m^{-1}$); see Eq. (6.5.12)
τ	dimensionless time
τ_b	bulk stress $ML^{-1}\ t^2$ ($N\ m^{-2}$)
τ_n	normal stress component $ML^{-1}\ t^{-2}$ ($N\ m^{-2}$)
τ_t	shear stress component $ML^{-1}\ t^{-2}$ ($N\ m^{-2}$)
τ_{xy}, τ_{yx}	stress components $ML^{-1}\ t^{-2}$ ($N\ m^{-2}$)
τ	stress $ML^{-1}\ t^{-2}$ ($N\ m^{-2}$)
Φ	$= 2\sigma/(\Delta PR_o)$
ϕ	velocity potential L^2t^{-1} (m^2s^{-1}); see Eqs. (3.4.6–7)
ϕ	angle in radial coordinates (rad)
ϕ_s	particle shape factor; see Eq. (7.2.2)
ϕ_{ij}	interaction parameters defined in Eq. (1.4.7)
$\chi = k/(\rho C_p)$	thermal diffusivity L^2t^{-1} (m^2s^{-1})
X	characteristic resistance $L^{-1}\ t^{-1}$ ($m^{-1}\ s^{-1}$)
ψ	stream function $L^2\ t^{-1}$ ($m^2\ s^{-1}$); see Eqs. (3.3.6–3.3.11)
ω	$= 2\pi f$ rad/s
$\tilde{\omega}$	angular velocity (s^{-1}); see Chapter 3
Ω	vorticity vector (s^{-1}); see Eqs. (3.3.1–3)
Ω_μ	interaction parameter; see Appendix 2

1.1 Introduction

Fluid flow phenomena are inherently associated with the majority of industrial processes that involve the extraction and refining of metals. Figure 1.1.1 shows a sketch of the *basic oxygen furnace* used for steel-making which provides a good illustration of the various fluid flow problems that one could encounter in metals processing systems.

It is seen that a stream of oxygen is being blown through a lance onto a slag–metal emulsion. The oxygen reacts with the bath components as a result of which further slag formation occurs; moreover, the carbon oxidized evolves in the form of CO bubbles. The rapid evolution of the carbon monoxide gas is thought to be responsible for both the formation of the slag–metal emulsion and the effective mixing of the bath.

It is thus seen that the BOF involves a broad range of fluid flow phenomena, including

- (1) the formation of (supersonic) jets,
- (2) the interaction of gas jets with melts, and
- (3) the nucleation and growth of gas bubbles, gas bubble driven circulatory flows, etc.

While we have not yet reached a complete, quantitative understanding of the detailed process mechanism, fluid flow theory, coupled with physical modeling experiments, has been very helpful in process improvement. In this regard, particular advances have been made in lance and in nozzle design.¹

Figure 1.1.2 shows a sketch of the fluid flow field in the mold region of a continuous casting machine; in essence this is a classical fluid flow problem—the interaction of a *confined jet* with its environment which has been

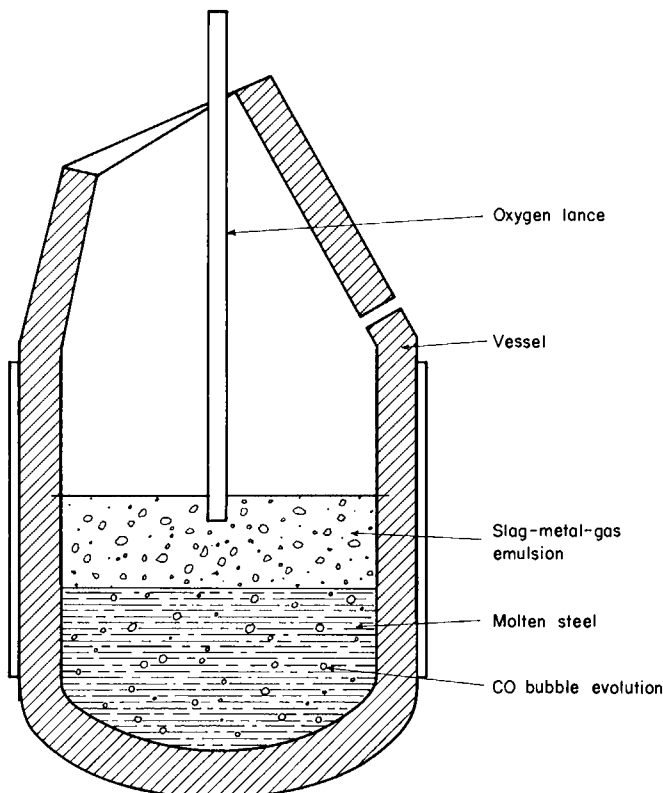


FIG. 1.1.1 Sketch of a basic oxygen furnace.

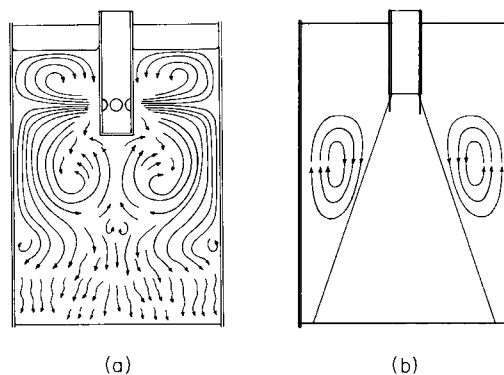


FIG. 1.1.2 Sketch of the velocity fields in the mold region of continuous casting systems²: (a) radial flow nozzles, (b) "straight" nozzles.

extensively studied because of its importance in combustion. The subsequently developed information on the fluid flow field in such confined jet systems, and in particular the role played by the geometry and the inlet nozzle configuration in affecting the flow field, have found a great deal of use in the design of continuous casting systems.²

Figure 1.1.3 shows the schematic layout of a steam jet ejector system used in conjunction with a vacuum degassing operation—for exhausting the gases removed from the melt.³

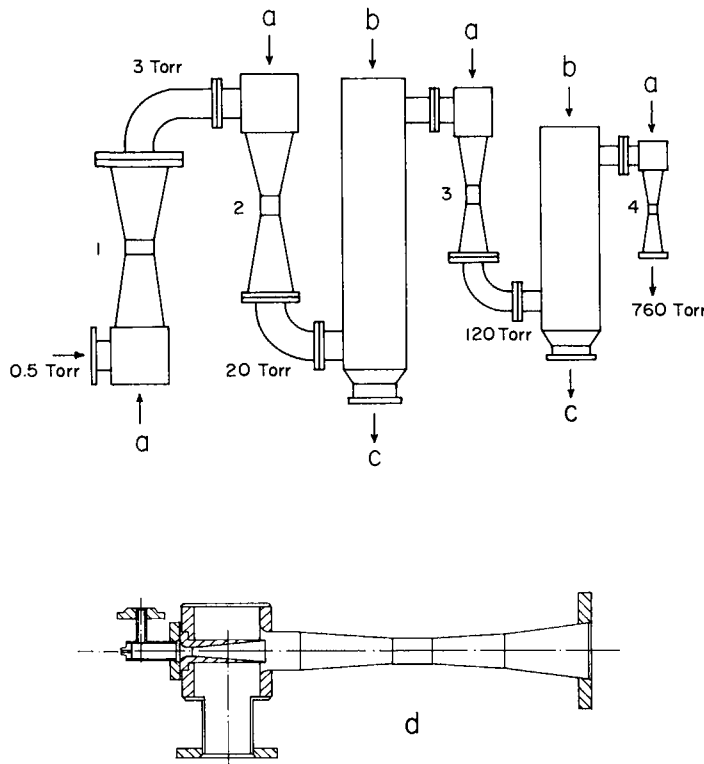


FIG. 1.1.3 Schematic layout of a steam jet ejector, using in-vacuum degassing operations³: a, stream entry; b, cooling water entry; c, cooling water exit; d, the actual injector.

Many other examples may be cited of metals processing operations in which fluid flow phenomena play a major, if not dominant role. Gas–solid systems of importance include the blast furnace, ore sintering, and roasting. Gas–liquid systems include vacuum degassing, copper converting, the gaseous deoxidation of copper, and argon stirring, in addition to the previously mentioned oxygen steel-making processes.

Liquid–solid systems involve scrap melting, fluid flow phenomena in solidification (macrosegregation), together with the melting of deoxidants and other alloying additions in the finishing part of the metals processing sequence.

Finally, liquid–liquid systems include the broad spectrum of slag–metal interactions, such as slag–metal mass transfer in steel-making, the coalescence and the flotation of inclusions, etc.

The problems encountered in these systems may be classified into two broad categories:

(a) Systems where the objective is to develop some overall relationship between some lumped parameters, such as the dependence of a flow rate on the pressure difference imposed, the time required for emptying a ladle, the nozzle size and shape required for producing a given flow rate, and the like. In the majority of cases these calculations are readily performed through the use of the well-understood and well-practiced principles of *overall mass, energy, and momentum balances*. The mathematical tools required for tackling such problems are usually simple, involving the manipulation of algebraic or simple differential equations.

(b) In contrast, in the second group of problems we seek more detailed information about the system, such as the velocity profiles rather than the volumetric flow rates, the patterns of turbulent energy dissipation rather than the total energy loss, and so on. The problems in this second category are much more complex and their tackling may require quite sophisticated mathematical tools, such as the numerical solution of nonlinear partial differential equations. While the actual methods to be used for formulating and solving problems of this type are reasonably well established, their application to metals processing operations is a more novel undertaking but one which is thought to be very worthwhile, in view of the major role played by fluid motion in these systems.

In this first chapter we shall introduce to the reader some of the basic concepts that will be used in the definition of overall mass, energy, and momentum balances in Chapter 2 and the differential type balances in Chapter 3.

1.2 Definition of Some Basic Units and Concepts

1.2.1 Definition of a Fluid

In this text we shall be dealing with the flow behavior of gases and liquids (melts) commonly termed as fluids. Before proceeding further, it is helpful to define what is meant by fluids. The essential property common to all fluids is that a volume of fluid cannot preserve its shape unless it is constrained

by surrounding forces. The fact that fluids assume the shape of the vessel in which they are contained and that this shape would be lost and the fluid would spread out if the container were broken may be regarded as ready, physical illustrations of this contention.

A more rigorous definition of a fluid would be to state that a fluid is a substance that deforms continuously under the action of a shear stress, no matter how small this shear stress may be. A comment should be made, furthermore, that there exists a special class of fluids, the so-called "non-Newtonian fluids," for which this definition would not be applicable. However, virtually all the fluids encountered in metals processing operations are Newtonian so that the above definition should be acceptable at least in the current context. We note that solids do deform to a finite extent if a shear stress is applied, but this deformation does not proceed continuously.

1.2.2 Basic Units and Dimensions

The quantitative representation of fluid flow phenomena requires us to use equations, both algebraic and differential type relationships. All equations describing physical phenomena should be dimensionally homogeneous; in other words, each distinct term in a given equation must have the same dimension, expressed in the same units.

Over the years, through accepted convention, various systems of units have been adopted by different scientific and engineering communities (e.g., the English system, the cgs system, the mks system).

In 1960 a new, rationalized set of units was recommended for international use termed the "Système International d'Unités" or SI units. In this system, which will be used throughout in this text, the unit of mass is the kilogram, the unit of length is the meter, and the unit of time is the second. Table 1.2.1 contains a listing of the units and dimensions of the principal basic and derived quantities used in fluid mechanics, together with comments regarding the nature of these quantities (e.g., scalar, vectorial).

A more detailed discussion of the definition of the more important quantities appearing in Table 1.2.1 will be given subsequently. Since SI units have not been universally accepted at the time of writing, it may be necessary on occasion to convert from other units to the SI system. This may be done with the aid of the conversion factors contained in Table 1.2.2. A more extensive list of conversion factors is available in Perry and Chilton,⁴ and Chiswell and Griff.⁵

1.2.3 Force

The definition of force is derived from Newton's second law of motion, which may be stated as

$$\mathbf{F} = m\mathbf{a} \quad (1.2.1)$$

TABLE 1.2.1

Units and Dimensions of Some Physical Quantities of Importance in Fluid Mechanics

Physical	Dimension	Name of unit	Unit symbol	Scalar	Vector
Basic units					
Mass	[M]	Kilogram	kg	x	
Length	[L]	Meter	m	x	
Time	[t]	Second	s	x	
Temperature	[T]	Degree Kelvin (or Centigrade)	°K (or °C)	x	
Derived units					
Acceleration	[Lt ⁻²]	Meter per second squared	m/s ²	x	
Angular acceleration	[t ⁻²]	Radian per second squared	rad/s ²	x	
Angular velocity	[t ⁻¹]	Radian per second	rad/s	x	
Area	[L ²]	Square meter	m ²	x	
Density	[ML ⁻³]	Kilogram per cubic meter	kg/m ³	x	
Dynamic viscosity	[ML ⁻¹ t ⁻¹]	Newton second per meter squared (or kilogram per meter per second)	N s/m ² (or kg/m s)	x	
Energy, work, quantity of heat	[ML ² t ⁻²]	Joule	J (≡ N m)	x	
Force	[MLt ⁻²]	Newton	N (≡ kg m/s ²)	x	x
Kinematic viscosity	[L ² t ⁻¹]	Meter squared per second	m ² /s	x	
Momentum	[MLt ⁻¹]	Kilogram meter per second (or newton second)	kg m/s (or N s)	x	x
Power	[ML ² t ⁻³]	Watt	W (≡ N m/s)	x	
Pressure, stress ^a	[ML ⁻¹ t ⁻²]	Newton per meter squared	N/m ²	x	x
Specific enthalpy, specific energy	[L ² t ⁻²]	Joule per kilogram (or meter squared per second squared)	J/kg (or m ² /s ²)	x	
Specific heat	[L ² t ⁻² T ⁻¹]	Joule per kilogram per degree Kelvin	J/kg °K	x	
Surface tension	[Mt ⁻²]	Newton per meter	N/m	x	
Velocity	[Lt ⁻¹]	Meter per second	m/s		x
Volume	[L ³]	Cubic meter	m ³	x	

^a Pressure is a scalar and stress is a tensor.

TABLE 1.2.2
Conversion Factors^a

Multiply	By	To obtain
atm	$(1.0133)(10^5)$	N/m ²
atm	1.0333	kg _f /cm ²
Btu	1055	J
Btu/lb °F	4187	J/kg °C
Btu/lb	2326	J/kg
cP	10^{-3}	kg/m s
ft ³	0.02832	m ³
dyn	10^{-5}	N
ft	0.3048	m
ft/s	1.097	km/hr
ft lb _f	1.356	J
gal (imp.)	1.2	gal (U.S.)
gal (U.S.)	$(3.785)(10^{-3})$	m ³
hp	746	W
hp hr	$(2.69)(10^6)$	J
kcal	4187	J
kg _f	9.81	N
kg _f /cm ²	10	m of water
kg _f /cm ²	735.6	mm of Hg
kg _f /cm ²	$(9.81)(10^4)$	N/m ²
km/hr	0.278	m/s
lb	0.4536	kg
lb _f	4.45	N
lb _f /in ²	6895	N/m ²
lb _f s/ft ²	47.9	kg/m s
liter	10^{-3}	m ³
mile	1609	m
P ^b	0.1	kg/m s
ft ²	0.093	m ²

^a R is the universal gas constant

$$\begin{aligned}
 &= 8317 \text{ J/kg mole } ^\circ\text{K} \\
 &= 1.986 \text{ kcal/kg mole } ^\circ\text{K} \\
 &= 1545 \text{ ft lb}_f/\text{lb mole } ^\circ\text{R} \\
 &= (8.206)(10^{-2}) \text{ atm m}^3/\text{kg mole } ^\circ\text{K} \\
 &= 62.3 \text{ mm Hg m}^3/\text{kg mole } ^\circ\text{K}
 \end{aligned}$$

The characteristic gas constant is the universal gas constant divided by the molecular weight of the gas. The characteristic gas constant for air is 287 J/kg °K.

^b Poise not to be confused with the unit *Poiseuille* which is 1 kg/ms.

where \mathbf{F} is force, m mass, and \mathbf{a} acceleration, or

$$\mathbf{F} = \frac{d(m\mathbf{u})}{dt}$$

It is seen from Eq. (1.2.1) that force is a vectorial quantity designated by the boldface notation in that it has both a magnitude and a direction. In the SI system the unit of force is the *newton* (N). The newton is the force which produces an acceleration of 1 m/s^2 if acting on a mass of 1 kg. We note from Table 1.2.2 that

$$1 \text{ N} = 4.45 \text{ lb}_f = 9.81 \text{ kg}_f$$

Let us now examine the forces that may act on fluids. If we consider an infinitesimal fluid element, the forces acting on such system may be divided into two categories, namely *body forces* and *surface forces*: Body forces are caused by the gravitational, electromagnetic fields and act on the bulk of the fluid element; these are usually represented as “force per unit mass of the element.” In contrast, surface forces represent the action of the surrounding fluid on the fluid element under consideration. These forces are usually expressed as force per unit area of the element.

1.2.4 Stress

Let us consider a fluid element of arbitrary shape, such as sketched in Fig. 1.2.1. Let us designate a small area ΔA on the surface of this element and suppose that the (surface) force exerted by the surrounding fluid on this small area ΔA is represented by ΔF . This force ΔF is a vectorial quantity which may be resolved into two components, ΔF_n which is normal to the area ΔA and ΔF_t , which forms a tangent to the infinitesimal area ΔA .

The quantities ΔF_n and ΔF_t are called the *normal force* and the *shear force*, respectively.

On noting that stress is defined as force per unit area, we may now consider two types of stresses acting on the fluid element:

$$\text{normal stresses } \tau_n \equiv (\Delta F_n / \Delta A)_{\Delta A \rightarrow 0} \quad (1.2.2)$$

$$\text{shear stresses } \tau_t \equiv (\Delta F_t / \Delta A)_{\Delta A \rightarrow 0} \quad (1.2.3)$$

More specifically the stress is identified by *both* the direction of the force and by the orientation of the area upon which this force acts.

Figure 1.2.2 shows a fluid element in the shape of a cube; also shown on this graph are the nine possible stress components that may act on the surface of this fluid element. The double subscript notation follows the convention that the first subscript designates the direction of the normal to the plane on which the stress acts, while the second subscript denotes the direction of the force which produces the stress.

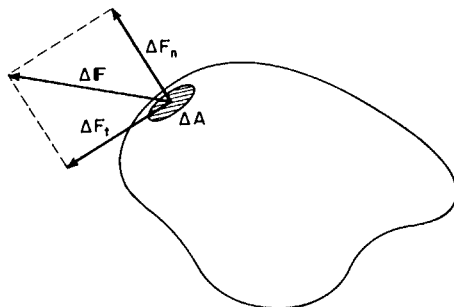


FIG. 1.2.1 The forces acting on an infinitesimal area on the surface of a fluid element.

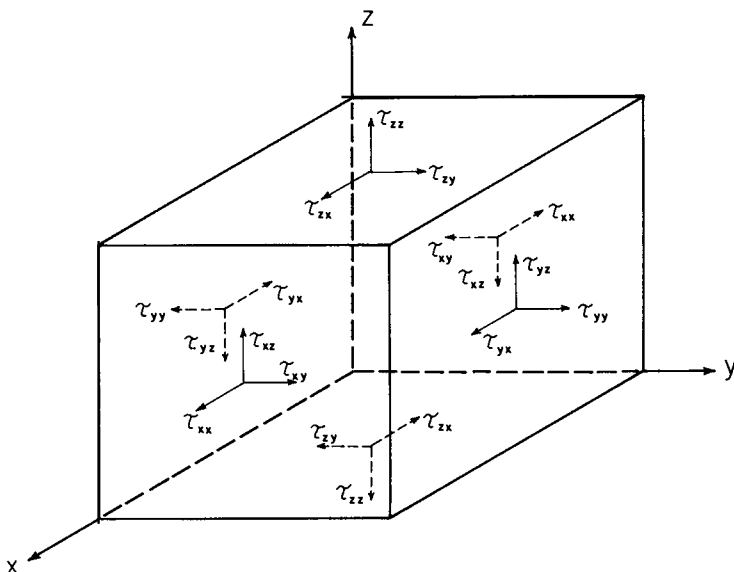


FIG. 1.2.2 Stresses acting on a fluid element.

It is readily seen that the quantities τ_{xx} , τ_{yy} , τ_{zz} denote normal stresses, while τ_{xy} , τ_{xz} , τ_{yx} , τ_{yz} , τ_{zx} , τ_{zy} designate shear stresses.

It is convenient to consider the nine stress components illustrated in Fig. 1.2.2 as the components of the stress tensor[†] τ defined as

$$\tau = \begin{pmatrix} \tau_{xx} & \tau_{xy} & \tau_{xz} \\ \tau_{yx} & \tau_{yy} & \tau_{yz} \\ \tau_{zx} & \tau_{zy} & \tau_{zz} \end{pmatrix} \quad (1.2.4)$$

[†] A brief discussion of vector and tensor notation is given in Appendix 1. A useful discourse on the use of vectors and tensors may be found in the text by Aris⁶ and by Bird *et al.*¹⁹

Here we shall state, without proof, that the stress tensor is symmetric; i.e.,

$$\tau_{xy} = \tau_{yx}, \quad \tau_{yz} = \tau_{zy}, \quad \tau_{zx} = \tau_{xz} \quad (1.2.5)$$

1.2.5 The Pressure Gradient

A particular case of surface forces acting on a fluid element is due to a pressure differential in the fluid. It is known from thermodynamics that pressure p has the same dimensions as stress, but unlike stress, which is a tensorial quantity, pressure is a scalar, which acts uniformly in all directions.

In some texts the bulk stress $\tilde{\tau}_b$ is defined as

$$\tilde{\tau}_b = \frac{1}{3}[\tau_{xx} + \tau_{yy} + \tau_{zz}] - p \quad (1.2.6)$$

where p is the thermodynamic pressure. It may be worthwhile to note that in a physical sense Eq. (1.2.6) implies that, when the fluid is at rest or when the *velocity is the same everywhere*, the bulk stress is numerically equal to the pressure.

Within this convention, the normal stress has to be visualized as being made up of two components, a contribution from pressure and a contribution from the viscous stresses associated with the linear deformation of the fluid element in the direction of the normal stress.

A problem of this type will be discussed in Chapter 8, dealing with expanding gas bubbles.

When shear stresses are absent, we can readily calculate the net force on a fluid element due to the pressure field. Let us consider a cubic space element sketched in Fig. 1.2.3. The force, due to pressure acting on the area $(\Delta y \Delta z)$ at x , is $p|_x (\Delta y \Delta z)$, while the force acting on the parallel surface at $(x + \Delta x)$ is given by

$$p|_{x+\Delta x} (\Delta y \Delta z)$$

so that the net force acting in the x direction, on unit volume of the fluid,

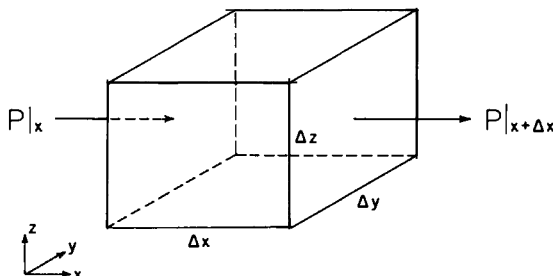


FIG. 1.2.3 The force due to pressure acting on a fluid element.

due to the difference in pressure between points x and $x + \Delta x$, is given by

$$F_{x,p} = \frac{(\Delta y \Delta z)p|_x - \Delta y \Delta z p|_{x+\Delta x}}{\Delta x \Delta y \Delta z} \quad (1.2.7)$$

On setting $\Delta x, \Delta y, \Delta z \rightarrow 0$ and recalling definition of the first derivative, Eq. (1.2.7) is written as

$$F_{x,p} = -\frac{\partial p}{\partial x} \quad (1.2.8)$$

By generalizing Eq. (1.2.8) in three dimensions, we have

$$\mathbf{F}_p = -\nabla p \quad \text{or} \quad -\text{grad } p = -\left(\frac{\partial p}{\partial x} + \frac{\partial p}{\partial y} + \frac{\partial p}{\partial z}\right) \quad (1.2.9)$$

Note that by forming the gradient (i.e., using the ∇ operator) of the scalar pressure field we obtained the force field, which is a *vector*.

Readers who may have difficulty with this concept should read the summary of vector and tensor operations given in Appendix 1. From this it will be apparent that the operation indicated on the right-hand side of Eq. (1.2.9) is the multiplication of a vector with a scalar, the product of which is a vector.

Equation (1.2.9) will be used subsequently in the general development of the equation of motion.

1.3 The Newtonian Definition of Viscosity

In order to illustrate the nature of viscosity let us consider the behavior of a thin fluid layer contained between two long and wide parallel plates, as sketched in Fig. 1.3.1. Let us assume that initially both the plates and the fluid are stationary but then at some fixed time the upper plate is made to move with a velocity U_x in the x direction, and this velocity is maintained at a constant value. As a result the fluid is also brought into motion and

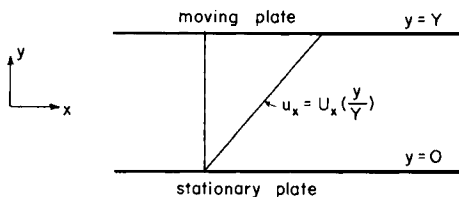


FIG. 1.3.1 Sketch of the fluid flow field developed between one stationary and one moving plate, for steady-state conditions.

experience has shown that, after a long enough time so that steady state has been attained and when the plates are sufficiently close, the velocity will vary linearly with distance between the moving and the stationary plate.

It has been found, moreover, that F_x , the force required to maintain the movement of the upper plate, is described by the following relationship:

$$F_x/A = \mu U_x/Y \quad (1.3.1)$$

where A is the surface area of the plate, Y the distance separating the two plates, and μ a constant of proportionality termed the viscosity.

If we note that the quantity F_x/A is in essence a shear stress and make use of the fact that the velocity profile is linear, Eq. (1.3.1) may be written in the following differential form:

$$\tau_{yx} = -\mu \frac{du_x}{dy} \quad (1.3.2)$$

Equation (1.3.2) expresses the experimental observation that for parallel flow the shear stress between adjacent fluid layers is proportional to the negative value of the velocity gradient. The constant of proportionality μ is termed the viscosity. *This is Newton's law of viscosity.*

All gases and most simple liquids, molten metals, and slags obey Eq. (1.3.2); these are termed Newtonian fluids. Our treatment in this text will be confined to Newtonian fluids. Certain polymers, slurries, and pastes do not obey Eq. (1.3.2); these fluids are termed non-Newtonian and their behavior is described in the specialist literature.⁷⁻⁹

It is noted that in some applications it is more convenient to provide an alternative interpretation for Eq. (1.3.2) by regarding τ_{yx} as *flux of x momentum in the y direction*, due to viscous forces.

The reader will recall from elementary physics that momentum is mass times velocity; as shown in Table 1.2.1, the units of momentum are (MLt^{-1}) and, since the velocity is a vector, momentum is a vectorial quantity also.

Since the term "flux" designates rate of flow (of a given quantity) per unit area, the reader will readily see that the terms *shear stress* and *momentum per unit area and unit time* are equivalent.

We shall see in Chapter 3, in the establishment of differential momentum balances, that momentum may be introduced into a volume element both by the inflowing fluid and by the existence of a shear stress at the surface of the element. Thus the equivalence of shear stress and momentum flux will become apparent in the formulation of differential momentum balances.

Let us now turn to the units of viscosity. Upon considering the units of the terms appearing in Eq. (1.3.2),

$$\tau_{yx} \quad [\text{N/m}^2], \quad u_x \quad [\text{m/s}], \quad y \quad [\text{m}]$$

The units of viscosity in the SI system are Ns/m^2 or kg/s m . We note that in

many, especially older, handbooks the viscosity of fluids is given in other units, namely the poise, or the centipoise. As was shown in Table 1.2.2,

$$1 \text{ P} = 0.1 \text{ N s/m}^2 \quad \text{and} \quad 1 \text{ cP} = 10^{-3} \text{ N s/m}^2$$

Let us illustrate the concepts developed in this section by working a simple numerical example:

Example 1.3.1 Cooling water is passed through a section of a furnace door which may be represented as consisting of two large parallel plates separated by a distance of 0.01 m, as sketched in Fig. 1.3.2a. Let the velocity profile be given by the following expression:

$$u_x [\text{m/s}] = 100[0.01y - y^2], \quad 0 \leq y \leq 0.01 \text{ m} \quad (\text{i})$$

which is also sketched in Fig. 1.3.2b. If the viscosity of water is 10^{-3} N s/m^2 calculate the shear stress profile.

SOLUTION Using Eq. (1.3.2), upon differentiating Eq. (i) we have

$$\tau_{yx}(y) = 10^{-3} \times 100[0.01 - 2y] = 0.1(0.01 - 2y) \quad (\text{ii})$$

The resultant profile is sketched in Fig. 1.3.2c, where it is seen that for this case the shear stress profile is linear and that the shear stress is zero at the central plane ($y = 0.005 \text{ m}$), where the velocity is at its maximum. The actual shear stress at the solid surface could also be calculated with the aid of Eq. (ii) by substituting $y = 0$ or $y = 0.01$.

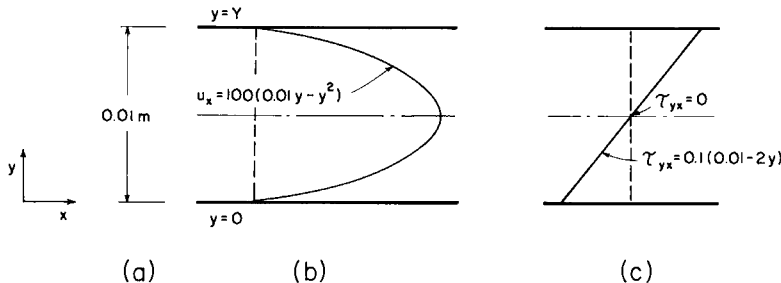


FIG. 1.3.2 Illustration for Example 1.3.1.

THE GENERALIZATION OF NEWTON'S LAW OF VISCOSITY

The viscosity defined by Eq. (1.3.2) is rather restrictive because only a one-dimensional, parallel flow field was considered. The definition of the viscosity may be generalized to three-dimensional flows through Stokes' hypothesis. A good discussion of this is available in the text by Schlichting.¹⁰

The relationship between the normal and the shear stresses and the velocity gradients in the cartesian coordinate system is given in Table 1.3.1.

TABLE 1.3.1

The Components of the Stress Tensor for Newtonian Fluids in Cartesian Coordinates^a

$$\tau_{xx} = -\mu[2\partial u_x/\partial x - \frac{2}{3}\nabla \cdot \mathbf{u}] \quad (1)$$

$$\tau_{yy} = -\mu[2\partial u_y/\partial y - \frac{2}{3}\nabla \cdot \mathbf{u}] \quad (2)$$

$$\tau_{zz} = -\mu[2\partial u_z/\partial z - \frac{2}{3}\nabla \cdot \mathbf{u}] \quad (3)$$

$$\tau_{xy} = \tau_{yx} = -\mu[\partial u_x/\partial y + \partial u_y/\partial x] \quad (4)$$

$$\tau_{yz} = \tau_{zy} = -\mu[\partial u_y/\partial z + \partial u_z/\partial y] \quad (5)$$

$$\tau_{zx} = \tau_{xz} = -\mu[\partial u_z/\partial x + \partial u_x/\partial z] \quad (6)$$

$$^a \nabla \cdot \mathbf{u} = \partial u_x/\partial x + \partial u_y/\partial y + \partial u_z/\partial z.$$

TABLE 1.3.2

Components of the Stress Tensor for Newtonian Fluids in Cylindrical Coordinates $(r, \theta, z)^a$

$$\tau_{rr} = -\mu[2\partial u_r/\partial r - \frac{2}{3}(\nabla \cdot \mathbf{u})] \quad (1)$$

$$\tau_{\theta\theta} = -\mu\left[2\left(\frac{1}{r}\frac{\partial u_\theta}{\partial \theta} + \frac{u_r}{r}\right) - \frac{2}{3}(\nabla \cdot \mathbf{u})\right] \quad (2)$$

$$\tau_{zz} = -\mu[2\partial u_z/\partial z - \frac{2}{3}(\nabla \cdot \mathbf{u})] \quad (3)$$

$$\tau_{r\theta} = \tau_{\theta r} = -\mu\left[r\frac{\partial}{\partial r}\left(\frac{u_\theta}{r}\right) + \frac{1}{r}\frac{\partial u_r}{\partial \theta}\right] \quad (4)$$

$$\tau_{\theta z} = \tau_{z\theta} = -\mu[\partial u_\theta/\partial z + (1/r)\partial u_z/\partial \theta] \quad (5)$$

$$\tau_{rz} = \tau_{zr} = -\mu[\partial u_z/\partial r + \partial u_r/\partial z] \quad (6)$$

$$^a (\nabla \cdot \mathbf{u}) = (1/r)\partial/\partial r(ru_r) + (1/r)\partial u_\theta/\partial \theta + \partial u_z/\partial z.$$

The corresponding expressions for cylindrical and spherical coordinates are given in Tables 1.3.2 and 1.3.3.

It is to be noted that in the designation of the subscripts for the components of the stress tensor we follow the same convention as done before; thus τ_{rz} in cylindrical coordinates expresses the fact that the force producing the stress acts in the z direction, while the surface on which the stress acts is cylindrical in shape and perpendicular to the radial coordinate r , as sketched in Fig. 1.3.3.

1.4 Factors That Affect the Viscosity

The viscosity of Newtonian fluids is affected by the temperature, the pressure, and in case of mixtures by the composition.

TABLE 1.3.3

Components of the Stress Tensor for
Newtonian Fluids in Spherical Coordinates $(r, \theta, \phi)^a$

$$\tau_{rr} = -\mu[2\frac{\partial u_r}{\partial r} - \frac{2}{3}(\nabla \cdot \mathbf{u})] \quad (1)$$

$$\tau_{\theta\theta} = -\mu\left[2\left(\frac{1}{r}\frac{\partial u_\theta}{\partial \theta} + \frac{u_r}{r}\right) - \frac{2}{3}(\nabla \cdot \mathbf{u})\right] \quad (2)$$

$$\tau_{\phi\phi} = -\mu\left[2\left(\frac{1}{r \sin \theta}\frac{\partial u_\phi}{\partial \phi} + \frac{u_r}{r} + \frac{u_\theta \cot \theta}{r}\right) - \frac{2}{3}(\nabla \cdot \mathbf{u})\right] \quad (3)$$

$$\tau_{r\theta} = \tau_{\theta r} = -\mu\left[r\frac{\partial}{\partial r}\left(\frac{u_\theta}{r}\right) + \frac{1}{r}\frac{\partial u_r}{\partial \theta}\right] \quad (4)$$

$$\tau_{\theta\phi} = \tau_{\phi\theta} = -\mu\left[\frac{\sin \theta}{r}\frac{\partial}{\partial \theta}\left(\frac{u_\phi}{\sin \theta}\right) + \frac{1}{r \sin \theta}\frac{\partial u_\theta}{\partial \phi}\right] \quad (5)$$

$$\tau_{\phi r} = \tau_{r\phi} = -\mu\left[\frac{1}{r \sin \theta}\frac{\partial u_r}{\partial \phi} + r\frac{\partial}{\partial r}\left(\frac{u_\phi}{r}\right)\right] \quad (6)$$

$$^a (\nabla \cdot \mathbf{u}) = \frac{1}{r^2}\frac{\partial}{\partial r}(r^2 u_r) + \frac{1}{r \sin \theta}\frac{\partial}{\partial \theta}(u_\theta \sin \theta) + \frac{1}{r \sin \theta}\frac{\partial u_\phi}{\partial \phi}.$$

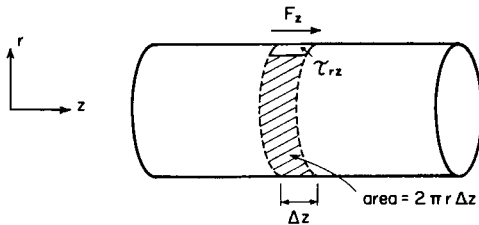


FIG. 1.3.3 Sketch of the shear stress component in an axially symmetrical cylindrical coordinate system. Shear force acts in the z direction, perpendicular to the area of the element, which is $2\pi r \Delta z$.

Table 1.4.1 gives typical values of the viscosity of gases and melts in order to provide the reader an indication of the actual numerical values involved.

The effect of temperature and pressure on the viscosity of fluids is illustrated in Fig. 1.4.1, where the reduced viscosity is plotted against the reduced temperature with the reduced pressure as a parameter. In this context the reduced viscosity, temperature, and pressure are defined as the ratio of the numerical value of these quantities to those at the critical point.

It is seen in Fig. 1.4.1 that the viscosity of gases increases with temperature while the viscosity of liquids decreases with increasing temperature.

TABLE 1.4.1
Viscosity of Fluids at Various Temperatures^{16,17,20}

Fluid	Temperature (°C)	Viscosity (cP)	N s/m ²
Hydrogen	0	0.0084	8.4×10^{-6}
	20.7	0.0088	8.8
	229	0.0126	12.6
	490	0.0167	16.7
	825	0.0214	21.4
Air	0	0.0171	17.1×10^{-6}
	18	0.0183	18.3
	229	0.0264	26.4
	409	0.0341	34.1
	810	0.0442	44.2
	1134	0.0521	52.2
Water	0	1.79	17.9×10^{-3}
	20	1.01	10.1
	60	0.469	4.69
	100	0.284	2.84
Iron	1550	6.7	6.7×10^{-3}
	1600	6.1	6.1
	1700	5.6	5.6
	1800	5.3	5.3
	1850	5.2	5.2

It is noted that the viscosity of gas is approximately proportional to the 0.6–0.8th power of the absolute temperature.

The viscosity of liquids (melts) is a much stronger function of temperature and this relationship may be expressed as

$$\mu = \mu_0 e^{-E_\mu/RT} \quad (1.4.1)$$

Here μ_0 is the viscosity of some reference temperature and the quantity E_μ is the activation energy for viscous flow. Typical values of E_μ are given in Table 1.4.2.^{11,12} Figure 1.4.2 illustrates the temperature dependence of viscosity for some common metals.

At pressures normally encountered in metals processing operations the viscosity of liquids is independent of pressure. Moreover, the viscosity of gases reaches a (pressure-independent) limit of absolute pressures below about 10 atm. It follows that for most systems of metallurgical interest the pressure dependence of viscosity is not significant.

The effect of composition on the viscosity of gases, molten metals, and slags is illustrated in Figs. 1.4.3, 1.4.4,¹³ and 1.4.5, respectively.

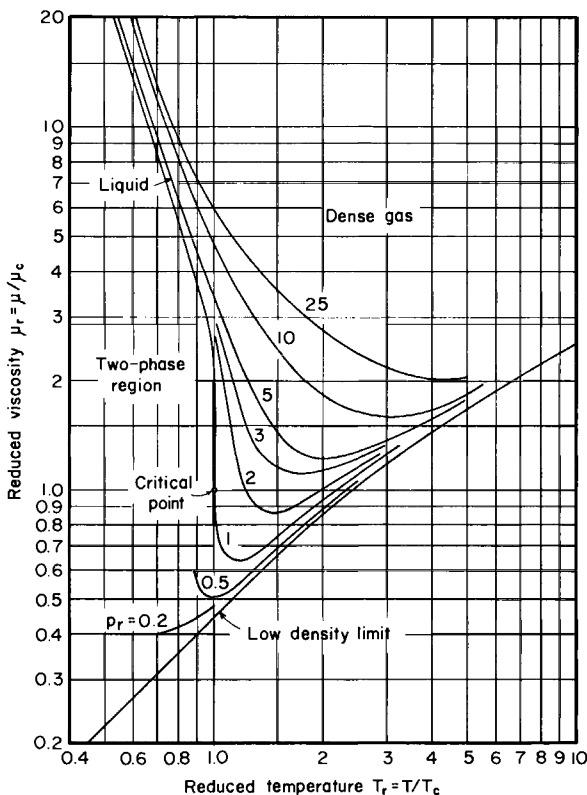


FIG. 1.4.1 The reduced viscosity as a function of the reduced temperature, with the reduced pressure as a parameter: μ_c , T_c , and p_c denote the values of the viscosity, temperature, and pressure at the critical conditions.²⁰

TABLE 1.4.2

Typical Values of E_μ for Various Metals^{11,12}

Metal	E_μ kcal/mole	$[E_\mu]$ J/kg mole
Hg	1.25	5.24×10^6
Na	2.44	10.22×10^6
Sn	2.91	12.19×10^6
Pb	3.92	16.42×10^6
Ag	7.5	31.42×10^6
Fe	17.0	71.23×10^6

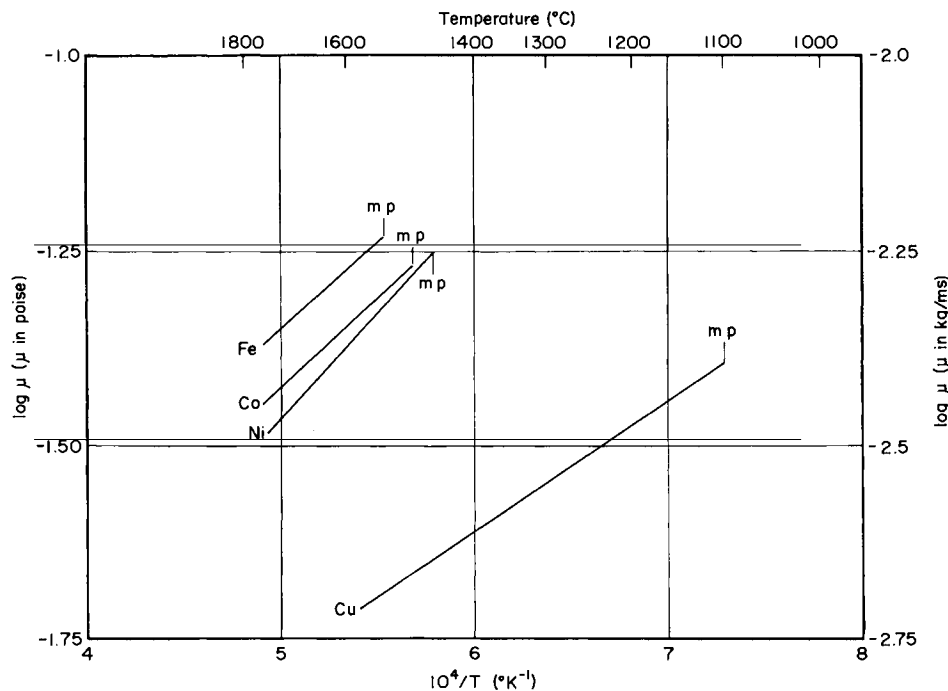


FIG. 1.4.2 The viscosities of some liquid metals as a function of temperature.¹²

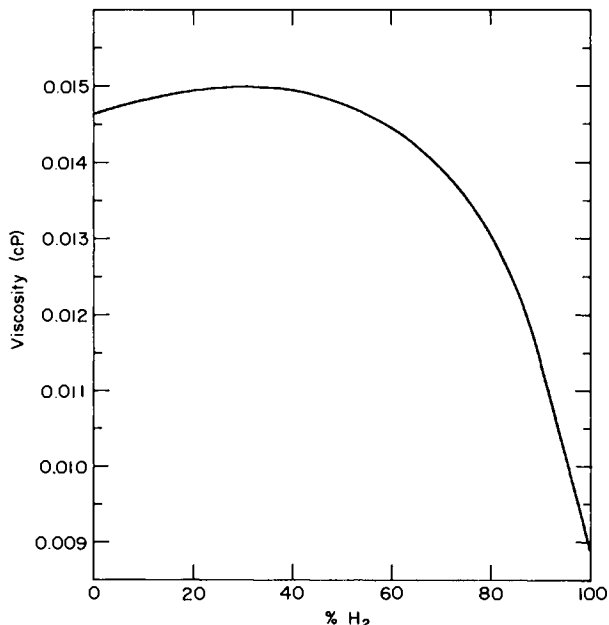


FIG. 1.4.3 The viscosity of hydrogen–carbon-dioxide mixtures at 15°C as a function of composition.⁴

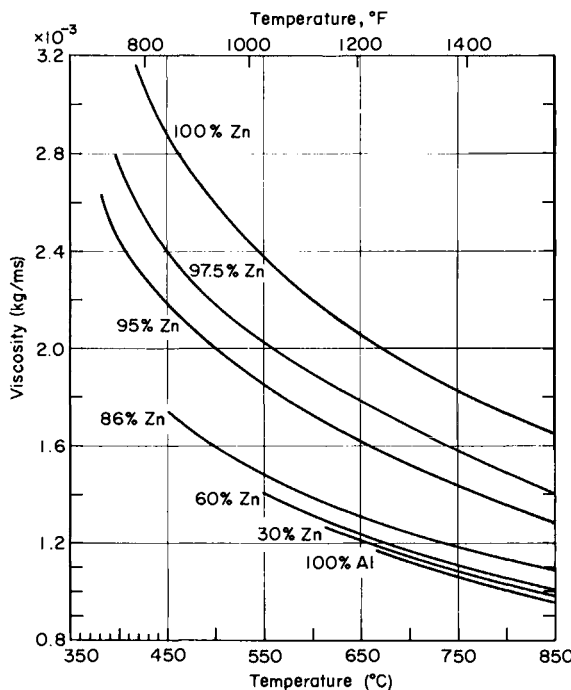


FIG. 1.4.4 The viscosity of molten zinc–aluminum solutions as a function of temperature and composition.¹³

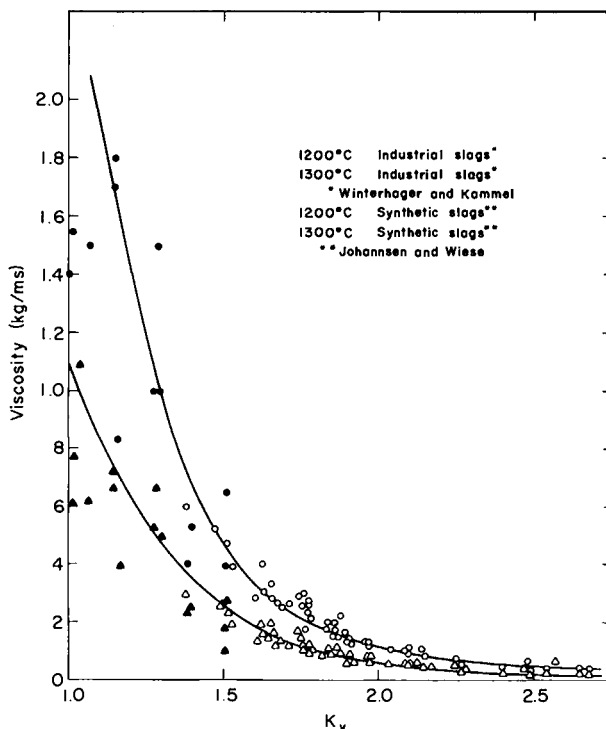


FIG. 1.4.5 The effect of composition on the viscosity of copper slags, cited from Szeckely and Themelis¹ after Toguri; Themelis, and Jennings.²¹ Here K_v is defined as $\text{wt\%FeO} + \text{Fe}_3\text{O}_4 + \text{CaO} + \text{MgO}$ divided by $\text{wt\%}(SiO_2 + Al_2O_3)$.

It is seen in Figs. 1.4.3–1.4.5 that the viscosity of gases, molten metals, and slags may be markedly dependent on composition; moreover, this composition dependence does not usually obey simple linear addition rules. In certain slag systems the viscosity of mixtures may be considerably smaller than that of any of the components from which the mixture is constituted. This fact is used to advantage in iron-making, steel-making, and in other metals processing operations where the slag composition is so adjusted to provide a desirable, low viscosity. The resultant fluid slags allow more ready slag–metal contacting, and also the easier discharge of the molten slag.

PREDICTION OF VISCOSITY

If numerical values of the viscosity are required it is preferable to use the results of experimental measurements. A good source of experimentally determined viscosities can be found in Szekely *et al.*^{1,12,14–18}

If measurements are not available, the viscosity of gases may be predicted, reasonably accurately, using the Chapman–Enskog theory and the Lennard–Jones potential, which leads to the following dimensional formula:

$$\mu = 2.67 \times 10^{-5} (MT)^{1/2} / \delta_c^2 \Omega_\mu \quad [\text{kg/ms}] \quad (1.4.2)$$

where M is the molecular weight of the species in kilograms, T the absolute temperature in degrees Kelvin, δ_c the collision diameter in Å = 10^{-10} m, Ω_μ a function of the dimensionless group $\kappa T/\epsilon$ given in Appendix 2, κ Boltzmann's constant, $R/N_0 = 1.38 \times 10^{-19}$ kg m² s⁻² molecule⁻¹ °K⁻¹, and ϵ is the energy parameter, kg m² s⁻² molecule⁻¹.

Numerical values of δ_c and ϵ are available in the literature for most common gases¹⁹; otherwise the following empirical formulas may be used for estimating these quantities:

$$\epsilon/\kappa = 1.15 T_b \quad (1.4.3)$$

$$\epsilon/\kappa = 1.92 T_m \quad (1.4.4)$$

where T_b and T_m are the boiling point and the melting point in absolute units, respectively, and

$$\delta_c = 1.22 \tilde{V}_m^{1/3} \quad (1.4.5)$$

where V_m is the molar volume of the melt at the freezing point in cubic centimeters per gram mole and δ_c is in angstrom units.

These methods are less reliable for estimating the viscosity of gas mixtures, especially if they contain polar components. However, the following empirical formula has been recommended for mixtures:

$$\mu_{\text{mix}} = \sum_{i=1}^n \left(x_i \mu_i \middle/ \sum_{j=1}^n x_j \phi_{ij} \right) \quad (1.4.6)$$

with

$$\phi_{ij} = \frac{1}{\sqrt{8}} \left(1 + \frac{M_i}{M_j} \right)^{-1/2} \left[1 + \left(\frac{\mu_i}{\mu_j} \right)^{1/2} \left(\frac{M_j}{M_i} \right)^{1/4} \right]^2 \quad (1.4.7)$$

where x_i and x_j are the molecular weights of species i and j and μ_i and μ_j are the viscosities of species i and j . The strongly nonlinear composition dependence of viscosity is readily seen from Eqs. (1.4.6) and (1.4.7). The use of these formulas is illustrated by the following example.

Example 1.4.1 Estimate the viscosity of a gas mixture containing 20% zinc vapor, 50% nitrogen, and 20% hydrogen, at 1000°C and 1 atm pressure.

SOLUTION From Eq. 1.4.2,

$$\begin{aligned} \mu_{Zn} &= 2.67 \times 10^{-5} (MT)^{1/2} / \delta^2 \Omega_\mu \\ &= 2.67 \times 10^{-5} \frac{(65.37 \times 1273)^{1/2}}{2.51^2 \times 1.638} \\ &= 7.45 \times 10^{-5} \text{ kg/m s} \end{aligned}$$

At 1273°K²⁰

$$\begin{aligned} N &= 500 \times 10^{-6} \text{ P} = 5 \times 10^{-5} \text{ kg/m s} \\ CO &= 480 \times 10^{-6} \text{ P} = 4.8 \times 10^{-5} \text{ kg/m s} \end{aligned}$$

Species	Mole fraction	M	μ_i (P)	$x_i(M_i)^{1/2}$	$x_i(M_i)^{1/2} \mu_i$
Zn	0.2	65.37	745×10^{-6}	1.62	1210×10^{-6}
N ₂	0.5	28.02	500×10^{-6}	2.65	1325×10^{-6}
CO	0.3	28.00	480×10^{-6}	1.59	762×10^{-6}
				5.86	<u>3297×10^{-6}</u>

Using Eq. (1.4.7),

$$\mu_{\text{mix}} = \frac{3297 \times 10^{-6}}{5.86} = 561 \times 10^{-6} \text{ P} = 5.6 \times 10^{-5} \text{ kg/m s}$$

Our understanding of the liquid state is much less complete than that of gases; for this reason the methods available for predicting the viscosities of liquids are usually not very reliable. An interesting discussion on the prediction of the viscosities of liquid metals is available in Ref. [10].

No satisfactory techniques have been developed for predicting the viscosities of the complex slags encountered in metals processing operations. However, some limited extrapolation of existing measurements is possible

by considering the nature and the equivalence of certain basic or acid components.^{1,2}

References

1. J. Szekely and N. J. Themelis, "Rate Phenomena in Process Metallurgy," Wiley, New York, 1971.
2. J. Szekely and R. T. Yadoya, *Metall. Trans.* **3**, 2673 (1972).
3. O. Winkler and T. Saito, eds., *Proc. Int. Conf. Vac. Metall. 4th, 1973*, p. 279 (1974).
4. R. H. Perry and C. H. Chilton, "Chemical Engineering Handbook, 5th ed., McGraw-Hill, New York, 1973.
5. B. Chiswell and E. C. Griff, "S.I. Units," Wiley, New York, 1971.
6. R. Aris, "Vectors, Tensors and the Differential Equations of Fluid Mechanics," Prentice-Hall, Englewood Cliff, New Jersey.
7. R. S. Brodkey, "The Phenomena of Fluid Motions," Chapter 15. Addison-Wesley, Reading, Massachusetts, 1967.
8. R. B. Bird, "Dynamics of Polymeric Liquids," Vol. I. Wiley, New York, 1977.
9. R. B. Bird, "Dynamics of Polymeric Liquids," Vol. II. Wiley, New York, 1977.
10. H. Schlichting, "Boundary Layer Theory," 6th ed., p. 13, McGraw Hill, New York, 1968.
11. N. H. Nachtrieb, *Adv. Phys.* **16**, 309 (1967).
12. F. D. Richardson, "Physical Chemistry of Melts in Metallurgy, Vol. I. Academic Press, New York, 1975.
13. "International Critical Tables," Vol. 5. McGraw-Hill, New York, 1929.
14. W. R. D. Jones and W. L. Bartlett, *J. Inst. Met.* **81**, 145 (1952-1953).
15. J. F. Elliott, M. Gleiser, and V. Ramakrishna, "Thermochemistry for Steelmaking," Vols. I and II. Addison-Wesley, Reading, Massachusetts, 1960 and 1963.
16. S. Levy and J. W. Mausteller, eds., "Liquid Metals Handbook," TID 5277. At Energy Comm., 1955.
17. E. McGannon, ed., "The Making, Shaping and Treating of Steel," 8th ed. U.S. Steel Corp. Pittsburgh, Pennsylvania, 1972.
18. R. D. Pehlke, W. F. Porter, R. F. Urban, and J. M. Gaines, eds., "BOF Steelmaking." The Iron and Steel Society of AIME, New York, 1977.
19. R. B. Bird, W. E. Stewart, and E. N. Lightfoot, "Transport Phenomena." Wiley, New York, 1960.
20. R. H. Perry, "Chemical Engineering Handbook," 4th ed., pp. 3-197. McGraw-Hill, New York, 1963.
21. J. M. Toguri, N. J. Themelis, and P. H. Jennings, *Can. Metall. Q.* **3**, 197 (1964).

2.1 Introduction

In the previous chapter we introduced the reader to some of the basic concepts that are used for characterizing moving fluids, such as the viscosity, the stress tensor, and the relationship between viscosity and the velocity gradient. These concepts were developed through the use of infinitesimal fluid elements which will be called *control volumes* in our subsequent discussion. The logical continuation of these ideas will be the development of the differential equations termed the *equation of motion* or the *Navier–Stokes equations*, which will be discussed in Chapter 3.

In this chapter we shall digress briefly and consider a group of important problems which may be tackled in a different way through the establishment of overall balances. In using this technique the system as a whole (e.g., a ladle, a nozzle, a duct) is taken as a control volume and then we proceed to establish a balance on some property of the system.

In general, overall balances yield simple algebraic equations, or, in case of unsteady-state systems, simple first-order differential equations. The mathematical simplicity afforded by this treatment makes it attractive for a broad range of problems where the objective is to obtain some overall relationship between variables, such as the time required to empty a ladle, the pressure drop required to attain a given rate of flow, or the sizing of orifices, nozzles, and the like. It has to be stressed, however, that this treatment is inappropriate if we wish to obtain detailed information about the actual velocity field, flow patterns, or the pressure distribution. The discussion of these problems has to be deferred until the material contained in Chapters 3 and 4 is presented.

2.2 The Integral Mass Balance

Let us consider an arbitrary control volume of finite size and of a mass, M_T , such as sketched in Fig. 2.2.1. Furthermore, let us designate an infinitesimal area on the surface of this control volume by dA ; the fluid flowing through this area is characterized by the vector \mathbf{u} which, as seen in the figure, forms an angle α with the normal \mathbf{n} drawn perpendicular to the surface dA .

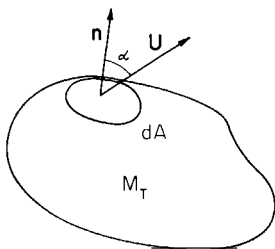


FIG. 2.2.1 An infinitesimal area on the surface of a finite control volume.

A mass balance over this control volume may now be written by expressing the fact that

$$-\left[\begin{array}{l} \text{total net rate of mass outflow} \\ \text{over the whole surface of the} \\ \text{control volume} \end{array} \right] = \left[\begin{array}{l} \text{the rate of change of} \\ \text{mass within the control} \\ \text{volume} \end{array} \right] \quad (2.2.1)$$

Using mathematical symbols the above statement may be expressed as

$$-\oint_A \rho(\mathbf{u} \cdot d\mathbf{A}) = \frac{d}{dt} \iiint_V \rho dV \equiv \frac{dM_T}{dt} \quad (2.2.2)$$

We note that the symbol \oint_A designates a surface integral over the whole surface area of the control volume. In this instance both \mathbf{u} and $d\mathbf{A}$ are considered as vectorial quantities because the surface dA does have a specific orientation.

The quantity on the right-hand side of Eq. (2.2.2) designates the accumulation or the rate of change of mass within the control volume.

In some instances it may be convenient to express the left-hand side of Eq. (2.2.2) in scalar rather than in vectorial quantities; thus, from Fig. 2.2.1 we have

$$-\oint_A \rho(\mathbf{u} \cdot d\mathbf{A}) = - \int_A \rho u \cos \alpha dA = \frac{dM_T}{dt} \quad (2.2.3)$$

Moreover, in many systems of practical interest fluid flows into a vessel and out of a vessel through well-defined areas having a simple geometry. Under

these conditions it is convenient to select the areas A_1, A_2, \dots, A_n such that they are perpendicular to the fluid stream that is passing through them. Such a system, containing one inlet and one outlet stream, is sketched in in Fig. 2.2.2.

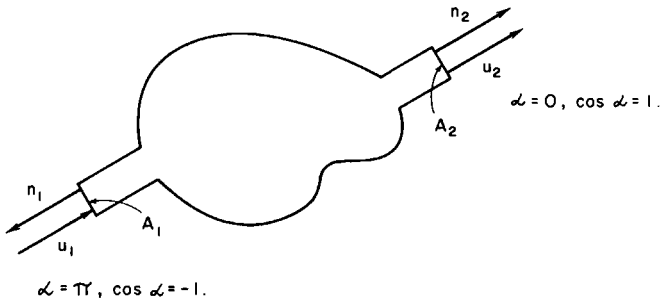


FIG. 2.2.2 A control volume with one inflowing stream, perpendicular to A_1 , and one outflowing stream, perpendicular to A_2 .

For the system shown in Fig. 2.2.2, Eq. (2.2.3) may be written as

$$\frac{dM}{dt} = - \int_{A_1 + A_2} \rho u \cos \alpha dA = \int_{A_1} \rho u dA - \int_{A_2} \rho u dA \quad (2.2.4)$$

Upon designating the mean velocity u_m ,

$$u_m = \int_A u dA / \int_A dA \quad (2.2.5)$$

We may write

$$\frac{dM_T}{dt} = u_{1,m} \rho_1 A_1 - u_{2,m} \rho_2 A_2 \quad (2.2.6)$$

or

$$\frac{dM_T}{dt} = w_1 - w_2 = -\Delta w \quad (2.2.7)$$

where $w = u \rho A$ is the mass flow rate (e.g., in kilograms per second); thus, $\Delta w = w_2 - w_1$. For steady-state conditions, Eq. (2.2.7) reduces to

$$w_1 = w_2$$

$$\left[\begin{array}{c} \text{rate of} \\ \text{mass input} \end{array} \right] = \left[\begin{array}{c} \text{rate of} \\ \text{mass output} \end{array} \right] \quad (2.2.8)$$

Let us illustrate the application of these ideas through a simple example.

Example 2.2.1 Molten steel is discharged from a ladle through a taphole, located at the bottom, as sketched in Fig. 2.2.3. If the average linear velocity of the steel through the taphole nozzle is given by

$$u_{2,m} = (2gh)^{1/2} \quad (i)$$

where h is the metal depth above the nozzle and g is acceleration due to gravity, calculate the time required for emptying the ladle.

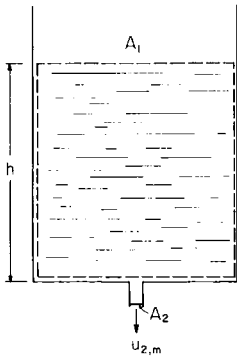


FIG. 2.2.3 Sketch of the system in Example 2.2.1.

Data

initial metal depth	3.5 m
nozzle diameter	0.075 m
ladle diameter	3.1 m
density of molten steel	$7.1 \times 10^3 \text{ kg/m}^3$
acceleration due to gravity	9.81 m/s^2

SOLUTION The control volume chosen is designated by the broken lines. Since no molten steel enters the system and steel is discharged only through area A_2 , the cross-sectional area of the nozzle, we can choose Eq. (2.2.7) as the starting point of our calculation. Thus we have

$$\frac{dM_T}{dt} = -w_2 = -u_{2,m}\rho A_2 \quad \text{because } w_1 = 0 \quad (ii)$$

but, since $u_{2,m} = (2gh)^{1/2}$ and $M_T = (hA_1\rho)$, Eq. (ii) may be written as

$$\frac{dh}{dt} = -\frac{\rho A_2}{\rho A_1}(2gh)^{1/2} \quad (iii)$$

where the subscripts in ρ have been omitted because the fluid is incompressible.

Equation (iii) has to be integrated for the boundary condition

$$h = h_i, \quad t = 0 \quad (\text{iv})$$

Thus we have

$$h_i^{1/2} - h^{1/2} = (A_2/A_1) \left(\frac{g}{2} \right)^{1/2} t \quad (\text{v})$$

which could be rearranged to obtain h as a function of t .

In the present case we seek the time which corresponds to $h = 0$; i.e.,

$$t_e = (2h_i/g)^{1/2} A_1/A_2$$

Upon substituting, we have

$$t_e = (3.5 \times 2/9.81)^{1/2} \left(\frac{3.1}{0.075} \right)^2, \quad h = 1220 \quad \text{s}$$

about 20 min.

We note that Example 2.2.1 provided simple illustrations of the overall mass balance. In many practical applications the realistic representation of the problem will require the statement of the other conservation equations, such as the mechanical energy balance or the overall momentum balance.

Nonetheless, it has to be stressed to the reader that any solution to fluid flow problems has to satisfy the overall mass balance.

2.3 The Integral Momentum Balance

The momentum of a fluid has been defined previously in Table 1.2.1 as mass times velocity. Because the velocity is a vector, the momentum itself is a vectorial quantity.

In flow systems it is more convenient to work in terms of momentum per unit volume, which we shall designate \mathbf{P} and define as

$$\mathbf{P} = \rho \mathbf{u} \quad (2.3.1)$$

The integral momentum balance equation has to express Newton's law:

$$\left[\begin{array}{l} \text{rate of change of momentum} \\ \text{within the control volume} \end{array} \right] = \left[\begin{array}{l} \text{net force acting on} \\ \text{the control volume} \end{array} \right] \quad (2.3.2)$$

Let us consider a macroscopic control volume of arbitrary shape, sketched in Fig. 2.2.1, and develop expressions for both the net accumulation of momentum with the control volume and for the sum of forces acting on this control volume. The momentum flux into the control volume at any

point on the external surface, due to the inflow of fluid, is given by

$$\mathbf{u}(\rho\mathbf{u})$$

In this context it is helpful to think of the quantity $(\rho\mathbf{u})$ as the “concentration of momentum.”

The total net rate at which momentum leaves the control volume is then given by summing these contributions over the whole surface of the control volume:

$$-\oint_A (\rho\mathbf{u}) \mathbf{u} \cdot d\mathbf{A} = -\oint_A \rho\mathbf{u} u \cos\alpha dA$$

The negative sign designates the fact that the outflow of momentum is being summed.

Let us now consider the forces acting on the control volume. These forces may be divided into three categories:

(1) *Forces due to pressure on the external surface of the control volume* are obtained by summing the pressure acting over the whole surface of the control volume:

$$\oint_A p d\mathbf{A} = \oint_A p \mathbf{n} dA$$

(2) *Forces on the internal surface of the control volume* or, more generally, the force exerted by the fluid on the solid walls of the container, are designated \mathbf{F}_{drag} .

(3) *External forces acting on the fluid*, such as gravity, an electromagnetic force field, etc., are designated as \mathbf{F}_{ext} .

Let us now proceed by combining all these terms in the momentum balance equation. Thus we have

$$\frac{d\mathbf{P}}{dt} = -\oint_A (\rho\mathbf{u}) \mathbf{u} \cdot d\mathbf{A} - \oint_A p d\mathbf{A} - \mathbf{F}_{\text{drag}} + \mathbf{F}_{\text{ext}} \quad (2.3.3)$$

$$\begin{bmatrix} \text{rate of change} \\ \text{of momentum} \end{bmatrix} = \begin{bmatrix} \text{net rate of outflow} \\ \text{of momentum} \end{bmatrix} + \begin{bmatrix} \text{forces acting on} \\ \text{the control volume} \end{bmatrix}$$

Equation (2.3.3) represents the statement of the integral momentum balance equation in its general form.

As discussed in connection with the overall mass balances, in many practical problems the fluid may be considered to enter and leave the system through well-defined areas of simple geometry. Under such conditions, sketched in Fig. 2.3.1, the overall momentum balance may be usefully sim-

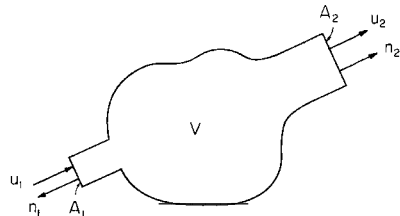


FIG. 2.3.1 Sketch of the system for the overall momentum balance.

$$\begin{array}{c} \text{y} \\ \text{x} \end{array}$$

$$u_x = |u| \cos \alpha$$

$$u_y = |u| \sin \alpha$$

plified. Thus we have

$$\begin{aligned} \frac{d\mathbf{P}}{dt} &= - \int_{A_1} (\rho \mathbf{u}) \mathbf{u} \cdot d\mathbf{A} - \int_{A_2} (\rho \mathbf{u}) \mathbf{u} \cdot d\mathbf{A} - \int_{A_1} p d\mathbf{A} \\ &\quad - \int_{A_2} p d\mathbf{A} - \mathbf{F}_{\text{drag}} + \mathbf{F}_{\text{ext}} \end{aligned} \quad (2.3.4)$$

If we select the surfaces A_1 and A_2 such that they are perpendicular to the direction of the flow (possible for simple flow situations), then we have

$$\begin{aligned} \frac{d\mathbf{P}}{dt} &= \int_{A_1} \rho \mathbf{u} u dA - \int_{A_2} \rho \mathbf{u} u dA + \int_{A_1} p dA \\ &\quad - \int_{A_2} p dA - \mathbf{F}_{\text{drag}} + \mathbf{F}_{\text{ext}} \end{aligned} \quad (2.3.5)$$

where the change in the sign of the first and the third terms reflects the fact that the appropriate orientation has been assigned to the surfaces A_1 and A_2 , which are no longer vectorial quantities but scalars. Or, upon performing the integration and using the mean velocities defined in Eq. (2.2.5), we obtain

$$\frac{d\mathbf{P}}{dt} = \rho_1(\mathbf{u}u)_{1,m} A_1 - \rho_2(\mathbf{u}u)_{2,m} A_2 + p_1 A_1 - p_2 A_2 - \mathbf{F}_{\text{drag}} + \mathbf{F}_{\text{ext}} \quad (2.3.6)$$

It is now convenient to introduce the quantities w or \mathbf{w} , which designate the absolute value and the vectorial mass flow rate, respectively, where

$$w = \rho u A \quad \text{and} \quad \mathbf{w} = \rho \mathbf{u} A$$

Then we have

$$\frac{d\mathbf{P}}{dt} = \frac{(u_{1,m}^2)}{u_{1,m}} \mathbf{w}_1 - \frac{(u_{2,m}^2)}{u_{2,m}} \mathbf{w}_2 + p_1 A_1 - p_2 A_2 - \mathbf{F}_{\text{drag}} + \mathbf{F}_{\text{ext}} \quad (2.3.7)$$

For the relatively flat velocity profiles encountered in turbulent systems[†] the terms

$$[u_{1,m}^2/u_{1,m}]w \text{ may be approximated by } \simeq u_m w$$

The vectorial nature of Eqs. (2.3.3–2.3.7) has to be stressed to the reader. In many practical applications, as illustrated in the example that follows, it is more convenient to work in terms of the x , y , and z components of the momentum balance.

Example 2.3.1 A horizontal water jet is made to strike a large planar solid surface (e.g., in the cooling of a steel strip), as sketched in Fig. 2.3.2. Estimate the total force exerted by the jet on the plate for the following conditions:

jet diameter	0.01 m
mean velocity	15 m/s
$\alpha = 30^\circ = \pi/6$	
$\rho = 1000 \text{ kg/m}^3$	

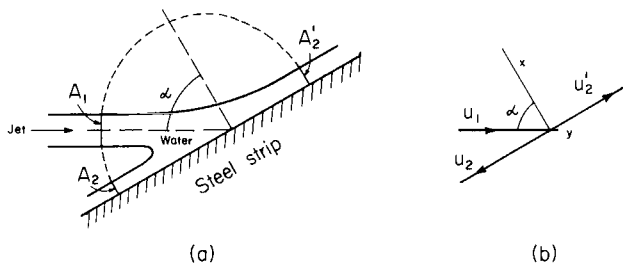


FIG. 2.3.2 Sketch of the system in Example 2.3.1.

SOLUTION Let us establish a coordinate system, such as sketched in Fig. 2.3.2a,b. It is seen that the direction x was chosen to be perpendicular to the plate, so that only the x component of the momentum balance equation will have to be considered in this instance.

Inspection of Fig. 2.3.2a shows that, as found by experience, upon striking the solid plate the fluid jet will not break up but by and large will flow parallel with it. The control volume selected is shown with broken lines; the surfaces across which flow occurs are drawn with a heavy line. The coordinate system and the principal velocities considered are also shown in Fig. 2.3.2b. Equation

[†] Turbulence phenomena will be discussed in Chapter 4.

(2.3.7) is the logical starting point, the x component of which is written as

$$\begin{aligned} dP_x/dt &= u_{1,m}u_{1,m}\rho A_1 \cos\alpha - \sum_i u_{2,m}u_{2,m}A_2 \cos\alpha + p_1A_1 \cos\alpha \\ &\quad - p_2A_2 \cos\alpha - F_{x,\text{drag}} + F_{x,\text{ext}} \end{aligned} \quad (\text{i})$$

However:

- (a) Since steady-state conditions are considered, $dP_x/dt = 0$.
- (b) The $u_{2,m,x} = u_{2,m} \cos\alpha$ terms are all zero because the flow across surface "2" has no x components.
- (c) Since both the jet and the plate are considered to be at atmospheric pressure there is not net force on the control volume due to a pressure difference.
- (d) Finally, in the present case we shall neglect the effect of gravity; thus, $F_{x,\text{ext}} = 0$.

It follows that the momentum balance equation is then written as

$$u_{1,m}^2 A_1 \rho \cos\alpha = -F_{x,\text{drag}} \quad (\text{ii})$$

i.e.,

$$F_x = -225 \times (3.14/4) \times 10^{-4} \times 0.86 \times 1000 = -152 \text{ N}$$

This is the force acting on the fluid. The force acting on the plate equals this numerically but acts in the opposite direction:

$$F_{x,\text{plate}} \equiv +152 \text{ N}$$

Two additional comments ought to be made at this stage. One of these is that the sign of the force in a given direction is given by the direction in which the momentum is increasing. Hence the negative sign of F_x in Example 2.3.1. In this case the direction of the force was probably obvious intuitively.

The second point that needs stressing is the fact that since momentum is a vectorial quantity a change in direction of the velocity (even if there is no change in its absolute value) will give rise to a net force, as illustrated in the following example.

Example 2.3.2 A stream of water flows smoothly over a curved vane as sketched in Fig. 2.3.3a. If we assume as first approximation that the absolute value of the velocity remains constant throughout, at 30 m/s, estimate the net force on the vane. The fluid stream may be regarded as cylindrical in shape with a diameter of 0.1 m.

SOLUTION This problem is very similar to that discussed in Example 2.3.1. Upon neglecting the effect of pressure and the external forces, the x

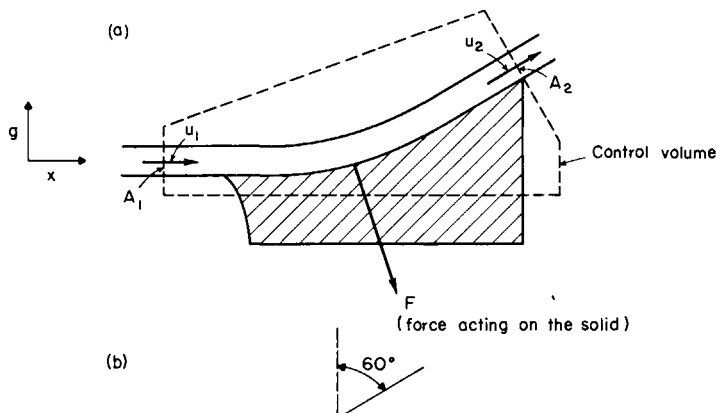


FIG. 2.3.3 Sketch of the system in Example 2.3.2.

component of the momentum balance equation [Eq. (2.3.7)] is written as

$$-F_x = \rho u_{1,m}^2 A_1 - \rho u_{2,m}^2 A_2 \cos \alpha \quad (\text{i})$$

The y component is given as

$$-F_y = 0 - \rho u_{2,m}^2 A_2 \sin \alpha \quad (\text{ii})$$

Upon substituting numerical values we have

$$F_x = -1000 \times (0.01 \times 3.14)/4 \times 900[1 - 0.5] \simeq -3530 \text{ N}$$

$$F_y = 1000 \times 900 \times (0.01 \times 3.14)/4 \times 0.866 \simeq 6120 \text{ N}$$

The resultant force *acting on the fluid* is given as

$$|F| = [(-3530)^2 + (6120)^2]^{1/2} = 7065 \text{ N}$$

This force is acting in the direction

$$\tan^{-1}(6120 / -3530) = -60^\circ$$

as sketched in Fig. 2.3.3b.

The net force acting on the vane (i.e., required to keep it in position) opposes the force acting on the fluid, the components of which have been calculated as $F_x = -3530 \text{ N}$ and $F_y = 6120 \text{ N}$. Calculations of this type, with due allowance for other physical factors that have been neglected here, such as friction, change of jet shape, etc., are of importance in turbine design.

More metallurgically oriented applications of the overall momentum balance will be given in subsequent chapters.

2.4 The Integral Mechanical Energy Balance (The Engineering Bernoulli Equation)

Let us consider a finite control volume through which a fluid is flowing, such as sketched in Fig. 2.3.1, and establish an overall mechanical energy balance. In forming such a balance we have to express the fact that the rate of change of mechanical energy within the control volume must equal the net inflow of mechanical energy, less the rate at which work is being done by the fluid. In this discussion our attention will be restricted to mechanical energy terms only, that is, kinetic energy, pressure energy, and potential energy. Regarding the possible work terms, only work done on the surroundings and the work done against frictional forces will be considered.

A more general statement of the conservation of energy, that is, the first law of thermodynamics, would have to include thermal effects since the same work terms appearing in the mechanical energy balance will necessarily produce heat. The presentation given here will be (largely) restricted to isothermal systems, and we will proceed on the tacit understanding that isothermality will be maintained through the abstraction or the addition of heat to the system.

This assumption is quite reasonable for most of the cases to be discussed here because the thermal energy produced by frictional effects tends to be small in most metals processing applications. A good discussion of more general energy balances is available in the texts by Bird *et al.* and Welty *et al.*²

Let us now consider the various forms of energy that have to be taken into account in the establishing of the integral mechanical energy balance.

(a) *Kinetic energy* $K_{E,T}$. The kinetic energy of the fluid contained in the control volume may be approximated by[†]

$$K_{E,T} = \iiint_{\tilde{V}} \frac{1}{2} \rho u_m^2 d\tilde{V} \quad (2.4.1)$$

(b) *Potential energy* Z_T . The potential energy of the fluid in the control volume is given by

$$Z_T = \iiint_{\tilde{V}} g\rho Z d\tilde{V} \quad (2.4.2)$$

In the present case, as a practical matter, the potential energy considered will be restricted to that due to gravity, defined in relation to a given datum

[†] This approximation is very good for turbulent flow. For laminar flow u_m^2 should be replaced by u_m^2/α where $\alpha \approx 1.3$.³

point. Here Z designates the height above this datum point. It is noted that both $K_{E,T}$ and Z_T have the dimension of energy, i.e., ML^2/t^2 or newton meters ($N\ m$); thus, they refer to the total energy combined within the control volume.

(c) The pressure energy per unit mass Π is defined as

$$\prod = \int_{p_1}^{p_2} \frac{1}{\rho} dp \quad (2.4.3)$$

We may now proceed by the statement of the mechanical energy by expressing the fact that energy is converted within the control volume, depicted in Fig. 2.3.1, into which fluid is flowing across area A_1 and from which fluid is flowing across area A_2 . For the general unsteady-state case this statement of energy conservation takes the following form:

$$\begin{aligned}
 \left[\frac{\text{rate of accumulation of}}{\text{kinetic and potential energy}} \right] &= \left[\frac{\text{mass}}{\text{flow rate}} \right] \times \left[\frac{\text{kinetic + potential energy}}{\text{energy per unit mass}} \right]_{\text{at inlet}} \\
 &\quad - \left[\frac{\text{mass}}{\text{flow rate}} \right] \times \left[\frac{\text{kinetic + potential energy}}{\text{energy per unit mass}} \right]_{\text{at outlet}} \\
 &\quad + \left[\frac{\text{mass}}{\text{flow rate}} \right] \times \left[\frac{\text{pressure energy}}{\text{per unit mass}} \right]_{\text{inlet}} - \left[\frac{\text{pressure energy}}{\text{per unit mass}} \right]_{\text{outlet}} \\
 &\quad + \left[\frac{\text{rate of work done}}{\text{on the surroundings}} \right] + \left[\frac{\text{rate of work done}}{\text{against frictional forces}} \right]
 \end{aligned} \tag{2.4.4}$$

It is noted that each of the terms in Eq. (2.4.4) has the dimension of (energy/time). Using the previously defined symbols, Eq. (2.4.4) takes the following form:

Certain comments may be helpful at this stage. The mechanical energy balance equation is written in terms of scalar quantities, because energy is a scalar; moreover, Eq. (2.4.5) is a balance written on the energy content of the control volume as a whole. The quantity W is the work done on the surroundings, which will be positive if we were to consider an expanding

piston and would be negative if we were to consider the work done by a pump in, e.g., a cooling water circuit. While the terms appearing in Eq. (2.4.5) are scalars, care has to be taken regarding the sign of these quantities.

When the system is at steady state, the left-hand side of Eq. (2.4.5) vanishes and under these conditions it is convenient to recast Eq. (2.4.5) in terms of energy/unit mass flow rate; thus, upon dividing by w we obtain the following:

$$\frac{u_{2,m}^2}{2} - \frac{u_{1,m}^2}{2} + g(Z_2 - Z_1) + \int_{p_1}^{p_2} \frac{dp}{\rho} + W' + E_f' = 0 \quad (2.4.6)$$

It is noted that in going from Eq. (2.4.5) to (2.4.6) allowance was made for the fact that, through the orientation of the areas A_1 and A_2 , u_1 and u_2 were implicitly defined as inlet and outlet velocities. Here $W' = W/w$ and $E_f' = E_f/w$.

The dimension of the terms appearing in Eq. (2.4.6) is energy/mass, i.e., $(L/t)^2$; $g(Z_2 - Z_1)$ represents the change in the potential energy of the fluid between levels "1" and "2". For horizontal systems this term is zero.

Equation (2.4.6) expresses the conservation of mechanical energy for steady-state systems and is frequently called the *Engineering Bernoulli Equation*.

Its importance lies in the fact that it provides a working relationship between the changes in the velocity, potential energy, and pressure of the fluid as it passes through the control surfaces "1" and "2".

For the solution of actual problems Eq. (2.4.6) constitutes a convenient algebraic relationship between the two terminal values of u , Z , \prod , and the work terms. Depending on the number of unknowns, additional relationships may be required for the definition of the problems. The most important of these, namely the dependence of E_f' on the system parameters will be discussed in the next section.

However, under certain conditions no work is being done on the surroundings, and moreover the frictional terms may be neglected also (e.g., short nozzles). Under these conditions, as illustrated in the following, Eq. (2.4.6) may be used directly to define the system.

THE ORIFICE METER

The flow of fluids through pipes or conduits may be measured by making the fluid pass through a constriction, thereby increasing its velocity, hence its kinetic energy. The actual flow rate may then be determined by measuring the corresponding change in pressure at constant potential energy.

One such typical arrangement, the orifice meter, is sketched in Fig. 2.4.1.

It is seen that the fluid approaches the orifice at a mean velocity $u_{1,m}$ through the cross-sectional area of the conduit A_1 and a pressure p_1 . At the

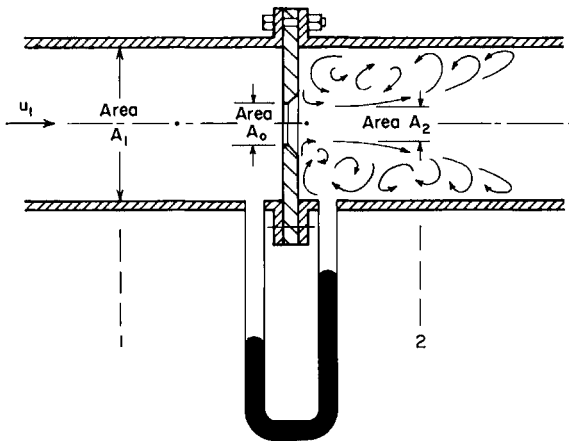


FIG. 2.4.1 Sketch of the orifice meter.

orifice the fluid passes through a constricted area A_2 and is accelerated to a velocity $u_{2,m}$ and is at a pressure p_2 .

The manometer, also shown in the sketch, is used to measure the pressure differential $(p_1 - p_2)$. Our objective is to relate the mass flow w to $(p_1 - p_2)$.

The control volume to be used in the calculation is sketched in Fig. 2.4.1; we then proceed by establishing an overall mass balance and an overall energy balance as follows:

For steady-state conditions Eq. (2.2.6) is the appropriate starting point for the mass balance, which is written as

$$u_{1,m}\rho_1 A_1 = u_{2,m}\rho_2 A_2 = w \quad (2.4.7)$$

In the absence of work done on the surroundings ($W' = 0$), when frictional effects are negligible ($E_t' = 0$) and for a horizontal pipe [$(Z_2 - Z_1) = 0$], Eq. (2.4.6) may be written as

$$\left(\frac{u_{2,m}^2}{2} - \frac{u_{1,m}^2}{2} \right) + \int_{p_1}^{p_2} \frac{dp}{\rho} = 0 \quad (2.4.8)$$

For an incompressible fluid

$$\int_{p_1}^{p_2} \frac{dp}{\rho} = \frac{p_2 - p_1}{\rho} \quad (2.4.9)$$

Thus upon substituting for the integral and upon eliminating $u_{1,m}$ with the aid of Eq. (2.4.7), Eq. (2.4.8) may be written as

$$u_{2,m} = \{2(p_1 - p_2)/\rho[1 - (A_2/A_1)^2]\}^{1/2} \quad (2.4.10)$$

As a practical matter the fluid, upon passing through the orifice, will accelerate to a higher velocity than $u_{2,m}$ due to the formation of a "vena contracta" somewhat downstream of the orifice. It follows that Eq. (2.4.10) would overestimate the flow rate. In order to relate the flow rate to the measurable quantity A_2 it is customary to introduce a correction factor, called the discharge coefficient C_D . Thus we have

$$u_{2,m} = C_D \{2(p_1 - p_2)/\rho [1 - (A_2/A_1)^2]\}^{1/2} \quad (2.4.11)$$

or

$$w = C_D A_2 \{2\rho(p_1 - p_2)/[1 - (A_2/A_1)^2]\}^{1/2} \quad (2.4.12)$$

Tabulated values of C_D are available for certain "standard" geometries. These values usually range between 0.6 and 0.8.

Example 2.4.1 A sharp edged orifice 0.03 m in diameter is installed in a water line 0.05 m in diameter, which supplies cooling water to an oxygen lance. If the pressure drop across the orifice is 200 mm mercury, calculate the water flow rate.

$$\begin{aligned} \text{Data} \quad C_D &= 0.8 \\ \rho &= 1000 \text{ kg/m}^3 \end{aligned}$$

Using Table 1.2.1,

$$200 \text{ mm Hg} = (200/735) \times 1.01 \times 10^5 \text{ N/m}^2 \simeq 2.72 \times 10^4 \text{ N/m}^2$$

Thus substitution into Eq. (2.4.10) yields

$$\begin{aligned} w &= 0.8 \times 7.06 \times 10^{-3} [2 \times 10^3 \times 2.72 \times 10^4 / (1 - 0.36)]^{1/2} \\ &\simeq 52 \text{ kg/s} \end{aligned}$$

2.5 The Friction Factor

The preceding discussion of the overall energy balance was restricted to systems where the work done against the frictional forces was negligible. There are, however, many cases where frictional forces are important; under these conditions the logical starting point is the statement of the overall mechanical energy balance, but an additional relationship is then required between the rate of work done against the frictional forces and the other parameters of the system. In the majority of cases this relationship had to be deduced from experimental measurements, and the friction factor, to be defined subsequently, provides a convenient means of representing this empirically obtained information. Let us consider a long, horizontal pipe of length L and of diameter d , sketched in Fig. 2.5.1, through which an incompressible fluid is flowing at a mean velocity u_m .

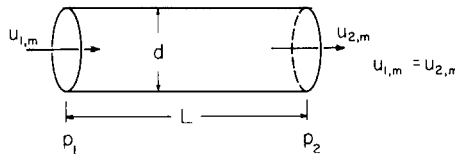


FIG. 2.5.1 Sketch showing the parameters used for defining the friction factor for flow through a pipe.

In establishing the overall mechanical energy balance let us consider that no work is done on the surroundings; thus for steady-state conditions Eq. (2.4.6) is written as

$$(p_1 - p_2)/\rho = E_f' \quad (2.5.1)$$

where E_f' is the rate of work done against the frictional force divided by the mass flow rate of fluid.

Equation (2.5.1) relates the pressure drop in the pipe to the work done against frictional forces.

During the early part of the century extensive measurements have been made of the pressure drop in pipes and it has been found convenient to represent this information in terms of friction factor correlations.

For straight pipes the friction factor f_{fr} is defined implicitly by the following expression:

$$p_1 - p_2 = 2f_{fr}[(L/d_c)\rho u_m^2] \quad (2.5.2)$$

or

$$f_{fr} = (p_1 - p_2)/2[(L/d_c)\rho u_m^2] \quad (2.5.3)$$

Using Eq. (2.5.1), f_{fr} and E_f' are related by

$$E_f' = 2f_{fr}(L/d_c)u_m^2 \quad (2.5.4)$$

It has to be stressed that, as defined in Eqs. (2.5.2)–(2.5.4), the friction factor is a constant of proportionality between the pressure drop or the rate of work done against frictional forces and the mean linear fluid velocity. The definitions given above apply to straight pipes only. Friction factors have been used to relate pressure drop and fluid velocity for other geometries and here care has to be taken to use a definition that is consistent with subsequent calculations, i.e., the system geometry, etc.

The friction factor f_{fr} is a dimensionless quantity, correlations for which are available for a number of geometries. Figure 2.5.2 shows a plot of f_{fr} against the Reynolds number

$$N_{Re} = u_m \rho d / \mu \quad (2.5.5)$$

which is based on a large number of experimental measurements.

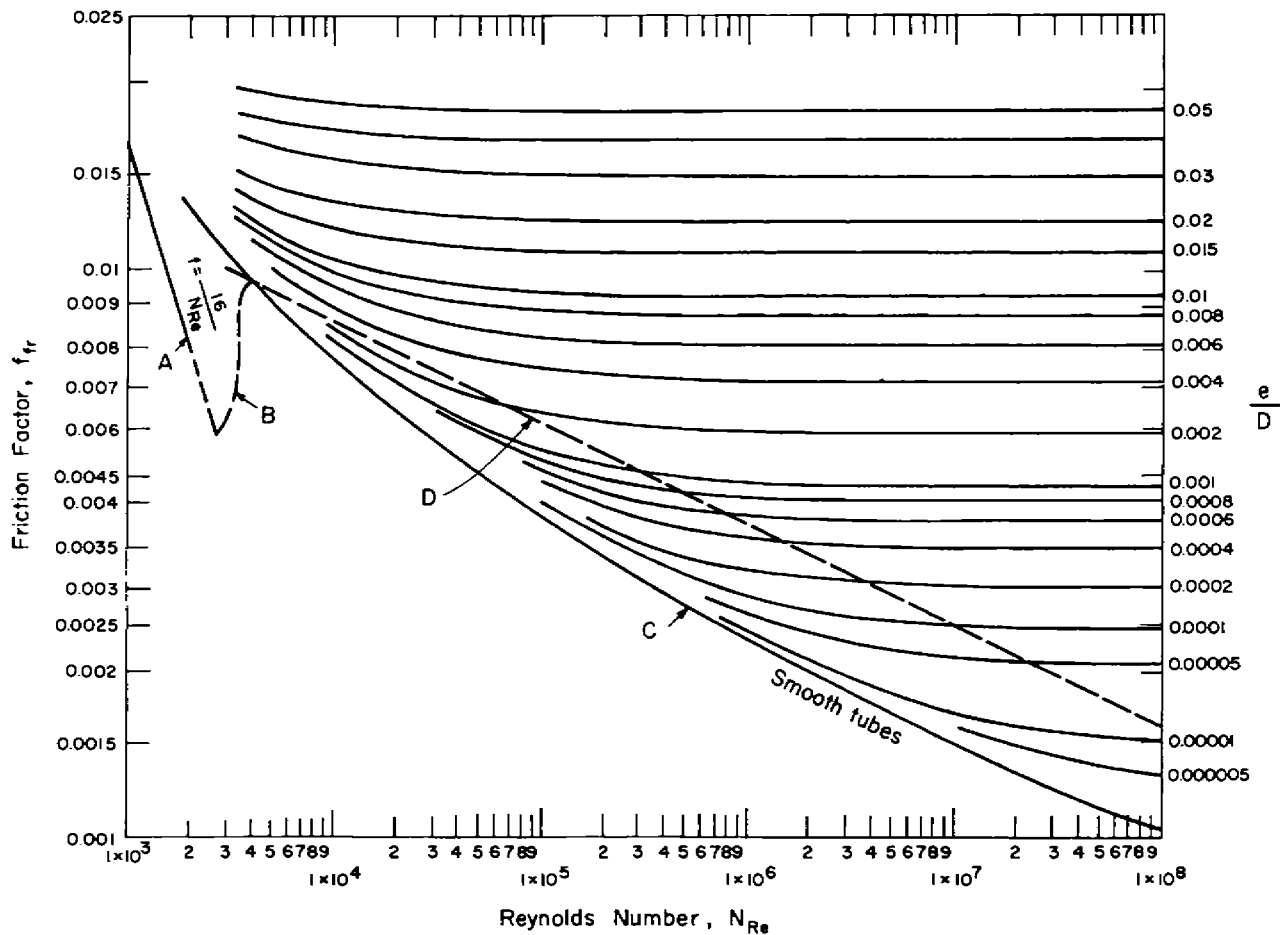


FIG. 2.5.2 The friction factor as a function of the Reynolds number for flow through pipes.³

It is seen that for $N_{Re} < 2000$ the experimental data are represented by a single line:

$$f_{fr} = 16/N_{Re} \quad (2.5.6)$$

This region corresponds to laminar flow, a concept which will be defined subsequently. When $N_{Re} > 3000$, which corresponds to turbulent flow, the friction factor depends both on N_{Re} and on e , the relative roughness of the pipe.

The region $2000 \leq N_{Re} < 3000$ corresponds to transition between laminar and turbulent flow and is rather ill-defined. We note finally that the correlation shown in Fig. 2.5.2 is valid for long pipes only, where $L/d_c > 50$.

Numerous correlations for short pipes and for other geometries may be found in the book by Knudsen and Katz.⁵

Let us illustrate the use of the friction factor by working a simple example.

Example 2.5.1 It is proposed to pump molten lead at 1000°K , at a rate of 1.0 ton/h through a horizontal pipe 2 cm in diameter and 100 m long. Calculate the pressure drop required and the theoretical power consumption for pumping.

<i>Data</i>	
viscosity of lead	0.012 g/cm s
density of lead	10 g/cm ³
e/d	4×10^{-3}

SOLUTION First of all we shall convert the numerical values of the parameters to SI units. Thus

$$\begin{aligned} \mu &= 1.2 \times 10^{-2} \times 10^{-1} \simeq 1.2 \times 10^{-3} \text{ kg/m s} \\ \rho &= 10 \times 10^3 = 10^4 \text{ kg/m}^3 \end{aligned}$$

Then we shall use Eq. (2.5.2) to calculate the pressure drop:

$$u_m = \frac{10^3}{10^3 \times 3.6 \times 10^3 [(0.02)^2 \times 3.14/4]} \simeq 0.88 \text{ m/s}$$

Thus

$$N_{Re} = \frac{0.88 \times 2 \times 10^{-2} \times 10^4}{1.2 \times 10^{-3}} \simeq 1.47 \times 10^5$$

Thus, from Fig. 2.5.2,

$$f_{fr} = 8 \times 10^{-3}$$

i.e., using Eq. (2.5.2),

$$(p_1 - p_2) = 2f_{fr}(L/d_c)\rho u_m^2 \quad (i)$$

i.e.,

$$\begin{aligned}(p_1 - p_2) &= 2 \times (8 \times 10^{-3}) \times \frac{100}{0.02} \times 10^4 \times 0.77 \\ &\simeq 6.16 \times 10^5 \text{ N/m}^2 \\ &\simeq 6.16 \text{ atm}\end{aligned}$$

In order to calculate the power requirements for pumping, let us consider that the pump *will perform work on the fluid*. It follows that the appropriate expression to use is Eq. (2.4.6), which for the present case is written as

$$-W' = (p_2 - p_1)/\rho \quad (\text{ii})$$

i.e.,

$$W' = -(6.16 \times 10^5)10^4 \simeq -61.6 \text{ (N m/s)/(kg/s)}$$

where the negative sign indicates that work was being done *on the fluid*. Let us recall that W' is power required per unit mass fluid flowing through the system; thus,

$$W = wW' = -(1000/3.6 \times 10^3) \times 61.6 \simeq 17.1 \text{ N m/s}$$

2.5.1 Flow through Noncircular Conducts

The friction factor correlations developed for circular pipes may be used for conduct of noncircular cross section provided d_h , the hydraulic mean diameter is used. The hydraulic mean diameter is defined as

$$d_h = \frac{4 \times \text{cross-sectional area}}{\text{wetted perimeter}}$$

For a circular pipe,

$$d_h = \frac{4(d^2\pi/4)}{\pi d} = d \quad (\text{i})$$

For a duct of rectangular cross section, say $l_1 \times l_2$,

$$d_h = 4l_1 l_2 / 2(l_1 + l_2) = 2l_1 l_2 / (l_1 + l_2) \quad (\text{ii})$$

Analogous considerations may be applied to other geometries, of course; if available, the correlations for the appropriate systems are preferable. A good discussion of flow through noncircular cross sections is available in Perry and other authors.⁴⁻⁶

2.5.2 Frictional Losses through Pipe Fittings

When a fluid flows through various pipe fittings, such as valves, T-junctions, elbows, etc., frictional losses will occur. For the purpose of

calculation it is convenient to represent these losses by assigning the frictional resistance of an equivalent pipe length to them.

A collection of these equivalent pipe lengths for various fittings is shown in Table 2.5.1.

TABLE 2.5.1
Equivalent Length of Pipe Fittings³

Fitting	Pipe diameters
45° elbows	15
90° elbows (standard radius)	30–40
90° square elbows	60
Entry from leg of T-piece	60
Entry into leg of T-piece	90
Unions and couplings	Generally very small
Globe valves fully open	60–300
Gate valve	
fully open	7
$\frac{3}{4}$ open	40
$\frac{1}{2}$ open	200
$\frac{1}{4}$ open	800

2.5.3 Flow through Open Channels

The friction factor may be used also for estimating uniform flow through open channels. Open channel flow may be of importance in metals processing operations in connection with flow of molten metals or slags through launders and troughs. However, most of the quite voluminous work on open channel flow has been done by civil engineers, motivated by the study of river and canal flow phenomena. Here we shall consider a particular somewhat idealised flow condition, namely uniform flow, sketched in Fig. 2.5.3,

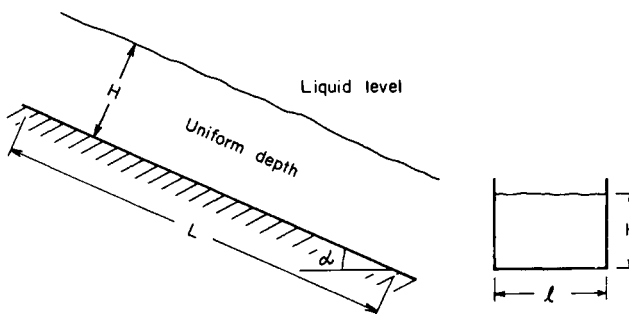


FIG. 2.5.3 Illustration of open channel flow.

TABLE 2.5.2

Typical Values of e_c ³

System	e_c (m)
Finished concrete	5×10^{-5}
Unfinished concrete	1.3×10^{-4}
Cast iron	$1.5-2 \times 10^{-4}$
Brick	$2-3 \times 10^{-4}$
Corrugated metal	$1.5-3 \times 10^{-3}$

where the depth of the liquid is uniform. Such uniform flow is established in long channels.

This problem may be formulated by writing a force balance in the following form:

$$AL\rho g \sin \alpha = \tau_{0,c} L(2H + l_1) \quad (\text{i})$$

$$\left[\begin{array}{l} \text{total mass of} \\ \text{fluid} \end{array} \right] \times \left[\begin{array}{l} \text{acceleration due to the} \\ \text{gravity component in the} \\ \text{direction of motion} \end{array} \right] = \left[\begin{array}{l} \text{shear stress on} \\ \text{the walls} \end{array} \right] \times \left[\begin{array}{l} \text{total contact area} \\ \text{between the channel} \\ \text{and the fluid} \end{array} \right]$$

where $\tau_{0,c}$ is the shear stress on the walls

$$A = l_1 H \quad (\text{ii})$$

and $(2H + l_1)$ is the wetted perimeter. We may define the friction factor $f_{fr,c}$ for open channel flow as

$$f_{fr,c} = \tau_{0,c}/2\rho u_m^2 \quad (\text{iii})$$

where u_m is the mean velocity. It has been found that, for most practical cases, when $N_{Re} > 5000$, $f_{fr,c}$ is independent of the Reynolds number[†] and is given by

$$f_{fr,c} = \frac{1}{8}(e_c/d_h)^{1/3} \quad (\text{iv})$$

where

$$d_h = 4(H \times l_1)/(2H + l_1) \quad (\text{v})$$

i.e., d_h is the hydraulic mean diameter and e_c is the surface roughness.

Typical values of e_c which may be used as rough calculations are given in Table 2.5.2.

The volumetric flow rate \tilde{Q} is given as

$$\tilde{Q} = u_m(Hl_1) \quad (\text{vi})$$

[†] In this context the Reynolds number is defined as $N_{Re} = u_m \rho d_h / \mu$.

Thus we may combine Eqs. (i)–(vi) to obtain the following expression:

$$\tilde{Q} = (Hl_1)d_h^{2/3}e^{-1/6}(g \sin \alpha)^{1/2} \quad (\text{vii})$$

Example 2.5.2 It is proposed to pass blast furnace hot metal through a trough, which we shall assume to be a straight, rectangular channel, 20 m long and 0.2 m wide, which forms an angle of 5° with the horizontal plane. Estimate the maximum metal throughput if the metal depth is not to exceed 0.15 m; e_c may be taken as 5×10^{-4} and $\mu = 5 \times 10^{-3}$ kg/m.s.

SOLUTION We shall use Eq. (vii); thus, we have

$$\begin{aligned} d_h &= (4 \times 0.15 \times 0.2)/(0.3 + 0.2) = 2.4 \\ \tilde{Q} &= 0.15 \times 0.2 \times 1.79 \times 3.54 \times 0.924 \\ \tilde{Q} &= 0.18 \text{ m}^3/\text{s} \\ w &= 7.1 \times 10^3 \times 0.18 \\ &= 1.25 \times 10^3 \text{ kg/s or } 1.25 \text{ ton/s} \end{aligned}$$

Finally let us check that the flow is turbulent:

$$N_{Re} = u_m \rho d_h / \mu$$

Thus

$$u_m = \frac{0.351}{0.03} = 11.7 \text{ m/s} \quad \text{and} \quad N_{Re} = \frac{11.7 \times 7.1 \times 10^3 \times 2.4}{5 \times 10^{-3}} = 4 \times 10^7$$

which is indeed turbulent.

The reverse problem that one might wish to calculate is to specify a runner and launder size and angle of inclination in order to provide a given throughput. Such a calculation would involve a trial and error procedure.

It has to be stressed to the reader that the problem discussed here takes a rather simplified view of open channel flow phenomena. For a fuller discussion of the complexities of open channel flow reference should be made to the specialist literature.^{7,8}

2.6 Compressible Fluids

The overall mass, momentum, and mechanical energy balances presented in the preceding sections are valid for both incompressible and compressible fluids. The reader will have noted, however, that all the examples given related to incompressible fluids, such as molten metals, slags, or water. While the same principles apply, the actual method of calculation differs in the case of compressible fluids. It has to be stressed that whether a fluid is to be regarded as compressible or incompressible depends not only on the nature

of the fluid but also on the *nature of the problem*. Thus, as will be shown, gases may be regarded as incompressible, for the purpose of calculation, provided the overall pressure drop is a small fraction of the total pressure in the system and the linear velocity does not approach that of the sound in the medium. In certain metals processing applications these restrictions are not met examples of these are gas flow in vacuum degassing systems, supersonic jets in oxygen steel-making, and the like.

For these situations a somewhat different approach has to be developed, which will be discussed in the following.

2.6.1 Some Thermodynamic Relationships

In solving compressible fluid flow problems certain thermodynamic relationships have to be used, primarily in conjunction with the evaluation of the integral $\int dp/\rho$. The specific heat at constant pressure and at constant volume are defined as

$$C_p = \left(\frac{\partial H}{\partial T} \right)_p \quad (2.6.1)$$

and

$$C_v = \left(\frac{\partial \tilde{U}}{\partial T} \right)_v \quad (2.6.2)$$

where \tilde{U} is the internal energy and

$$H = \tilde{U} + pv \quad (2.6.3)$$

is the enthalpy.

For a system which exchanges heat with its surroundings the conservation of energy may be written as

$$dQ = d\tilde{U} + p dv \quad (2.6.4)$$

where $v = 1/\rho$ is the specific volume. The entropy change, δs for a reversible process is given as

$$\delta s = \delta Q/T \quad (2.6.5)$$

For any irreversible or real process (where heat or mass transfer takes place)

$$\delta s \geq \delta Q/T \quad (2.6.6)$$

In the flow problems to be treated subsequently we shall assume ideal gas behavior. Ideal gas behavior is approximated by real gases at low (say below 10–20 atm) pressures.

For ideal gases *the equation of state* is given by

$$pv = p/\rho = p_1/\rho_1 = p_2/\rho_2 = RT/M_w \quad (2.6.7)$$

where R is the universal gas constant, $R = 8.32 \times 10^3 \text{ J/kg mole } ^\circ\text{K} = 1.99 \text{ kcal/kg mole } ^\circ\text{K}$, and M_w is the molecular weight.

The internal energy of ideal gases depends on the temperature only; thus,

$$\left(\frac{\partial \tilde{U}}{\partial v} \right)_T = 0 \quad (2.6.8)$$

The isothermal expansion of an ideal gas is given as [from Eq. (2.6.4) with $d\tilde{U} = 0$]

$$Q = \int_{v_1}^{v_2} p \, dv = RT/M_w \ln(v_2/v_1) \quad (2.6.9)$$

where Q is the amount of thermal energy that had to be communicated to the system in order to maintain isothermal conditions.

For adiabatic conditions it may be shown that the following relationship will apply, at least approximately:

$$pv^\gamma = p_1v_1^\gamma \quad (2.6.10)$$

where

$$\gamma = C_p/C_v \quad (2.6.11)$$

Upon substituting Eq. (2.6.11) the integral $\int_1^2 dp/v$ may then be evaluated as

$$\int_1^2 \frac{dp}{v} = \left(\frac{\gamma}{\gamma + 1} \right) p_1 v_1 \left[\left(\frac{p_2^{(\gamma+1)/\gamma}}{p_1} \right) - 1 \right] \quad (2.6.12)$$

The temperature change accompanying adiabatic expansion (or compression) is given by

$$T_1 v_1^{\gamma-1} = T_2 v_2^{\gamma-1} \quad (2.6.13)$$

Equations (2.6.10), (2.6.12), and (2.6.13) may now be used in conjunction with the overall energy balance for the solution of problems involving compressible fluids.

2.6.2 Flow of Compressible Fluids in Pipes

Let us consider a pipe of length L and of diameter d_c through which a compressible fluid gas is flowing. Let the upstream conditions be denoted by the suffix 1 and the downstream conditions be designated by the suffix 2, as sketched in Fig. 2.6.1.

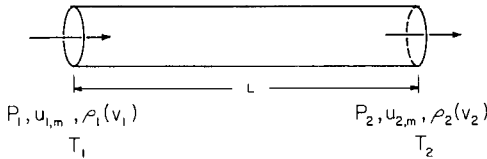


FIG. 2.6.1 Sketch representing the flow of a compressible fluid through a pipe.

For steady-state conditions the overall energy balance is written as

$$\frac{u_{2,m}^2}{2} - \frac{u_{1,m}^2}{2} + g(Z_2 - Z_1) + \int_{p_1}^{p_2} \frac{dp}{\rho} + W' + E_f' = 0 \quad (2.4.6)$$

Let us consider that the change in potential energy is negligible and that no work is being done on the surroundings. Then upon substituting for the friction factor from Eq. (2.5.4) we have the following:

$$\left(\frac{u_{2,m}^2}{2} - \frac{u_{1,m}^2}{2} \right) + \int_{p_1}^{p_2} \frac{dp}{\rho} + 2f_{fr} \frac{L}{d_c} u_m^2 = 0 \quad (2.6.14)$$

Let us introduce G , the mass flux, or the mass velocity, defined as

$$G = u_m \rho = u_m / v \quad (2.6.15)$$

The use of this quantity is helpful because G will remain constant along the pipe. Then upon writing Eq. (2.6.14) in a differential form we have the following:

$$G^2 v dv + v dp + 2f_{fr} G^2 v^2 (dL)/d_c = 0 \quad (2.6.16)$$

Let us divide by v^2 and then integrating over the whole length of the pipe we have

$$G^2 \ln \frac{v_2}{v_1} + \int_1^2 \frac{dp}{v} + \frac{2G^2}{d_c} \int_1^2 f_{fr} dL = 0 \quad (2.6.17)$$

As seen in Fig. 2.5.1 for high values of the Reynolds number, f_{fr} is independent of the linear velocity; thus,

$$\int_1^2 f_{fr} dL \approx f_{fr} L \quad (2.6.18)$$

For isothermal conditions and when the approximation in Eq. (2.6.18) is valid, upon using Eq. (2.6.10) we have

$$G^2 \ln \frac{p_1}{p_2} + \frac{(p_2^2 - p_1^2)M_w}{2RT} + 2f_{fr} G^2 \frac{L}{d_c} = 0 \quad (2.6.19)$$

or

$$G^2 \ln(p_1/p_2) + (p_2^2 - p_1^2)/2p_1v_1 + 2f_{fr}G^2L/d_c = 0 \quad (2.6.20)$$

When $p_1 \approx p_2$, the first term on the left-hand side of Eq. (2.6.20) is zero, which in a physical sense means that the kinetic energy change upon expansion is negligible.

Upon defining a mean density ρ_m as

$$\rho_m = 1/v_m = (p_1 + p_2)/2p_1v_1 \quad (2.6.21)$$

then Eq. (2.6.20) may be written as

$$p_1 - p_2 = 2f_{fr}\rho_m u_m^2 L/d_c \quad (2.6.22)$$

which is identical to the previously given expression, Eq. (2.5.2), for incompressible flow.

Example 2.6.1 In the operation of a vacuum degassing unit we wish to remove a gas mixture having a mean molecular weight of 10, a viscosity of 1.5×10^{-4} g/cm s, a rate of 0.2 kg/m² s. The vacuum degasser operates at an absolute pressure of 1 mm Hg. If the gases are passed through a duct 1 m in diameter and 80 m long, estimate the downstream pressure required. Assume the process to be isothermal at 1000°C and take the relative roughness of the duct as 2×10^{-4} .

SOLUTION First of all calculate the Reynolds number:

$$N_{Re} = Gd_c/\mu = (0.2 \times 1)/(1.5 \times 10^{-5}) \simeq 1.33 \times 10^4$$

Thus, from Fig. 2.5.1,

$$f_{fr} = 7.8 \times 10^{-3}$$

Let us now turn to Eq. (2.6.19), which has to be solved by trial and error. Upon substituting for the numerical values of the parameters (and converting millimeters mercury to newton per square meter) we have the following:

$$0.04 \ln(132/p_2) + p_2^2/(2.12 \times 10^6) - 0.082 + 0.0499 = 0$$

After trial and error

$$p_2 \simeq 61 \text{ N/m}^2 \quad \text{or} \quad \sim 0.46 \text{ mm Hg}$$

is the desired value of the downstream pressure.

It is seen that in the present case the change in pressure and hence the change in density was quite substantial (over a factor of 2) so that the assumption of incompressible flow would have led to erroneous results.

The reader is urged to perform the trial and error calculations, from which it will become apparent that the kinetic energy term played a major role. This term would have been ignored by assuming incompressible behavior.

Adiabatic flow problems may be calculated in a similar manner, but by substituting Eq. (2.6.12) for the $\int dp/v$ term in the energy balance equation.

There are circumstances when the flow is neither adiabatic nor isothermal, i.e., there is some heat exchange with the surroundings. Such problems are of particular importance in packed bed systems and their discussion will be deferred until Chapter 7.

2.6.3 The Concept of Sonic Velocity Supersonic Nozzles

Let us consider the isothermal flow of a compressible fluid through a pipe, such as discussed in the preceding example 2.6.1.

Upon rearrangement Eq. (2.6.20) may be solved explicitly for G to obtain

$$G^2 = \frac{p_1^2 - p_2^2}{2[\ln(p_1/p_2) + 2f_{fr}L/d_c]p_1v_1} \quad (2.6.23)$$

Upon examining Eq. (2.6.23) it is seen that for a fixed value of p_1 the mass velocity $G = 0$, both when $p_1 = p_2$ and when $p_2 = 0$. It follows from physical arguments that, for a fixed value of p_1 , G must have a maximum of some intermediate value of p_2 . This value of the downstream pressure, at which G is at a maximum, may be found by differentiation. Upon designating this value of p_2 by p_s and denoting the other corresponding parameters (e.g., density, velocity, and mass velocity by p_s , u_s , and G_s) we may write

$$G_s = u_s \rho_s = u_s/v_s \quad (2.6.24)$$

or

$$u_s = (p_s v_s)^{1/2} \quad (2.6.25)^{\dagger}$$

It can be shown[‡] that in these equations u_s corresponds to the speed of propagation of a pressure wave through the fluid or *to the velocity of sound in the fluid*.

In a physical sense this means that, if for a fixed set of upstream conditions the downstream pressure were reduced to below this critical value p_s , the velocity of the fluid would be faster than the rate at which the pressure wave can propagate through the system. In other words the upstream end of the

[†] Equation (2.6.25) readily follows from Eq. (2.6.23) upon differentiating the right-hand side and setting the result at zero.

[‡] For a readable but more detailed discussion of these phenomena the reader is referred to the texts by Shapiro,⁹ Brodkey,¹⁰ and Seshadri and Patankar.¹¹

nozzle would “not know” that the downstream pressure had been reduced below p_s .

The physical result of reducing the downstream pressure below the critical value is a discontinuity, called the shock wave. The physical appearance of a shock wave is illustrated in Fig. 2.6.2.

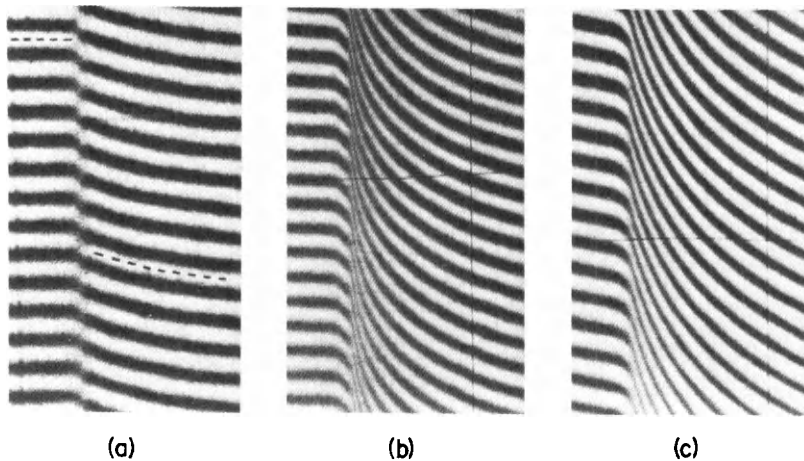


FIG. 2.6.2 Photograph of a shock wave. After Brodkey.¹⁰

The concept of a shock wave and of the finite rate at which the pressure wave can propagate through the system was illustrated using an isothermal system because the mathematics are somewhat tedious for the nonisothermal case. In practice it would be much more realistic to consider the system to be isentropic.

For isentropic conditions the sonic velocity is given by

$$u_s = (\gamma p_s v_s)^{1/2} = (\gamma R T / M_w)^{1/2} \quad (2.6.26)$$

At room temperature u_s is about 335 m/s in air and about 1280 m/s in hydrogen.

It follows from the foregoing that sonic velocities may not be exceeded in a pipe of constant cross section. However, it is possible to achieve supersonic velocities through the use of a convergent-divergent nozzle.

Let us consider a convergent-divergent nozzle, such as sketched in Fig. 2.6.3; as seen in the figure, plane 1 corresponds to the inlet, plane 2 designates the “throat,” i.e., the section, while plane 3 represents the outlet.

If we neglect the frictional, the potential energy terms, and assume that no work is being done on the surroundings, then the differential form of the

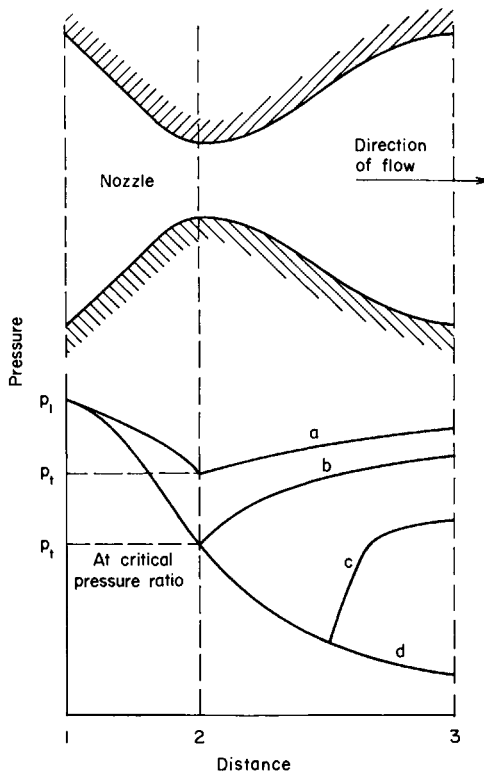


FIG. 2.6.3 The pressure profiles for gas flow through a convergent-divergent nozzle for (a) subsonic flow, (b) sonic velocity at the throat, (c) supersonic flow with shock formation, and for (d) supersonic flow without shock formation.

steady-state energy equation [e.g., Eq. (2.4.6)] may be written as

$$u_m du_m + v dp = 0 \quad (2.6.27)$$

Since $v = 1/\rho$ we can write

$$u_m du_m + \frac{dp}{d\rho} \frac{d\rho}{\rho} = 0 \quad (2.6.28)$$

However, since from Eq. (2.6.24)

$$\frac{dp}{d\rho} = u_s^2$$

the sonic velocity, i.e., the rate of propagation of the pressure wave, Eq. (2.6.28), may be expressed as

$$u_m du_m + u_s^2 d\rho/\rho = 0 \quad (2.6.29)$$

For a conduit of variable cross section the equation of continuity may be written as

$$\frac{d}{dL} (u_m \rho A) = 0 \quad (2.6.30)$$

which, upon performing the differentiation and rearrangement, is given as

$$du_m/u_m + d\rho/\rho + dA/A = 0 \quad (2.6.31)$$

Upon substituting for $d\rho/\rho$ from Eq. (2.6.3) we have

$$(du_m/u_m)(u_m^2/u_s^2 - 1) = dA/A \quad (2.6.32)$$

and $u_m/u_s = N_{Ma}$ is termed the Mach number. Thus Eq. (2.6.32) will take the following form:

$$du_m/u_m = [1/(N_{Ma}^2 - 1)] dA/A \quad (2.6.33)$$

Inspection of Eq. (2.6.33) shows that upon passing through a convergent-divergent nozzle, the fluid behaves in a drastically different manner, depending on whether the flow is supersonic or subsonic.

When the velocity is subsonic ($N_{Ma} < 1$) an increase in the cross-sectional area will cause a decrease in the linear velocity, and vice versa (a decrease in the cross-sectional area will increase the linear velocity). This behavior is to be expected intuitively.

However, Eq. (2.6.33) also shows that when the velocity is supersonic ($N_{Ma} > 1$), an increase in the cross-sectional area will lead in an increase in the linear velocity. The physical reason for this behavior is the fact that in supersonic flow the decrease in density exceeds the increase in the linear velocity, so that the passage has to diverge for the law of mass conservation to be satisfied.

The important consequence of this finding, sketched in Fig. 2.6.4, is that gases may be accelerated to supersonic velocities by using a convergent-divergent nozzle. These nozzles are so designed that sonic velocity is attained at the throat (i.e., plane 2 in Fig. 2.6.3) and then the fluid is further accelerated in the divergent section of the nozzle.

Inspection of Fig. 2.6.4 also shows that if supersonic velocity is not attained at the throat, the velocity will decrease rather than increase in the divergent section. The criteria for attaining sonic velocity at the throat of the nozzle may now be established as follows:

For adiabatic conditions the energy balance between planes 1 and 2 may be written as [where use has been made of Eq. (2.6.12)]

$$\frac{u_{m,2}^2}{2} - \frac{u_{m,1}^2}{2} = p_2 v_2 \left(\frac{\gamma}{\gamma - 1} \right) \left(\frac{p_1^{(\gamma-1)/\gamma}}{p_2} - 1 \right) \quad (2.6.34)$$

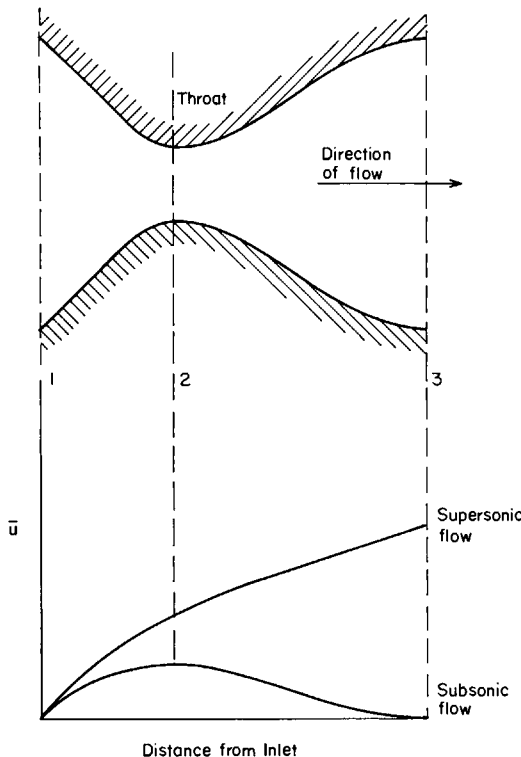


FIG. 2.6.4 Velocity profiles in a convergent-divergent nozzle.

Thus for

$$u_{m,2} = u_s = (\gamma p_s v_s)^{1/2} \quad (2.6.35)$$

the velocity at the throat may now be expressed as

$$N_{Ma}^2 = 1 = \frac{2}{\gamma - 1} \left(\frac{p_1^{(\gamma-1)/\gamma}}{p_2} - 1 \right) \quad (2.6.36)$$

It is seen that the criterion for the attainment of sonic velocity is defined in terms of $\gamma = C_p/C_v$, which is a property value of the gas, and the ratio p_2/p_1 , which is termed the *critical pressure ratio*:

$$(p_2/p_1)_{crit} = [p_2^{\gamma/(\gamma-1)} / (\gamma + 1)] \quad (2.6.37)$$

Values of $(p_2/p_1)_{crit}$ for various gases are given in Table 2.6.1.

If $(p_2/p_1) > (p_2/p_1)_{crit}$, sonic velocity will not be attained in the system. At this stage it may be instructive to illustrate the velocity and density profiles during the passage of a gas through a convergent-divergent nozzle.

TABLE 2.6.1
Critical Pressure Ratios for Various Gases

System	$(p_2/p_1)_{\text{crit}}$ at 288°K
Monoatomic gases and metal vapors	0.49
$\text{H}_2, \text{O}_2, \text{N}_2, \text{HCl}$	0.53
$\text{SO}_2, \text{CO}_2, \text{steam}$	0.55

These profiles are sketched in Fig. 2.6.5 for a particular case. It is seen that the velocity reaches $N_{\text{Ma}} = 1$ at the throat of the nozzle and then increases smoothly downstream, as the gas expands. The corresponding density profile indicates a continuous decrease in the density of the gas as it passes through the nozzle. No shock or discontinuity is seen in this example, thus, the profiles shown would correspond to the pressure profiles depicted in curve d of Fig. 2.6.3.

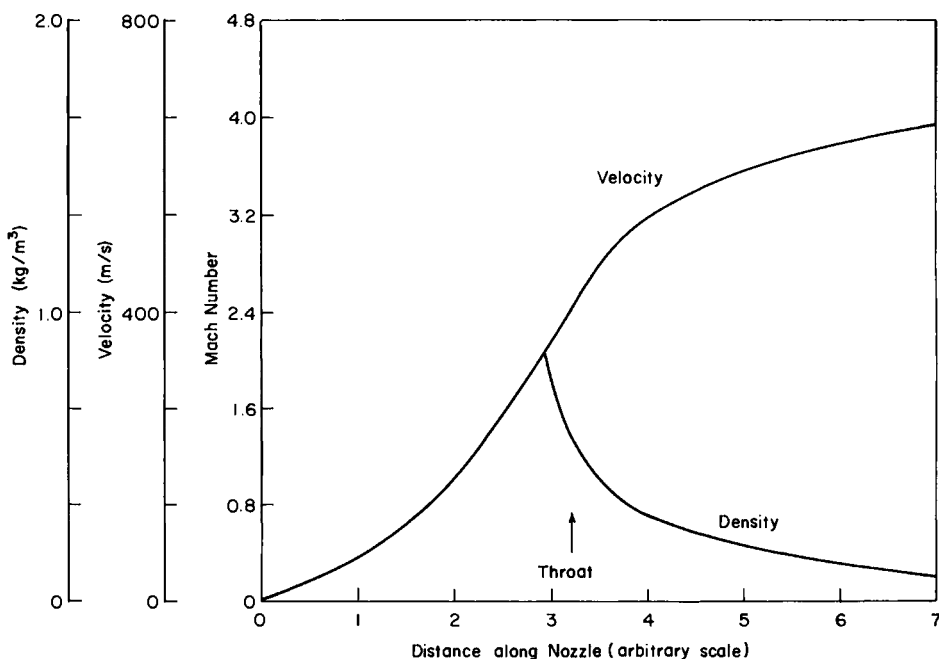


FIG. 2.6.5 Plot of the velocity profile and the corresponding density profile for supersonic flow through a nozzle.

Having established the criteria for sonic velocity at the throat the velocity ceiling in the divergent section may be calculated from

$$\frac{u_{m,3}^2}{2} - \frac{u_{m,2}^2}{2} = p_2 v_2 \left(\frac{\gamma}{\gamma - 1} \right) \left[1 - \left(\frac{p_3}{p_2} \right)^{(\gamma - 1)/2} \right] \quad (2.6.38)$$

where p_2 , v_2 , do of course correspond to p_s and v_s . Equations (2.6.36) and (2.6.38) together with the equation of state enable us to relate the velocity to the pressure in the various sections of the nozzle.

In many instances, however, it is more convenient to make use of information available in tabulated form such as given in Table 2.6.2 for the case of $\gamma = 1.4$. The first column in this table designates the Mach number; the second column gives the ratio (pressure in the nozzle to pressure at the inlet); the corresponding density ratio is given in the subsequent column. The following column denotes the ratio of the cross-sectional area of the

TABLE 2.6.2

Calculated Values of the Mach Number, the Pressure Ratio, and Other Related Parameters for the Isentropic Flow of an Ideal Gas¹⁰

N_{Ma}	p/p_1	ρ/ρ_1	A/A^*	T/T_1	$(p/p_1)(A/A^*)$
0.00	1.000000	1.000000	∞	1.000000	∞
0.10	0.99303	0.99502	5.8213	0.99800	5.7812
0.20	0.97250	0.98027	2.9635	0.99206	2.8820
0.30	0.93947	0.95638	2.0351	0.98232	1.9119
0.40	0.89562	0.92428	1.5901	0.96899	1.4241
0.50	0.84302	0.88517	1.3398	0.95238	1.12951
0.60	0.78400	0.84045	1.1882	0.93284	0.93155
0.70	0.72092	0.79158	1.09437	0.91075	0.78896
0.80	0.65602	0.74000	1.03823	0.88652	0.68110
0.90	0.59126	0.68704	1.00886	0.86058	0.59650
1.00	0.52828	0.63394	1.00000	0.83333	0.52828
1.20	0.41238	0.53114	1.03044	0.77640	0.42493
1.40	0.31424	0.43742	1.1149	0.71839	0.35036
1.60	0.23527	0.35573	1.2502	0.66138	0.29414
1.80	0.17404	0.28682	1.4390	0.60680	0.25044
2.00	0.12780	0.23005	1.6875	0.55556	0.21567
2.30	0.07997	0.16458	2.1931	0.48591	0.17538
2.60	0.05012	0.11787	2.8960	0.42517	0.14513
3.00	0.02722	0.07623	4.2346	0.35714	0.11528
4.00	0.00658	0.02766	10.719	0.23810	0.07059
7.00	0.00024	0.00261	104.143	0.09259	0.02516
10.00	0.00002	0.00050	535.938	0.04762	0.01263
∞	0.00000	0.00000	∞	0.00000	0.00000

nozzle to that of the throat (A^*), while the next column gives the corresponding temperature ratio.

The use of this table will be illustrated by a numerical example; however, before we do this let us remark that the actual total mean flow rate through the nozzle is of course readily calculated from

$$w_{\max} = u_s \rho_s A^* \quad (2.6.39)$$

Upon substituting for u_s from Eq. (2.6.35) and calculating ρ_s from isentropic expansion, after some manipulation we obtain the following:

$$w_{\max} = A^* \left[p_1 \rho_1 \gamma \left(\frac{2}{\gamma - 1} \right)^{(\gamma + 1)/(\gamma - 1)} \right]^{1/2} \quad (2.6.40)$$

which is based on the fact that the maximum velocity at the throat (A^*) is the sonic velocity. Here the units of w_{\max} are mass/time, i.e., kilograms per second. For oxygen, where $\gamma = 1.4$, Eq. (2.6.40) may be written as

$$w_{\max} = 0.47 A^* (p_1 \rho_1)^{1/2} \quad (2.6.41)$$

Example 2.6.2 Estimate the maximum mass flow rate of oxygen through a properly designed convergent–divergent nozzle for the following conditions:

inlet pressure 10 atm

inlet temperature 25°C

throat diameter 2 cm

$\gamma = 1.4$

SOLUTION First of all we convert to SI units. Thus

$$p_1 = 1.01 \times 10^6 \text{ N/m}^2$$

$$T_1 = 298^\circ\text{K}$$

$$A^* = 3.14 \times 10^{-4} \text{ m}^2$$

$$M_w = 32$$

$$\rho_1 = (32 \times 10^3 \times 10)/(2.4 \times 10^4) \simeq 13.3 \text{ kg/m}^3$$

Thus upon substituting in Eq. (2.6.41) we have

$$\begin{aligned} w_{\max} &= 0.47 \times 3.14 \times 10^{-4} \times (1.01 \times 10^6 \times 13.3)^{1/2} \\ &\simeq 0.54 \text{ kg/s} \end{aligned}$$

In this simple problem our sole concern was to calculate the mass flow rate through the nozzle and we paid no attention either to the geometry of the nozzle or to the pressure of the gas exiting the nozzle.

One would tend to calculate somewhat more complex problems in the design of a nozzle for a specific duty, as illustrated in the following example.

Example 2.6.3 We wish to supply oxygen to a 200-ton BOF plant at a rate of 5 kg/s through a single supersonic nozzle. It is desired that the gas should exit the nozzle with a velocity of at least $N_{Ma} = 1.5$, and in order to ensure smooth operation the pressure at the exit should be 1.05 atm. Specify the nozzle dimensions and the upstream oxygen pressure required.

SOLUTION We shall use Table 2.6.2 and work “backwards.” Selecting the entry corresponding to $N_{Ma} = 1.6$, the pressure ratio is $p/p_1 \simeq (p_{exit}/p_1) = 0.235$. Thus taking $p_{exit} = 1.05$ atm,

$$p_1 = (1.05/0.235) \times 1.01 \times 10^5 \simeq 4.51 \times 10^5 \text{ N/m}^2$$

The density at the inlet ρ_1 is given as

$$(32 \times 10^3 \times 4.46)/(2.4 \times 10^4) \simeq 5.95 \text{ kg/m}^3$$

Then A^* may be obtained from Eq. (2.6.40):

$$\begin{aligned} A^* &= 5[4.5 \times 10^5 \times 5.95 \times 1.40(2/2.4)^6]^{-1/2} \\ &\simeq 4.47 \times 10^{-3} \text{ m}^2 \end{aligned}$$

From Table 2.6.2 the pressure at the throat is given as

$$4.5 \times 10^5 \times 0.5 \simeq 2.38 \times 10^5 \text{ N/m}^2 \text{ or } 2.63 \text{ atm}$$

The corresponding temperature is given as

$$0.833 \times 298 \simeq 248^\circ\text{K}$$

The cross-sectional area of the nozzle at the exit is given as

$$1.25 \times 4.47 \times 10^{-3} \simeq 5.59 \times 10^{-3} \text{ m}^2$$

and the corresponding temperature is

$$0.661 \times 298 \simeq 197^\circ\text{K} \text{ or } -76^\circ\text{C}$$

A comment should be made on the fact that in current practice multiple hole lances are being used in oxygen steel-making processes. Nonetheless, the idea that the jet exiting the nozzle should have only a slightly higher pressure than that of the environment is being observed in nozzle design. A good description of the practical considerations involved in the design of nozzles for oxygen lances may be found in the articles by Smith¹² by Sharma *et al.*¹³ and in the BOF monograph.¹⁵

In closing it should be noted that the two groups of problems discussed in this section, namely subsonic flow of gases through pipes and supersonic flow through nozzles, represent but an introduction to a very complex field.

The approximations made here will be acceptable in the majority of calculations involving metals processing operations. A more rigorous treatment of this topic is available in the texts by Shapiro,⁹ Brodkey,¹⁰ and Massey.¹⁴

2.7 The Application of Overall Balances

In the preceding sections we introduced the reader to the overall mass, momentum, and energy balances, defined the friction factor, and showed how these overall balances may be applied to tackling problems involving compressible fluids. The worked examples in these earlier sections were relatively simple and served an illustrative purpose. The practical problems one is likely to encounter in materials processing tend to be rather more complex and are usually less well defined.

Because of the diversity of the problems that may arise there are no set rules for the application of the overall balance technique other than that it is important to recognize the essential features of the problem (ladle discharge, pipe flow, supersonic nozzle, etc.) and to select the control volume carefully, so that it corresponds to the physical reality of the system under consideration. In many instances the physical situation may be complex, and here engineering judgment has to be used to decide on the extent of simplification which is compatible with both the accuracy of the answer needed and the time available for computation. Some illustrative examples of these problems will be presented in this section.

Example 2.7.1 Figure 2.7.1 shows a sketch of an idealized cooling water circuit in which water is being pumped through an orifice meter (1), four valves, a processing unit (2), and a cooling tower. The total horizontal length of the pipe is 300 m and the vertical elevation to the cooling tower is 15 m. If the pressure drop through the processing unit is equivalent to a height loss of 10 m, calculate the pipe diameter required for circulating water at a rate of $0.1 \text{ m}^3/\text{s}$ if the pump has a capacity of 28,000 W at 100% efficiency.

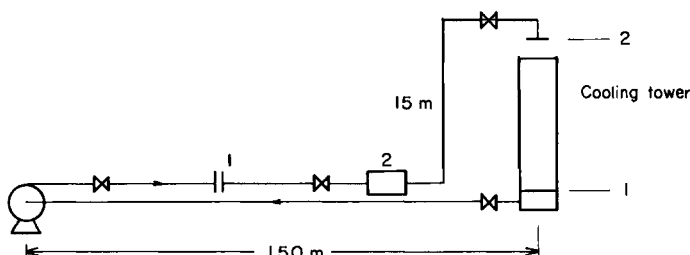


FIG. 2.7.1 An idealized cooling water circuit.

SOLUTION We shall use the overall energy balance equation given by Eq. (2.4.6). Upon substituting for the friction factor and allowing for the fact that the pump does work on the surroundings, we have the following:

$$\frac{u_{2,m}^2 - u_{1,m}^2}{2} + g(z_2 - z_1) + \int_{p_1}^{p_2} \frac{dp}{\rho} + W' + 2f_{fr} \frac{L}{d_c} u_m^2 = 0$$

We shall select the control surfaces as shown in the sketch.

Since the pressure is atmospheric at both surface 1 and surface 2,

$$\int_{p_1}^{p_2} \frac{dp}{\rho} = 0$$

By taking the datum level for the potential energy at plane 1,

$$g(z_2 - z_1) = (15 + 10)g$$

The velocities and the friction factor have to be evaluated by trial and error.

Let us guess

$$d_c = 25 \text{ cm} = 0.25 \text{ m}$$

$$Q = 0.1 \text{ m}^3/\text{s}$$

$$w = 100 \text{ kg/s}$$

$$G = 2.05 \times 10^3 \text{ kg/m}^2 \text{ s}$$

$$N_{Re} = \frac{2.05 \times 10^3 \times 0.25}{10^{-3}} = 5.12 \times 10^5$$

From Fig. 2.5.2

$$f_{fr} = 0.0033$$

Hence,

$$u_m = 2.05 \text{ m/s}$$

$$g(15 + 10) + W' + 2 \times 3.3 \times 10^{-3} \times 300 \frac{(2.05)^2}{0.25} = 0$$

$$245 + W' + 33.3 = 0$$

$$W' = -278 \text{ m}^2/\text{s}^2$$

$$\text{Power} = -278 \times 100 \text{ (kg m/s}^2\text{)(m/s)}$$

$$= -27,800 \text{ N m/s} = -27,800 \text{ W}$$

which is quite close to 28,000 W. Hence, $d_c = 0.25 \text{ m}$.

Example 2.7.2 Figure 2.7.2 shows a ladle containing molten steel which discharges into a tundish through a bottom pouring arrangement. If the ladle diameter is 3 m and the initial metal depth is 2.5 m, estimate the time

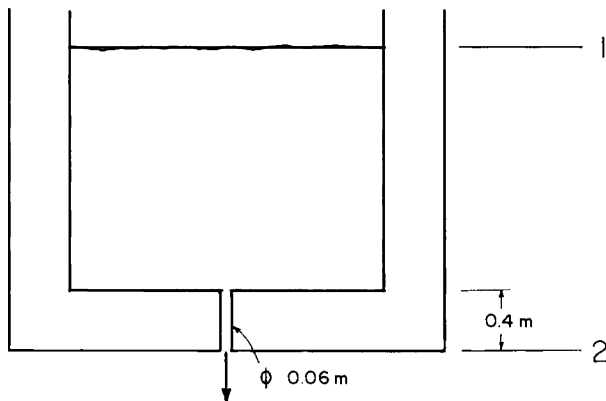


FIG. 2.7.2 Sketch of the ladle dimensions in Example 2.7.2.

required for emptying the ladle. As shown in the figure, the discharge nozzle is 0.4 m long, and 0.06 m in diameter. The density of molten steel is $7.1 \times 10^3 \text{ kg/m}^3$ and its viscosity is $1.5 \times 10^{-3} \text{ kg/m s}$.

SOLUTION This problem is similar to that discussed earlier in Example 2.2.1 except for the fact that in the previous case the velocity was given, while in the present case we can derive it. The overall mass balance [Eq. (2.2.7)] is written as

$$\frac{dM_T}{dt} = -w_2 = -u_{z,m}\rho A_2 \quad (\text{i})$$

The overall energy balance takes the following form:

$$u_{z,m}^2/2 - g(h + 0.4) = 0 \quad (\text{ii})$$

Hence

$$u_{z,m} = [2g(h + 0.4)]^{1/2} \quad (\text{iii})$$

The amount of metal in the ladle at a given time is

$$M_T = hA_1\rho \quad (\text{iv})$$

On combining the above, we have

$$A_1 \frac{dh}{dt} = -[2g(H + 0.4)]^{1/2} A_2$$

which is readily integrated to obtain

$$\int_0^{2.5} \frac{dh}{(h + 0.4)^{1/2}} = \left(\frac{A_2}{A_1}\right)(2g)^{1/2} t_e$$

Let $h + 0.4 = h^*$:

$$\int_{0.4}^{2.9} h^{*-1/2} dh^* = \left(\frac{A_2}{A_1}\right)(2g)^{1/2} t_e$$

$$h^{*1/2} \int_{0.4}^{2.9} = \left(\frac{A_2}{A_1}\right)(g/2)^{1/2} t_e$$

$$t_e = (A_2/A_1)(2/g)^{1/2}[2.9^{1/2} - 0.4^{1/2}]$$

$$= (3/0.06)^2(2/9.81)^{1/2}(1.071) \text{ s}$$

$$= (2500)(0.45)(1.071)$$

$$= 25 \times 45 \times 1.071$$

$$= 1204.87 \text{ s}$$

$$\approx 20 \text{ min}$$

Example 2.7.3 Let us consider a furnace, holding molten steel at 1600°C in an argon atmosphere initially at 1 atm pressure.

We wish to establish a reduced pressure of 1 mm Hg in the freeboard of the furnace by connecting the freeboard to a powerful vacuum pump.

If the pressure P_2 at the inlet to the pump is suddenly lowered to 0.5 mm Hg, estimate the time required for attaining 1 mm Hg in the freeboard of the vessel.

Data

freeboard height	1.5 m
vessel diameter	1 m
diameter of the pipe connecting the freeboard to the vacuum pump	0.25 m

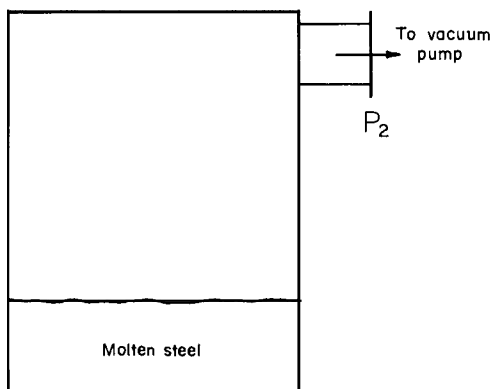


FIG. 2.7.3 Sketch of the system in Example 2.7.3.

Neglect the frictional resistance in the connecting pipe and assume a leakage of $0.01 \text{ m}^3/\text{s}$ of argon (at 1 atm and 300°K).

SOLUTION Define: $Q_1 = 0.01 \text{ m}^3/\text{s}$, molecular weight of argon is 40; hence,

$$\begin{aligned}\rho &= PM_w/RT = (1 \times 40)/(82.06 \times 300) \text{ g/cc} \\ &= 40/(82.06 \times 300) \times 10^3 \text{ kg/m}^3 = 1.62 \text{ kg/m}^3 \\ w_1 &= 0.0162 \text{ kg/s}\end{aligned}$$

The overall mass balance is

$$\frac{dM_T}{dt} = -(-w_e + u_{z,m}A_2\rho_2) \quad (\text{i})$$

Moreover, we have that

$$M_T = A_1 \times L \times \rho_1$$

where L is the freeboard height,

$$\rho_1 = P_1 M_w / RT$$

The energy balance now written for a compressible fluid is

$$\frac{u_{2,m^2}}{2} + \int_{P_1}^{P_2} \frac{dP}{\rho} + g(z_2 - z_1) = 0 \quad (\text{ii})$$

or

$$\frac{u_{2,m^2}}{2} + \int_{P_1}^{P_2} \frac{dP}{PM_w/RT} + gL = 0 \quad (\text{iii})$$

$$\frac{u_{2,m^2}}{2} + \frac{RT}{M_w} \int \frac{dP}{P} + gL = 0 \quad (\text{iv})$$

$$\frac{u_{2,m^2}}{2} + \frac{RT}{M_w} \ln \frac{P_2}{P_1} + gL = 0 \quad (\text{v})$$

$$\frac{u_{2,m^2}}{2} = \frac{RT}{M_w} \ln \frac{P_1}{P_2} - gL \quad (\text{vi})$$

The mass balance may now be recast as

$$A_1 L \frac{d\rho}{dt} = -(-w_1 + u_{2,m}A_2\rho_2)$$

or

$$\frac{A_1 LM_w}{RT} \frac{dP_1}{dt} = - \left[-w_1 + A_2 \frac{P_2 M_w}{RT} \left(\frac{RT}{M_w} \ln \frac{P_1}{P_2} - gL \right)^{1/2} \right] \quad (\text{vii})$$

so that

$$dP_1/dt = -[\alpha + (\beta \ln P_1/P_2 - \gamma)^{1/2}] \quad (\text{viii})$$

where

$$\begin{aligned} \alpha &= -w_1 \times RT/(M_w \times A_i L) \\ \beta &= (A_2/A_1 \times P_2/L)^2 RT/M_w \\ \gamma &= (A_2/A_1 \times P_2/L)^2 \times gL \\ \alpha &= -0.0162 \times \frac{8.314 \times 300}{40} \frac{1}{(3.14/4)(1)^2 \times 1.5} \text{ N/m}^2 \text{ s} \\ &= -(0.0162 \times 8.314 \times 30)/(3.14 \times 1.5) \\ &= -0.858 \text{ N/m}^2 \text{ s} \end{aligned}$$

Eq. (viii) may now be integrated numerically.

References

1. R. B. Bird, W. E. Stewart, and E. N. Lightfoot, "Transport Phenomena." Wiley, New York, 1960.
2. J. R. Welty, C. E. Wicks, and R. E. Wilson, "Fundamentals of Momentum, Heat and Mass Transfer." Wiley, New York, 1969.
3. J. M. Coulson and J. F. Richardson, "Chemical Engineering," 2nd ed., Vol. 1, p. 19. Pergamon, Oxford.
4. J. H. Perry, "Chemical Engineer's Handbook." 5th ed. McGraw-Hill, New York, 1973.
5. J. G. Kudsen and D. L. Katz, "Fluid Mechanics and Heat Transfer." McGraw-Hill, New York, 1968.
6. V. Streeter, ed., "Handbook of Fluid Mechanics." McGraw-Hill, New York, 1961.
7. F. M. Henderson, "Open Channel Flow." Macmillan, New York, 1966.
8. V. T. Chow, "Open Channel Hydraulics," McGraw-Hill, New York, 1959.
9. A. Shapiro, "The Dynamics and Thermodynamics of Compressible Fluid Flow." Ronald, New York, 1953.
10. R. A. Brodley, "The Phenomena of Fluid Motions." Addison-Wesley, Reading, Massachusetts, 1967.
11. C. V. Seshadri and S. V. Patankar, "Elements of Fluid Mechanics." Prentice-Hall of India Ltd., New Delhi, 1971.
12. G. C. Smith, *J. Met.* **18**, 846 (1966).
13. S. K. Sharma, J. W. Hlinka, and D. W. Kern, *I&SM* **4**, No. 7, (1977).
14. B. S. Massey, "Mechanics of Fluids." Van Nostrand-Reinhold, Princeton, New Jersey, 1970.
15. R. D. Pehlke, W. F. Porter, R. F. Urban, and J. M. Gaines, eds., "BOF Steelmaking," Vol. 2. The Iron and Steel Society, New York, 1975.

Chapter 3

The Differential Equations of Fluid Flow

In the previous chapter we introduced the reader to the technique of overall, macroscopic balances. It was shown that this is a very powerful tool for tackling a broad range of fluid flow problems where some overall relationship is required between the pressure drop and flow rate, the forces exerted on some body in contact with moving fluids, the power required for pumping, and the sizing of pipelines, nozzles, and the like. The mathematical manipulations were quite elementary, and the reader will have noticed that the principal variables involved bulk, averaged quantities, and that in the majority of cases certain empirical relationships had to be used (e.g., friction factor correlations, expressions for head losses in pipe fittings, etc.) to complete the definition of the problem.

While overall balances represent a very satisfactory engineering approach to many practical problems, there are many other equally important practical situations where more detailed information is required than available from the consideration of overall balances. Typical examples of such cases include knowledge of the velocity field in the mold region of a continuous casting machine, the flow patterns (i.e., detailed velocity profile) in vacuum degassing units, problems associated with the flotation characteristics of inclusion particles, and the like. For these more complex problems the differential equivalents of the previously given overall mass and momentum balance equations constitute the proper starting point for the formulation.

In this chapter we shall develop the differential equations of fluid flow. Regarding the organization of the material, in Section 3.1 we shall describe the differential mass balance that is the equation of continuity. Section 3.2 will be devoted to the differential momentum balance, i.e., the equation of motion. The stream function, velocity potential, and the vorticity will be introduced in Section 3.3, while simple ideal flow problems will be treated in Section 3.4.

Finally, Section 3.5 will be devoted to the discussion of a range of laminar fluid flow problems that can be formulated and tackled through the use of the differential equation of motion.

3.1 The Equation of Continuity

Let us consider a cubical stationary volume element $\Delta x \Delta y \Delta z$, sketched in Fig. 3.1.1, through which a fluid is flowing.

The equation of continuity expresses the conservation of mass over the element, in other words

$$\left[\begin{array}{c} \text{rate of} \\ \text{mass input} \end{array} \right] - \left[\begin{array}{c} \text{rate of} \\ \text{mass output} \end{array} \right] = \left[\begin{array}{c} \text{rate of accumulation of mass} \end{array} \right] \quad (3.1.1)$$

Since the orientation of the cube was so selected that faces 1A and 2A are perpendicular to the x axis, faces 1B and 2B are perpendicular to the y axis, etc. The input or output of material across these faces is readily calculated by forming the product (cross-sectional area) \times (fluid velocity) \times (fluid density).

Thus the net input of material in the x direction is given as

$$\Delta y \Delta z \rho u_x|_x - \Delta y \Delta z \rho u_x|_{x+\Delta x}$$

input across face 1A	output across face 2A
-------------------------	--------------------------

Writing similar expressions for the net input in the y and the z direction and upon noting that the accumulation of mass in the element is given by

$$\text{accumulation} = \Delta x \Delta y \Delta z \frac{\partial \rho}{\partial t}$$

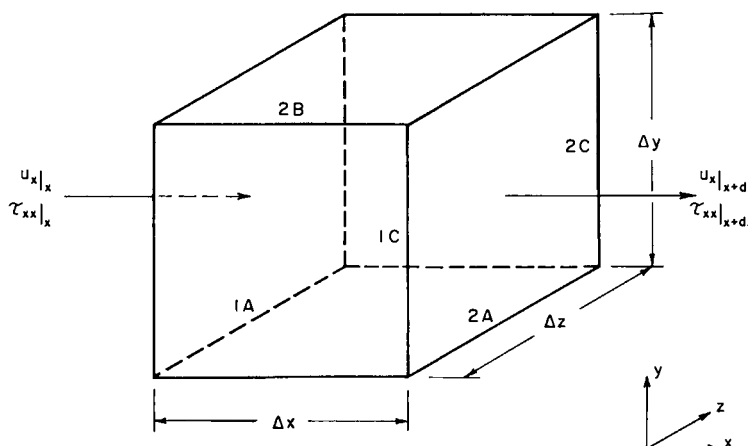


FIG. 3.1.1 A cubical volume element

the mass balance may be written as

$$\begin{aligned} \Delta z \Delta y [\rho u_x|_x - \rho u_x|_{x+\Delta x}] + \Delta x \Delta z [\rho u_y|_y - \rho u_y|_{y+\Delta y}] \\ + \Delta x \Delta y [\rho u_z|_z - \rho u_z|_{z+\Delta z}] = \Delta x \Delta y \Delta z \frac{\partial \rho}{\partial t} \end{aligned} \quad (3.1.2)$$

net input of material = accumulation

Upon dividing both sides by $\Delta x \Delta y \Delta z$ and setting $\Delta x, \Delta y, \Delta z \rightarrow 0$ and recalling the definition of the first derivative, that is,

$$u_x|_{x+\Delta x} - u_x|_x / \Delta x = \frac{\partial u_x}{\partial x}, \quad \text{when } \Delta x \rightarrow 0$$

then Eq. (3.1.2) may be expressed as

$$-\left[\frac{\partial}{\partial x} (\rho u_x) + \frac{\partial}{\partial y} (\rho u_y) + \frac{\partial}{\partial z} (\rho u_z) \right] = \frac{\partial \rho}{\partial t} \quad (3.1.3)$$

Or, using vector notation,

$$\frac{\partial \rho}{\partial t} = -\nabla \cdot (\rho \mathbf{u}) \quad (3.1.4)$$

Here ∇ is a vector differential operator, termed “del” or “nabla,” which is defined as

$$\nabla = \left(\mathbf{i} \frac{\partial}{\partial x} + \mathbf{j} \frac{\partial}{\partial y} + \mathbf{k} \frac{\partial}{\partial z} \right) \quad (3.1.5)$$

where \mathbf{i} , \mathbf{j} , and \mathbf{k} are unit vectors in the x , y , and z directions, respectively. The reader should note that the “dot” product of two vectors (∇ and \mathbf{u} in the present case) is a scalar quantity. The quantity $\nabla \cdot (\rho \mathbf{u})$ is sometimes called the divergence of $(\rho \mathbf{u})$.

For an arbitrary volume element of volume ΔV and surface A the divergence of $\rho \mathbf{u}$ is defined as

$$\text{div}(\rho \mathbf{u}) = \lim_{\Delta V \rightarrow 0} \iint_A (\rho \mathbf{u}) \cdot \mathbf{n} dA \quad (3.1.6)$$

where \mathbf{n} is the unit vector normal to the surface element dA . The definition of $\nabla \cdot \rho \mathbf{u} = \text{div}(\rho \mathbf{u})$ given by Eq. (3.1.6) is helpful in a physical sense, because it clearly shows that $\text{div}(\rho \mathbf{u})$ is the net outflow of material from the control volume. Thus for a fixed size of the control volume the negative of this net outflow must equal the rate of change of density, which is precisely what is expressed by Eq. (3.1.4).

The equation of continuity in cylindrical and in spherical coordinates is given in Table 3.1.1.

TABLE 3.1.1

The Equation of Continuity in Cylindrical and in Spherical Coordinates

Cylindrical coordinates (r, θ, z) :

$$\frac{\partial \rho}{\partial t} + \frac{1}{r} \frac{\partial}{\partial r} (\rho r u_r) + \frac{1}{r} \frac{\partial}{\partial \theta} (\rho u_\theta) + \frac{\partial}{\partial z} (\rho u_z) = 0 \quad (\text{i})$$

Spherical coordinates (r, θ, ϕ) :

$$\frac{\partial \rho}{\partial t} + \frac{1}{r^2} \frac{\partial}{\partial r} (\rho r^2 u_r) + \frac{1}{r \sin \theta} \frac{\partial}{\partial \theta} (\rho u_\theta \sin \theta) + \frac{1}{r \sin \theta} \frac{\partial}{\partial \phi} (\rho u_\phi) = 0 \quad (\text{ii})$$

In some cases it is convenient to represent Eq. (3.1.4) in terms of the substantial time derivative. Thus we have

$$\frac{D\rho}{Dt} = -\rho(\nabla \cdot \mathbf{u}) \quad (3.1.7)$$

where

$$\frac{D}{Dt}(\) = \frac{\partial}{\partial t}(\) + u_x \frac{\partial}{\partial x}(\) + u_y \frac{\partial}{\partial y}(\) + u_z \frac{\partial}{\partial z}(\) \quad (3.1.8)$$

In a physical sense $(D/Dt)()$, the substantial time derivative, designates the time derivative of a quantity evaluated on a path following the motion of the fluid.

For *steady-state condition* $\partial \rho / \partial t = 0$ and the equation of continuity is given as

$$\nabla \cdot (\rho \mathbf{u}) = 0 \quad (3.1.9)$$

or, when $\rho = \text{const}$, in Cartesian coordinates we have

$$\frac{\partial u_x}{\partial x} + \frac{\partial u_y}{\partial y} + \frac{\partial u_z}{\partial z} = 0 \quad (3.1.10)$$

The development of the equation of continuity on the preceding pages may have appeared as a trivial exercise to the reader. It has to be stressed however that, because the equation of continuity expresses the conservation of mass, it has to be satisfied always. In fact the equation of continuity is an integral and inherent part of the statement of any fluid flow problem.

3.2 The Equation of Motion

Let us consider a cubic space element $(\Delta x \Delta y \Delta z)$, such as sketched in Fig. 3.1.1, through which a fluid is flowing and establish a differential momentum balance.

On the analogy of the overall momentum balance presented in Section 2.4 the statement of the differential momentum balance has to express Newton's law:

$$\begin{aligned} & \left[\begin{array}{l} \text{rate of} \\ \text{momentum input} \\ \text{into the element} \end{array} \right] - \left[\begin{array}{l} \text{rate of} \\ \text{momentum output} \\ \text{from the element} \end{array} \right] \\ & + \left[\begin{array}{l} \text{sum of forces} \\ \text{acting on} \\ \text{the element} \end{array} \right] = \left[\begin{array}{l} \text{rate of momentum} \\ \text{accumulation} \\ \text{the element} \end{array} \right] \end{aligned} \quad (3.2.1)$$

The vectorial nature of Eq. (3.2.1) has to be stressed to the reader. Both the momentum and the forces acting on the fluid element are vectorial quantities.

Let us now examine the mechanism whereby the momentum may be transferred into and out of the volume element first and then let us proceed by considering the forces that act on the volume element.

3.2.1 Momentum Transfer

Momentum may be transferred due to bulk motion of the fluid, a mechanism which is termed the *convective transfer* of momentum.

Thus x momentum, i.e., the quantity (ρu_x) which has the dimension of momentum per unit volume, may be transferred into the element due to the velocity components u_x, u_y, u_z , giving rise to terms like $(\rho u_x)u_x, (\rho u_x)u_y, (\rho u_x)u_z$.

In this regard it may be helpful to think of (ρu_x) as the "concentration" of x momentum.

Momentum may be transferred also due to the components of the stress tensor acting on the element. The reader will recall that, in Chapter 1, Section 1.3, in the definition of the Newtonian viscosity, τ_{yx}, τ_{yz} , etc., i.e., the components of the stress tensor were interpreted as momentum fluxes.

3.2.2 Forces Acting on the Element

As discussed in Chapter 1, the forces acting on a fluid element may be divided into *surface forces*, which act on the surface of the element (e.g., due to pressure), and *body forces*, which act on the bulk of the element and are caused by a *force field* such as gravity or an externally imposed electromagnetic force field.

Let us now combine the terms of the momentum balance equation enumerated above to establish a balance on the x component of momentum.

TABLE 3.2.1

The Equation of Motion in Rectangular Coordinates (x, y, z)In terms of τ :

$$\begin{aligned} \text{x-component} \quad & \rho \left(\frac{\partial u_x}{\partial t} + u_x \frac{\partial u_x}{\partial x} + u_y \frac{\partial u_x}{\partial y} + u_z \frac{\partial u_x}{\partial z} \right) \\ & = -\frac{\partial p}{\partial x} - \left(\frac{\partial \tau_{xx}}{\partial x} + \frac{\partial \tau_{yx}}{\partial y} + \frac{\partial \tau_{zx}}{\partial z} \right) + \rho g_x \end{aligned} \quad (1)$$

$$\begin{aligned} \text{y-component} \quad & \rho \left(\frac{\partial u_y}{\partial t} + u_x \frac{\partial u_y}{\partial x} + u_y \frac{\partial u_y}{\partial y} + u_z \frac{\partial u_y}{\partial z} \right) \\ & = -\frac{\partial p}{\partial y} - \left(\frac{\partial \tau_{xy}}{\partial x} + \frac{\partial \tau_{yy}}{\partial y} + \frac{\partial \tau_{zy}}{\partial z} \right) + \rho g_y \end{aligned} \quad (2)$$

$$\begin{aligned} \text{z-component} \quad & \rho \left(\frac{\partial u_z}{\partial t} + u_x \frac{\partial u_z}{\partial x} + u_y \frac{\partial u_z}{\partial y} + u_z \frac{\partial u_z}{\partial z} \right) \\ & = -\frac{\partial p}{\partial z} - \left(\frac{\partial \tau_{xz}}{\partial x} + \frac{\partial \tau_{yz}}{\partial y} + \frac{\partial \tau_{zz}}{\partial z} \right) + \rho g_z \end{aligned} \quad (3)$$

For a Newtonian fluid with constant ρ and μ :

$$\begin{aligned} \text{x-component} \quad & \rho \left(\frac{\partial u_x}{\partial t} + u_x \frac{\partial u_x}{\partial x} + u_y \frac{\partial u_x}{\partial y} + u_z \frac{\partial u_x}{\partial z} \right) \\ & = -\frac{\partial p}{\partial x} + \mu \left(\frac{\partial^2 u_x}{\partial x^2} + \frac{\partial^2 u_x}{\partial y^2} + \frac{\partial^2 u_x}{\partial z^2} \right) + \rho g_x \end{aligned} \quad (1A)$$

$$\begin{aligned} \text{y-component} \quad & \rho \left(\frac{\partial u_y}{\partial t} + u_x \frac{\partial u_y}{\partial x} + u_y \frac{\partial u_y}{\partial y} + u_z \frac{\partial u_y}{\partial z} \right) \\ & = -\frac{\partial p}{\partial y} + \mu \left(\frac{\partial^2 u_y}{\partial x^2} + \frac{\partial^2 u_y}{\partial y^2} + \frac{\partial^2 u_y}{\partial z^2} \right) + \rho g_y \end{aligned} \quad (1B)$$

$$\begin{aligned} \text{z-component} \quad & \rho \left(\frac{\partial u_z}{\partial t} + u_x \frac{\partial u_z}{\partial x} + u_y \frac{\partial u_z}{\partial y} + u_z \frac{\partial u_z}{\partial z} \right) \\ & = -\frac{\partial p}{\partial z} + \mu \left(\frac{\partial^2 u_z}{\partial x^2} + \frac{\partial^2 u_z}{\partial y^2} + \frac{\partial^2 u_z}{\partial z^2} \right) + \rho g_z \end{aligned} \quad (1C)$$

Thus we have

$$\Delta y \Delta z [\rho u_x u_x|_x - \rho u_x u_x|_{x+\Delta x}] + \Delta x \Delta z [\rho u_x u_y|_y - \rho u_x u_y|_{y+\Delta y}] + \Delta x \Delta y [\rho u_x u_z|_z - \rho u_x u_z|_{z+\Delta z}]$$

(net input of x momentum due to convection)

$$+ \Delta y \Delta z [\tau_{xx}|_x - \tau_{xx}|_{x+\Delta x}]$$

(net diffusive input of x momentum due to the normal stress)

$$+ \Delta x \Delta z [\tau_{yx}|_y - \tau_{yx}|_{y+\Delta y}] + \Delta x \Delta y [\tau_{zx}|_z - \tau_{zx}|_{z+\Delta z}]$$

(net diffusive input of momentum due to shear stresses)

$$+ \Delta y \Delta z [p|_x - p|_{x+\Delta x}] + \rho F_{bx} (\Delta x \Delta y \Delta z)$$

(surface force due to pressure) + (body force in x direction)

$$= \Delta x \Delta y \Delta z \frac{\partial(\rho u_x)}{\partial t} \quad (3.2.2)$$

(accumulation of momentum).

Upon dividing both sides of Eq. (3.2.2) by $(\Delta x \Delta y \Delta z)$ and setting $\Delta x, \Delta y, \Delta z \rightarrow 0$ we obtain the x component of the overall momentum balance:

$$-\left[\frac{\partial}{\partial x} (\rho u_x u_x) + \frac{\partial}{\partial y} (\rho u_x u_y) + \frac{\partial}{\partial z} (\rho u_x u_z) \right]$$

(net convective input of momentum)

$$-\left[\frac{\partial}{\partial x} \tau_{xx} + \frac{\partial}{\partial y} \tau_{yx} + \frac{\partial}{\partial z} \tau_{zx} \right]$$

(net diffusive input of momentum)

$$-\frac{\partial p}{\partial x} + \rho F_{bx} = \frac{\partial(\rho u_x)}{\partial t} \quad (3.2.3)$$

$$\begin{bmatrix} \text{sum of forces acting} \\ \text{on the element} \end{bmatrix} = \begin{bmatrix} \text{accumulation} \\ \text{of momentum} \end{bmatrix}$$

The y and z components of the differential momentum balance equation are readily obtained by following an analogous procedure. Thus we have

$$\begin{aligned} &-\left[\frac{\partial}{\partial x} (\rho u_y u_x) + \frac{\partial}{\partial y} (\rho u_y u_y) + \frac{\partial}{\partial z} (\rho u_y u_z) \right] \\ &-\left[\frac{\partial}{\partial x} (\tau_{xy}) + \frac{\partial}{\partial y} (\tau_{yy}) + \frac{\partial}{\partial z} (\tau_{zy}) \right] - \frac{\partial p}{\partial y} + \rho F_{by} = \frac{\partial}{\partial t} \rho u_y \quad (3.2.4) \end{aligned}$$

for the y component and

$$\begin{aligned} &-\left[\frac{\partial}{\partial x} (\rho u_z u_x) + \frac{\partial}{\partial y} (\rho u_z u_y) + \frac{\partial}{\partial z} (\rho u_z u_z) \right] \\ &-\left[\frac{\partial}{\partial x} (\tau_{xz}) + \frac{\partial}{\partial y} (\tau_{yz}) + \frac{\partial}{\partial z} (\tau_{zz}) \right] - \frac{\partial p}{\partial z} + \rho F_{bz} = \frac{\partial}{\partial t} (\rho u_z) \quad (3.2.5) \end{aligned}$$

for the z component. The equivalent for the z component form of Eqs. (3.2.3)–(3.2.5) in cylindrical and in spherical coordinates is given in Tables 3.2.2 and 3.2.3.

It is convenient to write Eqs. (3.2.3)–(3.2.5) in vector notation as

$$\frac{\partial}{\partial t} \rho \mathbf{u} = -\nabla \cdot \rho \mathbf{u} \mathbf{u} - \nabla p - \nabla \cdot \boldsymbol{\tau} + \rho \mathbf{F}_b \quad (3.2.6)$$

TABLE 3.2.2

The Equation of Motion in Cylindrical Coordinates (r, θ, z)

In terms of $\boldsymbol{\tau}$:

$$\begin{aligned} r\text{-component} \quad & \rho \left(\frac{\partial u_r}{\partial t} + u_r \frac{\partial u_r}{\partial r} + \frac{u_\theta}{r} \frac{\partial u_r}{\partial \theta} - \frac{u_\theta^2}{r} + u_z \frac{\partial u_r}{\partial z} \right) \\ &= -\frac{\partial p}{\partial r} - \left(\frac{1}{r} \frac{\partial}{\partial r} (r \tau_{rr}) + \frac{1}{r} \frac{\partial \tau_{r\theta}}{\partial \theta} - \frac{\tau_{\theta\theta}}{r} + \frac{\partial \tau_{rz}}{\partial z} \right) + \rho g_r \end{aligned} \quad (1)$$

$$\begin{aligned} \theta\text{-component} \quad & \rho \left(\frac{\partial u_\theta}{\partial t} + u_r \frac{\partial u_\theta}{\partial r} + \frac{u_\theta}{r} \frac{\partial u_\theta}{\partial \theta} + \frac{u_r u_\theta}{r} + u_z \frac{\partial u_\theta}{\partial z} \right) \\ &= -\frac{1}{r} \frac{\partial p}{\partial \theta} - \left(\frac{1}{r^2} \frac{\partial}{\partial r} (r^2 \tau_{r\theta}) + \frac{1}{r} \frac{\partial \tau_{\theta\theta}}{\partial \theta} + \frac{\partial \tau_{\theta z}}{\partial z} \right) + \rho g_\theta \end{aligned} \quad (2)$$

$$\begin{aligned} z\text{-component} \quad & \rho \left(\frac{\partial u_z}{\partial t} + u_r \frac{\partial u_z}{\partial r} + \frac{u_\theta}{r} \frac{\partial u_z}{\partial \theta} + u_z \frac{\partial u_z}{\partial z} \right) \\ &= -\frac{\partial p}{\partial z} - \left(\frac{1}{r} \frac{\partial}{\partial r} (r \tau_{rz}) + \frac{1}{r} \frac{\partial \tau_{\theta z}}{\partial \theta} + \frac{\partial \tau_{zz}}{\partial z} \right) + \rho g_z \end{aligned} \quad (3)$$

For a Newtonian fluid with constant ρ and μ :

$$\begin{aligned} r\text{-component} \quad & \rho \left(\frac{\partial u_r}{\partial t} + u_r \frac{\partial u_r}{\partial r} + \frac{u_\theta}{r} \frac{\partial u_r}{\partial \theta} - \frac{u_\theta^2}{r} + u_z \frac{\partial u_r}{\partial z} \right) \\ &= -\frac{\partial p}{\partial r} + \mu \left[\frac{\partial}{\partial r} \left(\frac{1}{r} \frac{\partial}{\partial r} (r u_r) \right) + \frac{1}{r^2} \frac{\partial^2 u_r}{\partial \theta^2} - \frac{2}{r^2} \frac{\partial u_\theta}{\partial \theta} + \frac{\partial^2 u_r}{\partial z^2} \right] + \rho g_r \end{aligned} \quad (1A)$$

$$\begin{aligned} \theta\text{-component} \quad & \rho \left(\frac{\partial u_\theta}{\partial t} + u_r \frac{\partial u_\theta}{\partial r} + \frac{u_\theta}{r} \frac{\partial u_\theta}{\partial \theta} + \frac{u_r u_\theta}{r} + u_z \frac{\partial u_\theta}{\partial z} \right) \\ &= -\frac{1}{r} \frac{\partial p}{\partial \theta} + \mu \left[\frac{\partial}{\partial r} \left(\frac{1}{r} \frac{\partial}{\partial r} (r u_\theta) \right) + \frac{1}{r^2} \frac{\partial^2 u_\theta}{\partial \theta^2} + \frac{2}{r^2} \frac{\partial u_r}{\partial \theta} + \frac{\partial^2 u_\theta}{\partial z^2} \right] + \rho g_\theta \end{aligned} \quad (2A)$$

$$\begin{aligned} z\text{-component} \quad & \rho \left(\frac{\partial u_z}{\partial t} + u_r \frac{\partial u_z}{\partial r} + \frac{u_\theta}{r} \frac{\partial u_z}{\partial \theta} + u_z \frac{\partial u_z}{\partial z} \right) \\ &= -\frac{\partial p}{\partial z} + \mu \left[\frac{1}{r} \frac{\partial}{\partial r} \left(\frac{\partial u_z}{\partial r} \right) + \frac{1}{r^2} \frac{\partial^2 u_z}{\partial \theta^2} + \frac{\partial^2 u_z}{\partial z^2} \right] + \rho g_z \end{aligned} \quad (3A)$$

TABLE 3.2.3
The Equation of Motion in Spherical Coordinates (r, θ, ϕ)

In terms of τ :

$$\begin{aligned}
 \text{r-component} \quad & \rho \left(\frac{\partial u_r}{\partial t} + u_r \frac{\partial u_r}{\partial r} + \frac{u_\theta}{r} \frac{\partial u_r}{\partial \theta} + \frac{u_\phi}{r \sin \theta} \frac{\partial u_r}{\partial \phi} - \frac{u_\theta^2 + u_\phi^2}{r} \right) \\
 & = -\frac{\partial p}{\partial r} - \left(\frac{1}{r^2} \frac{\partial}{\partial r} (r^2 \tau_{rr}) + \frac{1}{r \sin \theta} \frac{\partial}{\partial \theta} (\tau_{r\theta} \sin \theta) \right. \\
 & \quad \left. + \frac{1}{r \sin \theta} \frac{\partial \tau_{r\phi}}{\partial \phi} - \frac{\tau_{\theta\theta} + \tau_{\phi\phi}}{r} \right) + \rho g_r
 \end{aligned} \tag{1}$$

$$\begin{aligned}
 \theta\text{-component} \quad & \rho \left(\frac{\partial u_\theta}{\partial t} + u_r \frac{\partial u_\theta}{\partial r} + \frac{u_\theta}{r} \frac{\partial u_\theta}{\partial \theta} + \frac{u_\phi}{r \sin \theta} \frac{\partial u_\theta}{\partial \phi} + \frac{u_r u_\theta}{r} - \frac{u_\phi^2 \cot \theta}{r} \right) \\
 & = -\frac{1}{r} \frac{\partial p}{\partial \theta} - \left(\frac{1}{r^2} \frac{\partial}{\partial r} (r^2 \tau_{r\theta}) + \frac{1}{r \sin \theta} \frac{\partial}{\partial \theta} (\tau_{\theta\theta} \sin \theta) \right. \\
 & \quad \left. + \frac{1}{r \sin \theta} \frac{\partial \tau_{\theta\phi}}{\partial \phi} + \frac{\tau_{r\theta}}{r} - \frac{\cot \theta}{r} \tau_{\phi\phi} \right) + \rho g_\theta
 \end{aligned} \tag{2}$$

$$\begin{aligned}
 \phi\text{-component} \quad & \rho \left(\frac{\partial u_\phi}{\partial t} + u_r \frac{\partial u_\phi}{\partial r} + \frac{u_\theta}{r} \frac{\partial u_\phi}{\partial \theta} + \frac{u_\phi}{r \sin \theta} \frac{\partial u_\phi}{\partial \phi} + \frac{u_r u_\phi}{r} + \frac{u_\theta u_\phi}{r} \cot \theta \right) \\
 & = -\frac{1}{r \sin \theta} \frac{\partial p}{\partial \phi} - \left(\frac{1}{r^2} \frac{\partial}{\partial r} (r^2 \tau_{r\phi}) + \frac{1}{r} \frac{\partial \tau_{\theta\phi}}{\partial \theta} + \frac{1}{r \sin \theta} \frac{\partial \tau_{\phi\phi}}{\partial \phi} \right. \\
 & \quad \left. + \frac{\tau_{r\phi}}{r} + \frac{2 \cot \theta}{r} \tau_{\theta\phi} \right) + \rho g_\phi
 \end{aligned} \tag{3}$$

In terms of velocity gradients for a Newtonian fluid with constant, ρ and μ ^a

$$\begin{aligned}
 \text{r-component} \quad & \rho \left(\frac{\partial u_r}{\partial t} + u_r \frac{\partial u_r}{\partial r} + \frac{u_\theta}{r} \frac{\partial u_r}{\partial \theta} + \frac{u_\phi}{r \sin \theta} \frac{\partial u_r}{\partial \phi} - \frac{u_\theta^2 + u_\phi^2}{r} \right) \\
 & = -\frac{\partial p}{\partial r} + \mu \left(\nabla^2 u_r - \frac{2}{r^2} u_r - \frac{2}{r^2} \frac{\partial u_\theta}{\partial \theta} - \frac{2}{r^2} u_\theta \cot \theta \right. \\
 & \quad \left. - \frac{2}{r^2 \sin \theta} \frac{\partial u_\phi}{\partial \phi} \right) + \rho g_r
 \end{aligned} \tag{1A}$$

$$\begin{aligned}
 \theta\text{-component} \quad & \rho \left(\frac{\partial u_\theta}{\partial t} + u_r \frac{\partial u_\theta}{\partial r} + \frac{u_\theta}{r} \frac{\partial u_\theta}{\partial \theta} + \frac{u_\phi}{r \sin \theta} \frac{\partial u_\theta}{\partial \phi} + \frac{u_r u_\theta}{r} - \frac{u_\phi^2 \cot \theta}{r} \right) \\
 & = -\frac{1}{r} \frac{\partial p}{\partial \theta} + \mu \left(\nabla^2 u_\theta + \frac{2}{r^2} \frac{\partial u_r}{\partial \theta} - \frac{u_\theta}{r^2 \sin^2 \theta} - \frac{2 \cos \theta}{r^2 \sin^2 \theta} \frac{\partial u_\phi}{\partial \phi} \right) + \rho g_\theta
 \end{aligned} \tag{2A}$$

$$\begin{aligned}
 \phi\text{-component} \quad & \rho \left(\frac{\partial u_\phi}{\partial t} + u_r \frac{\partial u_\phi}{\partial r} + \frac{u_\theta}{r} \frac{\partial u_\phi}{\partial \theta} + \frac{u_\phi}{r \sin \theta} \frac{\partial u_\phi}{\partial \phi} + \frac{u_r u_\phi}{r} + \frac{u_\theta u_\phi}{r} \cot \theta \right) \\
 & = -\frac{1}{r \sin \theta} \frac{\partial p}{\partial \phi} + \mu \left(\nabla^2 u_\phi - \frac{u_\phi}{r^2 \sin^2 \theta} + \frac{2}{r^2 \sin \theta} \frac{\partial u_r}{\partial \phi} \right. \\
 & \quad \left. + \frac{2 \cos \theta}{r^2 \sin^2 \theta} \frac{\partial u_\theta}{\partial \phi} \right) + \rho g_\phi
 \end{aligned} \tag{3A}$$

^a In these equations,

$$\nabla^2 = \frac{1}{r^2} \frac{\partial}{\partial r} \left(r^2 \frac{\partial}{\partial r} \right) + \frac{1}{r^2 \sin \theta} \frac{\partial}{\partial \theta} \left(\sin \theta \frac{\partial}{\partial \theta} \right) + \frac{1}{r^2 \sin^2 \theta} \left(\frac{\partial^2}{\partial \phi^2} \right)$$

Some comments may be appropriate on the terms appearing in Eq. (3.2.6). The quantity $\nabla \cdot \rho\mathbf{u}\mathbf{u}$ is not a simple divergence because $\rho\mathbf{u}\mathbf{u}$ is a dyadic product of two vectors, having nine components

$$\rho\mathbf{u}\mathbf{u} = \begin{vmatrix} \rho u_x u_x & \rho u_x u_y & \rho u_x u_z \\ \rho u_y u_x & \rho u_y u_y & \rho u_y u_z \\ \rho u_z u_x & \rho u_z u_y & \rho u_z u_z \end{vmatrix} \quad (3.2.7)$$

Nonetheless the physical meaning of $\nabla \cdot \rho\mathbf{u}\mathbf{u}$ is analogous to the concept of divergence discussed in Section 3.1, because it represents the *net outflow of momentum by convection*. It follows that $(-\nabla \cdot \rho\mathbf{u}\mathbf{u})$ corresponds to the net convective inflow of momentum.

The quantity $\nabla p \equiv \text{grad } p$ represents the pressure gradient. As shown in Appendix 1, the use of the operator, $\nabla \equiv \mathbf{i} \partial/\partial x + \mathbf{j} \partial/\partial y + \mathbf{k} \partial/\partial z$ on a scalar field, e.g., pressure, results in a vector.

The quantity τ is termed the stress tensor, which has nine components:

$$\tau = \begin{vmatrix} \tau_{xx} & \tau_{xy} & \tau_{xz} \\ \tau_{yx} & \tau_{yy} & \tau_{yz} \\ \tau_{zx} & \tau_{zy} & \tau_{zz} \end{vmatrix} \quad (3.2.8)$$

Finally \mathbf{F}_b is the body force per unit volume of the fluid. In the majority of applications \mathbf{F}_b may be replaced by \mathbf{g} , the vector due to the gravitational force.

In certain cases, however, \mathbf{F}_b will have to include electromagnetic forces. Such problems will be discussed in Chapter 5.

By using the substantial time derivative, defined in Eq. (3.1.8), and the form of the equation of continuity given in Eq. (3.1.7), Eq. (3.2.6) may be written in the following form:

$$\rho \frac{D\mathbf{u}}{Dt} = -\nabla p - \nabla \cdot \tau + \rho\mathbf{F}_b \quad \begin{matrix} \text{pressure} \\ \text{forces} \end{matrix} \quad \begin{matrix} \text{viscous} \\ \text{forces} \end{matrix} \quad \begin{matrix} \text{body} \\ \text{forces} \end{matrix} \quad (3.2.9)$$

$$\left[\begin{matrix} \text{(mass per unit volume)} \\ \times \text{acceleration} \end{matrix} \right] = \left[\begin{matrix} \text{sum of forces acting} \\ \text{on the element} \end{matrix} \right] \quad (3.2.10)$$

which shows a clear correspondence to Newton's law. At this stage it is of interest to compare Eq. (3.2.9) or Eq. (3.2.6) with the integral momentum balance that was given previously by Eq. (2.3.3) in Chapter 2. Both the differential and the integral balance equations provide a relationship between the velocity (introduced through the momentum), the pressure, and the forces acting on the element.

However, in the integral balance equation [Eq. (2.3.3)] empirical relationships (correlations) are required between the drag force (\mathbf{F}_{drag}) and the other

variables in order for the problem to be defined. The friction factor correlations presented in Section 2.5 were a good example of such empirical relationships.

In contrast, in the differential momentum balance, closure of the problem is possible on a fundamental basis because there exists a relationship between the components of the stress tensor τ and the velocity gradients.

These relationships, which constitute the generalization of Newton's law of viscosity, were given previously in Tables 1.3.1–1.3.3. Let us now proceed by substituting these relationships for τ_{xx} , τ_{xy} into the x , y , and z components of the equation of motion, previously given in Eqs. (3.2.3)–(3.2.5). Thus we have

$$\rho \frac{D u_x}{D t} = \frac{\partial}{\partial x} \left[2\mu \frac{\partial u_x}{\partial x} - \frac{2}{3} \mu \nabla \cdot \mathbf{u} \right] + \frac{\partial}{\partial y} \left[\mu \left(\frac{\partial u_x}{\partial y} + \frac{\partial u_y}{\partial x} \right) \right] + \frac{\partial}{\partial z} \left[\mu \left(\frac{\partial u_x}{\partial z} + \frac{\partial u_z}{\partial x} \right) \right] - \frac{\partial p}{\partial x} + \rho F_x \quad (\text{x component}) \quad (3.2.11)$$

$$\rho \frac{D u_y}{D t} = \frac{\partial}{\partial x} \left[\mu \left(\frac{\partial u_y}{\partial x} + \frac{\partial u_x}{\partial y} \right) \right] + \frac{\partial}{\partial y} \left[2\mu \frac{\partial u_y}{\partial y} - \frac{2}{3} \mu \nabla \cdot \mathbf{u} \right] + \frac{\partial}{\partial z} \left[\mu \left(\frac{\partial u_y}{\partial z} + \frac{\partial u_z}{\partial y} \right) \right] - \frac{\partial p}{\partial y} + \rho F_y \quad (\text{y component}) \quad (3.2.12)$$

and

$$\rho \frac{D u_z}{D t} = \frac{\partial}{\partial x} \left[\mu \left(\frac{\partial u_z}{\partial x} + \frac{\partial u_x}{\partial z} \right) \right] + \frac{\partial}{\partial y} \left[\mu \left(\frac{\partial u_z}{\partial y} + \frac{\partial u_y}{\partial z} \right) \right] + \frac{\partial}{\partial z} \left[2\mu \frac{\partial u_z}{\partial z} - \frac{2}{3} \mu \nabla \cdot \mathbf{u} \right] - \frac{\partial p}{\partial z} + \rho F_z \quad (\text{z component}) \quad (3.2.13)$$

Equations (3.2.11)–(3.2.13) together with the equation of continuity represent the general statement of the momentum balance for isothermal systems in the cartesian coordinate system.

In practice, in order to complete the definition of a problem, the initial and the boundary conditions have to be defined also; moreover, if the fluid is compressible the formulation must also include a relationship between pressure and density, i.e., the equation of state. The equivalent expressions are readily developed for cylindrical and for spherical coordinates through the use of Tables 3.2.2 and 3.2.3.

For nonisothermal systems Eqs. (3.2.11)–(3.2.13) have to be combined with the statement of the thermal energy balance, together with expressions for the temperature dependence of viscosity and the equation of state.

Even on their own Eqs. (3.2.11)–(3.2.13) appear to be quite formidable. However in most practical applications it is possible to make many simplifying assumptions, which then reduce these equations to a manageable form.

When both the density and the viscosity are constant, Eqs. (3.2.11)–(3.2.13) reduce to the following:

$$\rho \frac{D\mathbf{u}}{Dt} = \mu \nabla^2 \mathbf{u} - \nabla p - \rho \mathbf{F} \quad (3.2.14)$$

where $\nabla^2 = \partial^2(\)/\partial x^2 + \partial^2(\)/\partial y^2 + \partial^2(\)/\partial z^2$ is the Laplacian operator when applied to a vector field, i.e., $\nabla^2 \mathbf{u} \equiv \nabla(\nabla \cdot \mathbf{u})$. The result of the operation is a vectorial quantity.

Moreover, when gravity is the only body force to be considered we have

$$\rho \frac{D\mathbf{u}}{Dt} = \mu \nabla^2 \mathbf{u} - \nabla p + \rho \mathbf{g} \quad (3.2.15)$$

which is the well-known Navier–Stokes equation.

The equivalent forms of Eq. (3.2.14) in cylindrical and in spherical coordinates are given in Tables 3.2.2 and 3.2.3.

3.3 The Stream Function and Vorticity

While the appropriate form of the Navier–Stokes equation represents the logical starting point in the formulation of fluid flow problems, often it is more convenient to work in terms of some derived quantities, namely, the vorticity and the stream function.

3.3.1 The Vorticity

In a mathematical sense the vorticity is defined as

$$\boldsymbol{\Omega} = \text{curl } \mathbf{u} = \text{rot } \mathbf{u} = \nabla \times \mathbf{u} \quad (3.3.1)$$

which is seen in Appendix 1. It may be expressed as

$$\nabla \times \mathbf{u} = \begin{vmatrix} \mathbf{i} & \mathbf{j} & \mathbf{k} \\ \partial/\partial x & \partial/\partial y & \partial/\partial z \\ u_x & u_y & u_z \end{vmatrix} \quad (3.3.2)$$

or

$$\mathbf{i} \left[\frac{\partial u_z}{\partial y} - \frac{\partial u_y}{\partial z} \right] + \mathbf{j} \left[\frac{\partial u_x}{\partial z} - \frac{\partial u_z}{\partial x} \right] + \mathbf{k} \left[\frac{\partial u_y}{\partial x} - \frac{\partial u_x}{\partial y} \right] \quad (3.3.3)$$

In a physical sense $\boldsymbol{\Omega} \equiv \nabla \times \mathbf{u}$ is the vector of rotation of the fluid element.

The angular velocity ω at a given point in the fluid is defined as the speed with which a small, hypothetical paddle wheel, mounted on frictionless bearings, would rotate if placed there.

It can be shown that the following relationship exists between $\nabla \times \mathbf{u}$ and ω :

$$\omega = \frac{1}{2}(\nabla \times \mathbf{u}) = \frac{1}{2}\Omega \quad (3.3.4)$$

Figure 3.3.1 shows a number of physical situations that we can examine regarding the angular velocity.

Figure 3.3.1a shows a uniform velocity field, e.g., a large distance from boundary surfaces. Since all the paddles of the wheel would experience the same velocity, no rotation would occur under these circumstances. Thus

$$\omega = 0 \quad \text{or} \quad \operatorname{curl} \mathbf{u} = 0 \quad (3.3.5)$$

Such flows are called *irrotational*.

In contrast the situations depicted in Figs. 3.3.1b and c correspond to cases where the imaginary paddle wheel would rotate, because of the unequal velocities experienced by the different vanes. It has to be stressed to the reader that uniformity or nonuniformity of the field is not the necessary criterion for determining whether the flow is rotational. This point is illustrated in Fig. 3.3.1d, showing the flow field produced by a point source, e.g., a

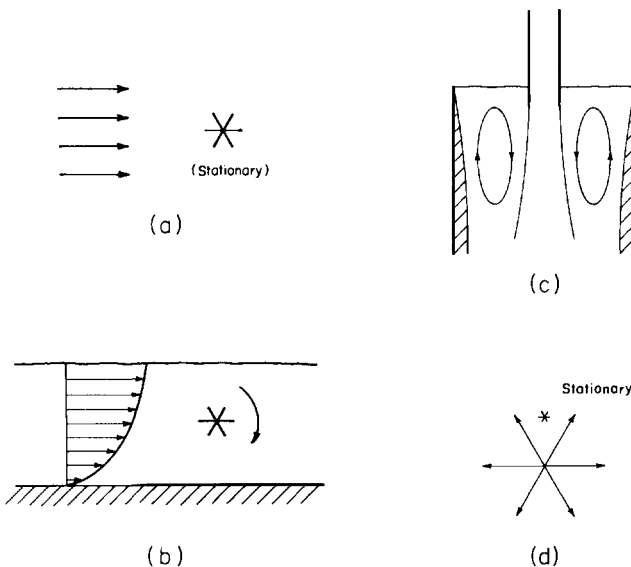


FIG. 3.3.1 Sketches of typical fluid flow situations, illustrating the concept of the vorticity: (a) parallel flow, (b) flow in an open channel, (c) flow in the mold region of a continuous casting system, and (d) flow from a point source.

fluid issuing from a small orifice into a large reservoir. Such a flow field would not be uniform, although spherical symmetry would be observed about the source. It is readily seen that the imaginary paddle wheel would not rotate if placed in such a flow field; thus the velocity field produced by a point source (or point sink) is irrotational.

Another interesting example of irrotational motion is that of the carriages in the Ferris wheel in fair grounds; although each carriage follows a circular path as the wheel turns, it does not rotate with respect to the earth—the passengers remain upright throughout the operation.

We note here that, in addition to its physical significance, the mathematical definition of the vorticity, as given in Eqs. (3.3.1)–(3.3.3), is very helpful in the manipulation of the Navier–Stokes equations. This problem will be discussed further in Section 3.5.6 and in subsequent chapters of this text.

3.3.2 *The Stream Function*

We have seen that in three-dimensional flows the velocity field may be represented by using the velocity vector \mathbf{u} or its three components, u_x , u_y , and u_z . In two-dimensional flows (which includes cylindrical, axisymmetrical systems) we have an alternative, often more convenient, representation available to us, through the use of the stream function.

For two-dimensional flows the stream function ψ is defined as

$$u_x = \frac{\partial \psi}{\partial y} \quad (3.3.6)$$

$$u_y = -\frac{\partial \psi}{\partial x} \quad (3.3.7)$$

for the cartesian coordinate system, and

$$u_r = -\frac{1}{r} \frac{\partial \psi}{\partial \theta} \quad (3.3.8)$$

$$u_\theta = \frac{\partial \psi}{\partial r} \quad (3.3.9)$$

in polar coordinates. The equivalent expression in cylindrical coordinates is given as

$$u_r = -\frac{1}{r} \frac{\partial \psi}{\partial z} \quad (3.3.10)$$

$$u_z = \frac{1}{r} \frac{\partial \psi}{\partial r} \quad (3.3.11)$$

A two-dimensional velocity field may then be represented on a stream function plot, showing lines of $\psi = \text{const}$, such as given in Fig. 3.3.2. The corresponding velocity map, given in terms of the velocity vector, is shown in Fig. 3.3.3, which could, of course, be readily calculated from Fig. 3.3.2 through the use of Eqs. (3.3.6) and (3.3.7). Inspection of Figs. 3.3.2 and 3.3.3 shows that the region where the streamlines are bunched together corresponds to regions of high velocity.

THE PHYSICAL SIGNIFICANCE OF THE STREAM FUNCTION AND OF THE STREAMLINES

The lines corresponding to $\psi = \text{const}$ usually termed *streamlines* have an important physical significance. For steady-state conditions the streamlines, defined through Eqs. (3.3.6)–(3.3.11), are identical to the *path lines* and the *streak lines* in the fluid flow field. The path lines would describe the paths traveled by a small fluid element as it moves through the system. The streak

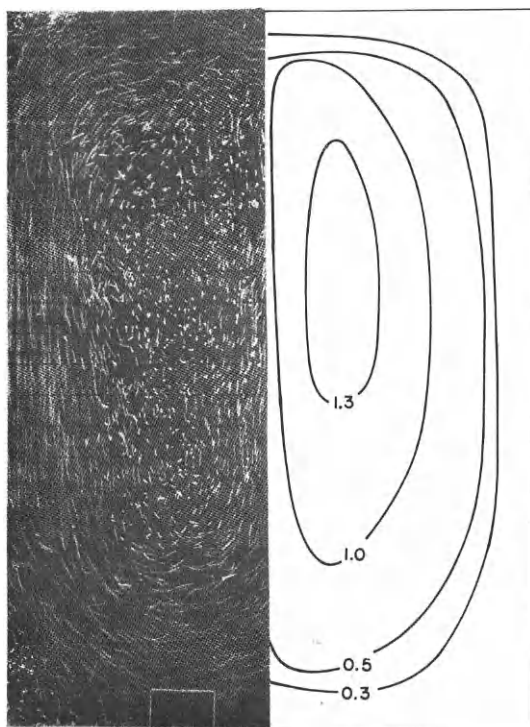


FIG. 3.3.2 Experimental and theoretical streamline plots.

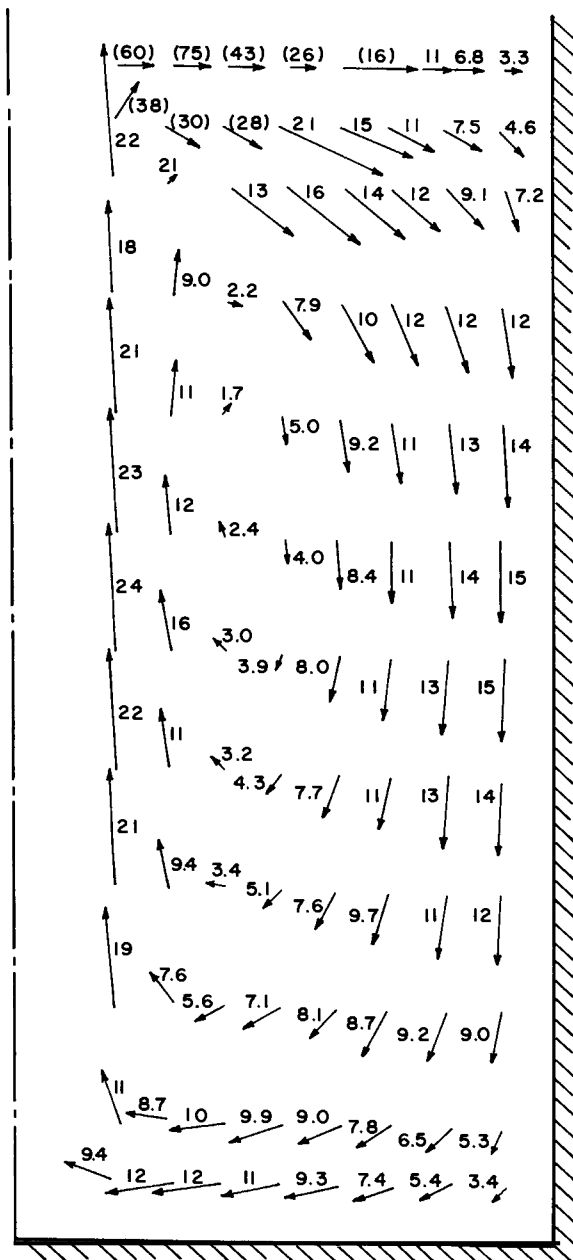


FIG. 3.3.3 Velocity map, corresponding to the streamline plot shown in Fig. 3.3.2. The numbers on the arrows denote the velocities in cm/s.

lines are the loci of all the fluid elements that had passed through some specific point in the flow field.

Both the path lines and the streak lines are of interest in flow visualization studies. Figure 3.3.4 shows the fluid path lines as obtained in a water model of a copper converter by using polystyrene tracer particles and time lapse photography.

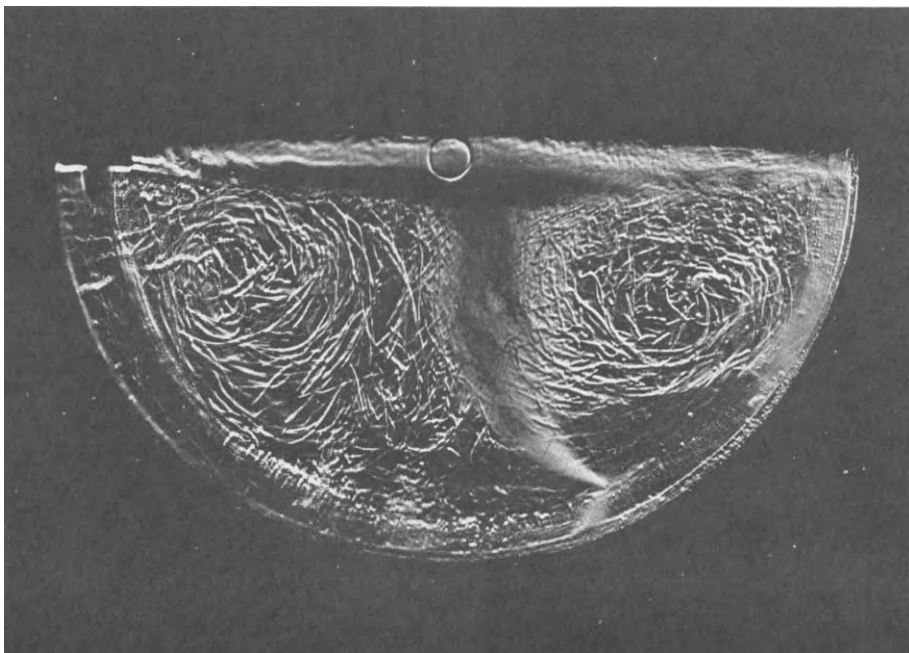


FIG. 3.3.4 Fluid path lines obtained in a water model of a copper converter. Photograph kindly supplied by Dr. P. Tarasoff of Noranda Mines Ltd., Pointe Claire, Quebec, Canada.

It is thus seen that, at least for steady-state conditions, there is a direct relationship between the streamlines and the experimentally obtainable streamlines and pathlines.

At this stage it may be worthwhile to comment on another important characteristic of the streamlines. Figure 3.3.5 shows two streamlines, ψ_1 and ψ_2 , in a fluid flow field.

For steady-state conditions the streamlines ψ_1 and ψ_2 would describe the path of a fluid element as it travels from points D to B and C to A, respectively. Since by definition no fluid would cross these streamlines, the mass rate of flow entering the system across surface DC must equal the mass flow rate

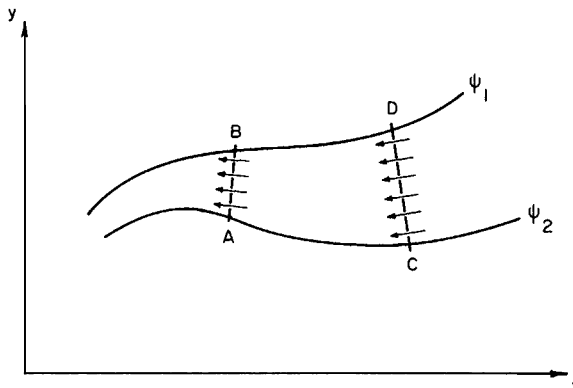


FIG. 3.3.5 Streamlines in a two-dimensional flow.

through surface BA. Thus we have

$$w \text{ crossing DC} = w \text{ crossing BA} \quad (3.3.12)$$

This behavior is consistent with the observation made in connection with Figs. 3.3.2 and 3.3.3 that closely bunched streamlines correspond to regions of high fluid velocity.

3.4 Some Special Solutions of the Navier-Stokes Equations

The reader will have noted the complexity of the general form of the Navier-Stokes equations that were developed in Section 3.2. In the majority of practical problems these equations may be usefully simplified, by neglecting certain terms which then reduces the mathematical or computational task to manageable proportions. In this section we shall consider two special classes of problems which may be tackled by using drastically simplified forms of the Navier-Stokes equations, namely inviscid, ideal fluid behavior and the very slow motion of highly viscous fluids. Both these types of problems represent extremes; nonetheless, the solutions that may be obtained are of considerable practical importance—for certain situations.

3.4.1 Ideal Fluid Behavior

Ideal flow solutions are obtained from the Navier-Stokes equations if we assume that the fluid is both incompressible and of zero viscosity. The reader may question whether solutions obtained for fluid flow problems on the assumption of zero viscosity have any practical value at all, since viscosity plays such a central role in transmitting stress through fluids. It is noted,

however, that the assumption of ideal (inviscid) behavior is quite appropriate for many fluid flow problems, *when the region of interest is not in the vicinity of solid surfaces and when recirculating flows are absent.*[†]

For ideal flow behavior the Navier–Stokes equations may be written as

$$\rho \frac{D\mathbf{u}}{Dt} = -\nabla p + \rho \mathbf{F} \quad (3.4.1)$$

the x component of which is given as

$$\rho \frac{Du_x}{Dt} = \rho \frac{\partial u_x}{\partial t} + \rho \left[u_x \frac{\partial u_x}{\partial x} + u_y \frac{\partial u_x}{\partial y} + u_z \frac{\partial u_x}{\partial z} \right] - \frac{\partial p}{\partial x} + \rho F_x \quad (3.4.2)$$

In addition the equation of continuity must be satisfied also. Thus for an incompressible fluid we have

$$\nabla \cdot \mathbf{u} = 0 \quad (3.4.3)$$

The solution of Eq. (3.4.1), often called the Euler equation, together with the equation of continuity, would still be quite a complex task.

However, if we assume furthermore that the flow field is irrotational, that is,

$$\nabla \times \mathbf{u} = 0 \quad (3.4.4)$$

when this assumption is appropriate, and only then, it is permissible to introduce the velocity potential ϕ , which is defined as

$$\mathbf{u} = \nabla \phi \quad (3.4.5)$$

or

$$u_x = \frac{\partial \phi}{\partial x}, \quad u_y = \frac{\partial \phi}{\partial y}, \quad u_z = \frac{\partial \phi}{\partial z} \quad (3.4.6)$$

Upon expressing the equation of continuity in terms of the velocity potential we have the following:

$$\nabla^2 \phi = 0 \quad (3.4.7)$$

[†] Inviscid behavior would be an inappropriate assumption in the vicinity of solid surfaces, because a fluid with zero viscosity could not satisfy the commonly imposed boundary condition that the fluid adjacent to a solid surface moves with the same velocity as the surface; i.e., it is stationary if the surface is stationary. In this context the reader may wish to recall the definition of viscosity in Section 1.3. If the fluid were inviscid in Fig. 1.3.1, the movement of the upper plate would *not* affect the fluid, because an inviscid fluid could not transmit shear due to velocity gradients. In the same context it should be remarked that in many instances recirculatory flows are caused by wall shear (e.g., in case of confined jets, or in the mold region of a continuous casting machine).

Thus for ideal fluids in an irrotational flow field we may obtain an expression for the velocity field through the solution of Eq. (3.4.7). This equation has the same form as Laplace's equation, for which numerous solutions are available not only in the field of fluid mechanics but also in the literature of heat conduction and electrostatics. A practical problem has to be faced though, in the solution of Eq. (3.4.7) is that many of the commonly used boundary conditions (e.g., specifying zero velocity at the bounding solid surfaces) cannot be used, because the *potential flow approximation is not valid in the vicinity of the solid boundaries*. In the majority of cases solutions are generated either by using the concept of sources and sinks or through conformal mapping.

We note that for two-dimensional systems, e.g., using the x and the y Cartesian coordinates, irrotationality may be expressed with the aid of the stream function as

$$\nabla^2 \psi = 0 \quad (3.4.8)$$

or

$$\frac{\partial^2 \psi}{\partial x^2} + \frac{\partial^2 \psi}{\partial y^2} = 0 \quad (3.4.9)$$

Under these conditions the statement of the ideal flow problem is given through Eqs. (3.4.7) and (3.4.8).

The reader may well wonder how one can state a fluid flow problem, albeit for ideal fluids, without invoking the equation of motion, i.e., the Euler equation in the present case. This is possible, because for irrotational flow there can be only one solution of the stream equation or the equation for the velocity potential that satisfies a given set of boundary conditions. Of course, the pressure distribution has to enter the solution thus obtained implicitly, through Eq. (3.4.2).

In seeking a solution to these equations we shall make use of the Cauchy-Riemann equations, which are stated here without proof.¹

If a functional relationship exists between complex numbers, such that

$$\phi(x, y) + i\psi(x, y) = F(x + iy) = F(\mathcal{X}) \quad (3.4.10)$$

where $i = \sqrt{-1}$ and $\mathcal{X} = (x + iy)$, thus a complex number, then the following relationship must be satisfied:

$$\frac{\partial \phi}{\partial x} = \frac{\partial \psi}{\partial y} \quad (3.4.11)$$

$$\frac{\partial \phi}{\partial y} = -\frac{\partial \psi}{\partial x} \quad (3.4.12)$$

Upon inspecting the definition of the stream function, as given by Eqs. (3.3.6) and (3.3.7), and that of the velocity potential, given by Eq. (3.4.6), it is readily seen that the Cauchy–Riemann equations are satisfied by this definition.

It follows that if the function $F(x + iy)$ is available for a given fluid flow situation, then the real part of this function will give the velocity potential, while the imaginary part will correspond to the stream function.

SOURCES AND SINKS IN IDEAL FLOW

Let us consider a two-dimensional system of infinite extent (e.g., a large, shallow reservoir) into which a fluid is discharged at a volumetric flow rate of Q .[†] Through a small opening, located at a coordinate point $x = 0, y = 0$.

The function representing the solution to Eqs. (3.4.7) and (3.4.8) for this case is given as

$$F(\mathcal{Z}) = \phi + i\psi = (Q/2\pi) \ln(x + iy) \quad (3.4.13)$$

After some manipulation, using polar coordinates, the real and the imaginary parts may be separated and we have

$$\phi = (Q/2\pi) \ln(x^2 + y^2)^{1/2} \quad (3.2.14)$$

and

$$\psi = (Q/2\pi) \tan^{-1}(y/x) \quad (3.4.15)$$

The resultant map, showing the streamlines and the isopotential lines for this case, is given in Fig. 3.4.1. It is seen that the streamline pattern indicates radially uniform flow from the source, while the lines of constant velocity potential, i.e., the isopotential lines, are concentric circles.

The actual velocity components may be obtained by differentiating Eqs. (3.4.14) and (3.4.15) in accordance with the definition of ϕ or ψ . Thus we have

$$u_x = \frac{\partial \phi}{\partial x} = \frac{\partial \psi}{\partial y} = \frac{Q}{2\pi} \left(\frac{x}{x^2 + y^2} \right) \quad (3.4.16)$$

and

$$u_y = \frac{\partial \phi}{\partial y} = -\frac{\partial \psi}{\partial x} = \frac{Q}{2\pi} \left(\frac{y}{x^2 + y^2} \right) \quad (3.4.17)$$

[†] Because the problem is two dimensional, the dimension of Q will have to be $(L^2/t) \times L$, where the last term is the depth of the reservoir.

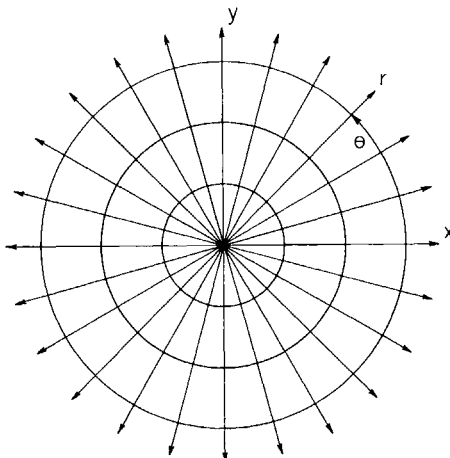


FIG. 3.4.1 Streamlines and isopotential lines for two-dimensional flow from a point source.

The absolute value of the velocity vector $|u|$ is given as

$$|u| = (u_x^2 + u_y^2)^{1/2} = Q/2\pi r \quad (3.4.18)$$

where $r^2 = x^2 + y^2$ is the radial distance from the source.

Example 3.4.1 Cooling water is introduced into a large shallow reservoir at a rate of $0.5 \text{ m}^3/\text{s}$. Calculate the x and y components of the velocity and the absolute value of the velocity, at a point $x = 2 \text{ m}$ and $y = 3 \text{ m}$ from the inlet. Assume that the water level is 0.2 m .

SOLUTION

$$Q' = 0.5/0.2 = 2.5 \text{ m}^2/\text{s}$$

Thus using Eqs. (3.4.16) and (3.4.17)

$$u_x = \frac{2.5}{2 \times 3.14} \times \frac{2}{4+9} = 0.061 \text{ m/s}$$

$$u_y = \frac{2.5}{2 \times 3.14} \times \frac{3}{4+9} = 0.092 \text{ m/s}$$

and

$$|u| = [(0.061)^2 + (0.092)^2]^{1/2} = 0.11 \text{ m/s}$$

Since Laplace's equation [i.e., in the present context Eqs. (3.4.7) and (3.4.8)] is linear, the solutions to it are capable of linear transformation; furthermore, any linear combination of solutions will be a solution also.

The important consequence of this behavior is the fact that knowing $\phi(x, y)$, $\psi(x, y)$ for a single source enables us to generate the solution for any combination of sources.

Thus for a point source of strength Q , located at $x = a$ and at $y = b$, we have

$$\phi = (Q/2\pi) \ln[(x - a)^2 + (y^2 - b)^2]^{1/2} \quad (3.4.19a)$$

The expressions for the velocity potential and for the stream function for sinks are identical to those previously given for sources, but for the opposing sign.

Thus the velocity potential for a system composed of a source at $x = 0$ and $y = 0$ and of a sink having the same strength but located at $x = a$ and $y = b$ is given as

$$\phi = \frac{Q}{2\pi} \ln \frac{(x^2 + y^2)^{1/2}}{[(x - a)^2 + (y - b)^2]^{1/2}} \quad (3.4.19b)$$

For a three-dimensional system the velocity potential for a point source located at $x = a$, $y = b$, $z = c$ is given as

$$\phi = Q/4\pi [(x - a)^2 + (y - b)^2 + (z - c)^2]^{-1/2} = Q/4\pi \mathcal{R} \quad (3.4.20)$$

where $\mathcal{R}^2 = (x - a)^2 + (y - b)^2 + (z - c)^2$.

These solutions for source-sink combinations, which are very readily generated through the use of the techniques described above, have found extensive use for petroleum reservoir engineering problems and for providing a quick estimate of the fluid flow field in packed bed reactors with side stream injection.²⁻⁴ Let us now turn to another very powerful tool for the solution of potential flow problems, namely conformal mapping.

THE USE OF CONFORMAL MAPPING FOR THE SOLUTION OF POTENTIAL FLOW PROBLEMS

Let us consider the parallel flow field shown in Fig. 3.4.2, where $u_x = U_\infty$ and $u_y = 0$ throughout the domain. Using the previously given definition of ϕ and ψ it is readily shown that for this flow field

$$\phi = U_\infty x \quad (3.4.21)$$

and

$$\psi = U_\infty y \quad (3.4.22)$$

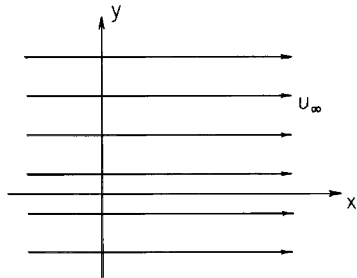


FIG. 3.4.2 Uniform ideal flow in the x - y co-ordinate system.

Upon recalling the Cauchy-Riemann criteria, as given in Eqs. (3.4.10)–(3.4.12), we note that this solution has the following form:

$$F(\mathcal{Z}) = U_{\infty}(x + iy) \quad (3.4.23)$$

We can now map this solution from the \mathcal{Z} -plane to some other plane through an appropriate transformation and through the application of conformal mapping. For example, let us consider the following transformation:

$$\mathcal{Z} = \mathcal{Z}'^2; \quad \text{i.e., } \mathcal{Z} = x'^2 - y'^2 + 2x'y'i \quad (3.4.24)$$

Then the transformed function $F(\mathcal{Z})$ becomes

$$F(\mathcal{Z}) = U_{\infty}z = U_{\infty}(x'^2 - y'^2) + 2U_{\infty}x'y'i \quad (3.4.25)$$

It follows that for this transformation the new functional relationships for the velocity potential and for the stream function are given as

$$\phi = U_{\infty}(x'^2 - y'^2) \quad (3.4.26)$$

and

$$\psi = 2U_{\infty}x'y' \quad (3.4.27)$$

It is readily shown that this transformation does indeed satisfy the Cauchy-Riemann conditions, since

$$\frac{\partial\psi}{\partial y'} = \frac{\partial\phi}{\partial x'} = 2U_{\infty}x' \quad (3.4.28)$$

and

$$-\frac{\partial\psi}{\partial x'} = \frac{\partial\phi}{\partial y'} = -2U_{\infty}y' \quad (3.4.29)$$

The streamline pattern and the corresponding map of the velocity potential corresponding to Eqs. (3.4.26) and (3.4.27) is shown in Fig. 3.4.3.

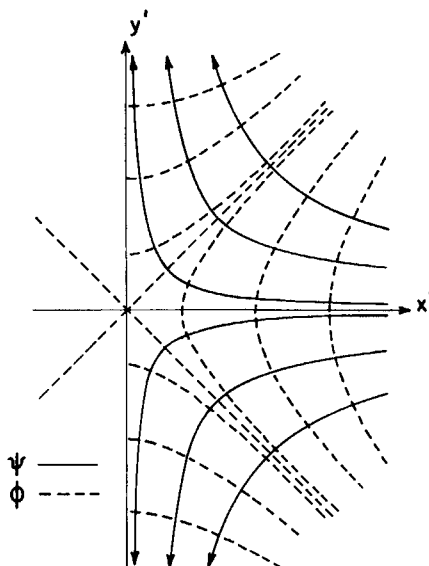


FIG. 3.4.3 The potential flow field corresponding to a jet impinging on a flat plate.

The actual expressions for the velocity components are readily obtained by differentiation, using the previously given definition of ϕ and ψ . Thus we have

$$u_x = \frac{\partial \phi}{\partial x} = 2U_\infty x' \quad (3.4.30)$$

and

$$u_y = -2U_\infty y' \quad (3.4.31)$$

The absolute value of the velocity $|u|$ is given as

$$|u| = (u_x^2 + u_y^2)^{1/2} = 2U_\infty(x'^2 + y'^2)^{1/2} \quad (3.4.32)$$

We note that inspection of Fig. 3.4.3 provides perhaps the best visual indication of the actual flow field produced by the transformation described above.

In a physical sense this flow field corresponds to the potential flow solution to the problem of a fluid jet impinging on a flat plate; the upper quadrant would represent potential flow around a rectangular corner. It has to be stressed that because of the assumption of zero viscosity this solution will not represent the actual conditions accurately in the immediate vicinity of the solid surface; the reader will note that the streamline pattern sketched in Fig. 3.4.3 would indicate finite velocities at the solid surface, which is, of course incorrect.

The conformal mapping procedure outline here may appear to be quite haphazard to the reader, because when suggesting the transformation $\mathcal{Z} = \mathcal{Z}'^2$ we gave no indication as to the specific fluid flow problem, i.e., geometry to which we sought to address ourselves. In fact the technique of conformal mapping is very well established and tables of transforms are available in several texts⁵⁻⁷ which are applicable over a broad range of geometries.

We note that the linearity of Laplace's equation allows us to generate a broad range of solutions by superimposition. As an example, we can write down immediately the expression for the stream function, for a situation where a point source of strength Q is placed at a location $(x = 0, y = 0)$ in a uniform flow field with a parallel velocity U_∞ in the x direction. This can be done by combining the expressions obtained earlier individually for these two flow situations, namely Eqs. (3.4.15) and (3.4.22). Thus we have

$$\psi = U_\infty y + (Q/2\pi) \tan^{-1}(y/x) \quad (3.4.33)$$

Equation (3.4.33) could be used for estimating the effect of a side stream, i.e., stack gas injection in the blast furnace on the overall velocity profile.

PRESSURE FIELD IN POTENTIAL FLOW

We note that in the developments presented here for obtaining the velocity profiles through the use of the velocity potential and the stream function no explicit account has been given of the pressure distribution within the system.

Once the velocity field is known, the pressure distribution within the system may be calculated, through the use of the Euler equations, namely Eq. (3.4.1).

In the absence of a body force field (i.e., horizontal flow or negligible potential energy change) and for steady state the Euler equations may be integrated to obtain

$$\frac{1}{2}|u|^2 + p/\rho = \text{const} \quad (3.4.34)$$

which is Bernoulli's equation; this is generally valid for irrotational flow and is also valid along a streamline in all other cases.

The constant may be eliminated if P and u are known at some reference point. Thus for flow impinging on a flat plate, depicted in Fig. 3.4.3, we have

$$p_0 - p = \frac{1}{2}\rho[u_x^2 + u_y^2]$$

Here p_0 denotes the stagnation pressure at the point indicated on the graph where $u_x = u_y = 0$.

Potential flow models, in conjunction with conformal mapping, have been used extensively for estimating the fluid flow field around spheres, cylinders, and other objects; a useful recent application of potential flow

theory has been in the area of bubble dynamics, more specifically in regard to gas bubbles in fluidized beds.⁸

Potential flow calculations were extremely popular before the advent of high-speed digital computers, because at that time the assumption of potential flow was the only available means for generating solutions to many important problems. At present the numerical solution of many two-dimensional fluid flow problems is a fairly straightforward matter; nonetheless, the potential flow approach might be attractive for providing a quick estimate of the flow field one might expect. In the majority of cases engineering judgment is required whether the potential flow solution is appropriate or the more involved computation is justified.

3.4.2 Laminar Viscous Flow—Very Slow Motion

In the preceding section we examined ideal fluid behavior in course of which zero viscosity was postulated. Under certain conditions this assumption enabled us to generate, quite readily, simple solutions to quite complex problems. The solutions thus obtained, however, were not applicable in the vicinity of solid boundaries.

The other extreme assumption that one can make is to postulate a very high viscosity and low linear fluid velocities. Under these conditions the viscous terms dominate and we may neglect the inertial terms, enclosed by the square brackets in the Navier-Stokes equations[†]:

$$\rho \left\{ \frac{\partial \mathbf{u}}{\partial t} + [(\mathbf{u} \cdot \nabla) \mathbf{u}] \right\} = -\nabla p + \mu \nabla^2 \mathbf{u} + \mathbf{F}_b \quad (3.4.35)$$

If in addition we assume steady-state conditions and neglect the body forces, Eq. (3.4.35) simplifies to

$$\nabla p = \mu \nabla^2 \mathbf{u} \quad (3.4.36)$$

Upon taking the divergence of both sides of Eq. (3.4.36)[†] we have

$$\nabla^2 p = 0$$

Moreover the divergence of the right-hand side of Eq. (3.4.36) may be written with the aid of the stream function as

$$\nabla^4 \psi = 0 \quad (3.4.37)$$

Through the use of Eqs. (3.4.36) and (3.4.37) useful solutions have been obtained for very slow motion past a sphere (Stokes' law) and for the hydrodynamic theory of lubrication. For a detailed discussion of these problems the reader is referred to the text by Schlichting.⁹

[†] Written for incompressible fluids, where $\nabla \cdot \mathbf{u} = 0$.

In metals and materials processing applications one should be justified in neglecting the inertial terms in the Navier-Stokes equations under certain circumstances, when the melt is highly viscous and when the linear velocities are low. Examples of such systems would include slag flow in copper reverberatory furnaces, flow in glass tanks, and fluid flow in the mushy zone of some solidifying melts.^{10,11}

3.5 Exact Solutions of the Navier-Stokes Equations

In the previous section we examined some limiting cases of the Navier-Stokes equations, pertaining either to inviscid, ideal fluids or to systems where the viscosity was so large that viscous forces dominated. In this section we shall consider the general, broad class of problems where both inertial and viscous effects have to be considered. Under these conditions the proper starting point in the statement of the problem is the *equation of continuity, the equation of motion together with the appropriate boundary conditions.*

The equation of continuity has been given as Eq. (3.1.7) and in Table 3.1.1.

The equation of motion has been given as Eq. (3.2.14) and in Tables 3.2.1 and 3.2.2—for incompressible fluids, with a constant viscosity.

Before proceeding further, some comment should be made regarding the boundary conditions. The boundary conditions usually employed in laminar fluid flow problems tend to express the following constraints:

- (1) The “no-slip” condition specifying that the velocity of the fluid is zero at surfaces where it is in contact with a stationary solid; alternatively, the fluid layer adjacent to a moving solid surface moves with the same velocity as the solid surface.
- (2) At the interface between two fluids we usually specify the continuity of the velocity and the stress. In other words, as sketched in Fig. 3.5.1,

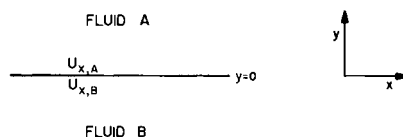


FIG. 3.5.1 Sketch showing the continuity of the velocity and of the shear stress at the interface separating two fluids.

$$U_{x,A}/_{y=0} = U_{x,B}/_{y=0}$$

$$U_{y,A}/_{y=0} = U_{y,B}/_{y=0} = 0$$

$$\tau_{y,x,A}/_{y=0} = \tau_{y,x,B}/_{y=0}$$

the velocity in one fluid at one side of the interface must equal the velocity in the other fluid at the “other side” of the interface; moreover, the shear stresses too must be equal. As a practical matter at gas–liquid interfaces we usually invoke the condition that the liquid does not transmit any shear stress to the gas, because the viscosity of gases is much less than that of liquids. In a mathematical sense this condition means specifying a zero velocity gradient at gas–liquid interfaces.

(3) There are cases which fall outside these two broad categories. If a gas–liquid, or liquid–liquid interface has a curvature, as in the case of bubbles, droplets, or some draining fluid films, then surface tension effects may have to be taken into account in the establishment of force (stress) balances, especially if the radius of curvature is small, i.e., small bubbles or droplets. The accumulation of surfactants may cause free liquid surfaces to behave as if they were rigid, etc.

Other, noteworthy boundary conditions that may be employed would include the *statement of symmetry*, i.e., the mathematical expression of the fact that the velocity gradient is zero across planes of symmetry or at the axis of symmetry. Moreover, in some cases the boundary conditions or constraints placed on the solution express some overall conservation relationship. Examples of this latter case will be given in connection with some film flow problems and with a problem concerning lubrication; in both these cases the streamlines are not parallel so that this additional conservation relationship is required.

For unsteady-state problems, e.g., the growth of gas bubbles in liquids, the initial conditions have to be specified also.

3.5.1 Problems Involving Film Flow

(A) FLOW OF A FALLING FILM

Let us consider the flow of a laminar film, on a vertical surface, such as sketched in Fig. 3.5.2. If we neglect the *entrance effects* associated with the introduction of the fluid, then we need concern ourselves only with the x component of the equation of motion. Working in the Cartesian coordinate system, for parallel flow,

$$u_y = u_z = 0 \quad (3.5.1)$$

Moreover, for an incompressible fluid the equation of continuity is written as

$$\partial u_x / \partial x = 0 \quad (3.5.2)$$

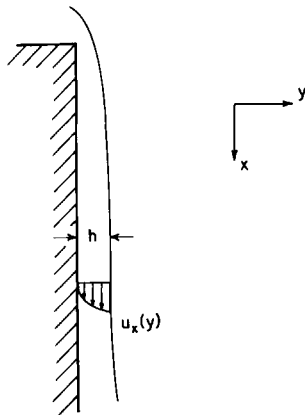


FIG. 3.5.2 Sketch of a vertical falling film.

Let us now turn to the x component of the Navier–Stokes equations as given by Eq. (3.2.11):

$$\begin{aligned} \rho & \left[\frac{\partial u_x}{\partial t} + u_x \frac{\partial u_x}{\partial x} + u_y \frac{\partial u_x}{\partial y} + u_z \frac{\partial u_x}{\partial z} \right] \\ &= \frac{\partial}{\partial x} \left[2\mu \frac{\partial u_x}{\partial x} - \frac{2}{3} \mu \nabla \cdot \mathbf{u} \right] + \frac{\partial}{\partial y} \left[\mu \left(\frac{\partial u_x}{\partial y} + \frac{\partial u_y}{\partial x} \right) \right] \\ &+ \frac{\partial}{\partial z} \left[\mu \left(\frac{\partial u_z}{\partial x} + \frac{\partial u_x}{\partial z} \right) \right] - \frac{\partial p}{\partial x} + \rho F_x \end{aligned} \quad (3.2.11)$$

The left-hand side of this equation is zero because

- (i) we assumed steady state, so that the time derivative vanishes,
- (ii) $\partial u_x / \partial x = 0$ because of continuity, and
- (iii) $u_y = u_z = 0$.

The first term in the square brackets on the right-hand side of Eq. (3.2.11) is zero because of the equation of continuity; the second term is also zero because the fluid is incompressible. The $\partial / \partial z$ derivative is zero because we consider no variations in the vertical direction; moreover, it may be shown that the pressure gradient $\partial p / \partial x$ approaches zero because the pressure is the same at the outer surface of the flux throughout.

Upon noting that the viscosity is constant and that the only body force is due to gravity, Eq. (3.2.11) simplifies to

$$\rho g_x = -\mu \frac{d^2 u_x}{dy^2}, \quad 0 \leq y \leq h \quad (3.5.3)$$

where, as seen in Fig. 3.5.2, h is the thickness of the film.

The boundary conditions are readily written down in accordance with the constraints (1) and (2); thus, we have

$$u_x = 0 \quad \text{at} \quad y = 0 \quad (\text{no slip condition}) \quad (3.5.4)$$

and

$$\frac{\partial u_x}{\partial y} = 0 \quad \text{at} \quad y = h \quad (3.5.5)$$

which stipulates that no shear is transmitted from the liquid to the gas which surrounds the film. The solution of Eqs. (3.5.3)–(3.5.5) yields the following expression:

$$u_x = (\rho g_x / 2\mu) [2hy - y^2] \quad (3.5.6)$$

from which it is seen that the velocity profile is parabolic. The maximum velocity occurs at $y = h$ and is given by

$$u_{x,\max} = (\rho g_x / 2\mu) h^2 \quad (3.5.7)$$

The average velocity $u_{x,m}$ is given as

$$u_{x,m} = \frac{1}{h} \int_0^h u_x(y) dy = \rho g_x h^2 / 3\mu \quad (3.5.8)$$

The mass flow rate per unit width w' is given as

$$w' = \int_0^h \rho u_x(y) dy = h \rho u_{x,m} = \rho^2 g_x h^3 / 3\mu \quad (3.5.9)$$

The validity of Eq. (3.5.6)–(3.5.9) is restricted to laminar film flow, i.e., to conditions when

$$N'_{Re,f} < 20 \quad (3.5.10)$$

Here $N'_{Re,f}$ is the film Reynolds number, defined as

$$N'_{Re,f} = 4hu_{x,m}\rho/\mu \quad (3.5.11)$$

It has been established that for the range $20 \leq N'_{Re,f} \leq 2000$ laminar flow is maintained, but with the formation of ripples and waves at the outer surface.^{12,13} The flow turns turbulent in the film, when $N'_{Re,f} > 2000$. Turbulence phenomena will be discussed in the next chapter.

The reader will note that the stipulation in Eq. (3.5.10) restricts the applicability of the laminar film flow equations derived here to quite thin films, especially in case of liquid metals, the density of which is high, as illustrated by the following example.

Example 3.5.1 Estimate the maximum allowable film thickness for a vertical falling film for it to satisfy the criterion for laminar flow^{12,13} in case of

- (a) molten steel, $\mu = 6.5 \times 10^{-3}$ kg/ms, $\rho = 7.1 \times 10^3$ kg/m³;
- (b) molten glass, $\mu = 10$ kg/ms, $\rho = 3 \times 10^3$ kg/m³;

for a vertical surface, $g_x = 9.81$ m/s².

Upon combining Eqs. (3.5.10) and (3.5.11) we have

$$20 \simeq 4hu_{x,m}\rho/\mu \quad (\text{i})$$

Substitution for $u_{x,m}$ from Eq. (3.5.8) yields after rearrangement

$$h = (15\mu^2/\rho^2g)^{1/3} \quad (\text{ii})$$

Thus for a steel film

$$h = \left(\frac{15 \times 4.23 \times 10^{-5}}{5.04 \times 10^7 \times 9.81} \right)^{1/3} \simeq 1.08 \times 10^{-4} \text{ m} \quad \text{or} \quad 0.108 \text{ mm}$$

It is highly questionable whether such a thin film could be maintained in a coherent form under experimental conditions. In contrast for molten glass,

$$h = \left(\frac{15 \times 100}{9 \times 10^6 \times 9.81} \right)^{1/3} \simeq 2.56 \times 10^{-2} \text{ m} \quad \text{or} \quad 25.6 \text{ mm}$$

which should be readily realizable in practice.

Let us turn our attention to a slight modification of the equations developed here which may be used for representing the drainage of liquid films from the walls of containers.

(B) THE DRAINAGE OF LIQUID FILMS

Figure 3.5.3 shows a sketch of a liquid film draining from the walls of a container.

In reality this is a very complex problem which involves unsteady motion and possibly more than one velocity component. Additional complications may arise if we seek to obtain an accurate representation of the region where the film meets the bulk of the receding fluid. A discussion of some of these problems has been presented by Tallmadge.¹⁴ Here we shall confine ourselves to a simple and very elegant development, which was proposed by Jeffreys.¹⁵

If we make the quasi steady-state approximation, i.e., ignore the acceleration terms in the Navier-Stokes equations, and assume parallel flow, then the

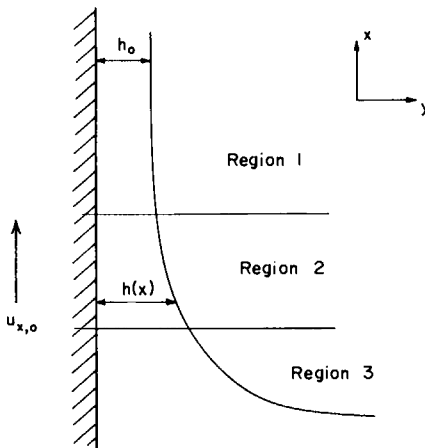


FIG. 3.5.3 Sketch of a liquid film draining from the walls of a container.

behavior of the receding film, sketched in Fig. 3.5.3, may be represented by the previously given film flow equation

$$-\mu \frac{\partial^2 u_x}{\partial y^2} = \rho g_x, \quad 0 \leq y \leq h(x, t) \quad (3.5.12)$$

This equation may be solved for u_x , just as was done in the preceding example; however, $h(x, t)$ is as yet unknown. The term h may be obtained from the following overall balance—written for a plate of unit width. Thus we have

$$-\frac{\partial h}{\partial t} = \frac{\partial}{\partial x} \int_0^h u_x dy \quad (3.5.13)$$

$\left[\begin{array}{l} \text{rate of decrease of} \\ \text{film thickness} \end{array} \right] = \left[\begin{array}{l} \text{net rate of} \\ \text{drainage} \end{array} \right]$

Upon substituting for u_x from Eq. (3.5.6) and on performing the integration we have

$$-\frac{\partial h}{\partial t} = \frac{d}{dx} \left(\frac{\rho g_x h^3}{3\mu} \right) = \frac{\rho g_x}{\mu} h^2 \frac{dh}{dx} \quad (3.5.14)$$

On noting that

$$h = 0 \quad \text{at} \quad x = 0, \quad t = 0 \quad (3.5.15)$$

Eq. (3.5.14) may be integrated to obtain

$$h = (\mu x / \rho g_x t)^{1/2} \quad (3.5.16)$$

which is the desired relationship between the film thickness h , time, and the vertical distance x .

Tallmadge¹⁴ has shown that Jeffreys' simple expression holds reasonably well, except for the very initial period of time when acceleration effects would become important. This is seen immediately by inspecting Eq. (3.5.16), which would give

$$\left(\frac{dh}{dx} \right) \rightarrow \infty \quad \text{as } x \rightarrow 0$$

which is clearly impossible.

We also note that Eq. (3.5.16) would not hold in the region where the draining fluid approaches the upper surface of the bulk fluid; here surface curvature effects could become important, as illustrated by the following problem.

(C) THE WITHDRAWAL OF SOLID BODIES FROM LIQUIDS

Let us now consider the slightly more complex problem involved in the continuous withdrawal of a solid body from a liquid. Such problems are of practical importance in the coating sheets, wires, and other bodies.

As seen in Fig. 3.5.4 the domain of interest may be divided into three regions.

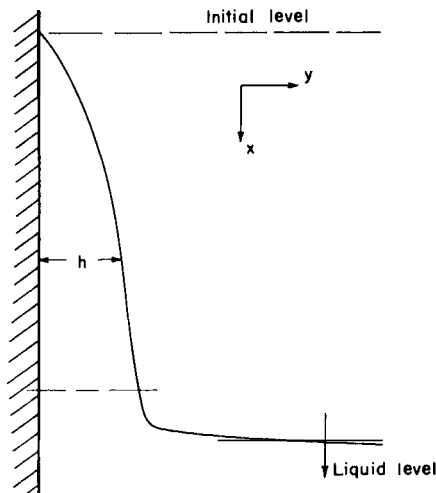


FIG. 3.5.4 Sketch of the fluid film developing on a vertical surface which is being withdrawn from a fluid.

In the upper region, some distance from the bulk liquid, the flow is parallel, and the effect of liquid curvature is negligible. The fluid flow behavior in this region may be described with the aid of the previously given Eq. (3.5.3).

In region 3 the effects of curvature predominate and the linear velocities are quite low, while in region 2 we have to consider both the effect of curvature and of flow.

Before proceeding further let us note that the meniscus of a liquid in contact with a vertical plate, such as sketched in Fig. 3.5.5, is given by the following relationship, which is obtained by minimizing the surface energy of the system¹⁶

$$\frac{d^2h}{dx^2} \left[1 + \left(\frac{dh}{dx} \right)^2 \right]^{3/2} = \frac{\rho g_x x}{\sigma} \quad (3.5.17)$$

where σ is the interfacial tension.

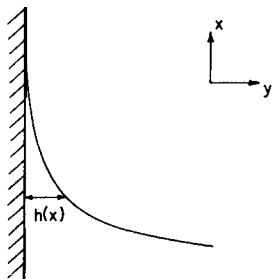


FIG. 3.5.5 Sketch of the meniscus at a vertical plate.

The solution of the differential equation (3.5.17) available in the text by Levich may be used for calculating the shape of the liquid surface in region 3, where the actual flow is quite small.

Region 2. If we consider that the film is thin in region 2, then only the x component of the equation of motion has to be taken into consideration; under these conditions we may also set $u_y = 0$, so that the equation of motion is given as

$$\mu \frac{d^2 u_x}{dy^2} + \rho g - \frac{\partial p}{\partial x} = 0 \quad (3.5.18)$$

In contrast to the behavior of thin films in parallel flow, previously discussed in (A) and (B), the pressure gradient is not zero in the present case; this pressure gradient is brought about by the curvature of the surface and

may be written as

$$-\frac{\partial p}{\partial x} = \sigma \frac{\partial^3 h}{\partial x^3} \quad (3.5.19)$$

Thus upon substituting from Eq. (3.5.19), Eq. (3.5.18) may be written as

$$\mu \frac{\partial^2 u_x}{\partial y^2} + \rho g_x + \sigma \frac{\partial^3 h}{\partial x^3} = 0 \quad (3.5.20)$$

which, with

$$u_x = U_{x,0} \quad \text{at } y = 0 \quad (3.5.21)$$

where $U_{x,0}$ is velocity of the plate, and

$$\frac{\partial u_x}{\partial y} = 0 \quad \text{at } y = h(x) \quad (3.5.22)$$

defines region 2.

Region 1. In this region, $0 \leq y \leq h_0$, parallel flow is observed; thus, we have

$$\mu \frac{\partial^2 u_x}{\partial y^2} = -\rho g_x \quad (3.5.23)$$

The statement of the problem is then completed by expressing continuity between regions 1 and 2. Thus we have

$$w_1 = w_2 \quad (3.5.24)$$

In general the system of Eqs. (3.5.17)–(3.5.23) has to be solved numerically, for the appropriate boundary conditions on h .¹⁹

Tallmadge¹⁷ has shown, however, that two convenient asymptotic solutions exist. For small values of the capillary number $N_{Ca} = U_{x,0}\mu/\sigma$ we have

$$h_0 = 0.95 [\mu^2 U_{x,0} / \sqrt{\sigma \rho g_x^{3/2}}]^{1/3} \quad (3.5.25)$$

while for large values of N_{Ca} the following solution holds:

$$h_0 = \mu U_{x,0}^{1/2} / \rho g \quad (3.5.26)$$

As seen in Fig. 3.5.6, Eq. (3.5.25) does seem to represent experimental measurements conducted with viscous fluids up to withdrawal speeds of about 0.5 m/s.

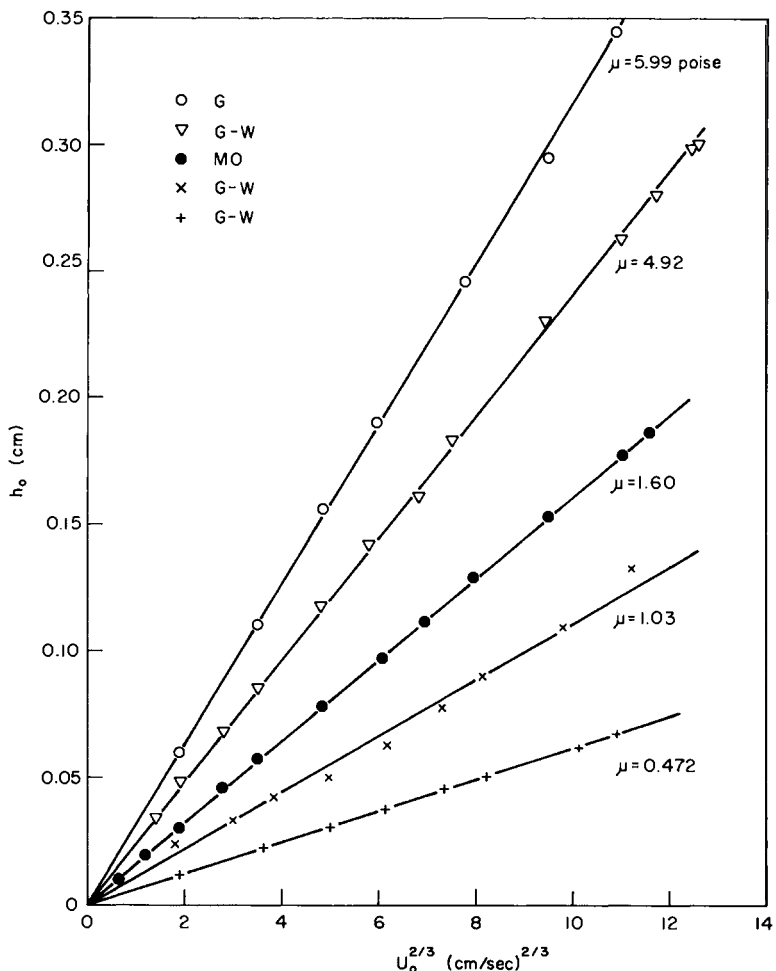


FIG. 3.5.6 The effect of fluid viscosity and withdrawal speed on the film thickness, after Talmadge.²⁰ Used with permission.

3.5.2 The Laminar Boundary Layer

Let us consider the flow of an incompressible fluid past a horizontal flat plate, as sketched in Fig. 3.5.7. It is seen in the sketch that the fluid, on approaching the plate with a uniform free stream velocity of $U_{x,\infty}$, is gradually retarded in the vicinity of the plate; the region in which the velocity of the fluid differs from that in the free stream is called the boundary layer, which is seen to grow progressively as we move in the x direction.

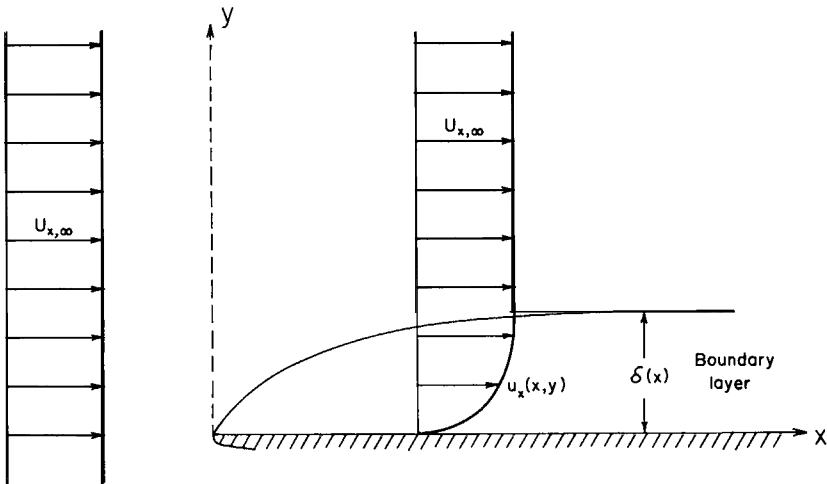


FIG. 3.5.7 Sketch of a laminar boundary layer developing on a flat plate.

Boundary layer type flows arise in numerous engineering problems, such as aircraft design, design of motor vehicle contours, etc.; specific metallurgical applications include heat transfer to steel strip in annealing and in heat treatment, mass transfer in pickling, and the entrainment of gases by molten metal streams.

For steady-state conditions, incompressible fluids, and for the two-dimensional (x and y) flow field considered here the equation of continuity and the equation of motion are available in Tables 3.2.1–3.2.3 and may be put in the following form:

$$\frac{\partial u_x}{\partial x} + \frac{\partial u_y}{\partial y} = 0 \quad (3.5.27)$$

$$u_x \frac{\partial u_x}{\partial x} + u_y \frac{\partial u_x}{\partial y} = -\frac{1}{\rho} \frac{\partial p}{\partial x} + \frac{\mu}{\rho} \left(\frac{\partial^2 u_x}{\partial x^2} + \frac{\partial^2 u_x}{\partial y^2} \right) \quad (3.5.28)$$

and

$$u_x \frac{\partial u_y}{\partial x} + u_y \frac{\partial u_y}{\partial y} = -\frac{1}{\rho} \frac{\partial p}{\partial y} + \frac{\mu}{\rho} \left(\frac{\partial^2 u_y}{\partial x^2} + \frac{\partial^2 u_y}{\partial y^2} \right) \quad (3.5.29)$$

In the statement of Eqs. (3.5.28) and (3.5.29) we retained both the pressure gradients and the velocity components u_x and u_y . Let us now proceed by estimating the order of magnitude of the terms appearing in these equations and decide on that basis which of the terms may be neglected. It hardly needs emphasis that this is a much more satisfactory and rigorous procedure than to dismiss terms or equations on purely qualitative arguments.

Let us consider the free stream (approach) velocity as the unit of magnitude for velocity and the length along the plate x as the unit of distance; let us assume furthermore that the thickness of the boundary layer δ is small compared to x .

The velocity u_x is of the order of unity because it varies from $U_{x,\infty}$ to 0 as y varies from δ to 0.

Since u_x may be expressed as

$$u_x = - \int_0^\delta \left(\frac{\partial u_y}{\partial y} \right) dx$$

it follows that $\partial u_x / \partial y$ is of the order $(1/\delta)$. From analogous considerations $\partial^2 u_x / \partial y^2$ is of the order $(1/\delta)^2$. Thus the order of magnitude of the x velocity components may be summarized as

$$\begin{array}{ccccc} u_x & \frac{\partial u_x}{\partial y} & \frac{\partial^2 u_x}{\partial y^2} & \frac{\partial u_x}{\partial x} & \frac{\partial^2 u_x}{\partial x^2} \\ (1) & (1/\delta) & (1/\delta)^2 & (1) & (1) \end{array}$$

The behavior of the last two terms follows readily from the fact that both u_x and x are assumed to be of the order of unity.

Let us now turn our attention to the y components of velocity. Upon considering that $\partial u_x / \partial x$ is of the order of unity, it follows from the equation of continuity [Eq. (3.5.27)] that $\partial u_y / \partial y$ must also be of the order of unity. Since y is of the order δ , the order of u_y must be of the order of δ also. It follows that $\partial^2 u_y / \partial y^2$ is of the order $1/\delta$. We may now summarize the order of the u_y terms as follows:

$$\begin{array}{ccccc} u_y & \frac{\partial u_y}{\partial y} & \frac{\partial^2 u_y}{\partial y^2} & \frac{\partial u_y}{\partial x} & \frac{\partial^2 u_y}{\partial x^2} \\ (\delta) & (1) & (1/\delta) & (\delta) & (\delta) \end{array}$$

Let us now restate the x and y components of the Navier-Stokes equation indicating the order of magnitude of the terms involved:

$$\begin{array}{lcl} u_x \frac{\partial u_x}{\partial x} + u_y \frac{\partial u_x}{\partial y} & = & -\frac{1}{\rho} \frac{\partial p}{\partial x} + \mu \left(\frac{\partial^2 u_x}{\partial x^2} + \frac{\partial^2 u_x}{\partial y^2} \right) \\ (1) & (1) & (1) \end{array} \quad (3.5.30)$$

for the x direction and

$$\begin{array}{lcl} u_x \frac{\partial u_y}{\partial x} + u_y \frac{\partial u_y}{\partial y} & = & -\frac{1}{\rho} \frac{\partial p}{\partial y} + \mu \left(\frac{\partial^2 u_y}{\partial x^2} + \frac{\partial^2 u_y}{\partial y^2} \right) \\ (\delta) & (\delta) & (1/\delta) \end{array} \quad (3.5.31)$$

for the y direction.

Upon examining Eq. (3.5.30), it is seen that on the right-hand side the term $\partial^2 u_x / \partial x^2$ is negligibly small compared to $\partial^2 u_x / \partial y^2$ and thus may be neglected. This finding is consistent with the qualitative reasoning that the principal mechanism of momentum transfer in the x direction is by convection, rather than by viscous diffusion.

We note, furthermore, that if the inertial terms, appearing on the left-hand side of Eq. (3.5.30), are of the same order as the remaining viscous term appearing on the right-hand side, then the quantity μ/ρ must be of the order of δ^2 . It follows from these arguments that the terms on the left-hand side of Eq. (3.5.31) are of the order δ and the last two terms of the right-hand side of Eq. (3.5.31) are also of at least δ order; as a consequence $-(1/\rho)(\partial p / \partial y)$ must also be of the order δ .

The importance consequence of this finding is that the y component of the equation of motion is small compared with the x component; i.e., the problem may be represented by considering Eq. (3.5.30), together with the equation of continuity. Using a similar argument, we may also show that in Eq. (3.5.30) the pressure term may be neglected for flat plates.

Thus the equations describing the velocity field in a steady-state incompressible boundary layer over a flat plate may be written as

$$\frac{\partial u_x}{\partial x} + \frac{\partial u_y}{\partial y} = 0 \quad (3.5.27)$$

and

$$u_x \frac{\partial u_x}{\partial x} + u_y \frac{\partial u_x}{\partial y} = (\mu/\rho) \frac{\partial^2 u_x}{\partial y^2} \quad (3.5.32)$$

The boundary conditions are given as

$$u_x = u_y = 0 \quad \text{at} \quad y = 0 \quad (3.5.33)$$

and

$$u_x = U_{x,\infty} \quad \text{at} \quad y = \infty \quad (3.5.34)$$

It has to be stressed to the reader that the seemingly lengthy development involved in establishing the order of magnitude of the various terms in the Navier-Stokes equations was entirely necessary. It is always essential to justify the neglecting of certain terms either a priori, as done here, or a posteriori by comparing the solutions obtained in the absence of simplifying assumptions with those resulting from the full set of equations.

A convenient way of solving the system of Eqs. (3.5.27)–(3.5.34) is by working in terms of a stream function and applying a coordinate transformation through which the partial differential equation is converted into an ordinary differential equation.

Let us introduce a similarity variable η defined as

$$\eta = y(U_{x,\infty}/vx)^{1/2} \quad (3.5.35)$$

and postulate, furthermore, that the solution of Eqs. (3.5.27)–(3.5.34) may be expressed in the following form:

$$\psi = (U_{x,\infty}xv)^{1/2}f(\eta) \quad (3.5.36)$$

Here ψ is the stream function and $f(\eta)$ is an as yet unknown function.

The reader will recall that in the cartesian coordinate system the stream function was defined as

$$u_x = \frac{\partial \psi}{\partial y} \quad (3.3.6)$$

and

$$u_y = -\frac{\partial \psi}{\partial x} \quad (3.3.7)$$

Thus by working in terms of the stream function, the equation of continuity is automatically satisfied (for a two-dimension system).

We may now proceed by generating the terms corresponding to u_x , u_y and their derivatives using Eq. (3.5.36) and then substitute the results into Eq. (3.5.32) to obtain the following:

$$u_x = U_{x,\infty}f' \quad (3.5.37)$$

$$u_y = \frac{1}{2}(U_{x,\infty}v/x)^{1/2}[\eta f' - f], \text{ etc.} \quad (3.5.38)$$

where

$$f' \equiv \frac{df(\eta)}{d\eta}$$

After some algebraic manipulation, Eq. (3.5.32) may be written in terms of the transformed variables η and f as

$$ff'' + 2f''' = 0 \quad (3.5.39)$$

In terms of the transformed variables the boundary conditions are written as

$$f = f' = 0, \quad \eta = 0 \quad (3.5.40)$$

[replacing Eq. (3.5.33)] and

$$f' = 1, \quad \eta = \infty \quad (3.5.41)$$

[replacing Eq. (3.5.34)].

The nonlinear ordinary differential equation (3.5.39) was first solved by Blasius¹⁸ using a power series expansion.

At present, over 50 years after Blasius' original article (based on his doctoral dissertation) the same task would be rather more easily accomplished using a digital computer, since many satisfactory techniques are available for the solution of the two-point boundary value problem posed by these equations.^{19,20}

The results of the numerical solution of Eqs. (3.5.39)–(3.5.41) are shown in Fig. 3.5.8 on a plot of the dimensionless horizontal and vertical velocity components against the dimensionless spatial variable.

We note that as specified by boundary condition (3.5.41) $u_x \rightarrow U_{x,\infty}$ as $\eta \rightarrow \infty$, but as a practical matter this condition is approached as $\eta \approx 5.0$. We note, furthermore, that the limiting value of the normal velocity component u_y is given as

$$u_y \rightarrow 0.865(U_{x,\infty} v/x)^{1/2} \quad \text{as } \eta \rightarrow \infty$$

i.e., $\eta \approx 5$.

If we designate, somewhat arbitrarily, the thickness of the boundary layer as the distance where $u_x/U_{x,\infty} \approx 0.99$, then from Fig. 3.5.8 we have the following expression for the boundary layer thickness:

$$\delta(x) \approx 5.0(vx/U_{x,\infty})^{1/2} \quad (3.5.42)$$

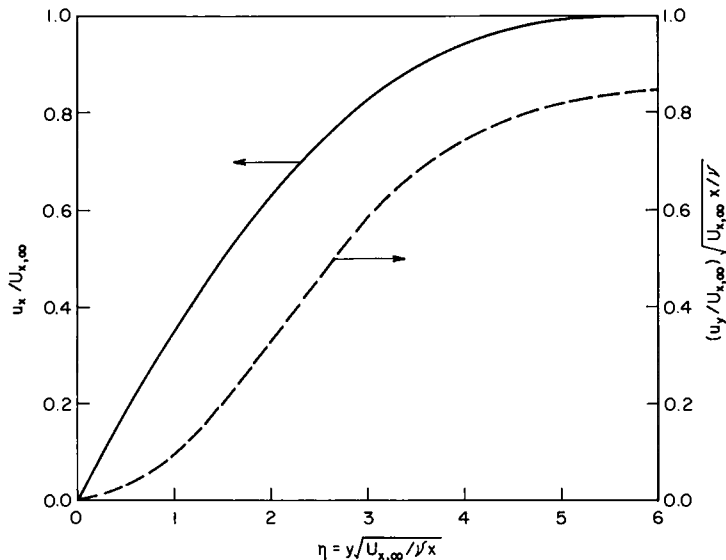


FIG. 3.5.8 The dimensionless velocity profiles for a boundary layer formed on a flat plate.

Before proceeding further, the limits of validity of these calculations have to be stressed to the reader. The boundary layer equations developed here are valid only for *laminar flow*, which for the present system means that the Reynolds number, defined in terms of the length of plate x ,

$$N_{Re,x} = U_{x,\infty} x / v$$

has to be smaller than 2×10^5 .

Another point that should be noted is that these equations are not valid in the immediate vicinity of the "leading edge," i.e., in the region of $x \approx 0$, because the assumptions made that the x components dominate the equation of motion, i.e., that x is large compared to δ , would not be valid here.

A further discussion of this problem is available in the text by Brodkey.⁷

A more satisfactory definition of the boundary layer is through the displacement thickness $\delta^*(x)$:

$$\begin{aligned}\delta^*(x) &= \int_0^\infty \left(1 - \frac{u_x}{U_{x,\infty}}\right) dy \\ &= 1.72(vx/U_{x,\infty})^{1/2}\end{aligned}\quad (3.5.43)$$

In a physical sense the product of the displacement thickness and the free stream velocity gives the volumetric rate at which the free stream is being retarded (per unit plate width) due to the presence of the flat plate.

Conversely, if the plate were moving and the bulk of the fluid were stationary, the product of the displacement thickness and the velocity of the plate would give the volumetric rate of fluid entrainment.

The above property of the displacement thickness is useful because it enables us to calculate the rate at which moving plates or metal streams would entrain the surrounding fluid medium. This problem is of particular importance in the estimation of air entrainment by poured metal streams, which could result in deoxidation. The displacement thickness of boundary layers formed on cylindrical bodies has been calculated by Glauert and Lighthill,²¹ whose results are shown in Fig. 3.5.9 on a plot of $\Delta/\pi R_c^2$ against $vz/U_{z,\infty} R_c^2$. Here R_c is the radius of the cylindrical body, or stream, z is the axial coordinate, representing the length of the body, U_z is the axial velocity, and

$$\Delta = \pi[(\delta^* + R_c)^2 - R_c^2] \quad (3.5.44)$$

is the cross-sectional area equivalent to the displacement thickness. It follows that the mass rate of entrainment by a moving cylindrical body (or stream) is given as

$$w = U_{z,\infty} \rho_f \Delta \quad (3.5.45)$$

Let us illustrate the use of Fig. 3.5.9 and of the accompanying equations by working a simple example.

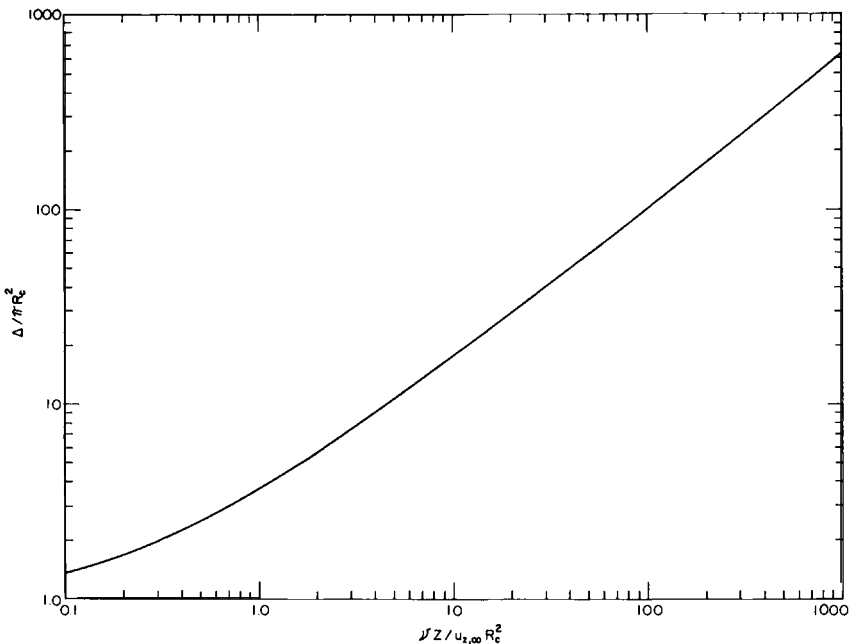


FIG. 3.5.9 The displacement thickness of the boundary layer formed on a thin cylindrical body.

Example 3.5.2 Estimate the amount of air entrained by a tapped steel stream, which may be regarded as a solid cylinder 0.02 m in diameter, 0.8 m long, and moving with a linear velocity of 1 m/s. The properties of the surrounding air may be estimated as

$$v = 1.25 \times 10^{-4} \text{ m}^2/\text{s}, \quad \rho_f = 0.34 \text{ kg/m}^3$$

SOLUTION The abscissa in Fig. 3.5.9 is

$$\frac{vz}{U_{z,\infty} R_c^2} = \frac{1.25 \times 10^{-4} \times 1}{1 \times 4 \times 10^{-4}} \sim 0.31$$

Thus

$$\Delta/\pi R_c^2 \sim 2.0$$

or

$$\Delta = 2.0 \times 3.14 \times 4 \times 10^{-4} = 2.51 \times 10^{-3} \text{ m}^2$$

Thus

$$w = 1 \times 0.34 \times 2.51 \times 10^{-3} \simeq 8.53 \times 10^{-4} \text{ kg/s}$$

We note that when the stream is broken up into droplets the air entrainment is increased—see K. Schwerdfeger, *Metall. Trans.*, 1979, in press.

We note that in addition to the examples mentioned earlier, namely entrainment problems, moving metal strips, etc., boundary layer phenomena play an important role in a broad range of materials processing operations. Some examples of these will be given in subsequent parts of this text. For a very thorough treatment of boundary layer flows the reader is referred to the classical book by Schlichting.⁹

3.5.3 Problems in Pipe Flow

In the majority of practical cases, gases or liquids are transported through circular pipes. While in most instances the flow is turbulent and the problems that arise may be tackled by employing *overall balances* as discussed in the preceding chapter, it is instructive to examine a limited number of laminar pipe flow problems, as will be done subsequently.

(A) LAMINAR FULLY DEVELOPED FLOW THROUGH A CIRCULAR PIPE

Let us consider the steady flow of incompressible fluid through a long straight pipe, some distance from the inlet, as sketched in Fig. 3.5.10.

This situation is conveniently represented in terms of the cylindrical coordinate system, for fully developed flow; i.e., if entrance effects are neglected only the axial velocity component u_z has to be considered.

Thus from Table 3.2.1 the equation of continuity is written as

$$\frac{\partial u_z}{\partial x} = 0 \quad (3.5.46)$$

Then using this result and Table 3.2.2 the z component of the equation of motion takes the following form:

$$\mu \left[\frac{1}{r} \frac{\partial}{\partial r} \left(r \frac{\partial u_z}{\partial r} \right) \right] = \frac{\partial p}{\partial z}, \quad 0 \leq r \leq R \quad (3.5.47)$$

For a fixed value of the pressure gradient this is a second-order ordinary differential equation; thus, two boundary conditions are needed. These have to specify that the velocity is zero at the walls of the pipe (i.e., the no-slip

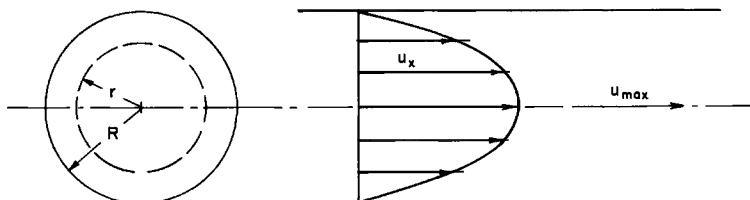


FIG. 3.5.10 Sketch of the coordinate system and the velocity profile for laminar flow through a pipe.

condition); the second boundary condition is provided by the stipulation of symmetry about the center line. Thus we have

$$u_z = 0 \quad \text{at} \quad r = R \quad (3.5.48)$$

and

$$\frac{\partial u_z}{\partial r} = 0 \quad \text{at} \quad r = 0 \quad (3.5.49)$$

Upon considering that $\partial p / \partial z = \text{const}$, Eq. (3.5.47) is readily integrated once, to obtain

$$\mu r \frac{du_z}{dr} = \frac{r^2}{2} \left(\frac{\partial p}{\partial z} \right) + C_1 \quad (3.5.50)$$

by invoking the boundary condition in Eq. (3.5.49),

$$C_1 = 0$$

Subsequent integration gives

$$u_z = \left(\frac{\partial p}{\partial z} \right) \frac{r^2}{4} + C_2 \quad (3.5.51)$$

Then upon evaluating C_2 from the boundary condition contained in Eq. (3.5.48) we obtain

$$u_z = - \left(\frac{\partial p}{\partial z} \right) \frac{R^2}{4\mu} \left[1 - \left(\frac{r}{R} \right)^2 \right] \quad (3.5.52)$$

We note that the velocity profile is parabolic, just as we found for the laminar flow of a vertical falling film in Section 3.5.1, and that the maximum velocity occurs at the center line, i.e., at $r = 0$:

$$u_{z,\max} = - \left(\frac{\partial p}{\partial z} \right) R^2 / 4\mu \quad (3.5.53)$$

The volumetric flow rate through the pipe Q is given as

$$Q = \int_0^R u_z(r) 2\pi r dr = - \frac{\pi R^4}{8\mu} \left(\frac{\partial p}{\partial z} \right) \quad (3.5.54)$$

or upon designating the pressure drop over a finite pipe length L by Δp we have

$$Q = -(\Delta p / 8L\mu) \pi R^4 \quad (3.5.55)$$

which is the celebrated *Hagen–Poiseuille* equation for laminar flow through a pipe.

The reader should recall that an identical result to that given by Eq. (3.5.55) has been presented in Chapter 2 using the friction factor correlation.

The average linear velocity through the pipe $U_{z,m}$ is given as

$$u_{z,m} = \frac{\int_0^R u_z(r) 2\pi r dr}{\int_0^R 2\pi r dr} = \frac{Q}{\pi R^2} = -\left(\frac{\partial p}{\partial z}\right) \frac{R^2}{8\mu} = \frac{1}{2}(u_{z,max}) \quad (3.5.56)$$

Laminar flow through pipes does not occur very frequently in industrial practice, except when highly viscous fluids, such as molasses or molten glass, are being handled. However, the Hagen–Poiseuille equation is of considerable practical interest in viscometry. Thus, if a fluid is passed through a capillary tube over which a known pressure drop is imposed and the volumetric flow rate is measured for a known geometry, the viscosity is the only unknown and may be calculated from Eq. (3.5.55).

(B) ENTRANCE EFFECTS IN PIPE FLOW

In the discussion of the previous example we assumed *fully developed flow*; that is, we considered the portion of the pipe which was sufficiently downstream from the inlet so that the complexities associated with the entrance of the fluid to the pipe did not have to be taken into consideration. Let us now examine this problem.

The flow field to be expected when the fluid enters the pipe[†] is sketched in Fig. 3.5.11. It is seen that the fluid, which approaches the pipe with a flat velocity profile, is progressively retarded as it is brought into contact with the pipe walls so that a *boundary layer develops*. When these boundary layers formed on the walls coincide, the fluid assumes the velocity field predicted by Eq. (3.5.52), i.e., that corresponding to fully developed laminar flow.

The flow field in the entrance region is three dimensional physically but the problem may be stated mathematically in terms of two spatial variables because of the axial symmetry.

Using the expression developed for the equation of continuity and motion in cylindrical coordinates in Tables 3.2.1 and 3.2.2 and neglecting the θ component we have

$$\frac{1}{r} \frac{\partial}{\partial r}(ru_r) + \frac{\partial}{\partial z}(u_z) = 0 \quad (\text{continuity}) \quad (3.5.57)$$

$$\rho \left(u_r \frac{\partial u_z}{\partial r} + u_z \frac{\partial u_z}{\partial z} \right) = -\frac{\partial p}{\partial z} + \mu \left[\frac{1}{r} \frac{\partial}{\partial r} \left(r \frac{\partial u_z}{\partial r} \right) + \frac{\partial^2 u_z}{\partial z^2} \right] \quad (3.5.58)$$

This problem was tackled by numerous investigators, including Langhaar,²² Boussinesq,²³ and Sparrow.²⁴ A detailed description of

[†] Analogous consideration would apply to flow between parallel flat plates.

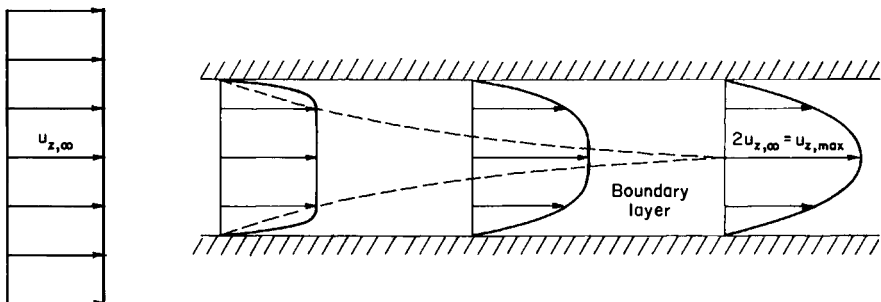


FIG. 3.5.11 The entrance region for laminar flow through a circular pipe.

Langhaar's elegant solution is available in the text by Brodkey [7]. A comparison of some of the solutions is given in Fig. 3.5.12, which shows a plot of the ratio: (velocity at the center line of the pipe)/(free stream velocity of the approaching stream). In fully developed laminar flow the maximum velocity is twice the average velocity; this ratio is seen to vary from unity at the entrance to the pipe to the value of two when fully developed flow is attained.

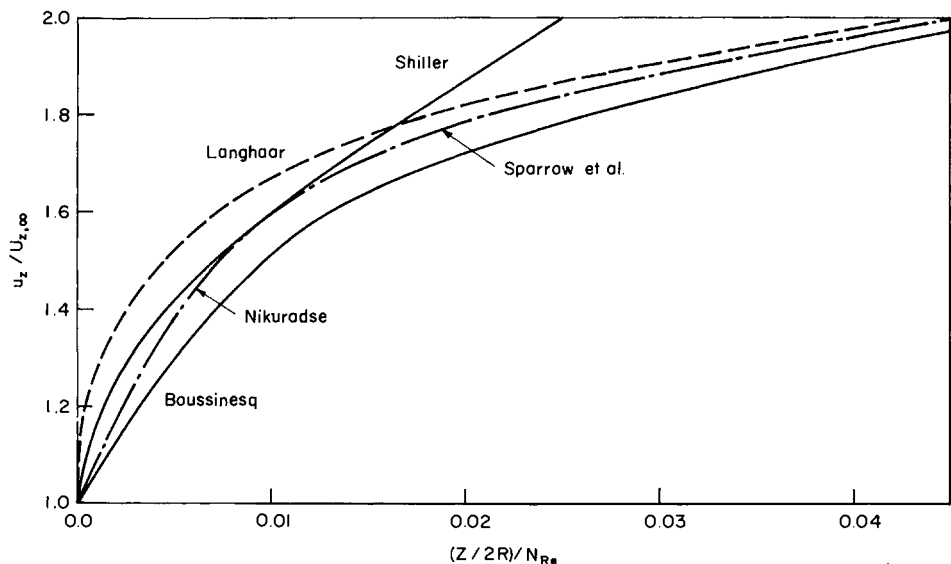


FIG. 3.5.12 A comparison of the solutions for the entrance region of a cylindrical pipe.

Inspection of Fig. 3.5.12 shows that the entrance length L_e may be represented by the following relationship:

$$L_e/2R \approx 0.06N_{Re} \quad (3.5.59)$$

where $N_{Re} = 2U_m \rho R / \mu$ is the Reynolds number.

Equation (3.5.59) is helpful because it defines the region beyond which the Hagen–Poiseuille equation is valid. We note that the flow field is rather more complex in the entrance region to pipes; moreover, the frictional resistance to flow is rather higher in this zone. If flow measurement devices are to be installed it is important that these not be located in the entrance region. Moreover, if we wish to use the Hagen–Poiseuille equation for the measurement of viscosity, care has to be taken that the capillary is long enough, so that the entrance length is a negligible proportion of its total length.

(c) UNSTEADY FLOW IN A PIPE

All the pipe flow problems discussed so far involved steady state conditions. Let us now consider a simple transient problem namely the commencement of fully developed laminar flow in a pipe, resulting from a suddenly imposed pressure gradient.

For fully developed laminar flow both the θ and the r components of the velocity are zero; thus, the equation of motion may be written as[†]

$$\rho \frac{\partial u_z}{\partial t} = -\frac{\partial p}{\partial z} + \mu \left[\frac{\partial^2 u_z}{\partial r^2} + \frac{1}{r} \frac{\partial u_z}{\partial r} \right] \quad (3.5.60)$$

The boundary conditions have to specify that initially the fluid is stationary, the velocity is zero at the walls and that symmetry is observed about the centerline. Thus we have

$$u_z = 0 \quad \text{at } t = 0 \quad (3.5.61a)$$

$$u_z = 0 \quad \text{at } r = R \quad (3.5.61b)$$

$$\frac{\partial u_z}{\partial r} = 0 \quad \text{at } r = 0 \quad (3.5.61c)$$

This problem was solved by Szymanski,²⁵ and only the final result will be given here:

$$u_z = -\frac{\partial p}{\partial z} \frac{R^2}{4\mu} \left[1 - \left(\frac{r}{R} \right)^2 - 8 \sum_{n=1}^{\infty} \frac{J_0(\alpha_n r/R)}{\alpha_n^3 J_0'(\alpha_n)} e^{-\alpha_n \tau} \right] \quad (3.5.62)$$

where $\tau = \mu t / \rho R^2$. Here J_0 is a Bessel function of first kind and α_n , $n = 1, 2, 3$, are the zeros of this Bessel function.[†]

The solution, as given by Eq. (3.5.62) is shown in Fig. 3.5.13 in graphical form. It is seen that steady-state conditions would be attained when $\tau \approx 1$;

[†] The equation of continuity requires that $\partial u_z / \partial z = 0$, which is being met by Eq. (3.5.60).

[†] A good discussion of Bessel functions is available in Sherwood *et al.*²⁶ or in Sokolnikoff and Redheffer.⁶

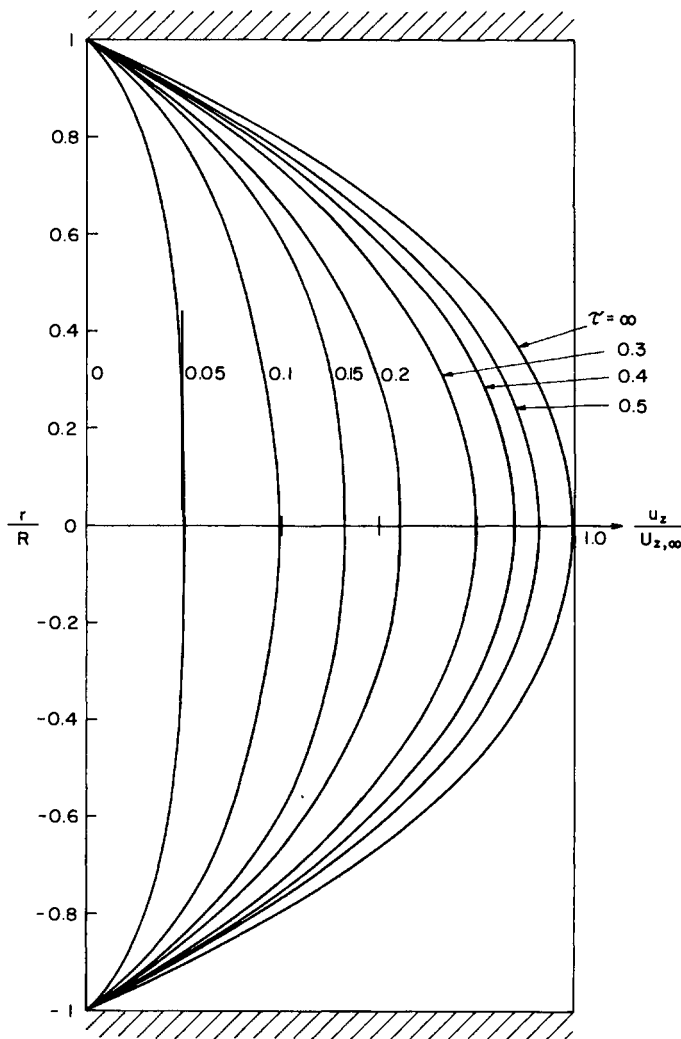


FIG. 3.5.13 The development of the velocity profile in a circular pipe during the startup period; $\tau = \mu t / \rho R^2$.

although there is some question whether the initial condition of suddenly imposing a pressure gradient on the system is entirely realistic.

3.5.4 The Hydrodynamic Theory of Lubrication

In fluid flow problems associated with lubrication the flow is definitely laminar; indeed, the viscous forces predominate under these conditions.

Lubrication problems do arise in materials processing operations, not only in connection with the conventional machinery employed in these systems but also in some special, metallurgically oriented operations, such as wire drawing and continuous casting.

Here we shall confine our discussion to a simplified treatment of lubrication in a bearing; nonetheless, these considerations form the basis of the analysis of more complex problems. Let us examine the flow field in a wedge-shaped gap between a slide block and a plane guide surface, such as sketched in Fig. 3.5.14.

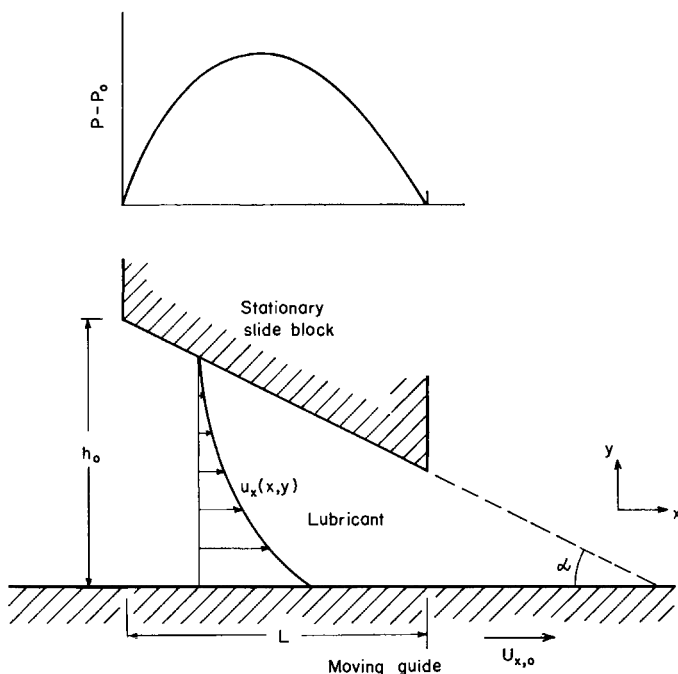


FIG. 3.5.14 Sketch of the slide-block-guide assembly for an idealized problem in the lubrication of bearings.

We shall consider that the slide block remains stationary while the guide moves in the x direction; as a result fluid is being entrained in the x direction. The flow field has to be two dimensional because of the angle formed by the slide block and the guide. Here $h(x)$ denotes the vertical distance between the slide block and the guide while h_0 is the value of h at $x = 0$.

However, if $L \gg h(x)$, as is the case in practice, only the x component of the equation of motion has to be considered. One could develop quantitative

arguments in support of this contention as was done in connection with the boundary layer equations.

Thus the equation of motion may be written in the following form:

$$\frac{\partial p}{\partial x} = \mu \frac{\partial^2 u_x}{\partial y^2} \quad (3.5.63)$$

The equation of continuity has to express the fact that the volumetric flow rate (per unit width Q') must be constant at each cross section; this constraint is somewhat similar to that employed for the flow of thin films which add a variable thickness. Thus we have

$$Q' = \int_0^{h(x)} u_x dy = \text{const} \quad (3.5.64)$$

The boundary conditions specifying “no-slip” at the solid surfaces are written as

$$u_x = U_{x,0} \quad \text{at } y = 0 \quad (3.5.65)$$

$$u_x = 0 \quad \text{at } y = h(x) \quad (3.5.66)$$

$$p = p_0 \quad \text{at } x = 0, \quad x = L \quad (3.5.67)$$

If we postulate that $(\partial p / \partial x)$ is a function of x only Eq. (3.5.63) is readily integrated to obtain

$$u_x = U_{x,0} \left(1 - \frac{y}{h(x)} \right) - \frac{h^2(x)y}{2\mu} \left(\frac{\partial p}{\partial x} \right) \left(1 - \frac{y}{h(x)} \right) \quad (3.5.68)$$

At this stage the pressure gradient is an as yet unknown quantity. In order to define $\partial p / \partial x$ let us substitute for u_x in the equation of continuity from Eq. (3.5.68) to obtain

$$Q' = \frac{U_{x,0}h(x)}{2} - \frac{h^3(x)}{12\mu} \frac{\partial p}{\partial x} \quad (3.5.69)$$

Thus

$$\frac{\partial p}{\partial x} = 12\mu \left[\frac{U_{x,0}}{2h^2(x)} \right] - \frac{Q'}{h^3(x)} \quad (3.5.70)$$

Or by integrating between the limits $x = 0$ and $x = x$ we have

$$p(x) = p_0 + 6\mu U_{x,0} \int_0^x \frac{dx}{h^2(x)} - 12\mu Q' \int_0^x \frac{dx}{h^3(x)} \quad (3.5.71)$$

Upon noting that $p = p_0$ at $x = L$ we have

$$Q' = \frac{1}{2} U_{x,0} \int_0^L \frac{dx}{h^2(x)} / \int_0^L \frac{dx}{h^3(x)} \quad (3.5.72)$$

which is the desired relationship between the volumetric flow rate of the lubricant (per unit width) and the shape of the gap between the slide block and the plane guide.

We note that it is readily seen from the form of Eq. (3.5.72) and the boundary conditions that the pressure in the gap has to show a maximum at some intermediate distance from the inlet, as sketched in the upper part of Fig. 3.5.14. In the inlet region flow occurs against the pressure gradient.

Further manipulation of these equations is possible to define the optimal shape of the gap between the slide block and the plane guide. A good discussion of this is available in the text by Schlichting⁹. The application of the theory of lubrication to wire drawing has been presented by Christopherson and Dawson²⁷ and Sturgeon and Tattersall.²⁸

3.5.5 Flow in the Vicinity of a Rotating Disk

Flow phenomena associated with thin, rotating disks are of considerable importance in metals research, because this geometry provides a good practical means of contacting a solid with a liquid in a well-defined fluid flow regime. Rotating disk electrodes have been used in polarography and in many other electrochemical studies. A good description of mass transfer phenomena in the rotating disk geometry has been presented by Levich¹⁶; at present our attention will be confined to a brief discussion of the fluid flow phenomena.

Figure 3.5.15 shows a sketch of the rotating disk system, in three-dimensional, cylindrical coordinates. It is seen that the flat disk rotates about an axis perpendicular to its plane with an angular velocity $\tilde{\omega}$.

The rotation of the disk gives rise to three velocity components:

u_θ , the tangential component results from the viscous drag;

u_r , the radial component results from the centrifugal forces; while

u_z , the axial velocity component arises from continuity, i.e., from the need to replace the fluid in the vicinity of the disk that has moved away in the radial and the tangential direction.

For incompressible three-dimensional flow, with symmetry about θ , the equation of continuity is given as

$$\frac{1}{r} \frac{\partial}{\partial r} (ru_r) + \frac{\partial u_z}{\partial z} = 0 \quad (3.5.73)$$

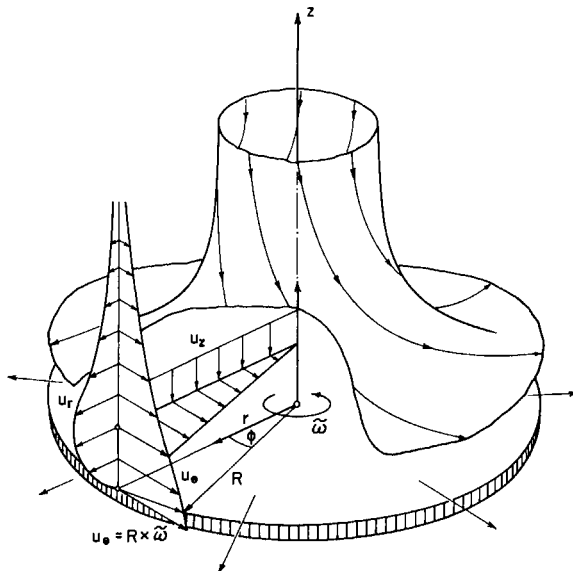


FIG. 3.5.15 Sketch of the flow field developed in a fluid in which a disk is rotating.

For steady-state conditions the three components of the equation of motion may be written as

$$u_r \frac{\partial u_r}{\partial r} - \frac{u_\theta^2}{r} + u_z \frac{\partial u_r}{\partial z} = -\frac{1}{\rho} \frac{\partial p}{\partial r} + \frac{\mu}{\rho} \left[\frac{\partial^2 u_r}{\partial r^2} + \frac{\partial}{\partial r} \left(\frac{u_r}{r} \right) + \frac{\partial^2 u_r}{\partial z^2} \right] \quad (3.5.74)$$

(radial component)

$$u_r \frac{\partial u_\theta}{\partial r} + \frac{u_r u_\theta}{r} + U_z \frac{\partial u_\theta}{\partial z} = \frac{\mu}{\rho} \left[\frac{\partial^2 u_\theta}{\partial r^2} + \frac{\partial}{\partial r} \left(\frac{u_\theta}{r} \right) + \frac{\partial^2 u_\theta}{\partial z^2} \right] \quad (3.5.75)$$

(tangential component)

$$u_r \frac{\partial u_z}{\partial r} + u_z \frac{\partial u_z}{\partial z} = -\frac{1}{\rho} \frac{\partial p}{\partial z} + \frac{\mu}{\rho} \left[\frac{\partial^2 u_z}{\partial r^2} + \frac{1}{r} \frac{\partial u_z}{\partial r} + \frac{\partial^2 u_z}{\partial z^2} \right] \quad (3.5.76)$$

(axial component)

The boundary conditions may be written as

$$u_r = 0 \quad \text{at } z = 0 \quad (3.5.77)$$

$$u_\theta = r \tilde{\omega} \quad \text{at } z = 0 \quad (3.5.78)$$

$$u_z = 0 \quad \text{at } z = 0 \quad (3.5.79)$$

(all expressing the “no-slip” condition). In addition we have that

$$u_r = 0 \quad (3.5.80)$$

$$u_\theta = 0 \quad (3.5.81)$$

at $z = \infty$.

We note that we have no boundary conditions referring to the outer edge of the disk (i.e., at $r = R$) because the disk is regarded as infinitely large, or, in other words, the edge effects are neglected. This will, however, not prevent us from applying the velocity profile obtained to a disk of finite dimensions.

As discussed in Schlichting⁹ the system of Eqs. (3.5.73)–(3.5.79) has been solved by a similarity transformation. The similarity variable ξ was defined as

$$\xi = z(\tilde{\omega}/v)^{1/2} \quad (3.5.82)$$

Furthermore, it was postulated that the solution may be sought in the following form:

$$u_r = r\tilde{\omega}F(\xi) \quad (3.5.83)$$

$$u_\theta = r\tilde{\omega}G(\xi) \quad (3.5.84)$$

$$u_z = (v\tilde{\omega})^{1/2}H(\xi) \quad (3.5.85)$$

where $F(\xi)$, $G(\xi)$, and $H(\xi)$ are functions to be determined. Figure 3.5.16 shows the computed profiles of the functions $F(\xi)$, $G(\xi)$, and $H(\xi)$ obtained by the numerical integration of the governing equations. A perhaps better

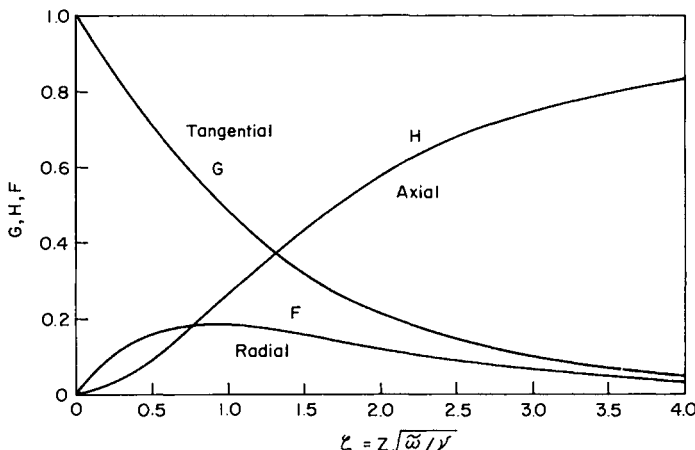


FIG. 3.5.16 The functions describing the axial, tangential, and radial velocity components for the rotating disk problem.

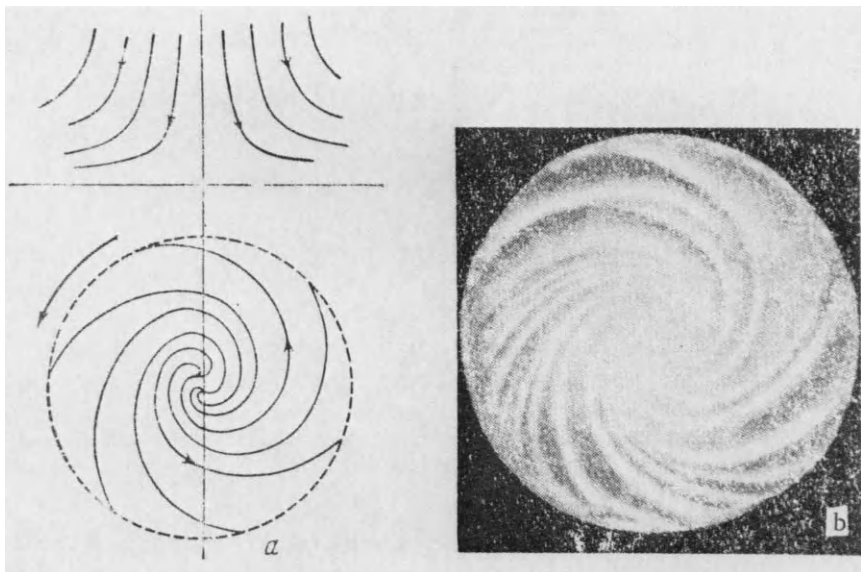


FIG. 3.5.17 Distribution of the streamlines at the surface of a rotating disk: (a) calculated values, (b) streamlines etched on the surface of a rotating disk. After Levich,¹⁶ reproduced with permission.

visualization of the actual flow pattern is provided in Fig. 3.5.17, which indicates the position of the streamlines.

We may define, somewhat arbitrarily, a boundary layer thickness for the rotating disk, say δ_ω , where the axial component attains some 80% of its limiting value and the tangential velocity component is less than 5% of its value at the surface of the disk. Using the information in Fig. 3.5.16 we have

$$\delta_\omega \sim 3.6(v/\tilde{\omega})^{1/2} \quad (3.5.86)$$

As discussed by Levich, Eq. (3.5.86) provides a fundamental basis for the interpretation mass transfer data obtained for a rotating disk system.

3.5.6 The Navier-Stokes Equations Written as Vorticity Transport Equations

Let us consider the fluid flow field established in the system sketched in Fig. 3.5.18, where a liquid is held in a rectangular container which extends from $x = 0$ to $x = L$ and from $y = 0$ to $y = H$ and is large in the z direction. The upper surface of the container is covered by a solid sheet which is in contact with the liquid and moves at a constant velocity $U_{x,0}$.

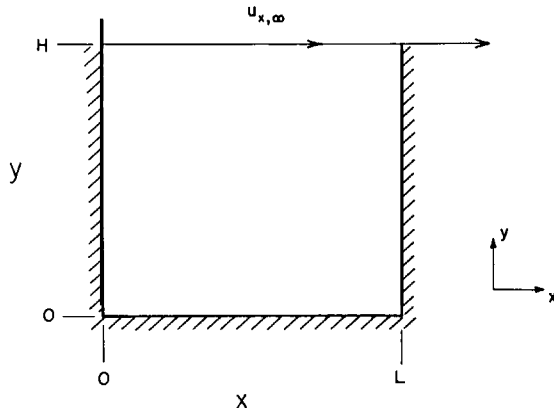


FIG. 3.5.18 Sketch of the system for the mechanically driven circulation system discussed in Section 3.5.6.

The problem is then to describe the resultant steady-state velocity field. Such a system may be a highly idealized representation of the fluid flow field in certain pickling tanks.

Let us proceed by stating the appropriate forms of the Navier–Stokes equations, and indicate the manipulations possible to express these in a form suitable for machine computation. The equation of continuity is given as follows for an incompressible fluid and for steady-state conditions:

$$\frac{\partial u_x}{\partial x} + \frac{\partial u_y}{\partial y} = 0 \quad (3.5.87)$$

The two components of the equation of motion are given as

$$u_x \frac{\partial u_x}{\partial x} + u_y \frac{\partial u_x}{\partial y} = -\frac{1}{\rho} \frac{\partial p}{\partial x} + \frac{\mu}{\rho} \left[\frac{\partial^2 u_x}{\partial x^2} + \frac{\partial^2 u_x}{\partial y^2} \right] \quad (3.5.88)$$

$$u_x \frac{\partial u_y}{\partial x} + u_y \frac{\partial u_y}{\partial y} = -\frac{1}{\rho} \frac{\partial p}{\partial y} + \frac{\mu}{\rho} \left[\frac{\partial^2 u_y}{\partial x^2} + \frac{\partial^2 u_y}{\partial y^2} \right] \quad (3.5.89)$$

The boundary conditions are given as

$$\begin{aligned} u_x &= u_y = 0 && \text{at } y = 0 \\ && & \text{at } x = 0, x = L \\ u_y &= 0, \quad u_x = U_{x,0} && \text{at } y = H \end{aligned} \quad (3.5.90)$$

In many applications it is convenient to rewrite Eqs. (3.5.88) and (3.5.89) in terms of the vorticity Ω defined by Eqs. (3.3.1)–(3.3.3). For a

two-dimensional Cartesian system the z component of Ω is defined as

$$\Omega_z = \left(\frac{\partial u_y}{\partial x} - \frac{\partial u_x}{\partial y} \right) \quad (3.5.91)$$

Let us now proceed by differentiating Eq. (3.5.88) with respect to y and differentiating Eq. (3.5.89) with respect to x . Upon performing these operations and then subtracting Eq. (3.5.88) from (3.5.89) and using Eq. (3.5.91) we obtain the following:

$$u_x \frac{\partial \Omega_z}{\partial x} + u_y \frac{\partial \Omega_z}{\partial y} = \frac{\mu}{\rho} \left[\frac{\partial^2 \Omega_z}{\partial x^2} + \frac{\partial^2 \Omega_z}{\partial y^2} \right] \quad (3.5.92)$$

Equation (3.5.92) is the *vorticity transport equation*, which expresses the conservation of vorticity.

Often it is convenient to introduce the stream function defined as

$$u_x = \frac{\partial \psi}{\partial y} \quad (3.5.93)$$

$$u_y = -\frac{\partial \psi}{\partial x} \quad (3.5.94)$$

As discussed earlier, it is readily shown that by working in terms of the stream function the equation of continuity is automatically satisfied. The vorticity and the stream function are related by the following expression:

$$\Omega_z = -\nabla^2 \psi = -\left(\frac{\partial^2 \psi}{\partial x^2} + \frac{\partial^2 \psi}{\partial y^2} \right) \quad (3.5.95)$$

In many practical computational schemes it is convenient to replace Eqs. (3.5.88) and (3.5.89) and Eq. (3.5.87) by Eqs. (3.5.92) and (3.5.95). We could, of course, work entirely in terms of the vorticity and the stream function by putting Eqs. (3.5.92) in the following form:

$$\frac{\partial \psi}{\partial y} \left(\frac{\partial \Omega_z}{\partial x} \right) - \frac{\partial \psi}{\partial x} \left(\frac{\partial \Omega_z}{\partial y} \right) = \frac{\mu}{\rho} \left[\frac{\partial^2 \Omega_z}{\partial x^2} + \frac{\partial^2 \Omega_z}{\partial y^2} \right] \quad (3.5.96)$$

In stating the problem in a suitable form for computation, the boundary conditions represented by Eq. (3.5.90) have to be expressed in terms of the vorticity or the stream function. In the present case this may be done quite readily, because the zero velocities stipulated at the solid walls require that the stream function be a constant—which may be taken as zero. The actual computational schemes required for solving problems of this kind are discussed in Roache²⁹ and Peaceman and Rachford.³⁰

3.6 Concluding Remarks

In this chapter we introduced the reader to the differential equations of fluid flow, together with the solutions to some key classical problems. While the Navier-Stokes equations developed here are valid for laminar flow only the significance of the material presented here is much broader than the restriction of laminar flow implies. Notwithstanding the fact that laminar motion is not very common in the majority of metals processing operations carried out on an industrial scale, the basic concepts discussed in this chapter, such as the definition of the stream function, the vorticity, and the like, are applicable to both laminar and to turbulent motion. Moreover, the general philosophy of setting up fluid flow problems illustrated throughout in the chapter is applicable to both laminar and turbulent systems.

In the immediately preceding section we sought to illustrate the use of the Navier-Stokes equations for solving some problems of practical interest in metals processing or metals processing research. This selection, however, is far from encyclopedic; a very broad range of interesting laminar flow problems are presented in the texts listed under general reading at the end of this chapter.

In closing we should perhaps stress again to the reader that the technique of overall balances described in Chapter 2 and the differential balances given in the present chapter are largely complementary. The choice of the particular approach to be adopted must depend critically on the nature of the problem.

References

1. J. G. Knudsen and D. L. Katz, "Fluid Mechanics and Heat Transfer." McGraw-Hill, New York, 1958.
2. V. Streeter, ed., "Handbook of Fluid Mechanics." McGraw-Hill, New York, 1961.
3. J. Szekely and N. J. Themelis, "Rate Phenomena in Process Metallurgy." Wiley, New York, 1971.
4. N. Standish, ed., "Blast Furnace Aerodynamics." Wollongong, Australia, 1975.
5. R. V. Churchill, "Complex Variables and Applications." McGraw-Hill, New York; 1948; see also Knudsen and Katz.²
6. I. S. Sokolnikov and R. M. Redheffer, "Mathematics of Physics and Modern Engineering." McGraw-Hill, New York, 1966.
7. R. S. Brodkey, "The Phenomena of Fluid Motions." Addison-Wesley, Reading, Massachusetts, 1957.
8. J. F. Davidson and D. Harrison, "Fluidized Particles." Cambridge Univ. Press, London and New York, 1963.
9. H. Schlichting, "Boundary Layer Theory," 6th ed., Chapter 6. McGraw-Hill, New York, 1968.
10. J. Szekely and J. H. Chen, "The Chemical Metallurgy of Iron and Steel," p. 218 Iron Steel Inst., London, 1971.
11. J. Szekely and A. Jassal, *Metall. Trans.* **9B**, 387 (1978).

12. S. R. Talby, and S. Portalski, *Trans. Inst. Chem. Eng.* **14**, 114 (1962).
13. S. Portalski and A. J. Clegg, *Chem. Eng.* **8a**, No. 26, 770 (1971), No. 27, 1257 (1972).
14. J. Tallmadge, *AICheJ.* **10**, 777 (1964).
15. H. Jeffreys, *Proc. Cambridge Philos. Soc.* **26**, 204 (1930).
16. V. Levich, "Physicochemical Hydrodynamics," p. 373. Prentice-Hall, Englewood Cliffs, New Jersey, 1962.
17. J. A. Tallmadge, *AICheJ.* **11**, 403 (1965).
18. Z. Blasius, *Z. Math. Phys.* **56**, 1–37 (1908).
19. W. H. Ray and J. Szekely, "Process Optimization, with Applications in Metallurgy and in Chemical Engineering." Wiley, New York, 1973.
20. H. B. Keller, "Numerical Methods for Two Point Boundary Value Problems." (Blaisdell), New York, 1968.
21. M. B. Glauert and M. J. Lighthill, *Proc. R. Soc. London, Ser. A* **204**, 188, (1954).
22. H. L. Langhaar, *Trans. AIME* **64**, A55 (1942).
23. J. Boussinesq, *C. R. Hebd. Seances Acad. Sci.* **113**, 49 (1891).
24. E. M. Sparrow, S. H. Lin, and T. S. Lundgren, *Phy. Fluids* **7**, 338 (1964).
25. P. J. Szymanski, *Math. Pure Appl. Ser. 9* **11**, 67–107 (1932).
26. T. K. Sherwood, H. S. Mickley, and C. E. Reid, "Applied Mathematics in Chemical Engineering." McGraw-Hill, New York, 1957.
27. D. G. Christopherson and D. Dawson, *Proc. R. Soc. London, Ser. A* **251**, 550 (1959).
28. G. M. Sturgeon and G. H. Tattersall, *Wire Ind.* **26**, 1183 (1959).
29. P. J. Roache, "Computational Fluid Dynamics." Hermosa Publishers, Albuquerque, New Mexico, 1972.
30. D. W. Peaceman and H. H. Rachford, *J. Soc. Ind. Appl. Math.* **3**, 28 (1955).

In the previous chapter we introduced the reader to the basic differential equations of fluid flow, the Navier–Stokes equations. We noted that these expressions were restricted to *laminar systems*, and thus we had to assign a definite domain of validity to the equations, developed for representing a range of fluid flow problems. This was usually done by stating the upper limits of the Reynolds number for which these solutions were valid, e.g., 2300 for pipe flow, 10^5 for laminar boundary layers, 20 for laminar falling films, etc.

As noted in many practical situations these restrictions are not met, either because the velocity is large or, perhaps more frequently, because of the large size of the equipment (large value of the characteristic length in the Reynolds number); under these conditions the flow field is turbulent.

If the problem of interest concerns some macroscopic, overall behavior of the system, such as the development of a relationship between pressure drop and volumetric flow rate through a conduit, or the calculation of the drag force on a body, then the use of the overall balance technique, described in Chapter 2, may be the most satisfactory approach. The empirical correlations employed in the use of this technique are not really different *in concept* although will differ numerically, depending on whether the flow field is turbulent or laminar.

In contrast, if we wish to study the detailed velocity profiles and the fine structure of the flow field, a subject to which this chapter is devoted, there are very substantial differences between laminar and turbulent behavior. In a physical sense these differences are due to the fact that even in a macroscopically steady situation the fluctuations in the key parameters, such as velocity, pressure, etc., inherently associated with turbulence are unsteady-state phenomena. These turbulent fluctuations and other phenomena stemming

from them play a crucial role in determining the behavior of turbulent systems.

The mathematical consequence of these turbulent fluctuations is that in these systems momentum transfer can no longer be described in terms of the velocity gradients and the Newtonian definition of viscosity but rather much more complex and yet less satisfactory relationships have to be invoked for relating the momentum flux to the local velocity gradient.

It follows that turbulent flow phenomena are much more complex than laminar flow behavior; moreover, turbulence phenomena are much less well understood. Nonetheless, turbulent flow is encountered in the majority of metals processing operations, including BOF steelmaking, vacuum degassing, mixing in teemed streams, electromagnetic stirring, continuous casting, copper converting, fluid flow in the Hall-Cell, etc. Moreover, it is generally accepted that a better understanding of the structure of the flow field in these systems could play a major role in both process improvement and the development of improved processes. These factors provide very powerful incentives for the study of the very complex and as yet inadequately understood phenomena which will be described in this chapter.

The work that has been done on the study of turbulent flow phenomena may be divided into three groups: namely,

- (a) Experimental study of turbulent flows, aimed at both the measurement of velocity fields and the parameters that characterize turbulent behavior.
- (b) The statistical study of turbulence, aimed at the development of the mathematical tools for representing the fluctuating, random nature of turbulence and ultimately to predict the behavior of turbulent flow fields from first principles.
- (c) Semiempirical computational techniques aimed at the prediction of the velocity fields and dispersion in turbulent flows of engineering interest.

Unfortunately, the connection between these three areas of study is rather tenuous at the present. The statistical theory of turbulence indicates the types of measurements that are desirable but is as yet not successful at predicting these. The recently developed computational techniques are heavy users of computer time and are not yet in full agreement with measurements, except for a few special cases.

In the treatment that will be presented subsequently, the emphasis will be on the engineering techniques that are available to us for predicting the behavior of turbulent fluid flow fields. However, the presentation of these has to be preceded by a discussion of the physical nature of turbulence together with a very cursory introduction to the elements of the statistical theory of turbulence.

Regarding the organization of the material in Section 4.1 we shall describe some physical manifestations of turbulent flow behavior; Section 4.2 is devoted to the mathematical characterization of turbulent systems, while the differential equations of turbulent flow are developed in Section 4.3. In Section 4.4 we shall present applications of turbulence models for representing some basic fluid flow situations, like turbulent boundary layers, turbulent film flow, and turbulent recirculatory systems. Finally, the concluding remarks are contained in Section 4.5.

4.1 Some Physical Manifestations of Turbulent Flow Behavior

Figure 4.1.1, taken from a sketch of Leonardo da Vinci¹ depicting the flow behavior produced by a stream of water falling into a pool, provides an elegant summary of many key features of turbulent flows. The overall circulation of the pool is readily evident as are the circulating smaller eddies of various sizes; the artist provides a vivid impression of the chaotic turmoil in this pool agitated by the incoming water stream. We should note that very closely related phenomena are of crucial importance in metallurgical practice in tapping, ingot casting, and continuous casting. Nonetheless, and notwithstanding the fact that nearly six centuries passed since Leonardo da Vinci

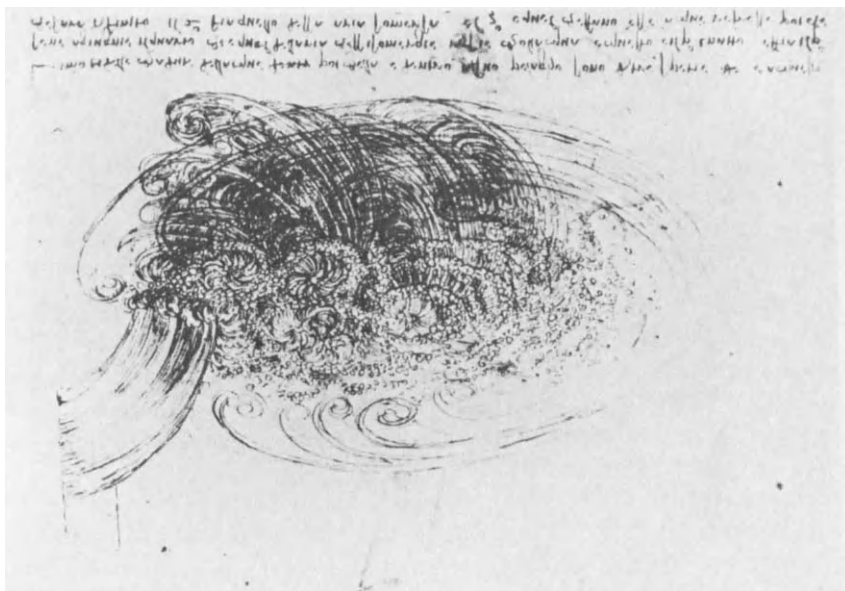


FIG. 4.1.1 The formation of eddies and entrained gas bubbles when a water stream impinges onto a liquid pool, as sketched by Leonardo de Vinci in 1509.

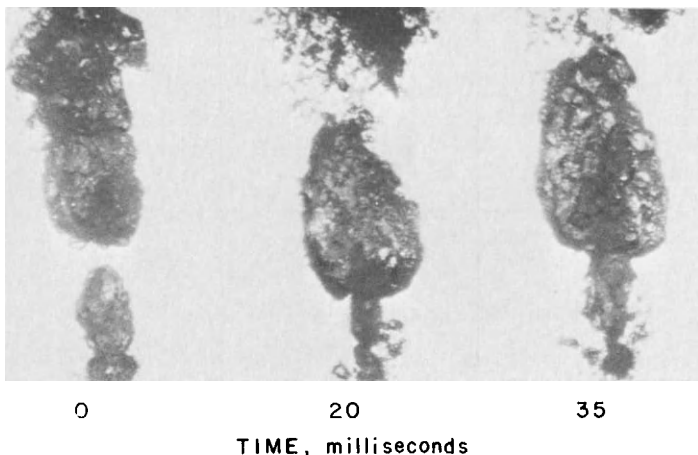


FIG. 4.1.2 Still photograph of showing the surface instabilities when an air jet is injected into water.²

recorded his observations, the full quantitative description of the phenomena depicted in Fig. 4.1.1 has still eluded us.

Other qualitative manifestations of turbulent behavior are shown in Fig. 4.1.2 depicting a submerged air jet in water² where the unsteadiness of the flow and the surface instabilities at the air-water interface are readily apparent. Submerged gas jets are of great importance in metals processing and will be discussed in greater detail in Chapter 9.

Finally, Fig. 4.1.3 shows the formation of eddies in open channel flow. Let us now consider some quantitative and semiquantitative aspects of turbulent behavior.

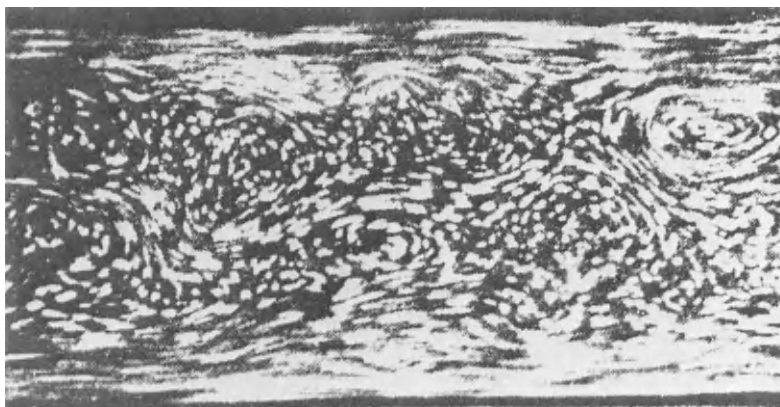


FIG. 4.1.3 Eddy formation in turbulent flow through a horizontal channel.

4.1.1 Comparison of Laminar and Turbulent Flow through Pipes

In his now classical experiments, Osborne Reynolds examined the factors that determine the resistance to fluid flow through pipes. He found that at low velocities the pressure drop was linearly proportional to the mean fluid velocity ($U_{z,m}$), as one would expect from the Hagen–Poiseuille equation [Eq. (3.5.55)], but above a certain critical velocity there was an abrupt increase in the pressure drop, which was then proportional to $U_{z,m}$ raised to a power of about 1.8–2.0.

From these studies Reynolds deduced that the dimensionless group, subsequently termed the Reynolds number, provides a criterion whereby the behavior of the system could be predicted. For pipe flow when the Reynolds number defined as

$$N_{Re} = U_{z,m} \rho 2R / \mu \quad (4.1.1)^{\dagger}$$

was less than about 2300, the flow was laminar and the Hagen–Poiseuille equation was obeyed while above this value the pressure drop was proportional to $U_{z,m}^{1.8-2.0}$.

In another series of experiments Reynolds injected a dye tracer into water flowing through a glass tube. He found that under certain conditions, corresponding to $N_{Re} < 2300$, i.e., to laminar flow, the dye streak introduced in the center retained its identity and remained in its original axial position during its travel through the pipe, as illustrated in Fig. 4.1.4a. In contrast for other conditions, corresponding to $N_{Re} > 2300$, the dye was quickly and uniformly dispersed throughout the tube within a short distance of the injection, as sketched in Fig. 4.1.4b.

The rapidity with which mass and momentum may be transferred in turbulent flow in contrast to laminar systems, as demonstrated by Reynolds' experiments at the turn of the century, constitute an important feature of turbulent behavior.

Another macroscopically observable property of turbulent flows through pipes relates to the velocity profile. The reader will recall from Chapter 3 that for laminar flow

$$u_z/U_{z,max} = 1 - (r/R)^2 \quad (4.1.2)$$

and

$$U_{z,m}/U_{z,max} = \frac{1}{2} \quad (4.1.3)$$

[†] In a physical sense the Reynolds number represents the ratio

$$\frac{(\text{characteristic length})(\text{fluid velocity})}{\text{kinematic viscosity}} = \frac{\text{inertia forces}}{\text{viscous forces}}$$

Viewed in this light it should be readily apparent that for small values of the Reynolds number the viscous forces predominate; hence, the flow is laminar. In contrast, when inertia forces predominate, i.e., the Reynolds number is large, then the flow is turbulent.

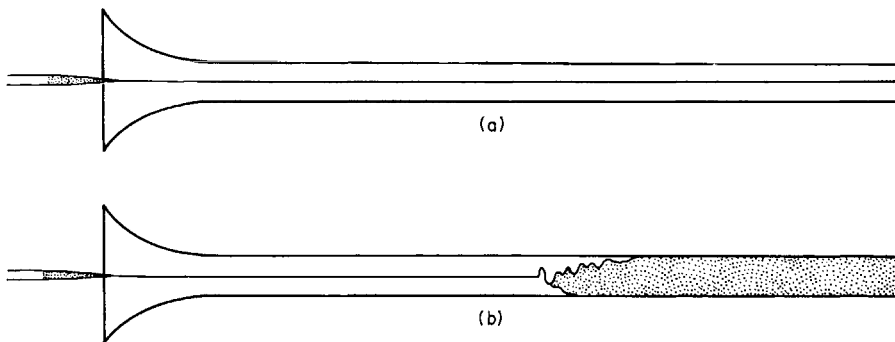


FIG. 4.1.4 Sketch illustrating Reynolds' experiment involving the behavior of a dye streak injected into water flowing through a horizontal pipe. (a) laminar flow, (b) turbulent flow.

In contrast, it has been found experimentally that for turbulent flow through pipes

$$\bar{u}_z/\bar{U}_{z,\max} = (1 - r/R)^{1/7} \quad (4.1.4)$$

and

$$\bar{U}_{z,m}/\bar{U}_{z,\max} = 0.8 \quad (4.1.5)$$

We note that the overbar quantities, i.e., \bar{u}_z , $\bar{U}_{z,m}$, etc., represent time-averaged, or time-smoothed values, the definition of which will be given subsequently. At this stage it is sufficient to say that these are the velocities that one would determine using a conventional Pitot tube.

The behavior represented by Eqs. (4.1.2)–(4.1.4) is illustrated in Fig. 4.1.5,³ showing the velocity distribution for laminar and for turbulent flow, corresponding to the same Reynolds number.[†]

It is seen that for turbulent flow the velocity profile is quite flat in the central core, compared to the parabolic profile for laminar conditions. However, the velocity gradients are much steeper in the vicinity of the wall for turbulent flow.

THE FLUCTUATING NATURE OF TURBULENT FLOW

If the fluid velocity is observed in a turbulent system it is found that even for macroscopically steady conditions (i.e., $U_{z,m}$ const) there are appreciable fluctuations in the local velocity with time. These fluctuations, the frequency of which may be several hundreds or thousands per second, may be detected

[†] The reader may query how both turbulent and laminar regimes may exist above $N_{Re} > 2300$ for pipe flow. The answer is that for these conditions turbulent flow may exist, i.e., instabilities or eddies will propagate if introduced. However, by careful control, e.g., the use of smooth pipes and smooth inlets, it is possible to maintain laminar flow up to $N_{Re} \approx 10,000$.

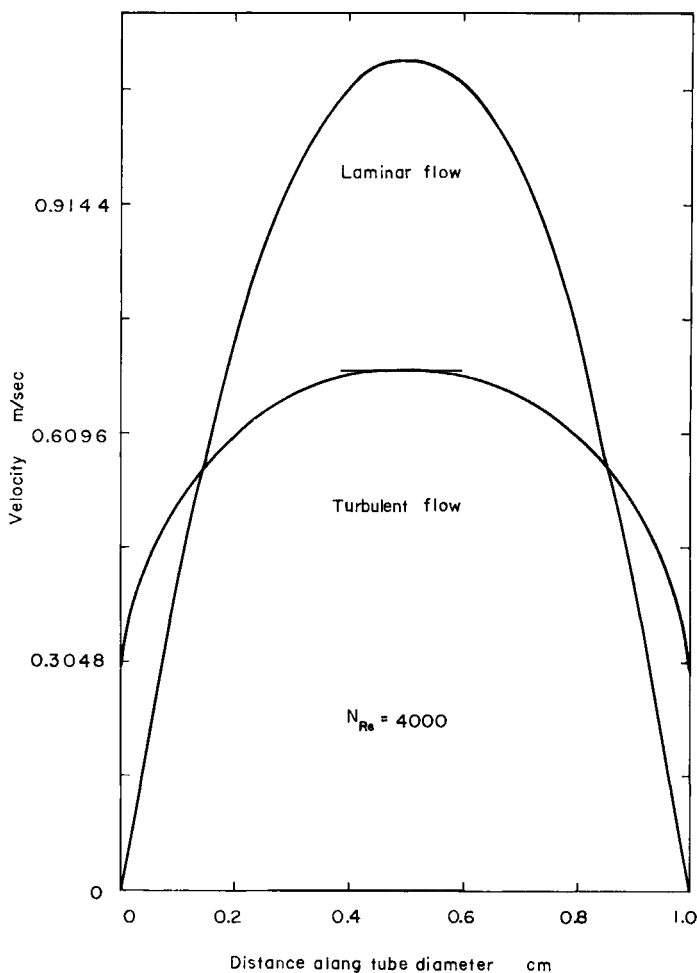


FIG. 4.1.5 Comparison of laminar and turbulent velocity profiles at the same Reynolds number as quoted by Bird *et al.*³

with the aid of special instruments, such as hot film anemometers and Laser-Doppler anemometers, which will be described in Chapter 10.

As will be discussed subsequently, the quantitative representation of turbulent flow behavior requires us to characterize both the mean (i.e., time averaged) velocity and the nature of the fluctuations (i.e., their amplitude and frequency). The very irregular nature of the fluctuations apparent in Fig. 4.1.6⁴ should give a good indication of the complexity of the problems involved in the description of turbulence phenomena.

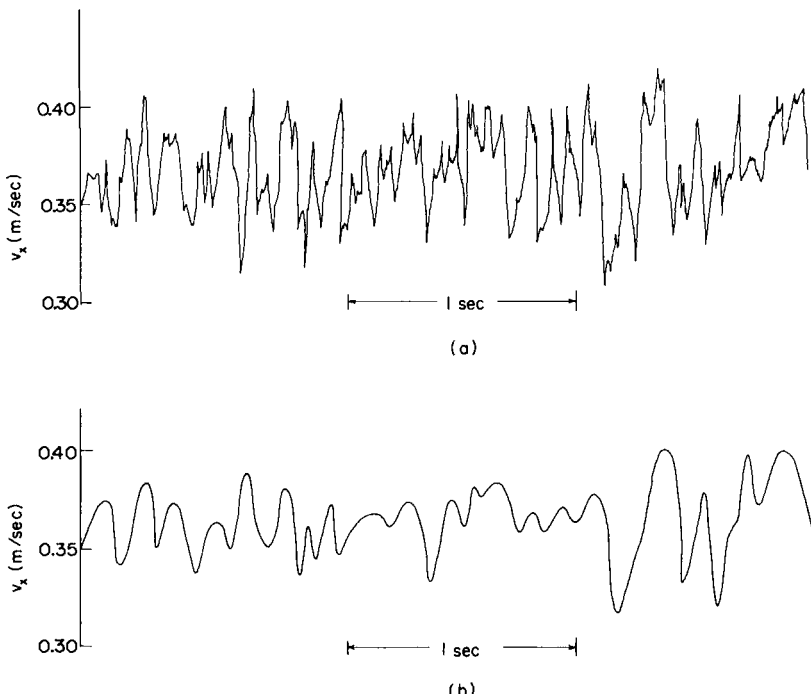


FIG. 4.1.6 The fluctuation of the axial velocity component in pipe flow, at a Reynolds number of 6500, as reported by Davies.⁴ Curve (a) represents the actual measurements, while curve (b) represents a smoothed version. The frequency of the larger eddies is about 11 Hz.

EDDIES IN TURBULENT FLOW

The reader has seen in Figs. 4.1.1 and 4.1.4 that an essential feature of turbulent flows is the existence of fluid elements where rapid, local circulating flow occurs. It is noted that these elements, which are formed and destroyed continually, are termed *eddies*. At this stage it may be worthwhile to examine Fig. 4.1.7 in which the occurrence of the different types of eddies is illustrated. We note that large eddies exist some distance from the wall and that much of the kinetic energy of the fluid is associated with the large and the medium size eddies.

In the motion of the large eddies viscous dissipation is negligible, thus, the energy degradation occurs by the large eddies transferring their energy to the smaller eddies where the kinetic energy is then consumed due to viscous dissipation. In essence, Fig. 4.1.7 is an oversimplification of physical reality because there exists a whole spectrum of eddy sizes; the viscous dissipation takes place in the lower range of this spectrum and the kinetic energy is contained in the range encompassing the larger eddies. The actual

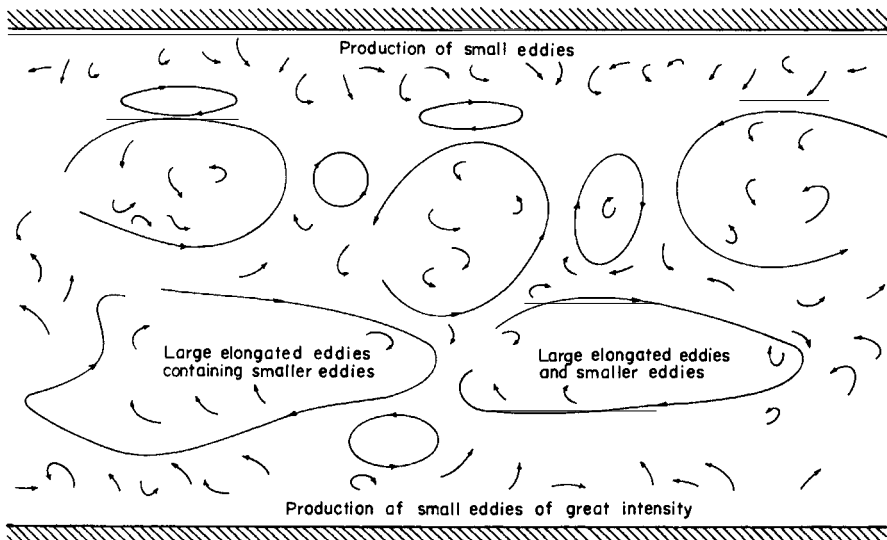


FIG. 4.1.7 Schematic representation of the distribution of eddies in pipe flow, indicating that the larger eddies are located near the center, while the small eddies are being produced in the vicinity of the solid surfaces.

characterization of the eddy size distribution and the description of the energy spectrum form an important part of the statistical theory of turbulence.

4.2 The Quantitative Characterization of Turbulent Flow

In this section we shall introduce the reader to some of the basic concepts employed for the quantitative characterization of turbulent flow behavior.

4.2.1 Some Concepts in the Statistical Theory of Turbulence—the Time-Smoothed and the Fluctuating Velocity Components

Let us reexamine the previously shown Fig. 4.1.6 and define the time-averaged (time-smoothed) value of the velocity component in the z direction as follows:

$$\bar{u}_z = \frac{1}{t_0} \int_0^{t_0} u_z(t) dt \quad (4.2.1)$$

where the length of the time interval t_0 was chosen to be large compared to the reciprocal frequency of the turbulent oscillations. The instantaneous velocity u_z may be expressed as the sum of the time-smoothed velocity and the fluctuating component:

$$u_z = \bar{u}_z + u'_z \quad (4.2.2)$$

as illustrated in Fig. 4.2.1.

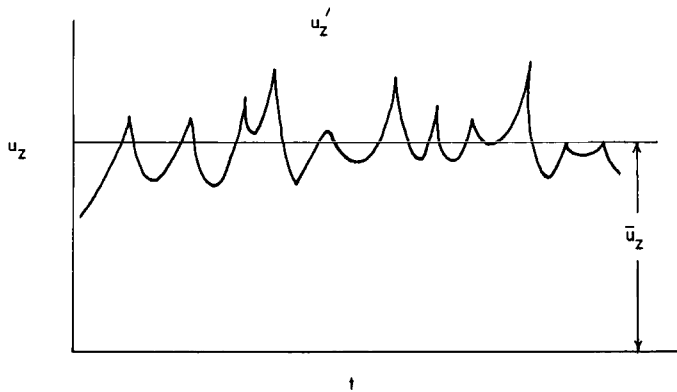


FIG. 4.2.1 Time-averaged and fluctuating velocity components in turbulent flow.

Similar considerations may be applied to the other velocity components and to the pressure within the system. Thus we have

$$\begin{aligned} u_x &= \bar{u}_x + u_x', u_y = \bar{u}_y + u_y' \\ p &= \bar{p} + p', \quad \text{etc.} \end{aligned} \quad (4.2.3)$$

By definition, the time-smoothed value of the fluctuating components must equal zero, i.e.,

$$\bar{u}_z' = \frac{1}{t_0} \int_0^{t_0} u_z' dt \equiv 0 \quad (4.2.4)$$

However, the time-smoothed value of the square of the fluctuating component, i.e.,

$$\overline{(u_z')^2} = \frac{1}{t_0} \int_0^{t_0} (u_z')^2 dt \quad (4.2.5)$$

need not equal zero; moreover, the time-smoothed value of the cross products of the fluctuating components, i.e., $\overline{u_x' u_z'}, \overline{u_y' u_z'}, \overline{u_x' u_y'}$ need not be zero either. These quantities play an important role in the characterization of turbulent flows.

We define the intensity of turbulence as the ratio of the root mean square (rms) velocity fluctuations to the time-smoothed value of the velocity in the same direction. Thus we have

$$\frac{[(\bar{u}_x')^2]^{1/2}}{\bar{u}_x} \quad \frac{[(\bar{u}_y')^2]^{1/2}}{\bar{u}_y} \quad \text{and} \quad \frac{[(\bar{u}_z')^2]^{1/2}}{\bar{u}_z}$$

These turbulence intensities range from about 0.02 to 0.12 for flow through pipes, but may have much higher values for certain recirculating flows and the region of low time-averaged velocities of turbulent jets.

Figure 4.2.2 shows measurements of both the time-smoothed velocity profile and the fluctuating velocity components u'_x and u'_y reported by Reichardt⁵ on an investigation in a wind tunnel. It is seen that for this geometry the velocity fluctuations perpendicular to the direction of the flow do not vary very much across the width of the conduit, while the fluctuating velocity in the direction of the flow exhibits a very sharp maximum quite close to the wall. In the center of the conduit the fluctuating components are quite close in magnitude.

The quantities $\rho u'_x u'_y$, $\rho u'_z u'_x$, etc., have the dimension of stress and are called the *Reynolds stresses*. These Reynolds stresses designate the momentum transfer in the system due to the turbulent fluctuations.

Figure 4.2.3 shows a plot of both the total shear stress and the shear stress contributed by the Reynolds stresses for the flow situation that was previously given in Fig. 4.2.2. It is seen that the Reynolds stresses constitute the dominant mechanism of momentum transfer, everywhere, except in the

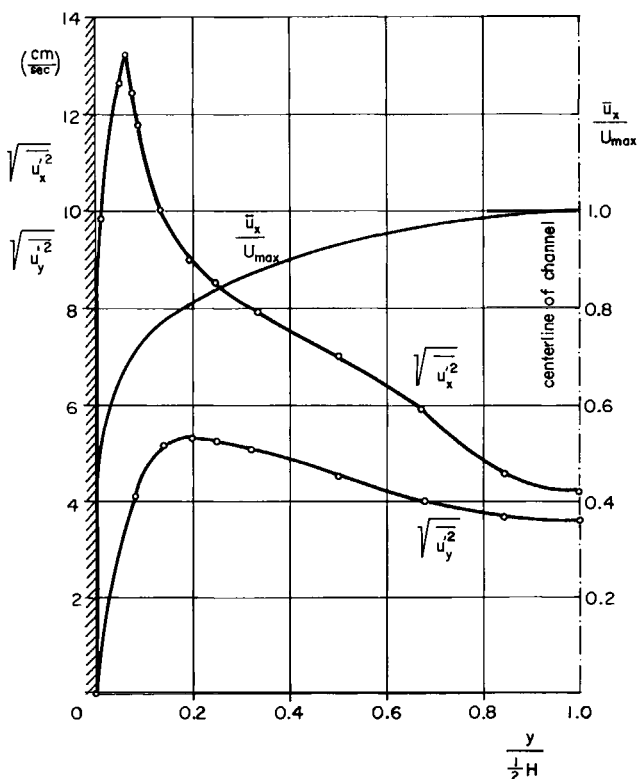


FIG. 4.2.2 Experimentally measured spatial variation of the fluctuating and the time-smoothed velocity components in a wind tunnel; after Reichardt.⁵

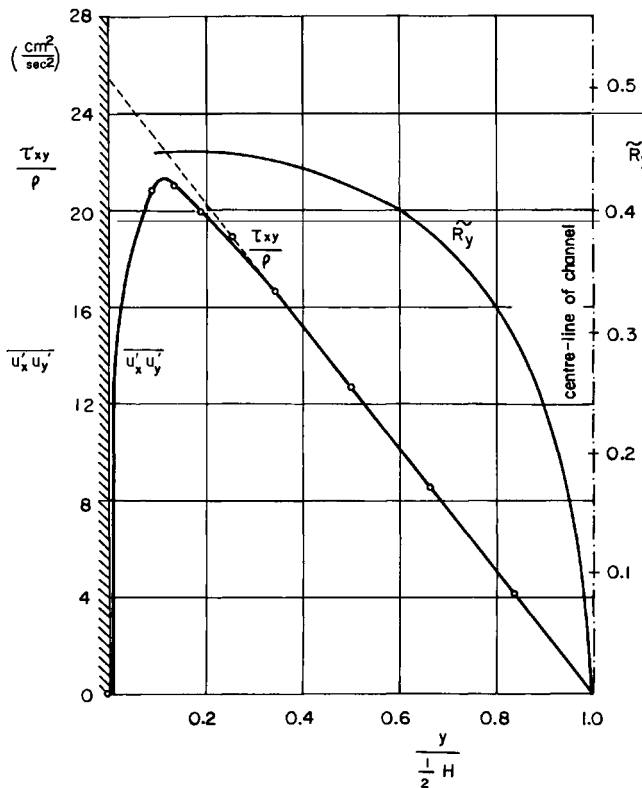


FIG. 4.2.3 Plot of the total shear stress, the turbulent shear stress, and the correlation coefficient for the same system that was previously described in Fig. 4.2.2.

vicinity of the wall where the viscous transfer of momentum is important. We note, furthermore, that there is no shear transmitted across the central plane of symmetry, which should be consistent with physical reasoning. In this central plane the fluctuations are random, $[(\bar{u}_x')^2]^{1/2} \approx [(\bar{u}_z')^2]^{1/2}$, so that $\bar{u}_x' \bar{u}_y' \approx 0$. Such flow behavior is termed *isotropic turbulence*.

CORRELATIONS, CORRELATION COEFFICIENTS

An important tool in the study of turbulence is the development of relationships between the turbulent fluctuations that occur

- (a) over the same time period at adjacent locations, and
- (b) at identical locations over different time periods.

These relationships are called *correlations*. Many such relationships can be developed and for a full discussion of these the reader is referred to the specialist literature.⁶⁻⁹

In the following we shall confine ourselves to a very cursory treatment, of an illustrative nature.

Taylor¹⁰ defined a correlation coefficient R_t the following way:

$$\tilde{R}_t = [(u_x')_t(u_x')_{t+\Delta t}] / \bar{u}_x^2 \quad (4.2.6)$$

In a physical sense \tilde{R}_t defines the relationship between the fluctuating velocity u_x' at time t and the same quantity at time $t + \Delta t$. It follows readily that when $\Delta t = 0$ these two velocities are identical; i.e., $\tilde{R}_t = 1$. In contrast, when Δt is large, $\tilde{R}_t \rightarrow 0$. Equation (4.2.6) may be regarded also as an implicit relationship giving the time over which an eddy, represented by these fluctuations, preserves its identity. The quantity \tilde{R}_t is also called the auto-correlation coefficient.

An alternative representation of the relationship between eddies is possible by comparing the fluctuating velocity components over the same time period but at different points in space. This is illustrated in Fig. 4.2.4, where the upper two velocity fluctuations were obtained at locations which were close to each other. These two traces are very similar and thus show a *high correlation*. One may say loosely that the upper two traces refer to measurements made *within the same eddy*.

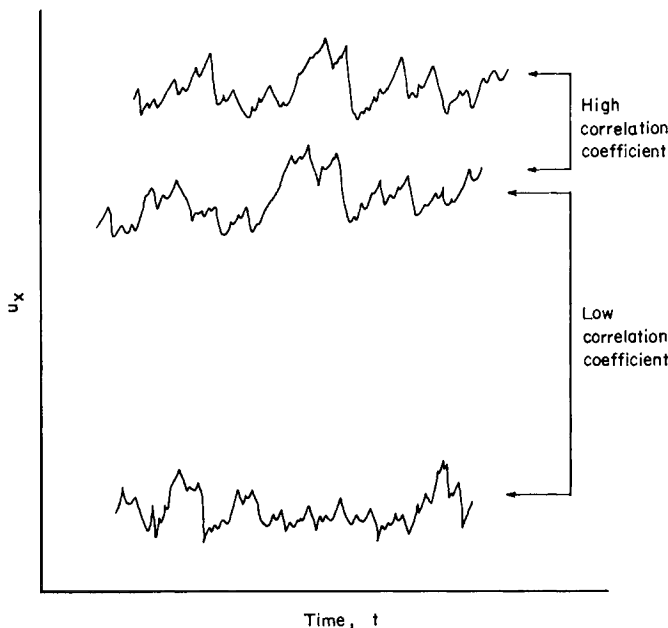


FIG. 4.2.4 Sketch illustrating the correlation of velocity fluctuations in turbulent flow.

In contrast, the lower two traces, showing measurements carried out at points located some distance apart, are dissimilar and thus show a *low correlation*.

This latter example is usually termed the *Eulerian viewpoint* of turbulence.

Upon examining this problem a little more quantitatively, let us cite the classical experiment of Taylor¹⁰ who studied the correlation between the axial and the radial fluctuating velocity components in pipe flow. He defined his correlation coefficient $R_r(r)$ as follows:

$$R_r(r) = [u_z'|_{r=0} u_r'|_{r=r}] / \sqrt{(u_z')^2_{r=0}} \sqrt{(u_r')^2_{r=r}} \quad (4.2.7)$$

As indicated by Eq. (4.2.7) the correlation coefficient $\tilde{R}_r(r)$ relates the fluctuating axial velocity component measured at the center of the pipe to the fluctuating radial velocity component measured at various radial positions. The plot of the measured values of $\tilde{R}_r(r)$ against r/R is shown in Fig. 4.2.5. It is seen that at the center of the pipe the axial and the radial fluctuating components are the same; thus, the correlation coefficient is unity

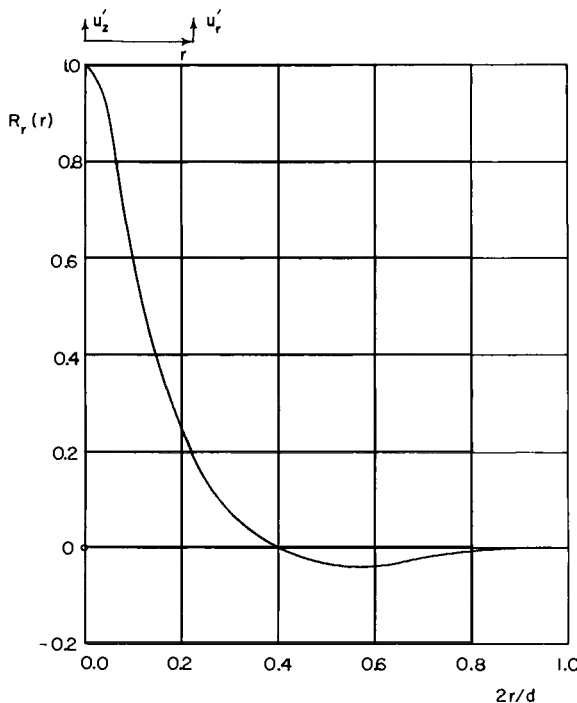


FIG. 4.2.5 The correlation between the fluctuating axial and radial velocity components in pipe flow as a function of position, reported by Taylor and quoted by Schlichting.⁶ The negative values of $R_r(r)$ have no physical meaning.

here. However the correlation coefficient decreases quite rapidly as we move away from the center of the pipe. The integral of the correlation function

$$L_r = \int_0^R \tilde{R}_r(r) dr \quad (4.2.8)$$

has the dimension of length and may be regarded as the characteristic *length scale of turbulence*. Loosely interpreted L would give the *macroscale*, i.e., the mean size, of the large eddies which contain most of the energy in the system. In the example discussed,

$$L_r \simeq 0.07 R \quad (4.2.9)$$

In general, L_r would be some finite fraction of the pipe diameter for pipe flow. It has to be stressed to the reader that just as many definitions of the correlation coefficients is possible there may be diverse ways of estimating the length scale. At this stage we should recall Fig. 4.1.7 which indicated that in general there is a wide distribution of eddy sizes, so that some mean value, such as defined by Eq. (4.2.9), need not be very meaningful.

THE NATURE OF ENERGY ASSOCIATED WITH TURBULENT FLOW

Let us recall the fluctuating velocity component depicted in Fig. 4.1.6. We note that we defined the time-smoothed value of the velocity and also quantified the *amplitude* of the fluctuations through the definition of the intensity of turbulence. Let us now turn our attention to the frequency of the fluctuations and to the energy associated with these.

Let n denote the frequency of fluctuations and $F(n) dn$ designate the fraction of the root mean square fluctuations, say $\sqrt{\langle u_z' \rangle^2}$, that fall within this frequency range. The function $f(n)$ thus represents the spectral distribution of $\sqrt{\langle u_z' \rangle^2}$. A plot of the experimentally obtained $F(n)$ data for boundary layer flow is shown in Fig. 4.2.6, which indicates that the spectral distribution function decreases quite rapidly for smaller frequencies. Also shown in the plot are theoretical lines, indicating that

$$F(n) \sim n^{-5/3} \quad \text{and} \quad F(n) \sim n^{-7}$$

for moderate and high values of the frequency. A qualitatively similar behavior is seen in Fig. 4.2.7, which shows measurements obtained for the turbulent flow of toluene through 25- and 50-mm pipes.

We note that, as the frequency of fluctuations is inversely proportional to the size of the eddies (i.e., to the length scale), Figs. 4.2.6 and 4.2.7 indicate that most of the energy due to the velocity fluctuations is associated with the large eddies, i.e., those with the lower frequency.

The actual energy dissipation due to the turbulent fluctuations takes place in the smaller eddies where the viscous forces predominate. It may be

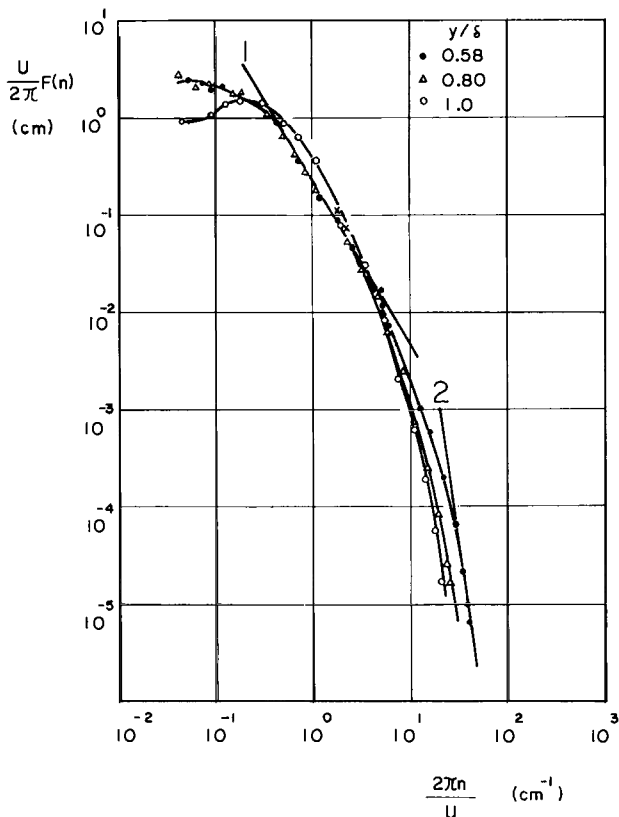


FIG. 4.2.6 Frequency spectrum of the longitudinal fluctuations in a turbulent boundary layer, formed over a flat plate, as cited by Schlichting. The discrete data points represent measurements at various distances from the solid surface, while curves 1 and 2 correspond to theoretical models, predicting $F(x)n^{-5/3}$ and $F(x)n^{-7}$, respectively.

shown that, in Cartesian coordinates, the energy dissipation rate $\dot{\epsilon}$ is given by the following expression:

$$\dot{\epsilon} = \nu \left[2 \left(\frac{\partial u_x'}{\partial x} \right)^2 + 2 \left(\frac{\partial u_y'}{\partial y} \right)^2 + 2 \left(\frac{\partial u_z'}{\partial z} \right)^2 + \left(\frac{\partial u_x'}{\partial y} + \frac{\partial u_y'}{\partial x} \right)^2 + \left(\frac{\partial u_x'}{\partial z} + \frac{\partial u_z'}{\partial x} \right)^2 + \left(\frac{\partial u_y'}{\partial z} + \frac{\partial u_z'}{\partial y} \right)^2 \right] \quad (4.2.10)$$

When turbulence is both homogeneous and isotropic, Eq. (4.2.10) may be usefully simplified. A turbulent field is termed homogeneous when the statistical distributions are the same at every point in space (in the pipe flow

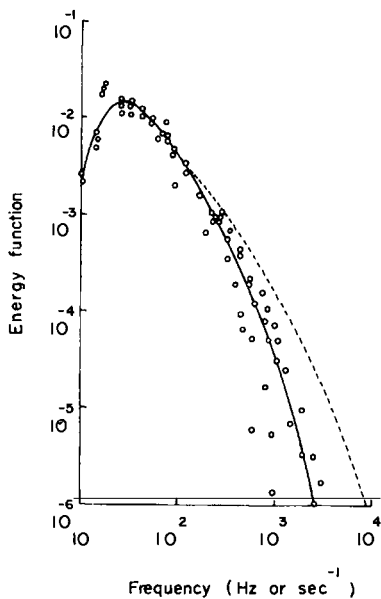


FIG. 4.2.7 The dependence of the energy function on the eddy frequency, as quoted by Davies.⁴

examples discussed, this would be true only in the center line of the pipe). The flow field is called isotropic when the distributions remain invariant with respect to arbitrary rotation or other transformation of the coordinate system.

For these conditions (which incidentally are quite rarely realized or even approached by practically important systems) the turbulent dissipation may be written as

$$\dot{\varepsilon} = 15v \left(\frac{\partial u_x}{\partial x} \right)^2 \quad (4.2.11)$$

In contrast to the macroscale, we can also define a *microscale* which may be loosely interpreted as the size of the smallest energy-containing eddy—where most of the viscous dissipation actually takes place. Kolmogorov¹² suggested that this microscale η may be defined as

$$\eta \simeq (v^3/\dot{\varepsilon})^{1/4} \quad (4.2.12)$$

where ϵ is the turbulent dissipation defined in Eqs. (4.2.10) and (4.2.11).

Example 4.2.1 If in an electromagnetically stirred ASEA-SKF furnace the turbulent dissipation is¹² 100 erg/cm³s estimate the microscale and compare its length to a typical inclusion size, say 20 μ m.

SOLUTION We shall use Eq. (4.2.12). Since $1 \text{ erg} = 1 \text{ g cm}^2/\text{s}^2$ and for steel $v = 8 \times 10^{-3} \text{ cm}^2/\text{s}$, upon substituting into Eq. (4.2.12) we have

$$\eta \text{ [cm]} = [(8 \times 10^{-3})^3 / 10^2]^{1/4} \simeq 0.84 \times 10^{-2} \text{ cm} \quad \text{or} \quad 84 \mu\text{m}$$

It is thus seen that in this case the microscale of turbulence is of the same order of magnitude as the size of the inclusion particles. We note that the parameters used in the statistical theory of turbulence, such as the correlation coefficients, the energy spectra, the length scale, and the dissipation, will not be extensively used in subsequent computations. However, these quantities do provide a useful insight into the general nature of turbulent flow and the concepts of the statistical theory of turbulence should find more widespread use in the future development of turbulence modeling. Let us conclude the present discussion by describing a simple but very effective technique for representing the velocity distribution in turbulent flow fields through the use of “universal velocity profiles.”

4.2.2 *The Use of Universal Velocity Profiles for Representing Turbulent Velocity Fields*

Because of the obvious practical importance of turbulent flow phenomena in pipes and other conduits, very extensive velocity measurements have been reported on these systems. A schematic representation of these measurements is sketched in Fig. 4.2.8, which shows a plot of the velocity profile for turbulent flow near a surface.

It is seen that some distance from the surface the velocity profile is relatively flat—this region is commonly called the *turbulent core*.

In the immediate vicinity of the wall, viscous forces predominate which results in a steep velocity gradient; this region is usually called the laminar sublayer, although studies have shown (cite Hanratty) that turbulent eddies do penetrate this zone. Finally, there exists an intermediate region, termed the *buffer layer*, where both turbulent and viscous effects are important.

For flow through pipes the definition of these zones and the corresponding velocity profiles is possible through the use of the so-called “universal velocity profiles.” For the representation of his extensive experimental measurements, Nikuradze¹³ defined the following quantities:

$$u^* = (\tau_0 / \rho)^{1/2} \quad (\text{friction velocity}) \quad (4.2.13)$$

$$u^+ = \bar{u}_z / u^* \quad (\text{dimensionless velocity}) \quad (4.2.14)$$

$$y^+ = y u^* \rho / \mu \quad (\text{dimensionless distance}) \quad (4.2.15)$$

where u^* is the friction velocity, τ_0 the shear stress at the wall, previously defined in Chapter 2, u^+ the dimensionless velocity, and \bar{u}_z the time-smoothed velocity component in the z direction.

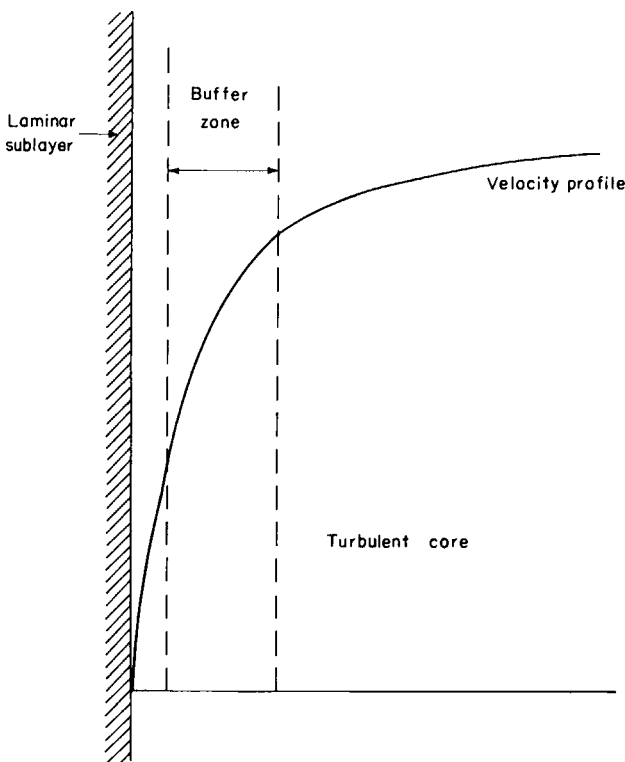


FIG. 4.2.8 Sketch of the velocity profile for turbulent flow in the vicinity of a solid surface.

Nikuradze suggested that the dimensionless velocity profile may be represented by the following expressions:

$$u^+ = y^+ \quad \text{for } 0 \leq y^+ \leq 5 \quad (\text{laminar sublayer}) \quad (4.2.16)$$

$$u^+ = -3.05 + 5 \ln y^+ \quad \text{for } 5 \leq y^+ < 30 \quad (\text{buffer layer}) \quad (4.2.17)$$

and

$$u^+ = 5.5 + 2.5 \ln y^+ \quad \text{for } y^+ > 30 \quad (\text{turbulent core}) \quad (4.2.18)$$

Figure 4.2.9 shows a plot of Eqs. (4.2.16)–(4.2.18) together with experimental data, as reported by Deissler.¹⁴ It is seen that, while the velocity measurements are reasonably well represented by these equations, the fact that three distinct expressions have to be used for the modeling of a continuous, smooth curve has certain major disadvantages.

A useful development by Deissler has been the suggestion that the laminar sublayer and the buffer layer may be modeled by a single, albeit

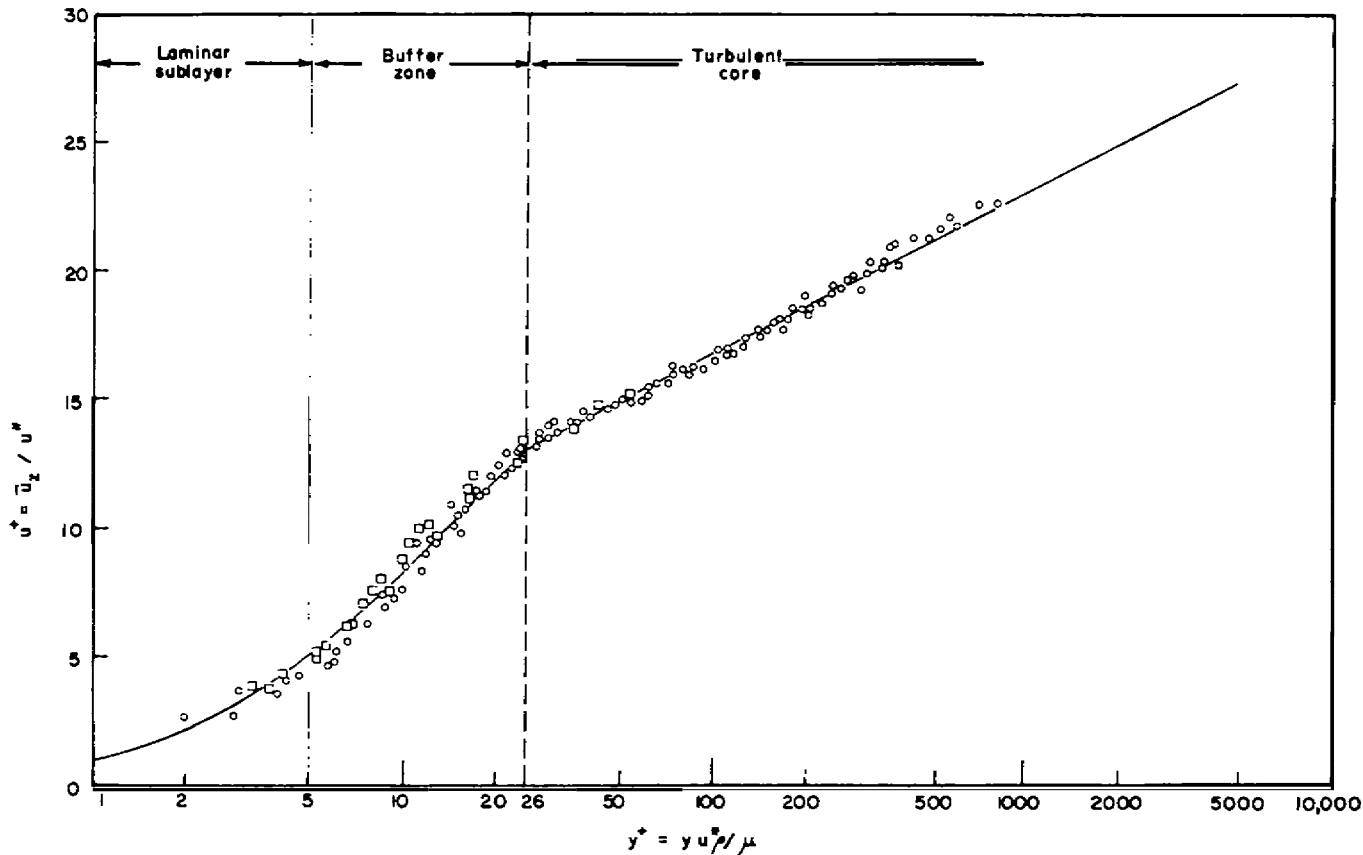


FIG. 4.2.9 Sketch of the "universal velocity profile" for flow through a pipe, after Deissler.¹⁴

implicit relationship which has the following form:

$$u^+ = \int_0^{y^+} \frac{dy^+}{1 + n^2 u^+ y^+ [1 - \exp(-n^2 u^+ y^+)]}, \quad 0 \leq y^+ \leq 26 \quad (4.2.19)$$

where $n \approx 0.124$. Since Eq. (4.2.19) contains u^+ on both the left-hand and the right-hand sides, it has to be solved iteratively. This solution is also shown in Fig. 4.2.9.

While these simple algebraic relationships provide little insight into the actual structure of the turbulent flow, the technique of universal velocity profiles and the further developments based upon it (namely Schlichting,⁶ Knudsen and Katz¹⁵) have been used successfully for estimating velocity profiles for a range of turbulent flow systems. In Section 4.4 of this chapter we shall cite an application of this method for estimating the behavior of turbulent films.

4.3 The Differential Equations of Turbulent Flow

In the preceding two sections the reader was introduced to some of the qualitative and quantitative manifestations of turbulent flow behavior.

The majority of the material presented was descriptive or interpretive and, with the exception of the universal velocity profile, could not be used for predicting the behavior of turbulent systems. In this section we shall develop the differential equations of turbulent flow; these expressions will parallel quite closely the Navier–Stokes equations that were used for describing laminar flow in the preceding chapter. There are two major differences, however. The turbulent fluctuations, i.e., the fluctuating velocity components, introduced additional terms in the equation of motion; moreover, the Newtonian definition of viscosity which was used to relate the stress components to the velocity gradients in laminar flow will have to be replaced by much more complex and less satisfactory relationships.

4.3.1 The Equation of Continuity in Turbulent Flow

Let us consider a stationary cubical fluid element $\Delta x \Delta y \Delta z$, such as was shown in Fig. 3.1.1, through which a fluid is flowing. We can now proceed by writing the equation of continuity, i.e., Eq. (3.1.3), by representing the velocity components as the sum of the time-smoothed and the fluctuating quantities, namely

$$u_x = (\bar{u}_x + u'_x), \quad u_y = (\bar{u}_y + u'_y), \quad \text{and} \quad u_z = (\bar{u}_z + u'_z)$$

Thus for the Cartesian coordinate system, and upon assuming incompressible behavior, we have

$$\frac{\partial}{\partial x}(\bar{u}_x + u'_x) + \frac{\partial}{\partial y}(\bar{u}_y + u'_y) + \frac{\partial}{\partial z}(\bar{u}_z + u'_z) = 0 \quad (4.3.1)$$

Upon time smoothing each term, i.e., applying the operator $1/t_0 \int_{t_0}^t (\) dt$, the fluctuating components will disappear because $(1/t_0) \int_{t_0}^t u_x' dt \equiv 0$; thus, we have

$$\frac{\partial \bar{u}_x}{\partial x} + \frac{\partial \bar{u}_y}{\partial y} + \frac{\partial \bar{u}_z}{\partial z} = 0 \quad (4.3.2)$$

or

$$\nabla \cdot \mathbf{u} = 0 \quad (4.3.3)$$

Naturally we also have that $\nabla \cdot \mathbf{u}' = 0$.

It follows that the time-smoothed equation of continuity is identical to that developed for laminar flow; this identity would, of course, hold irrespective of the coordinate system employed. This finding is reasonable on physical grounds, provided the control volume chosen is large compared to the average eddy size.

This stipulation is of course rather more restrictive than the analogous constraint used in laminar flow; in laminar flow, unless we consider gases at very low absolute pressures, one can take for granted that the control volume chosen will be large compared to the mean free path of the molecules. As seen in Section 4.2 [e.g., Eq. (4.2.9)] eddies can be large enough to be only one order of magnitude smaller than the characteristic dimension of the container.

4.3.2 The Equation of Motion

Let us rewrite the x component of the equation of motion for an incompressible fluid, e.g., using Table 3.2.1, and again replacing the instantaneous velocity and pressure terms by the sum of the time-smoothed and the fluctuating components. Thus we have

$$\begin{aligned} \rho \frac{\partial}{\partial t} (\bar{u}_x + u_x') &= \mu \nabla^2 (\bar{u}_x + u_x') \\ &\quad \text{viscous transfer} \\ &\quad \text{of momentum} \\ &- \rho \left[\frac{\partial}{\partial x} (\bar{u}_x + u_x') (\bar{u}_x + u_x') + \frac{\partial}{\partial y} (\bar{u}_y + u_y') (\bar{u}_x + u_x') \right. \\ &\quad \left. + \frac{\partial}{\partial z} (\bar{u}_z + u_z') (\bar{u}_x + u_x') \right] \\ &\quad \text{convective transfer} \\ &\quad \text{of momentum} \\ &- \frac{\partial}{\partial x} (\bar{p} + p') + \rho (\bar{F}_x + F_x') \\ &\quad \text{body force} \\ &\quad \text{pressure force} \end{aligned} \quad (4.3.4)$$

Upon time smoothing both sides of Eq. (4.3.4) we have the following:

$$\begin{aligned} \rho \frac{\partial \bar{u}_x}{\partial t} &= \mu \nabla^2 \bar{u}_x - \rho \left[\frac{\partial}{\partial x} (\bar{u}_x \bar{u}_x) + \frac{\partial}{\partial y} (\bar{u}_y \bar{u}_x) + \frac{\partial}{\partial z} (\bar{u}_z \bar{u}_x) \right] \\ &\quad - \rho \left[\frac{\partial}{\partial x} (\bar{u}_x' \bar{u}_x') + \frac{\partial}{\partial y} (\bar{u}_y' \bar{u}_x') + \frac{\partial}{\partial z} (\bar{u}_z' \bar{u}_x') \right] - \frac{\partial \bar{p}}{\partial x} + \rho \bar{F}_x \end{aligned} \quad (4.3.5)$$

Inspection of Eq. (4.3.5) shows that it is very similar (in terms of the time-smoothed quantities) to the previously given Navier–Stokes equations but for the fact that additional terms arise upon time smoothing. These quantities $\rho u_x' u_x'$, $\rho u_y' u_x'$, and $\rho u_z' u_x'$ which have the dimension of stress or momentum flux are usually termed the Reynolds stresses. Let us define the components of the turbulent stress tensor $\tau^{(t)}$ as

$$\bar{\tau}_{xx}^{(t)} = \rho u_x' u_x', \quad \bar{\tau}_{xy}^{(t)} = \rho u_x' u_y', \quad \bar{\tau}_{xz}^{(t)} = \rho u_x' u_z', \quad \text{etc.} \quad (4.3.6)$$

Then the equation of motion for incompressible fluids may be written as

$$\rho \frac{D \bar{u}}{Dt} = -\nabla \bar{p} - \nabla \cdot \tau^{(l)} - \nabla \cdot \bar{\tau}^{(t)} + \rho \bar{F}_b \quad (4.3.7)$$

where $\tau^{(l)}$ is the laminar stress tensor which has been defined in Eq. (3.2.9) for laminar flow, while $\bar{\tau}^{(t)}$ is the turbulent stress tensor,

$$\begin{aligned} \bar{\tau}^{(t)} &\equiv \begin{vmatrix} \bar{\tau}_{xx}^{(t)} & & & \\ & \bar{\tau}_{xz}^{(t)} & & \\ & & \bar{\tau}_{zz}^{(t)} & \\ \hline \bar{\tau}_{zx}^{(t)} & & & \\ & \bar{\tau}_{yy}^{(t)} & & \\ & & \bar{\tau}_{zz}^{(t)} & \\ \hline \rho \bar{u}_x' \bar{u}_x' & & & \\ \hline \rho \bar{u}_z' \bar{u}_x' & \rho \bar{u}_x' \bar{u}_z' & & \\ \hline & \rho \bar{u}_z' \bar{u}_z' & & \end{vmatrix} \\ &\equiv \begin{vmatrix} \rho \bar{u}_x' \bar{u}_x' & & & \\ & \rho \bar{u}_x' \bar{u}_z' & & \\ & & \rho \bar{u}_z' \bar{u}_z' & \\ \hline \rho \bar{u}_z' \bar{u}_x' & & & \end{vmatrix} \end{aligned} \quad (4.3.8)$$

The components of the turbulent stress tensor may be measured experimentally. One such set of measurements has been given previously in Fig. 4.2.3, where it was seen that the turbulent stress tensor predominates in the turbulent core but the laminar diffusion of momentum is the dominant mechanism in the laminar sublayer.

For laminar flow problems the next step, following the statement of the equation of motion of the type given by Eq. (4.3.7), was to substitute for the components of the stress tensor using Newton's law of viscosity, which then resulted in a differential equation relating the derivatives of the velocity to the pressure field and to the body force field in the system.

This operation is much less straightforward for turbulent flows because there exists no unequivocal or universal relationship between the components of the turbulent stress tensor and the time-smoothed velocity gradients.

For laminar flow this relationship was well defined and the constant of proportionality was the Newtonian viscosity which was a property of the fluid.[†]

For turbulent systems the relationship between the components of $\bar{\tau}^{(t)}$ and the time-smoothed velocity gradients is much more complex and is a property of the system.

It follows from the foregoing discussion that before we can proceed with the integration of the turbulent Navier–Stokes equations, functional relationships or models are needed for relating $\bar{\tau}^{(t)}$ and the velocity gradients.

4.3.3 Models of Turbulent Transport

BOUSSINESQ'S CONCEPT OF EDDY VISCOSITY

The first attempt at relating the turbulent shear stress to the velocity gradient was due to Boussinesq, who in 1877 proposed the following expression¹⁶:

$$\bar{\tau}_{yx}^{(t)} = \rho \overline{u_y' u_x'} = -\mu_t \frac{\partial \bar{u}_x}{\partial y} \quad (4.3.9)$$

Here μ_t is the eddy viscosity or the apparent turbulent viscosity which is strongly dependent on the location. One would expect, therefore, that

$$\mu_t \gg \mu \quad \text{in the turbulent core}$$

(e.g., Fig. 4.2.7 or 4.2.8) and

$$\mu_t \ll \mu \quad \text{in the vicinity of the wall}$$

i.e., in the laminar sublayer.

While Boussinesq did not suggest any specific functional relationship for μ_t , Eq. (4.3.9) proposed by him is very important, because it provides a rational framework for the analysis of turbulent flow, through the development of such relationships.

PRANDTL'S MIXING LENGTH MODEL¹⁷

In 1925 Prandtl proposed the following expression for defining μ_t the turbulent eddy viscosity which appeared in Boussinesq's model:

$$\mu_t = \rho l_m^2 \frac{\partial \bar{u}_x}{\partial y} \quad (4.3.10)$$

[†] We have to make a tacit acknowledgment that major complexities do arise even in case of laminar flow if the fluid is non-Newtonian. However, non-Newtonian behavior is very seldom encountered in metals or slag processing operations.

Here l_m is termed the mixing length which, loosely interpreted, plays the same role in the movement of the eddies as does the mean free path in the movement of gas molecules. While this analogy is not very good in a physical sense, through the use of suitable expressions for l_m considerable success has been achieved in the representation of turbulent velocity profiles of certain simple flows. Before proceeding further, it may be instructive to examine in a little more detail the hypotheses that led to Prandtl's mixing length model.

Implicit in these considerations is the postulate that the total shear is

$$\bar{\tau}_{yx} = \tau_{yx} + \bar{\tau}_{yx}^{(t)} \quad (4.3.11)$$

i.e.,

$$\bar{\tau}_{yx} = \mu_{\text{eff}} \frac{\partial \bar{u}_x}{\partial y} \quad (4.3.12)$$

where

$$\mu_{\text{eff}} = \mu + u_t \quad (4.3.13)$$

Prandtl proposed that the turbulent viscosity μ_t may be represented by

$$\mu_t = \rho l_m u_t \quad (4.3.14)$$

where u_t is some random turbulent velocity, which may be estimated from

$$\mu_t = l_m \left| \frac{\partial u_x}{\partial y} \right| \quad (4.3.15)$$

It is readily seen that by combining Eqs. (4.3.14) and (4.3.15) we obtain the original "mixing length model." However, it is possible to use expressions other than Eq. (4.3.15) for defining u_t , and indeed this is the path followed by the more complex turbulence models.

Let us return now to Eq. (4.3.10) which defined the turbulent viscosity in terms of the absolute value of the velocity gradient and the mixing length. Before we can proceed further an additional relationship is required through which l_m may be defined.

In his original paper Prandtl proposed that l_m may be related to the distance from the wall, say

$$l_m = 0.4y \quad (4.3.16)$$

where y represents the normal distance from a solid surface. While this simple expression is very appealing from the computational viewpoint, the results obtained through its use were not found to be in a very good agreement with measurements. In a recent review Launder and Spalding¹⁸ suggested, however, that Prandtl's mixing length model can be used successfully for modeling a range of basically undirectional (nonrecirculating) flows,

Nikuradse's formula:

$$\frac{l_m}{R} = 0.14 - 0.08(1 - r'/R)^2 - 0.06(1 - r'/R)^4$$

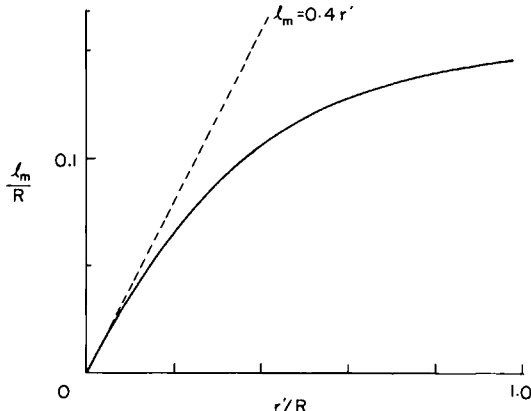


FIG. 4.3.1 Nikuradse's formula for the position dependence of the mixing length for pipe flow.

such as flow through a pipe, boundary layer flow, the behavior of *free jets*, etc., provided appropriate expressions are used for defining l_m . These authors gave numerous, recommended relationships for l_m together with a critical review of the comparison of the predictions based on these models with actual measurements. Here we shall confine our attention to the application of the modified mixing length model to representing pipe flow.

TURBULENT FLOW THROUGH PIPES

Nikuradse proposed the following relationship for l_m for turbulent flow through pipes:

$$l_m/R = 0.14 - 0.08(1 - r'/R)^2 - 0.06(1 - r'/R)^4 \quad (4.3.17)$$

Here R is the radius of the pipe and r' is the radial distance measured from the wall. Figure 4.3.1 shows a plot of l_m/R against r'/R . It is seen that the mixing length is zero at the wall[†] and that it reaches a rather flat maximum in the center of the pipe.

Having the formula for l_m we may now state the momentum balance equation for pipe flow.

[†] It should be noted that even Eq. (4.3.17) is not accurate in the vicinity of the wall, because it does not predict a rapid enough decline in the turbulent viscosity as the solid surface is being approached. This problem will be discussed subsequently.

Using the expression from Table 3.2.2 for the equation of motion for steady-state flow in a cylindrical coordinate system we have

$$\frac{d}{dr} [r' \bar{\tau}_{rz}] = -\frac{\Delta p}{\Delta z} = \frac{2}{R \tau_0} \quad (\text{using an overall balance}) \quad (4.3.18)$$

On noting that

$$\tau_{rz} = - \left[\mu \frac{d\bar{u}_z}{dr} + \mu_t \frac{d\bar{u}_z}{dr'} \right] \quad (4.3.19)$$

and then substituting for μ_t from Eqs. (4.3.9), (4.3.10), and (4.3.17) we have

$$\begin{aligned} \frac{d}{dr} \left[r \left\{ \mu \frac{d\bar{u}_z}{dr} + \left(0.14 - 0.08 \left(1 - \frac{r'}{R} \right)^2 - 0.06 \left(1 - \frac{r'}{R} \right)^4 \right)^2 R^2 \rho \left| \frac{d\bar{u}_z}{dr'} \right| \frac{d\bar{u}_z}{dr'} \right\} \right] \\ = \Delta p / \Delta z \end{aligned} \quad (4.3.20)$$

which is a highly nonlinear ordinary second-order differential equation, which has to be solved for the following boundary conditions:

$$\bar{u}_z = 0, \quad r' = 0 \quad (4.3.21)$$

and

$$d\bar{u}_z/dr' = 0 \quad \text{at} \quad r' = R \quad (4.3.22)$$

This is a two-point boundary value problem which, because of its nonlinearity, has to be solved using a digital computer. The techniques available for solving problems of this type have been reviewed by Finlayson¹⁹, Ray and Szekely²⁰, Patankar and Spalding²¹, and Keller²².

Figure 4.3.2 shows a comparison of predictions based on these considerations and measurements, as cited by Launder and Spalding.¹⁸ The very good agreement is readily apparent.

Example 4.3.1 Let us assume that the data depicted in Fig. 4.3.2 refer to water flowing through a pipe 1 m in diameter at a mean linear velocity of 3.2 m/s. Using Fig. 4.3.2 and the previously developed relationships: (1) calculate the mixing length l_m at a position halfway between the wall and the center line; (2) estimate μ_t at this position and compare it with the molecular value of 10^{-3} kg/ms.

SOLUTION Using Eq. (4.3.17),

$$l_m/0.5 = 0.14 - 0.08 \times 0.25 - 0.06 \times 0.625$$

$$l_m = 0.041 \quad \text{m}$$

From Eq. (4.15),

$$\bar{U}_{z,\max} \approx 3.2/0.8 = 4 \quad \text{m/s}$$

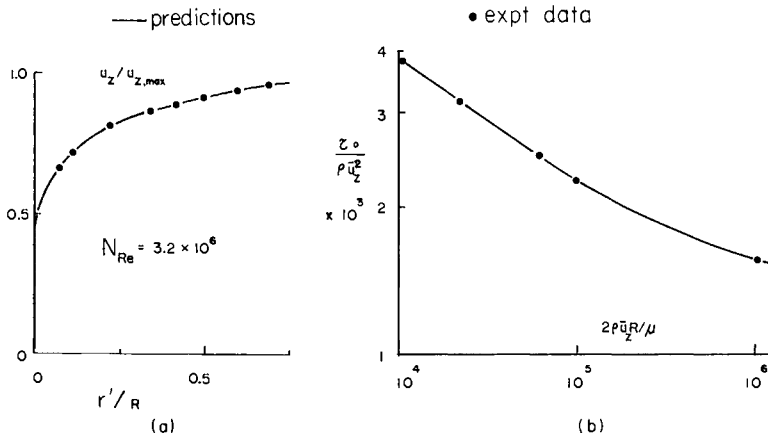


FIG. 4.3.2 A comparison between experimental measurements and theoretical predictions regarding turbulent flow in a pipe: (a) the velocity profile, (b) the drag coefficient.

Then, from Fig. 4.3.2,

$$\left. \frac{d\bar{u}_z}{dr} \right|_{r'=0.25} \simeq 0.8 \text{ s}^{-1}$$

Thus upon substitution into Eq. (4.3.10) we have

$$\mu_t = 10^3 \times 1.68 \times 10^{-3} \times 0.8 = 1.34 \text{ kg/ms}$$

which is over a thousand times larger than the molecular value.

The numerical example cited above shows that, for the system considered, in the turbulent core, laminar effects may be neglected. Laminar effects are, however, important in the vicinity of the wall (cf. the laminar sublayer). Inspection of Eq. (4.3.14) shows that the mixing length would tend to vary linearly with the distance from the wall. Careful measurements have shown that this postulate would overestimate the turbulent contribution in the wall region, so when accurate information is required in the vicinity of the wall the use of Van Driest's expression is recommended, which takes the following form:

$$\mu_{\text{eff}} = \mu + \mu_t \quad (4.3.23)$$

and

$$\mu_t = l_m \rho \left| \frac{d\bar{u}_z}{dr} \right| \quad (4.3.24)$$

with

$$l_m = 0.435 r' [1 - \exp(r' \tau_0^{1/2} \rho^{1/2} / 26\mu)] \quad (4.3.25)$$

$$\text{Formula for } \mu_{\text{eff}}: \mu_{\text{eff}} = \mu + \rho \ell_m^2 \left| \frac{\partial u}{\partial r} \right|$$

$$\text{Formula for } \ell_m: \ell_m = k r' \left[1 - \exp \left(- \frac{r' \tau_0^{1/2} \rho^{1/2}}{A \mu} \right) \right]$$

with $A = 26.0$

Resulting distribution :

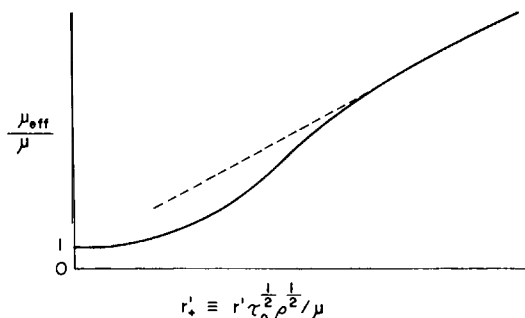


FIG. 4.3.3 Sketch of the ratio: μ_{eff}/μ calculated on the basis of Van Driest's hypothesis, in the vicinity of a solid wall. The broken line represents the regular mixing length model.

Figure 4.3.3 shows a sketch of the ratio μ_{eff}/μ_t as calculated by both the simple mixing length model and through the use of Van Driest's modification. It is seen that this latter method provides an asymptotic rather than a linear approach to unity in the wall region, which is in better accord with observations.

This modification is of particular importance if we are interested in the local shear stress near the wall and in the calculation of heat or mass transfer rates.

For a more detailed discussion of the various formulas available for estimating the mixing length for a range of flow situations the reader is referred to the texts by Spalding and co-workers.^{18,21} The simple mixing length model described on the preceding pages is attractive because it enables us to calculate certain basically undirectional flows quite accurately without recourse to excessive computational labor. However the model does suffer from some basic drawbacks which are enumerated in the following:

- (1) Specific expressions are required for the mixing length which may not be available for the system of interest.

(2) The mixing length model implies zero turbulent viscosity, and hence on analogy zero eddy diffusivity at positions where the velocity gradient is zero. This is contrary to experience (e.g., the simple mixing length model would suggest that there is no material or thermal transport due to eddies in the centerline of a pipe in turbulent flow which is clearly not true).

(3) Mixing length models have not been satisfactory for the representation of complex flow fields, i.e., recirculatory flows.

These shortcomings of the mixing length type models may be overcome by using more complex modeling equations for the turbulent viscosity.

ONE-EQUATION MODELS

Equations (4.3.11)–(4.3.13) represent the starting point in the so-called “one-equation models” of turbulent flow.

Furthermore, μ_t , the turbulent viscosity, is given by the following expression:

$$\mu_t = \rho l_m K^{1/2} \quad (4.3.26)$$

Here l_m is the previously defined mixing length and K is the kinetic energy, due to the turbulent fluctuations in the velocity. More specifically K is defined as

$$K = \frac{1}{2} [u_x'^2 + u_y'^2 + u_z'^2]$$

i.e., half the sum of the time-smoothed values of the square of fluctuating velocity components. The dimension of $K^{1/2}$ is velocity, so that formally Eqs. (4.3.26) and (4.3.14) are equivalent. However, rather than postulating, as done in the mixing length model, that K (or u_t) may be related to the time-smoothed velocity gradient in the present case, K will be computed from a differential equation, expressing the conservation of this quantity. The concept of defining the turbulent viscosity as a product of the mixing length and the turbulence energy was suggested independently by Kolmogorov²³ and by Prandtl.²⁴ However, these ideas could not be put to practical use until the availability of powerful digital computers. A good discussion of the subsequent specific computational schemes and underlying developments is available in the monograph by Launder and Spalding.¹⁸

The considerations that lead to the establishment of a differential balance on the turbulent energy are not as clear cut or rigorous as the balance equations in laminar flow; nonetheless, it is instructive to follow the reasoning developed by Rotta²⁵ and co-workers in the statement of this balance for boundary layer type flows.

Let us consider a turbulent boundary layer type flow, such as discussed in Section 3.5.2 and sketched in Fig. 4.3.4. As shown in Section 3.5.2, in these

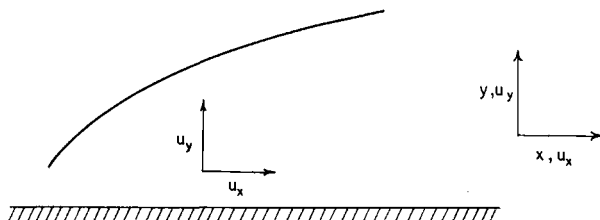


FIG. 4.3.4 Sketch of a turbulent boundary layer.

systems momentum is being transferred in the direction of the flow (x) by convection, while in the direction perpendicular to the flow momentum is being transferred due to both convection and diffusion (i.e., viscous shear).

We can use similar arguments to suggest that in the turbulent field the diffusive transfer in the direction of the flow may be neglected, although in this case the mechanism for the diffusive transfer is not molecular but is associated with the turbulent fluctuations. For steady-state conditions the time-smoothed equations may be written as

$$\rho \left(\bar{u}_x \frac{\partial K}{\partial x} + \bar{u}_y \frac{\partial K}{\partial y} \right) = - \frac{\partial}{\partial y} \left[\rho u_y' K' + \overline{u_y' p'} \right] \quad \begin{matrix} \text{convective} \\ \text{transport of } K \end{matrix}$$

$$- \rho u_y' u_x' \frac{\partial \bar{u}_x}{\partial y} \quad \begin{matrix} \text{turbulent diffusive} \\ \text{transfer of } K \end{matrix} - \mu \sum_j \left(\frac{\partial u_i'}{\partial x_j} \right)^2 \quad \begin{matrix} \text{production of } K \\ \text{dissipation of } K \end{matrix} \quad (4.3.27)$$

where $x_j \equiv x, y, z$.

However, before we can proceed further the fluctuating quantities appearing in Eq. (4.3.27) have to be replaced with measurable or predictable parameters. Following Prandtl, the diffusive component may be approximated by

$$(\rho \overline{u_x' K'} + \overline{p' u_y'}) \approx (\mu_t / \sigma_K) \frac{\partial K}{\partial y} \quad (4.3.28)$$

where σ_K is the turbulent Prandtl number for the diffusion of K , usually taken as unity.

The production term is the previously defined Reynolds stress for a one-dimensional flow; thus, we may write

$$- \rho \overline{u_x' u_y'} = \mu_t \frac{\partial \bar{u}_x}{\partial y} \quad (4.3.29)$$

If we consider that (viscous) dissipation takes place in the smallest eddies near the wall, it is reasonable to suppose that these are not much affected

by direction or position; thus, upon assuming isotropy, using Eq. (4.2.12) we may write

$$\mu \sum \left(\frac{du_i}{\partial x_j} \right)^2 = C_D (\rho K^{3/2}/l) \quad (4.3.30)$$

where C_D is a coefficient.

Thus summarizing the assumptions made, the turbulence energy balance equation for boundary layer type flows may be expressed as

$$\rho \left(\bar{u}_x \frac{\partial K}{\partial x} + \bar{u}_y \frac{\partial K}{\partial y} \right) = \frac{\partial}{\partial y} \left[\frac{\mu_t}{\sigma_K} \frac{\partial K}{\partial y} \right] + \mu_t \left(\frac{\partial \bar{u}_x}{\partial y} \right)^2 - C_D \frac{\rho K^{3/2}}{l_m} \quad (4.3.31)$$

convection diffusion generation dissipation

Thus for a turbulent boundary layer type problem the equation of continuity and the equation of motion have to be solved in conjunction with the definition of the turbulent viscosity [Eq. (4.3.26)] and the balance equation for the turbulence energy [Eq. (4.3.31)].

These equations are coupled because the turbulent viscosity appears in the equation of motion and the velocity terms appear in the balance equations for the turbulent energy, the (position dependent) value of which is needed for defining μ_t .

The computational task is complex because the equations to be solved are simultaneous, nonlinear partial differential equations; however, numerous well-documented programs are available in the literature.^{18,21,26,27}

In using the “one-equation model” before the statement of the problem is completed, information is required on (a) the boundary conditions for Eq. (4.3.31), and (b) the mixing length l_m has to be specified.

Spalding and co-workers suggested that in the vicinity of solid walls the convection and diffusion of turbulence energy may be negligible; thus, upon equating the production of turbulence energy [Eq. (4.3.29)] and its dissipation [Eq. (4.3.30)] we have

$$(\tau/\rho K)_{wall} \simeq C_D^{1/2} \quad (4.3.32)$$

where $C_D \simeq 0.08$ and $\tau = \tau_0$ the shear stress at the wall.

Some boundary conditions for nonsolid boundaries (i.e., for submerged jets and rising streams of gas bubbles) have been discussed by Asai and Szekely³⁰ who suggested some tentative relationships applicable to these systems. It is noted that Eq. (4.3.3) together with the definition of the length scale is just one example of the one-equation models that have been proposed. Notable contributions to this field have been made by Bradshaw *et al.*²⁸ and by Nee and Kovaszny.²⁹

The drawback of “one-equation models” is the fact that the mixing length still has to be specified and that it is unlikely that simple relationships

will be available, or could be developed for describing the mixing length for complex fields. Nonetheless, the one-equation models have been used for calculating the behavior of turbulent boundary layers and for computing the fluid flow field in the mold region of a continuous casting machine.³⁰

We note that the relatively simple form of Eq. (4.3.31) was due to the fact that we employed the simplifying assumptions usually associated with boundary layer equations.

For a truly two-dimensional flow field in rectangular coordinates the equations expressing turbulent momentum balance and the conservation of K may be written as follows:

$$\rho \left[\frac{\partial}{\partial x} \left(\xi_z \frac{\partial \bar{\psi}}{\partial y} \right) - \frac{\partial}{\partial y} \left(\xi_z \frac{\partial \bar{\psi}}{\partial x} \right) \right] - \frac{\partial^2}{\partial x^2} \left(\mu_e \frac{\partial \bar{\xi}}{\partial z} \right) - \frac{\partial^2}{\partial y^2} \left(\mu_e \frac{\partial \bar{\xi}}{\partial z} \right) = 0 \quad (4.3.33)$$

where

$$\xi_z = \frac{\partial \bar{u}_y}{\partial x} - \frac{\partial \bar{u}_x}{\partial y} \quad (4.3.34)$$

is the vorticity and

$$\bar{u}_y = - \frac{\partial \bar{\psi}}{\partial x} \quad (4.3.35)$$

$$\bar{u}_x = \frac{\partial \bar{\psi}}{\partial y} \quad (4.3.36)$$

is the stream function

$$\mu_{\text{eff}} = \mu + \mu_t \quad (4.3.23)$$

and

$$\mu_t = \rho l_m K^{1/2} \quad (4.3.26)$$

Moreover, for two-dimensional flow K is given by

$$\begin{aligned} & \rho \left[\frac{\partial}{\partial x} \left(K \frac{\partial \bar{\psi}}{\partial y} \right) - \frac{\partial}{\partial y} \left(K \frac{\partial \bar{\psi}}{\partial x} \right) \right] - \left[\frac{\partial}{\partial x} \left(\frac{\mu_t}{\sigma_K} \frac{\partial K}{\partial x} \right) + \frac{\partial}{\partial y} \left(\frac{\mu_t}{\sigma_K} \frac{\partial K}{\partial y} \right) \right] \\ &= 2\mu_t \left[\left(\frac{\partial \bar{u}_x}{\partial x} \right)^2 + \left(\frac{\partial \bar{u}_y}{\partial y} \right)^2 + \frac{1}{2} \left(\frac{\partial \bar{u}_y}{\partial x} + \frac{\partial \bar{u}_x}{\partial y} \right)^2 \right] - \frac{C_D \rho K^{3/2}}{l_m} \end{aligned} \quad (4.3.37)$$

We note that by writing Eqs. (4.3.33) and (4.3.37) in terms of the vorticity, the two components of the equation of motion could be consolidated into a single expression, as was done for the case of laminar flow in the previous chapter; moreover, by working in terms of the stream function, the equation of continuity was automatically satisfied.

The equivalent expressions to Eqs. (4.3.33)–(4.3.37) in cylindrical coordinates will be cited in the next section in connection with a worked example.

The earlier mentioned drawback of one-equation models, namely that the mixing length has to be specified, makes them essentially inapplicable to a broad range of complex flow fields, including turbulent recirculatory flows, which are of considerable practical importance in many metals processing operations, such as argon-stirred ladles, BOF steelmaking, vacuum degassing, and the like. These problems may be tackled through the use of rather more complex models, where the mixing length, or some equivalent quantity, is not specified through the use of an algebraic equation but rather has to be calculated from an additional differential equation.

TWO-EQUATION MODELS

As noted earlier, Kolmogorov was the first who suggested that the turbulent viscosity be determined as the product of two factors: a characteristic energy and the reciprocal of a characteristic frequency—both of which should be evaluated as a solution of differential equations.

The principal postulates of the two-equation models are summarized in the following:

(a)

$$\mu_t = \rho K W^{-1/2} \quad (4.3.38)$$

where

$$l_m = (K W)^{1/2} \quad (4.3.39)$$

and W is the mean square of the frequency of the turbulent eddies or the gradient of the acceleration of the turbulent field.

(b) K the turbulence energy is calculated by solving the appropriate conservation equation, i.e., Eq. (4.3.31), for a boundary layer type flow, Eq. (4.3.37) for two-dimensional flow in rectangular coordinates, etc.

(c) W the square of the mean frequency has to be obtained through the solution of a differential, conservation equation. Spalding proposed the following expression for defining W :

$$\begin{aligned} & \frac{\partial}{\partial x} \left(W \frac{\partial \bar{\psi}}{\partial y} \right) - \frac{\partial}{\partial y} \left(W \frac{\partial \bar{\psi}}{\partial x} \right) - \frac{\partial}{\partial x} \left(\frac{\mu_t}{\sigma_w} \frac{\partial W}{\partial x} \right) - \frac{\partial}{\partial y} \left(\frac{\mu_t}{\sigma_w} \frac{\partial W}{\partial y} \right) \\ &= C_1 \mu_t (\nabla \xi_z)^2 + C_3 \frac{W}{K} 2 \mu_t \left[\left(\frac{\partial \bar{u}_x}{\partial x} \right)^2 + \left(\frac{\partial \bar{u}_y}{\partial y} \right)^2 \right. \\ & \quad \left. + \frac{1}{2} \left(\frac{\partial u_y}{\partial x} + \frac{\partial u_x}{\partial y} \right) \right] - C_2 \rho W^{3/2} \quad (4.3.40) \\ & \qquad \qquad \qquad \text{(generation-dissipation)} \end{aligned}$$

Here $C_1 \approx 3.5$, $C_2 \approx 0.17$, $C_3 \approx 1.04$, and $\sigma_w \approx 1$.

It has to be stressed to the reader that, notwithstanding the similarities between the conservation equations for K and for W , there is little fundamental basis for writing transport equations for the frequency term. Nonetheless the use of the two parameters, namely K and W , has in conjunction with the procedure outlined above been quite successful for the representation of turbulent recirculating flows. The formalism presented here represents just one of the numerous techniques that has been proposed recently, for modeling the turbulent viscosity, through the use of two sets of independent equations. A good review of recent work in this field is available in Launder and Spalding.^{18,31}

We may summarize the material presented in this section by stating that formally the turbulent equations of motion are very similar to the equation of motion developed earlier for laminar flow, although some additional terms appear as a result of the turbulent fluctuations.

The evaluation of these additional terms, i.e., the Reynolds stresses, is the major problem in the study of turbulent flow systems.

Numerous empirical and semiempirical expressions have been proposed for relating the turbulent (eddy) viscosity to the macroscopically measurable properties of the system. For simple, boundary layer type flows, if our prime interest is in the velocity profile, some modification of Prandtl's original mixing length model may give sufficiently accurate results.

If we wish to assess the extent of turbulent mixing, then a better definition of the turbulent energy dissipation pattern is required. The turbulent energy pattern may be calculated with the aid of "one-equation models" where a transport type expression is used for computing the turbulent energy. The use of this technique leads to greatly increased computational complexity because several nonlinear partial differential equations have to be solved simultaneously. Nonetheless, certain preprogrammed computational algorithms are available for performing this task.

These one-equation models are in general inadequate for the representation of turbulent recirculating flows. The modeling of these required the so-called two-equation models, where both the turbulence energy and some length or reciprocal frequency terms have to be evaluated through solving transport-based equations.

This procedure is quite complex, and cannot be justified except on a pragmatic basis since it seems to produce results which are in reasonable agreement with measurements. It is highly probable that these techniques will be greatly refined in the near future, although the greater accuracy and generality will be achieved at the expense of considerably increased computational labor.

Let us conclude this chapter by presenting some detailed computed results for some systems of practical importance.

4.4 Some Solutions of the Turbulent Equation of Motion

We concluded the preceding chapter with the presentation of some exact solutions of the equation of motion. The reader will recall that the actual statement of these problems was quite straightforward through the use of the equations of continuity and the equation of motion, which were available in tabulated form. In some cases simple analytical solutions could be obtained (e.g., for the flow of a falling film, steady laminar flow through pipes, etc.) and even in the more complex problems the computational task was quite straightforward.

The situation is very different for turbulent systems. While many of the classical laminar flow problems were solved at the turn of the century or even before, the vast majority of solutions generated for turbulent flow problems owe their existence to the high-speed digital computer.

In the following we shall present the solution of some key turbulent flow problems and the reader will see that even simple systems such as film flow require computer solution. Another important consideration is the fact that simplifying assumptions are almost inherently made when tackling turbulent fluid flow problems; for this reason it is very important, whenever possible, to verify the predictions made by direct comparison with measurements.

4.4.1 Turbulent Flow of a Vertical Falling Film

Let us consider the flow of a falling film on a vertical surface, where the film Reynolds number $N'_{Re,f} = 4hU_{x,m}\rho/\mu$ is large enough, so that the system is turbulent.

The reader will recall from the discussion presented in Section 3.5.1 that the flow is laminar in falling films when $N'_{Re,f} < 20$ and turbulent when $N'_{Re,f} > 1000$. The formation of surface waves and rippling has been observed in the intermediate region. A very good, detailed description of film flow phenomena is available in the review article by Fulford.³²

In principle, we could represent the behavior of a turbulent falling film by writing on the analogy of the treatment developed in Section 3.5.1 for the system sketched in Fig. 4.4.1:

$$-\frac{d}{dy} \left(\mu_{eff} \frac{du_x}{dy} \right) = \rho g, \quad 0 \leq y \leq h \quad (4.4.1)$$

where some appropriate expression, e.g., mixing length, etc., may be used for relating μ_{eff} to y , the distance from the surface. Since a portion of the film adjacent to the solid surface will be laminar, the accurate representation of the laminar and the transition regions would have to be an important feature of the relationship used.

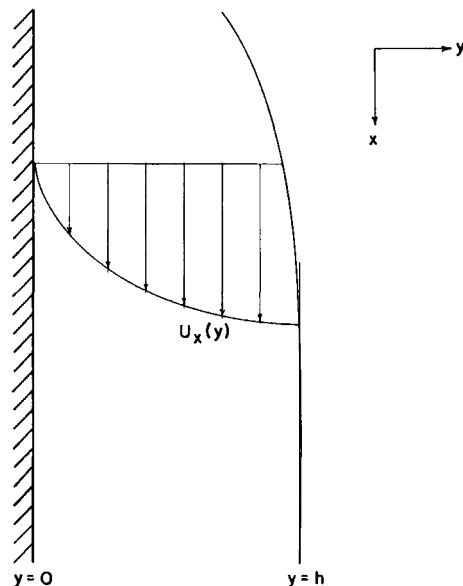


FIG. 4.4.1 Sketch of a turbulent falling film.

A rather simpler approach was proposed by Dukler and Bergelin in 1952³³, who suggested that the universal velocity profile may be used, in conjunction with an overall force balance to represent turbulent falling films.

Let us recall from Section 4.2 that the universal velocity profile, proposed by Nikuradse, took the following form:

$$u_x^+ = y^+, \quad 0 \leq y^+ \leq 5 \quad (4.4.2)$$

$$u_x^+ = -3.05 + 5.0 \ln y^+, \quad 5 \leq y^+ \leq 30 \quad (4.4.3)$$

and

$$u_x^+ = 5.5 + 2.5 \ln y^+, \quad y^+ > 30 \quad (4.4.4)$$

where

$$u_x^+ = u_x/u_x^* \quad (4.4.5)$$

$$u_x^* = \tau_0 g / \rho \quad (\text{friction velocity}) \quad (4.4.6)$$

and

$$y^+ = u^* \rho y / \mu \quad (\text{dimensionless distance}) \quad (4.4.7)$$

Now w' , the mean flow rate per unit width of the plate, may be obtained by integrating the velocity profile over the film thickness. Thus we have

$$w' = \mu \int_0^\beta u^+ dy^+ \quad (4.4.8)$$

where

$$\beta = u^* \rho h / \mu \quad (4.4.9)$$

is the dimensionless film thickness. Upon substituting for u^+ from Eqs. (4.4.2)–(4.4.4) we have

$$\begin{aligned} \frac{w'}{\mu} &= \int_0^5 y^+ dy^+ + \int_5^{30} (-3.05 + 5 \ln y^+) dy^+ \\ &+ \int_{30}^{\beta} (5.5 + 2.5 \ln^n y^+) dy^+ \end{aligned} \quad (4.4.10)$$

Upon performing the integration, we have

$$w'/\mu = -63 + 3.0\beta + 2.5\beta \ln \beta \quad (4.4.11)$$

which may be solved numerically. In order to complete the solution a further relationship is needed for h . This is readily obtained from an overall force balance:

$$\tau_0 = \rho g \quad (4.4.12)$$

Thus

$$\beta = \rho g^{1/2} h^{3/2} / \mu \quad (4.4.13)$$

Thus through the combined use of Eqs. (4.4.11) and (4.4.13) we can calculate the mass flow rate w' corresponding to a given film thickness or, vice versa, calculate the film thickness associated with a given mass flow rate.

Figure 4.4.2 shows a plot of the experimental measurements of film thickness, encompassing the transition range of Reynolds numbers. The ordinate on this plot is the Nusselt film thickness N_T defined as

$$N_T = h(g/v^2)^{1/3} \quad (4.4.14)^{\dagger}$$

In addition to the measurements Fig. 4.4.3 also shows the predicted Nusselt film thickness for laminar flow, the curve predicted by Dukler's equation and another prediction based on a correlation proposed by Brotz,³⁴ which may be put in the following form:

$$N_T = 6.82 \times 10^{-2} (N'_{\text{Re,f}})^{2/3} \quad (4.4.15)$$

It is seen that even in the transition region the conventional laminar flow expression would substantially underestimate the film thickness, which is clearly consistent with the fact that the presence of the eddies provides for a more effective momentum transfer across the film which then prevents steep velocity gradients.

[†] For inclined surface we have $N_T = h(g \sin \theta/v^2)^{1/3}$.

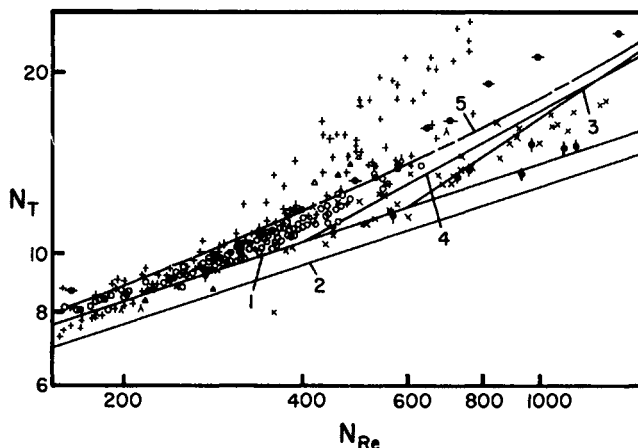


FIG. 4.4.2 Experimental measurements of the film thickness, plotted in terms of N_T , the Nusselt parameter, as a function of the Reynolds number in the transition regime; after Fulford.³³ The numbers on the continuous lines designate theoretical predictions by 1 Nusselt, 2 Kapitsa, 3 Brotz, 4 Brauer, 5 Dukler.

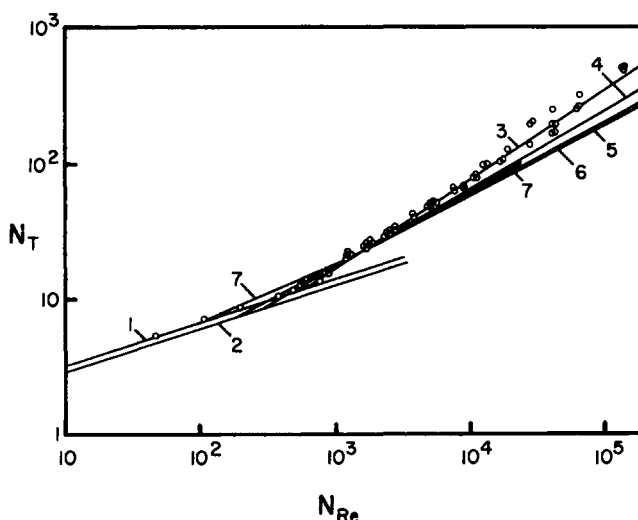


FIG. 4.4.3 Comparison of experimentally measured film thickness with predictions based on various correlations; after Fulford.³² The numbers on the continuous lines designate theoretical predictions by 1 Nusselt, 2 Kapitsa, 3 Brotz, 4 Zhivalkin, 5 Brauer, 6 Feind, 7 Dukler. For the detailed references see the article by Fulford.³²

In the transition region both the Brotz formula and Dukler's equation should provide more or less reliable estimates of the film thickness. However, as shown in Fig. 4.4.3, the Brotz formula designated by line 3 should be preferred at high Reynolds numbers and also for flow through open channels with a small inclination to the horizontal.

Let us illustrate the use of the Brotz formula on a simple example.

Example 4.4.1 In a lead refining process we wish to pass a film of molten lead over a vertical surface at a rate of $(100 \text{ kg/s})/\text{m}$ width. Estimate the film thickness (a) using the Brotz equation and (b) assuming laminar flow.

DATA Viscosity of lead, $1.6 \times 10^{-3} \text{ kg/ms}$; density of lead, $\sim 10^4 \text{ kg/m}^3$; thus $v = 1.6 \times 10^{-7} \text{ m}^2/\text{s}$.

SOLUTION Since $w' = 100 \text{ kg/ms}$,

$$N'_{\text{Re},f} = \frac{4 \times 100}{1.6 \times 10^{-3}} \simeq 2.5 \times 10^5$$

so that the flow is definitely turbulent. Then, using Eqs. (4.4.14) and (4.4.15), we have

$$h \left[\frac{9.81}{(1.6 \times 10^{-7})^2} \right]^{1/3} = 6.82 \times (2.5 \times 10^5)^{2/3}$$

i.e., $h \simeq 3.9 \times 10^{-3} \text{ m}$. If we assume laminar flow, which would be a very poor assumption since $N'_{\text{Re},f} = 2.5 \times 10^5$, then the film thickness may be calculated from Eq. (3.5.9), which upon rearrangement yields

$$h = \left(\frac{3\mu w'}{\rho^2 g} \right)^{1/3} = \left(\frac{3 \times 1.6 \times 10^{-3} \times 400}{9.81 \times 10^8} \right)^{1/3} = 1.25 \times 10^{-3} \text{ m}$$

This value is less than a third of what we calculated for turbulent flow and is therefore in error to a considerable extent.

It should be noted that while the expressions developed by Dukler or by Brotz may be used for estimating film thicknesses, gross simplifying assumptions were introduced in the development of these equations.

In particular, while an expression corresponding to the "turbulent core" has been employed for representing the outer surface of the film, as shown by Levich³⁵, the flow is not turbulent in this region. The reason for this behavior is that surface tension would tend to damp out the eddies near the free surface. This damping of surface eddies has been studied by Davies⁴ who was able to relate the thickness of the layer where the damping occurred to the surface tension and to the eddy size. The important practical consequence of this finding is the fact that, notwithstanding the turbulence within the film

from the viewpoint of heat transfer or mass transfer, the outer layers of turbulent films will behave as if they were laminar.

4.4.2. Turbulent Boundary Layers

Let us consider the development of a turbulent boundary layer such as sketched in Fig. 4.4.4. It is seen that the fluid approaching a flat plate with a free stream velocity of $\bar{U}_{x,\infty}$ is being retarded through the formation of a boundary layer. As discussed in Section 3.5.2, in the vicinity of the leading edge this boundary layer is laminar and its behavior may be represented with the aid of the (laminar) Navier-Stokes equations. However, when $N_{Re} = \bar{U}_{x,\infty} L / v > 10^5$, the flow is known to turn turbulent, although a thin region close to the solid surface will remain laminar. On the analogy of pipe flow phenomena this region is called the *laminar sublayer*.

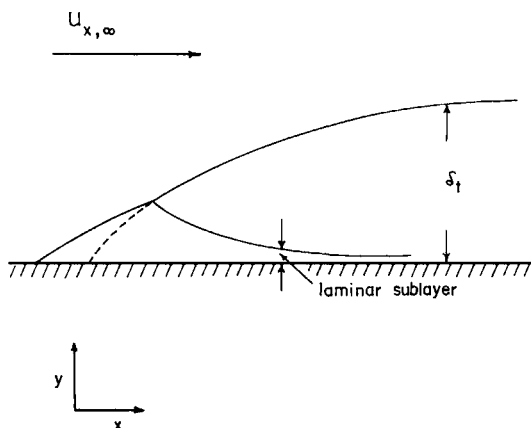


FIG. 4.4.4 Sketch of a turbulent boundary layer.

By using the approximations discussed in Section 3.5.2 for an incompressible fluid, the differential equations representing the flow field within the boundary layer may be written as[†]

$$\partial \bar{u}_x / \partial x + \partial \bar{u}_y / \partial y = 0 \quad (\text{continuity}) \quad (4.4.16)$$

$$\rho \left[\bar{u}_x \frac{\partial \bar{u}_x}{\partial x} + \bar{u}_y \frac{\partial \bar{u}_x}{\partial y} \right] = \frac{\partial}{\partial y} \left(\mu_{\text{eff}} \frac{\partial \bar{u}_x}{\partial y} \right) \quad (4.4.17)$$

[†] As we mentioned earlier this boundary condition is an approximation, because through its use we postulate that the turbulent boundary layer commences at the leading edge. More accurate expressions are available in the literature.⁴

where $\mu_{\text{eff}} \equiv \mu + \mu_t$ may be calculated by using one of the techniques described in the preceding section.

If our principal objective is to obtain insight into the distribution of the turbulent shear stresses in the system and also to calculate heat or mass transfer phenomena, this would be the proper approach to take. A good, detailed discussion of the various computational procedures available for this purpose is found in the monograph by Patankar and Spalding.²¹

If, however, our objective is more modest and all we wish to do is to calculate the boundary layer thickness and the drag force on the plate, a greatly simplified procedure is available through the use of von Karman's integral analysis.³⁶ If we assume, as a first approximation, that the domain of interest is such that the initial, laminar portion of the boundary layer forms a negligibly small fraction of the total length considered, an overall momentum balance across the boundary layer may be written as

$$\frac{d}{dx} \int_0^{\delta_t} \rho (\bar{U}_{x,\infty} - \bar{u}_x) \bar{u}_x dy = \tau_0 \quad (4.4.18)$$

$\left[\begin{array}{l} \text{rate of change} \\ \text{of momentum} \end{array} \right] \quad \left[\begin{array}{l} \text{shear stress on the} \\ \text{surface of the plate} \end{array} \right]$

Here δ_t is the thickness of the turbulent boundary layer. Let us postulate furthermore that (a) the one seventh power relationship experimentally observed for pipes may be applied here, namely Section 4.1; moreover, (b) let us assume that τ_0 , the shear stress at the surface, may be described by using an empirical relationship found for pipe flow. Thus applying (a) we have

$$\bar{u}_x / \bar{U}_{x,\infty} = (y/\delta_t)^{1/7} \quad (4.4.19)$$

Moreover, the empirical expression for τ_0 may be written as

$$\tau_0 = 0.0225 \rho U_{x,\infty}^2 (v/\bar{U}_{x,\infty} \delta_t)^{1/4} \quad (4.4.20)$$

We may now proceed by substituting for \bar{u}_x from Eq. (4.4.19) and for τ_0 from Eq. (4.4.20) in the left-hand side and the right-hand side of Eqs. (4.4.18), respectively.

Then upon performing the integration we obtain

$$(7/72) \frac{d\delta_t}{dx} = 0.0225 (v/\bar{U}_{x,\infty} \delta_t)^{1/4} \quad (4.4.21)$$

which may be integrated for the boundary condition

$$\delta_t = 0 \quad \text{at} \quad x = 0$$

to yield

$$\delta_t/x = 0.37 (\bar{U}_{x,\infty} x/v)^{-0.2} \quad (4.4.22)$$

Inspection of Eq. (4.4.22) shows that the thickness of the turbulent boundary layer is proportional to $x^{4/5}$, while as it was shown in Section 3.5.2 the thickness of the laminar boundary layer is proportional to $x^{1/2}$.

On the analogy of the considerations employed for laminar boundary layers we may define a displacement thickness δ_t^* as

$$\delta_t^*(x) = \int_0^\infty \left(1 - \frac{\bar{u}_x}{\bar{U}_{x,\infty}}\right) dy$$

and it may be shown that

$$\delta_t^*(x)/x = 0.046(\bar{U}_{x,\infty}x/v)^{-0.2} \quad (4.4.23)$$

Finally, we may also define the local skin friction coefficient in the following manner:

$$C_{f,x} = \tau_0 / (\frac{1}{2}\rho \bar{U}_{x,\infty}^2) \quad (4.4.24)$$

and it may be shown that

$$C_{f,x} = 0.0576(v/\bar{U}_{x,\infty}x)^{0.2}$$

or integrated over a length L we have

$$C_{f,L} = 0.072(v/\bar{U}_{x,\infty}L)^{0.2} \quad (4.4.25)$$

Figure 4.4.5 shows a plot of $C_{f,L}$ against the Reynolds number and it is seen that the simple analysis presented here seems to be in reasonable agreement with measurements. An easy refinement of this analysis was proposed by Prandtl, who used the logarithmic "universal velocity profile"

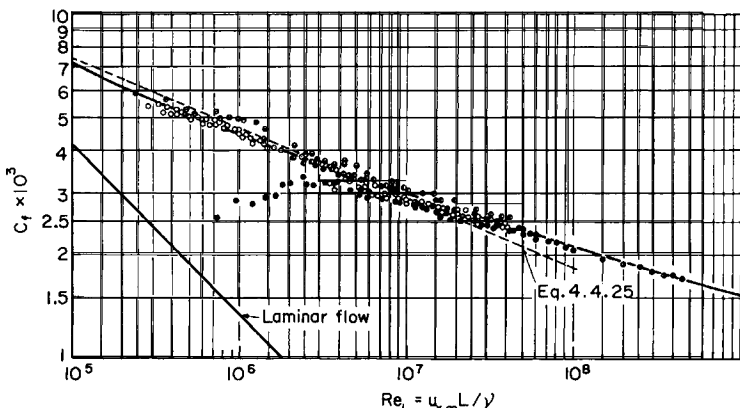


FIG. 4.4.5 Plot of the friction coefficient against the Reynolds number for flow over a flat plate.

instead of the “seventh power law” and obtained slightly better agreement with measurement at higher values of the Reynolds number.

Example 4.4.2 Estimate the volumetric rate at which ambient air is being entrained by a unit width of a moving strip in a hot strip mill.

DATA strip velocity, 12 m/s; strip length, 50 m; ν of air at 700°K; 66 m^2/s .

SOLUTION It is convenient to work in terms of the displacement thickness $\delta_t^*(x)$. Using Eq. (4.4.23), we have

$$\begin{aligned}\delta_t^* &= 50 \times 0.046(12 \times 50/66)^{-0.2} \\ &\simeq 1.47 \quad \text{m}\end{aligned}$$

Hence the volumetric rate of entrainment is

$$1.47 \times 12 \sim 17.7 \quad \text{m}^3/\text{s}$$

per unit width of strip.

4.4.3 The Water Model of an Argon-Stirred Ladle

Figure 4.4.6 shows a sketch of an argon-stirred ladle, where it is seen that a stream of argon bubbles, introduced through an axisymmetrically located nozzle, entrain a liquid metal core, which in turn gives rise to circulating currents within the system. Such argon agitation (albeit not with centrally located nozzles, because off-central nozzle location provides for an improved mixing efficiency) is being used for homogenizing molten steel contained in ladles.

Since this is an axisymmetrical recirculating flow system, the statement of the problem is readily accomplished by writing the equivalent expressions, to Eqs. (4.3.33)–(4.3.36), (4.3.26), (4.3.37), and (4.3.40) in a cylindrical coordinate system. Thus we have

$$\begin{aligned}r^2 \rho \left[\frac{\partial}{\partial z} \left(\frac{\bar{\xi}_\theta}{r} \frac{\partial \bar{\Psi}'}{\partial r} \right) - \frac{\partial}{\partial r} \left(\frac{\bar{\xi}_\theta}{r} \frac{\partial \bar{\Psi}'}{\partial z} \right) \right] - \frac{\partial}{\partial z} \left[r^3 \frac{\partial}{\partial z} \left(\mu_{\text{eff}} \frac{\bar{\xi}_\theta}{r} \right) \right] \\ - \frac{\partial}{\partial r} \left[r^3 \frac{\partial}{\partial r} \left(\mu_{\text{eff}} \frac{\bar{\xi}_\theta}{r} \right) \right] = 0 \quad \begin{bmatrix} \text{the vorticity} \\ \text{transport equation} \end{bmatrix} \quad (4.4.26)\end{aligned}$$

where

$$\bar{\xi}_\theta = \frac{\partial \bar{u}_r}{\partial z} - \frac{\partial \bar{u}_z}{\partial r} \quad (4.4.27)$$

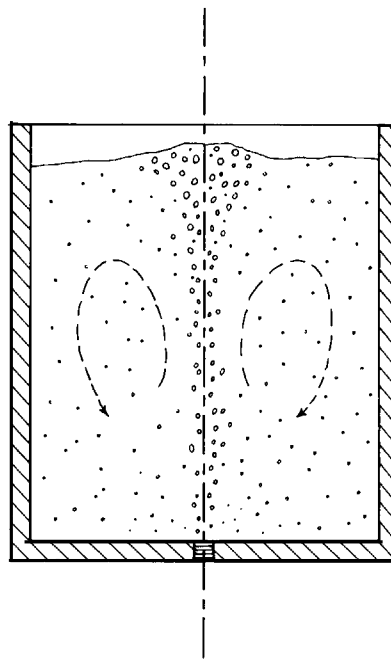


FIG. 4.4.6 Sketch of an argon-stirred ladle.

and

$$\bar{u}_r = -\frac{1}{r} \frac{\partial \bar{\psi}}{\partial z} \quad (4.4.28)$$

$$u_z = \frac{1}{r} \frac{\partial \bar{\psi}}{\partial r} \quad (4.4.29)$$

with

$$\frac{\partial}{\partial z} \left(\frac{1}{r} \frac{\partial \bar{\psi}}{\partial z} \right) + \frac{\partial}{\partial r} \left(\frac{1}{r} \frac{\partial \bar{\psi}}{\partial r} \right) + \bar{\xi}_\theta = 0 \quad (4.4.30)$$

Here

$$\mu_{\text{eff}} = \mu + \mu_t \quad (4.4.31)$$

and

$$\mu_t = \rho K W^{-1/2} \quad (4.3.38)$$

The quantities K and W are then obtained through the solution of the following conservation equations:

$$\begin{aligned} \frac{\partial}{\partial z} \left(K \frac{\partial \bar{\psi}}{\partial r} \right) - \frac{\partial}{\partial r} \left(K \frac{\partial \bar{\psi}}{\partial z} \right) - \frac{\partial}{\partial z} \left[r \left(\mu + \frac{\mu_t}{\sigma_K} \right) \frac{\partial K}{\partial z} \right] - \frac{\partial}{\partial r} \left[r \left(\mu + \frac{\mu_t}{\sigma_K} \right) \frac{\partial K}{\partial r} \right. \\ \left. \text{(convection)} \right. \\ = r \left[2\mu_t \left\{ \left(\frac{\partial \bar{u}_z}{\partial z} \right)^2 + \left(\frac{\partial \bar{u}_r}{\partial r} \right)^2 + \frac{1}{2} \left(\frac{\partial \bar{u}_r}{\partial z} + \frac{\partial \bar{u}_z}{\partial r} \right)^2 \right\} \right. \\ \left. \text{(generation)} \right. \\ - r C_D \rho K^{3/2} / (K/W)^{1/2} \right. \\ \left. \text{(dissipation)} \right] \end{aligned} \quad (4.4.32)$$

[conservation of K].

The corresponding conservation equation for W is written as[†]

$$\begin{aligned} \frac{\partial}{\partial z} \left(W \frac{\partial \bar{\psi}}{\partial r} \right) - \frac{\partial}{\partial r} \left(W \frac{\partial \bar{\psi}}{\partial z} \right) - \frac{\partial}{\partial z} \left[r \left(\mu + \frac{\mu_t}{\sigma_W} \right) \frac{\partial W}{\partial z} \right] - \frac{\partial}{\partial r} \left[r \left(\mu + \frac{\mu_t}{\sigma_W} \right) \frac{\partial W}{\partial r} \right] \\ = r \left[C_1 \mu_t (\nabla \xi_\theta)^2 + 2C_3 \frac{W}{K} \mu_t \left\{ \left(\frac{\partial \bar{u}_z}{\partial z} \right)^2 \right. \right. \\ \left. \left. + \left(\frac{\partial \bar{u}_r}{\partial r} \right)^2 + \frac{1}{2} \left(\frac{\partial \bar{u}_r}{\partial z} + \frac{\partial \bar{u}_z}{\partial r} \right)^2 \right\} \right] - C_2 \rho W^{3/2} \end{aligned} \quad (4.4.33)$$

The “constants” appearing in these equations were assigned the following tentative values by Spalding:

$$C_D = 0.09, \quad C_1 = 3.5, \quad C_2 = 0.17$$

$$C_3 = 1.04, \quad \sigma_K = \sigma_W = 0.9$$

The boundary conditions for Eqs. (4.4.26)–(4.4.33) are readily stated for the solid surfaces, by specifying “no-slip” for the velocities and “equilibrium” between the generation and the dissipation terms for the turbulent energy; moreover, the stipulation of “zero-shear” may be invoked at the free surface, as a reasonable approximation.

The main practical difficulty is to assign realistic boundary conditions at the interface between the core containing the argon bubbles and the rest of the fluid.

In recent work, as a first approximation, the experimentally measured linear velocities were used as the boundary condition.³⁴ Figure 4.4.7 shows a comparison between the theoretically predicted streamline pattern and

[†] Some reservations regarding the physical justification for writing conservation equations for W have been discussed in Section 4.3.

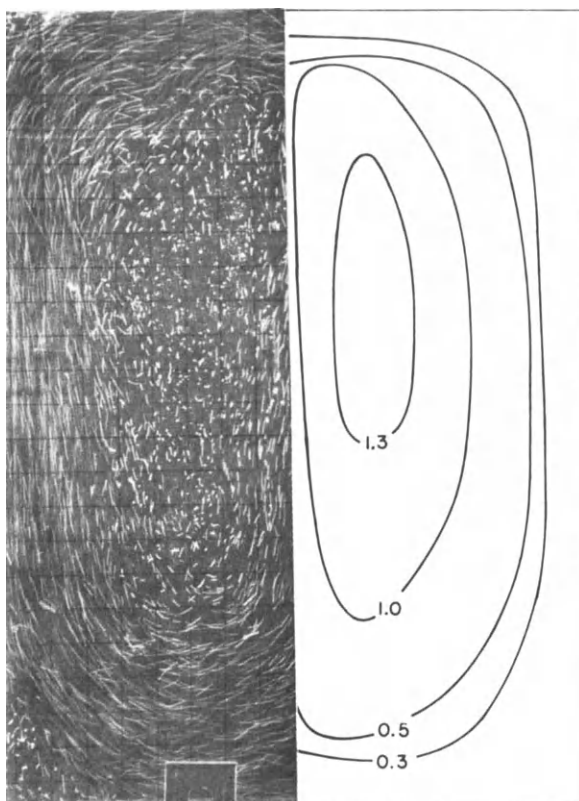


FIG. 4.4.7 Comparison between the theoretically predicted streamline pattern and the experimentally obtained streamline pattern for a water model of an argon-stirred ladle.³⁴

the streakline pattern that has been determined experimentally using time lapse photography. Figures 4.4.8 and 4.4.9 show a comparison between the experimentally determined velocity profiles and those predicted, using a two-equation model of turbulence.

It is seen that there appears to be reasonable, if not fully quantitative, correspondence between measurements and predictions, which augurs well for the usefulness of this computational method.

4.5 Concluding Remarks

In this chapter we introduced the reader to turbulence phenomena. While much of the material presented may have appeared to the reader as quite abstract and of great mathematical complexity, the practical importance of

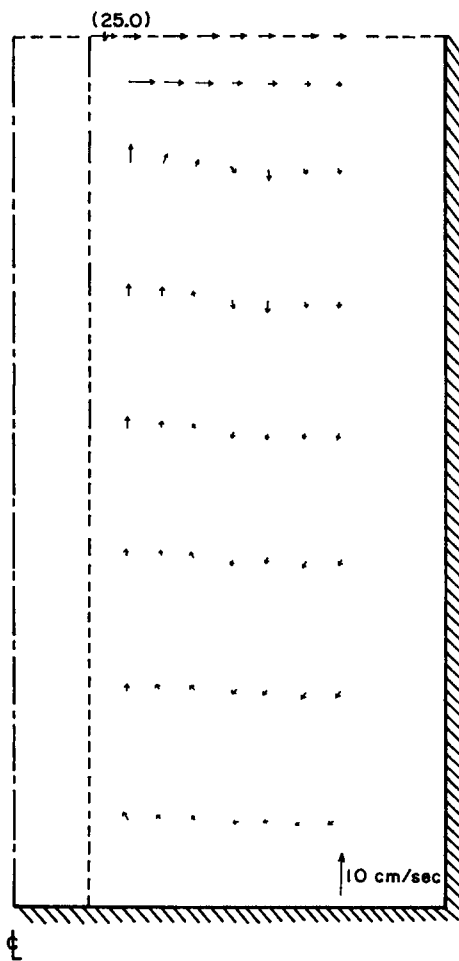


FIG. 4.4.8 Experimentally determined velocity profile in a water model of an argon-stirred ladle.³⁴

turbulence phenomena has to be stressed very strongly; the majority of the flow systems encountered in metals processing operations are in the turbulent regime.

The reader will have noted the rather tenuous connection between the statistical, descriptive material presented on turbulence phenomena in Section 4.2 and the last two sections, devoted to the prediction of turbulent flow systems. Indeed in the majority of cases we have to rely on largely empirical inputs if we wish to calculate turbulent flows.

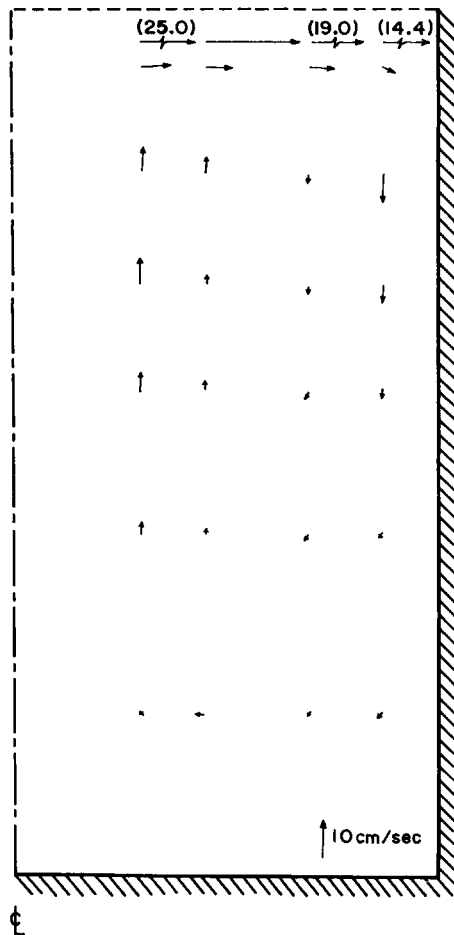


FIG. 4.4.9 Theoretically predicted velocity profiles for a water model of an argon-stirred ladle.³⁴

A great deal of experience has been accumulated by aerodynamicists and mechanical engineers with regard to certain types of turbulent flows, notably flow through pipes, jets, and boundary layer phenomena. Thus the behavior of these systems may be predicted with reasonable accuracy by combining empirical information with semitheoretical models. Alas, these systems, with the exception of jets, which will be discussed in Chapter 9, are of no great importance in metals processing, although turbulent flow through channels and turbulent film flows do have definite applications.

In contrast, turbulent recirculating flows, such as encountered in argon-stirred ladles, vacuum degassing, continuous casting, BOF and Q-BOP

steelmaking, teemed-stream—melt interactions of electromagnetically stirred vessels, etc., are of crucial importance in most metals processing and refining systems.

While the methods available for the modeling of these flow situations are far from perfect (see the discussion of two-equation models in Section 4.3), these techniques show much promise for a marked improvement of our understanding of these phenomena.

References

1. Leonardo da Vinci, about 1509, reproduced by permission from Her Majesty Queen Elizabeth II.
2. M. McNallan, Ph.D. Thesis, Massachusetts Institute of Technology, Cambridge, Massachusetts, 1976.
3. R. B. Bird, W. E. Stewart, and E. N. Lightfoot, "Transport Phenomena." Wiley, New York, 1969.
4. J. T. Davies, "Turbulence Phenomena." Academic Press, New York, 1972.
5. H. Reichardt, *NACA Tech. Memo. 1047* (1943).
6. H. Schlichting, "Boundary Layer Theory." McGraw-Hill, New York, 1968.
7. R. S. Brodkey, "The Phenomena of Fluid Motions." Addison-Wesley, Reading, Massachusetts, 1967.
8. J. Lumley and H. Tennekes, "Turbulence." McGraw-Hill, New York, 1972.
9. J. O. Hinze, "Turbulence," 2nd ed. McGraw-Hill, New York, 1975.
10. G. I. Taylor, *Proc. R. Soc. London, Ser. A* **151**, 421 (1935); **164**, 15 (1938).
11. A. N. Kolmogorov, *Dokl. Akad. Sci. SSSR* **30**, 301 (1941); **31**, 538 (1941); **32**, 16 (1941).
12. K. Nakanishi and J. Szekely, *Trans. Iron Steel Inst. Jpn.* **15**, 522 (1975).
13. J. Nikuradse, *Ver. Dsch. Ing. Forsch.* **356** (1932).
14. R. G. Deissler, *NASA Tech. Note D-2138* (1950); *Natl. Advis. Comm. Aeronaut., Rep. 1210* (1955).
15. J. G. Knudsen and D. L. Katz, "Fluid Mechanics and Heat Transfer." McGraw-Hill, New York, 1958.
16. T. V. Boussinesq, *Mem. Pres. Acad. Sci., Paris* **23**, 46 (1877).
17. L. Prandtl, *ZAMM* **5**, 136 (1925).
18. B. E. Launder and D. B. Spalding, "Lectures in Mathematical Models of Turbulence," Chapter 2. Academic Press, New York, 1972.
19. B. A. Finlayson, "The Method of Weighted Residuals and Variational Principles." Academic Press, New York, 1972.
20. W. H. Ray and J. Szekely, "Process Optimization with Applications in Metallurgy and Chemical Engineering." Wiley, New York, 1973.
21. S. V. Patankar and D. B. Spalding, "Heat and Mass Transfer in Boundary Layers." Intertex Books, London, 1970.
22. H. B. Keller, "Numerical Methods for Two Point Boundary Value Problems." Ginn (Blaisdell), New York, 1968.
23. A. N. Kolmogorov, *Izv. Akad. Nauk SSSR, Ser. Fiz.* **6**, No. 1-2, 56 (1942).
24. L. Prandtl, *Nachr. Akad. Wiss. Goettingen* (1945), cited by ref 18.
25. J. C. Rotta, *Z. Phys.* **129**, 547 (1951).
26. A. D. Gosman, W. M. Pun, A. K. Runchal, D. B. Spalding, and M. Wolfshtein, "Heat and Mass Transfer in Recirculating Flows." Academic Press, New York, 1969.
27. C. W. Chang, Ph.D. Thesis, State University of New York at Buffalo (1976).

28. P. Bradshaw, D. H. Ferriss, and N. P. Atwell, *J. Fluid Mech.* **28**, 593 (1967).
29. V. W. Nee and L. S. G. Kovasznay, *Phys. Fluids* **12**, 473 (1969).
30. J. Szekely and S. Asai, *Trans. Iron Steel Inst. Jpn.* **15**, 270 (1975).
31. B. E. Launder and D. B. Spalding, "Lectures in Mathematical Models of Turbulence." Academic Press, New York, 1972.
32. G. D. Fulford, *Adv. Chem. Eng.* **5**, 151 (1964).
33. A. E. Dukler and O. P. Bergelin, *Chem. Eng. Prog.* **48**, 557 (1952).
34. J. Szekely, J. C. Wang, and K. M. Kiser, *Metall. Trans.* **7B**, 287 (1976)
35. V. Levich, "Physicochemical Hydrodynamics." Prentice-Hall, Englewood Cliffs, New Jersey, 1962.
36. E. R. G. Eckert and R. M. Drake, "Heat and Mass Transfer." McGraw-Hill, New York.

5.1 Introduction

The reader will recall that in the general statement of the equation of motion in the preceding two chapters the following vectorial representation was employed:

$$\rho \frac{D\mathbf{u}}{Dt} = \mu \nabla^2 \mathbf{u} + \rho \mathbf{F}_b' - \nabla p \quad (5.1.1)$$

for laminar flow and

$$\rho \frac{D\mathbf{u}}{Dt} = \nabla(\mu_{\text{eff}} \cdot \nabla \mathbf{u}) + \rho \mathbf{F}_b' - \nabla p \quad (5.1.2)$$

for turbulent flow.

The quantity \mathbf{F}_b' for turbulent flow appearing in these equations is the body force acting on unit volume of the fluid. In the majority of practical fluid flow problems this body force is due to gravity only. However, in other processing applications, when molten metals or ionic conducting slags are made to flow in a strong magnetic field, additional body forces will arise due to the electromagnetic force field generated.

Practical examples of such systems include induction-stirred ladles, electromagnetic pumping, the operation of high-frequency melting units, some aspects of electroslag refining, the operation of the Hall cell in the electrowinning of aluminum, and the like.

Figure 5.1.1. shows a sketch of some of the industrial systems, where electromagnetic stirring may play an important role in determining the overall process kinetics. Thus (a) shows an induction furnace, where the current passed through the coils induces current in the melt, held in a

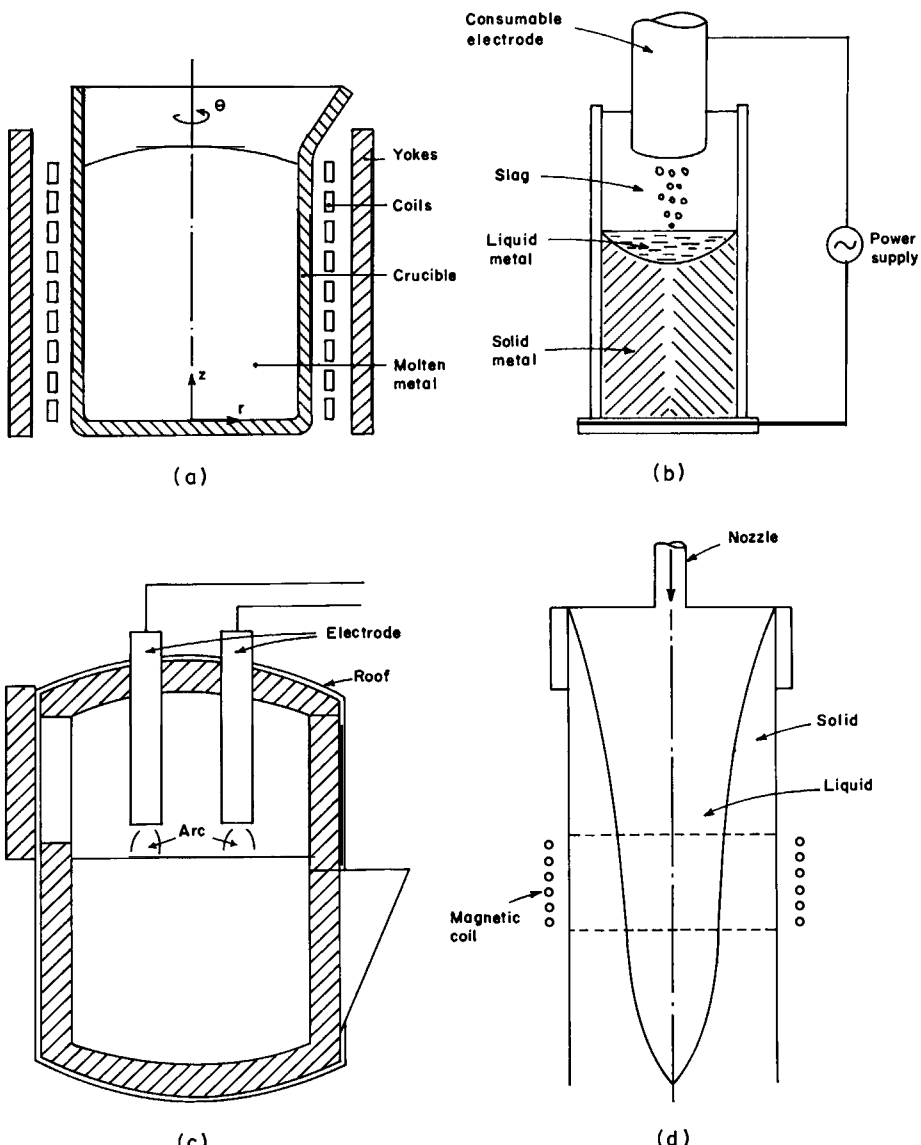


FIG. 5.1.1 Sketch of systems where electromagnetically driven flows may be of importance: (a) induction furnace, (b) electroslag refining, (c) electric arc furnace, (d) induction-stirred continuous casting system.

crucible. The induced current produces an electromagnetic field, which in turn causes motion of the melt.

In the electroslag refining process, sketched in (b), current is passed from a consumable metal electrode through a molten slag to a molten liquid pool. The passage of the current through the conducting slag and the metal pool produces an electromagnetic force field, which in turn generates flow.

In the arc furnace, sketched in (c), the current passes through the molten metal pool, and this again results in induced motion.

Finally, the induction coils, placed around a continuous casting machine, indicated in (d), also generate flow, which in turn may improve the surface quality of the material produced.

The reader may recall from his studies in physics the classical experiments of Oersted and Biot in the early part of the nineteenth century that wires carrying electric currents produced deflections in the permanent magnets placed in their neighborhood. The quantitative description of this *magnetic induction* was due to Ampere in 1825.

In 1831 Faraday examined the behavior of currents in circuits that were placed in magnetic fields that varied with time. Faraday observed that a transient current is induced in a circuit if

- (a) a steady current flowing in an adjacent circuit is turned on or off,
- (b) the adjacent circuit with a steady current is moved relative to the first circuit,
- (c) a permanent magnet is moved relative to the circuit.

These observations, which form the basis of power generation and the operation of electric machinery, provided some of the most important building blocks for the laws of electrodynamics.[†]

In qualitative terms the consequence of these findings is that if current is passed through conducting coils that surround a ladle or mold containing a molten metal, i.e., conductor itself, this current will induce an electromagnetic force field, which in turn will produce motion in the melt.

This is the principle of induction stirring and induction melting; this latter operation makes use of the energy dissipated by the induced current. Another important consequence of these relationships is that the passage of a current through (an ionic) conductor, such as occurring in electroslag refining and in the electrowinning of aluminum, will produce an electromagnetic force field and hence a body force causing motion.

The scientific field devoted to the study of the interaction of electromagnetic and fluid flow phenomena is called electromagnetodynamics or

[†] A good discussion of elementary electrodynamics is available in the texts by Krauss and Carrer¹ and Ponofsky and Phillips.²

often (erroneously) magnetohydrodynamics.[†] This field, which encompasses classical electrodynamics, magnetodynamics, and fluid mechanics, has undergone a very dramatic growth motivated by its relevance to electro-physics, geophysics, plasma research, and novel techniques of power generation.

While the analogous problems in metals processing are of considerable practical importance these have received very little attention up to recent times. Although the mathematical tasks involved are quite substantial, there is an important challenge in the adaptation of the techniques developed in electromagnetodynamics for space and plasma research to metals processing applications.

The obvious limitations on space will allow us but a cursory introduction to this field; the interested reader is urged to follow up the supplementary reading recommended at the end of the chapter. Regarding the organization of the material to be presented here, the definition of the basic concepts and the statement of Maxwell's equations will be given in Section 5.2, together with equations of motion and the key dimensionless numbers that are used for characterizing these systems. Finally, some specific metallurgical applications are presented in Section 5.3.

5.2 The Principal Parameters in Electrodynamics

Table 5.2.1 provides a summary of the principal parameters employed in the description of electrodynamic phenomena. The constants of proportionality used in conjunction with these quantities are given in Table 5.2.2. The quantities appearing in Table 5.2.3 are interrelated through the celebrated Maxwell's equations which form the basis of electrodynamics. Using the MHD approximation, a full discussion of which is available in the texts by Hughes³ and Jackson,⁴ the Maxwell's equations may be written as

$$\nabla \times E = -\frac{\partial \mathbf{B}}{\partial t} \quad (5.2.1)$$

$$\nabla \times H = \mathbf{J} \quad (5.2.2)$$

$$\nabla \cdot \mathbf{J} = 0 \quad (5.2.3)$$

$$\nabla \cdot \mathbf{B} = 0 \quad (5.2.4)$$

Moreover, for a moving fluid, Ohm's law takes the following form:

$$\mathbf{J} = \sigma_e [\mathbf{E} + \mathbf{u} \times \mathbf{B}] \quad (5.2.5)$$

[†] Strictly speaking, the term hydrodynamics would imply phenomena associated with water.

TABLE 5.2.1
The Principal Parameters in Electrodynamics Phenomena

Symbol	Quantity	Unit
D	Electric flux density	volt-farad/m ² or coulomb/m ²
B	Magnetic flux density	weber/m ² or tesla
J	Conduction current density	ampere/m ² , A/m ²
H	Magnetic field	ampere/m, A/m
E	Electric field	volt/meter, V/m

TABLE 5.2.2
The Constants of Proportionality
in Electrodynamics

Symbol	Quantity	Units
ϵ	Permittivity	farad/m
σ_e	Electrical conductivity	ohm m ⁻¹
μ_m	Magnetic permeability	henry/m
ρ_e	Charge unit	coulomb/m

We note here that

$$\mathbf{J} = \sigma_e \mathbf{E} \quad (5.2.5a)$$

would be the familiar expression for Ohm's law. The second term on the right-hand side of Eq. (5.2.5) represents the current due to the convective motion of the melt. It has been found that in many practical applications relating to induction stirring, the melt velocities are low enough that the convective term may be neglected, so that one may use Eq. (5.2.5a) as a reasonable approximation.

The body force \mathbf{F}_b due to the electromagnetic force field, sometimes called *Lorentz force*, is given as

$$\mathbf{F}_b = \mathbf{J} \times \mathbf{B} \quad (5.2.6)$$

It is readily apparent that in electromagnetically driven flow problems that Navier-Stokes equations, namely Eqs. (5.1.1) and (5.1.2), and the Maxwell equations, namely Eqs. (5.2.1)–(5.2.4), are coupled, through the expression for the Lorentz force, or Eq. (5.2.6). By the appropriate manipulation of the variables, other forms of the Maxwell's equations may be written down, which may be convenient for particular applications. A good discussion of these is available in the text by Hughes and Young.³

By combining Eq. (5.2.6) and Eq. (5.1.1) or (5.1.2) we have

$$\rho \frac{D\mathbf{u}}{Dt} = \mu \nabla^2 \mathbf{u} + \rho \mathbf{g} + \mathbf{J} \times \mathbf{B} - \nabla p \quad (5.2.7)$$

for laminar flow and

$$\rho \frac{D\mathbf{u}}{Dt} = \nabla(\mu_{\text{eff}} \nabla \mathbf{u}) + \rho \mathbf{g} + \mathbf{J} \times \mathbf{B} - \nabla P \quad (5.2.8)$$

for turbulent flow. Equations (5.2.7) or (5.2.8) together with the Maxwell equations (5.2.1)–(5.2.4) and Ohm's law [Eq. (5.2.5) or (5.2.5a)] and their appropriate boundary conditions represent the complete statement of the problem.

The complexity of the problem should be readily apparent to the reader; this is aggravated by the coupled nature of these equations, namely the velocity vector appears in Eq. (5.2.5) whereas the Lorentz force, i.e., the $\mathbf{J} \times \mathbf{B}$ term appears in the equation of motion.

Two additional complicating factors should be noted here. One of these is the fact that in many MHD problems the electromagnetic boundary conditions, i.e., the values of \mathbf{H} , \mathbf{B} , \mathbf{E} , and \mathbf{J} at the surfaces bounding the conducting fluid, are not immediately available, but have to be obtained as a result of sometimes tedious field calculations.

Another, much more fundamental problem is posed by the fact that an electromagnetic force field tends to damp out turbulent fluctuations.⁵ It follows that in general the use of the turbulent viscosity μ_t in Eq. (5.2.8) would be questionable in a strong electromagnetic field, for a conducting fluid. Unfortunately at present we do not have adequate quantitative information which would allow us to describe the effect of an electromagnetic field on turbulence phenomena. As will be discussed subsequently, however, this difficulty does not arise in many furnace applications, on an industrial scale, because the electromagnetic force field does not penetrate much beyond the laminar sublayer. Nevertheless, this problem could be quite important in the case of laboratory scale furnaces. While the governing equations were seen to be quite complex, under certain conditions appreciable simplification is possible through the identification of the dominant terms, as will be illustrated in the following. In many practical applications it is convenient to recast Eq. (5.2.1) in terms of the magnetic flux intensity. Thus after some manipulation we have

$$\frac{\partial \mathbf{B}}{\partial t} = \nabla \times (\mathbf{u} \times \mathbf{B}) + \eta_m \nabla^2 \mathbf{B} \quad (5.2.9)$$

which is called the induction equation. The quantity

$$\eta_m = 1/\sigma_e \mu_m \quad (5.2.10)$$

is called the magnetic diffusivity. Equation (5.2.9) may be regarded as the transport equation for the magnetic flux intensity. The first term on the right-hand side corresponds to the convective transport, while the second term represents the “diffusive transport” of \mathbf{B} .

If the governing equations are made dimensionless, the following dimensionless group appears naturally from the statement of the problem:

$$N_{Re,m} = U_0 L_0 \sigma_e \mu_m \equiv U_0 L_0 / \eta_m \quad (5.2.11)$$

Here U_0 and L_0 are the characteristic velocity and the characteristic length of the system, respectively. $N_{Re,m}$ is called the *magnetic Reynolds number*, which is a measure of the ratio (magnetic convection)/(magnetic diffusion). When the magnetic Reynolds number is small the diffusive transport of the magnetic flux is much larger than the convective transport; thus, the induction equation (5.2.9) may be simplified to

$$\frac{\partial \mathbf{B}}{\partial t} = (1/\sigma_e \mu_m) \nabla^2 \mathbf{B} \quad (5.2.12)$$

Under such conditions the magnetic transport equation may be uncoupled from the equation of motion which renders the computational task much easier.

As a practical matter $N_{Re,m} < 1$ in many induction furnace applications, as illustrated by the following example.

Example 5.2.1 Calculate the magnetic Reynolds number for an induction furnace, containing molten steel.

DATA characteristic velocity, 0.1 m/s; characteristic length, 0.5 m; μ_m , 1.26×10^{-6} henry/m; σ_e , 1.4×10^6 (ohm m) $^{-1}$.

Then from Eq. (5.2.11),

$$N_{Re,m} = 0.1 \times 0.5 \times 1.26 \times 10^{-6} \times 1.4 \times 10^6 \simeq 0.09$$

It follows that the magnetic Reynolds number is indeed much smaller than unity.

Two other important dimensionless groups that are helpful in characterizing electromagnetically driven flows are the Hartmann number N_{Ha} and the magnetic Prandtl number $N_{Pr,m}$, defined as follows:

$$N_{Ha}^2 = \sigma_e B_0^2 L_0^2 / \mu \equiv \sigma_e U_0 B^2 / (\mu U_0 / L^2) \quad (5.2.13)$$

In physical terms the Hartmann number represents the ratio

$$\frac{\text{(electromagnetic) ponderomotive force}}{\text{viscous force}}$$

The Hartmann number appears as an important dimensionless group in one of the classical electromagnetically driven flow problems, namely the Hartmann Problem, to be discussed in the subsequent section. It is helpful in assessing the relative importance of the electromagnetic driving forces acting on the system. The magnetic Prandtl number is defined as

$$N_{\text{Pr},m} = v/\eta_m = N_{\text{Re},m}/N_{\text{Re}} \quad (5.2.14)$$

It designates the ratio: (ability of the fluid to transmit the magnetic field)/(ability of the fluid to transmit vorticity).

For most liquid metal systems this ratio is usually small, thus, for mercury $N_{\text{Pr},m} \simeq 10^{-7}$, while for molten steel $N_{\text{Pr},m} \simeq 7.5 \times 10^{-7}$, so that the magnetic field diffuses much faster than vorticity. It follows that the convective transport of the magnetic field may be neglected compared to its diffusive transport. This contention is consistent with the argument developed in simplifying Eq. (5.2.9) to obtain (5.2.12).

At this stage, it is worthwhile to summarize what we have done here. By applying the MHD approximation, the electromagnetically driven flow problem in metals processing was stated, by writing the (turbulent) Navier–Stokes equations, with the Lorentz force (i.e., the $\mathbf{J} \times \mathbf{B}$ term) constituting the body force:

$$\rho \frac{D\mathbf{u}}{Dt} = \nabla(\mu_{\text{eff}} \nabla \mathbf{u}) + \rho \mathbf{g} + \mathbf{J} \times \mathbf{B} - \nabla p \quad (5.2.8)$$

The body force term $\mathbf{J} \times \mathbf{B}$ has to be obtained from the solution of Maxwell's equations, namely (5.2.1)–(5.2.4), and Ohm's law (5.2.5). In general this would be a very complex, mutually coupled system of differential equations. However, because the magnetic Reynolds number is small in liquid metal systems, the terms involving the melt velocity may be usually neglected; thus, the propagation of the magnetic flux intensity may be expressed as

$$\frac{\partial \mathbf{B}}{\partial t} = (1/\sigma_e \mu_m) \nabla^2 \mathbf{B} \quad (5.2.12)$$

or, written in terms of \mathbf{H} the magnetic field, we have

$$\frac{\partial \mathbf{H}}{\partial t} = (1/\sigma_e \mu_m) \nabla^2 \mathbf{H} \quad (5.2.12a)$$

Furthermore, Ohm's law is given as

$$\mathbf{J} = \sigma_e \mathbf{E} \quad (5.2.5a)$$

Thus Eqs. (5.2.7) or (5.2.8), (5.2.5), and (5.2.12) represent the principal governing equations. As will be shown subsequently, for induction furnace applications the solution of the problem proceeds as follows:

(1) We solve Eq. (5.2.12), which is like the diffusion equation, for the appropriate boundary conditions, to obtain the magnetic flux density \mathbf{B} , or the magnetic field \mathbf{H} . Because of the simplifying assumptions made, we can do this independently of the fluid flow field.

An alternative procedure, discussed by Evans,⁶ involves the use of mutual inductances and numerical techniques to obtain the Lorentz force.

(2) Once \mathbf{B} or \mathbf{H} is known, we can use the appropriate Maxwell equation(s) [e.g., (5.2.2)] to calculate \mathbf{J} the current density.

(3) Then the $\mathbf{J} \times \mathbf{B}$ product may be formed, only certain components of which have a nonzero value, for use in the integration of the Navier–Stokes equations. This latter procedure can be carried out numerically, as discussed in Chapter 4.

The solution of electromagnetically driven flow problems for systems other than induction furnaces may be somewhat more complex and some comments on these will be given subsequently.

Before proceeding with the consideration of specific cases, it may be worthwhile to develop some general relationships between the key parameters in induction furnace operation. A full discussion of the detailed mathematical manipulations involved in the development of these equations is available in papers by Szekely and Chang.^{7–9}

Let us consider Eq. (5.2.8):

$$\rho \frac{D\mathbf{u}}{Dt} = \nabla(\mu_{\text{eff}} \cdot \nabla \mathbf{u}) + \rho \mathbf{g} + \mathbf{J} \times \mathbf{B} - \nabla P \quad (5.2.8)$$

At high melt velocities, if the inertial forces dominate, we may neglect all but the third term (the electromagnetic driving force) in Eq. (5.2.8). Then for steady-state operation we have

$$\rho(\mathbf{u} \cdot \nabla \mathbf{u}) = \mathbf{J} \times \mathbf{B} \quad (5.2.15)$$

In assessing the order of magnitude of these terms, we may write:

$$O\{\mathbf{u} \cdot \nabla \mathbf{u}\} \sim \rho u_0^2 / L \quad (5.2.15a)$$

where u_0 and L designate a characteristic velocity and the characteristic length respectively.

Moreover, through the appropriate manipulation of the Maxwell equations, we may also write that

$$\mathcal{O}\{\mathbf{J} \times \mathbf{B}\} \sim \sigma_e B_0 f L \quad (5.2.16)$$

where B_0 is the characteristic magnetic flux intensity, and f is the frequency. On taking

$$B_0 \sim \mu_m J_0 L \quad (5.2.17)$$

and upon combining Eqs. (5.2.15)–(5.2.17), we have

$$\rho U_0^2 / L \sim \sigma_e f L^3 J_0^2 \mu_m^2 \quad (5.2.18)$$

or

$$U_0 \sim J_0 (\sqrt{\sigma_e f / \rho}) L^2 \mu_m \quad (5.2.19)$$

which indicates that the characteristic velocity is proportional to the coil current and to the square of the linear dimension of the apparatus. This relationship is helpful in qualitative assessment of scale-up. We note that the linear relationship between the coil current and the characteristic velocity has been verified experimentally by Dragunkina and Tir;¹⁰ some recent work by Evans and Tarapore^{6,11} indicated, however, that this linearity is not always observed.

THE NATURE OF THE STIRRING FORCE

The body force, or the Lorentz force, which drives the flow, may be expressed as

$$\mathbf{J} \times \mathbf{B} = -\nabla \left(\frac{1}{\mu_m} \frac{B^2}{2} \right) + \frac{1}{\mu_m} \mathbf{B} \cdot \nabla \mathbf{B} \quad (5.2.20)$$

The first term of the right-hand side is the magnetic pressure gradient, which in itself does not produce motion. The second term, however, is the one responsible for producing the motion. It follows that the extent to which the $\mathbf{J} \times \mathbf{B}$ product is not derivable as a gradient of a scalar [i.e., the first term on the right-hand side of Eq. (5.2.20)] is the measure of the stirring force.

Finally, it may be shown that the following expression may be used for estimating the ratio [energy input for stirring]/[energy input for (joule) heating]:

$$\mathcal{O}\left\{ \frac{(\mathbf{J} \times \mathbf{B}) \cdot \mathbf{u}}{\mathbf{J}/\sigma} \right\} \sim U_0 / f L \quad (5.2.21)$$

This is consistent with current operational guidelines in that low frequencies are being employed when stirring is desired, e.g., in the ASEA-SKF process, while high frequencies are being used when heating is the objective.

It should be remarked that if we wish to maximize the energy input that is being used for stirring, there exists an optimum frequency for accomplishing this objective.

Finally we note that for induction furnace applications, on the basis of experience and computations, it is possible to estimate the flow pattern in the system, depending on the coil arrangement. When the coils are placed essentially symmetrically, a *traveling wave* may be generated through the use of polyphase connections; in contrast, standing waves may be generated through a single-phase coil design.

The resultant flow patterns are sketched in Fig. 5.2.1, where it is seen that traveling waves generate two circulating loops, where the direction of the velocity near the wall coincides with the direction of the wave as shown in (a) and (b). In contrast, as seen in (c), a standing wave results in four circulating loops. This latter flow behavior is characteristic of most laboratory scale induction furnaces.

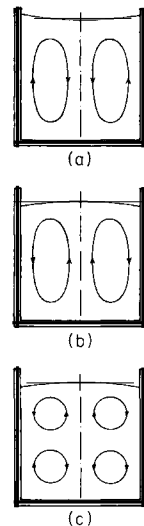


FIG. 5.2.1 Idealized flow patterns in induction furnaces: (a) upward-traveling magnetic field, (b) downward-traveling magnetic field, (c) standing wave.

When the coils are not placed symmetrically, the resultant flow patterns are somewhat distorted; a discussion of this problem has been presented by Evans and Tarapore¹¹ and also by Szekely and Chang.¹² In the following we shall present the outline of the formulation and computed velocity fields for certain systems of interest in metals processing.

5.3 MHD Applications in Metals Processing

In this section we shall examine a range of problems for which solutions, albeit approximate, may be generated with the aid of MHD theory.

The first of these is a particularly simple flow problem, where essentially one-dimensional flow is being generated by the imposition of a uniform, steady magnetic flux density on the system. Such flow problems are not of very great importance in metals processing, but because of their simplicity they provide a very useful illustration of the principles that were discussed in the preceding sections.

The remainder of the problems to be discussed relate to the operation of induction furnaces, and wherever possible the predictions based on the modeling equations will be compared with measurements. Because of limitations on space, electroslag refining systems will not be treated here, although papers dealing with this subject will be referenced at the end of the chapter.

The approach to be taken in the formulation of all these problems to be discussed in the following sections will be to assume that the boundary conditions for the magnetic flux or the magnetic field will be available. In practice this is not always the case, although the method of calculating in-

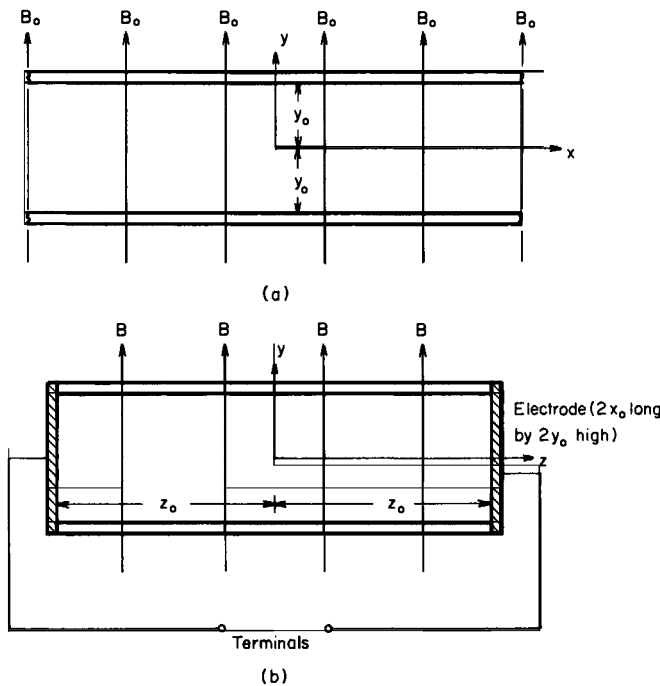


FIG. 5.3.1 The channel geometry for Hartmann flow.

duced magnetic fields is reasonably well documented. In some recent studies of electromagnetic stirring phenomena the actual magnetic field has been determined experimentally in the empty vessel—for such problems, the postulate that the magnetic boundary conditions are available will of course be correct. Let us now consider some of these problems in detail.

5.3.1 One-Dimensional Laminar MHD Flow Due to a Steady Electromagnetic Force Field—the Hartmann Problem

Let us consider one of the simplest problems in magnetoelectrodynamics, the flow of a conducting fluid between two parallel plates in a magnetic field, the so-called Hartmann problem. The system is sketched in Fig. 5.3.1a and b. It is seen that the plates, between which the fluid is flowing, are separated by a distance $2y_0$; moreover, we shall postulate that the channel is very wide, $z_0 \gg y_0$, so that the flow field may be regarded as one dimensional.

Let us apply a uniform magnetic induction B_0 in the y direction, which will then result in an induced magnetic field H_x and an induced velocity component u_x , as sketched in Fig. 5.3.2.

The problem is then to calculate both the velocity field and the current resulting from this arrangement. A simple physical argument indicates that the current flows predominantly in the z direction, between the electrodes, as

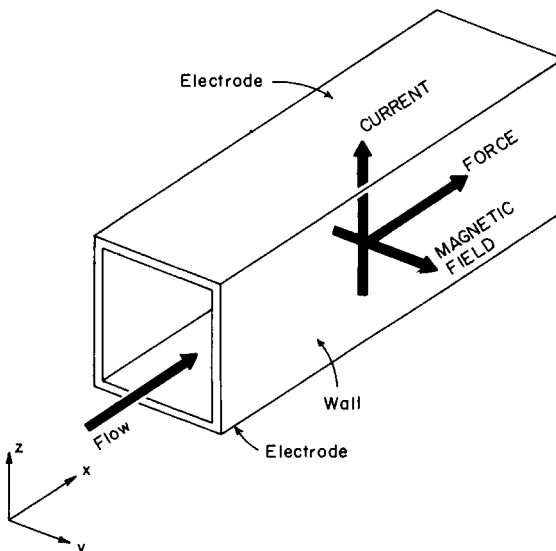


FIG. 5.3.2 Sketch showing the dominant directions of the current, magnetic field, and force field in Hartmann flow.

seen in Fig. 5.3.1b. Let us now state the problem mathematically by writing down both the appropriate components of Maxwell's equations and the Navier–Stokes equations; in the statement of the latter we shall have to include the extra body force term resulting from the electromagnetic force field. Maxwell's equations were given previously as Eqs. (5.2.1)–(5.2.4).

Since the induced magnetic field is constant, $\partial \mathbf{B} / \partial t = 0$, then from (5.2.1)

$$\nabla \times \mathbf{E} = 0 \quad (5.3.1)$$

Let us now refer to Eq. (5.2.2):

$$\nabla \times \mathbf{H} = \mathbf{J} \quad (5.2.2)$$

Upon writing down the components of this expression we have

$$\frac{\partial H_z}{\partial y} = J_x \quad (5.3.2)$$

$$-\frac{\partial H_x}{\partial y} = J_z \quad (5.3.3)$$

$$J_y = 0 \quad (5.3.4)$$

On noting that $B_y = B_0$, the three components of the Navier–Stokes equation may be expressed as

$$\mu \frac{\partial^2 u_x}{\partial y^2} = \frac{\partial p}{\partial x} + B_0 J_z \quad (\text{x direction}) \quad (5.3.5)$$

$$\frac{\partial p}{\partial y} = J_z B_x - J_x B_z \quad [(\text{y direction}), \text{ assuming } u_y = 0] \quad (5.3.6)$$

$$\mu \frac{\partial^2 u_z}{\partial y^2} = \frac{\partial p}{\partial z} - B_0 J_x \quad (\text{z direction}) \quad (5.3.7)$$

Finally Ohm's law may be written as

$$J_x = \sigma_e [E_x - B_0 u_z] \quad (5.3.8)$$

and

$$J_z = \sigma_e [E_z + B_0 u_x] \quad (5.3.9)$$

If from the consideration of the geometry we set

$$J_x, \quad H_z, \quad u_z, \quad \text{and} \quad E_x = 0 \quad (5.3.10)$$

then on combining Eqs. (5.3.5) and (5.3.9) we have

$$\mu \frac{\partial^2 u_x}{\partial y^2} = \frac{\partial p}{\partial x} + \sigma_e [E_z + B_0 u_x] B_0 \quad (5.3.11)$$

Equation (5.3.11) is the equation of motion for the system; the force terms appearing on the right-hand side denote the sum of the pressure force and the additional body force due to the electromagnetic force field.

Equation (5.3.11) may be readily integrated for the boundary conditions specifying no-slip at the walls, i.e.,

$$u_x = 0 \quad \text{at} \quad y = \pm y_0$$

Since E_z and B_0 are constant, we have

$$u_x = \frac{y_0^2}{N_{\text{Ha}}^2} \left[\frac{1}{\mu} \frac{\partial p}{\partial x} + \frac{N_{\text{Ha}}}{y_0} \left(\frac{\sigma_e}{\mu} \right)^{1/2} E_z \right] \left[\frac{\cosh N_{\text{Ha}}(y/y_0)}{\cosh N_{\text{Ha}}} - 1 \right] \quad (5.3.12)$$

Here $N_{\text{Ha}} = y_0 B_0 (\sigma_e / \mu)^{1/2}$ is the Hartmann number which has been defined in Eq. (5.2.13). It is readily seen on inspection of Eq. (5.3.12) that when $N_{\text{Ha}} \rightarrow 0$ this expression will reduce to

$$u_x \approx -\frac{1}{\mu} \left(\frac{\partial p}{\partial x} \right) \left[\frac{y^2 - y_0^2}{2} \right] \quad (5.3.13)$$

which is the well-known result for laminar flow between two parallel planes—in the absence of electromagnetic effects.

The terminal voltage between the two plates, $-z_0$ and $+z_0$, is given by

$$V_T = - \int_{-z_0}^{z_0} E_z dz = -2z_0 E_z \quad (5.3.14)$$

It is instructive to express Eq. (5.3.12) in the following dimensionless form:

$$\tilde{u}_x = \frac{1}{N_{\text{Ha}}^2} (1 - N_{\text{Ha}} \tilde{V}_T) \left(\frac{\cosh N_{\text{Ha}} \tilde{y}}{\cosh N_{\text{Ha}}} - 1 \right) \quad (5.3.15)$$

where

$$\tilde{y} = \frac{y}{y_0}, \quad \tilde{u}_x = u_x / (y_0^2 / \mu) \frac{\partial p}{\partial x}$$

and

$$\tilde{V}_T = V \left/ \left[2y_0 z_0 / (\sigma_e \mu)^{1/2} \left(\frac{\partial p}{\partial x} \right) \right] \right.$$

The dimensionless volumetric flow rate \tilde{Q} is given as

$$\tilde{Q} = 2 \int_0^1 \tilde{U} d\tilde{y} = \frac{2}{N_{\text{Ha}}^2} (1 - N_{\text{Ha}} \tilde{V}_T) \left(\frac{\tanh N_{\text{Ha}}}{N_{\text{Ha}}} - 1 \right) \quad (5.3.16)$$

Inspection of Eq. (5.3.16) shows that the net flow is zero when $\tilde{V}_T = N_{\text{Ha}}^{-1}$. Figure 5.3.3 shows a plot of \tilde{Q} against the Hartmann number for various

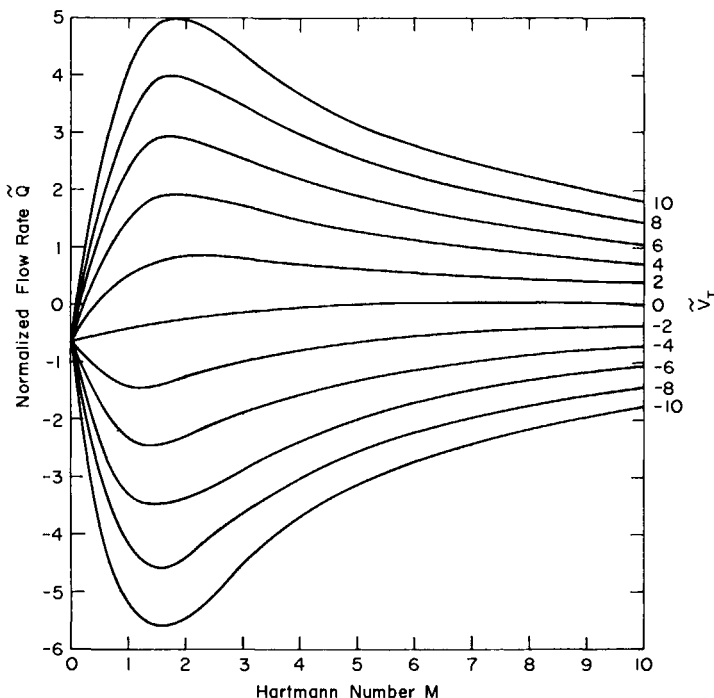


FIG. 5.3.3 Plot of the dimensionless flow rate against the Hartmann number, with the dimensionless terminal voltage as a parameter of Hartmann flow.

parametric values of \tilde{V}_T . It is seen that for a given value of the terminal voltage there exists an optimum value of the Hartmann number, which maximizes the volumetric flow rate. This behavior is to be expected, because $\tilde{Q} \rightarrow 0$ as $N_{Ha} \rightarrow \infty$. In order to provide the reader with a better feel for the numerical quantities involved, let us work a simple numerical example.

Example 5.3.1 Liquid mercury is being pumped in a rectangular channel of halfwidth 0.05 m through the application of an electromagnetic force field. If we assume that the other dimensions of the channel are large, and that there is no externally imposed pressure field, calculate the maximum fluid velocity for the following conditions:

B_0 , the magnetic flux density, 0.01 Wb/m^2

E_z , the electric field, 0.1 V/m

μ , the viscosity of mercury, 1.55 N s/m^2

σ_e , the electric conductivity of mercury, $1.07 \times 10^6 \text{ (ohm m)}^{-1}$

SOLUTION First of all, let us calculate the Hartmann number. Using the definition given in Eq. (5.2.13) we have

$$\begin{aligned} N_{\text{Ha}} &= y_0 B_0 \frac{\sqrt{\sigma_e}}{\mu} \\ &= 0.05 \times 0.01 \times \frac{\sqrt{1.07 \times 10^6}}{1.55} = 0.415 \end{aligned}$$

Let us refer to Eq. (5.3.12). On noting that $u_x = u_{x,\max}$ at $y = 0$, for $\partial P / \partial x = 0$, we have

$$u_{x,\max} = \frac{y_0}{N_{\text{Ha}}} \frac{\sqrt{\sigma_e}}{\mu} E_z \left(\frac{1}{\cosh N_{\text{Ha}}} - 1 \right)$$

i.e.,

$$u_{x,\max} = \frac{0.05}{0.415} \times 830 \times (-0.1) \left(\frac{1}{1.08} - 1 \right) \sim 0.79 \text{ m/s}$$

The Reynolds number for this case is approximately

$$N_{\text{Re}} = \frac{0.79 \times 0.1 \times 1.36 \times 10^4}{1.55} \sim 690$$

so that the flow is laminar. Thus the use of the molecular viscosity is justified. We note that because of the strong electromagnetic force field imposed on the system, which penetrates throughout the domain, the flow would have been laminar even at much higher Reynolds numbers, because a strong electromagnetic force field tends to damp out turbulence, as discussed in Romig *et al.*⁵

It has to be stressed to the reader that the problem discussed here is one of the simplest ones in the field of electromagnetodynamics. A much fuller discussion of the Hartmann problem and its variations is available in the text by Hughes and Young.³

5.3.2 The Velocity Fields in Melts with a Traveling Electromagnetic Force Field

In many instances in metals processing operations, when the stirring of the melt is the prime objective, a traveling electromagnetic field is employed in induction furnaces (stirrers), through the use of a polyphase coil connection. Such an arrangement is used in the ASEA-SKF furnace, in induction coils, employed for induction stirring of continuous casting systems. A good discussion of the ASEA-SKF system is available in the article by Sundberg,¹³ while an interesting application of electromagnetic stirring has been discussed by Iwata *et al.*¹⁴

In the following we shall present a discussion of how these problems may be formulated, together with a selection of some computed results and actual measurements—for the sake of comparison. The treatment will emphasize the important conceptual steps; thus, not all the mathematical details will be given—however, these may be found in the appropriate references.

CALCULATION OF THE ELECTROMAGNETIC FORCE FIELD

The starting point in the calculation of the electromagnetic force field is given by the Maxwell equations, which were previously defined in Eqs. (5.2.1)–(5.2.4), together with Ohm's law (5.2.5a) and the definition of the Lorentz force (5.2.6).

As a practical matter, it is convenient to work in terms of the vector potential \mathbf{A} , which is defined as

$$\mathbf{B} = \nabla \times \mathbf{A} \quad (5.3.17)$$

and

$$\mathbf{E} = -\partial \mathbf{A} / \partial t \quad (5.3.18)$$

with

$$\nabla \cdot \mathbf{A} = 0 \quad (5.3.19)$$

It may be shown, moreover, that upon combining the above definition with the Maxwell equations, we obtain:

$$\nabla^2 \mathbf{A} = \mu_m \sigma_e \partial \mathbf{A} / \partial t \quad (5.3.20)$$

which is of the same form as the diffusion equation. For cylindrical symmetry, which is appropriate to most furnace applications and also to the induction stirring of cylindrical billets, Eq. (5.3.20) may be written as

$$\frac{1}{r} \frac{\partial}{\partial r} \left(r \frac{\partial A_\theta}{\partial r} \right) + \frac{\partial^2 A_\theta}{\partial z^2} - \frac{A_\theta}{r^2} = \mu_m \sigma \frac{\partial A_\theta}{\partial t} \quad (5.3.21)$$

with $A_z = A_r = 0$.

Upon using Eq. (5.3.17) we have

$$B_z = \left(\frac{1}{r} \right) \frac{\partial (r A_\theta)}{\partial r} \quad (5.3.22)$$

and

$$B_r = -\frac{\partial A_\theta}{\partial t} \quad (5.3.23)$$

Moreover, upon using Ohm's law (5.2.5a) together with (5.3.18), we obtain

$$J_\theta = -\sigma \frac{\partial A_\theta}{\partial t} \quad (5.3.24)$$

The two components of the body force field [i.e., the nonzero terms of the $(\mathbf{J} \times \mathbf{B})$ product] are then

$$F_z = -J_\theta B_r \quad (5.3.25)$$

and

$$F_r = J_\theta B_z \quad (5.3.26)$$

FLUID FLOW EQUATIONS

For cylindrical symmetry the equations of motion are written as

$$\begin{aligned} \rho \left(u_r \frac{\partial u_r}{\partial r} + u_z \frac{\partial u_r}{\partial z} \right) &= -\frac{\partial P}{\partial r} + \left[\frac{\partial}{\partial r} \left(\frac{\mu_e}{r} \frac{\partial}{\partial r} (ru_r) \right) \right. \\ &\quad \left. + \frac{\partial}{\partial z} \left(\mu_e \frac{\partial u_r}{\partial z} \right) \right] + J_\theta B_z \quad (r \text{ component}) \end{aligned} \quad (5.3.27)$$

$$\begin{aligned} \rho \left[u_r \frac{\partial u_z}{\partial r} + u_z \frac{\partial u_z}{\partial z} \right] &= \frac{\partial P}{\partial z} + \left[\frac{1}{r} \frac{\partial}{\partial r} \left(\mu_e r \frac{\partial u_z}{\partial r} \right) \right. \\ &\quad \left. + \frac{\partial}{\partial z} \left(\mu_e \frac{\partial u_z}{\partial z} \right) \right] - J_\theta B_r \quad (z \text{ component}) \end{aligned} \quad (5.3.28)$$

Upon introducing the vorticity ξ and the stream function ψ ,

$$\xi = \frac{\partial u_r}{\partial z} - \frac{\partial u_z}{\partial r} \quad (5.3.29)$$

and

$$u_r = \frac{1}{r} \frac{\partial \psi}{\partial z} \quad (5.3.30)$$

$$u_z = -\frac{1}{r} \frac{\partial \psi}{\partial r} \quad (5.3.31)$$

The equation of motion is written as

$$\begin{aligned} \frac{\partial}{\partial z} \left(\frac{\xi}{r} \frac{\partial \psi}{\partial r} \right) - \frac{\partial}{\partial r} \left(\frac{\xi}{r} \frac{\partial \psi}{\partial z} \right) \\ + \frac{1}{\rho} \left[\frac{\partial}{\partial r} \left(\frac{\mu_e}{r} \frac{\partial}{\partial r} (r\xi) \right) + \frac{\partial}{\partial z} \left(\frac{\mu_e}{r} \frac{\partial}{\partial z} (r\xi) \right) \right] \\ + \frac{1}{\rho} \left[\frac{\partial}{\partial z} (J_\theta B_z) + \frac{\partial}{\partial r} (J_\theta B_r) \right] = 0 \end{aligned} \quad (5.3.32)$$

where $\mu_e = \mu + \mu_t$ is the effective viscosity. As discussed in Szekely *et al.*^{7-9,11,12,15} calculation proceeds first by evaluating the spatially dependent F_z and F_r ; these values are then substituted into the equation of motion, namely (5.3.32), which is then solved in conjunction with the subsidiary equations for the turbulent viscosity.

We note here that the calculation of the electromagnetic force field is particularly straightforward, if \mathbf{H} or \mathbf{B} may be specified at the melt boundary. Otherwise this boundary condition has to be deduced from the coil current distribution.

For a *traveling wave*, produced by a polyphase connection, the coil current may be represented by the following expression:

$$J_\theta = J_0 e^{j(\omega t - kz)} \quad (5.3.33)$$

where J_0 is the absolute value of the coil current; j is $\sqrt{-1}$; ω the angular frequency, $2\pi f$ rad/s; f the frequency, in hertz; k the wave number, $1/\lambda$; λ the wavelength; z the axial coordinate; and t is the time.

MELT VELOCITIES IN AN ASEA-SKF FURNACE

ASEA-SKF furnaces are often used in ladle refining processes, for deoxidation and for the final adjustment of the bath composition in specialty steel manufacture. In order to promote agitation a traveling wave is being used and low-frequency coil current is being employed. Figure 5.3.4 shows a sketch of an ASEA-SKF system and Table 5.3.1 lists typical operating parameters for a 50-ton furnace used by the Kawasaki Steel Corporation.

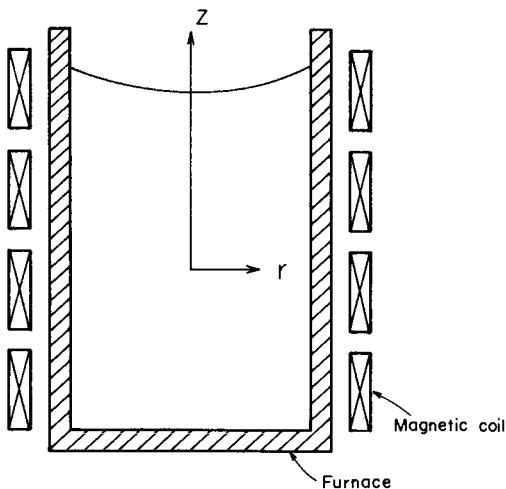


FIG. 5.3.4 Sketch of an ASEA-SKF system.

TABLE 5.3.1
Numerical Values of Parameters Used in the Computation

ρ	Density of the melt	7.2 g cm ⁻³
μ	Viscosity of the melt	6 cp
Z	Bath depth	1.70 m
A	Bath radius	1.13 m
$1/\sigma_e$	Specific resistivity	1.4×10^{-6} ohm m
μ_m	Magnetic permeability	1.26×10^{-6} henry/m
ϵ	Permittivity	8.85×10^{-2} F/m
f	Frequency	1.4 Hz
H_{zo}	Maximum strength of the magnetic field measured in the z direction at the inner wall	470 g or 3.69×10^4 AT/m

The computed axial body force component is plotted as a function of the distance from the wall in Fig. 5.3.5 and it is seen that the field penetrates the melt to quite an appreciable distance. The computed map of the velocity field is shown in Fig. 5.3.6, where it is seen that velocities up to 0.5–0.6 m/s are being predicted. The map of the computed turbulent energy profiles is

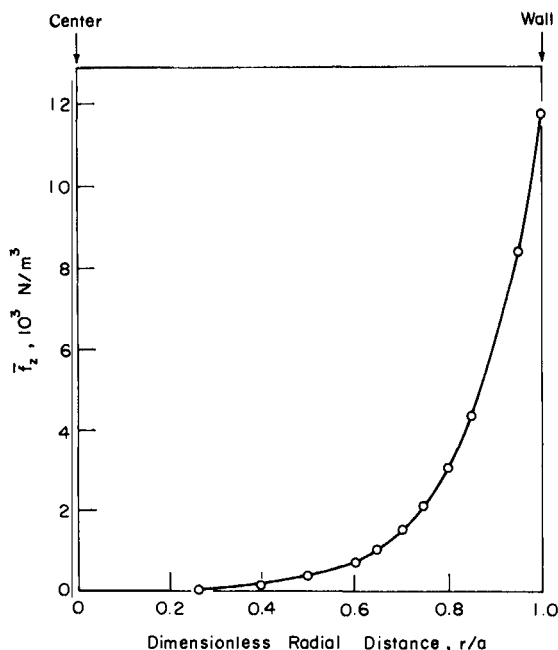


FIG. 5.3.5 The computed axial body force component in an ASEA-SKF furance.¹⁵

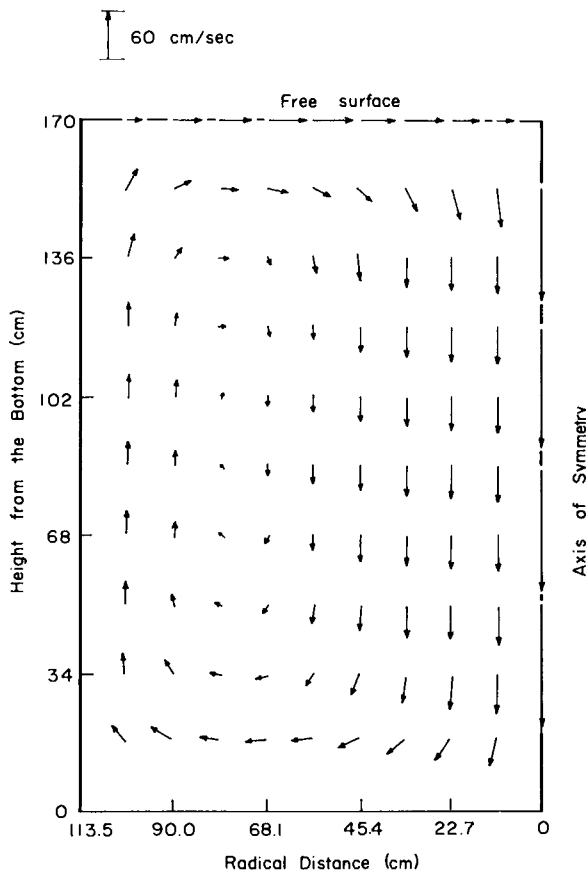


FIG. 5.3.6 The computed velocity field in an ASEA-SKF furnace.¹⁵

given in Fig. 5.3.7, which indicates that the flow is highly turbulent in the central core of the vessel. Unfortunately, no direct measurements of the velocity fields or turbulent kinetic energy profiles are available on this system, in order to provide a test of these predictions. However, tracer dispersion measurements have been reported on this system¹⁶ and the knowledge of the flow field and of the map of the turbulent viscosities allows predictions to be made of this tracer dispersion. Figure 5.3.8 shows a plot of both the experimentally measured tracer content of samples taken from the bath, as a function of time, together with the theoretical predictions for the tracer dispersion. It is seen that while the individual data points cannot be represented by the model, the actual time required for the homogenization of the bath is quantitatively predicted.

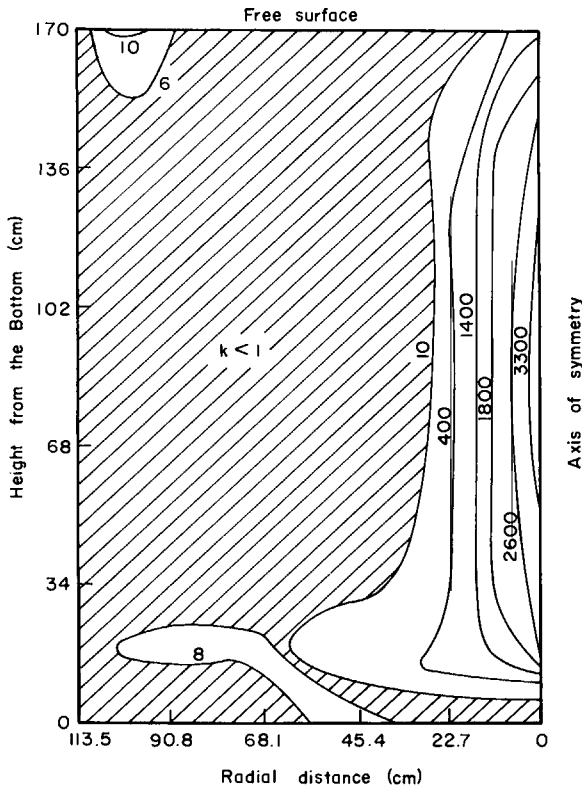


FIG. 5.3.7 The computed distribution of the turbulent kinetic energy [in $(\text{cm}/\text{s})^2$] in an ASEA-SKF furnace.¹⁵

Upon illustrating these principles, using another example,¹⁷ Fig. 5.3.9 shows a sketch of an inductively stirred low melting alloy system where experimental measurements were made of both the electromagnetic force field produced and of the velocity profiles within the melt.

The property values of the system are summarized in Table 5.3.2. Figures 5.3.10a and b show the computed and the experimentally measured maps of the velocity vector, respectively. The excellent agreement between measurements and predictions is readily apparent.

5.3.3 Velocity Fields in Metals with a Stationary Electromagnetic Field

In the majority of induction furnaces, where heating is the prime objective, single-phase coil arrangement is used, which then results in a stationary field.

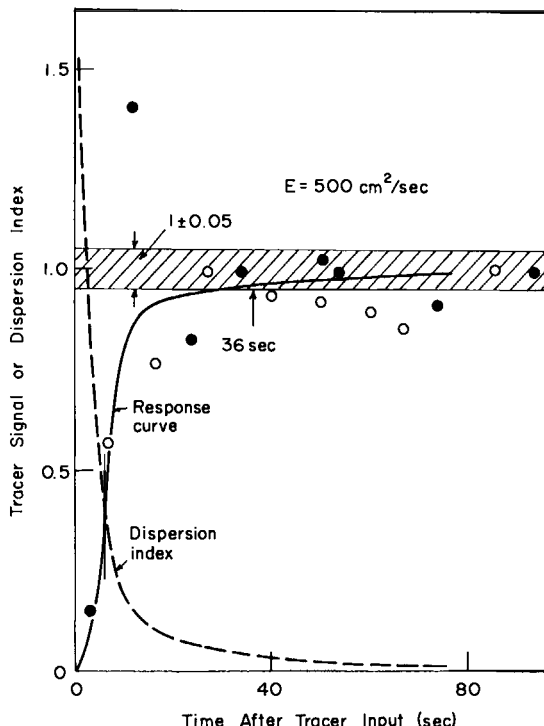


FIG. 5.3.8 Comparison of the experimentally measured and computed tracer dispersion in an ASEA-SKF furnace.¹⁵ ● Observed (LN-1). ○ Observed (SN-1).

The coil current for such systems, using uniformly spaced coils, may be approximated by

$$J_\theta = J_0 e^{j\omega t} \sin kz \quad (5.3.34)$$

When the coils are not uniformly spaced, either a Fourier series expansion has to be used, as discussed by Lavers and Biringer,¹⁸ or, alternatively, numerical techniques have to be employed, as suggested by Evans.^{6,11}

Figures 5.3.11a and b show experimentally measured and theoretically predicted profiles of the surface velocity in an induction-stirred unit, some 0.29 m in diameter, containing a mercury pool 0.20 m high, as reported by Evans and Tarapore.⁶ The reasonably good, at least semiquantitative, agreement between experimental measurements and theoretical predictions is again apparent.

Figure 5.3.12 shows both experimentally measured maximum melt velocities in induction-stirred aluminum melts, as reported by Dragunkina and Tir,¹⁰ and predictions of these velocities, for corresponding conditions, proposed by Szekely and Chang.^{8,9}

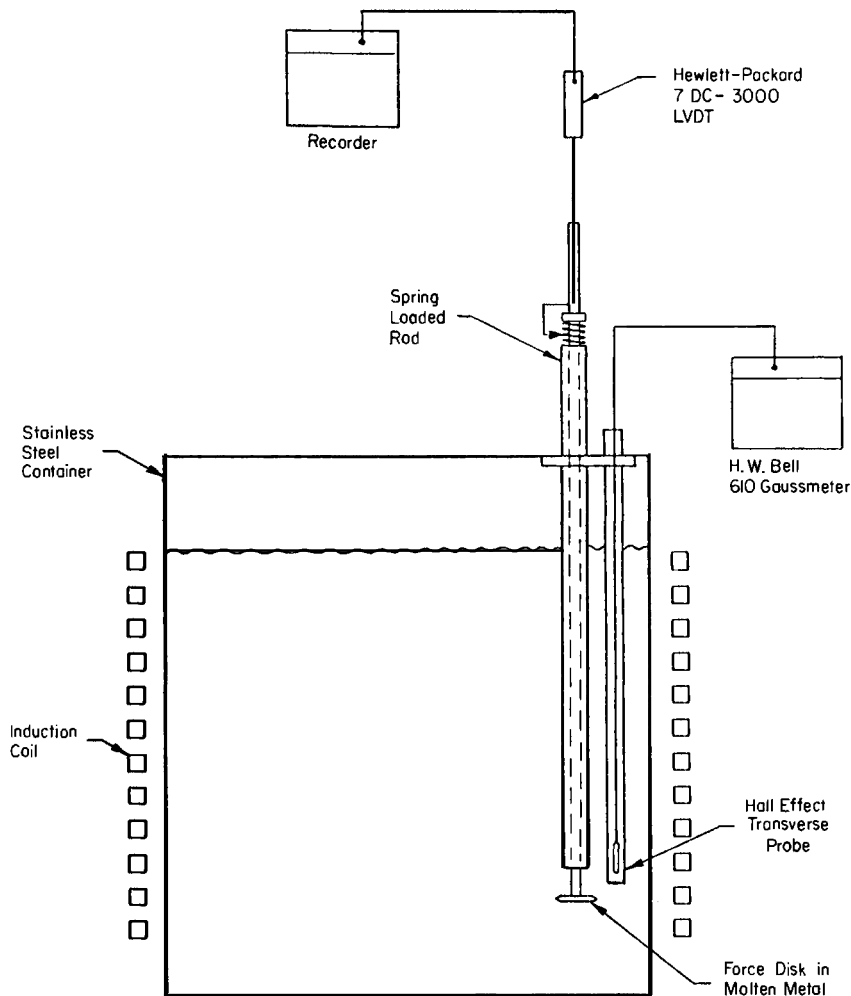


FIG. 5.3.9 Sketch of the experimental arrangements for measuring the velocity distribution in an induction-stirred low alloy system.¹⁷

TABLE 5.3.2

Principal Property Values Used in the
Computation of Figs. 5.3.10a

Metal density	10.7 g/cm ³
Metal viscosity	1.7 cp
Electrical conductivity	9.00×10^5 ohm ⁻¹ m ⁻¹
Magnetic permeability	1.26×10^{-6} henry/m
Magnetic flux intensity	0.024 Wb/m ²
Vessel height	50 cm
Vessel diameter	25.4 cm

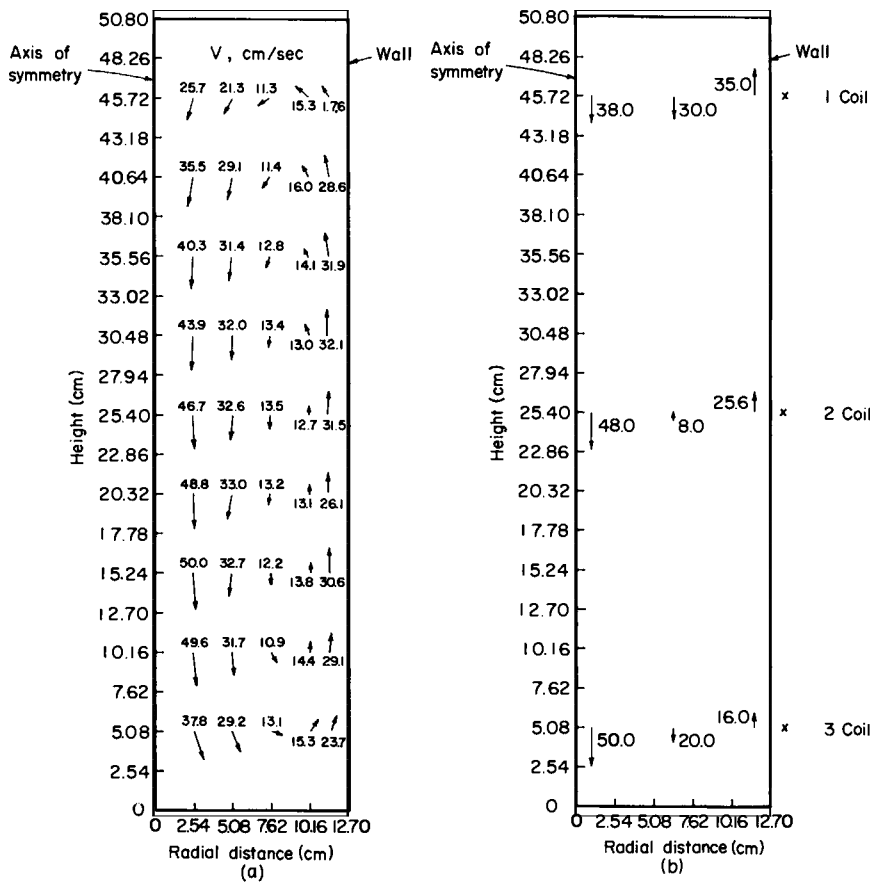


FIG. 5.3.10 A comparison of the experimentally measured and the theoretically predicted velocity fields in an inductively stirred low alloy system¹⁷: (a) predictions, (b) measurements.

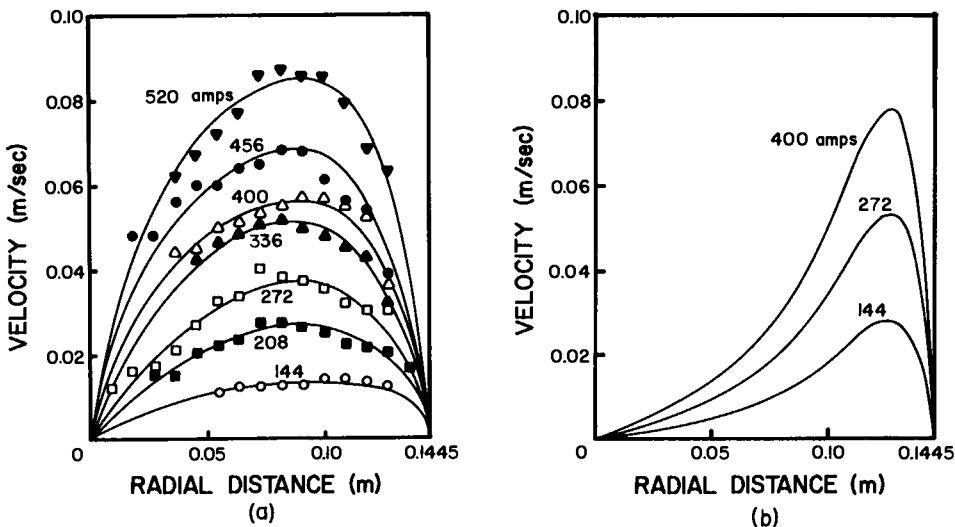


FIG. 5.3.11 Comparison of the experimentally measured and the theoretically predicted velocity profiles on the surface of an inductively stirred mercury bath⁶: (a) measurements, (b) predictions. Original figures kindly supplied by Prof. J. W. Evans.

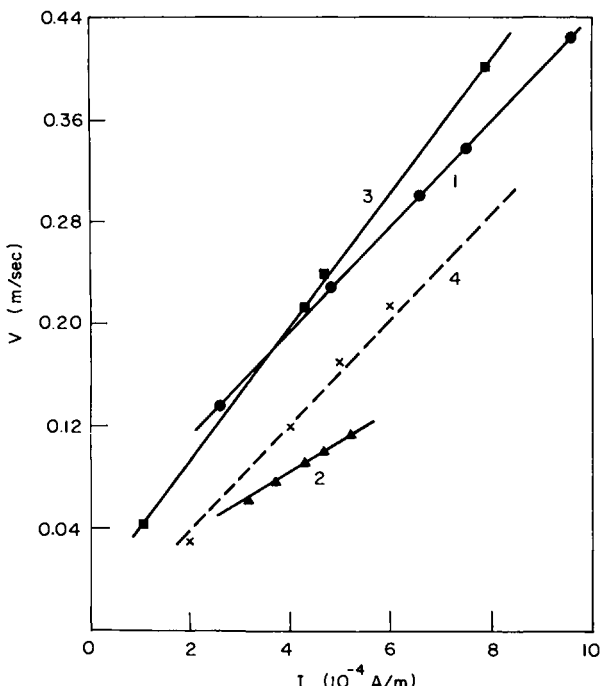


FIG. 5.3.12 The effect of the current on the maximum velocities in an induction-stirred furnace, holding molten aluminum¹⁰: 1, $f = 50 \text{ Hz}$ with cover; 2, $f = 2500 \text{ Hz}$ with cover; 3, $f = 50 \text{ Hz}$ without cover; 4, $f = 1060 \text{ Hz}$ without cover.

It is seen that both measurements and predictions indicate that, in accordance with Eq. (5.2.19), there appears to be a linear relationship between the maximum velocity and the coil current. Furthermore, the predicted velocities, for 1060 Hz (shown by the broken line), appear to fall between those measured for 2500 Hz and 60 Hz, depicted by the solid lines connecting the solid squares (circles) and solid triangles, respectively.

Therefore, the melt velocities and tracer dispersion rates predicted through the solution of Maxwell's equations and the turbulent Navier-Stokes equations appear to be in reasonable, if not entirely quantitative, agreement with actual measurements, over a broad range of conditions, and for a variety of metals systems.

5.4 Concluding Remarks

In this chapter we introduced the reader to electromagnetically driven flows. The subject matter covered is perhaps the most complex in the entire

text; nonetheless, it was thought worthwhile to discuss these problems because of both their importance in metals processing and the very rapid advances that are being made in the understanding of these phenomena.

From a purely fluid flow viewpoint, electromagnetically driven flows may be regarded as differing from the other flow problems only because of the presence of the additional body force, the Lorentz force. However, the calculation of this Lorentz force is a crucial part of tackling any MHD flow problem.

The interested reader is urged to follow through the references listed for additional reading at the end of this chapter.

In conclusion one should state that the principles of electromagnetically driven flows, as applied to metals processing, are now reasonably well understood and the predictions based on the theory have been verified, at least semiquantitatively, for a number of practical cases.

A great deal of work has yet to be done, however, on the application of these principles to problems in scrap melting in induction furnaces, flows in aluminum smelting, electromagnetically driven flows in electroslag remelting, and in arc furnace practice. The interested reader may find these topics very fertile areas for further research.

References

1. J. D. Krauss and K. D. Carrer, "Electromagnetics," 2nd ed. McGraw-Hill, New York, 1966.
2. W. K. H. Panofsky and M. Phillips, "Classical Electricity and Magnetism." Addison Wesley, Reading, Massachusetts, 1955.
3. W. F. Hughes and F. J. Young. "The Electromagnetodynamics of Fluids." Wiley, New York, 1966.
4. J. D. Jackson, "Classical Electrodynamics." Wiley, New York, 1962.
5. M. Romig, J. Hartnett and T. F. Irvine, eds. *Adv. Heat Transfer* 1, 268 (1964).
6. J. W. Evans and A. Tarapore, *Metall. Trans.* **7B**, 343 (1976).
7. J. Szekely and C. W. Chang, *I&SM* 4, 190 (1977).
8. J. Szekely and C. W. Chang, *I&SM* 4, 196 (1977).
9. J. Szekely and C. W. Chang, *J. Met.* **28**, 6 (1976).
10. N. I. Dragunkina and L. L. Tir, *Magn. Gidrodin.* **2**, 137 (1966).
11. J. W. Evans and A. Tarapore *Metall. Trans.* **8B**, Part II (1977).
12. J. Szekely and C. W. Chang, "Electromagnetically Drive Flows." Wiley, New York, to be published.
13. Y. Sundberg, *ASEA J.* **44**, No. 4, 71 (1971)
14. H. Iwata, K. Yamada, T. Fujita, and K. Nayashi, *Trans. Iron Steel Inst. Jpn.* **16**, 374 (1976).
15. J. Szekely and K. Nakanishi, *Metall. Trans.* **6B**, 245 (1975).
16. K. Nakanishi, J. Szekely, T. Fujii, Y. Mihara, and S. Iwaoka, *Metall. Trans.* **6B**, 111 (1975).
17. J. Szekely, C. W. Chang, and R. E. Ryan, *Metall. Trans.* **8B**, 333 (1977).
18. J. D. Lavers and P. P. Biringer, *Elektrowaerme Int.* **29**, 232 (1971).

Recommended Reading

Electrodynamics

- J. D. Krauss and K. D. Carrer, "Electromagnetics." 2nd ed. McGraw-Hill, New York, 1966.
W. K. H. Panofsky and M. Phillips, "Classical Electricity and Magnetism." Addison Wesley, Reading, Massachusetts, 1955.
W. F. Hughes and F. J. Young, "The Electromagnetodynamics of Fluids." Wiley, New York, 1966.

Electro-Slag Refining

- Proceedings of the 5th International Conference on Vacuum Metallurgy and Electro-Slag Refining (J. G. Kruger, E. Plockinger, O. Winkler, and H. Winterhager, eds.), Munich, Germany, 1976.
B. E. Paton, ed., "Electro-Slag Furnaces." Kiev, 1976 (in Russian).
A. H. Dilawari and J. Szekely, *Met. Trans.* **8B**, 123 (1977); also *ibid.* **9B**, 77 (1978).
M. Choudhary and J. Szekely, Proceedings of the 1979 Vacuum Metallurgy Conference, The American Vacuum Society, New York.

6.1 Introduction

In Chapters 2–5 we examined a broad range of flow problems and discussed that the *driving forces* responsible for these flows could be divided into *body forces* and *surface forces*. Typical examples of body force driven flows included falling films, discussed in Chapter 3, and the emptying of ladles, described in Chapter 2; in both these cases the body force was provided by gravity. Chapter 5 was devoted to the discussion of the rather special case of body force driven flows, electromagnetodynamics.

Typical examples of flow resulting from forces acting on the surface of a control volume, or a macroscopic element, include flow through pipes, or packed beds, or boundary layer type flows, also discussed in Chapters 2–4.

A common feature of all these flow situations was the fact that the force field generating the flow could be defined essentially independently of the flow system, or rather the expressions for the body force field or for the pressure fields acting on the boundaries of a fluid body could be uncoupled from the fluid flow equations themselves. In a mathematical sense the gravitational force field acting on a falling film could be uniquely defined without the solution of the Navier–Stokes equations; in the same way, upon using the MHD approximation, for liquid metals, the electromagnetic body force field was defined, such that it was uncoupled from the Navier–Stokes equations. This uncoupling of the driving force from the fluid flow equations afforded useful simplification.

In this chapter we shall discuss two groups of problems: namely, natural convection driven flows and surface tension driven flows, both of which are of considerable practical importance in metals processing operations.

In natural convection the driving force is provided by a body force due to density differences in the fluid, caused either by temperature or by concentration gradients within the system. Natural convection occurs frequently in metals processing operations because of the large differences between the temperature of molten metals and that of the environment.

Surface tension driven flows are caused by gradients in surface tension at gas–melt or slag–metal interfaces. The principal reason for such gradients in surface tension is that the interfacial tension is in general composition dependent, so that in many mass transfer processes the presence of lateral concentration gradients will produce gradients in surface tension and hence surface tension driven flows. These problems are of particular interest in slag corrosion and in the kinetics of slag metal reactions.

A common feature of both natural convection and of surface tension driven flows is the fact that the flow is a direct consequence of a chemical or physical process occurring in the fluid, such as convective heat or mass transfer. It follows that the definition of these fluid flow problems has to be undertaken in conjunction with the study of these other transfer processes. In other words, *the driving force for the flow is inherently coupled both with the flow itself and with these other transport processes*. This “two-way” coupling of transport processes renders the study of these flow phenomena rather more complex.

Regarding the organization of this chapter, a brief introduction to convective heat and mass transfer will be given in Section 6.2, and both laminar and turbulent natural convection will be discussed in Section 6.3. The definition of surface tension will be presented in Section 6.4 together with some typical property values of relevance to molten metal and slag systems. Finally, some examples of surface tension driven flows in metals processing will be given in Section 6.5.

6.2 Convective Heat and Mass Transfer

In this section we shall introduce the reader to the elements of convective heat and mass transfer; since our main motivation is to provide some background for the treatment of natural convection problems, the treatment will be necessarily very brief. Comprehensive treatments of convective heat and mass transfer are available in numerous texts.^{1–5}

6.2.1 *The Definition of Thermal Conductivity*

The reader will recall that in Chapter 1 we stated the Newtonian definition of viscosity as the constant of proportionality between the components of the stress tensor and the velocity gradient. Fourier’s law of heat conduction

expresses a similar, if somewhat simpler, relationship between the heat flux and the temperature gradient. Thus we have

$$\begin{aligned} \mathbf{q} &= -k\mathbf{\nabla}T \\ \left[\begin{array}{c} \text{heat flux} \\ \text{vector} \end{array} \right] &= \left[\begin{array}{c} \text{thermal} \\ \text{conductivity} \end{array} \right] \left[\begin{array}{c} \text{temperature} \\ \text{gradient} \end{array} \right] \end{aligned} \quad (6.2.1)$$

so that the heat flux vector is proportional to the negative of the temperature gradient; that is, in qualitative terms, thermal energy flows from regions of high temperature to regions of low temperatures, and the constant of proportionality, k , is called the thermal conductivity of the medium.[†]

Written in terms of its components, Eq. (6.2.1) takes the following form:

$$q_x = -k \frac{\partial T}{\partial x}, \quad q_y = -k \frac{\partial T}{\partial y}, \quad q_z = -k \frac{\partial T}{\partial z} \quad (6.2.2)$$

The units in Eqs. (6.2.1) and (6.2.2) are as follows:

\mathbf{q} , the heat flux, is given in energy/(surface area) (time), i.e., in joules/m² s or watts/m² in the SI system. (Other units are still used: Btu/h ft², kcal/m² s, cal/cm² s, etc.)

T is given in °K (or in °C or °F).

$\mathbf{\nabla}$ is given in 1/m (or in 1/ft, 1/cm), and hence

k is given in watts/m °K (or in Btu/h ft °F, kcal/m °C, etc.).

Conversion factors between these units are available in Bird *et al.*¹

Table 6.2.1 shows a listing of the numerical values of the thermal conductivities of selected gases, molten metals, and slags.^{6,7} It is seen that the thermal conductivity of gases tends to be low, while the thermal conductivity of metals is quite high; molten slags occupy an intermediate position between these extremes.

The analogy between heat conduction and viscous transport may be emphasized by defining κ , the thermal diffusivity, in the following manner:

$$\kappa = k/c_p\rho \quad (6.2.3)$$

where c_p is the specific heat and ρ is the density. The dimension of κ is (length)²/time.

Thus we may write, e.g.,

$$\tau_{xy} = -v \frac{d(u_x \rho)}{dy} \quad (6.2.4)$$

[†] We note that a further assumption is inherent in the statement of Fourier's equation, as given by Eq. (6.2.1), in that the medium is assumed to be isotropic. This is a reasonable assumption for fluids, but need not hold for solid materials.

TABLE 6.2.1

The Thermal Conductivities of Selected Gases
and Molten Metals^{6,7}

Material	Temperature (°K)	Thermal conductivity (W/m °K = kg m/s³ °K)
Hydrogen	100	6.79×10^{-2}
	200	1.28×10^{-1}
	300	1.77×10^{-1}
Oxygen	100	9.02×10^{-3}
	200	1.83×10^{-2}
	300	2.65×10^{-3}
Aluminum	973	103.2
	1063	121.2
Lead	603	16.3
	973	15.0

for viscous transport and

$$q_y = -\kappa \frac{d}{dy} (c_p \rho T) \quad (6.2.5)$$

for the conductive transport of thermal energy. The ratio

$$\nu/\kappa = N_{Pr} \quad (6.2.6)$$

is called the Prandtl number, which has an important physical significance. It designates the following ratio: (ability of the fluid to transmit momentum)/(ability of the fluid to transmit thermal energy).

For gases the Prandtl number is approximately unity: ($N_{Pr} \approx 0.7$ for air at room temperature). For liquids, including molten slags, $N_{Pr} \gg 1$ for liquid metals $N_{Pr} < 1$ ($N_{Pr} \approx 0.2$ for molten steel and $N_{Pr} \approx 0.02$ for molten lead).

6.2.2 Formulation of Convective Heat Transfer Problems

In the formulation of convective heat transfer problems, we have to recognize that, in general, in a moving fluid, thermal energy is transported both by conduction and by the movement of the fluid itself.

Let us consider a rectangular volume element, through which a fluid is flowing. On the analogy of the differential momentum balance developed in Chapter 3, the conservation of thermal energy may now be expressed by the mathematical statement of the following:

$$\begin{aligned} & \left[\begin{array}{l} \text{net input of thermal} \\ \text{energy by conduction} \end{array} \right] + \left[\begin{array}{l} \text{net input of thermal energy} \\ \text{due to fluid motion} \end{array} \right] + \left[\begin{array}{l} \text{rate of heat} \\ \text{generation} \end{array} \right] \\ &= \left[\begin{array}{l} \text{rate of accumulation} \\ \text{of thermal energy} \end{array} \right] \end{aligned} \quad (6.2.7)$$

Thus we have

$$\begin{aligned}
 & \left[-k \frac{\partial T}{\partial x} \Big|_x + k \frac{\partial T}{\partial x} \Big|_{x+\Delta x} \right] \Delta y \Delta z + \left[-k \frac{\partial T}{\partial y} \Big|_y + k \frac{\partial T}{\partial y} \Big|_{y+\Delta y} \right] \Delta x \Delta z \\
 & + \left[-k \frac{\partial T}{\partial z} \Big|_z + k \frac{\partial T}{\partial z} \Big|_{z+\Delta z} \right] \Delta x \Delta y \\
 & + [u_x \rho c_p T \Big|_x - u_x \rho c_p T \Big|_{x+\Delta x}] \Delta y \Delta z \\
 & + [u_y \rho c_p T \Big|_y - u_y \rho c_p T \Big|_{y+\Delta y}] \Delta z \Delta x \\
 & + [u_z \rho c_p T \Big|_z - u_z \rho c_p T \Big|_{z+\Delta z}] \Delta x \Delta y \\
 & + \Delta x \Delta y \Delta z q''' \\
 & \quad \text{(rate of heat generation)} \\
 & = \left(\rho c_p \frac{\partial T}{\partial t} \right) \Delta x \Delta y \Delta z \\
 & \quad \text{(accumulation)}
 \end{aligned} \tag{6.2.8}$$

Upon dividing both sides by $\Delta x \Delta y \Delta z$ and on setting $\Delta x \rightarrow 0$, $\Delta y \rightarrow 0$, and $\Delta z \rightarrow 0$, for constant physical properties we have

$$\frac{\partial T}{\partial t} + u_x \frac{\partial T}{\partial x} + u_y \frac{\partial T}{\partial y} + u_z \frac{\partial T}{\partial z} = \frac{\dot{q}'''}{\rho c_p} + \kappa \left[\frac{\partial^2 T}{\partial x^2} + \frac{\partial^2 T}{\partial y^2} + \frac{\partial^2 T}{\partial z^2} \right] \tag{6.2.9}$$

which may be written as

$$\frac{DT}{Dt} = \kappa \nabla^2 T + \dot{q}'''/\rho c_p \tag{6.2.9a}$$

where

$$\frac{D}{Dt} (\) \equiv \frac{\partial}{\partial t} (\) + u_x \frac{\partial}{\partial x} (\) + u_y \frac{\partial}{\partial y} (\) + u_z \frac{\partial}{\partial z} (\) \tag{6.2.10}$$

is the substantial time derivative.

Equation (6.2.9) is the usual starting point in the statement of convective heat transfer problems. This equation may be appropriately simplified for one- or two-dimensional situations or for systems that exhibit cylindrical or spherical symmetry.^{1,4}

6.2.3 Definition of the Binary Diffusion Coefficient

As Newton's law of viscosity relates the velocity gradient to the local shear stress and Fourier's law relates the heat flux to the temperature gradient, Fick's law expresses a proportionality between the mass or the molar flux and the local concentration gradient for a binary system; thus we have

$$\mathbf{J}_A = -D_{AB} \nabla C_A \tag{6.2.11}$$

or

$$J_{Ay} = -D_{AB} \frac{\partial C_A}{\partial y} \quad (6.2.11a)$$

Here \mathbf{J}_A is the vector designating the molar flux of species A, relative to the molar average velocity of the binary mixture. C_A is the molar concentration of the diffusing species A and D_{AB} is the binary diffusion coefficient. The dimensions of the quantities appearing in Eq. (6.2.11) are as follows:

J_A	kg mole/m ² s
C_A	kg mole/m ³
D_{AB}	m ² /s

When the concentration of the diffusing species is small, Eq. (6.2.11) simplifies to

$$\mathbf{N}_A = -D_{AB} \nabla C_A \quad (6.2.12)$$

or

$$\mathbf{N}_{Ay} = -D_{AB} \frac{\partial C_A}{\partial y} \quad (6.2.12a)$$

where \mathbf{N}_A is the molar flux in fixed spatial coordinates. We note that both the components of the stress τ and that of the heat flux \mathbf{q} were defined within the framework of a spatially fixed coordinate system.[†]

It is seen that the dimension of the binary diffusion coefficient is (length)²/time, which is identical to that of the kinematic viscosity and the thermal diffusivity. Thus the analogy between the transfer of mass, energy, and momentum is readily apparent on comparing Eqs. (6.2.12a), (6.2.5), and (6.2.4):

$$N_{Ay} = -D_{AB} \frac{\partial C_A}{\partial y} \quad (6.2.12a)$$

$$q_y = -\kappa \frac{d(c_p \rho T)}{dy} \quad (6.2.5)$$

$$\tau_{xy} = -v \frac{d(u_x \rho)}{dy} \quad (6.2.4)$$

Some typical values of the binary diffusion coefficient are given in Table 6.2.2 for gases, and melts.^{4,8}

[†] The need for working with J_A , rather than N_A , in systems where the concentration of the diffusing species is not small is discussed in detail in Bird *et al.*¹ In brief, when the diffusing species is present at appreciable concentration levels, the diffusive movement of this species will result in *bulk flow*, the effect of which has to be taken into consideration; this is done by using the molar flux relative to the molar average velocity.

TABLE 6.2.2
Diffusivities of Some Gases and Melts^{4,10}

System	Temperature (°K)	$D_{A-B}(m^2/s)$
Gases		
H ₂ O in N ₂	298	0.26×10^{-4}
H ₂ O in O ₂	623	1.3×10^{-4}
CO ₂ in O ₂	773	0.9×10^{-4}
H ₂ in H ₂ O	773	5.15×10^{-4}
H ₂ in H ₂ O	1173	11.4×10^{-4}
Melts		
Cu in Cu ₂ S melt (19.8% S)	1433	7.49×10^{-9}
Cu in Cu ₂ S melt (19.8% S)	1529	10.10×10^{-9}
Fe in 2.5% C iron melt	1773	9.0×10^{-9}
C in 3.5% C iron melt	1823	6.0×10^{-9}
Cu in 39% CaO, 21% Al ₂ O ₃ ,	1673	0.067×10^{-9}
Si in 40% CaO, 20% Al ₂ O ₃ , 40% SiO ₂ slag	1703	0.01×10^{-9}
Fe in 43% CaO, 22% Al ₂ O ₃ , 35% SiO ₂ slag	1773	$0.21-0.50 \times 10^{-9}$
Fe in 61% FeO, 39% SiO ₂ slag	1548	9.6×10^{-9}

It is seen that the binary diffusion coefficient is some four orders of magnitude larger for gases than for molten metals, while the diffusivity in slags tends to be about one order of magnitude smaller than in molten metals.

On the analogy of the definition of the Prandtl number, the ratio

$$\nu/D_{A-B} = N_{Sc} \quad (6.2.13)$$

has an important physical significance. It is termed the Schmidt number and it represents the ratio: (ability of the fluid to transmit momentum)/(ability of the fluid to transmit matter by diffusion).

For gases the Schmidt number is close to unity (as in the Prandtl number). For melts, including liquid metals and slags, the Schmidt number is much larger than unity, usually of the order of 100–10,000. This indicates that in the liquid state viscous transfer proceeds more readily than diffusion.

6.3 Formulation of Convective Mass Transfer Problems

In formulating convective mass transfer problems allowance has to be made for the fact that material is transported due to both diffusion and bulk flow of the fluid. As in the statement of convection heat transfer let us consider a rectangular volume element, through which a fluid is flowing; then for a

binary mixture the conservation of the diffusing species A may be expressed as

$$\begin{aligned} & [\text{net input of A by diffusion}] + [\text{net input of A by bulk flow}] \\ & + \left[\begin{array}{l} \text{rate of generation of A} \\ \text{due to a chemical reaction} \end{array} \right] = [\text{accumulation of A}] \end{aligned} \quad (6.3.1)$$

If we consider that the diffusing species is present at a low concentration level so that the diffusive flux \mathbf{N}_A is given by Eq. (6.2.12), then, following procedures essentially identical to those described for convective heat transfer, we have

$$\begin{aligned} \frac{\partial C_A}{\partial t} + u_x \frac{\partial C_A}{\partial x} + u_y \frac{\partial C_A}{\partial y} + u_z \frac{\partial C_A}{\partial z} \\ = \dot{r}_A''' + D_{AB} \left[\frac{\partial^2 C_A}{\partial x^2} + \frac{\partial^2 C_A}{\partial y^2} + \frac{\partial^2 C_A}{\partial z^2} \right] \end{aligned} \quad (6.3.2)$$

which may be written as

$$\frac{DC_A}{Dt} = D_{AB} \nabla^2 C_A + \dot{r}_A''' \quad (6.3.2a)$$

which is closely analogous to the previously described Eqs. (6.2.9) and (6.2.9a) for convective heat transfer. Here \dot{r}_A''' is the rate at which species A is being generated due to chemical reaction.

It has to be stressed to the reader that in natural convection problems u_x , u_y , and u_z , the components of the velocity vector which appeared in the conservation equations (6.2.9) and (6.3.2), are not given a priori, but are the result of the temperature or concentration gradients within the system and have to be calculated in conjunction with the computation of these quantities.

Figures 6.3.1–6.3.3 show some typical examples of flows driven by natural convection. Figure 6.3.1 shows a sketch of the temperature and velocity profiles that one would expect to develop when a vertical surface at temperature T_w is in contact with an infinite fluid having a temperature T_∞ , such that $T_w > T_\infty$.

The temperature of the fluid in contact with the vertical surface is T_w , while the bulk temperature assigned to the fluid, T_∞ , is approached at some finite distance from the vertical wall. The heated fluid in the vicinity of the fluid expands and the resultant buoyancy force causes that portion of the fluid to rise. Since the velocity has to be zero at the wall and also in the bulk of the fluid, the resultant velocity profile must show a maximum at some intermediate distance from the solid surface, as sketched in Fig. 6.3.1. Also

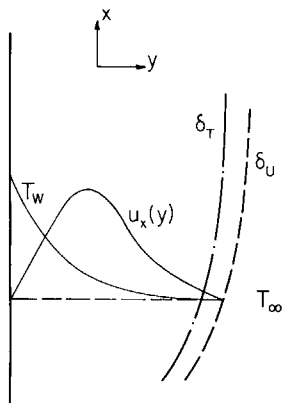


FIG. 6.3.1 Sketch of the temperature and the velocity profiles developed when a vertical plate at a temperature T_w is immersed into a fluid of infinite extent having a temperature T_2 .

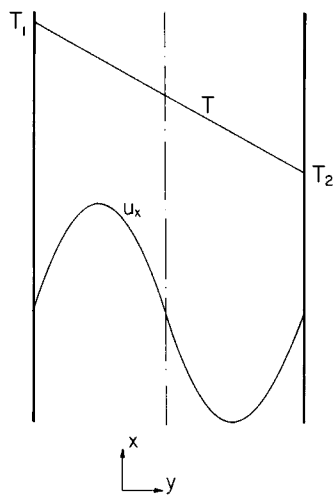


FIG. 6.3.2 Temperature and velocity profiles in a vertical slot, the walls of which are kept at different temperatures.

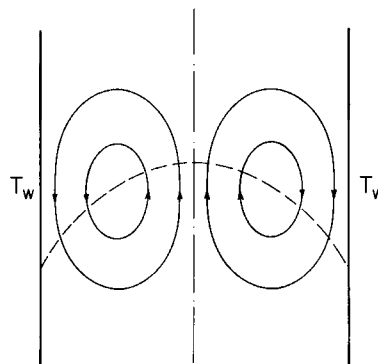


FIG. 6.3.3 Sketch of the streamline pattern and the temperature profile in a fluid in a rectangular container, at some intermediate time. Initially the fluid was at a temperature T_i , but the vertical walls are then kept at a temperature T_w such that $T_i > T_w$.

shown in this graph are the *velocity* and the *thermal* boundary layers. Velocity boundary layers have been discussed earlier in Chapters 3 and 4. Just as the velocity boundary layer denotes the portion of the fluid where the velocity differs from that in the bulk, the thermal boundary layer in this context denotes the portion of the fluid where the temperature differs from that in the bulk.

Figure 6.3.2 shows a sketch of the temperature and the velocity fields developed in a long, narrow vertical slot, the vertical walls of which are kept at different temperatures. As shown by Bird *et al.*¹ for a narrow slot and for moderate temperature differences the temperature profile is linear and the velocity field is symmetrical, corresponding to upward flow in the vicinity of the heated plate and downward flow in the neighborhood of the cold plate.

Finally, Fig. 6.3.3 depicts the behavior of an inherently transient system; a fluid initially of temperature T_i is kept in a rectangular container, the vertical walls of which from time zero are kept at a temperature T_w such that ($T_i > T_w$). As a result unsteady-state heat transfer takes place from the fluid to the vertical walls and the temperature profiles and streamline patterns corresponding to an intermediate time are shown in the graph. It is seen that two circulating loops are established and that flow is in a downward direction in the vicinity of the walls.

The situations seen in Figs. 6.3.1 and 6.3.3 are quite common in metals processing practice. Natural convection in the vicinity of vertical furnace walls would correspond to Fig. 6.3.1, while the transient natural convection in ladles and in molds is represented, if in a somewhat idealized manner, by Fig. 6.3.3.

Let us now proceed by discussing the quantitative formulation of natural convection problems, together with the presentation of some selected computed results.

6.3.1 Laminar Natural Convection

In the statement of laminar natural convection problems we have to express the equation of continuity, the equation of motion, and the conservation of thermal energy, or of the diffusing species (in case of mass transfer).

THE THERMAL BOUNDARY LAYER

In order to illustrate the procedure adopted for formulation, let us consider the system depicted in Fig. 6.3.1. As discussed in the analysis of boundary layer problems, for a two-dimensional system we have to consider two velocity components u_x and u_y .

Motion occurs predominately in the x direction so that only the x component of the equation of motion has to be considered.

Upon assuming, furthermore, steady-state conditions and that the physical properties are independent of temperature, except for the effect of the temperature dependence of the fluid density which is responsible for driving the flow,[†] we have the following:

$$\frac{\partial u_x}{\partial x} + \frac{\partial u_y}{\partial y} = 0 \quad (\text{equation of continuity}) \quad (6.3.3)$$

$$u_x \frac{\partial u_x}{\partial x} + u_y \frac{\partial u_x}{\partial y} = v \frac{\partial^2 u_x}{\partial y^2} - \frac{1}{\rho} \frac{\partial p}{\partial x} + g_x \quad (\text{equation of motion}) \quad (6.3.3a)$$

and

$$u_x \frac{\partial T}{\partial x} + u_y \frac{\partial T}{\partial y} = \kappa \frac{\partial^2 T}{\partial y^2} \quad (\text{thermal energy balance equation}) \quad (6.3.3b)$$

Equation (6.3.3a) is identical to Eq. (3.5.32) written for the laminar boundary layer in forced flow, except for the fact that the gravity term and the pressure gradient have been both retained. Equation (6.3.3b) is a somewhat simplified version of the convective heat transfer equation (6.2.9) made possible by the usual boundary layer approximation, by the two-dimensional nature of the problem, and by neglecting heat generation.

However, there is a major difference between Eq. (6.3.3a) and the equation of motion discussed in Chapter 3, predicated by the fact that the pressure gradient in the system is produced solely by the changes in density within the fluid. Thus we may write

$$\frac{\partial p}{\partial x} \approx \frac{dp}{dx} = \rho_m g_x \quad (6.3.4)$$

where ρ_m is the mean density of the fluid at a given position. Since this density ρ_m corresponds to some temperature T_m , we can expand ρ about its value ρ_m in Taylor series to obtain

$$\rho = \rho_m + \left(\frac{\partial \rho}{\partial T} \right)_{T_m} (T - T_m) + \dots \quad (6.3.5)$$

On neglecting the higher order terms and upon recalling that

$$-\frac{1}{\rho} \left(\frac{\partial \rho}{\partial T} \right)_\rho = \beta \quad (6.3.6)$$

[†] A good discussion of the appropriateness of this assumption has been presented by Gebhart.²

is the volumetric coefficient of thermal expansion, we may combine Eqs. (6.3.4)–(6.3.6) to obtain

$$-\frac{1}{\rho} \frac{\partial p}{\partial x} + g_x = -\frac{g_x(\rho_m - \rho)}{\rho} = g_x \beta(T - T_m) \quad (6.3.7)$$

Thus the equation of motion takes the following form:

$$u_x \frac{\partial u_x}{\partial x} + u_y \frac{\partial u_x}{\partial y} = v \frac{\partial^2 u_x}{\partial y^2} + \beta g_x(T - T_m) \quad (6.3.8)$$

Thus the statement of the problem is then given through Eqs. (6.3.3), (6.3.3b), and (6.3.8). The coupling between the equation of motion and the thermal energy balance equation is readily apparent.

The boundary conditions have to express the fact that the velocity is zero at the wall and at an infinite distance from the wall and that the temperature is specified both at the wall and in the bulk of the fluid (at an infinite distance from the wall). Thus we have

$$u_x = 0 \quad \text{at } y = 0 \quad (6.3.9)$$

$$u_y = 0 \quad \text{at } y = 0 \quad (6.3.10)$$

$$u_x = 0 \quad \text{at } y = \infty \quad (6.3.11)$$

$$T = T_w \quad \text{at } y = 0 \quad (6.3.12)$$

$$T = T_\infty \quad \text{at } y = \infty \quad (6.3.13)$$

The system of Eqs. (6.3.3), (6.3.3b), and (6.3.8) is readily solved for these boundary conditions through the use of a similarity transformation.⁹ Let us define

$$\theta = (T - T_\infty)/(T_w - T_\infty) \quad (6.3.14)$$

and seek the solution of the equation of motion (6.3.3b) in the following form:

$$\psi = 4vCx^{3/4}\xi(\eta) \quad (6.3.15)$$

where ψ is the stream function

$$\left(u_x = \frac{\partial \psi}{\partial y}, u_y = -\frac{\partial \psi}{\partial x} \right), \quad \eta = Cy/x^{1/4} \quad (6.3.16)$$

$$C = [g_x \beta(T_w - T_\infty)/(4v^2)]^{1/4} \quad (6.3.17)$$

and $\xi(\eta)$ is an as yet unknown function.

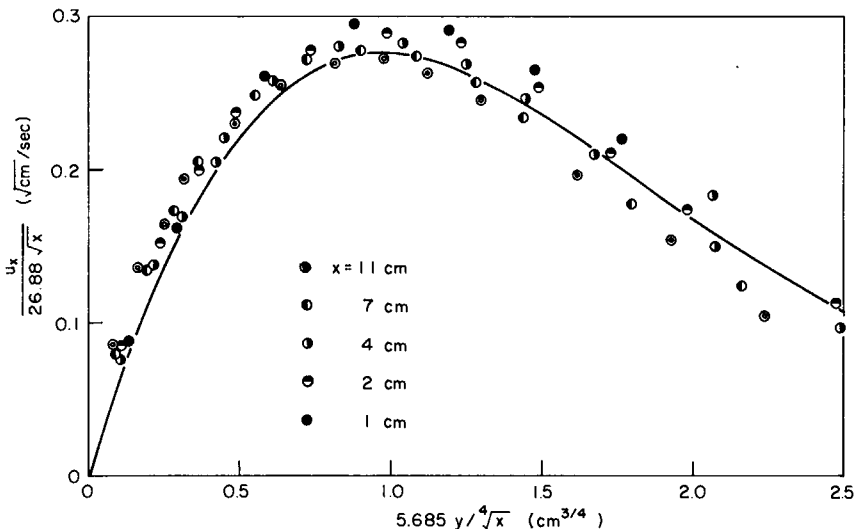


FIG. 6.3.4 A comparison between the measured and the calculated velocity profiles for natural convection of air in the vicinity of a vertical plate, on a dimensional plot. The discrete points represent the measurements, while the continuous line is the computed curve.¹¹

Through the use of the reduced variables the equation of motion (6.3.8) and the thermal energy balance equation (6.3.3b) may be expressed in the following form:

$$\xi''' + 3\xi\xi'' - 2(\xi')^2 + \theta = 0 \quad (6.3.18)$$

and

$$\theta'' + 3N_{Pr}\xi\theta' = 0 \quad (6.3.19)$$

where

$$\theta' = \frac{d\theta}{d\eta}, \quad \theta'' = \frac{d^2\theta}{d\eta^2}, \quad \xi''' = \frac{d^3\xi}{d\eta^3}$$

etc.

It is thus seen that the two partial differential equations were reduced to ordinary differential equations, by means of the coordinate transformation. We note, furthermore, that since we are working in terms of the stream function, the equation of continuity is automatically satisfied.

The boundary conditions for Eqs. (6.3.21)–(6.3.22) are also readily transcribed, but these details are not reproduced here.[†] Equations (6.3.21) and (6.3.22) are readily solved numerically. Figure 6.3.4 shows a comparison

[†] A good discussion of the mathematical details of the above coordinate transformation is available in the texts by Gebhard² or Eckert and Drake.³

between actual experimental measurements reported by Schmidt and Beckmann¹⁰ and predictions based on the numerical solution described by Pohlhausen.¹¹ The good agreement between measurements and predictions is readily apparent.

A more comprehensive dimensionless plot of the computed velocity fields and the dimensionless temperature fields is given in Figs. 6.3.5 and 6.3.6, respectively.¹² The Prandtl number is a parameter on both these plots and the quantity appearing on the horizontal axis is

$$N_{Gr} = g_x x^3 \beta (T_w - T_\infty) / v^2 \quad (6.3.20)$$

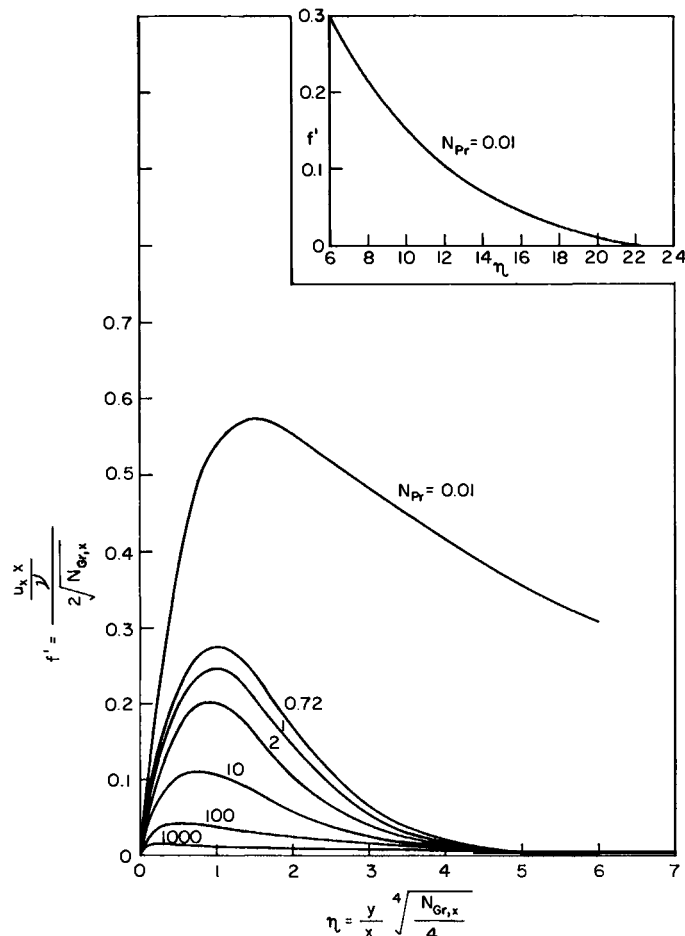


FIG. 6.3.5 Plot of the dimensionless velocity profile for natural convection about a vertical plate, after Ostrach.¹²

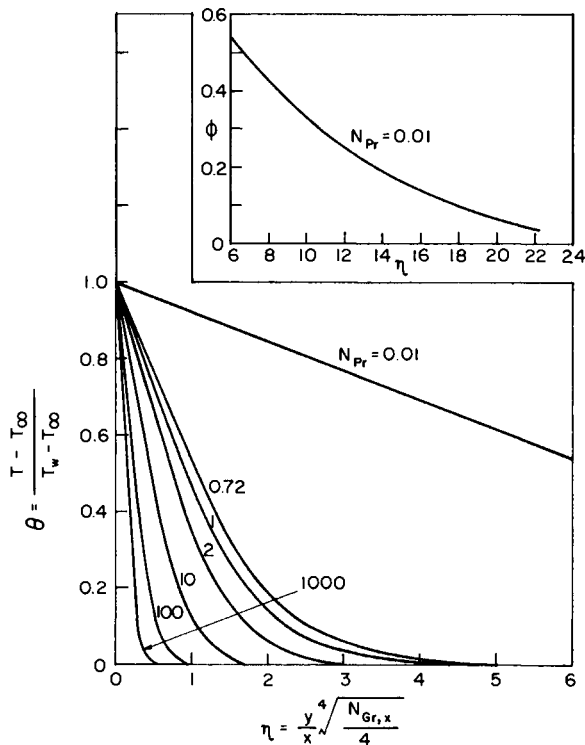


FIG. 6.3.6 Plot of the dimensionless temperature profile for natural convection about a vertical plate, after Ostrach.¹²

the Grashof number. The Grashof number is an important dimensionless group, which is formed when the differential equation describing the equation of motion in natural convection is made dimensionless. Its physical significance is the ratio: (buoyancy force)(inertial force)/(viscous force)². Inspection of Figs. 6.3.5 and 6.3.6 shows that we may define a boundary layer thickness in terms of

$$y = \delta \quad (6.3.21)$$

or

$$y = \delta_T \quad (6.3.22)$$

corresponding to the value of η at which the dimensionless velocity or the dimensionless temperature approaches zero.

It is seen from the form of the coordinate transformation or from the definition of η that $\delta \propto x^{1/4}$ or $\delta_T \propto x^{1/4}$, i.e., in thermal natural convection the

thickness of the velocity or thermal boundary layers depends rather less strongly on the distance from the “leading edge” than is the case for forced convection (in forced convection δ or $\delta_T \alpha x^{1/2}$). It is seen, moreover, on comparing Figs. 6.3.5 and 6.3.6 that when the Prandtl number is in the region of unity, the thermal and the velocity boundary layers coincide. When $N_{Pr} \gg 1$, as is the case for slags, $\delta > \delta_T$; in contrast, when $N_{Pr} \ll 1$, as is the case for liquid metals, $\delta_T > \delta$. This point is illustrated by the following example.

Example 6.3.1 A large vertical surface is in contact with a melt of infinite extent under steady-state conditions. If the plate is 100°C cooler than the bulk temperature of the melt, estimate the thickness of the laminar thermal and velocity boundary layers 0.1 m from the leading edge, and the maximum fluid velocity at that location for the following conditions:

- (a) The fluid is molten steel, with the following property values:

$$\begin{aligned}\beta &= 10^{-3} \text{ }^{\circ}\text{K}^{-1} & \mu &= 6.7 \times 10^{-2} \text{ kg/m, s} \\ k &= 20.9 \text{ W/m }^{\circ}\text{K} & C_p &= 0.71 \text{ kJ/kg }^{\circ}\text{K} \\ \rho &= 7.1 \times 10^3 \text{ kg/m}^3\end{aligned}$$

- (b) The fluid is molten slag, with the following property values:

$$\begin{aligned}\beta &= 2.7 \times 10^{-4} \text{ }^{\circ}\text{K}^{-1} & C_p &= 1.25 \text{ kJ/kg }^{\circ}\text{K} \\ k &= 2.09 \text{ W/m }^{\circ}\text{K} & \mu &= 5.0 \text{ kg/m s} \\ \rho &= 3.0 \times 10^3 \text{ kg/m}^3\end{aligned}$$

SOLUTION (a) Let us start by calculating the Grashof and the Prandtl numbers:

$$N_{Gr} = \frac{9.81 \times (0.1)^3 \times 10^{-3} \times 100}{(9.4 \times 10^{-7})^2} \simeq 1.11 \times 10^9$$

$$N_{Pr} = \frac{0.71 \times 10^3 \times 6.7 \times 10^{-3}}{20.9} \simeq 0.23$$

From Fig. 6.3.6, by interpolation, say the thickness of the thermal boundary layer, corresponds to

$$\eta = 18$$

Thus

$$(\delta_T/x)(N_{Gr,x}/4)^{1/4} \simeq 18$$

hence

$$\delta_T \simeq 0.014 \text{ m}$$

The corresponding thickness of the velocity boundary layer is estimated from Fig. 6.3.5. Thus

$$\eta \simeq 14$$

hence

$$\delta \simeq 0.011 \text{ m}$$

Thus the velocity boundary layer is thinner than the thermal boundary layer, which is to be expected, since $N_{Pr} < 1$. From Fig. 6.3.5 the maximum velocity is estimated from

$$f' = u_x x / 2\sqrt{N_{Gr,x}} \simeq 0.45$$

hence

$$\begin{aligned} u_{x,\max} &\simeq 0.45 \times 2 \times 9.4 \times 10^{-7} \times 3.31 \times 10^4 / 0.1 \\ &\simeq 0.28 \text{ m/s} \end{aligned}$$

(b)

$$\begin{aligned} N_{Gr} &= 9.81 \times (0.1)^3 \times 2.7 \times 10^{-4} \times 100 / (1.66 \times 10^{-3})^2 \simeq 96.3 \\ N_{Pr} &\simeq 1.25 \times 10^3 \times 5.0 / 2.09 \simeq 2.99 \times 10^3 \end{aligned}$$

From Fig. 6.3.6 the thickness of the thermal boundary layer corresponds to

$$\eta \simeq 0.3$$

Thus

$$(\delta_T/x)(N_{Gr,x}/4)^{1/4} \simeq 0.1$$

hence

$$\delta_T \simeq 0.1 \times 0.1 / 2.21 \simeq 4.5 \times 10^{-3} \text{ m}$$

The corresponding thickness of the velocity boundary layer is rather more difficult to estimate from Fig. 6.3.5, but is of the order of 0.1–0.15 m. The maximum velocity is about

$$(10^{-2}/0.1) \times 2 \times 9.81 \times 1.66 \times 10^{-3} \simeq 3.3 \times 10^{-3} \text{ m/s}$$

i.e., very much smaller than for case (a).

It is stressed to the reader the above considerations are valid for laminar flow only, which, for boundary layer type flows, mean that $N_{Gr}N_{Pr} < 10^9$.[†]

GENERAL STATEMENT OF LAMINAR NATURAL CONVECTION

The modeling equations developed on the proceeding stages were stated on the basis of the boundary layer assumptions. Many systems, particularly

[†] The quantity $N_{Gr}N_{Pr}$ is usually called the Rayleigh number, N_{Ra} .

those in enclosed cavities (e.g., natural convection in molds, ladles, or in the electrolytic refining of copper), involve truly two-dimensional flows; the formulation of these problems is best carried out using a general statement of natural convection.

In general, assuming incompressible behavior (except for the generation of the body force term), the equations of continuity, motion, and thermal energy balance take the following form:

$$\nabla \cdot \mathbf{u} = 0 \quad (\text{equation of continuity}) \quad (6.3.23)$$

$$\rho \frac{D\mathbf{u}}{Dt} + \mathbf{g}\rho\beta(T - T_\infty) = -\nabla p + \mu\nabla^2\mathbf{u} \quad (\text{equation of motion}) \quad (6.3.24)$$

and

$$\frac{DT}{Dt} = \kappa\nabla^2T \quad (\text{thermal energy balance equation}) \quad (6.3.25)$$

Of the multidimensional natural convection problems, a great deal of work has been reported on the behavior of rectangular cavities. For a two-dimensional cavity the governing equations take the following form:

$$\frac{\partial u_x}{\partial x} + \frac{\partial u_y}{\partial y} = 0 \quad (\text{continuity}) \quad (6.3.26)$$

$$\frac{\partial T}{\partial t} + u_x \frac{\partial T}{\partial x} + u_y \frac{\partial T}{\partial y} = \kappa \left(\frac{\partial^2 T}{\partial x^2} + \frac{\partial^2 T}{\partial y^2} \right) \quad (\text{energy balance}) \quad (6.3.27)$$

$$\frac{\partial u_y}{\partial t} + u_x \frac{\partial u_x}{\partial x} + u_y \frac{\partial u_x}{\partial y} = g\beta[T - T_i] - \frac{1}{\rho_m} \frac{\partial p}{\partial x} + v \left(\frac{\partial^2 u_x}{\partial x^2} + \frac{\partial^2 u_x}{\partial y^2} \right) \quad (6.3.28)$$

and

$$\frac{\partial u_y}{\partial t} + u_x \frac{\partial u_y}{\partial x} + u_y \frac{\partial u_y}{\partial y} = -\frac{1}{\rho_m} \frac{\partial p}{\partial y} + v \left(\frac{\partial^2 u_y}{\partial x^2} + \frac{\partial^2 u_y}{\partial y^2} \right) \quad (\text{equation of motion}) \quad (6.3.29)$$

As discussed in Schlichting¹² these equations may be rearranged using the stream function and the vorticity and then solutions can be obtained numerically. In general this problem is thought to be well understood, and as illustrated in Fig. 6.3.7¹⁸ the predictions based on the modeling equations were found to be in reasonable agreement with measurements.

The general trend exhibited by rectangular slots, where a temperature difference is imposed on the opposing vertical faces, while the horizontal planes are insulated, is sketched in Fig. 6.3.8 for various values of $N_{Gr}N_{Pr}$.

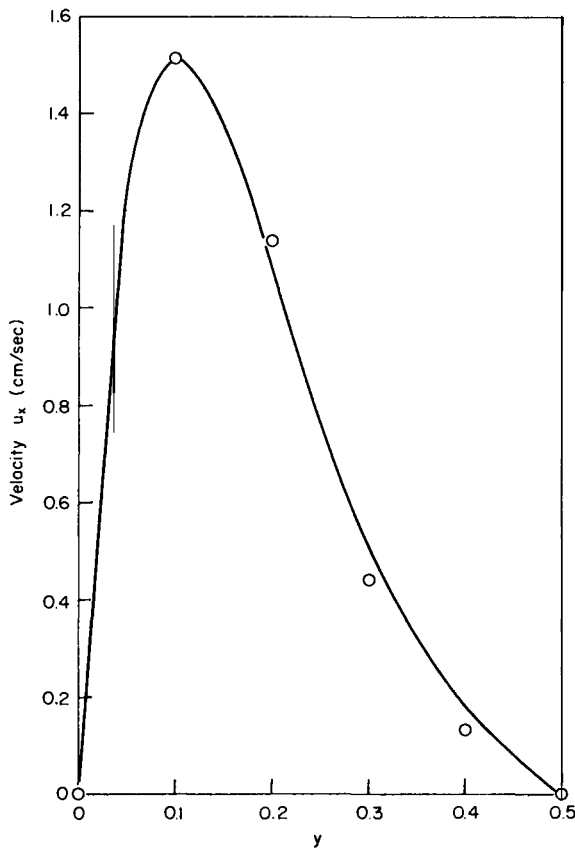


FIG. 6.3.7 Comparison of the experimentally measured velocity profile for natural convection in a cavity by Elder (○) with the theoretical predictions of Szekely and Todd¹³ shown by the solid line.

It is seen in (a) that when $N_{Gr}N_{Pr} < 500$, which in a physical sense would correspond either to very small temperature differences or to very thin fluid layers, the temperature profile is linear and the flow field is essentially symmetrical.

At intermediate values of the Rayleigh number depicted in (b) i.e., $500 \leq N_{Gr}N_{Pr} \leq 10^5$, there is a distortion in both the linearity of the temperature profiles and in the symmetry of the velocity fields. In fact, the formation of the thermal and the velocity boundary layers is readily discernible.

Finally, (c) shows the temperature and the streamline pattern for $N_{Gr}N_{Pr} > 10^5$. The establishment of secondary flows is clearly seen, which

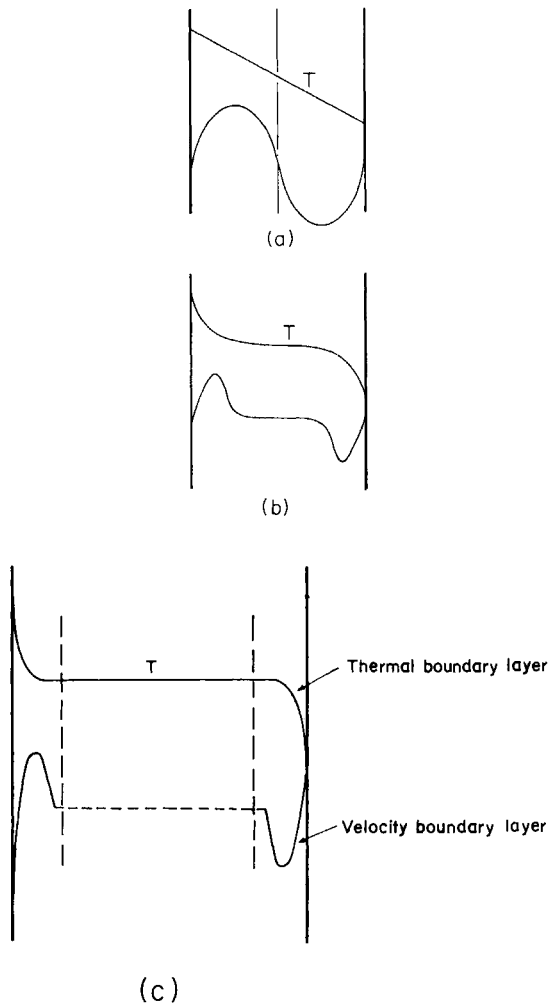


FIG. 6.3.8 Temperature and velocity profiles resulting from natural convection in rectangular slots: (a) $N_{Gr}N_{Pr} < 500$; (b) $500 \leq N_{Gr}N_{Pr} \leq 10^5$; (c) $N_{Gr}N_{Pr} > 10^5$.

in turn results in a large flat portion of the temperature profile in the central portion of the system.

Work has also been done on transient natural convection in cavities; here if the initial state corresponds to a stagnant fluid layer, the establishment of the flow field has to be preceded with transient conduction, with the corresponding development of temperature gradients in the fluid. As shown by

Szekely and Todd,¹³ an interesting aspect of the transient cooling of liquid metals is that since the transfer of heat can proceed much faster than the transfer of momentum (the Prandtl number is small!) convection currents may persist in the system long after the attainment of uniform temperatures.

More recently, particularly interesting measurements and predictions have been reported on the application of these concepts to solidifying metallic systems by Weinberg and co-workers^{14,15} and by Szekely and Jassal¹⁶ on a room-temperature model of a binary solidifying mixture. Figure 6.3.9, taken from this latter paper, shows a comparison between measured and the predicted transient velocity field in a rectangular cavity, where solidification takes place.

It is noted that in using laminar flow models for the velocity and the temperature fields in rectangular cavities the solutions tend to break down, when $N_{Gr}N_{Pr} > 3 \times 10^5$. This condition marks the onset of secondary flows

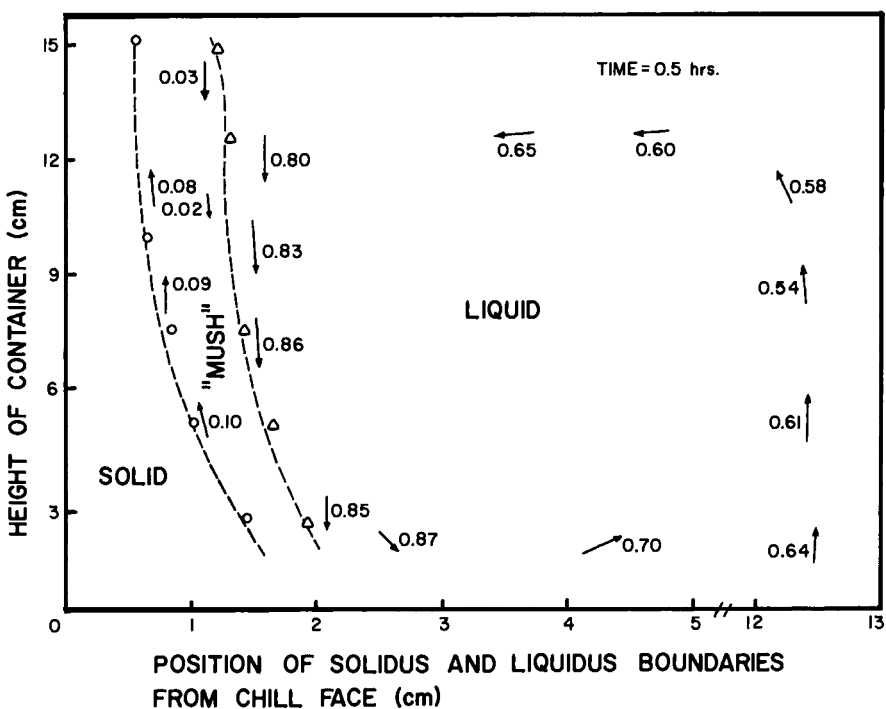


FIG. 6.3.9b (Cont.)

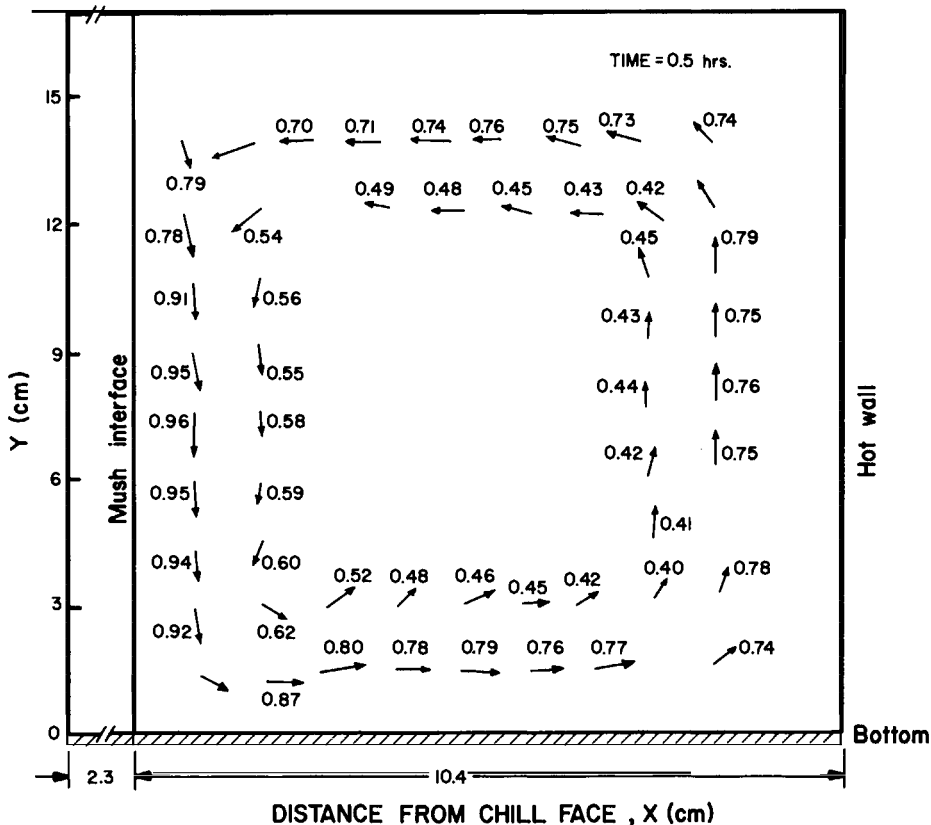


FIG. 6.3.9(b) Theoretically predicted velocity fields in the liquid and the two-phase regions of a solidifying binary system, after Szekely and Jassal¹⁶.

in a physical sense and under these conditions the numerical methods tend to become unstable.¹³

6.3.2 Turbulent Natural Convection

The expressions developed on the preceding pages were restricted in their validity to laminar flow conditions, i.e., to $N_{Gr}N_{Pr} < 10^9$ for boundary layer flows and $N_{Gr}N_{Pr} < 3 \times 10^5$ for natural convection in cavities. In a physical sense these restrictions imply either small temperature differences or small linear size, i.e., short length for the leading edge in boundary layer flows, or small widths in case of cavities.

When these restrictions are not met the *flow becomes turbulent* and, on the analogy of the material presented in Chapter 4, a different mathematical apparatus has to be developed for the modeling of these flows.

PHYSICAL MANIFESTATIONS OF TURBULENT NATURAL CONVECTION

Figure 6.3.10 shows an interferogram depicting the transition from laminar to turbulent flow in a boundary layer formed on a heated vertical plate in air. The onset of instabilities, in the form of waves, is readily apparent.

Other physical manifestations of turbulent flow in natural convection include the thickening of the boundary layer and an increase in the local rate of heat transfer from the heated surface into the surrounding fluid.

Yet other manifestations, consistent with those mentioned above, include more effective momentum transfer and enhanced lateral mixing. It is to be stressed however that, in contrast to forced flow problems, in natural convection the transition from laminar flow to turbulent flow is gradual, rather than abrupt. Thus in case of natural convection in cavities when $N_{Gr}N_{Pr} > 3 \times 10^5$ secondary flows will be established, and then on a further increase in the Grashof Prandtl product, smaller eddies are formed and the flow turns turbulent.

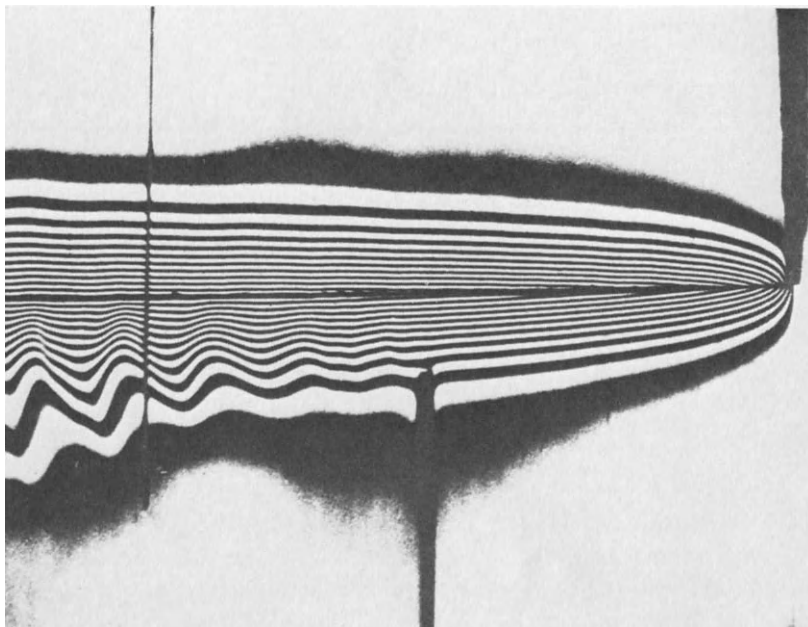


FIG. 6.3.10 Interferograms showing the transition from laminar to turbulent flow in natural convection. Photograph kindly supplied by Professor B. Gebhard of the state University of New York of Buffalo.

A considerable amount of work, both experimental and analytical, has been done on turbulent boundary layer flow in natural convection. Much of this effort has been directed toward the analysis of the heat transfer rates in these systems; however, some very useful measurements on temperature and velocity profiles have also been reported in the literature^{17,18}; moreover, recently some very interesting computational approaches have been described.^{19,20}

Particularly noteworthy is a recent paper by Plumb and Kennedy²¹ who applied the so-called $K-\epsilon$ model of Jones and Launder²² for representing these systems.

In examining boundary layer flow, the problem was stated as

$$\rho u_x \frac{\partial u_x}{\partial x} + \rho u_y \frac{\partial u_y}{\partial y} = 0 \quad (\text{continuity}) \quad (6.3.30)$$

$$\begin{aligned} \rho u_x \frac{\partial u_x}{\partial x} + \rho u_y \frac{\partial u_x}{\partial y} &= \frac{\partial}{\partial y} \left[(\mu + \mu_T) \frac{\partial u}{\partial y} \right] \\ &\quad + \rho g \beta (T - T_{\infty}) \quad (\text{equation of motion}) \end{aligned} \quad (6.3.31)$$

and

$$u_x \frac{\partial T}{\partial x} + u_y \frac{\partial T}{\partial y} = \frac{1}{\rho} \frac{\partial}{\partial y} \left[\left(\frac{\mu}{N_{Pr}} + \frac{\mu_T}{\sigma_T} \right) \frac{\partial T}{\partial y} \right] \quad (\text{energy balance}) \quad (6.3.32)$$

These authors solved Eqs. (6.3.30)–(6.3.32) in conjunction with a two-equation model for the turbulent viscosity; Figs. 6.3.11 and 6.3.12 show plots of the computed temperature and velocity profiles.

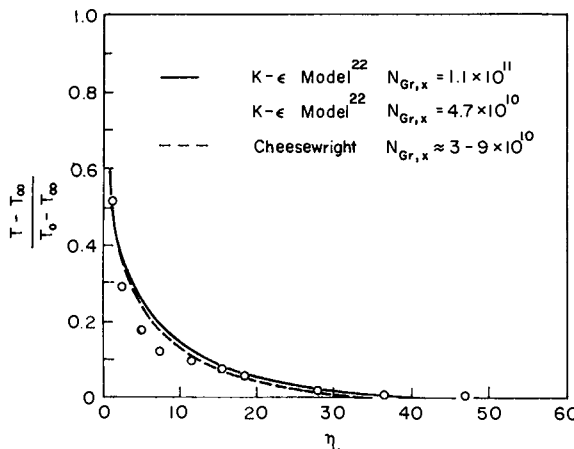


FIG. 6.3.11 A comparison of experimentally measured and theoretically predicted temperature profiles in a turbulent boundary layer in natural convection, after Plumb and Kennedy.²¹ Original graph kindly provided by Professor L. A. Kennedy of the State University of New York at Buffalo.

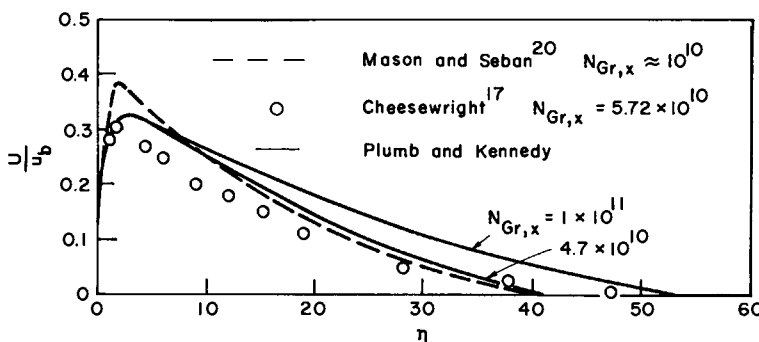


FIG. 6.3.12 A comparison of the experimentally measured and the theoretically predicted velocity profiles in a turbulent boundary layer in natural convection, after Plumb and Kennedy.²¹ Original graph kindly provided by Professor L. A. Kennedy of the State University of New York at Buffalo.

It is seen that there is reasonable agreement between the predictions based on these modeling equations and the experimental measurements of Cheesewright.¹⁷ It follows that this approach is reasonable and should be applicable to a broad range of metals processing problems.

It is thought, however, that the closely related problem area, namely turbulent natural convection in cavities, and in particular the transient turbulent natural convection, would be rather more difficult to tackle computationally.

6.4 Surface Tension Driven Flows

In the following two sections we shall discuss surface tension driven flows; Section 6.4 is devoted to the definition of surface tension and to the presentation of typical values of the interfacial tension for systems of metallurgical interest. The actual surface tension driven flows will then be discussed in Section 6.5.

DEFINITION OF SURFACE TENSION

When two fluids, a liquid and a gas, or two liquids are in contact with each other, in general they are separated by a thin layer or region termed *an interface*, the properties of which are different from those of the bulk phases. It has been suggested by Young²³ in 1805 that from a mechanical standpoint the system behaves as if it consisted of two homogeneous fluids, separated by a uniformly stretched membrane of infinitesimal thickness.

It has to be stressed to the reader that, while this representation is very convenient from the mathematical standpoint, it does not correspond to

physical reality. Because of the nature of the molecular forces, these differ in the bulk from those in the interfacial region (the attractive and repulsive forces are necessarily different between like and unlike molecules). From a molecular standpoint the fluids cannot be regarded as homogeneous throughout the domain, including the interfacial regions.

In fact, the application of continuum concepts to the interfacial regions can cause appreciable conceptual and practical difficulties. A discussion of these problems is beyond the scope of this text and the reader is referred to Rideal and Davies²⁴ and Defay and Prigogine²⁵ for a full treatment of these problems.

In physical terms the above statement by Young represents the definition of surface tension, or interfacial tension. In order to define the interfacial tension in quantitative mathematical terms, let us consider a surface AB of arbitrary shape, sketched in Fig. 6.4.1, separating phases I and II.

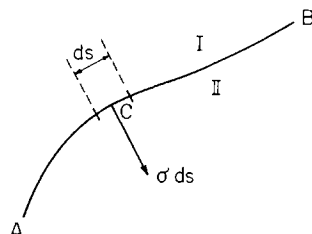


FIG. 6.4.1 Sketch for the definition of the surface tension.

In order to define the tension in this surface at some point C, let us consider the surface element δs . If across this element, region II exerts a force $\sigma \delta s$ tangential to the surface, then σ is called the *surface* or the *interfacial tension* at this point.

The surface is said to be in a state of uniform tension if

- (1) at each point σ is perpendicular to the dividing line and has the same value irrespective of the direction of this line, and
- (2) σ has the same value at all points on the interface.

As we shall see subsequently, there are cases when this condition is not observed and there are local variations in σ because of either concentration or temperature gradients. Under these conditions the gradients in σ can result in surface tension driven flows.

An important physical manifestation of surface tension is that work is required to deform the surface AB; in practice such work has to be performed against surface tension forces when a gas bubble expands in a liquid or when a liquid or gas stream is broken up. In the latter case surface tension forces would oppose the creation of a fresh surface.

From a practical viewpoint, in metals processing systems, the effect of interfacial (surface) tension forces may be divided into the following two categories:

(a) *In stationary* systems the mechanical equilibrium between surface tension forces and the other forces acting on the system determines the shape of the interfacial regions, namely the shape of a gas bubble, a metal droplet in slag, or the meniscus of a metal surface in the vicinity of an immersed solid body.

(b) *In moving* systems surface tension forces may resist the motion imposed by other forces, as is the case in the growth of gas bubbles in liquids, the damping of turbulent fluctuations at the free surface of liquids and in atomization. In all these cases, surface tension resists the formation of fresh surface.

In another group of situations local gradients in surface tension, caused by local gradients in concentration or temperature, give rise to flow and in certain cases interfacial turbulence may also result.

In this section we shall discuss some manifestations of surface tension in stationary systems and will also present typical measured values of the interfacial tension for slag–metal–gas systems.

The dynamic aspects of interfacial tension and surface tension driven flows will be discussed in Section 6.5.

6.4.1 *The Shape of a Surface as Dictated by Mechanical Equilibrium: The Shape of a Spherical Cap*

Let us consider a portion of a spherical surface which separates two phases, as sketched in Fig. 6.4.2a. Let us designate the pressures in phases I and II by p_1 and p_{II} , respectively.

A more detailed consideration of the system is given in Fig. 6.4.2b, which also shows the coordinate system employed. More specifically, R denotes the radius of the sphere forming the cap while R' is the radius of the base. On recalling Fig. 6.4.1 we note that surface tension exerts a force $\sigma \delta s$, on each element of length δs of the circumference of the base.

The resolved part of this force along the C-Z axis is

$$-\sigma \cos \alpha' \delta s$$

The sum of all such contributions is

$$-\int_0^{2\pi R'} \sigma \cos \alpha' \delta s = -\frac{2\sigma}{R} \pi R'^2 \quad (6.4.1)$$

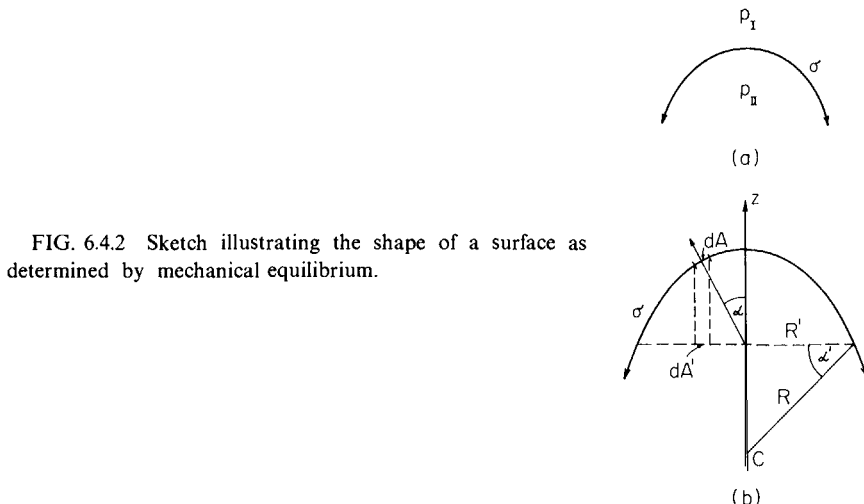


FIG. 6.4.2 Sketch illustrating the shape of a surface as determined by mechanical equilibrium.

Since the system is symmetrical about the z axis all forces normal to z must be equal. Thus the condition of mechanical equilibrium may be written as

$$(p_{II} - p_I)\pi R'^2 = (2\sigma/R)\pi R'^2 \quad (6.4.2)$$

or

$$P_{II} - P_I = 2\sigma/R \quad (6.4.3)$$

which is the famous Kelvin equation. In physical terms the Kelvin equation means that because of surface tension, a spherical surface having a radius of curvature R maintains equilibrium between two phases under conditions such that the phase on the concave side has a larger pressure than the phase on the convex side. When $R \rightarrow \infty$, $p_{II} \rightarrow p_I$. An important consequence of this relationship is the fact that because of surface tension the pressure within a gas bubble must be larger than the pressure in the surrounding liquid at the surface of the bubble. The smaller the size of the bubble and the higher the value of the surface tension the larger is this pressure difference.

6.4.2 The Equilibrium Shape of an Arbitrary Surface : An Alternative Approach

Previously we defined the surface tension in terms of the mechanical properties of the system. An alternative approach discussed by Levich²⁶ would be to work in terms of the free energy of the system.

Upon considering a one-component system (i.e., a liquid in contact with its own vapor, etc.), let us designate the two phases by the subscripts I and

II and postulate, as before, that each of these phases is homogeneous up to the interface which itself is infinitely thin. Then we may define F_Σ , the surface free energy, as

$$F^\Sigma = F_T - (F_I + F_{II}) \quad (6.4.4)$$

where F_T is the total free energy of the system; F_I and F_{II} are the free energies of the bulk phases I and II, respectively; F_Σ is the thermodynamic potential for which the temperature and the surface area Σ are the independent variables.[†] Thus we may define

$$\sigma = \left(\frac{\partial F^\Sigma}{\partial \Sigma} \right)_T \quad (6.4.5)$$

which is the surface free energy per unit area at constant temperature.

The work done on the isothermal reversible expansion of the surface, dW , is then given as

$$dW = -\sigma d\Sigma \quad (6.4.6)$$

We may now recall that thermodynamic equilibrium for an isothermal system requires that the free energy of the system be at a minimum. Thus at equilibrium we may write

$$\delta F_T = 0 \quad (6.4.7)$$

The criterion posed by Eq. (6.4.7) may then be used to define the surface configuration which will minimize the total free energy of the system. The mathematical technique for minimizing the line or surface integral of an unknown function and thus evaluating this function is called the calculus of variations. A good discussion of the calculus of variations is available in the texts by Sokolnikov and Redheffer²⁷ and Collins.²⁸ Elegant treatments involving the use of variational calculus for defining the shape of the interfacial regions have been discussed by Levich²⁶ and by Matvejevich.²⁹

Here we shall confine ourselves to presenting the results derived by Levich for the shape of a meniscus in the vicinity of a solid wall, such as sketched in Fig. 6.4.3.

By establishing a force balance and minimizing the free energy of the system we have

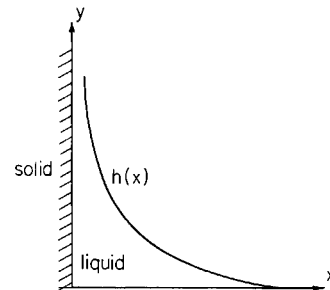
$$\rho gy = \sigma/R_I + \text{const} \quad (6.4.8)$$

where R_I , the radius of curvature, is given by

$$\frac{1}{R_I} = \frac{d^2 h / dx^2}{[1 + (dh/dx)^2]^{3/2}} \quad (6.4.9)$$

[†] For multicomponent systems, F^Σ will also depend on the composition.

FIG. 6.4.3 Meniscus formed in the vicinity of a vertical plate immersed in a fluid.



Upon combining Eqs. (6.4.8) and (6.4.9) and after some arithmetic we obtain the following expression for the shape of the meniscus:

$$h(x) = -\left(\frac{\sigma}{\rho g}\right)^{1/2} \cosh^{-1} 2\left(\frac{\sigma}{2gx^2}\right)^{1/2} + \left(\frac{2\sigma}{\rho g}\right)^{1/2} \left(2 - \frac{\rho gx^2}{2\sigma}\right)^{1/2} + \text{const} \quad (6.4.10)$$

where the constant is determined by the value of the contact angle.

We note that two types of menisci may exist, depending on the value of the contact angle, as sketched in Fig. 6.4.4.

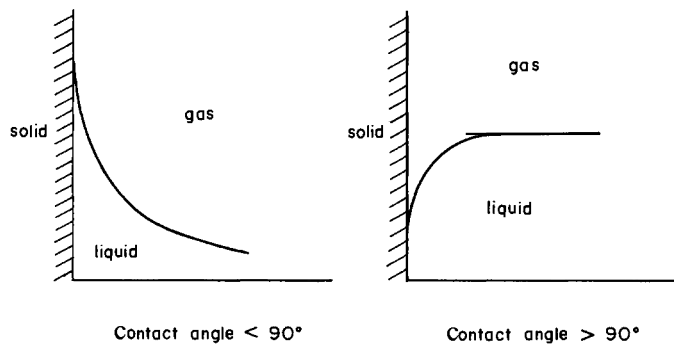


FIG. 6.4.4 The effect of the contact angle on the shape of the meniscus formed in the vicinity of a vertical plate immersed in a fluid.

6.4.3 The Contact Angle

If a liquid droplet is placed onto a solid surface, the actual shape of the droplet at equilibrium will be determined by four factors; namely

- σ_{S-L} , surface tension between the solid and the liquid
- σ_{S-G} , surface tension between the gas and the solid
- σ_{L-G} , surface tension between the gas and the liquid
- θ , "the contact angle"

At equilibrium we may write

$$\sigma_{S-G} - \sigma_{S-L} = \sigma_{L-G} \cos \theta \quad (6.4.11)$$

Figure 6.4.5 shows typical examples of gas–solid–melt contacts. Here 6.4.5a shows a situation where $\theta < \pi/2$, while 6.4.5b corresponds to $\theta > \pi/2$, which is usually the case for liquid metals on refractory surfaces.

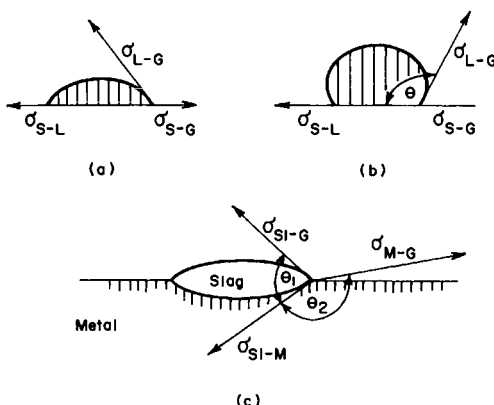


FIG. 6.4.5 The contact angle for drops on (a) solids, (b) on a liquid metal, (c) on the arrows showing the direction of the forces.

Finally, Fig. 6.4.5c depicts the case of a slag droplet on the surface of a metal pool, where two contact angles have to be considered, namely, slag–gas and slag–metal.

Upon considering 6.4.5c, the criterion for mechanical equilibrium is given by

$$\sigma_{M-G}/\sin \theta_1 = \sigma_{S1-G}/\sin \theta_2 \equiv \sigma_{S1-M}/\sin(2\pi - \theta_1 - \theta_2) \quad (6.4.12)$$

from which one can deduce the criteria *for spreading*.

More specifically, the quantity

$$\alpha_{spr} = [\sigma_{M-G} - \sigma_{S1-G} - \sigma_{S1-M}] \quad (6.4.13)$$

is usually termed the spreading coefficient; when this bracketed term is larger than zero, the slag will spread across the metal surface.

Another practical point that should be made here is that the shape assumed by a molten metal or slag droplet, when placed onto a flat surface in a given atmosphere, was shown to depend on the contact angle and on the interfacial tension. This property of the system may be used for the experimental determination of the surface tension and of the contact angles, as discussed by Hondros.³⁰

6.4.4 Typical Values of the Surface Tension

The surface tension of liquid metals in contact with inert gases and slags tends to be higher than that of water (~ 0.07 N/m) or light organics (0.02–0.04 N/m). Some typical values of the surface tension of liquid metals and slags are given in Table 6.4.1 and 6.4.2, respectively, where it is seen that the surface tension of liquid metals ranges from about 0.34 to 1.7 N/m, while the surface tension of metal oxides and halides varies from about 0.07 to 0.7 N/m.

In a physical sense these high absolute values of the interfacial tension mean that both the damping effects of interfacial tension and the intensity of surface tension driven flows are appreciably higher in metallic melts (and in slags) than would be the case for aqueous or organic systems.

It is noted that the property values given in Tables 6.4.1 and 6.4.2 referred to one-component systems. The interfacial tension is strongly composition dependent, as illustrated in Figs. 6.4.6 and 6.4.7.

Figure 6.4.6 shows the effect of SiO_2 content on the surface tension of binary silicates while Fig. 6.4.7 shows the effect of various alloying additions to aluminum on its surface tension. Figures 6.4.8 and 6.4.9 show the effect

TABLE 6.4.1
Surface Tension of Liquid Metals

Metal	Temperature (°C)	Surface tension	N/m
Cu	1120	1280	1.2
Ag	970	920	0.92
Au	1070	1127	1.127
Zn	420	750	0.75
Cd	330	550	0.55
Hg	20	465	0.465
Ga	30	725	0.725
In	160	340	0.340
Te	450	460	0.460
Si	1420	~725	0.725
Ti	~1670	1510	1.51
Sn	~240	~550	0.550
Pb	400	445	0.445
Sb	640	395	0.395
Bi	400	375	0.375
Cr	1540	>1590	1.59
W	3380	2310	2.31
Mn	~1250	>1300	1.3
Fe	1550	1788	1.788
Co	1550	1886	1.886
Ni	1550	1934	1.934
Pt	1800	1699	1.699

TABLE 6.4.2
Surface Tension of Some Oxides,
Sulphides, and Halides

Substance	T (°C)	σ (N/m)
NaCl	1000	0.098
NaBr	900	0.091
NaI	700	0.084
KBr	900	0.09
KI	800	0.085
RbCl	828	0.069
RbBr	831	0.081
RbI	772	0.072
CsF	826	0.096
CsCl	830	0.078
CsBr	808	0.072
CsI	821	0.063
NaNO ₃	350	0.115
KNO ₃	350	0.109
FeO (in equilibrium with Fe)	1420	0.585
Al ₂ O ₃	2050	0.690
SiO ₂	1800	0.307
GeO ₂	1150	0.259
P ₂ O ₅	100	0.060
B ₂ O ₃	1000	0.082
Cu ₂ S	1200	0.4
NiS	1200	0.577
CoS	1200	0.488
PbS	1200	0.2
Sb ₂ S ₃	1200	0.094

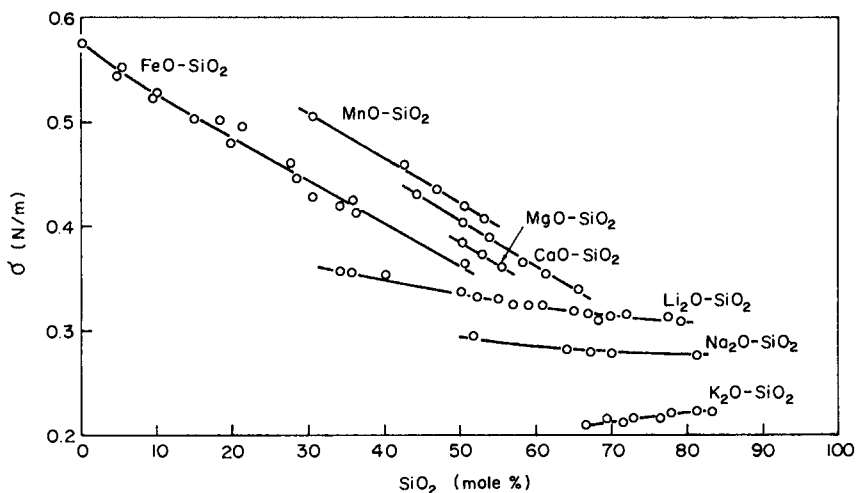


FIG. 6.4.6 The surface tension of some binary silicates, by T. B. King, as quoted by Richardson.⁸

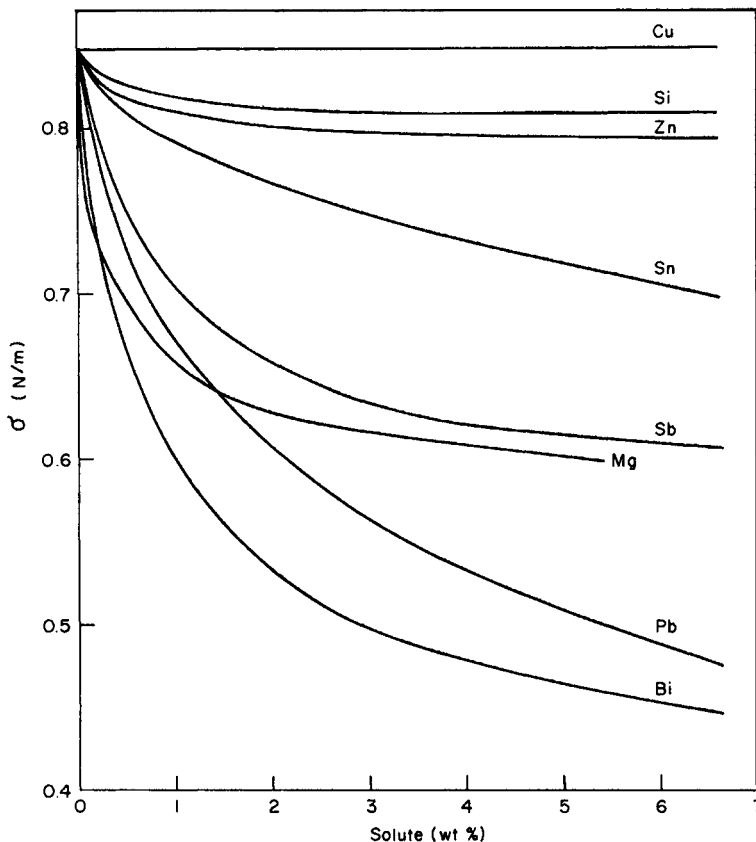


FIG. 6.4.7 The surface tension of molten aluminum, as affected by the presence of various alloying elements, by Korolkov, as cited by Richardson.⁸

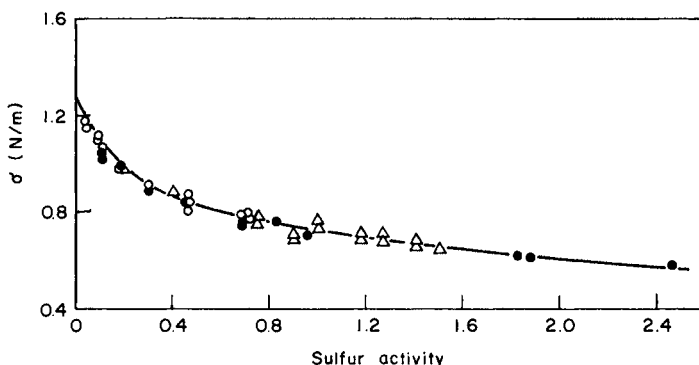


FIG. 6.4.8 The effect of sulfur activity of the surface tension of molten iron at 1450°C, reported by Kozakievitch, cited by Richardson.⁸

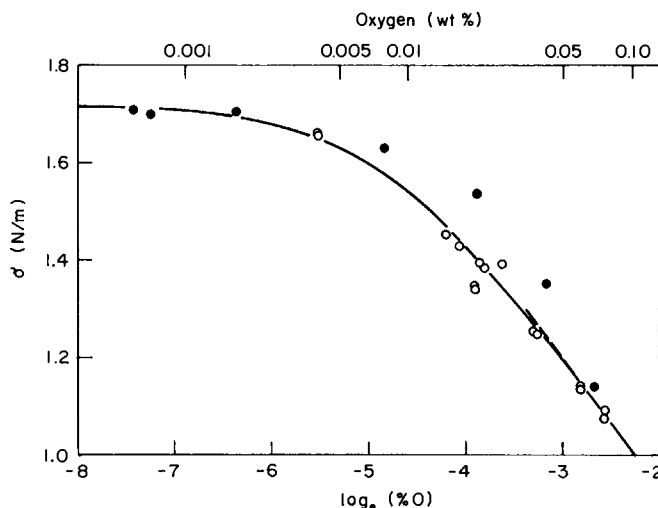


FIG. 6.4.9 The effect of the surface tension of molten iron, containing oxygen at 1550°C, reported by Swisher and Turkdogan, cited by Richardson.⁸

of sulfur activity and the effect of oxygen content on the surface tension of liquid iron.

It is seen that in all these cases the interfacial tension is markedly reduced by the presence of the second component. The very marked effect of sulfur and oxygen on the interfacial tension of liquid iron is particularly noteworthy. The manifestation of this strong dependence on oxygen content of the interfacial tension will be discussed in the subsequent section.

6.5 Surface Tension Effects in Dynamic Systems

In this section we shall examine the effect of interfacial tension on the dynamic behavior of systems. As noted earlier, these effects may be classified into two broad categories; namely,

(a) when surface tension effects tend to retard the flow, such as in the initial stages of bubble growth or the damping of turbulence at free surfaces, and

(b) surface tension driven flows.

6.5.1 The Effects of Surface Tension on the Growth of Gas Bubbles in Liquids

Let us consider the growth of a spherical bubble in a liquid, sketched in Fig. 6.5.1. It is seen that the pressure inside the bubble is designated P_G , while the pressure in the liquid, in contact with the bubble, is denoted by P_L ; the pressure in the liquid, at an infinite distance from the bubble, is

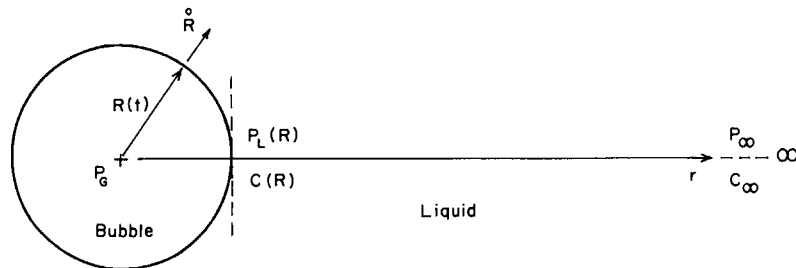


FIG. 6.5.1 Sketch showing the parameters describing the growth of a gas bubble in a liquid.

termed P_∞ . Finally, the instantaneous bubble radius and the velocity of the bubble surface are designated by $R(t)$ and $\dot{R}(t)$, respectively. In practice bubble growth will occur, because of the transfer of a solute (or vapor) from the liquid to the bubble surface. However, this aspect of the problem will not be considered here. Physical reasoning suggests that, in order for growth to occur,

$$P_G > P_L > P_\infty \quad (6.5.1)$$

As discussed in Chapter 3, such a system may be represented by writing the equation of continuity and the equation of motion. For spherical coordinates the equation of continuity takes the following form:

$$r u_r^2 = \text{const} \equiv R \dot{R}^2 \quad (6.5.2)$$

For spherical coordinates the equation of motion is given as

$$\frac{\partial u_r}{\partial t} + u_r \frac{\partial u_r}{\partial r} = \frac{1}{\rho_L} \frac{\partial P_L}{\partial r}, \quad r > R \quad (6.5.3)$$

Upon substituting for u_r from Eq. (6.5.2) on, then integrating between the limits $r = R$ and $r = \infty$, we obtain[†]

$$R \ddot{R} + \frac{3}{2} \dot{R}^2 = \frac{1}{\rho_L} [P_L(R) - P_\infty] \quad (6.5.4)$$

Equation (6.5.4) relates the growth rate and the acceleration of the bubble surface to the difference in pressure at infinity and in the liquid phase at the surface of the bubble. In practical cases we need to relate the growth of the bubble to the pressure inside the gas phase, forming the bubble. This may be done by expressing the continuity of the normal stress at the gas-liquid interface. Thus we have

$$P_L(R) + (2\sigma/R) + \tau_{rr,L}(R) = P_G(R) - \tau_{rr,G}(R) \quad (6.5.5)$$

[†] The detailed steps involved are discussed in Szekely and Themelis⁴ and Martins.³³

Upon noting that

$$\tau_{rr,G}(R) \approx 0 \quad (6.5.6)$$

and

$$\tau_{rr,L}(R) = -2\mu \frac{\partial u_r}{\partial r} \quad (6.5.7)$$

we obtain

$$P_L(R) = P_G(R) - (2\sigma/R) - 2\mu(\dot{R}/R) \quad (6.5.8)$$

Equation (6.5.8) expresses the fact that the pressure inside the gas bubble [$P_G(R)$] is larger than the pressure in the liquid at the surface of the bubble because of the need to balance both the surface tension and the viscous forces.

It is seen from the form of Eq. (6.5.8) that the role of surface tension forces in limiting the growth of gas bubbles is limited to the initial stages when the bubbles are small. This point is illustrated in Fig. 6.5.2, which shows computed curves of the bubble radius against time with the quantity $\phi = 2\sigma/\Delta PR_0$ as a parameter.

Further examples of the effect of surface tension in limiting or affecting bubble growth are discussed in Chapter 8.

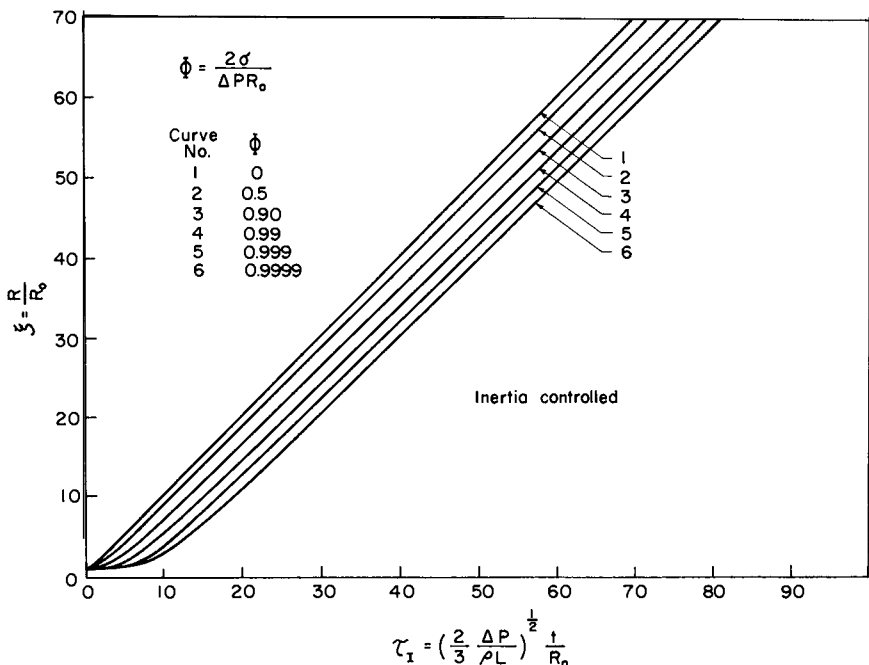


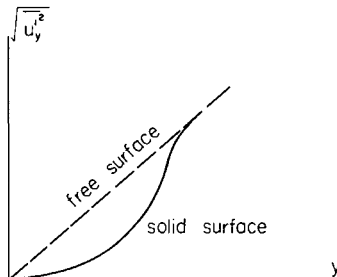
FIG. 6.5.2 Plot showing the effect of the surface tension parameter on the growth of spherical bubbles in the inertia controlled regime, after Szekely and Martins.³³

6.5.2 The Effect of Surface Tension in Damping Turbulence on Free Surfaces

It is an experimental observation that turbulent eddies are strongly restrained at a free gas–liquid surface. It has been demonstrated, using talc powder tracers, that while the velocity component perpendicular to the surface is zero, turbulent fluctuations persist in the direction parallel to the free surface. This behavior is in marked contrast to that found for solid surfaces, in the vicinity of which both normal and parallel fluctuating velocity components were extinguished.

Figure 6.5.3 shows a sketch depicting the dependence of $\sqrt{u_y'^2}$ (the normal velocity component) on distance from a solid and a free liquid surface.

FIG. 6.5.3 Sketch showing the dependence of the fluctuating normal velocity component on distance from the surface: solid line, solid bounding surface; broken line, free surface.



It is seen that for a liquid bounded by a solid wall the fluctuating velocity component (and hence the intensity of turbulence) decays exponentially on approaching the wall, e.g., as predicted by Dreissler's formula which was discussed in Chapter 4.

In contrast at a free gas–liquid surface the relationship between $\sqrt{u_y'^2}$ and distance is approximately linear.

Eddies on approaching a free surface are resisted by two forces; namely, (1) gravity resists the vertical deformation of the free surface and (2) surface tension resists the deformation of the surface, i.e., the formation of a protuberance. If we assign an approach velocity to the eddy, say u_0 , then a momentum balance may be written as

$$\tilde{c}\rho u_0^2 = 2\sigma/R + h_{\max}^* \rho g \quad (6.5.9)$$

where \tilde{c} is a coefficient, 0.7–1.0, R is the radius of curvature of the deformation, and h_{\max}^* is the maximum value of the vertical deformation; thus ρgh_{\max}^* is the maximum hydrostatic head opposing the eddy.

On the basis of experiments with submerged vertical liquid jets, sketched in Fig. 6.5.4, Davies³⁴ suggested the following relationship:

$$R = \tilde{c}^2 / 8y_{\max}^* \quad (6.5.10)$$

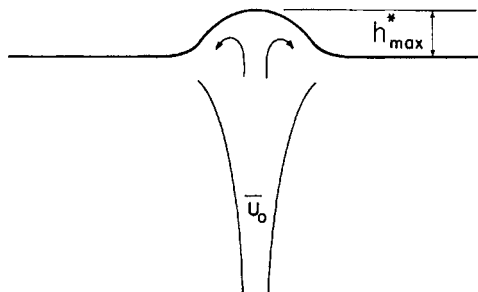


FIG. 6.5.4 Sketch of a submerged vertical jet.

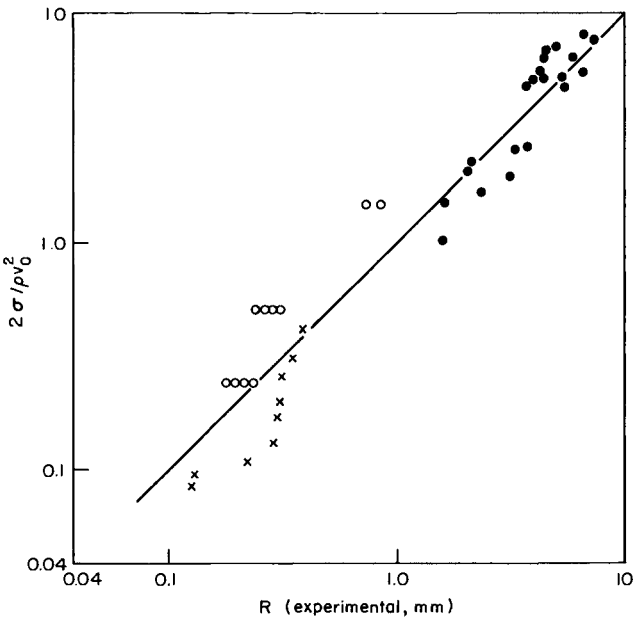
where \tilde{l} is the mean eddy size. Thus Eq. (6.5.9) may be written as

$$\tilde{c}\rho u_0^2 = (2/R)[\sigma + l^2 \rho g/16] \quad (6.5.11)$$

Davies suggested that the quantity in the brackets be termed the “equivalent surface tension” or

$$\sigma_{\text{equiv}} = [\sigma + \tilde{l}^2 \rho g/16] \quad (6.5.12)$$

Figure 6.5.5 shows a plot of the experimentally measured values of $2\sigma/\rho u_0^2 \equiv 2\sigma_{\text{equiv}}/\rho u_0^2$ against the radius of curvature for a vertical submerged jet.

FIG. 6.5.5 Plot of the dimensionless “equivalent” surface tension against the photographically measured radii of curvature for submerged jets, after Davies.³⁴

These results indicate the validity of Eq. (6.5.11) with $\tilde{c} \approx 1$. In using the quantity σ_{equiv} it is helpful to assess the relative importance of the surface tension and the hydrostatic forces. These two forces are equal when

$$\tilde{l}^2 \rho g / 16 = \sigma \quad \text{or} \quad \tilde{l} = 4(\sigma/\rho g)^{1/2}. \quad (6.5.13)$$

Thus for water

$$\sigma = 0.072 \text{ N/m}, \quad \rho = 10^3 \text{ kg/m}^3, \quad \tilde{l} = 0.011 \text{ m} \quad \text{or} \quad 11 \text{ mm}$$

Hence, for eddies smaller than this value, surface tension forces would dominate in damping turbulence near the free surface.

For molten steel

$$\sigma = 1.5 \text{ N/m}, \quad \rho = 7.1 \times 10^3 \text{ kg/m}^3.$$

Hence,

$$\tilde{l} = 0.018 \text{ m.}$$

For practical purposes it is helpful to define δ_σ as the thickness of the region where turbulence is damped by surface tension or hydrostatic forces in the vicinity of the free surface.

On the basis of experiments Davies suggested the following expression:

$$\delta_\sigma \approx (\nu \sigma_{\text{equiv}} / 0.4 \rho u_0^3)^{1/2} \quad (6.5.14)$$

which is very similar in form to the expression proposed by Levich²⁶ on purely theoretical grounds.

Example 6.5.1 Estimate the thickness of the laminar sublayer due to surface tension damping for the following conditions:

Assume that $\sigma \approx \sigma_{\text{equiv}}$.

Molten steel

$$\begin{aligned} \mu &= 5.5 \times 10^{-3} \text{ kg/m.s} & \sigma &= 1.5 \text{ N/m} \\ \rho &= 7.1 \times 10^3 \text{ kg/m}^3 & u_0 &\approx 0.1 \text{ m/s} \end{aligned}$$

SOLUTION Use Eq. (6.5.14); thus,

$$\nu = 7.7 \times 10^{-7} \text{ m}^2/\text{s}$$

$$\begin{aligned} \delta_\sigma &= \left[\frac{7.7 \times 10^{-7} \times 1.5 \times 10^3}{0.4 \times 7.1 \times 10^3} \right]^{1/2} \\ &\approx 6 \times 10^{-4} \text{ m} \quad \text{or} \quad 0.6 \text{ mm} \end{aligned}$$

which is very small.

6.5.3 Surface Tension Driven Flows at Gas–Solid–Liquid Interfaces

An interesting manifestation of surface tension driven flows is the phenomenon of “flux line corrosion”; this is the accelerated attack on a refractory wall by a melt in the vicinity of a gas–melt–solid interface.

These problems have been well documented in the literature of glass technology,³⁵ but are perhaps best illustrated on the behavior of a physical model system sketched in Fig. 6.5.6, which shows the dissolution pattern of an ice cube partially immersed in an aqueous alcohol solution. The region in the immediate vicinity of the solid ice surface is richer in water than the region some distance from the surface. Since the interfacial tension of aqueous alcohol solutions in contact with air depends on the composition (the higher the water content, the larger is the value of σ), a gradient in surface tension will be established in the vicinity of the gas–solid–liquid interface. This gradient in turn produces flow which accelerates the melting in the interfacial region.

The situation is complicated further by the fact that water is heavier than alcohol and hence natural convection too will play a role in defining motion. The resultant flow pattern is indicated on the inset of the graph.

A mathematical analysis of such systems for viscous fluids, where the flow is laminar, has been put forward by Stanek and Szekely.³⁶ The physical system considered is sketched in Fig. 6.5.7, which indicates a rectangular slot with one soluble wall. The governing equations take the following form:

$$\frac{\partial u_x}{\partial x} + \frac{\partial u_y}{\partial y} = 0 \quad (\text{continuity}) \quad (6.5.15)$$

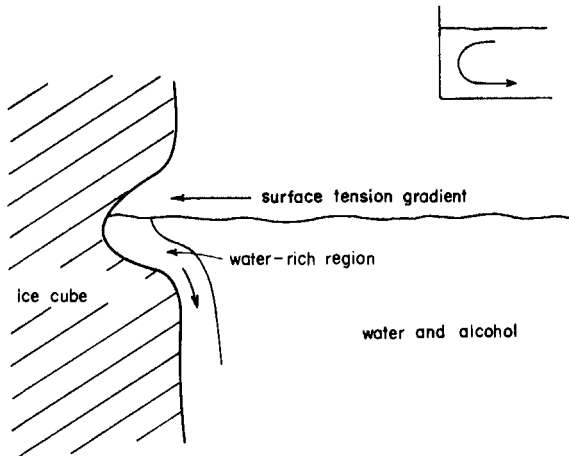


FIG. 6.5.6 The dissolution pattern of an ice cube, partially immersed in an aqueous alcohol solution.

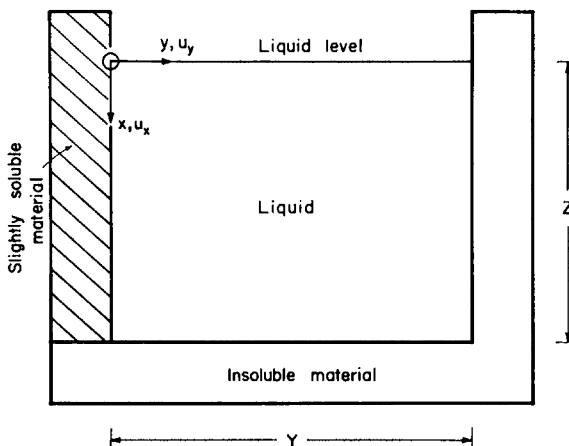


FIG. 6.5.7 Sketch of the system: a container with one soluble wall, containing liquid, which was studied by Stanek and Szekely.³⁶

$$\frac{\partial u_x}{\partial t} + u_x \frac{\partial u_x}{\partial y} + u_y \frac{\partial u_x}{\partial y} = g \left(\frac{\rho - \rho_0}{\rho} \right) - \frac{1}{\rho_0} \frac{\partial p}{\partial x} + v \left[\frac{\partial^2 u_x}{\partial x^2} + \frac{\partial^2 u_x}{\partial y^2} \right] \quad (6.5.16)$$

$$\frac{\partial u_y}{\partial t} + u_x \frac{\partial u_y}{\partial x} + u_y \frac{\partial u_y}{\partial y} = - \frac{1}{\rho} \frac{\partial p}{\partial y} + v \left[\frac{\partial^2 u_y}{\partial y^2} + \frac{\partial^2 u_y}{\partial x^2} \right] \quad (\text{equation of motion}) \quad (6.5.17)$$

$$\frac{\partial C}{\partial t} + u_x \frac{\partial C}{\partial x} + u_y \frac{\partial C}{\partial y} = D \left[\frac{\partial^2 C}{\partial x^2} + \frac{\partial^2 C}{\partial y^2} \right] \quad (\text{convective diffusion equation}) \quad (6.5.18)$$

The concentration of the diffusing species and the liquid density are related by the following expression:

$$\rho_0/\rho = 1 + \beta C \quad (6.5.19)$$

where ρ_0 is the density of the solvent and ρ is the density of the solution with a concentration C . The boundary conditions are readily written down; these have to specify the following:

- (a) zero velocity at the solid surface,
- (b) zero vertical velocity component at the free surface,
- (c) zero concentration gradient perpendicular to all the solid surfaces except the soluble wall, and
- (d) fixed concentration at the soluble wall.

The main boundary condition of interest at the free surface is the relationship between the local shear stress and the gradient in surface tension, which

TABLE 6.5.1

Circulation Patterns, as Affected by
 $d\sigma/dC$ and $(\rho - \rho_0)/\rho$

$d\sigma/dC$	Rotation	$(\rho - \rho_0)/\rho$	Rotation
+	↷	-	↷
+	↷	+	↷
-	↷	-	↶
-	↷	+	↶

may be written as

$$-\mu \frac{\partial u_y}{\partial x} = \frac{\partial \sigma}{\partial y} \quad \text{at } x = 0 \quad (6.5.20)$$

but since $\sigma = f(C)$, we have

$$-\mu \frac{\partial u_y}{\partial x} = \left(\frac{d\sigma}{dC} \right) \left(\frac{\partial C}{\partial y} \right) \quad \text{at } x = 0 \quad (6.5.21)$$

Equations (6.5.15)–(6.5.21) may be put in a dimensionless form and then integrated numerically, e.g., using the alternating direction implicit method.³⁷ A selection of computed results has been presented in Stanek and Szekely.³⁶ It is noted that, since both natural convection and surface tension will produce flow, the following circulation patterns are possible, depending on the sign of the quantities $(\rho - \rho_0)/\rho$ and $d\sigma/dC$, where ρ_0 is the density of the pure solvent as illustrated in Table 6.5.1.

When the direction of circulation due to natural convection and surface tension driven flow coincides, the flow pattern is unambiguous. Calculations have shown that, when these two factors would produce opposing flow fields, initially the surface tension term would predominate, while for longer times the circulation due to the body force field would become dominant.

Figure 6.5.8 shows a set of typical computed results, for a case where natural convection is absent and when $d\sigma/dC$ is positive. The concentration isopleths are shown in 6.5.8a, which are seen to be distorted near the free surface, as caused by the flow toward the soluble wall.

The clockwise circulation pattern is consistent with that indicated in Table 6.5.1, while the dissolution pattern, sketched in 6.5.8c, shows the effect of the surface tension driven flow in producing a highly localized corrosion.

Another interesting manifestation of surface tension driven flows in the slag corrosion of refractories is the phenomenon of “upward drilling.” In physical terms, “upward drilling” represents the accelerated corrosion of refractories in glass melting furnaces, in the presence of gas bubbles. A photograph showing the results of such corrosion is shown in Fig. 6.5.9,

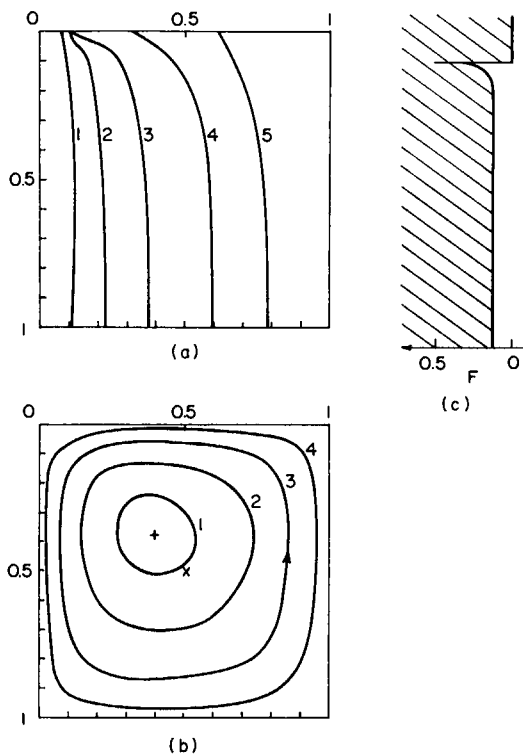


FIG. 6.5.8 Computed results for the system depicted in Fig. 6.5.7: (a) concentration isopleths, (b) the streamline pattern, (c) the dissolution pattern.

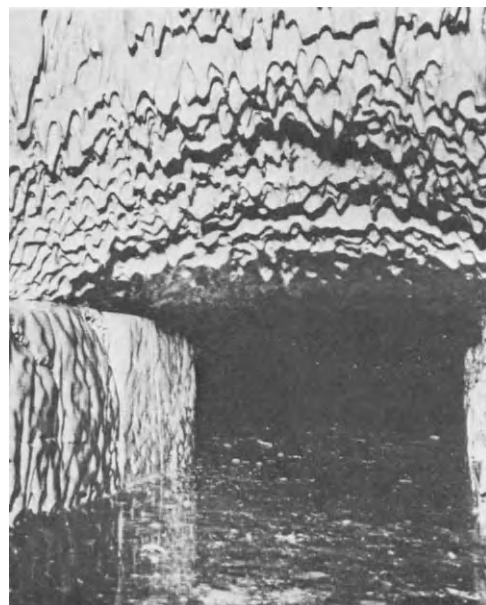


FIG. 6.5.9 The damage caused to the roof of a glass melting furnace, due to "upward drilling" bubbles, after Davies.³⁴

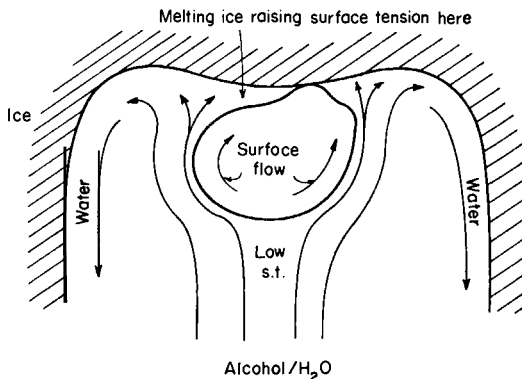


FIG. 6.5.10 Sketch depicting a model of the “upward drilling process” using the ice – water + alcohol system.

and the actual mechanism of the process is sketched in Fig. 6.5.10. It is seen that the local dissolution of the refractory in the vicinity of the bubble causes a local gradient in interfacial tension (as was the case in the previous example) and that the gas bubble acts as a “lubricant” helping the surface tension driven flow. This in turn accelerates the dissolution process.

6.5.4 Interfacial Turbulence

A particular example of surface tension driven flows at gas–melt or melt–slag interfaces is the establishment of interfacial turbulence. Such interfacial turbulence, while not quantitatively understood, is of considerable practical importance because it may appreciably enhance mass transfer rates between the two phases.

When a surface active solute is transferred across an interface, unstable surface tension gradients may occur which, in turn, generate a phenomenon usually termed *interfacial turbulence*. In this context surface active agent means any solute or component variation in the concentration of which it alters the interfacial tension of the system. Good metallurgical examples would include the transfer of oxygen or sulfur across a gas–molten steel interface, etc.

A simple physical example of such interfacial turbulence is the phenomenon observed in the vaporization of ether from an unstirred aqueous solution. Talc particles sprinkled on the free surface of such a system would show abrupt local movements, indicating surface turbulence. The physical explanation of this behavior is sketched in Fig. 6.5.11, which shows a liquid in contact with a gas (or another liquid) where a solute is transferred from the liquid to the other phase.

Because of this transfer the solute concentration at the interface (C_i) will be less than the solute concentration in the bulk (C_B). The interfacial tension

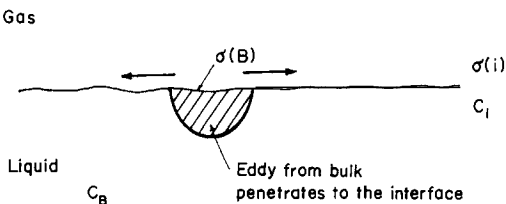


FIG. 6.5.11 The mechanism of surface tension driven interfacial turbulence.

between the liquid and the gas depends on the solute concentration. Now when an eddy travels from the bulk of the liquid to the surface there will be a sharp local concentration gradient at the point where the eddy reaches the free surface. Since the interfacial tension is concentration dependent, this in turn will produce a sharp local gradient in interfacial tension. The radial flow resulting from such interfacial tension gradients will cause the fluid to be replaced from the bulk, and hence the process is self-perpetuating.

Elegant experimental measurements of interfacial turbulence on aqueous-organic systems have been reported by numerous investigators, starting with Thompson³⁸ in 1855, Marangoni³⁹ in 1871[†] (after whom this effect has been named), and others. Elegant mathematical models of interfacial turbulence have been proposed by Sternling and Scriven⁴⁰ although it is not quite certain whether this model provides more than a qualitative representation of these phenomena.

Figure 6.5.12 shows a Schlieren photograph of interfacial turbulence induced by the stream of $\text{Fe}(\text{NO}_3)_3$ solution into a 50-mM $\text{Fe}(\text{NO}_3)_3$ solution layered above a 0.1% indium amalgam. The eddies formed are readily apparent.⁴¹

Since the interfacial tension of liquid metals and slags is quite high, surface tension driven flows can play a major role in enhancing gas-metal and slag-metal mass transfer rates. Very interesting work has been done in this field by Brimacombe and co-workers^{41,42} who demonstrated the effect of oxygen jetting onto the surface of liquid tin and liquid iron. The mechanism of the surface tension driven flow for such systems is sketched in Fig. 6.5.13.

It is seen that a metal oxide is formed where the oxygen jet impinges on the liquid metal surface. As discussed before, this metal oxide will spread if the following inequality is satisfied:

$$\sigma_{\text{Me-Gas}} > \sigma_{\text{MeO-Gas}} + \sigma_{\text{Me-MeO}} \quad (6.5.22)$$

[†] Both Thompson and Marangoni observed interfacial turbulence resulting from the preferential vaporization of alcohol from fortified wines or spirits; no doubt a most enjoyable pastime.

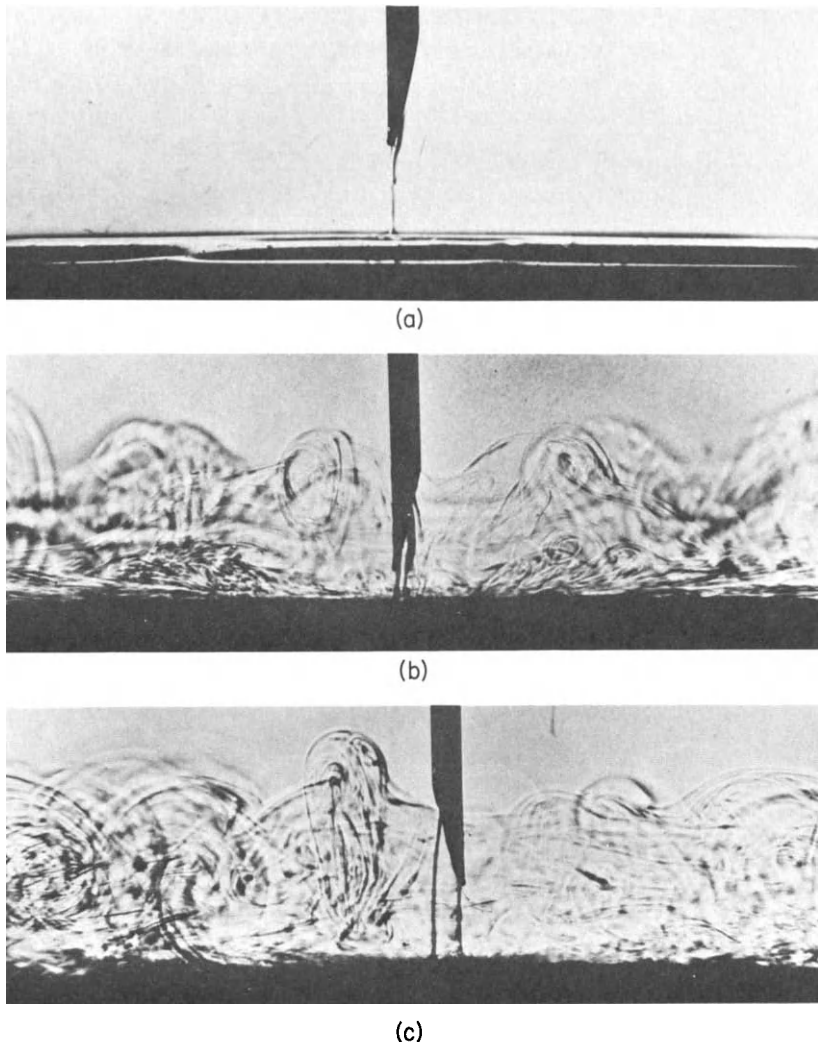


FIG. 6.5.12 Schlieren photograph of interfacial turbulence: (a) Fe^{3+} stream from syringe falling onto amalgam; (b) interface stirring due to sudden twitch; $[\text{In}]_{b_0} = 0.1 \text{ wt\%}$, $(\text{Fe}^{3+})_{b_0} = 49 \text{ mM}$, $(\text{Fe}^{3+})_s = 738 \text{ mM}$; (c) interfacial twitching with another Fe^{3+} ion solution; $[\text{In}]_b = 0.1 \text{ wt\%}$, $(\text{Fe}^{3+})_{b_0} = 49 \text{ mM}$, $(\text{Fe}^{3+})_s = 492 \text{ mM}$. After Brimacombe and Richardson.⁴²

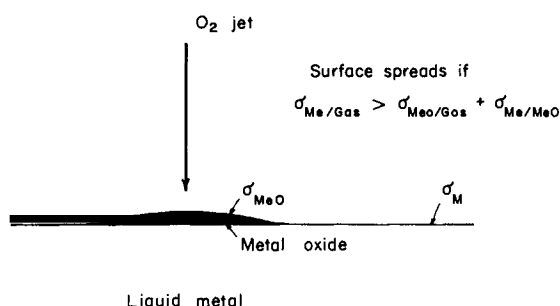


FIG. 6.5.13 The mechanism of interfacial turbulence produced when oxygen is jetted onto the surface of a metallic melt.

This phenomenon is often characterized by using a spreading coefficient α_{spr} , defined as

$$\alpha_{\text{spr}} = \sigma_{\text{Me-Gas}} - (\sigma_{\text{MeO-Gas}} + \sigma_{\text{Me-MeO}}) \quad (6.5.23)$$

α_{spr} values as high as 0.2 N/m may be found for certain metallic systems.

Figures 6.5.14 and 6.5.15 show photographs depicting interfacial turbulence observed by Brimacombe⁴² on jetting oxygen onto the surface of tin and copper melts respectively. The spreading of the hot spot, corresponding to the oxide formed, is readily apparent.

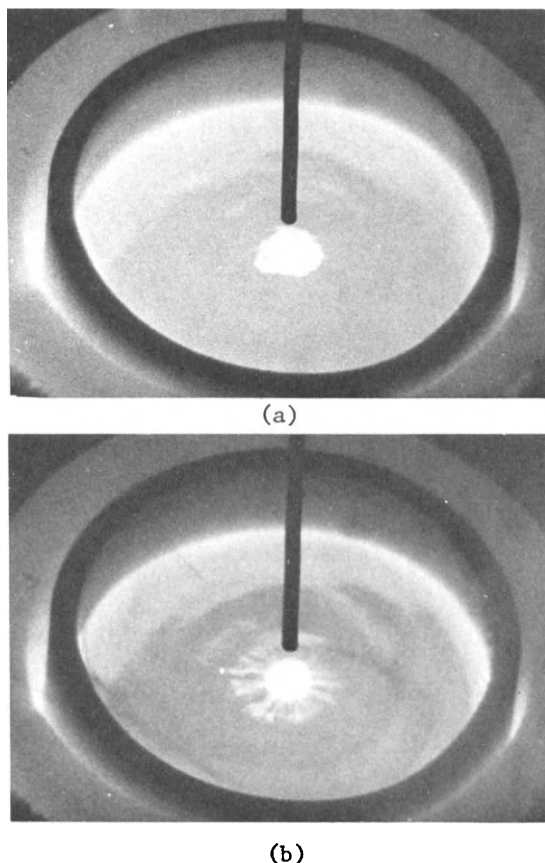


FIG. 6.5.14 Interfacial turbulence observed by Brimacombe when jetting oxygen onto a tin melt: (a) Bright oxide patch beneath oxygen delivery tube vibrates rapidly; distortion of the rim reflection on the surface is evident. (b) Two minutes later, spots of oxide move radially from center patch; the oxider appear as streaks due to the slow shutter speed (1/125 s); ripples can be seen on the surface. Magnification 1.4X. Photograph kindly supplied by Professor J. K. Brimacombe of the University of British Columbia.

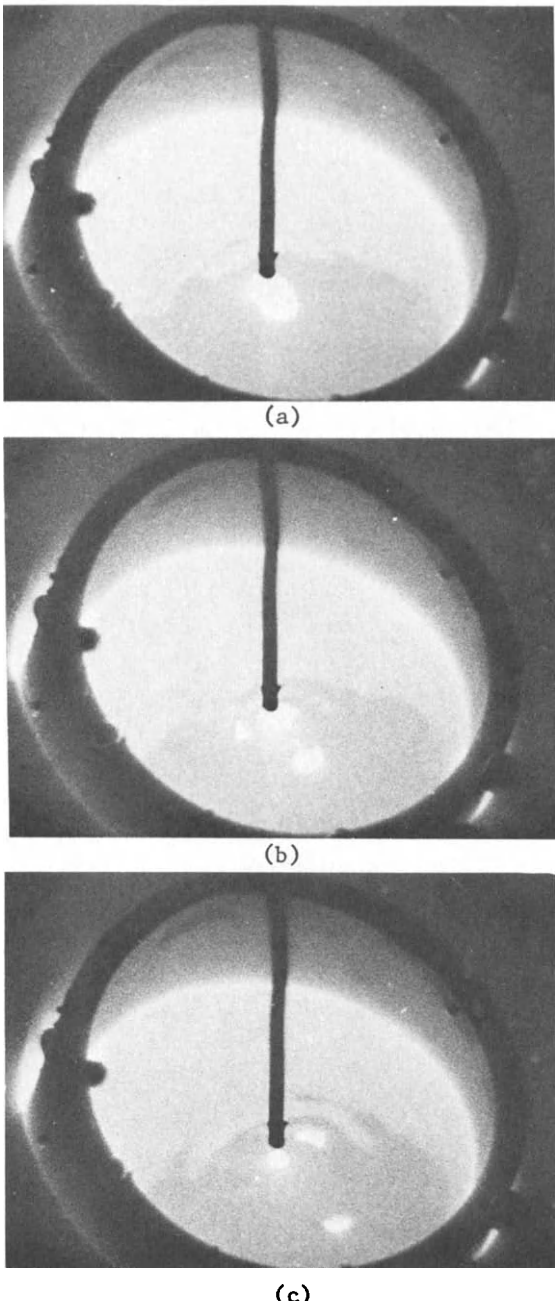


FIG. 6.5.15 Interfacial turbulence observed by Brimacombe when jetting oxygen onto copper melt: (a) 0 s; central oxide patch begins to part; rim reflection is irregular, indicating surface motion. (b) 0.0066 s; oxide patch has split into three sections moving away from center. (c) 0.013 s; one spot of oxide (lower left) has dissolved, the others continue moving outward; note the marked distortion of the rim reflection. Shutter speed 1/750 s; magnification 1.4X. Photograph kindly supplied by Professor J. K. Brimacombe of the University of British Columbia.

While the detailed mechanism of interfacial turbulence is not adequately understood, the existence and importance of these phenomena in gas-metall and slag-metall reactions has been readily demonstrated.

References

1. R. B. Bird, W. E. Stewart, and E. N. Lightfoot, "Transport Phenomena." Wiley, New York, 1960.
2. B. Gebhard "Heat Transfer," 2nd ed. McGraw-Hill, New York, 1971.
3. E. R. G. Eckert and R. M. Drake, "Analysis of Heat and Mass Transfer." McGraw-Hill, New York, 1972.
4. J. Szekely and N. J. Themelis, "Rate Phenomena in Process Metallurgy." Wiley, New York, 1971.
5. W. M. Rohenow and H. Choi, "Heat, Mass and Momentum Transfer." Prentice-Hall, Englewood Cliffs, New Jersey, 1961.
6. J. O. Hirschfelder, C. F. Curtiss, and R. B. Bird, "Molecular Theory of Gases and Liquids." Wiley, New York, 1959.
7. "Reactor Handbook," AEC, AECD-3646. U.S. Govt. Printing Office, Washington, D.C., 1955.
8. F. D. Richardson, "Physical Chemistry of Melts in Metallurgy." Academic Press, New York, 1975.
9. H. Schlichting, "Boundary Layer Theory." McGraw-Hill, New York, 1968.
10. E. Schmidt and W. Beckmann, *Forsch. Ingenieur wes.* **1**, 391 (1930).
11. E. Pohlhausen, *Z. Angen. Math. Mech.* **1**, 115 (1921).
12. S. Ostrach, *Natl. Advis Comm Aeronaut., Rep.* **1111** (1953).
13. J. Szekely and M. R. Todd, *Int. J. Heat Mass Transfer* **14**, 467 (1971).
14. M. J. Stewart and F. Weinberg, *Metall. Trans.* **3**, 333 (1972).
15. L. C. MacAuley and F. Weinberg, *Metall. Trans.* **4**, 2097 (1973).
16. J. Szekely and A. Jassal, *Metall. Trans.* **9B**, 389 (1978).
17. Cheesewright, R., *J. Heat Transfer* **90**, 1-8 (1968).
18. C. Y. Warner and V. S. Arpacı, *Int. J. Heat Mass Transfer* **11**, 1225 (1968).
19. T. Cebeci and A. Khattab, *J. Heat Transfer* **97**, 1117 (1975).
20. H. B. Mason and R. A. Seban, *Int. J. Heat Mass Transfer* **17**, 1329 (1974).
21. O. A. Plumb and L. A. Kennedy, *J. Heat Transfer* (in press).
22. W. P. Jones and B. E. Launder, *Int. J. Heat Mass Transfer* **15**, 301 (1972).
23. T. Young *Phil. Trans. Roy. Soc.* **95**, 65 (1805).
24. E. K. Rideal and J. T. Davies, "Interfacial Phenomena." Academic Press, New York, 1963.
25. R. Defay and I. Prigogine, "Surface Tension and Adsorption." Longmans, London 1966.
26. V. Levich, "Physicochemical Hydrodynamics." Prentice-Hall, Englewood Cliffs, New Jersey, 1962.
27. I. S. Sokolnikov and R. M. Redheffer, "Mathematics of Physics and Modern Engineering." McGraw-Hill, New York, 1966.
28. R. E. Collins, "Mathematical Methods for Physicists and Engineers." Van Nostrand Reinhold, Princeton, New Jersey, 1968.
29. E. Matijevich, ed., "Advances in Inter-Facial Phenomena." Academic Press, New York.
30. E. D. Hondros, in "Physicochemical Measurements in Metals Research" (R. A. Rapp, ed.), vol. 4, Part II, Chapter 8, Wiley, New York, 1970.
31. P. Kozakevich and G. Urbain, *Sci. Rev. Metall. (Paris)* **58**, 930 (1961).
32. T. B. King, in "Physical Chemistry of Melts," p. 35. Inst. Min. Metall., London, 1953.
33. G. P. Martins, Ph.D. Thesis, State University of New York at Buffalo (1969).

34. J. T. Davies, "Turbulence Phenomena," Academic Press, New York, 1972.
35. E. Vago and C. E. Smith, *Proc. Int. Congr. Glass Technol.* 7th, 1962.
36. V. Stanek and J. Szekely, *Chem. Eng. Sci.* **25**, 699 (1970).
37. D. W. Peaceman and H. H. Rachford, *J. Soc. Ind. Appl. Math.* **3**, 28 (1955).
38. J. Thomson, *Philos. Mag. [5]* **10**, 330 (1855).
39. C. Marangoni, *Ann. Phys. Chem. []* **143**, 337 (1871).
40. C. V. Sternling and L. E. Scriven, *AIChEJ.* **5** 514 (1959).
41. J. K. Brimacombe and F. D. Richardson, *Inst. Min. Metall., C Trans., Sect.* **82**, 63 (1973).
42. J. K. Brimacombe, in "Physical Chemistry of Process Metallurgy" (J. H. E. Jeffes and R. J. Tait, eds.), p. 175. Inst. Min. Metall., London, 1974.

Many metals and materials processing operations involve systems where fluids and particles are being contacted or where the objective is to separate fluid-particle mixtures. Typical examples of fluid-particle contacting operations include the iron blast furnace (slowly moving bed of solids, moving gas stream), the fluidized bed roasting of sulfide ores (both solids and gases moving), and the flotation of inclusion particles in steel processing (both the melt and the solid particles are in motion). Examples of fluid-particle separation processes include the operation of cyclones (both solids and gases moving), filtration (fixed bed of solids, moving fluid), and the operation of a thickener (solids settling, fluid essentially stationary).

The diversity of problems and of physical situations that one may encounter within the general framework of solid-fluid systems would indicate that a thorough, exhausting treatment of this subject area would require a much greater volume than can be devoted to the discussion of this topic in the present text. For this reason the treatment to be developed here will be largely introductory, but references for further reading will be given through the chapter.

It is to be noted, moreover, that the physical situations to be described in this chapter are rather more complex than the topics covered in the preceding chapters (Chapters 3-6); accordingly, in the treatment to be presented here use will be made of empirical and semiempirical relationships, of the type described in Chapter 2, dealing with macroscopic balances. In the majority of cases the governing equations used as a starting point for the statement of a problem will be empirical relationships, rather than fundamental physical laws. This factor will render the results rather less rigorous and rather less general. Nonetheless, this approach is thought to

be very useful because of the important, practical problems of considerable interest that may be tackled this way.

Regarding the organization of the chapter, the first section will be devoted to the behavior of single particles; packed bed systems will be discussed in Section 7.2, where some brief comments will be made also on filtration. Section 7.3 will be devoted to fluidized beds, with some brief comments on conveyed systems and spouted beds. Finally, sedimentation and filtration will be discussed in Section 7.4.

7.1 Single Particle Fluid Systems

7.1.1 *The Steady Motion of Particles in Fluids: The Drag Coefficient*

Although under certain circumstances it is possible to calculate the velocity profile around a regularly shaped solid particle from the solution of the Navier-Stokes equations,[†] in the general case it is perhaps more convenient to evaluate the force acting on a moving particle with the aid of an empirical drag coefficient, or friction factor.

When a particle and the fluid in which it is immersed are in motion relative to each other, a force, usually termed drag force, is exerted on the particle. This drag force F_d may be expressed as

$$F_d = C_d A_p (\rho U_b^2 / 2) \quad (7.1.1)$$

where C_d is the dimensionless drag coefficient (somewhat analogous to the friction factor defined in Chapter 2 for flow through conduits), A_p the cross-sectional area of the particle projected on a plane perpendicular to the direction of motion, and U_b the relative fluid to particle velocity in the bulk of the fluid. It has been found experimentally that the drag coefficient is a function of both the particle Reynolds number, defined as

$$N_{Re,p} = 2R_p U_b \rho / \mu \quad (7.1.2)$$

and also of the shape of the particle.

Figure 7.1.1¹ shows a plot of an experimentally determined relationship between the drag coefficient and $N_{Re,p}$.² Inspection of Fig. 7.1.1 shows that this plot may be divided into four distinct regions as follows:

- (i) $10^{-3} < N_{Re,p} < 2$. *Creeping flow or Stokes' law region.* In this region the drag coefficient is linearly proportional to the inverse of the

[†] See, for example, R. S. Brodkey, "The Phenomena of Fluid Motions," p. 104, the discussion of creeping flow around a sphere. Addison-Wesley, Reading, Massachusetts, 1967.

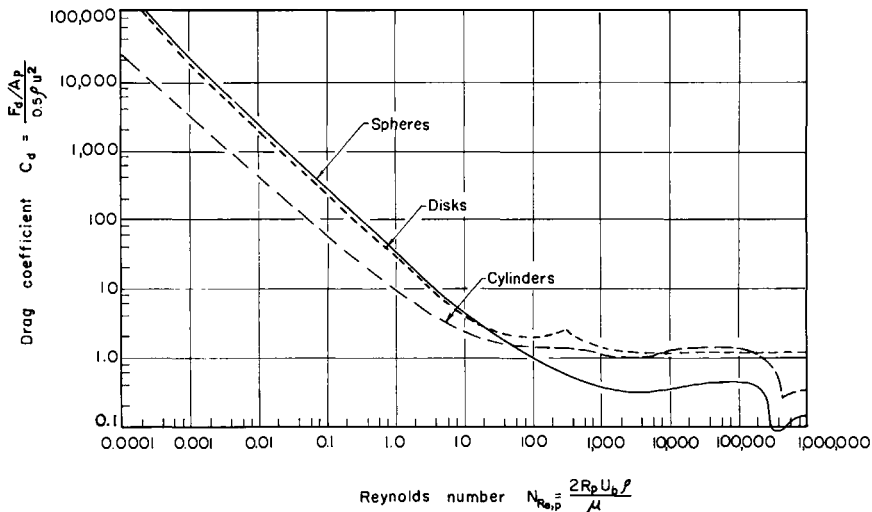


FIG. 7.1.1 Plot of the drag coefficient against the particle Reynolds number for spheres, disks, and cylinders; after Lapple and Shepherd.¹

particle Reynolds number and may be written as

$$C_d = 24/N_{Re,p} \quad (7.1.3)$$

Upon substituting for C_d from Eq. (7.1.3) in Eq. (7.1.1) and on noting that, for a spherical particle, $A_p = \pi R_p^2$, we have

$$F_d = 6\pi R_p U_b \mu \quad (7.1.4)$$

This equation is called Stokes' law, in honor of Stokes, who derived this relationship analytically from the solution of the Navier-Stokes equations in 1851.

(ii) $2 \leq N_{Re,p} \leq 500$. *Intermediate region.* In this region the experimental data may be represented by the following approximate relationship:

$$C_d \simeq 18.5/N_{Re,p}^{0.6} \quad (7.1.5)$$

(iii) $500 \leq N_{Re,p} \leq 2 \times 10^5$. *Newton's law region.* In this region the drag coefficient is approximately constant and is independent of the Reynolds number:

$$C_d \simeq 0.44 \quad (7.1.6)$$

(iv) $N_{Re,p} > 2 \times 10^5$. Finally, in this region the drag coefficient drops to a rather low value of 0.09 from which it rises slowly for higher values of the Reynolds number.

The physical picture corresponding to the dependence of the drag coefficient on the particle Reynolds number, depicted in Fig. 7.1.1, is sketched in Fig. 7.1.2. It is seen that in the Stokes' law region (a) the streamline pattern is nearly symmetrical; the streamline pattern is progressively distorted in the transition region (b), (c). In Newton's law region (d) separation occurs

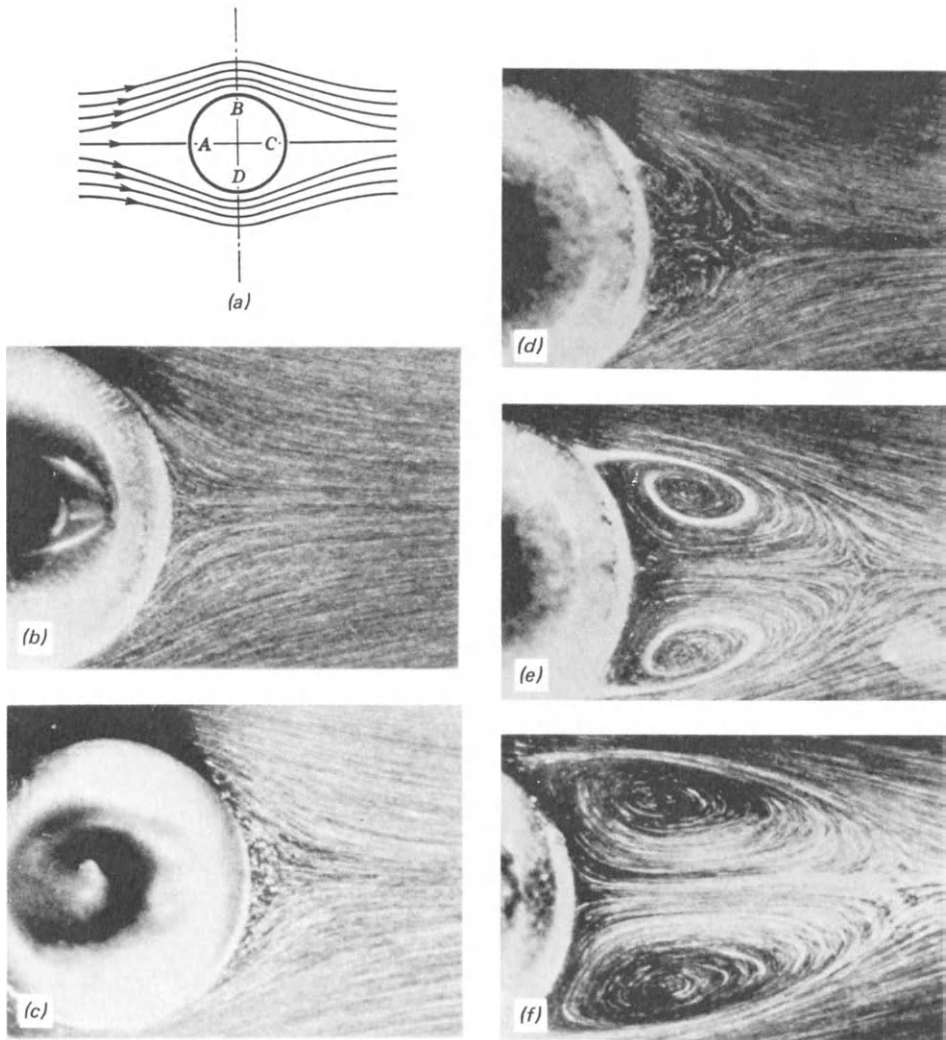


FIG. 7.1.2 Streamlines for a fluid flowing past a sphere: (a,b) symmetrical streamline pattern at low Reynolds numbers, (c) distortion of the streamline pattern at moderate Reynolds number, (d) separation in the Newton's law region, (e,f) separation of the boundary layer moved forward at very high Reynolds numbers.

with the formation of eddies at the rear of the sphere. Finally, in region (e, f) the point of separation is moved forward with a corresponding reduction in the drag force exerted on the particle.

THE TERMINAL FALLING VELOCITY

An important use of the expressions developed for representing the drag force acting on particles is the calculation of the terminal falling (or rising) velocity.

If a particle falls (dust in air) or rises (inclusions in molten steel) in a fluid it will accelerate until the force of gravity (or some other body force field) producing this motion is exactly balanced by the forces that resist this motion. For a stationary fluid from this point onward the particle will move at a constant speed, termed the terminal falling (or rising) velocity.

The value of this terminal velocity is readily obtained by equating the body force (usually the force of gravity) which acts on the particle to the drag force. Thus for the creeping flow (Stokes' law) region we have

$$F_d = \left(\frac{4}{3}\pi\right)R_p^3(\rho_p - \rho)g = 6\pi R_p U_t \mu \quad (7.1.7)$$

i.e.,

$$U_t = \frac{2R_p^2}{9g\mu} (\rho_p - \rho)g \quad (7.1.8)$$

where ρ_p is the density of the solid particle.

The equivalent expression for Newton's law region (iii) is given as

$$U_t = [6R_p g(\rho_p - \rho)/\rho]^{1/2} \quad (7.1.9)$$

Similar expressions may be derived for the other regions. It has to be stressed to the reader that the equations developed here are limited in validity:

- (a) to spherical solid particles,
- (b) to steady-state motion,
- (c) to particle movement in a stagnant fluid or in a fluid where turbulence is absent and the velocity field is uniform,
- (d) to single particles moving a long distance from solid surfaces.

The constraints listed under (a)–(d) above may appear to be unduly restrictive for the simple equations (7.1.8) or (7.1.9) to have any practical value.

In reality these simple relationships have been used quite extensively for estimating the behavior of a broad range of systems. In some cases these convenient equations are applicable within the desired degree of accuracy; in other situations their use may be highly misleading.

Let us first illustrate the application of Eq. (7.1.8) on a simple example and then proceed to discuss the implications of the constraints listed under (a)–(d) above.

Example 7.1.1 Calculate the terminal rising velocity of a 20- μm diameter solid inclusion particle in a stagnant melt of molten steel.

DATA Density of inclusion particle, $2.7 \times 10^3 \text{ kg/m}^3$; density of molten steel, $7.1 \times 10^3 \text{ kg/m}^3$; viscosity of molten steel, $5.5 \times 10^{-3} \text{ kg/m s (Ns/m}^2)$. The inclusion particle may be taken as spherical.

SOLUTION First of all we shall try using Eq. (7.1.8), i.e.,

$$U_t = \frac{2 \times 10^{-10}}{9 \times 5.5 \times 10^{-3}} (2.7 - 7.1) \times 10^3 \times 9.81 = 1.74 \times 10^{-4} \text{ m/s}$$

Let us check that Eq. (7.1.8) is applicable by evaluating the particle Reynolds number,

$$N_{Re,p} = \frac{2 \times 2.0 \times 10^{-5} \times 1.74 \times 10^{-4} \times 7.1 \times 10^3}{5.5 \times 10^{-3}} \simeq 9 \times 10^{-3}$$

The system is in the creeping flow region; thus, Eq. (7.1.8) was applicable.

Let us now comment on the consequences of the constraints placed on the applicability of the simple expressions developed for the terminal falling velocity.

(a) Spherical, solid particles

It has been suggested³¹ that the previously developed expressions for the drag coefficients C_d may be used for nonspherical particles if a correction factor is employed. This correction factor does not differ much from unity if the major axes of the particle are approximately of the same magnitude. The equations developed here are valid for solid particles only. Very small gas bubbles or liquid droplets would tend to behave like solids because surface tension effects tend to make their outer surface rigid. For larger bubbles or drops, internal circulation and possibly deformation would render the predictions for the terminal rising velocities given in this section inappropriate. These problems will be discussed in detail in Chapter 8.

(b) Unsteady motion of particles

When a solid particle is accelerated or decelerated during its motion in a fluid, the statement of Newton's second law (mass times acceleration

equals the sum of the forces acting on the particle) takes the following form⁴:

$$\begin{aligned} \frac{4}{3}\pi R_p^3 \rho_p \frac{dU}{dt} &= +\frac{4}{3}\pi R_p^3 (\rho_p - \rho)g &+ -\frac{C_d \pi R_p^2}{2} \rho U |U| \\ &\quad \text{(mass \times acceleration)} & \quad \text{(force due to gravity)} & \quad \text{(drag force)} \\ -\tilde{C}_A \frac{4}{3}\pi R_p^3 \rho \frac{dU}{dt} &- C_H R_p^2 (\pi \rho \mu)^{1/2} \int_0^t \frac{dU}{d\tau} \frac{d\tau}{\sqrt{t-\tau}} \\ &\quad \text{(added mass effect)} & \quad \text{(history term)} \end{aligned} \quad (7.1.10)$$

Some comment should be made regarding the physical significance of the terms appearing in Eq. (7.1.10). The term on the left-hand side is mass times acceleration. The first term on the right-hand side is the force due to gravity and the second term is the drag force which will always oppose the direction of motion; hence, the absolute value sign on one of the velocities. The third term corresponds to the “added mass,” which allows for the fact that not only the particle has to be accelerated but also a portion of the fluid which adheres to the particle. The value of the added mass coefficient \tilde{C}_A has been taken as $\frac{1}{2}^{5-7}$; alternatively, it has been assumed to depend on the particle velocity and on the acceleration.

The last term on the right-hand side is designated the “history term” through the use of which an attempt is made to allow for the dependence of the instantaneous drag on the state of development of the fluid motion around the sphere. In the classical literature C_H was assigned a value of 6.0 while in more recent work C_H was allowed to vary with the velocity and the acceleration. It is to be noted that if we were to neglect all but the second and the third terms in Eq. (7.1.10) the problem would reduce to the evaluation of the steady-state, terminal falling velocity.

In many practical situations the acceleration effects described above may be safely neglected because by far the major portion of the path traveled by the particle will be at the steady, terminal velocity. Examples of such cases would include the settling of solid particles in quiescent liquids, where the path to be traveled is many hundred or thousand times larger than the particle diameter. Other examples would include the free settling of dust particles in air and in some gravitational settling apparatus. Acceleration effects could be safely ignored also in the flotation of inclusion particles, although there are other factors that would have to be considered in such case. The relative importance of the period of acceleration or deceleration may be assessed quite readily by solving the simple, first-order differential equation consisting of the first three terms in Eq. (7.1.10). Many problems of this type are discussed in Coulson and Richardson.³

There exists, however, an important group of problems where the trajectory of a solid particle in a fluid is dominated by the acceleration effects described above.

These problems are of great practical importance in the addition of deoxidants to molten steel baths. Most deoxidants, such as aluminum or some ferroalloys, have a much lower density than molten steel, so when deoxidant particles are dropped into ladles or other metal pools, these are first decelerated and then accelerated during their rise to the metal surface. While this trajectory of deoxidant particles is greatly complicated by other factors, such as partial dissolution, heat generation, and the bulk motion of the melt, the deceleration followed by the change in the direction of the velocity and subsequent acceleration of a lighter particle dropped into a heavy fluid remains an essential component of the problem. These problems, which are of considerable practical interest in the effective contacting of deoxidants with steel melts, have been studied by Guthrie and co-workers.^{8,9}

In a series of elegant model experiments these authors determined the trajectories of wood spheres, dropped into vessels containing water. Attempts were made to interpret the measurements with the aid of the numerically

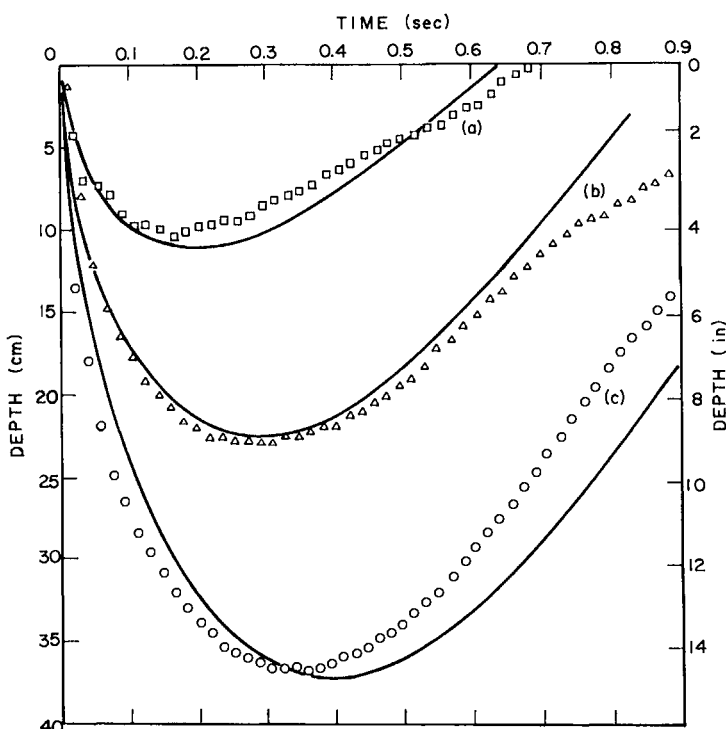


FIG. 7.1.3 Comparison of the measured and the computed trajectories of wood spheres dropped into water; after Guthrie *et al.*⁹ Notation: (a) $d_p = 0.0107 \text{ m}$, $\rho_p = 716 \text{ kg/m}^3$, $U_o = 7.74 \text{ m/s}$; (b) $d_p = 0.0269 \text{ m}$, $\rho_p = 711 \text{ kg/m}^3$, $U_o = 8.09 \text{ m/s}$; (c) $d_p = 0.0488 \text{ m}$, $\rho_p = 727 \text{ kg/m}^3$, $U_o = 8.21 \text{ m/s}$. Original drawing kindly provided by Professor R. I. L. Guthrie of McGill University.

integrated Eq. (7.1.10), but it was found that equally satisfactory, or even better, results could be obtained if the history term were neglected. It was found, however, that it was essential to retain the "added mass effect," i.e., the third term on the right-hand side of Eq. (7.1.10). Figure 7.1.3 shows a typical set of experimental measurements, denoted by the discrete data points, together with predictions based on Eq. (7.1.10) (neglecting the history term), designated by the continuous curves. It is seen that the agreement between predictions and measurements is quite reasonable, especially regarding the maximum depth of penetration, which is a factor of practical interest.

(c) The effect of motion in the bulk of the fluid

The expressions developed for the terminal falling (or rising) velocity are restricted either to stagnant fluids or to systems where the flow is laminar and the velocity field is uniform. Under these conditions the actual instantaneous velocity of the particle with respect to a fixed frame of reference has to be calculated by adding vectorially the fluid velocity and the terminal velocity of the particle. Problems of this type have been discussed by Stanek and Szekely,¹⁰ and Szekely¹¹ and Asai in connection with the movement of inclusion particles in solidifying melts. If the particle moves in a turbulent fluid flow field (as is often the case for the movement of inclusions in stirred melts) the situation is much more complicated.

In a macroscopic sense the actual drag force acting on the particle will depend on the turbulence level and also on the particle Reynolds number. A good review of published data on this problem has been prepared by Torobin and Gauvin.¹²

In the microscopic sense the interaction between the particle and the turbulent flow field will depend on the relative magnitude of the particle and the eddies in the system. If the particle is large, compared to the scale of the turbulence, its motion is not greatly affected by the turbulent fluctuations; at the other extreme, when the particle is small, compared to the size of the eddies, it will act as a tracer, following the detailed motion of the fluid.¹³

The situation is rather more complicated in the intermediate case. Some useful introductory comments dealing with these problems may be found in the text by Brodkey,⁴ which also contains numerous references.

(d) The effect of solid surfaces

The presence of solid surfaces in the vicinity of the moving particles may markedly affect the drag force. An elegant and detailed treatise of these problems is available in the text by Happel and Brenner.¹⁴ In essence the movement of a particle in the vicinity of solid surfaces may be affected two ways. One of these is due to the fact that the velocity gradients may cause an

imbalance in the forces acting on the particle which results in rotation of the particle. The other effect is that on approaching a solid surface, as sketched in Fig. 7.1.4, fluid has to be displaced. The viscous resistance to flow, indicated on the sketch, will cause an apparent increase in the drag force.

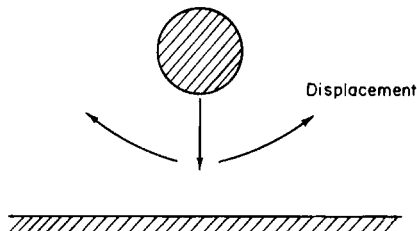


FIG. 7.1.4 Displacement of the fluid as a solid particle approaches a solid surface.

Happel and Brenner¹⁴ suggested the following relationship for representing this increase drag force:

$$F_d/F_{d,\infty} = [1 - \tilde{k}(F_\infty/6\pi\mu Ul)]^{-1/2} \quad (7.1.11)$$

where F_d and $F_{d,\infty}$ are the drag force and the drag force a large distance from the surface; \tilde{k} a constant 0.5–1.0, depending on geometry; and l is the distance between the center of the particle and the wall. This increased drag force as a particle approaches a wall (or when a moving surface approaches a particle) is of practical interest in problems dealing with the entrapment of inclusion particles by advancing solidification fronts.^{15,16}

Notwithstanding the complicating factors mentioned here, the simple expressions for the drag force and for the terminal falling velocity derived earlier for idealized conditions are helpful for estimating the behavior of solid particles in more complex situations.

Let us conclude this section by illustrating the application of the simple expressions for the drag force for calculating the separation characteristics of a gas–solid cyclone.

THE OPERATION OF A CYCLONE

Figure 7.1.5 shows a sketch of a cyclone separator. It is seen that the gas is introduced into a cylindrical vessel tangentially (at a velocity of the order of 30–50 m/s), and the cleaned gas is taken off through a central outlet at the top. The solids are thrown outwards (due to the centrifugal force) against the walls of the vessel and are then collected at the central base of the unit. Experimental measurements on cyclones have shown that the gas moves downwards in a spiraling flow pattern and then rises to leave through the central outlet. The tangential component of the velocity was found to predominate throughout the system, except for a central core, which has a diameter, some 0.4 times that of the outlet pipe.

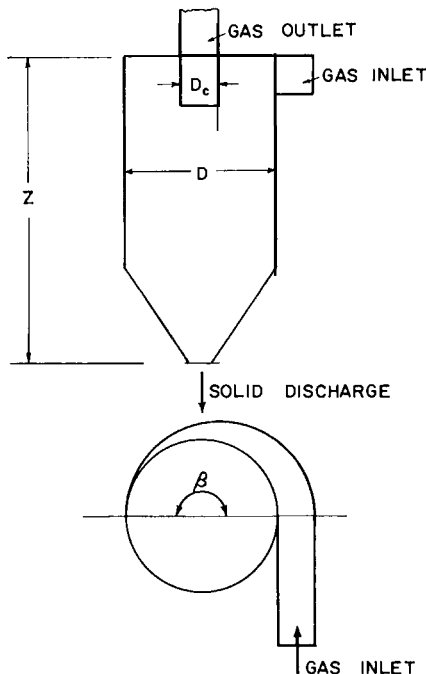


FIG. 7.1.5 A cyclone separator.

A particle in the cyclone is subjected to two opposing forces in the radial direction; the centrifugal force tends to throw the particle toward the wall, while the drag force acting on the particle will tend to carry the particle through the outlet. Both these forces depend on the radius of rotation and on the size of the particles; thus, particles of different size will tend to rotate at different radii. As the outward force on the particles increases with an increasing tangential velocity and the inward (drag) force increases with the radial components, the cyclone separator should be so designed as to maximize the tangential component and minimize the radial component. This is usually accomplished by introducing the gas stream with a high tangential velocity and by making the height of the separator large.[†]

For a spherical particle of diameter R_p , rotating in the cyclone at a radius r , the centrifugal acceleration is U_{tg}^2/r , where U_{tg} is the tangential velocity component; here we have assumed tacitly that there is no slip between the particle and the gas stream.

The inward drag of the fluid on the particle produces an acceleration of

$$6\pi R_p \mu U_r / \frac{4}{3}\pi R_p^3 \rho_p = \frac{9\mu}{2R_p^2 \rho_p} U_r \quad (7.1.12)$$

[†] The present discussion is limited to gas cyclones, such that $\rho_p \gg \rho$.

where u_r is the radial velocity component and we have assumed that the particle is small enough to be in the Stokes law region.

Let us proceed by expressing the properties of the fluid and of the particles in terms of the terminal falling velocity, previously defined by Eq. (7.1.8), for the Stokes law region, i.e.,

$$U_t = \frac{2R_p^2}{9\mu} \rho_p g \quad (7.1.12a)$$

where we assumed that $\rho_p \gg \rho$, which is reasonable for gas-solid systems.

The radius at which the particle will rotate may be calculated by equating the inward and the outward acting forces; thus, we have

$$\frac{U_{tg}^2/r}{(\text{outward acceleration})} = \frac{(U_r/U_t)g}{(\text{inward acceleration})} \quad (7.1.13)$$

where the mass of the particle has been canceled on both sides of Eq. (7.1.13) and, on the right-hand side, the combined proper y values were represented through the use of the terminal falling velocity.

On rearranging we have

$$U_t = (U_r/U_{tg}^2)rg \quad (7.1.14)$$

Thus the larger the terminal falling velocity of the particle (i.e., large heavy particles) the larger its radius of rotation and thus the easier the separation.

If we assume that a particle will be separated, provided it tends to rotate outside the central core of radius $0.4R_0$, the terminal falling velocity of the smallest particle which will be retained may be found by substituting $r = 0.4R_0$ in Eq. (7.1.14), i.e.,

$$U_t = (U_r/U_{tg}^2)(0.4R_0)g \quad (7.1.15)$$

where R_0 is the radius of the offtake pipe.

The radial velocity U_r may be estimated from

$$U_r \simeq U_{tg0} A_i / 2\pi r Z \quad (7.1.16)$$

where U_{tg0} is the inlet velocity in the inlet duct, A_i the cross-sectional area of the inlet duct, and Z is the height of the cyclone.

Moreover, the tangential velocity may be estimated from the following semiempirical relationship:

$$U_{tg} = U_{tg0}(R_c/r)^{1/2} \quad (7.1.17)$$

Upon combining Eqs. (7.1.14)–(7.1.17) we finally obtain the desired relationship between the terminal falling velocity of the smallest particle, which is

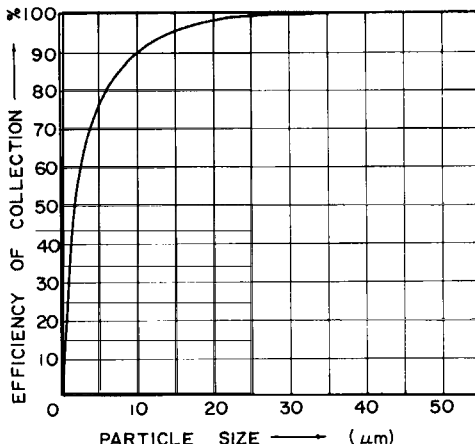


FIG. 7.1.6 A typical cyclone efficiency curve.

just retained by the cyclone, and the operating characteristics of the cyclone system:

$$U_t = 0.2A_iR_0g/\pi ZR_c U_{tg0} \quad (7.1.18)$$

where R_0 is the radius of the cyclone. Written in terms of the particle dimension we have

$$R_p = \left(\frac{0.9A_iR_0\mu}{\pi ZR_c\rho_p U_{tg0}} \right)^{1/2} \quad (7.1.19)$$

For properly designed industrial cyclones this cutoff size is usually of the order of 5–10 μm .

It is noted that for practical conditions the minimum size that may be separated by cyclones is not provided by a step-function type relationship but rather the cyclone efficiency is a smooth curve, as illustrated in Fig. 7.1.6. Some of the smaller particles may be retained by the system because of agglomeration, while particles larger than the cutoff radius could be lost because of turbulence effects or due to their bouncing off the walls. A good, practical discussion of the design criteria for cyclones may be found in Ter Linden¹⁷ and Stairmand.¹⁸

7.2 Flow through Packed Beds

Systems where a packed bed of solids is contacted with a moving gas stream are quite common in metallurgical practice. While one may wish to draw a distinction between situations, where the solids are fixed and are thus processed in a batchwise arrangement, or are moving slowly and are processed continuously, the rate of movement of the solids is always much

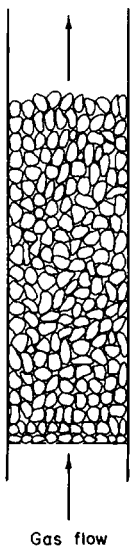


FIG. 7.2.1 Sketch of a packed bed.

slower than that of the gas and the gas flow is usually unaffected by the solid movement. It follows that the actual gas flow through such systems does not depend much on whether the solids are moving or not, so these two cases may be treated together.[†]

7.2.1 Fluid Flow through Uniform Packed Beds

Perhaps the simplest way that a packed bed may be visualized is to consider a vertical tube, filled with particles of uniform size, such as sketched in Fig. 7.2.1. Such an assembly of particles represents a rather complex geometry, and while a number of interesting studies have been made of the flow field in packed bed assemblies^{20–22} for most practical problems the packed bed has to be treated as a continuum and the relationship between pressure and flow rate has to be determined with the aid of empirical correlations. A uniformly packed bed of particles is usually characterized by the following parameters: the void fraction, the particle size, and the particle shape factor. The void fraction ϵ_v is defined as

$$\epsilon_v = \frac{\text{total volume of bed} - \text{volume of solid particles}}{\text{total volume of bed}} \quad (7.2.1)$$

The size of a nonspherical particle is usually expressed in terms of the volume equivalent diameter d_p , defined as the diameter of a sphere which

[†] The downward movement of the solids in the iron blast furnace does cause a rearrangement of solid feed layers, which in turn affects the gas distribution. This problem has been discussed by Poveromo *et al.*¹⁹

has the same volume as the particle, together with the particle shape factor ϕ_s , defined as

$$\phi_s = \frac{\text{surface area of sphere of equal volume of the particle}}{\text{surface area of particle}} \quad (7.2.2)$$

Clearly, $\phi_s = 1$ for spheres. Typical shape factors for naturally occurring materials would range from about 0.5 to 0.9.²³ The void fraction of packed beds, containing uniformly sized particles, tends to range from about 0.3 to 0.6.

Of the numerous correlations proposed for relating the pressure drop to the gas flow rate the Ergun equation²⁴ is perhaps the most widely accepted[†]:

$$\frac{\Delta P}{Z} = 150 \frac{(1 - \epsilon_v)^2}{\epsilon_v^3} \frac{\mu U_0}{(\phi_s d_p)^2} + 1.75 \frac{1 - \epsilon_v}{\epsilon_v^3} \frac{\rho U_0^2}{\phi d_p} \quad (7.2.3)$$

where ΔP is the pressure drop, Z the bed depth, and U_0 is the fluid velocity through the empty column. Before proceeding further, let us illustrate the use of the Ergun equation by working a simple example:

Example 7.2.1 Calculate the pressure drop for a laboratory scale packed bed, through which air is being passed, for the following conditions:

column diameter,	0.2 m	ϵ_v ,	0.45
column height,	1.5 m	volumetric gas flow rate,	0.04 m ³ /s
particle diameter,	0.01 m	viscosity of air,	1.85×10^{-5} kg/ms
ϕ_s ,	0.85	density of air,	1.21 kg/m ³

SOLUTION The linear velocity U_0 is given as

$$\frac{0.04}{(0.2)^2 3.14/4} = 1.27 \text{ m/s}$$

Then using Eq. (7.2.3) we have

$$\begin{aligned} \Delta P = 1.5 & \left[150 \frac{(1 - 0.45)^2}{(0.45)^3} \times \frac{1.85 \times 10^{-5} \times 1.27}{(0.85 \times 0.01)^2} \right. \\ & \left. + 1.75 \frac{1 - 0.45}{(0.45)^3} \times \frac{1.21 \times (1.27)^2}{0.85 \times 0.01} \right] \end{aligned}$$

i.e.,

$$\Delta P = 1.5 [243 + 2430] = 3.99 \times 10^3 \text{ N/m}^2$$

[†] Recent work by Gauvin and Katta has indicated that the Ergun equation is not appropriate for systems that contain particles of low sphericity.

It is seen, moreover, that for this example the inertial term, i.e., the second term in the Ergun equation, predominates.

Inspection of Eq. (7.2.3) shows that at low fluid velocities the viscous term predominates, whereas at high fluid velocities the pressure drop is proportional to the square of the fluid velocity and thus the inertial term is dominant. It has been suggested that this domination by the inertial term is due to the sudden expansion of the gas as it passes through the constrictions produced by the packed particles, rather than due to the onset of turbulence in the larger channels.²⁵

Most systems of practical interest are composed of mixtures of particles, rather than having a uniform matrix. When there exists a range of particle sizes, but these are uniformly mixed, the use of the surface area mean diameter is recommended. The surface area mean diameter \bar{d}_p is defined as follows:

$$\bar{d}_p = \frac{1}{\sum \frac{X_n'}{d_{p,n}}} \quad (7.2.4)$$

Here X_n' is the fraction of solids, which have a diameter $d_{p,n}$. It is seen from the form of Eq. (7.2.4) that in the averaging procedure the weighting is by the specific surface.

A major problem in relating the pressure drop to flow rate in case of particle mixtures is the difficulty in predicting the void fraction.

In his now classical work Furnas²⁶ has shown that the void fraction in a two-component mixture of solid particles may be markedly affected by both the ratio of the particle sizes and by the relative proportion of the components. This behavior is illustrated in Fig. 7.2.2, where it is seen that a void fraction as low as 0.23 may be obtained under certain circumstances. The physical explanation for this behavior is readily made by considering that if there is a large disparity in size the small particles may partially fill the voids within the matrix of the large particles.

This behavior has two important practical consequences: One of these is the fact that it is very difficult to predict, from first principles, the void fraction of systems composed of mixtures of particles; thus, the experimental determination of this parameter is highly desirable. (The void fraction of packed beds containing closely sized particles too depends on the mode of packing, thus on the manner in which the column was filled.)

The second point to be made is that in the operation of a system composed of mixtures of particles, the size and shape of the individual components may play a major role in determining the overall pressure drop—even for systems having identical mean particle sizes. Problems of this type are well known in blast furnace practice and have gained attention recently in connection with the use of formed coke in blast furnaces, because formed coke tends to be smaller and more regularly shaped than conventional coke.

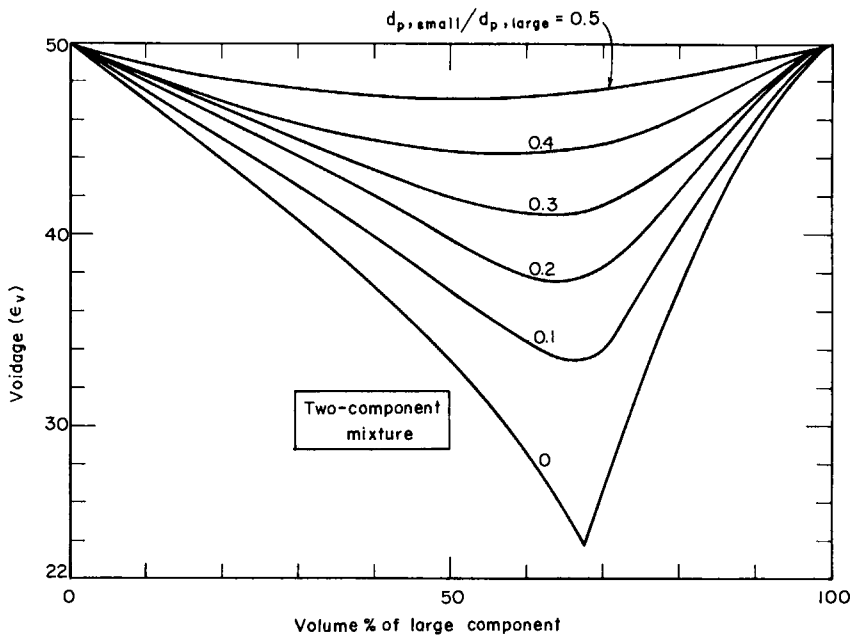


FIG. 7.2.2 The void fraction in a packed bed, composed of two sizes of spheres as affected by the particle size ratio and the composition; after Furnas,³⁰ as quoted by Zenz and Othmer.²⁶

Another important problem affecting the flow resistance of blast furnace burdens is provided by the fact that the distribution of the solid charge is not uniform, but there exist distinct layers of coke, sinter, and pellets, such as sketched in Fig. 7.2.3. It has been shown, as a result of recent work by Schultz and Abel²⁷ and Szekely and Propster,²⁸ that the interfacial region between the two adjacent layers exhibits a local minimum in porosity, similarly to that seen in Fig. 7.2.2, and hence may offer an appreciable resistance to flow. This problem is of considerable importance in the optimization of blast furnace burdens.

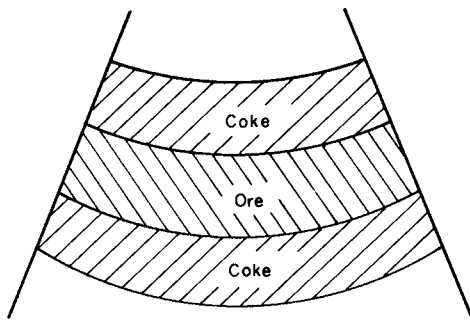


FIG. 7.2.3 Coke and ore layers in the stack of a blast furnace.

Strictly speaking, the Ergun equation is valid for uniform flow, for isothermal conditions, and for incompressible fluids. As noted in Chapter 2, in this context a fluid may be regarded as incompressible, when the pressure drop across the bed is small compared to the absolute pressure. In the iron blast furnace, in sinterbeds, and in blast furnace stoves conditions are strongly nonisothermal; moreover, in the iron blast furnace the overall pressure drop is quite significant, compared with the absolute environmental pressure. In applying the Ergun equation to these systems we may either write Eq. (7.2.3) in a differential form and then integrate the resultant expressions over the appropriate temperature path²⁹ or, alternatively, the property values have to be evaluated at some mean pressure and temperature.

7.2.2 Nonuniform Flow of Fluids through Packed Beds

In many real, industrial packed bed systems it is unrealistic to assume a one-dimensional flow field (or a spatially uniform resistance to flow) which was implicit in the statement of the Ergun equation. There may be numerous reasons for the existence of spatially nonuniform flow fields in real, industrial packed bed systems; some of these are enumerated in the following:

- (a) Flow maldistribution may occur as a result of nonuniform packing, e.g., the segregation of particles of different size on loading, the development of localized regions of low porosity, etc. It is to be noted that some preferential flow will necessarily occur in the vicinity of the walls of packed beds, even if these are packed with particles of uniform size.³⁰
- (b) Flow maldistribution may occur as a result of lateral variations in the bed temperature, because as seen from the form of the Ergun equation the temperature of the system does affect the resistance to flow.
- (c) Finally, uneven flow will occur when the gas is supplied to the system in a spatially nonuniform manner, e.g., there are side streams, rather than the gas being introduced only through a distributor, as sketched in Fig. 7.2.1.

Formulations for representing the three-dimensional flow of fluids through packed beds have been developed by Radestock and Jeschar³¹ and by Stanek and Szekely.³²

For incompressible fluids the three-dimensional, vectorial form of the Ergun equation may be written as[†]

$$-\nabla P = \mathbf{u}(f_1 + f_2 u) \quad (7.2.5)$$

[†] The possible pitfalls involved in writing simply the components of Eq. (7.2.5), e.g., $\frac{\partial p}{\partial x} = u_x(f_1 + f_2|u_x|)$, etc., instead of Eq. (7.2.5), have been discussed by Stanek and Szekely.³²

where

$$f_1 = \frac{150\mu(1 - \epsilon_v)^2}{(\phi_s d_p)^2 \epsilon_v^3} \quad (7.2.6)$$

and

$$f_2 = \frac{1.75\rho(1 - \epsilon_v)}{\phi_s d_p \epsilon_v^3} \quad (7.2.7)$$

are the flow resistance parameters in the Ergun equation. If we consider incompressible fluids, using the $\nabla \times$ or curl operator on both sides of Eq. (7.2.5), the pressure term may be eliminated and we obtain

$$\nabla \times \mathbf{u} - \mathbf{u} \times \nabla [\ln(f_1 + f_2 u)] = 0 \quad (7.2.8)$$

which is a vector equation containing \mathbf{u} , the velocity vector as the only variable. In addition the equation of continuity has to be satisfied also:

$$\nabla \cdot \mathbf{u} = 0 \quad (7.2.9)$$

Upon finding the velocity field, through the solution of Eq. (7.2.8) and (7.2.9) the pressure distribution may be evaluated from

$$\nabla^2 p = -\mathbf{u} \cdot \nabla (f_1 + f_2 u) \quad (7.2.10)$$

The appropriate forms of these equations for compressible fluids is available in Stanek and Szekely.³³ Perhaps the most important practical application of these expressions would be for cylindrical systems with an axial symmetry and where the particle Reynolds number is large enough ($N_{Re,p} > 150$) so that the viscous term may be neglected in the Ergun equation, i.e., $f_1 \approx 0$.

Under these conditions, Eq. (7.2.8) may be written in terms of the stream function as

$$\begin{aligned} \frac{\partial^2 \psi}{\partial r^2} \left[2 \left(\frac{\partial \psi}{\partial r} \right)^2 + \left(\frac{\partial \psi}{\partial z} \right)^2 \right] + \frac{\partial^2 \psi}{\partial z^2} \left[2 \left(\frac{\partial \psi}{\partial z} \right)^2 + \left(\frac{\partial \psi}{\partial r} \right)^2 \right] + \left[\left(\frac{\partial \psi}{\partial r} \right)^2 + \left(\frac{\partial \psi}{\partial z} \right)^2 \right] \\ \times \left[\frac{\partial \psi}{\partial z} \frac{\partial \ln f_2}{\partial z} + \frac{\partial \psi}{\partial r} \left(\frac{\partial \ln f_2}{\partial r} - \frac{2}{r} \right) \right] + 2 \frac{\partial^2 \psi}{\partial r \partial z} \left(\frac{\partial \psi}{\partial r} \right) \left(\frac{\partial \psi}{\partial z} \right) = 0 \end{aligned} \quad (7.2.11)$$

where

$$u_z = -\frac{1}{r} \frac{\partial \psi}{\partial r} \quad (7.2.12)$$

and

$$u_r = \frac{1}{r} \frac{\partial \psi}{\partial z} \quad (7.2.13)$$

We note that the formulation allows f_2 , the resistance parameter, to be spatially variable—in an axisymmetric manner.

The boundary conditions for Eq. (7.2.11) are quite straightforward; the velocity has to be zero at the walls, which means that the stream function has to be constant. Moreover, symmetry has to be observed about the axis of the cylindrical vessel.

The only problem is posed by specifying the conditions at the inlet and at the exit. As shown by experimental work³⁴ it is reasonable to consider that the pressure is constant over both the inlet and the exit surfaces, which enables us to write

$$\frac{\partial \psi}{\partial z} = 0 \quad (7.2.14)$$

at the inlet and at the exit. The predictions based on Eqs. (7.2.11)–(7.2.14) or their equivalent forms have been tested experimentally and, as shown in Figs. 7.2.4 and 7.2.5, the agreement between measurements and predictions is

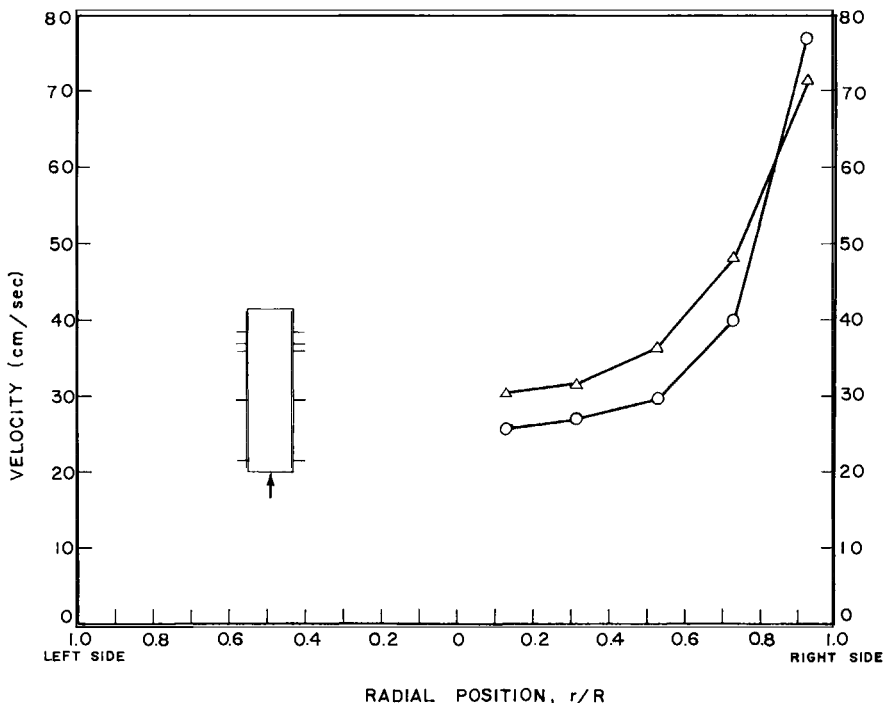


FIG. 7.2.4 Comparison of the predicted and the experimentally measured outlet velocities for parallel flow through a uniformly packed bed of glass spheres; after Szekely and Poveromo.³⁴
 \triangle Predicted. \circ Experimental.

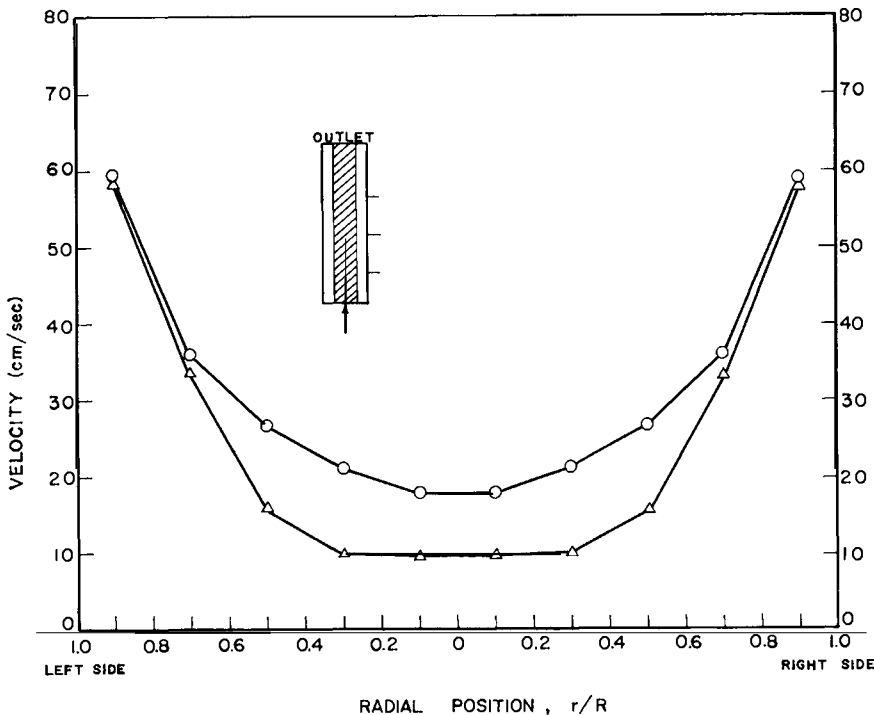


FIG. 7.2.5 Comparison between the experimentally measured and the theoretically predicted outlet velocity profiles for a packed bed, the inner core of which was packed with 1-mm glass spheres, while the outer shell contained 3-mm glass spheres, after Szekely and Poveromo.³⁴ △ Predicted. ○ Experimental.

quite reasonable. It is to be noted that Fig. 7.2.4 depicts the behavior of a uniformly packed bed and the preferential flow near the wall is quite apparent here. This preferential flow is associated with the existence of a high-porosity region; the existence of such porosity distribution has been reported by Benanati and Brosilow³⁵ and their data have been in the computation of the void fraction distribution in the theoretical curves.

The preferential flow near the walls is thought to be particularly important when the ratio: (bed diameter)/(particle diameter) is less than about 50.

The measurements shown in Figs. 7.2.4 and 7.2.5 provide a direct verification of the use of the vectorial form of the empirical Ergun equation for representing nonuniform flows in packed beds. It should be noted, however, that the Ergun equation is a macroscopic relationship. It follows that the use of this expression, or the use of relationships derived from it, become questionable when applied to distances that are comparable to the size of the particles that make up the packing.

7.2.3 The Countercurrent Flow of Gases and Liquids through Packed Beds

The countercurrent flow of liquids and gases through packed beds is very commonly encountered in the chemical industry in connection with the operation of gas absorption and distillation processes. This physical situation occurs less frequently in metals processing operations; nonetheless, there are some very important applications.

Perhaps the simplest equivalent (if not the most important) of the chemical processing operation is heat or mass transfer between gas and molten metal streams in a packed bed system, such as described by Warner, in connection with the separation of lead-zinc mixtures.³⁶ The most significant practical application of the countercurrent flow of gases and melts in

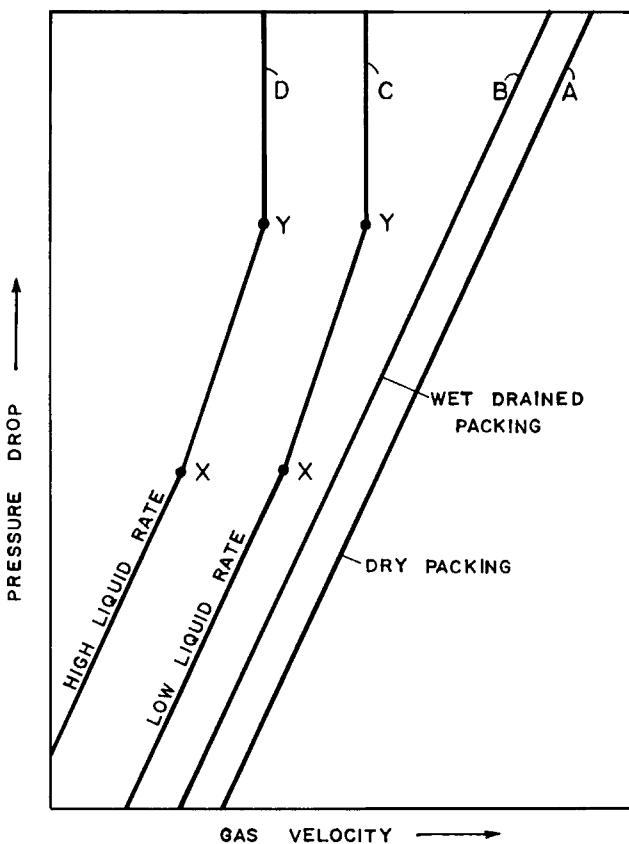


FIG. 7.2.6 Pressure drop as a function of the gas flow rate for wet and dry packing.

packed beds is the flow of molten iron and slag through the coke bed, in the bosh region of the iron blast furnace.³⁷

In our understanding and description of these systems we can borrow heavily from the great deal of experience accumulated by the chemical process industry, while recognizing the differences in behavior that may be caused by the nature of molten metals. As in the case of flow through packed beds in the absense of another phase, our prime interest in these problems is to develop a relationship between the pressure drop and the (gas) flow rate.

The general behavior of these systems is sketched in Fig. 7.2.6 on a plot of the linear gas velocity against the overall pressure drop across the bed. (It is assumed that the particle Reynolds number is high enough, so that the inertial term dominates in the Ergun equation.)

Curve A on the extreme right depicts the behavior of dry packing (in the absence of a melt), where it is seen that on a logarithmic plot a straight line relationship is obtained between the gas velocity and the pressure drop. This behavior is to be expected from the Ergun equation.

Curve B shows the behavior of a system which has been flooded with a liquid, allowed to drain, and then a gas is being passed through it. It is seen, as perhaps expected, that the presence of some adhering liquid tends to increase the pressure drop, by decreasing the void fraction, i.e., the space available for gas flow.

The behavior of curve C showing the relationship between pressure drop and gas flow rate for the countercurrent flow of a liquid and a gas is more interesting. It is seen that at low gas velocities curve C is parallel to the two previous curves, albeit the absolute value of the pressure drop is higher. However, as the gas flow rate is increased above a certain point X, the pressure drop starts to increase much more rapidly with the gas velocity, until eventually point Y is reached, when the curve becomes almost vertical.

Curve D, drawn for a higher liquid flow rate, is qualitatively similar in behavior to curve C, except for the fact that the breaks in this curve occur at relatively lower gas flow rates.

The conditions designated by point X are usually described as the *loading point*, while point Y indicates the onset of flooding. In a physical sense flooding conditions correspond to a situation when the liquid fills most of the pores and the gas has to bubble through the liquid, so that a very high pressure drop is required to maintain the gas flow. As the gas passes upward, it prevents the drainage of the liquid, which then builds up over the packing. Another physical manifestation of flooding phenomena is that the pressure drop across the bed may fluctuate quite wildly.

In a practical sense flooding is an undesirable condition which has to be avoided in the operation of process equipment; indeed, in many cases the

onset of flooding may define the maximum practicable rates at which a given process equipment may be operated. It has been suggested that operation in the vicinity of the "loading point" would provide a reasonable compromise between good utilization of equipment space and at the same time adequate safeguards against flooding.

Numerous empirical correlations have been proposed for predicting the onset of flooding in packed bed systems. Figure 7.2.7 shows a plot of one of the earlier correlations³⁸ together with measurements reported on the nitrogen mercury and the helium mercury system³⁹ and some data obtained with slags.⁴⁰ It is seen that while there exists substantial scatter (the full line too represents quite widely scattered data points) the Sherwood–Shipley–Holloway correlation appears to provide quite a good representation of measurements obtained with liquid metals and slags.

The parameters appearing in this plot are defined as follows: G_g , mass velocity of the gas, $\text{kg/m}^2\text{s}$; G_L , mass velocity of the liquid, $\text{kg/m}^2\text{s}$; a_p , surface area per unit volume of packing, m^{-1} ; ϵ_v , void fraction of the dry bed, kg/m s ; $C_f = (a_p/\epsilon^3) \text{ m}^{-1}$; μ , viscosity of the melt.

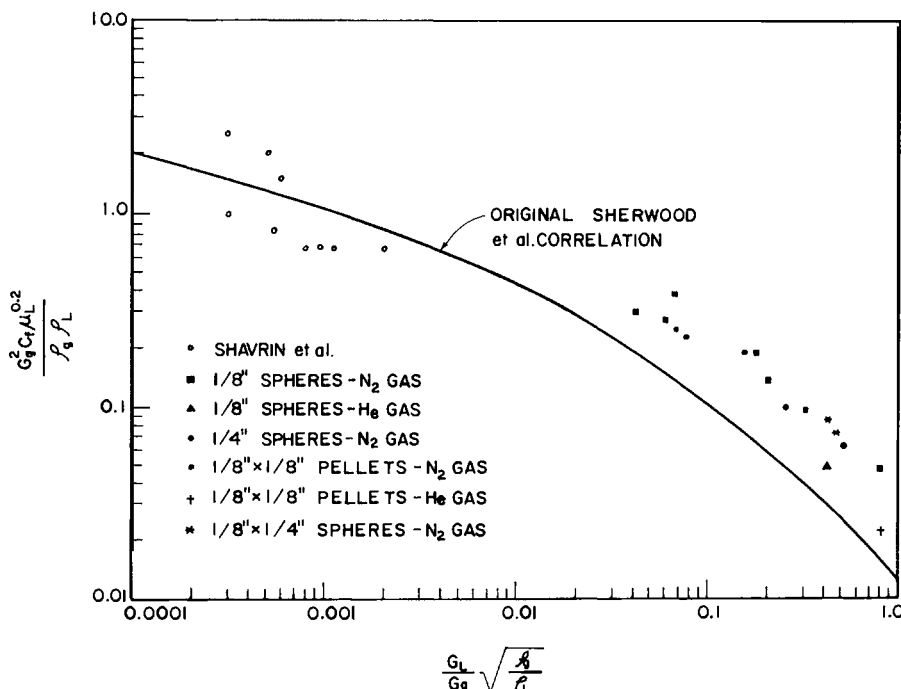


FIG. 7.2.7 Flooding correlation of Sherwood *et al.*³⁸ also showing the experimental measurements of Szekely and Mendrykowski³⁹ and Shavrin *et al.*⁴⁰

At first sight it may be somewhat surprising that the wholly empirical correlation of Sherwood *et al.*³⁸ would provide such a good representation of data obtained with molten metals, the density and interfacial tension of which is so much higher than that of the liquids used in obtaining the original plot.

It is of interest to note in this context that, while the exact mechanism of flooding is not quite fully understood, it has been suggested that different phenomena are responsible for the onset of flooding, depending on the liquid rate.⁴¹

At high liquid rates flooding occurs, even at low gas velocities, because there is just not enough free cross section available to allow the passage of the gas. In contrast, flooding may occur at low liquid rates (and at high linear gas velocities) because the gas may shear off droplets from the liquid film, which could then be carried upward. One would expect, therefore, that systems with liquid metals or slags would tend to flood under less severe conditions (i.e., earlier) at high liquid rates, while flooding would require higher gas flow rates for the same system at low liquid rates. The data points appearing on the right-hand side of Fig. 7.2.7 seem consistent with this argument.

Let us illustrate the application of Fig. 7.2.6 by working a numerical example.

Example 7.2.2 In the operation of a blast furnace the following parameters have been deduced:

$$G_g = 3 \text{ kg/m}^2\text{s};$$

$$G_L = 5.5 \text{ kg/m}^2\text{s};$$

$$\rho_L = 7.1 \times 10^3 \text{ kg/m}^3;$$

$$\rho_G = 0.35 \text{ kg/m}^3;$$

$$\mu_L = 5.5 \times 10^{-3} \text{ kg/m-s; and } C_f = 270.$$

Using Fig. 7.2.7 estimate whether flooding occurs.

SOLUTION The abscissa in Fig. 7.2.7 is given as $(G_L/G_g)(\rho_G/\rho_L)^{1/2} = 0.0128$. The ordinate is given as $G_g^2 C_f \mu_L / \rho_G \rho_L \approx 0.37$, which would be just below the flooding line.

As a final comment on countercurrent gas-liquid flows through packed beds, let us note that if the objective is to bring about the efficient contacting of a liquid metal-gas system in such an arrangement, problems may be caused by the inadequate wetting of the solid particles. In other words, although the gas and the melt are being contacted in a countercurrent fashion, not all the surface area of the packing is actually available for any transfer process.

This problem has been studied by Mackie,⁴² who has shown that the actual availability of the surface area may be greatly reduced for liquid metals, especially at low liquid flow rates. Mackie's results are illustrated in Fig. 7.2.8.

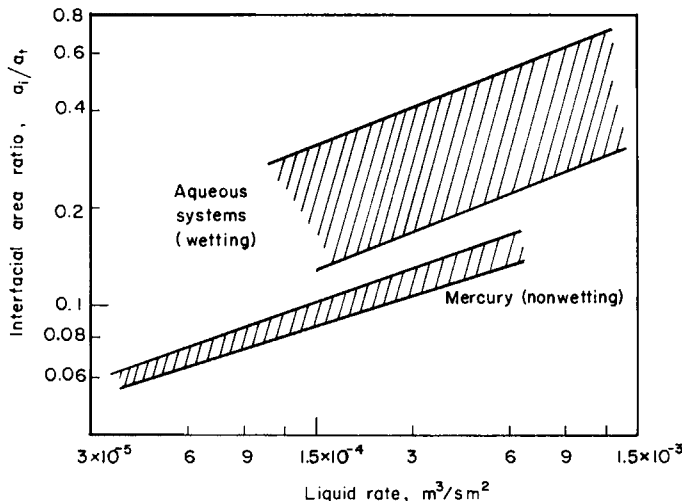


FIG. 7.2.8 Plot of the ratio: interfacial area available to total interfacial area for the counter current flow of gases and liquids through packed beds; after Mackie.⁴²

7.3 Fluidized Beds and Conveyed Systems

Fluidized systems represent a potentially attractive alternative to fixed bed operations for gas-solids contacting. The nature of fluidization is perhaps best illustrated by considering the upward flow of a fluid through a packed bed of solids, as sketched in Figs. 7.3.1a-c, for progressively increasing fluid flow rates.

It is seen that at low fluid velocities the system behaves like a *packed bed*; thus, the relationship between the pressure drop across the bed and the flow rate is given by the *Ergun equation*, which was described in the preceding section. As the fluid velocity is increased this will cause a corresponding increase in the pressure drop across the bed until a state is reached when the pressure drop across the bed equals the weight of the bed. At this point, illustrated in Fig. 7.3.1b, the particles in the bed will become rearranged so as to offer less resistance to the flow and the *bed expands* to attain the loosest possible packing. At higher fluid velocities the bed expands further, the particles become freely suspended in the gas stream, and the *bed attains the fluidized state*.

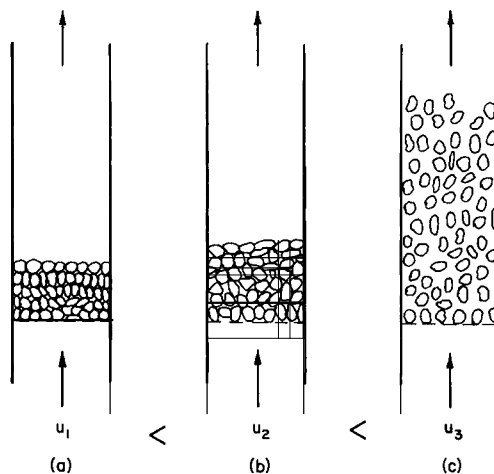


FIG. 7.3.1 Schematic representation of (a) a fixed bed, (b) a fixed bed having its maximum voidage, and (c) a fluidized bed.

From a macroscopic point of view, gas–solid fluidized beds may be regarded as well-stirred, boiling liquids; the liquidlike properties of fluidized beds are readily shown in Fig. 7.3.2.

This behavior of fluidized systems represents the major attractiveness of these systems for effecting gas–solid reactions. The good solids mixing helps to minimize temperature variations and renders these systems attractive for carrying out highly exothermic or endothermic chemical reactions. The liquidlike properties of fluidized beds make them very attractive from the viewpoint of solids handling.

The principal drawback of fluidized beds is their inability to handle sticky materials which could lead to agglomeration and eventually to the blockage of the whole system; the corresponding increase in the power

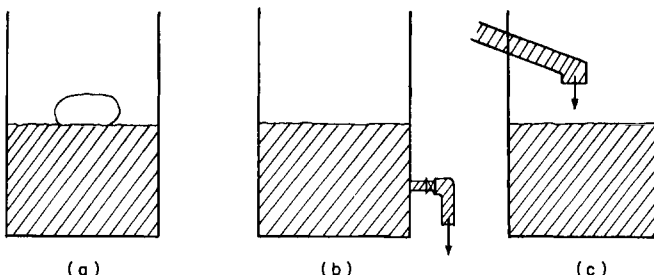


FIG. 7.3.2 Liquidlike properties of fluidized beds: (a) Light bodies are buoyant in fluidized beds; (b) fluidized beds may be “drained”; (c) feeding of solids into fluidized beds.

dissipation entailed in keeping the bed fluidized could also be a major disadvantage. Fluidized beds have been used extensively in the chemical industry for carrying out heterogeneous catalytic reactions (catalytic cracking, manufacture of naphthalene, etc.), especially where close temperature control and frequent catalyst regeneration was necessary. In metals and minerals processing operations fluidized beds have been used for the roasting of sulfide ores, for the combustion of solid fuels, and also for iron oxide reduction.

7.3.1 Some General Properties of Fluidized Systems: The Fluidization Curve

The onset of fluidization sketched in Fig. 7.3.1 may be represented conveniently through the use of the *fluidization curve*, shown in Fig. 7.3.3. In this graph the pressure drop across the bed is plotted against gas velocity as a logarithmic scale; here line AB corresponds to the pressure drop across the *fixed bed* before fluidization takes place, and region BC represents the rearrangement of the bed to provide the minimum fluidization voidage, when the pressure drop across the bed equals the weight of the bed. The bed is considered fluidized at point C and the corresponding voidage ϵ_{mf} is the minimum voidage of the fluidized bed. The broken line DE shows the pressure-drop-gas-velocity relationship for a packed bed, with an initial voidage of ϵ_{mf} . The ABC curve represents the ideal behavior of gas-solid fluidized beds. There are many systems that do not follow this

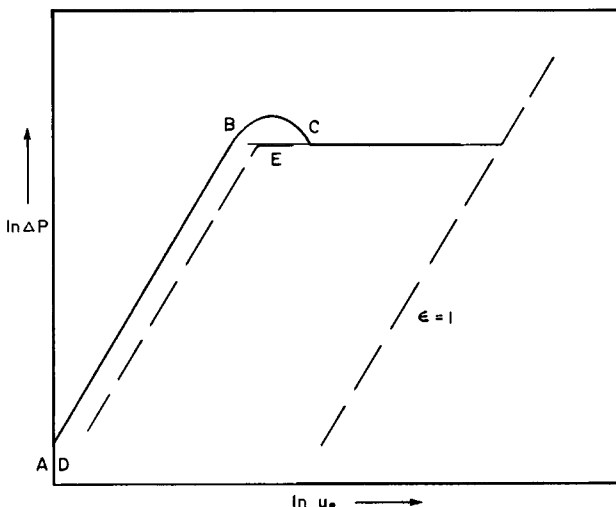


FIG. 7.3.3 The fluidization curve, showing the effect of the gas velocity on the pressure drop on a logarithmic plot.

pattern exactly, channeling and slugging being typical examples. In a physical sense channeling corresponds to the preferential flow of the gas through certain vertical sections of the bed; thus, under these conditions a part of the bed may become fluidized while the remainder stays in a packed state. Slugging means the presence of rather large gas bubbles, which occupy most of the cross section of the bed; the periodic collapse of the bed as the particles fall through these large bubbles then causes the fluctuations noted in Fig. 7.3.3. For a further discussion of slugging and other nonideal behavior of fluidized systems the reader is referred to the specialist literature.^{43,44}

THE MINIMUM FLUIDIZATION VELOCITY

As noted earlier, at the onset of fluidization the pressure drop across the bed equals the weight of the bed; this relationship may then be used in conjunction with the Ergun equation to calculate the minimum fluidization velocity, i.e., the minimum gas velocity at which fluidization is initiated.

Upon considering unit cross-sectional area of the bed, we have

$$\frac{\Delta P}{\text{pressure drop}} = Z_{mf} \left(1 - \epsilon_{mf}\right) g (\rho_p - \rho) \quad (7.3.1)$$

weight of the bed

Here Z_{mf} is the height of the bed at the minimum fluidization velocity and ρ_p and ρ are the densities of the solid particles and of the gas, respectively.

Upon substituting for $\Delta P/Z_{mf}$ from the Ergun equation, i.e., Eq. (7.2.3), after some algebra we obtain

$$\frac{1.75}{\phi_s \epsilon_{mf}^3} \left(\frac{d_p U_{mf} \rho_g}{\mu} \right)^2 + \frac{150(1 - \epsilon_{mf})}{\phi_s^2 \epsilon_{mf}^3} \left(\frac{d_p U_{mf} \rho}{\mu} \right) = \frac{d_p^3 \rho (\rho_p - \rho) g}{\mu^2} \quad (7.3.2)$$

For a given particle size and ϵ_{mf} , Eq. (7.3.2) provides a quadratic relationship for determining the minimum fluidization velocity.

We note that as a practical matter the minimum fluidization velocity depends quite strongly on ϵ_{mf} , the void fraction at the onset of fluidization; the value of ϵ_{mf} will in general depend on both the nature of the material and on the particle size, as illustrated in Fig. 7.3.4.

When neither ϵ_{mf} nor ϕ_s are known, the following approximate formula may be used for estimating the minimum fluidization velocity:

$$U_{mf} = \frac{d_p^2 (\rho_p - \rho) g}{1650 \mu} \quad \text{for } N_{Re,p} < 20 \quad (7.3.3)$$

and

$$U_{mf}^2 = \frac{d_p (\rho_p - \rho) g}{24.5 \rho} \quad \text{for } N_{Re,p} > 1000 \quad (7.3.4)$$

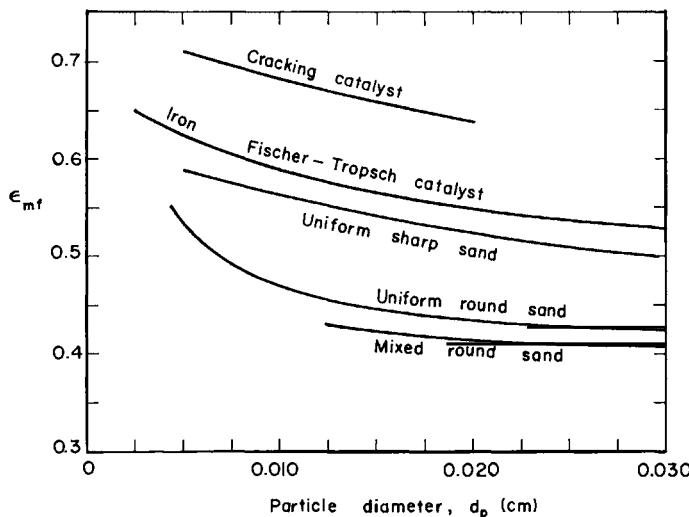


FIG. 7.3.4 The minimum voidage at the onset of fluidization for various materials.⁴³

Example 7.3.1 Estimate the minimum fluidization velocity for hematite particles 100 μm in diameter, in hydrogen at 900°C, and at 1 atm pressure.

DATA $\rho_p = 5.25 \times 10^3 \text{ kg/m}^3$; $\mu = 2.2 \times 10^{-5} \text{ kg/m.s}$; $\rho = 2.05 \times 10^{-2} \text{ kg/m}^3$.

SOLUTION Let us try Eq. (7.3.3) first. Thus,

$$U_{mf} = \frac{10^{-8} \times 5.25 \times 10^3 \times 9.81}{1.650 \times 10^3 \times 2.2 \times 10^{-5}} = 0.0141 \text{ m/s}$$

The corresponding particle Reynolds number is

$$\frac{0.0141 \times 2.05 \times 10^{-2} \times 10^{-4}}{2.2 \times 10^{-5}} \simeq 1.3 \times 10^{-3}$$

which is well within the range over which Eq. (7.3.3) is applicable.

7.3.2 Elutriation and Entrainment of Particles

The lower limit of gas velocities in fluidized beds is set by the minimum fluidization velocity, although in practice the majority of the systems are operated well above this value. The upper limit of gas velocities that may be employed is determined by the rate at which particles are elutriated from the system. As a first approximation the elutriation velocity, i.e., the rate at

which a particle of given size is swept out of the bed, may be estimated from the terminal falling velocity, defined in Section 7.1.

The ratio U_t/U_{mf} , which represents the theoretical limits of the operation, has been shown to vary from about 90 for small particles to about 10 for large particles. In practice, if elutriation is to be avoided, or minimized, these limits are even narrower because most beds contain a range of particle sizes. Practical experience has shown that in fluidized beds, particles, the terminal falling velocity of which is smaller than the superficial gas velocity, are not entrained immediately but rather elutriation takes place at a finite rate. The rate at which fines are elutriated may be represented by the following expression:

$$-\frac{dE_i}{dt} = k_E E_i \quad (7.3.5)$$

where E is the mass of particles of size $d_{p,i}$ in the bed and k_E [1/time] is the elutriation constant; thus, $\frac{dE_i}{dt}$ is the rate at which particles are swept out of the bed.

Figure 7.3.5 shows a plot, based on the data of Yagi and Aoichi,⁴⁵ from which k_E may be estimated. On the ordinate E_i/A_B denotes the mass of

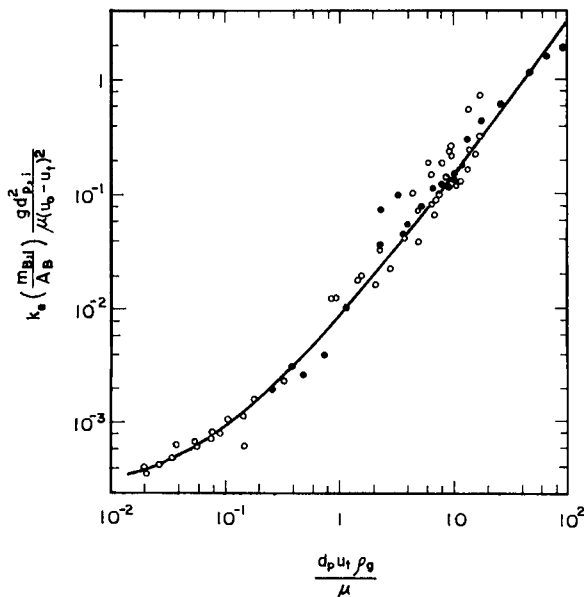


FIG. 7.3.5 Correlation for the elutriation constant; after Yagi and Aoichi.⁴⁵ ○ Continuous operation. ● Batch operation.

particles of a given size ($d_{p,i}$) per unit cross-sectional area of bed and U_0 designates the linear gas velocity in the empty column. Examination of Fig. 7.3.5 shows that the higher the difference between the terminal falling velocity and the linear gas velocity the higher the numerical value of the elutriation constant. In contrast deeper beds would tend to reduce the rate of elutriation.

Example 7.3.2 Hematite particles are reduced with hydrogen in a fluidized bed at 900°C. The mean particle size is 200 µm, the linear gas velocity is 1.5 m/s, and the bed diameter is 1 m. If initially the bed contains 3000 kg of particles of size 50 µm, estimate the amount retained after 30 min of operation.

SOLUTION Using the property values given in Example 7.3.1 and Eq. (7.1.8),

$$U_t = \left(\frac{2}{9} \mu \right) R_p^2 \rho_p g$$

i.e.,

$$U_t = \frac{(5 \times 10^{-5})^2 \times 5.25 \times 10^3 \times 9.81}{9 \times 2.2 \times 10^{-5}} = 0.65 \text{ m/s}$$

The particle Reynolds number appearing on the abscissa of Fig. 7.3.5 is

$$\frac{d_p u_t \rho}{\mu} = \frac{5 \times 10^{-5} \times 2.05 \times 10^{-2} \times 0.65}{2.2 \times 10^{-5}} = 0.03$$

Hence from Fig. 7.3.5 the ordinate is 1.3×10^{-3} , so that

$$k_E \frac{E_i}{A_B} \frac{g d_{p,i}^2}{\mu (u_0 - u_t)^2} = 1.3 \times 10^{-3}$$

i.e.,

$$k_E = \frac{1.3 \times 10^{-3} \times 2.2 \times 10^{-5} (1.5 - 0.65)^2 \times 0.785}{9.81 \times 3 \times 10^3 \times (5 \times 10^{-5})^2} \approx 2.2 \times 10^{-4} \text{ s}^{-1}$$

Then on integrating Eq. (7.3.5) we have

$$E_i/E_{i,0} = e^{-k_E t}$$

i.e.,

$$E_i/E_{i,0} = \exp(-2.2 \times 10^{-4} \times 1.8 \times 10^3) = 0.67$$

So that after 30 min of operation some 67% or 2020 kg of the fines would still remain in the bed, notwithstanding the fact that the linear gas velocity

in the system far exceeds the terminal falling velocity of the fines. It is thus seen that the bed acts as a filter for the fines.

7.3.3 Bubbles in Fluidized Beds

It has been shown that in most gas-solid fluidized systems of practical interest a portion of the gas, equivalent to the amount required to maintain the bed in a fluidized state, is more or less uniformly distributed in the bed, whereas the remainder passes through in the form of *gas bubbles*.

Davidson and Harrison studied bubbling phenomena in fluidized beds extensively and have shown that the rising velocity of gas bubbles in fluidized beds may be estimated with the aid of the Davies and Taylor equation,⁴⁶ which was originally developed for the rise of large (spherical cap) gas bubbles in liquids:

$$U_B = 0.79g^{1/2}V_B^{1/6} = 0.711(gd_B)^{1/2} \quad (7.3.6)$$

where U_B and V_B are the rising velocity and bubble volume, respectively, and d_B is the diameter of a spherical bubble of volume V_B .

The velocity of a bubble of maximum stable size in a fluidized bed was estimated by Harrison as

$$U_{B,S} = U_t \quad (7.3.7)$$

where $U_{B,S}$ is the rising velocity corresponding to the maximum stable bubble size; the argument here is that, when the rising velocity of the bubble is larger than the terminal falling velocity of the particles (U_t) solids would be drawn into the wake, which would cause the bubble to break up. Figure 7.3.6 provides a convenient way of estimating the maximum stable bubble size.

When a stream of bubbles rises through a bed then the velocity of an individual bubble is affected by the presence of the other bubbles. For these circumstances Davidson and Harrison suggested the following expression for estimating the rising velocity of the bubbles:

$$U_B = U_0 - U_{mf} + 0.711(gd_B)^{1/2} \quad (7.3.8)$$

Gas bubbles have a major influence on the operation of fluidized systems. The presence of bubbles is responsible for the good solids mixing, which is a desirable feature. On the other hand, the gas passing through in the form of bubbles is not brought into intimate contact with the bed, as is the gas contained in the continuous, i.e., emulsion, phase of the system. Kunii and Levenspiel⁴³ developed a comprehensive model for representing the interaction between gas bubbles (the discontinuous phase) and the emulsion phase of gas-solid fluidized beds.

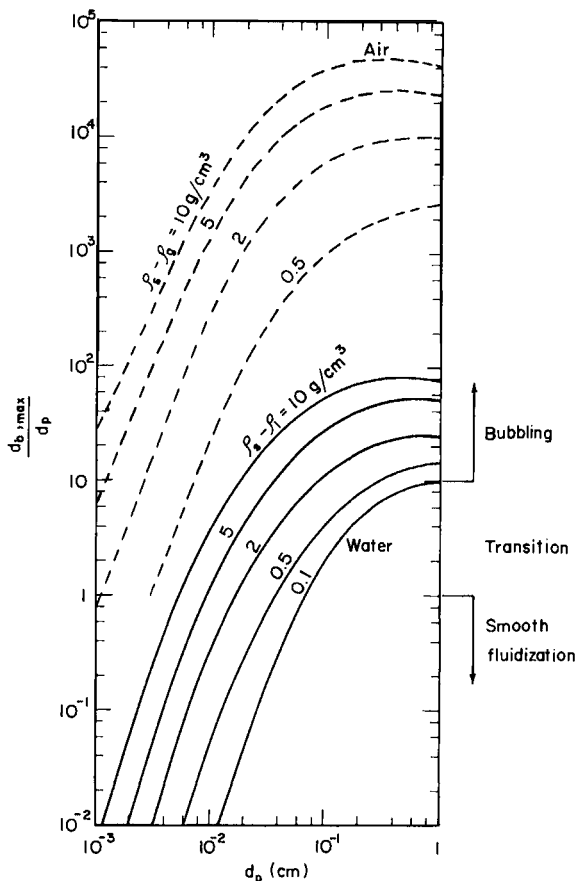


FIG. 7.3.6 The effect of the particle size on the maximum bubble size in fluidized beds.⁴³

They considered three groupings of bubbling systems, as depicted in Fig. 7.3.7:

- (i) small bubbles, where $U_B \approx U_{mf}$;
- (ii) large bubbles, where $U_B > 5U_{mf}$;
- (iii) an intermediate region, where $U_{mf} < U_B < 5U_{mf}$.

Unless the beds are very shallow, small bubbles do not play an important role in modifying the transfer processes between the gas and the solids.

Large bubbles, however, do provide a means for the bypassing of the bed by gas; in other words, the gas passing through the system in the form of large bubbles will necessarily have a less intimate contact with the solids than the gas contained in the emulsion phase. Thus in describing gas-solid

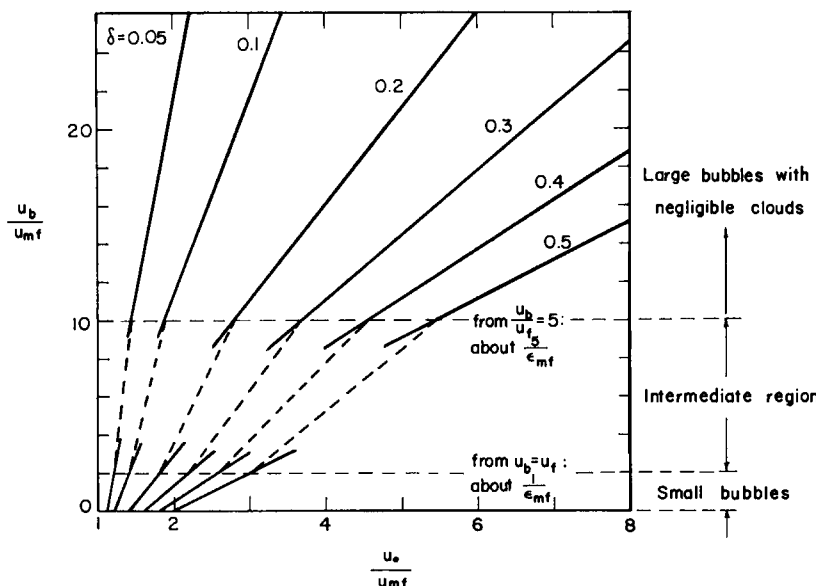


FIG. 7.3.7 Bubbling regimes in fluidized beds. The quantity δ is the fraction of the bed occupied by the bubble phase.⁴³

contacting in these systems, allowance must be made for transfer between the gas bubble phase and the emulsion phase of the bed.

A detailed discussion of these phenomena is available in the text by Kunii and Levenspiel;⁴³ some further metallurgical examples are also presented in a monograph by Szekely *et al.*⁴⁷

7.3.4 Pneumatically Conveyed Systems

In order to illustrate the nature of pneumatic conveying let us reexamine Figs. 7.3.1 and 7.3.3, which were given previously. It was shown that, when a gas is blown vertically through a packed bed of solids, at a given gas velocity the bed expands so as to attain the loosest possible packing and then on a subsequent increase in the gas velocity the bed became fluidized. Further increases in the volumetric flow rate of the gas causes part of this gas to pass through the system in the form of bubbles. We also noted that, if the superficial gas velocity exceeds the terminal falling velocity of some of the particles, these fines are elutriated at some finite rate.

However, if a gas were blown through the system at a rate which exceeds the terminal falling velocity of the bulk of the particles contained in the bed, the particles would be swept out of the bed; alternatively, if operated at these rates, particles could be *conveyed* through conduits.

Such systems are usually called *pneumatically conveyed* and may operate either through horizontal or through vertical conduits. The volumetric ratio (gas flow rate)/(solids flow rate) is usually 20–80 in these systems.

The actual purpose of pneumatically conveyed systems is, as the name implies, to transport material, but in some cases chemical reactions are also being carried out; these latter systems are termed transfer line reactors.

The two principal questions that need answering in the design and operation of pneumatic transport installations is the ratio of the gas to solids flow rate required to bring about transport and the pressure drop needed to provide the required gas flow rate.

THE SALTATION VELOCITY AND CHOKING PHENOMENA

It has been found experimentally that in the horizontal pneumatic transport of solids there has to be a minimum linear gas velocity, for a given set of operating conditions (conduit size, solids flow rate, etc.), to prevent the settling or saltation of the solid particles. Such settling or saltation would, of course, result in the blockage of the conduit.

The phenomenon of saltation is illustrated in Fig. 7.3.8 on a plot of the pressure gradient in the horizontal conduit against the linear gas velocity, for various values of the solids flow rate G_s . The line corresponding to $G_s = 0$ corresponds to the frictional loss due to the gas flow alone, while the curves designated G_{s1} , G_{s2} , etc., show the behavior of the system for progressively increasing solids flow rates. Upon considering the curve corresponding to G_{s1} , starting at point C, it is seen that as the linear gas velocity is reduced (at a constant solids loading) this will cause the pressure drop to fall also, until point D is reached. At this stage the solid particles will begin to settle and a dynamic equilibrium is being established between this settled layer and the mixture above. At point D the resistance to flow increased very sharply and a further reduction in the linear gas velocity would cause a further increase in the pressure drop, as indicated by the EF portion of the curve. As seen in Fig. 7.3.8, qualitatively similar behavior is observed for higher solids loading except for the fact that the “break” occurs at higher gas velocities. The critical gas velocity, corresponding to point D, is termed the saltation velocity $U_{c,s}$. As a practical matter, a horizontally conveyed system has to be operated above this saltation velocity.

The information available for calculating the saltation velocity is far from adequate; nonetheless, a first-order estimate may be made by following a procedure suggested by Zenz and Othmer.⁴⁸ Figure 7.3.9 shows a plot of

$$\frac{U_{c,s,m}}{4g\mu(\rho_p - \rho)^{1/3}/9\rho^2 R_c^{0.4}}$$

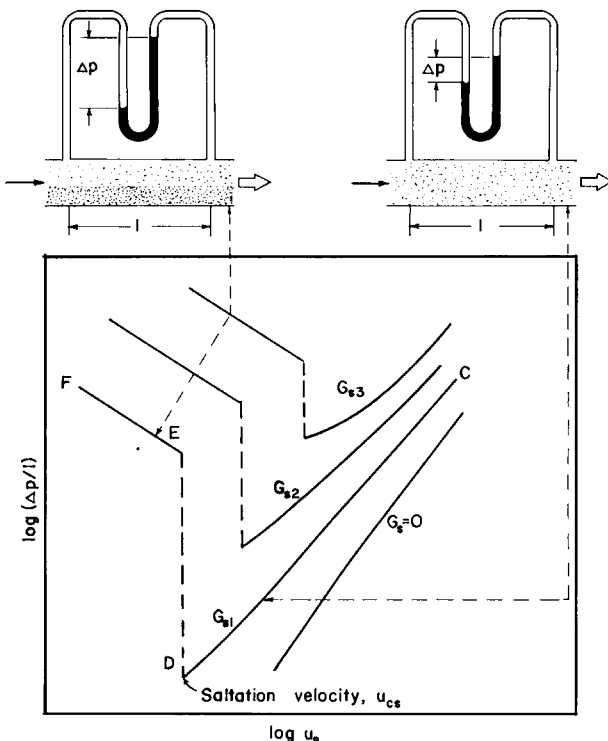


FIG. 7.3.8 The behavior of solids conveyed by a gas stream in a horizontal pipe. The ordinate gives the pressure gradient, while the abscissa designates the linear gas velocity.⁴⁸

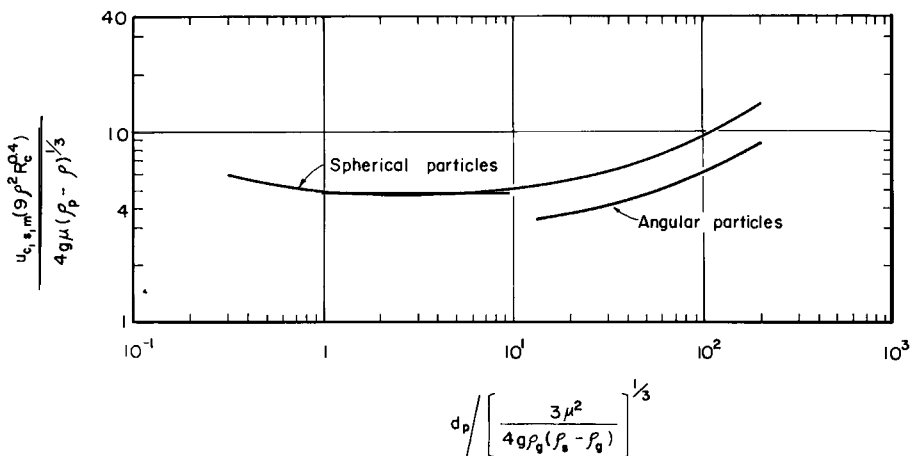


FIG. 7.3.9 Correlation for the saltation velocity of uniformly sized solids; after Zenz and Othmer.⁴⁸

against

$$\frac{d_{p,m}}{(3\mu^2/4g\rho(\rho_p - \rho))^{1/3}}$$

from which the saltation velocity of uniformly sized solids of diameter $d_{p,m}$ may be calculated.

Here R_c is the radius of the conduit. For a mixture of sizes, we compute $U_{c,s,m1}$ and $U_{c,s,m2}$, the velocity required to convey the smallest and the largest particles in the mixture, and then find n , the slope of the straight line connecting these two points in Fig. 7.3.9. The value of n thus obtained may then be used, in conjunction with Fig. 7.3.10, to calculate the critical saltation velocity. An alternative, and perhaps more satisfactory way, of sizing pipelines for the horizontal conveying of solids is through the use of the minimum safe velocities, listed in Table 7.3.1 for a variety of systems.

In vertical pneumatic conveying the concept of choking is somewhat analogous to the saltation phenomenon discussed above. The choking phenomenon for the vertical conveying of a lean gas-solid mixture is sketched in Fig. 7.3.11 on a plot of the linear gas velocity against the (vertical) pressure gradient. Here again (as in the case of Fig. 7.3.8) $G_s = 0$ designates the flow of the solids free gas stream, while $G_{s,1}$ and $G_{s,2}$ denote progressively higher solids loading. It is seen on examining curve $G_{s,1}$, say starting from point C, that the pressure gradient (i.e., the overall pressure drop) decreases as the linear gas velocity is lowered at constant solids loading, down to point D. From this point onwards, any further decrease in the linear gas velocity will

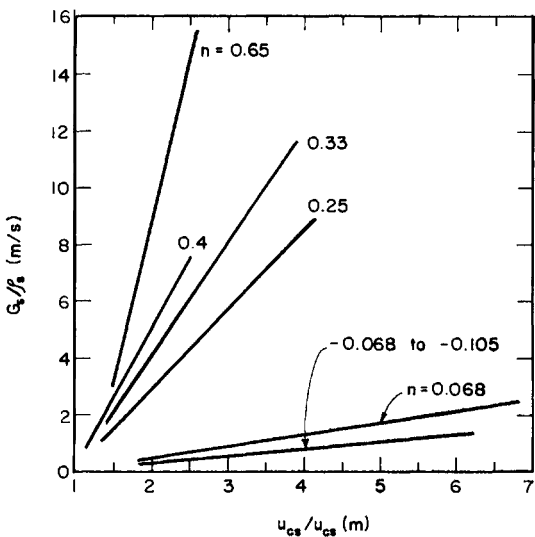


FIG. 7.3.10 The saltation velocity for a solid mixture; after Zenz and Othmer.⁴⁸

TABLE 7.3.1
Safe Values for Pneumatic Conveying^a

Material	Average bulk density (kg m ⁻³)	Approximate size (1000 μ = 1 mm)	Minimum safe air velocity (m s)		Maximum safe density for flow (g cm ⁻³)	
			Horizontal	Vertical	Horizontal	Vertical
Coal	0.72×10^3	< 12.7 mm	15.3	12.2	0.012	0.016×10^{-3}
Coal	0.72×10^3	< 6.35 mm	12.2	9.2	0.016	0.024×10^{-3}
Wheat	0.75×10^3	4.76 mm	12.2	9.2	0.024	0.032×10^{-3}
Cement	$1.04-1.44 \times 10^3$	95% < 88 μ	7.6	1.5	0.16	0.96×10^{-3}
Pulverized coal	0.56×10^3	100% < 380 μ . 75% < 76 μ	4.6	1.5	0.11	0.32×10^{-3}
Pulverized ash	0.72×10^3	90% < 150 μ	4.6	1.5	0.16	0.48×10^{-3}
Bentonite	$0.77-1.04 \times 10^3$	95% < 76 μ	7.6	1.5	0.16	0.48×10^{-3}
Silica flour	$0.80-0.96 \times 10^3$	95% < 105 μ	6.1	1.5	0.08	0.32×10^{-3}
Phosphate rock	1.28×10^3	90% < 152 μ	9.2	3.1	0.11	0.32×10^{-3}
Common salt	1.36×10^3	5% < 152 μ	9.2	3.1	0.08	0.24×10^{-3}
Soda ash (light)	0.56×10^3	66% < 105 μ	9.2	3.1	0.08	0.24×10^{-3}
Soda ash (dense)	1.04×10^3	50% < 177 μ	12.2	3.1	0.048	0.16×10^{-3}
Sodium sulphate	$1.28-1.44 \times 10^3$	100% < 500 μ . 55% < 105 μ	12.2	3.1	0.08	0.24×10^{-3}
Ground bauxite	1.44×10^3	100% < 105 μ	7.6	1.5	0.13	0.64×10^{-3}
Alumina	0.93×10^3	100% < 105 μ	7.6	1.5	0.096	0.48×10^{-3}
Magnesite	1.60×10^3	90% < 76 μ	9.2	3.1	0.16	0.48×10^{-3}
Uranium dioxide	3.52×10^3	100% < 152 μ . 50% < 76 μ	18.3	6.1	0.16	0.96×10^{-3}

^a Adapted from Zentz and Othmer.⁴⁸

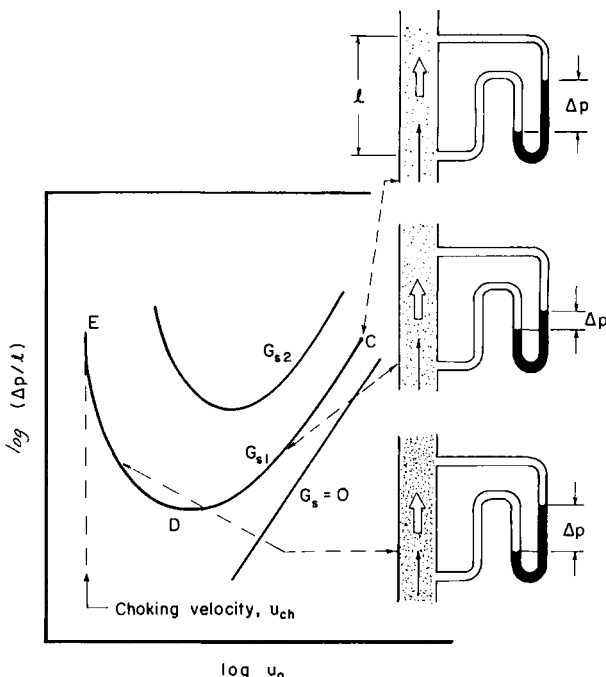


FIG. 7.3.11 The behavior of a lean gas–solids mixture in vertical conveying.

cause a rapid decrease in the voidage, with a corresponding increase in the static head and the pressure drop, until point E is reached, when the bulk density of the bed becomes too great and the bed collapses into a slugging mode. The superficial velocity at point E is called the choking velocity U_{ch} .

It follows from the foregoing that any vertical conveying system has to be operated *above the choking velocity*. The conditions when a lean gas–solid mixture collapses into a choking mode may be represented by the following expression:

$$G_{s,ch} = \rho_p(1 - \epsilon_{ch})(U_{ch} - U_t) \quad (7.3.9)$$

where $G_{s,ch}$ is the solids mass velocity corresponding to choking, ϵ_{ch} the void fraction corresponding to choking, and U_t is the terminal falling velocity of the solid particles. Zenz and Othmer suggested that ϵ_{ch} does not depend very much on the size of the solid particles, but that it is a strong function of the solids density. These authors also found that for closely sized particles the choking velocity can be approximated by the saltation velocity $U_{c,s}$.

Table 7.3.1 also contains useful information on the safe values of the linear gas velocity for the vertical pneumatic conveying of solids, for quite a range of materials.

THE PRESSURE DROP IN PNEUMATIC CONVEYING

The pressure drop in the pneumatic conveying of solids may be calculated by using somewhat analogous expressions to those developed in Chapter 2 for the flow of homogeneous fluids. Thus we may write

$$\Delta p = \rho_m g \Delta h + [\text{static head}] + U_s G_s [\text{kinetic energy of the solids}] + \Delta p_f [\text{frictional loss}] \quad (7.3.10)$$

where Δp is the overall pressure drop and ρ_m is the mean density of the mixture, i.e.,

$$\rho_m = \rho_p(1 - \epsilon_v) + \rho\epsilon_v \quad (7.3.11)$$

The acceleration term $U_s G_s$ may be also written as

$$U_s G_s = U_s \rho U_0 (G_s / G) \quad (7.3.12)$$

where G is the combined gas plus solids mass velocity through the conduit, and Δp_f is the pressure loss due to friction at the wall, which may be written as

$$\Delta p_f = \frac{2f'_s(U_0 G_s / U_s G)}{(\rho U_0^2 Z / d_t)} \quad (7.3.13)$$

where f'_s is the friction factor for the mixture, some values of which are given in Table 7.3.2, d_t the diameter of the conduit, and Z is the length of the conduit. The linear velocity of the solids U_{s1} may be estimated from

$$U_s \approx U_0 - U_t \quad (7.3.14)$$

TABLE 7.3.2

Values of Coefficient f'_s versus Air Velocities

Solids and their size	Pipe diameter d_t (mm)	Air velocity U_0 (m/s)					
		5	10	15	20	30	40
Limestone, various sizes up to 3.2 mm	Horizontal 51	0.020	0.017	0.004	0.0033	0.0033	0.0033
Salt 76–252	Horizontal 44.4	0.03	0.0065	—	—	—	—
	Vertical 44.4	0.035	0.018	0.016	—	—	—
Sand, 0.8–1.4 mm	Horizontal 44.4	0.018	0.005	0.0045	—	—	—
Coal, 0–1 mm	Horizontal 25.4	—	—	0.014	0.0011	0.0011	—

^a Adapted from Zentz and Othmer.⁴⁸

7.4 Sedimentation and Filtration

In this section we shall provide a brief treatment of processes that are available for the separation of liquids from solids, namely sedimentation and filtration. These two processes, often carried out sequentially, are of considerable practical importance in minerals processing and also in the treatment of solid wastes. One good practical example may be the recovery of the primarily iron oxide dust emitted from the basic oxygen furnace. This dust is removed from the gas stream exiting the furnace, e.g., through the action of wet venturi scrubbers. The gas-liquid suspension is allowed to undergo a sedimentation step and the sludge from these settling tanks (thickeners) is then filtered. The filtrate is recycled and the solid residue (filter cake) is pelletized and returned to the furnace or to the sinter-plant.

Notwithstanding the great and growing practical importance of sedimentation and filtration processes, at least in part due to their relevance to environmental problems, our basic understanding of these is rather incomplete at present. For this reason the brief treatment that follows will be largely qualitative and only some rather oversimplified cases will be described in a quantitative manner.

7.4.1 *Sedimentation*

In the sedimentation of concentrated suspensions, particles move downwards due to the action of gravity and an equal volume of liquid is displaced due to this motion. When the concentration of a suspension is low, the distances between adjacent particles are large compared with the size of the particles; thus, the effects of mutual interference may be disregarded. The rate of settling of a given solid particle under these conditions is not effected by the others and may be calculated using the techniques described in Section 7.1.

Such conditions are usually termed free settling. At high solids concentrations the interaction of the individual particles can no longer be neglected; this process is commonly termed "hindered settling," which corresponds to the operation of industrial thickeners. The main reasons for the modification of the settling rate of particles in a concentrated suspension are as follows:

- (a) The large particles are settling relative to a suspension of smaller ones so that the effective density and viscosity of the fluid are increased.
- (b) The upward velocity of the fluid displaced during settling is appreciable in a concentrated suspension and the apparent settling velocity is less than the actual velocity relative to the fluid.
- (c) The velocity gradients in the fluid close to the particles are increased as a result of the change in the area and shape of the spaces available for liquid flow.

(d) The smaller particles tend to be dragged downwards by the motion of the large particles and therefore accelerated.

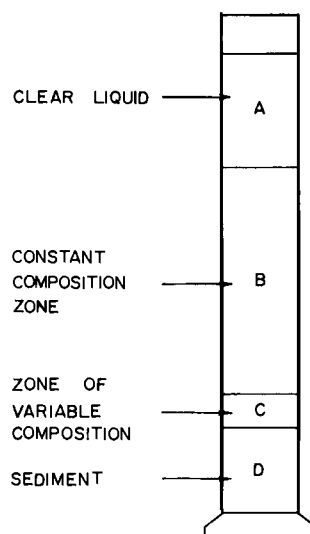
(e) Because the particles are closer together in a concentrated suspension, flocculation is more marked in an ionized solvent and the effective size of the small particles is increased.

Figure 7.4.1 shows a schematic sketch of the sedimentation process. After a brief initial period an interface is established between the clear liquid (at the top) and the suspension. The suspension moves downward at a constant rate and a layer of sediment builds up at the bottom of the container. When the clear liquid interface approaches the sediment, its rate of fall decreases until a "critical settling point" is reached, when a direct interface is formed between the sediment and the clear liquid. Further sedimentation results solely from the consolidation of the sediment, with the occluded liquid being forced upwards through the loosely packed solid particles.

The sketch in Fig. 7.4.1 shows an intermediate stage in the settling process, where there is an interference between the suspension and the clear, uppermost layer. Moreover the suspension may be divided into a constant composition zone and a zone of variable composition. In some cases no constant composition zone has been observed. It has been found that the rate of sedimentation remains constant, until the "critical settling point" is reached, through the disappearance of both zones B and C.

The sedimentation rates of fine suspensions are very difficult to predict from first principles and it is desirable to determine these experimentally for a given application. Certain general trends have been observed however.

FIG. 7.4.1 Sketch showing the sedimentation of concentrated suspensions.



The height of the suspension does not affect the rate of sedimentation, in general. This is illustrated in Fig. 7.4.2 on a plot of the sludge line (i.e., the upper surface of region D in Fig. 7.4.1) against time, for two different slurry heights. It is seen that the two curves are similar and the ratio OD/OD' is constant throughout. It follows that if a curve is obtained for a given initial height, sedimentation curves may be constructed (for identical suspension) for different initial heights, through the use of this procedure.

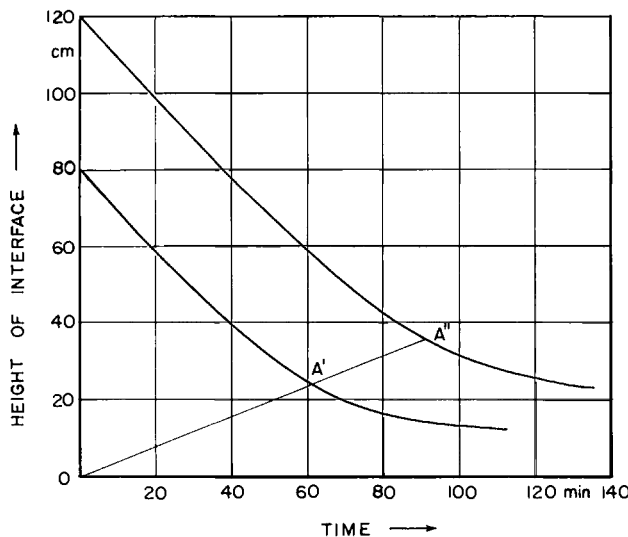


FIG. 7.4.2 The effect of the height on the sedimentation of a 3% CaCO_3 suspension; after Coulson and Richardson.³

Figure 7.4.3 shows the effect of solids concentration on the sedimentation rate, for a particular system. It is seen that, as noted earlier, the higher the concentration the lower the sedimentation rate, because of the progressively increasing upward velocity of the displaced liquid. The broken line, denoting the CD interface, sketched earlier in Fig. 7.4.1, will, of course, increase with time because of the accumulation of the sediment at the bottom of the container.

The sedimentation of coarse suspensions, which is of academic interest only is somewhat easier to interpret. Richardson and Zaki,⁴⁹ in the interpretation of their experimental measurements, proposed the following relationship between U_t , the terminal falling velocity and infinite dilution, and U_c , the settling velocity of the suspension:

$$U_c/U_t = \epsilon_v^n \quad (7.4.1)$$

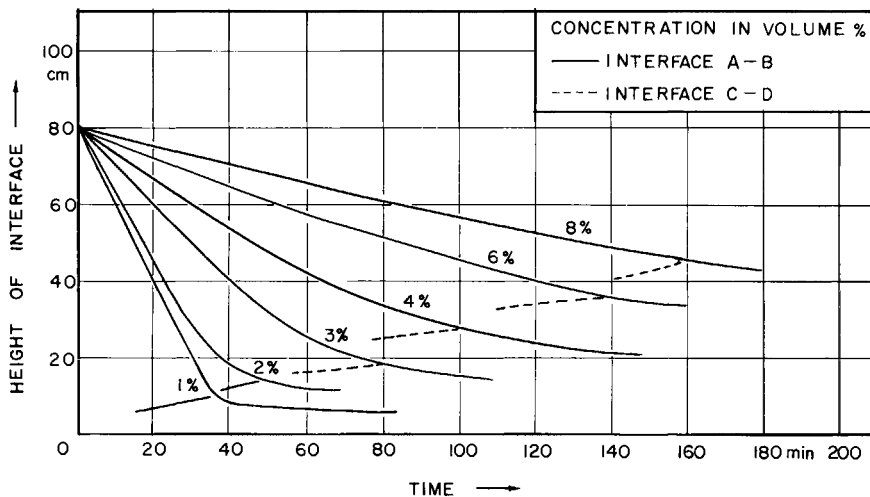


FIG. 7.4.3 The effect of the concentration on the sedimentation of CaCO_3 suspensions; after Coulson and Richardson.³

where ϵ_v is the void fraction and n is a constant. By using elegant arguments, based on dimensional analysis, these authors showed that when $N_{\text{Re},p} < 0.2$ and $N_{\text{Re},p} > 500$ the parameter n depends only on the ratio (tube diameter)/(particle diameter). More specifically,

$$n = 4.6 + 20 \frac{d_p}{d_t} \quad \text{for } N_{\text{Re},p} < 0.2 \quad (7.4.2)$$

and

$$n = 2.4 \quad \text{for } N_{\text{Re},p} > 500 \quad (7.4.3)$$

For the intermediate regime n was found to depend on both the particle Reynolds number and on the ratio d_p/d_t . The detailed empirical expressions for this region are available in the text by Coulson and Richardson.³

It has to be stressed that Eqs. (7.4.1)–(7.4.3) are valid for coarse suspensions only. The principal practical use of experimental measurements obtained on sedimentation rates, such as were sketched in Figs. 7.4.1–7.4.3, is to obtain information for the design of industrial thickeners. Figure 7.4.4 shows a sketch of a continuous thickener, which is seen to consist of a large shallow tank with a flat bottom. The solid–liquid suspension is being fed at the center, some distance below the surface of the liquid, in a manner to cause as little disturbance as possible. The thickened liquid (i.e., the concentrated suspension) is removed through an outlet located at the bottom. The solids deposited on the floor of the tank are directed towards the outlet

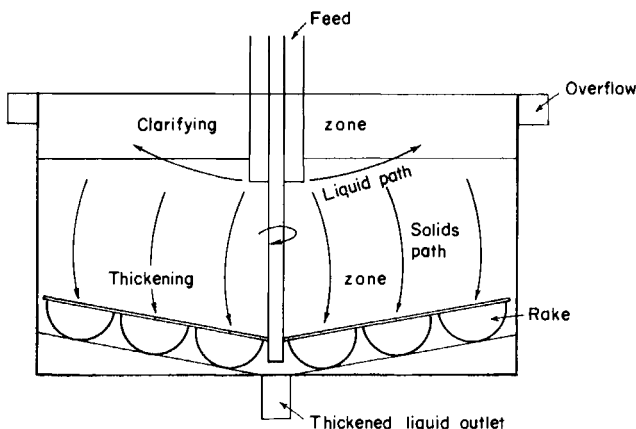


FIG. 7.4.4 A continuous thickener.

by means of slowly rotating rates. The clarified liquid is removed through an overflow.

As seen in the sketch the liquid is moving radially outward and upward, in the direction of the overflow, so the thickener must be so designed that the upward liquid velocity is less than the settling velocity of the particles (i.e., of the suspension) in order to avoid the entrainment of solids. Moreover, the desired degree of thickening is achieved by providing the necessary residence time. A more basic discussion of sedimentation phenomena is available in the text by Wallis⁵⁰ and a good discussion on the design of thickeners is available in the specialist literature.⁵¹

7.4.2 Filtration

Filtration is a process whereby a solid is separated from a liquid through the use of a porous medium, which retains the solids but allows the fluid to pass. In general the pores of the filter medium are tortuous in shape and larger than the particles which are to be separated; moreover, the filter tends to work efficiently only after an initial deposit has been trapped in the medium.

In actual practice a broad range of geometries and physical arrangements have been employed to carry out filtration, but the basic principle is conveniently illustrated in the sketch shown in Fig. 7.4.5. It is seen that a *slurry*, containing suspended solids, is passed through suitable supported *filter cloth*; the solids are retained, and form the *filter cake*, while the liquid is passed through both the cake and the cloth forms the *filtrate*.

It is readily seen that the filter cake builds up gradually over the medium (i.e., the cloth in the present case) and that this build-up will represent a progressively increasing resistance to flow.

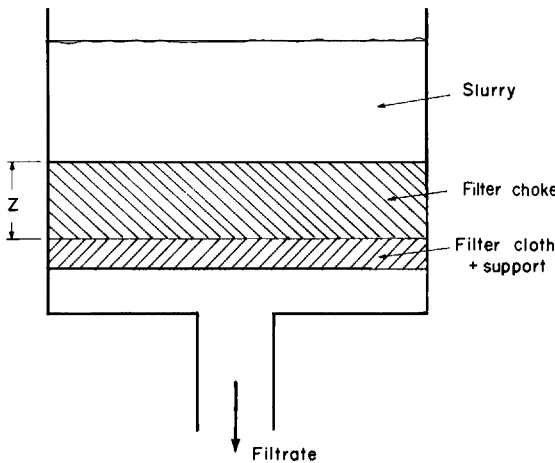


FIG. 7.4.5 Sketch of a filter.

If we assume that the cake formed is incompressible (quite a poor assumption usually), then the progress of the filtration process is easily represented through the use of the expressions developed in Section 7.2 for flow through packed beds.

If we assume, furthermore, that the viscous term dominates in the Ergun equation, the volumetric flow rate of the filtrate through the cake may be written as

$$\frac{1}{A} \frac{dV}{dt} = \frac{\Delta p}{\chi \mu Z} \quad (7.4.4)$$

where A is the cross-sectional area of the filter, $\frac{dV}{dt}$ the volumetric flow rate of the filtrate, Δp the pressure drop, Z the instantaneous thickness of the cake, and χ is the characteristic resistance, which corresponds to the viscous resistance terms in the Ergun equation. On noting that $\frac{1}{A} \frac{dV}{dt}$ corresponds to the linear velocity of the filtrate, Eq. (7.4.4) is identical to Darcy's equation. If \tilde{v} is used to designate the volume of cake deposited by unit volume of filtrate, then we have

$$Z = \tilde{v} V/A \quad (7.4.5)$$

Thus on substituting into Eq. (7.4.4) we obtain

$$\frac{1}{A} \frac{dV}{dt} = \frac{A^2 \Delta p}{\chi \mu V \tilde{v}} \quad (7.4.6)$$

Actually in the statement of Eq. (7.4.6) we neglected the resistance to flow produced by the filter cloth, which should be of particular significance in the initial stages of the process. If we represent this resistance by an equivalent cake thickness, say Z , Eq. (7.4.6) is written as

$$\frac{dV}{dt} = \frac{A \Delta p}{\chi \mu [V \tilde{v}/A] + Z} \quad (7.4.7)$$

Equation (7.4.7) is readily integrated, provided an additional relationship is specified between Δp or V and time. In many practical operations the pressure is built up gradually in the initial stages, during which time dV/dt is approximately constant. So one may represent the process by the following initial conditions:

$$V = 0 \quad \text{at} \quad t = 0 \quad (7.4.8a)$$

$$\frac{dV}{dt} = \text{const} \quad \text{for} \quad 0 < t < t_1 \quad (7.4.8b)$$

and

$$\Delta p = \text{const} \quad \text{for} \quad t > t_1 \quad (7.4.8c)$$

Then we may write

$$\frac{V_1}{t_1} = \frac{A^2 \Delta p}{u \chi \mu [V_1 + Z A / \tilde{v}]} \quad \text{or} \quad V_1^2 + \frac{LA}{\tilde{v}} = \frac{A^2 \Delta p}{\chi \mu v} t_1 \quad (7.4.9)$$

where V_1 is the volume of filtrate collected at the end of the constant rate pressure. Then we may integrate Eq. (7.4.7) for constant Δp and for the initial condition

$$V = V_1 \quad \text{at} \quad t = t_1 \quad (7.4.10)$$

to obtain

$$\frac{1}{2}(V^2 - V_1^2) + \frac{ZA}{\tilde{v}}(V - V_1) = \frac{A^2 \Delta p}{\chi \mu v}(t - t_1) \quad (7.4.11)$$

or, on rearranging,

$$\frac{t - t_1}{V - V_1} = \frac{\chi \mu \tilde{v}}{2A^2 \Delta p}(V - V_1) + \frac{r \mu \tilde{v} V_1}{A^2 \Delta p} + \frac{\chi \mu Z}{A \Delta p} \quad (7.4.12)$$

It follows from the form of Eq. (7.4.12) that a plot of $(t - t_1)/(V - V_1)$ against $V - V_1$ should have a linear portion, from the slope of which the specific cake resistance χ may be deduced. A good discussion of the use of these expressions for the evaluation of filter performance and for the scaling of filtration equipment is available in Purchas *et al.*^{52,53}

References

1. C. E. Lapple and D. Shepherd, *Ind. Eng. Chem.* **32**, 605 (1940).
2. R. H. Perry and C. H. Chilton, eds., "Chemical Engineer's Handbook," 5th ed. McGraw-Hill, New York, 1973.
3. J. M. Coulson and J. F. Richardson, "Chemical Engineering," Vol. 2, p. 439. Pergamon, Oxford, 1955.
4. R. J. Brodkey, "The Phenomena of Fluid Motions," p. 621. Addison-Wesley, Reading, Massachusetts, 1967.
5. L. D. Landau and E. M. Lifshitz, "Fluid Mechanics." Pergamon, Oxford, 1959.
6. A. B. Bassett, *Philos. Trans. R. Soc. London*, **179**, 43 (1888).
7. F. Odar and W. S. Hamilton, *J. Fluid Mech.* **18**, 302 (1964).
8. L. Gourtsoyannis, H. Henein, and R. I. L. Guthrie, in "The Physical Chemistry of the Production and Use of Alloy Additives" (J. Farrell, ed.). AIME, New York, 1974.
9. R. I. L. Guthrie, R. Clift, and H. Henein, *Metall. Trans.* **6**, 321 (1975).
10. J. Szekely and V. Stanek, *Metall. Trans.* **1**, 119 (1970).
11. J. Szekely and S. Asai, *Ironmaking Steelmaking* **2**, 205 (1975).
12. L. B. Torobin and W. H. Gauvin, *Can. J. Chem. Eng.* **37**, 129–141, 167–176, and 224–236 (1959).
13. S. K. Friedlander, *AICHE J.* **3**, 381 (1957).
14. J. Happel and H. Brenner, "Low Reynolds Number Hydrodynamics." Prentice-Hall, Englewood Cliffs, New Jersey, 1965.
15. B. Chalmers and D. R. Uhlman, *J. Appl. Phys.* **35**, 2986 (1964).
16. G. F. Bolling and J. Cisse, *J. Cryst. Growth* **10**, 56 (1971).
17. A. J. Ter Linden, *Proc. Inst. Mech. Eng., London* **160**, 1949 233.
18. C. J. Stairmand, *Trans. Inst. Chem. Eng.* **29**, 356 (1951).
19. J. J. Poveromo, J. Szekely, and M. Propster, Wollongong, Australia.
20. J. Happel and H. Brenner, "Low Reynolds Number Hydrodynamics," Chapter 8. Prentice-Hall, Englewood Cliffs, New Jersey, 1965.
21. B. P. LeClair and A. E. Hamielec, *Ind. Eng. Chem. Fundam.* **7**, 542 (1968).
22. B. P. LeClair and A. E. Hamielec, *Ind. Eng. Chem.* **8**, 602 (1969).
23. D. Kunii and D. Levenspiel, "Fluidization Engineering," G5. Wiley, New York, 1968.
24. S. Ergun, *Chem. Eng. Prog.* **28**, 89 (1952).
25. E. F. Blick, *Ind. Eng. Chem., Process Des. Dev.* **5**, 90 (1960).
26. C. C. Furnas, cited by F. A. Zenz and D. F. Othmer, "Fluidization and Fluid Particle Systems." Van Nostrand-Reinhold, Princeton, New Jersey, 1960.
27. H. Schultz and O. Abel, *Arch. Eisenhuettenwes.* **45**, 279 and 445 (1976).
28. J. Szekely and M. Propster, *Ironmaking Steelmaking* **7**, 15 (1977).
29. J. Szekely and R. J. Carr, *Trans. Met. Soc. AIME* **212**, 918 (1968).
30. J. Price, *Aust. Inst. Eng., Mech. Chem. Trans.* No. 1, p. 7 (1968).
31. J. Radestock and R. Jeschar, *Chem.-Ing.-Tech.* **43**, 355 (1971).
32. V. Stanek and J. Szekely, *AICHE J.* **20**, 980 (1974).
33. V. Stanek and J. Szekely, *Can. J. Chem. Eng.* **51**, 22 (1973).
34. J. Szekely and J. J. Poveromo, *AICHE J.* **21**, 769 (1975).
35. R. R. Benanati and C. B. Brosilow, *AICHE J.* **8**, 359 (1962).
36. N. A. Warner, *Chem. Eng. Sci.* **11**, 149 (1959).
37. H. E. McGannon, ed., "The Making and Shaping and Treating of Steel." US Steel Corp., Pittsburgh, Pennsylvania, 1972.
38. T. K. Sherwood, G. H. Shipley, and F. H. L. Holloway, *Ind. Eng. Chem.* **30**, 765 (1938).
39. J. Szekely and J. Mendrykowski, *Chem. Eng. Sci.* **27**, 959 (1971).
40. S. V. Sharvin, I. N. Sakhov, and B. V. Ipatov, *Izv. Chern. Met.* **9**, 5 (1962).

41. N. Standish, *Chem. Eng. Sci.* **23**, 51 and 945 (1968).
42. N. A. Warren and P. J. Mackie, *Chem. Eng. Sci.* **28**, 2141 (1973).
43. D. Kunii and D. Levenspiel, "Fluidization Engineering." Wiley, New York, 1969.
44. J. F. Davidson and D. Harrison, "Fluidization." Elsevier, Amsterdam, 1973.
45. S. Yagi and T. Aoichi, cited by Kunii and Levenspiel.
46. R. M. Davies and G. I. Taylor, *Proc. R. Soc. London, Ser. A* **200**, 375 (1950).
47. J. Szekely, J. W. Evans, and H. Y. Sohn, "Gas-Solid Reactions." Academic Press, New York, 1976.
48. F. A. Zenz and D. F. Othmer, "Fluidization and Fluid-Particle Systems." Van Nostrand-Reinhold, Princeton, New Jersey, 1960.
49. J. F. Richardson and W. N. Zaki cited by J. M. Coulson and J. F. Richardson, "Chemical Engineering," Vol. 2, p. 520. Pergamon, Oxford, 1955.
50. G. B. Wallis, "One Dimensional Two Phase Flow." McGraw-Hill, New York, 1969.
51. R. F. Stewart, in "Chemical Engineering Practice" (H. W. Cremer and T. Davies, eds.)," Vol. 3. Academic Press, New York, 1957.
52. P. B. Purchase, "Industrial Filtration of Liquids." Cleveland, Ohio, 1957.
53. G. D. Dickey, "Filtration." Van Nostrand-Reinhold, Princeton, New Jersey, 1961.

8.1 Introduction

The interaction of gas bubbles and droplets with melts plays a very important role in many metals processing operations. Gas-bubble–melt interactions are of importance in copper converting, vacuum degassing, argon stirring, and in the solidification of rimming ingots. The dispersion of metal droplets in a continuous slag phase encountered in oxygen steelmaking (both the BOF and the Q-BOP) and the resultant large, interfacial area are thought to be responsible for the very fast overall reaction rates found in these systems. In contrast the separation of finely divided copper droplets from the slag is one of the major problems encountered in the continuous smelting of copper ores in the Noranda Process.

From a practical viewpoint our interest in gas-bubble melt or droplet melt systems is usually twofold. Often the concern is to predict the overall rate of reaction between the dispersed (bubble or droplet) phase and the melt, while in other instances the objective is to characterize the fluid motion, such as circulation induced by a stream of gas bubbles or flotation characteristics of inclusion particles.

It has been suggested that in the majority of real systems of practical interest the overall rate at which a dispersed bubble or droplet phase reacts with a continuous melt is not controlled by chemical kinetics but by the physical processes, such as diffusion and the nature of the dispersion itself. This point is illustrated in Table 8.4.1,¹ which indicates the greatly enhanced overall reaction rates per unit volume that are attainable in dispersed systems.

Regarding the organization of this chapter, Section 8.2 is devoted to bubble formation—both by nucleation and at orifices, and the motion of gas bubbles in liquids (melts) is discussed in Section 8.3. Dispersed gas bubble

TABLE 8.2.1

Drag Coefficients

Range of bubble radius, cm	Drag coefficient, \mathcal{F}
$0.015 \leq R \leq 0.04$	$216 v^2/gR^3$
$0.07 \leq R \leq 0.3$	$(8R^2/3) \times 1.82\rho_l g/\sigma$
$R < 0.3$	2.56

systems are treated in Section 8.4, while the behavior of droplets is discussed in Section 8.5.

It is noted that the behavior of gas bubbles in liquids (including liquid metals) has been studied quite extensively in recent years. As a result the growth and motion of single bubbles in liquids is reasonably well understood. However, most systems of practical, industrial interest involve gas–liquid dispersions, bubble swarms, or foams. Our understanding of these systems is much less satisfactory. Notwithstanding their practical importance, even less is known about the formation of droplets (atomization) and the behavior of slag metal emulsions.

8.2 Bubble Formation

Bubbles may form in melts through spontaneous nucleation from supersaturated solutions or, alternatively, gas bubbles may be introduced into liquids by the injection of a gas stream through nozzles or orifices.

8.2.1 Bubble Nucleation

As discussed by Richardson² a very high degree of supersaturation (say of the order of 50–100 atm) must exist in order that homogeneous nucleation of the bubbles may occur. For this reason it is generally thought that gas bubble nucleation in melts of metallurgical interest is heterogeneous; that is, bubbles are formed either at solid surfaces in contact with the melt or on the surface of solid particles (impurities) present in the melt.

In order to illustrate heterogeneous nucleation, let us consider a horizontal surface of a container covered with a melt, which contains a series of small cavities; as sketched in Fig. 8.2.1, initially there exists some gas trapped at the bottom of this cavity.

The pressure inside this small, initial gas bubble $P_{r,G}$ is given by Kelvin's equation:²

$$P_{r,G} = P_a + 2\sigma/R \quad (8.2.1)$$

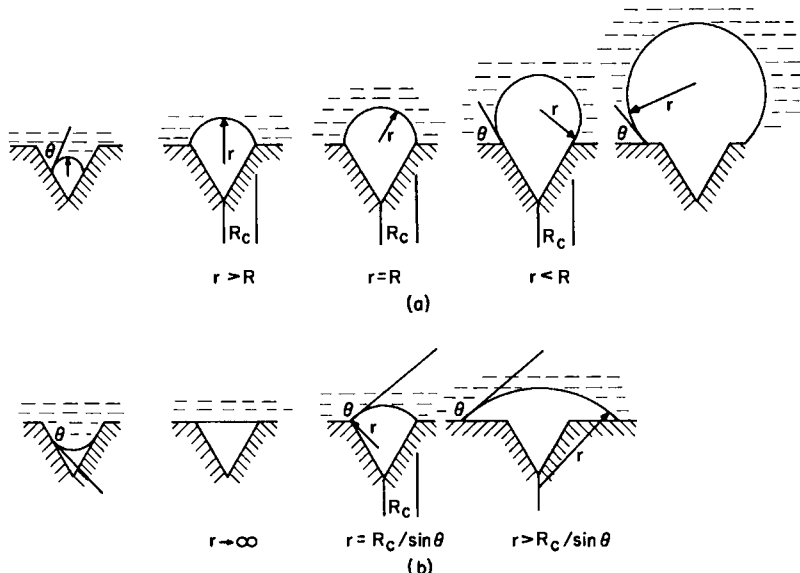


FIG. 8.2.1 Growth of a gas bubble in a cavity located on the wall of a container: (a) for a contact angle $\theta < \pi/2$, (b) for a contact angle $\theta > \pi/2$.

where P_a is the pressure in the liquid at the level of the bubble, σ the surface tension, and r is the radius of curvature. If the supersaturation pressure, with respect to the transferred component, exceeds $P_{r,G}$, the bubble will grow, as illustrated by the successive stages. Finally, once the bubble reaches a size when the buoyancy forces exceed the surface tension forces, detachment will occur.

Upon taking, somewhat arbitrarily, a typical surface tension value of 1000 dyn/cm (1.0 N/m) and a cavity radius of say 10^{-2} mm, then it is seen that a supersaturation of about 2 atm would be sufficient to initiate heterogeneous nucleation. It follows that heterogeneous nucleation may occur much more readily in melts than the formation of gas bubbles by homogeneous nucleation. It should be noted, furthermore, that most refractories tend to be porous so that the surfaces in contact with melts usually contain an adequate number of nucleation sites.

The bubble growth process, sketched in Fig. 8.2.1, has been extensively studied, both in connection with nucleate boiling and with nucleation due to solute transfer. In his now classical formulation, Scriven³ has shown that the following approximate relationship may be used for estimating the bubble radius R , as a function of time:

$$R = 2\beta(D_{AB}t)^{1/2} \quad (8.2.2)$$

where β is defined by

$$\frac{C_{\infty} - C_{eq}}{\rho_G} = 2\beta^3 e^3 \int_{\beta}^{\infty} \left(\frac{1}{\tilde{r}^2} e^{-\tilde{r}^2} - 2\beta^3/\tilde{r} \right) d\tilde{r} \quad (8.2.3)$$

where $(C_{\infty} - C_{eq})$ is concentration of the transferred species in the bulk of the melt minus the concentration of the transferred species at the bubble surface. ρ_G is the density of the gas in the bubble—in the same units as C or C_{eq} , and D_{AB} is the binary diffusivity of the transferred species in the melt. A plot of β against $(C_{\infty} - C_{eq})/\rho_G$ is available in the literature.^{3,4} It is noted, however, that when $\beta > 10$ the following approximate expression is valid:

$$\beta \approx (C_{\infty} - C_{eq})/\rho_G \quad (8.2.4)$$

Equations (8.2.2) and (8.2.4) may be used for estimating the growth of the bubble while attached to the nucleation site. The bubble becomes detached from the site when the buoyancy force exceeds the surface tension force which opposes the creation of fresh surface and hence detachment.

The bubble diameter at which detachment occurs (d_B) may be estimated using the Fritz equation

$$d_B = 0.860\theta [2\sigma/g(\rho_L - \rho_G)]^{1/2} \quad (8.2.5)$$

where θ is the contact angle in radians.

Equations (8.2.2) and (8.2.5) may now be combined to calculate the time required for a bubble to grow to its detachment diameter (t_d). On noting the bubble frequency at a given nucleation designated by f , we have the following:

$$f = \frac{1}{t_d} = \left(\frac{16D_{A-B}}{d_B^2} \right) \left[\frac{C_{\infty} - C_{eq}}{\rho_G} \right]^2 \quad (8.2.6)$$

It is to be stressed that Eq. (8.2.6) provides only a very rough estimate because of the numerous simplifying assumptions made in its derivation.

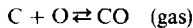
As discussed by Szekely and Martins⁵ and Szekely and Fang⁶ Eq. (8.2.2) is inapplicable when the growth rate is very fast (e.g., in vacuum degassing); moreover, in the initial stages of growth, when surface tension and viscous effects could also become important, this simple expression would not be appropriate.

It is noted, furthermore, that the bubbles which become detached from nucleation sites may be much smaller than predicted by Eq. (8.2.5) in the presence of forced or natural convection currents which would exert an additional force favoring detachment.

The most serious limitation inherent in the use of Eq. (8.2.6) is our ability to predict the number of active nucleation sites that may exist on a given surface in a bath, at any given time. It follows that while the above treatment

provides useful insight into the mechanism of heterogeneous nucleation in melts, it cannot be used for predicting the total rate at which gas bubbles would evolve from a given surface.

Example 8.2.1 In the open hearth steelmaking process carbon monoxide bubbles are nucleated at the bottom of the bath, due to the reaction



where C and O are dissolved in the melt.

If we assume that the overall rate is controlled by the diffusion of oxygen and that the driving force $(C - C_{\text{eq}}) = 1.5 \times 10^{-7} \text{ kg mole/m}^3$ let us calculate (a) the growth rate of the bubbles, and (b) the bubble frequency at a given site.

DATA $D_{\text{A-B}} = 1.1 \times 10^{-8} \text{ m}^2/\text{s}$, $\rho_{\text{G}} = 10^{-8} \text{ kg mole/m}^3$.

SOLUTION Thus

$$f(\beta) = (C_{\infty} - C_{\text{eq}})/\rho_{\text{G}} = 15$$

so that, from (8.2.4),

$$\beta \simeq 15$$

Then using Eq. (8.2.2) we have

$$R = 2 \times 15(1.1 \times 10^{-8}t)^{1/2} \quad \text{or} \quad R = 3.15 \times 10^{-3}t^{1/2} \quad (\text{i})$$

so that in $\frac{1}{2}$ s the bubble would grow to about 4.4 mm in diameter. It is to be stressed that Eq. (i) would not be valid in the initial stages of growth because of the simplifying assumption made in its derivation.^{5,6}

The detachment diameter d_B is readily calculated from Eq. (8.2.5). On taking $\theta = 2.10$ and $\sigma = 1.2 \text{ N/m}$ (1200 dyn/cm) we have:

$$d_B = 0.86 \times 2.1 \left(\frac{2.4}{9.81 \times 7.1 \times 10^3} \right)^{1/2} = 0.0106 \text{ m} \quad \text{or} \quad 10.6 \text{ mm}$$

On substituting this value of d_B in Eq. (8.2.6) we have

$$f = \frac{1}{t_d} = \frac{16 \times 1.1 \times 10^{-8}}{1.12 \times 10^{-4}} [15]^2 = 0.35 \text{ bubbles/s}$$

8.2.2 Bubble Formation at Nozzles

While the physical phenomena involved in bubble formation at nozzles are similar for low-temperature aqueous and high-temperature molten metal systems, there is sufficient difference in detail to justify the separate treatment of these phenomena.

BUBBLE FORMATION IN AQUEOUS AND ORGANIC SYSTEMS,
WHICH WET THE ORIFICE OR NOZZLE MATERIAL

When a gas is made to flow through a submerged nozzle, very different behavior is observed at high and at low gas flow rates. At high flow rates, as indicated in Fig. 8.2.2, a more or less continuous jet is formed, while at low flow rates, as seen in Fig. 8.2.1b, the formation of discrete bubbles is

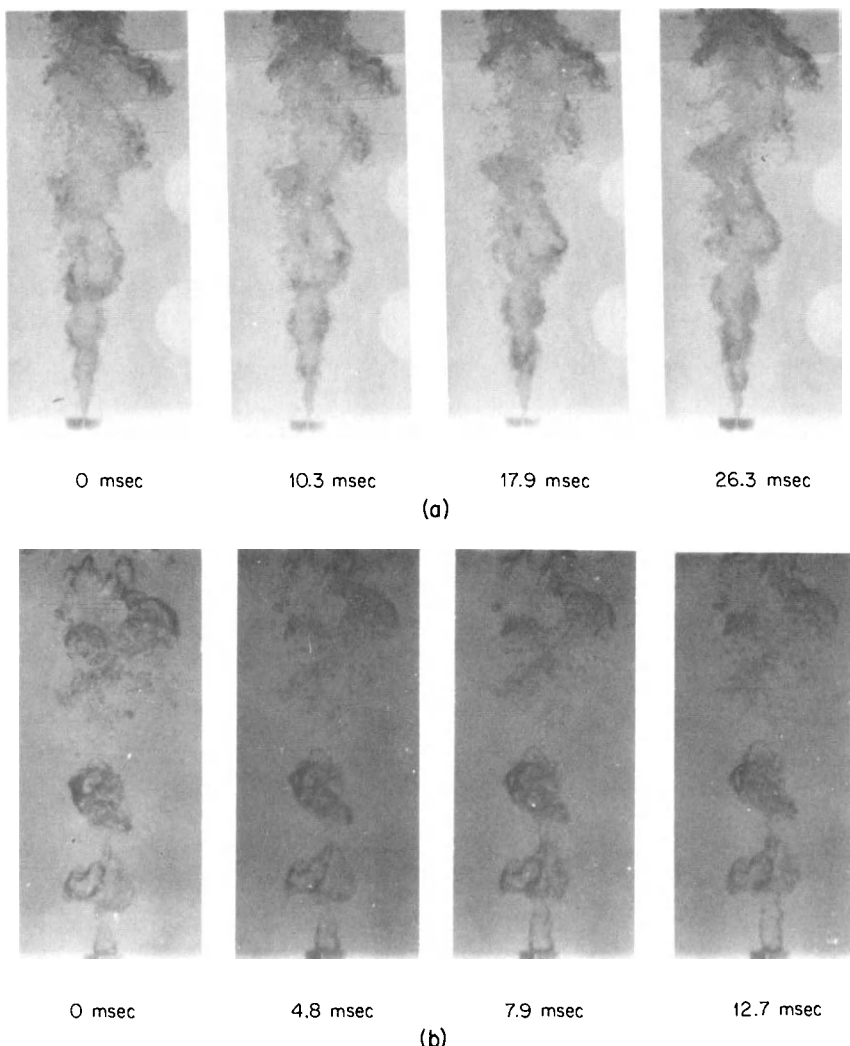


FIG. 8.2.2 Photographs depicting a gas stream issuing from a nozzle into water: (a) jet formation at high gas flow rates, (b) formation of discrete bubbles at low flow rates. Courtesy of Dr. M. McNallan, Department of Materials Science and Engineering, MIT.

observed. Leibson *et al.*⁷ suggested on the basis of experiments with air-water systems that discrete bubbles are formed when

$$N_{Re,0} = ud_0\rho/\mu < 2100 \quad (8.2.7)$$

while jet type behavior was postulated by these authors for nozzle Reynolds numbers larger than about 2100. While it is not clear that the transition from the bubbling regime to the jet regime occurs at a nozzle Reynolds number of 2100 in case of liquid metals, the existence of a transition is to be expected as the gas flow rate is increased. In this chapter we shall confine our attention to the bubbling regime, while submerged jets are discussed in Chapter 9.

A good review of experimental and theoretical work on the formation of bubbles at orifices has been presented by Kumar and Kuloor,⁸ who concluded that a general model describing bubble formation over a broad range of conditions is not available, and indeed the complexity of these phenomena would make the development of such a comprehensive model quite difficult.

Figure 8.2.3 shows a sketch of the growth of a gas bubble, while attached to an orifice. It is seen that in the initial stage (Fig. 8.2.3a) the bubble tends to expand, while essentially maintaining its shape; as seen in Fig. 8.2.3b, after the bubble has grown to a given size its shape tends to deform and a "neck" is being established. Finally, Fig. 8.2.3c shows the bubble on detachment.

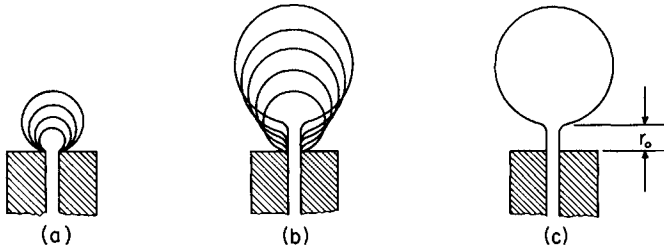


FIG. 8.2.3 Bubble formation at an orifice; after Kumar and Kuloor.⁸ (a) Expansion stage, (b) detachment stage, (c) condition of detachment.

Consideration of the physics of bubble growth would indicate that the growth and detachment of gas bubbles in liquids is affected by several factors, including surface tension, viscosity, liquid inertia, and the upstream pressure. As discussed by Kumar and Kuloor, convenient asymptotic analysis of the growth and detachment process are available for special cases when the overall rate is limited by only one or two of these parameters. Paradoxically though, in many instances these simple analyses do not correspond to the problems of real, practical significance.

At very low gas flow rates through an orifice immersed in a liquid, the bubble diameter on detachment and thus the bubble frequency are determined by a balance between the surface tension and the buoyancy force:⁹

$$\frac{\pi}{6} d_B^3 g(\rho_L - \rho_G) = \pi d_0 \sigma, \quad N_{Re,0} < 500, \quad \text{or} \quad d_B = \left[\frac{6d_0 \sigma}{g(\rho_L - \rho_G)} \right]^{1/3} \quad (8.2.8)$$

where $N_{Re,0} = ud_0/\mu = 4Q\rho/d_0\mu$ is the nozzle Reynolds number and Q is the volumetric flow rate of the gas.

Equation (8.2.8) was found consistent with a large number of experimental measurements—albeit on aqueous and on organic systems. However, since surface tension effects were included, it is likely that this equation would hold, at least approximately, for molten metal systems.

The region $N_{Re,0} > 500$ was investigated by Leibson *et al.*⁷ using the air-water system, and a selection of their measurements is shown in Fig. 8.2.4. Within the range $500 \leq N_{Re,0} \leq 2100$, these authors were able to represent their measurements by the following empirical correlation:

$$d_B = 0.046d_0^{0.5}N_{Re,0}^{1/3} \quad (8.2.9)$$

We note that Eq. (8.29) is a dimensional relationship, where d_B and d_0 are in meters.

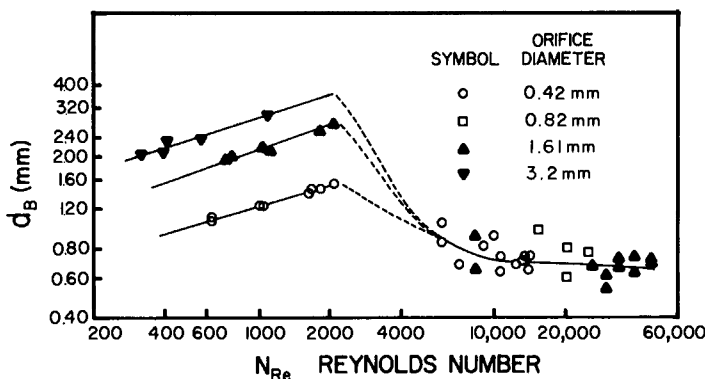


FIG. 8.2.4 Bubble size as a function of the orifice Reynolds number, for the formation of air bubbles in water; after Leibson *et al.*⁷

As seen in Fig. 8.2.4, for $N_{Re,0} > 5000$ a more or less constant bubble size was being obtained. As noted earlier, in this region a continuous jet rather than discrete bubbles were found to form, and the bubble size shown in the graph is the result of jet breakup.

By establishing a balance between inertial and buoyancy forces (and neglecting surface tension and viscous effects) Davidson and Harrison¹⁰ derived the following expression for the bubble size:

$$d_B \simeq 1.3Q^{6/5}/g^{3/5} \quad (8.2.10)$$

It can be readily shown that Leibson's empirical expression and the above, theoretically derived equation are quite similar in form. Figure 8.2.5 shows a comparison between the predictions based on Eq. (8.2.10) and measurements reported by numerous investigators on the air-water system; the reasonable agreement is readily apparent.

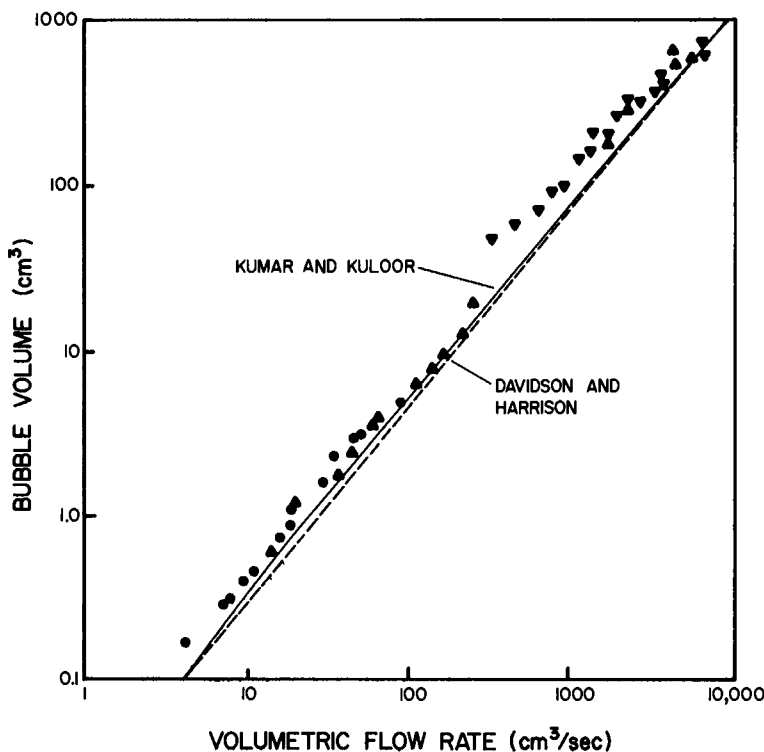


FIG. 8.2.5 Comparison between Eq. (8.2.10) and measurements reported by Kumar and Kuloor⁸ and Harrison and Davidson.¹⁰

A range of more complex models for bubble formation at orifices have been reviewed by Kumar and Kuloor,⁸ who also present a useful description of the experimental techniques available for the study of bubble formation at orifices.

It is noted that more recent work on bubble formation at nozzles and orifices has pointed to additional complexities, notably the formation of double or even triple bubbles and the effect of the antechamber size. A discussion of these will be given subsequently in conjunction with the behavior of gas bubbles in metallic melts.

BUBBLE FORMATION AT NOZZLES SUBMERGED IN MOLTEN METALS

Until recent times, little work has been done on gas bubble formation in liquid metals systems, mainly because of the experimental difficulties involved; however, a number of very recent papers, notably by Guthrie and Irons,¹¹ Anderini and Foster,¹² and Sano and Mori¹⁴ have shed considerable light on the behavior of these systems. In this regard the work of Guthrie and Irons is particularly helpful because it also provides a good review of the relevant literature.

Figure 8.2.6 indicates the principal difference between liquid metal and aqueous systems, regarding bubble formation. For gas bubble formation in aqueous or organic systems, when the liquid wets the nozzle, the bubble forms at the tip of the capillary, as shown on the left-hand side of Fig. 8.2.6 and was sketched in greater detail in Fig. 8.2.3. In contrast for nonwetting systems the bubble tends to form at the outer circumference of the nozzle,

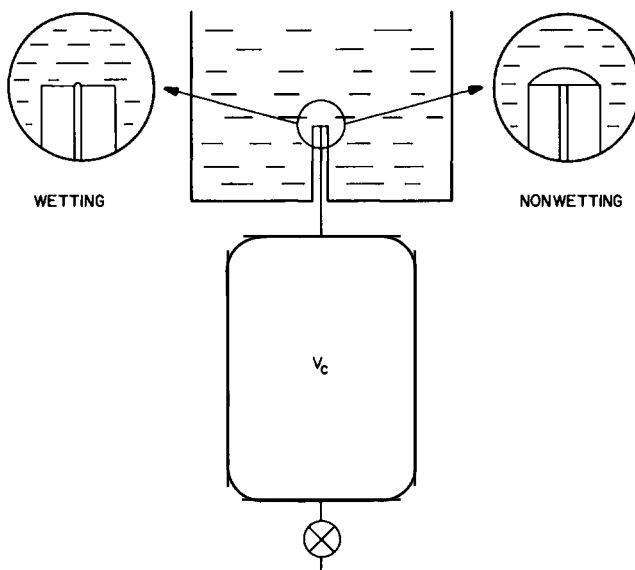


FIG. 8.2.6 Schematic sketch of bubble formation of an orifice allowing for both wetting or nonwetting fluids and for the antechamber effect; after Guthrie and Irons.¹¹

as sketched on the right-hand side of Fig. 8.2.6. An important consequence of this behavior is that the expression for the bubble diameter on detachment has to be appropriately modified. Thus for liquid metal systems at low gas flow rates the balance between surface tension and buoyancy forces gives the following relationship:

$$d'_{B,d} = \left[\frac{6d_{n,o}\sigma}{\rho(\rho_L - \rho_G)} \right]^{1/2} \quad (8.2.11)$$

where $d_{n,o}$ is the outside diameter of the nozzle.

Inspection of Figs. 8.2.6 and 8.2.7 points to another refinement that has to be considered in the modeling of bubble formation at nozzles, namely the effect of the antechamber, or the volume of the gas train, designated by V_c . This chamber volume is defined as the volume between the last large pressure drop (i.e., a valve) and the actual nozzle or orifice.

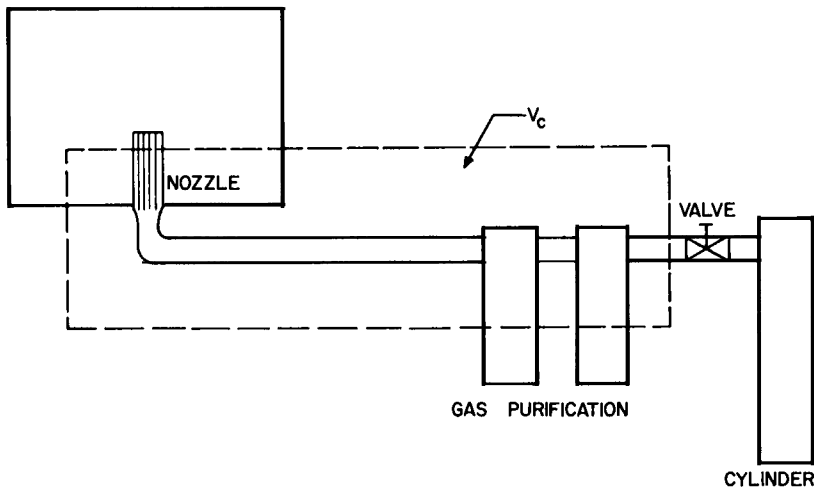


FIG. 8.2.7 Sketch illustrating the physical definition of V_c . After Guthrie and Irons.¹¹

In a physical sense, during the formation of the bubble, there is a gradual pressure build-up in the antechamber, the net result of which is that when the bubble is released, the final volume on detachment is larger than calculated from the "static balance" and given by Eqs. (8.2.10) and (8.2.11) for wetting and nonwetting systems, respectively.

The actual analysis of this phenomenon has been discussed by Guthrie¹¹ and by others, but here we shall confine our attention to the presentation of the final results.

The effect of the antechamber is conveniently represented in terms of a dimensionless capacitance group, which for nonwetting systems may be defined as

$$\tilde{N}_c' = 4\rho_L g V_c / \pi d_o d_{n,o} P_s \quad (8.2.12)$$

where V_c is the volume of the antechamber, ρ the density of the melt, and P_s is the pressure of the nozzle. It has been suggested that at low flow rates Eq. (8.2.12) has to be modified to allow for the effect of the capacitance of the gas train. On denoting this modified bubble detachment diameter as $(d'_{B,d})_{\text{eff}}$ we have

$$\begin{aligned} (d'_{B,d})_{\text{eff}} &= d_{B,d} && \text{for } \tilde{N}_c' < 1 \\ (d'_{B,d})_{\text{eff}} &= (\tilde{N}_c')^{1/3} d_{B,d} && \text{for } 1 \leq \tilde{N}_c' \leq 9 \\ (d'_{B,d})_{\text{eff}} &\simeq 2.08 d_{B,d} && \text{for } \tilde{N}_c' > 9 \end{aligned} \quad (8.2.13)$$

It follows that for small antechamber volumes, i.e., when $\tilde{N}_c' > 1$, the capacitance effect may be neglected. However, the role played by the capacitance number may well explain the apparent discrepancies between the results of the various investigators.

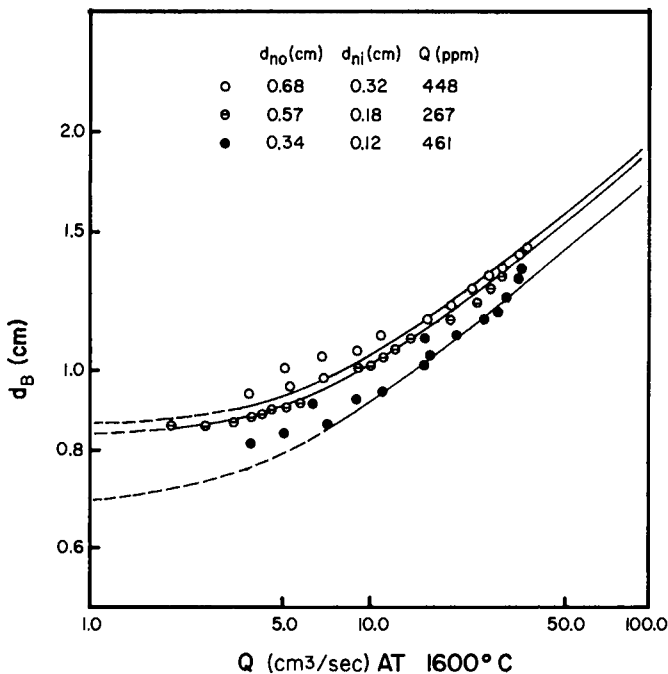


FIG. 8.2.8 Comparison of experimentally measured bubble sizes in molten iron, at different impurity levels, with predictions based on Eq. (8.2.14).¹¹

Sano and Mori¹⁴ proposed the following semiempirical relationship to represent measurements obtained in molten iron:

$$(d'_{B,d})_{\text{eff}} = \left[\frac{3\sigma d_{n,o}}{\rho g} \tilde{N}'_c + \left(\frac{9\sigma^2 d_{n,o}}{\rho^2 g^2} \tilde{N}'_c + \frac{10Q_G^2 d_{n,o}}{g} \right)^{1/2} \right]^{1/3} \quad (8.2.14)$$

where, as before, $d_{n,o}$ is the outer diameter of the nozzle.

It is stressed that Eq. (8.2.14) is an empirical relationship, written in cgs units; thus, $(d'_{B,d})_{\text{eff}}$ is given in centimeters, the density in grams per cubic centimeter, the volumetric gas flow rate in cubic centimeters per second, etc.

Figure 8.2.8 shows a plot of the experimentally measured bubble sizes in molten iron; it is seen that these measurements are reasonably well interpreted by using Eq. (8.2.11). Perhaps of even greater interest is Fig. 8.2.9, which shows the experimental measurements, together with those reported by Leibson, which were given previously in Fig. 8.2.4.

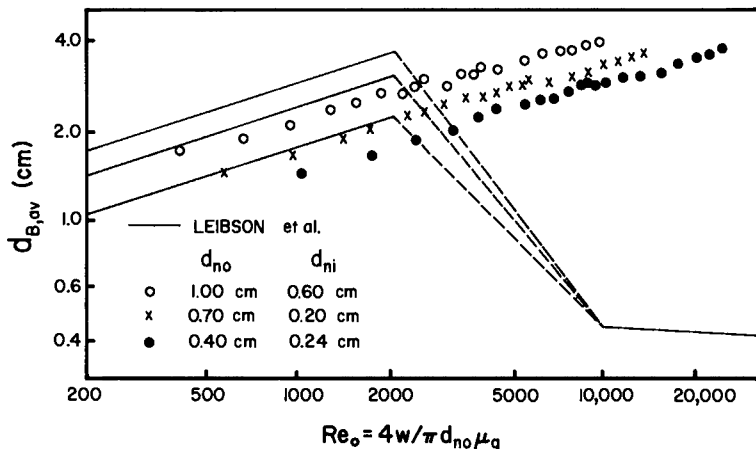


FIG. 8.2.9 A comparison of the experimental measurements of Sano and Mori¹⁴ with Leibson's equation.

It is seen, that the drastic lowering of the bubble size, for $N_{Re} > 5000$, was not found experimentally for liquid metal systems. This discrepancy may be attributed to the fact that, for larger values of the Reynolds number, Leibson found that turbulence in the liquid caused a breakup of the bubbles. For liquid metals the higher interfacial tension may have prevented such a breakup, at least up to the Reynolds numbers explored by Sano and Mori.¹⁴

Finally, Fig. 8.2.10 shows a plot of the bubble diameters against the gas flow rate for a variety of molten metal systems, illustrating the pronounced effect of the capacitance number, particularly for low gas flow rates; after Guthrie and Irons.¹¹

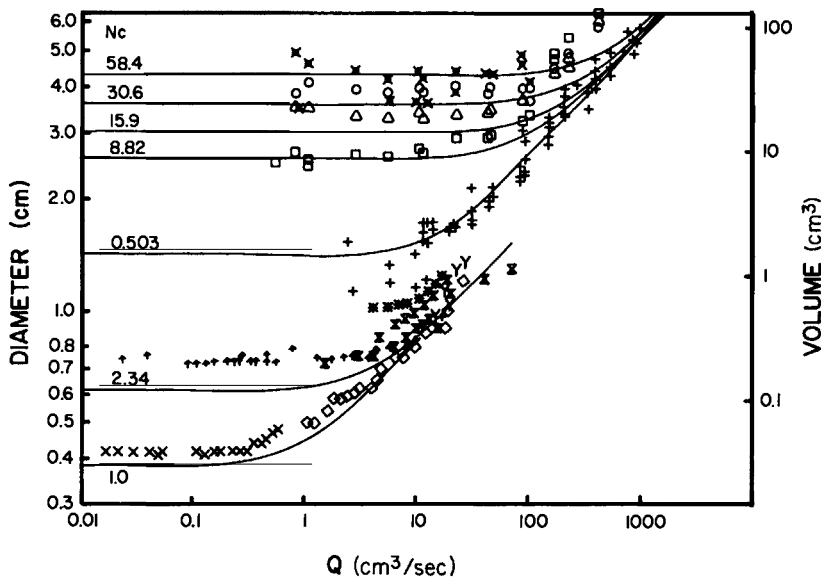


FIG. 8.2.10 A comparison of experimentally measured bubble diameters in molten metals with predictions based on the analysis of Guthrie and Irons,¹¹ showing the effect of the capillary number.

Let us illustrate the use of Eq. (8.2.14) by working a simple example.

Example 8.2.2 Estimate the size of the gas bubbles formed, when injecting nitrogen into molten iron at 1600°C at a volumetric flow rate of 30 cm³/s (at 1600°C). The effective nozzle diameter may be taken as 1.0 cm, the interfacial tension is 1600 dyn/cm, and the capacitance number $\tilde{N}_c' = 1$.

SOLUTION Let us substitute these numerical values into Eq. (8.2.14). Thus we have

$$(d'_{B,d})_{\text{eff}} = \left[\left(\frac{3 \times 1600 \times 1}{7.1 \times 981} \right)^2 + \left(\frac{9 \times (1600)^2 \times 1}{(7.1)^2 (981)^2} + \frac{10 \times (30)^2 \times 1}{981} \right)^{1/2} \right]^{1/3}$$

$$= [0.68 + (0.47 + 9.17)^{1/2}]^{1/3} \sim 1.56 \text{ cm}$$

It is seen, furthermore, that for the conditions chosen both the surface tension forces and liquid inertia play a role in determining the bubble size, but the inertial effects are more important.

8.3 The Motion of Gas Bubbles in Liquids

The velocity with which bubbles rise through a liquid is determined principally by the buoyancy force that drives the bubble upwards, and the

viscous and form drag that tend to retard this motion. When these forces are balanced, the bubble rises at a constant velocity.

Similar considerations led to the calculation of the terminal falling velocity of solids in fluids discussed in Chapter 7 and, as will be shown subsequently, identical considerations may be applied to describing the motion of liquid droplets in liquids. In fact, the principles that govern the movement of droplets and bubbles are similar, but because traditionally these two fields have developed separately, we shall treat these two topics separately. There are two major differences between the motion of bubbles and solid particles in fluids.

(i) In general the bubble is not rigid; thus, the forces acting upon it may deform its shape.

(ii) The gas contained in the bubble may undergo circulation, which in turn would affect the drag force. This point is illustrated in Fig. 8.3.1.¹⁵

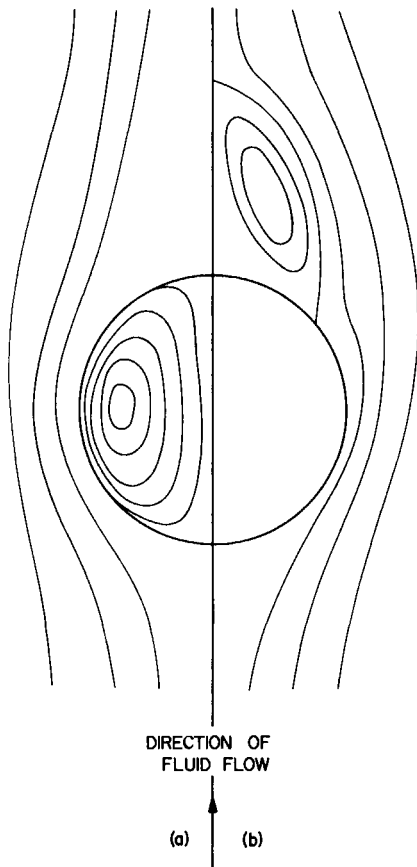


FIG. 8.3.1 Liquid streamlines around a gas bubble: (a) with gas circulation, (b) without circulation in the bubble. After Johnson *et al.*¹⁵

A great deal of theoretical work has been done on the rising velocity and shape of gas bubbles in liquids, and in most cases theory is in quite good agreement with measurements. In this section we shall present a phenomenological description of bubble behavior with only an occasional reference to the underlying theory.

The principal parameters which characterize the motion of bubbles are bubble Reynolds number,

$$N_{Re,b} = d_b U \rho_L / \mu_L \quad (8.3.1)$$

Weber number,

$$N_{We} = d_b U^2 \rho_L / \sigma \quad (8.3.2)$$

or Eotvos number,

$$N_{Eo} = g d_e^2 (\rho_L - \rho_G) / \sigma \quad (8.3.3)$$

and Morton number,

$$N_{Mo} = g \mu_L^4 / \rho_L \sigma^3 \quad (8.3.4)$$

Useful work, characterizing the rising velocity of gas bubbles in liquids, has been done by Peebles and Garber,¹⁶ Hartunian and Sears,¹⁷ Haberman and Morton,¹⁸ Hadamard and Rybczynski,¹⁹ Levich,²⁰ and others.

A recent paper by Grace *et al.*²¹ provides a rather elegant map of the gas bubble domains that one may encounter in practice. Figures 8.3.2 and 8.3.3 indicates the important regions of bubble behavior in terms of the Eotvos number and the Reynolds number.

The following general comments should be made:

(1) When the Reynolds number is small, say $N_{Re} < 1$, the bubbles are spherical in shape. Physically this corresponds to small bubbles.

(2) When the Reynolds number is large, say $N_{Re} > 1000$, and the Eotvos number is also large, say $N_{Eo} > 50$, spherical cap bubbles are formed. This corresponds to large bubbles, rising in liquids of low or of moderate viscosity.

(3) At intermediate values of the Reynolds number and large values of the Eotvos group, skirted or dimpled bubbles are formed. Physically this corresponds to the behavior of large gas bubbles in highly viscous liquids.

(4) Finally, at intermediate values of the Reynolds number and of the Eotvos number, ellipsoidal and "whirling" bubbles are found, which may oscillate and rise in a circular path.

Correlations and also fundamental studies exist to enable the prediction or estimation of the rising velocities of the bubbles in all these regions, but the situation is clearcut only at very low and at very high Reynolds numbers, as discussed in the following paragraphs.

1. *Very small bubbles*: $N_{Re,b} < 2$. Under these conditions, the bubbles are spherical, and tend to behave like rigid spheres. It follows from the

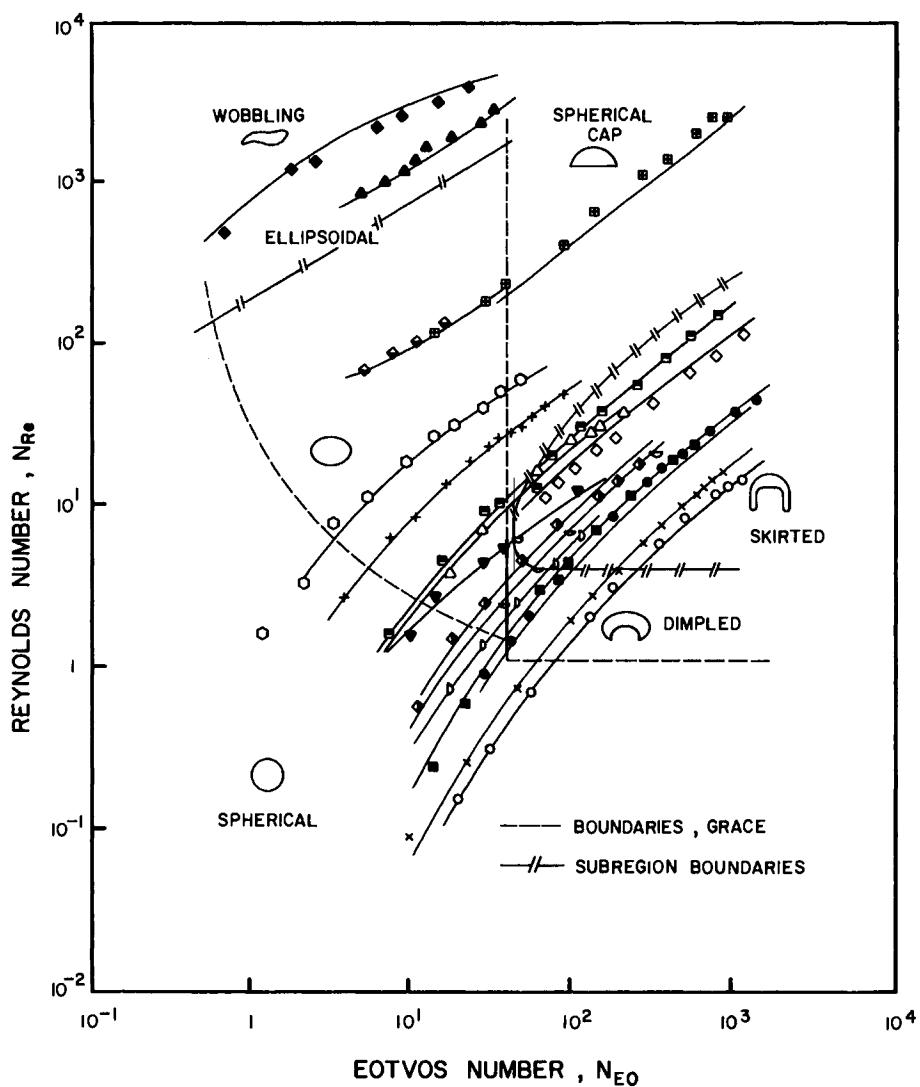


FIG. 8.3.2 Regions of bubble behavior, on a plot of the Reynolds number against the Eotvos number; after Grace *et al.*²¹ Note that this treatment includes both gas bubbles and liquid droplets rising in liquids. Original figures kindly supplied by Prof. Grace of McGill University.

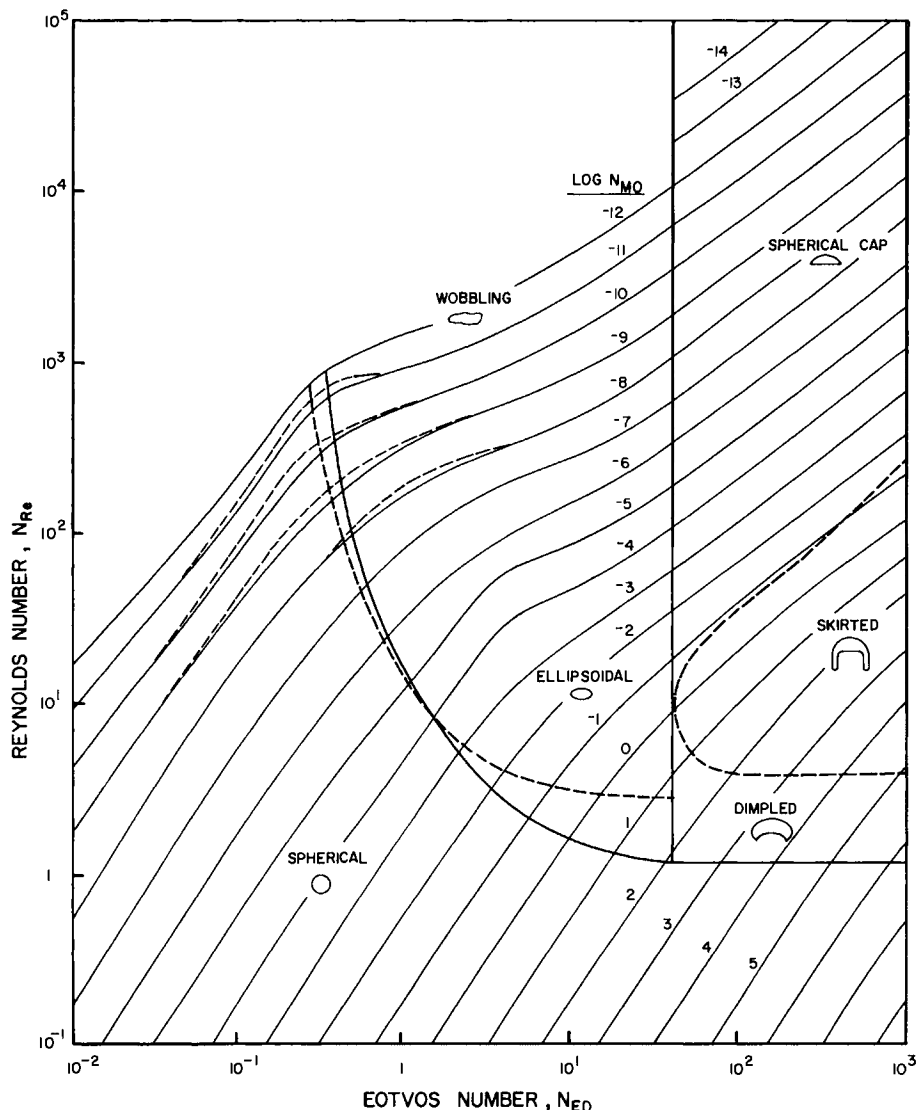


FIG. 8.3.3 Regions of bubble behavior on a plot of the Reynolds number against the Eotvos number (Morton number) after Grace *et al.*²¹ Original figures kindly supplied by Prof. Grace of McGill university.

discussion in the previous chapter that Stokes' law applies; thus, the terminal rising velocity U_t is given by

$$U_t = \frac{d_b^2}{18\mu} g(\rho_L - \rho_G) \quad (8.3.5)$$

2. *Spherical-cap bubbles*: $N_{Re,b} > 1000$, $N_{We} > 18$, or $N_{Eo} > 50$. Bubbles larger than about 1 cm in diameter when rising in liquids of low or intermediate viscosity, e.g., in water or in liquid metals, are of spherical-cap shape and rise at a terminal velocity, which is apparently independent of the properties of the liquid. Typical examples of spherical-cap bubbles are shown in Fig. 8.3.4.²²

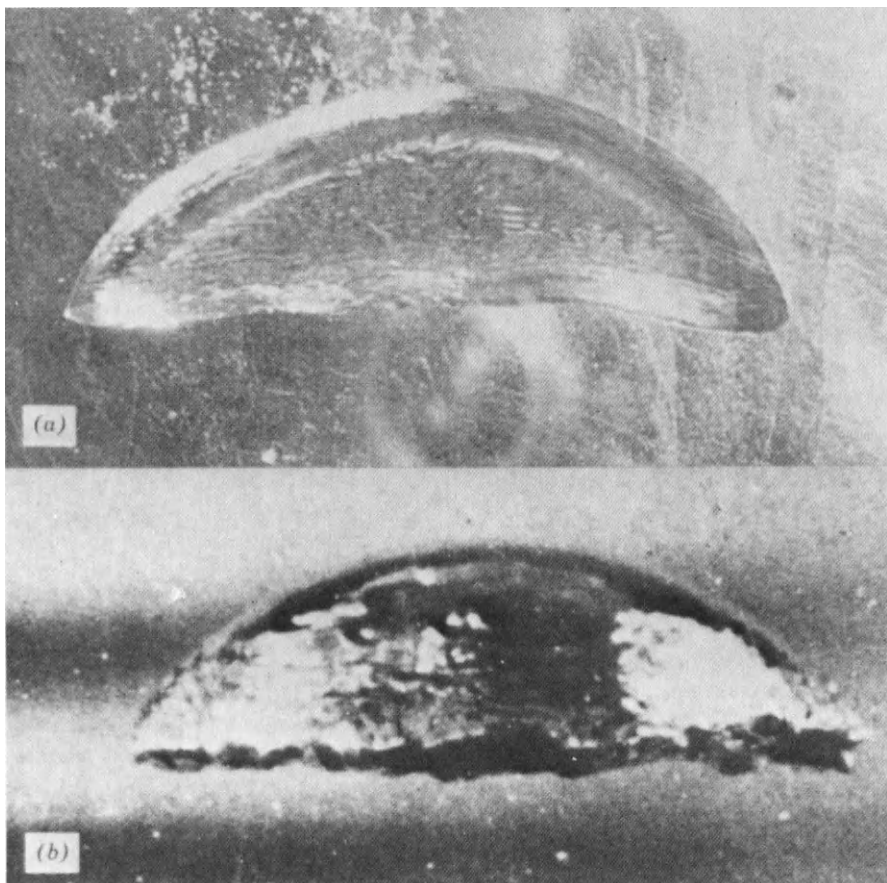


FIG. 8.3.4 Typical examples of spherical-cap bubbles: (a) a two-dimensional argon bubble (base 8 cm) rising in mercury, (b) a nitrogen bubble (base 7.3 cm) rising in a column of water; photograph kindly supplied by Prof. Davenport of McGill University.

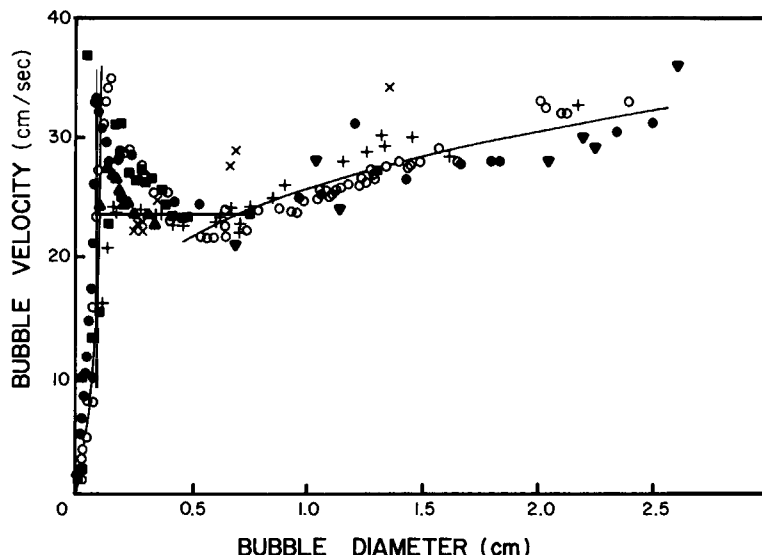


FIG. 8.3.5 The rising velocity of single bubbles in water. The symbols represent the results of nine different studies, as cited by Van Krevelen and Hofstijzer.⁹

An equation for the rising velocity of such bubbles was derived by Davies and Taylor^{21a} and can be expressed as

$$U_t = 0.79g^{1/2}V_B^{1/6} \quad \text{or} \quad U_t = 1.02(gd_B/2)^{1/2} \quad (8.3.6)$$

Figure 8.3.5 shows the results of nine separate investigations aimed at the experimental measurement of the rising velocities of air bubbles in water. The appreciable scatter in the measurements is readily apparent, but it is noted that this scatter is rather less pronounced in the limiting regions corresponding to low and high values of the Reynolds number, namely the Stokes' law region and the spherical cap region. In contrast, the scatter is rather more pronounced at intermediate bubble sizes, which would correspond to the spheroidal or the oscillating bubbles.

Numerous measurements have been carried out to ascertain the applicability of Eq. (8.3.6) to liquid-metal-gas systems.^{22,23} Since at large bubble Reynolds numbers inertial effects predominate, it is perhaps not surprising that Eq. (8.3.6) holds reasonably well for a range of Newtonian liquids, including water, mercury, and molten silver.

Figure 8.3.6 shows a plot of the rising velocity of spherical-cap bubbles of air in water and in mercury. At small bubble diameters there is good agreement between the measurements and the predictions; the discrepancy observed at larger bubble diameters was attributed to wall effects. However, the data for mercury and for water are still in very close agreement in this region.

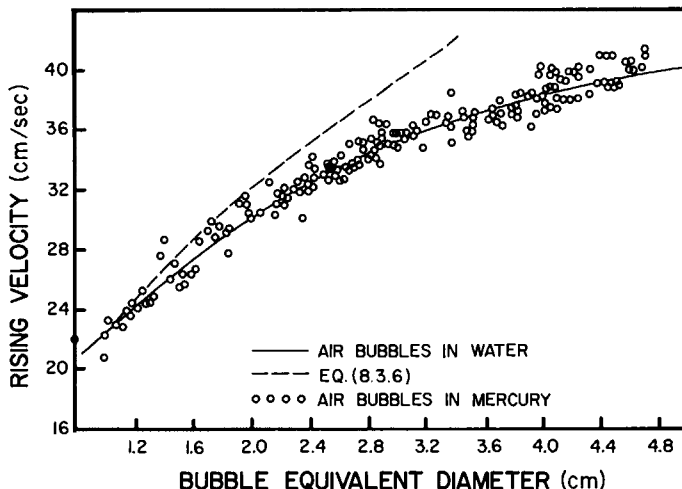


FIG. 8.3.6 The rising velocities of spherical cap bubbles in water and in mercury; after Davenport.^{22,23}

GROWTH OF A RISING BUBBLE

Equations (8.3.5) and (8.3.6) apply to bubbles of unchanging size. In practical systems bubbles will expand as they rise through a melt (liquid) because they experience a progressively reduced static head. This effect may not be very significant for many aqueous systems, the freeboard of which is at atmospheric pressure; however, the much greater density of molten metals will cause an appreciable expansion of a gas bubble, even on a rise through a relatively shallow depth. Thus a gas bubble would experience a twofold increase in its volume on rising through a 0.76-m depth of mercury or a 1.4-m depth of molten iron, the surface of which is exposed to atmospheric pressure. The expansion would, of course, be greater if the free surface of the melt is at a reduced pressure, as in the case of vacuum degassing systems.^{24,25}

For moderate rates of bubble expansion it is reasonable to assume that the pressure inside the bubble is the same as the static pressure in the liquid at the level of the bubble and that the changes in the terminal rising velocity of the bubble due to the bubble expansion occur instantaneously.

Under these conditions it is a very straightforward matter to describe the trajectory of the bubble, as affected by its expansion.^{26,27}

The pressure inside the bubble, P_x , at a height x above the orifice, is given by

$$P_x = P_o - g\rho_L x \quad (8.3.7)$$

where P_o is the pressure just above the orifice.

For spherical-cap bubbles to be considered here, we have

$$U_t = 0.79g^{1/2}V_B^{1/6} \quad (8.3.8)$$

Since $U_t = dx/dt$ we may write

$$dx/dt = 0.79g^{1/2}V_B^{1/6} \quad (8.3.9)$$

The equation of state is written as

$$P_x V_x = P_o V_o \quad (8.3.10)$$

On designating the liquid depth above the orifice by $x = H$, we have

$$P_o = P_{atm} + \rho_L g H \quad (8.3.11)$$

On combining Eqs. (8.3.8)–(8.3.10) we have

$$dx/dt = 0.79g^{1/2} \left[\frac{P_o V_o}{P_o - \rho_L g x} \right]^{1/6} \quad (8.3.12)$$

which is readily integrated for the boundary condition

$$x = 0 \quad \text{at} \quad t = 0 \quad (8.3.13)$$

to obtain

$$t = \frac{1.08}{g^{1/2}(P_o V_o)^{1/6} \rho_L g} [P_o^{7/6} - (P_o - \rho_L g x)^{7/6}], \quad 0 \leq x \leq H \quad (8.3.14)$$

Equation (8.3.13) provides the desired relationship between the position of the bubble (x) and time for spherical-cap bubbles. Once x is known as a function of time, the instantaneous volume V_x is readily obtained from Eqs. (8.3.7) and (8.3.10).

Analogous procedures may be used for deriving an expression for the trajectory of spherical bubbles in the Stokesian regime. As noted earlier, however, the intermediate region between rigid spherical bubbles and spherical-cap bubbles is rather less defined, so that predictions in this regime are likely to be less accurate.

It has to be stressed that the applicability of Eq. (8.3.13) is restricted to conditions when the rate of expansion of the bubble is relatively low.

When a gas bubble rises in a liquid, the freeboard of which is evacuated, as is the case in vacuum degassing, two complicating factors will arise. One of these is associated with the fact that a rapidly expanding bubble has to accelerate the surrounding fluid, and so the pressure inside the bubble has to be larger than the static pressure in the liquid at the level of the bubble. The other factor is that on rapid expansion the drag force has to be modified, so it is no longer realistic to assume, as we have done before, that the bubble will attain its terminal velocity instantaneously. This second effect is analogous to Bassett's problem, discussed in Section 7.1.

THE TRAJECTORY OF A RAPIDLY EXPANDING BUBBLE

In developing expressions for the trajectory of a rapidly rising bubble, let us consider the system sketched in Fig. 8.3.7, where a bubble of radius $R(t)$ is rising in a liquid, the freeboard of which is at a reduced pressure P_t . If, as before, x denotes the distance of the bubble from the top surface, then the pressure in the liquid at the level of the bubble is given by

$$P_{x,\infty} = P_t + \rho g x \quad (8.3.15)$$

However, the pressure inside the bubble, $P_{x,G}$, is larger than $P_{x,\infty}$, when rapid growth occurs, because a pressure gradient is required in the liquid in the vicinity of the bubble to accelerate the surrounding fluid.

This problem may be formulated with the aid of the differential equations developed in Chapter 3. Upon considering the expansion of the spherical bubble, the equation of continuity for the surrounding liquid may be written as

$$r^2 u_r = R_B^2 \dot{R}_B \quad (8.3.16)$$

where r is the radial distance in the liquid, measured from the bubble surface, $u_r(r)$ the radial velocity in the liquid at r , $R_B = R_B(t)$ is the bubble radius at a given time t , and

$$\dot{R}_B = \frac{dR_B}{dt}, \quad \ddot{R}_B = \frac{d^2 R_B}{dt^2}$$

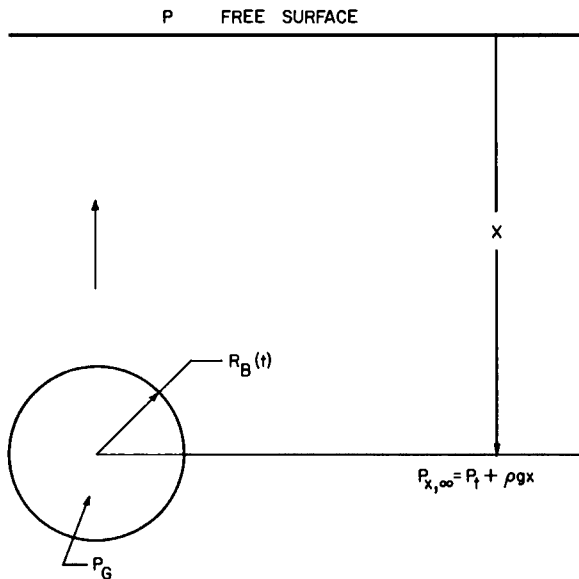


FIG. 8.3.7 Sketch of the system for the rapidly expanding bubble.

The equation of motion in the liquid, for a spherically symmetrical system, is written as

$$\partial u_r / \partial t + u_r \partial u_r / \partial r = (1/\rho_L) \partial P_r / \partial r + (2\mu/\rho) \partial^2 u_r / \partial r^2 \quad (8.3.17)$$

where P_r is the pressure. Upon substituting from the equation of continuity (8.3.16) and using the chain rule of differentiation the terms on the left-hand side of Eq. (8.3.16) are expressed as

$$u_r = R_B^{-2} \dot{R}_B / r^2 \quad (8.3.18)$$

$$\frac{\partial u_r}{\partial r} = -\frac{2R_B^{-2} \dot{R}_B}{r^3} \quad (8.3.19)$$

$$\frac{\partial u_r}{\partial t} = r^{-2} [R_B^{-2} \ddot{R}_B + 2R_B \dot{R}_B^2] \quad (8.3.20)$$

Upon substituting into Eq. (8.3.17) and on neglecting the viscous term we have

$$\frac{1}{r^2} [R_B^{-2} \ddot{R}_B + 2R_B \dot{R}_B^2] + \frac{1}{2r^5} [R_B^{-4} \dot{R}_B^2] = -\frac{1}{\rho_L} \frac{\partial P_r}{\partial r} \quad (8.3.21)$$

Equation (8.3.21) is integrated between the limits

$$P_r = P_{x,\infty} \quad \text{at} \quad r = \infty \quad (8.3.22)$$

and

$$P_r = P_{x,G} \quad \text{at} \quad r = R_B \quad (8.3.23)$$

to obtain

$$R_B \ddot{R}_B + \frac{3}{2} \dot{R}_B^2 = -[(P_{x,\infty} - P_{x,G})/\rho_L] \quad (8.3.24)$$

In physical terms Eq. (8.3.22) expresses the fact that for a rapidly expanding bubble (i.e., when \ddot{R}_B and \dot{R}_B are large) $P_{x,G}$, the pressure inside the bubble, is larger than $P_{x,\infty}$, the pressure in the liquid at the same level as the bubble.[†] Thus on combining Eqs. (8.3.15) and (8.3.24) we have

$$P_{x,G} = P_t + \rho g x + (\ddot{R}_B R_B + \frac{3}{2} \dot{R}_B^2) \rho_L \quad (8.3.25)$$

It may be shown³¹ that after some manipulation the following expression may be developed for relating $R(t)$ and its derivatives to time:

$$[P_t - \rho g x + (\ddot{R}_B R_B + \frac{3}{2} \dot{R}_B^2) \rho_L] \frac{dR}{dt} = \frac{R}{3} \rho g u \quad (8.3.26)$$

[†] For an expanding bubble $P_{x,G} > P_{x,\infty}$; under certain circumstances both viscous forces and surface tension forces may play an important role in limiting bubble growth. A good discussion of these problems is available in Szekely *et al.*^{28,29}

where $u = dx/dt$ is the rising velocity of the bubble, which may be estimated with the aid of Bassett's equation:

$$\frac{du}{dt} + \frac{3u}{R} \frac{dR}{dt} + \frac{3}{4} \mathcal{F}(u^2/R) - 2g = 0 \quad (8.3.27)$$

The expressions for the drag coefficient are given in Table 8.2.1.

Equations (8.3.25) and (8.3.26) were integrated numerically; details of the procedure, including a listing of the program, are available in Fang.³¹

Figures 8.3.7 and 8.3.8 show a comparison between predictions and measurements regarding the bubble radius as a function of position and the

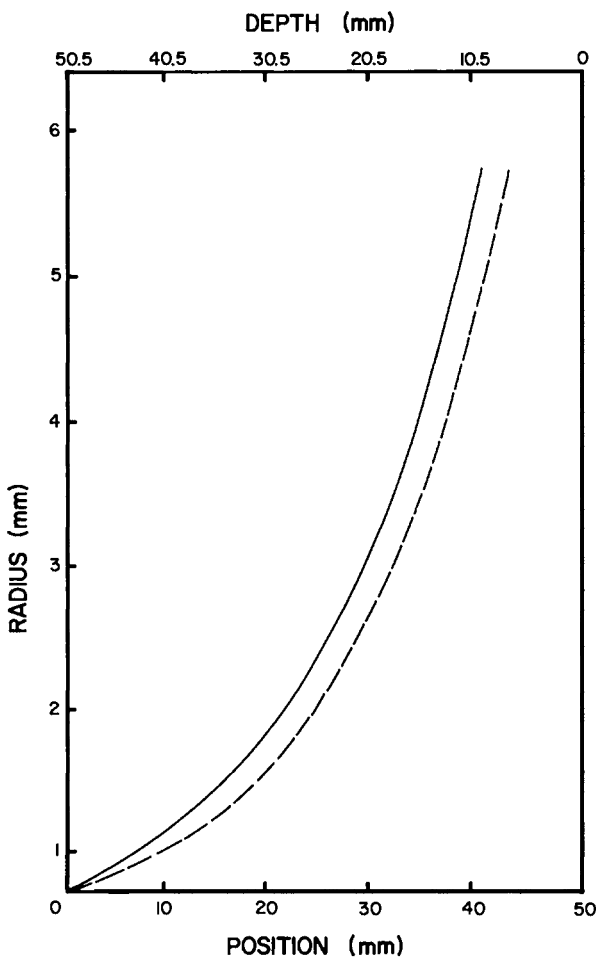


FIG. 8.3.8 Plot of the bubble radius against position for the growth of a *n*-pentane bubble in *n*-tetradecane at a freeboard pressure of 1 mm Hg; after Szekely and Fang.³⁰ — Predicted. --- Experimental.

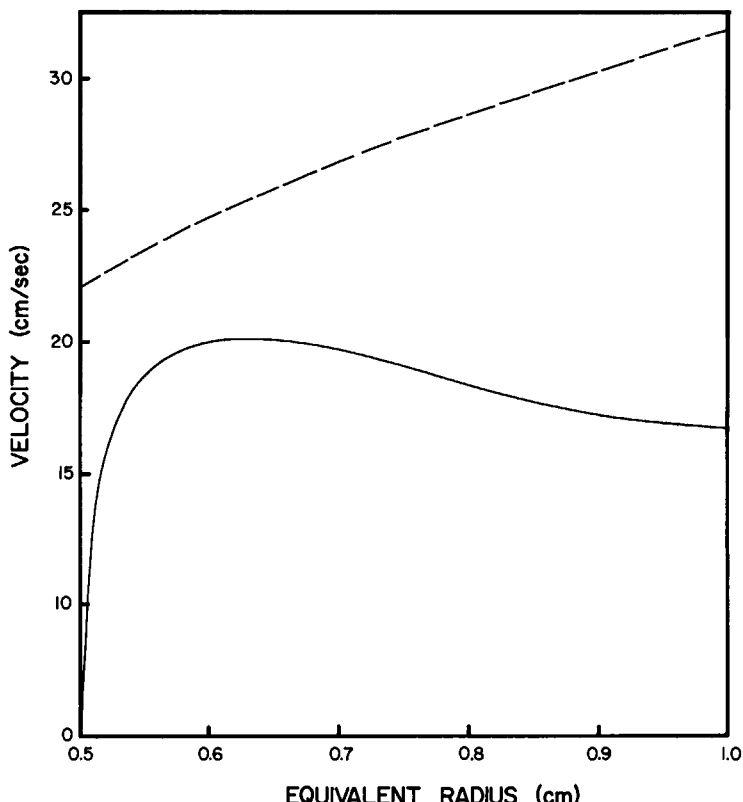


FIG. 8.3.9 Computed curves showing the position of the velocity of an inert bubble rising in mercury for a top pressure of 1 mm Hg, an initial radius of 5 mm, and an initial depth of 50 mm.

position of the bubble as a function of time, for the growth of n-pentane bubbles in n-tetradecane.[†] The top pressure at the freeboard was 1 mm Hg. It is seen that there was reasonably good agreement between measurements and predictions. On inspection of Fig. 8.3.7 it is seen that the Basset term appears to be quite important because the position of the bubble appears to be a linear function of time, notwithstanding the very appreciable growth, as indicated in Fig. 8.3.8.

Figure 8.3.4 shows the trajectory of a nitrogen bubble, rising in mercury; also shown, with a broken line, is the bubble velocity that would have been computed for the equivalent bubble radius by neglecting the effect of rapid expansion and the Basset equation. The very appreciable discrepancies are

[†] We note that, strictly speaking, there is another complicating factor, namely that these bubbles were growing also due to the effect of mass transfer. While this effect was taken into account in the computation of Figs. 8.3.6 and 8.3.7, it is glossed over in the presentation given here.

readily apparent. It would seem therefore that one would not be justified in neglecting these effects when bubbles rise in liquids, the freeboard of which is evacuated, as is the case in vacuum degassing.

8.4 Dispersed Bubble Systems

The previously presented discussion of single bubble behavior shows that in many instances it is possible to develop theoretical predictions for the growth and rising velocity of single bubbles as affected by the properties of the fluid, which were in quite good agreement with measurements.

While work with single bubbles is appropriate in the laboratory, in virtually all industrial systems we have to be concerned with multiple bubbles and dispersed bubble systems.

The behavior of dispersed bubble systems is not very well understood. Virtually all the measurements that have been reported in the literature relate to the interaction of air bubbles with water and to other essentially room temperature systems. Moreover, the interpretations developed for these measurements have been largely empirical so that the extrapolation of these findings to the interaction of molten metals or slags with gas bubbles is rather problematic.

Extensive reviews of the behavior of dispersed bubble systems are available,³²⁻³⁴ albeit devoted to applications in distillation and gas absorption. An interesting brief review of dispersed bubble systems as applied to metals processing has been presented by Turkdogan.³⁵ Furthermore, a good illustration of the role played by nature of the dispersion, i.e. the interfacial area on the processing rate, is given in Table 8.4.1.

Dispersed bubble systems are usually formed by the injection of a gas stream into a liquid (melt) through one or multiple orifices. In some cases, however, bubbles are formed through heterogeneous nucleation. Metals processing examples of the former include argon-stirred ladles, the Q-BOP bottom-blown oxygen steelmaking process, the AOD Process, copper converting, the gaseous deoxidation of copper, and the like. Multiple bubble systems formed through nucleation include the open hearth steelmaking process and the BOF (BOP), the basic oxygen furnace.

The principal parameters used for the characterization of multiple bubble systems are the superficial velocity $U_{B,s}$, the mean bubble velocity $U_{B,m}$, the void fraction or gas holdup ϵ_G , the surface area per unit volume S , and the mean bubble diameter \bar{d}_p . Here

$$U_{B,S} = \frac{\text{volumetric flow rate of gas}}{\text{cross-sectional area of vessel}}$$

and

$$\epsilon_G = \frac{\text{volume of gas bubbles}}{\text{volume of gas and liquid}}$$

It is noted that $U_{B,m}$, the mean bubble rising velocity, may be considerably larger than the terminal rising velocity of a bubble, having the same size, because of the upward movement of the liquid. This behavior is illustrated in Fig. 8.4.1.³⁶

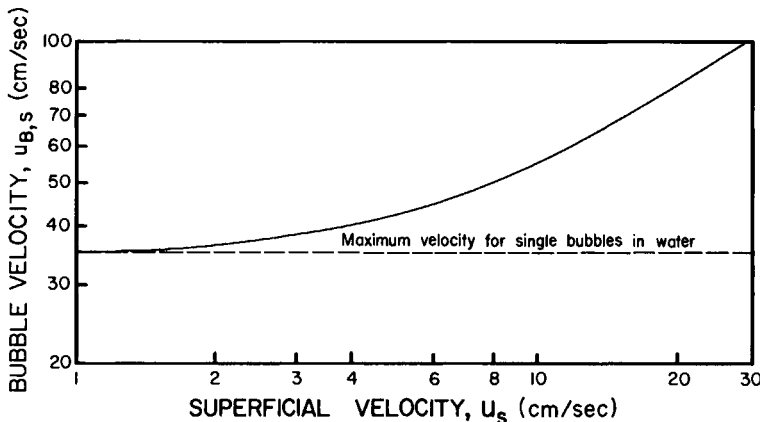


FIG. 8.4.1 Plot of the bubble velocity against the superficial gas velocity for bubble swarms; after Yoshida and Akita.³⁶

The principal practical interest in the study of these systems is to relate the superficial gas velocity $U_{B,S}$ to the holdup and to the mean bubble size.

Dispersed bubble systems may be divided, somewhat arbitrarily, into the following three categories:

- (i) Bubbling systems, where discrete bubbles are formed, and the melt is the continuous phase, and the void fraction or fractional holdup is relatively small, say $\epsilon_G < 0.3$.
- (ii) Froths, illustrated in Fig. 8.4.2, where the melt (liquid) constitutes the continuous phase, but the void fraction is of the order of 0.4–0.6.
- (iii) Foams, illustrated in Fig. 8.4.3, more specifically, cellular foams, where $\epsilon_G \approx 0.9$ –0.98.

Among the metals processing systems argon-stirred ladles and the gaseous deoxidation of copper would fall into category (i), Q-BOP operation and the AOD system would correspond to category (ii), while the slag, or more precisely the slag–metal–gas emulsion, tends to form a foam in the BOF system.³⁷

Ideally, it would be desirable if an explicit relationship were available between the superficial gas velocity and the gas holdup. Unfortunately, no generally valid relationships have been developed, even for aqueous systems, although most authors agree that increasing the superficial gas velocity tends

TABLE 8.4.1

The Rate of Processing per Unit Volume
for Various Metallurgical Operations^a

Process	Rate of processing (ton m ⁻³ min ⁻¹) ^b
Electrolytic winning of aluminum	0.00005
Electrolytic refining of copper	0.0005
Reverberatory matte smelting	0.0007
Iron blast-furnace	
(overall)	0.002
(lower half)	0.004
Open hearth steelmaking	0.002
Copper converting	0.004
Noranda copper process (enriched air)	0.005
Anode refining for copper	0.008
Harris lead refining	0.03
Top-blown oxygen converter for steel	0.05
Sintering for iron and zinc blast-furnaces	0.06
Bottom-blown oxygen converter for steel	0.07
Electroslag melting of steel	0.10
Spray steelmaking	0.10
Spray degassing of steel	0.15

^a From Richardson¹.

^b Of solids and liquids: if air is included, rate for iron blast-furnace is raised about 4 times, copper converting 4 times, Noranda process 4 times, and sintering twice.

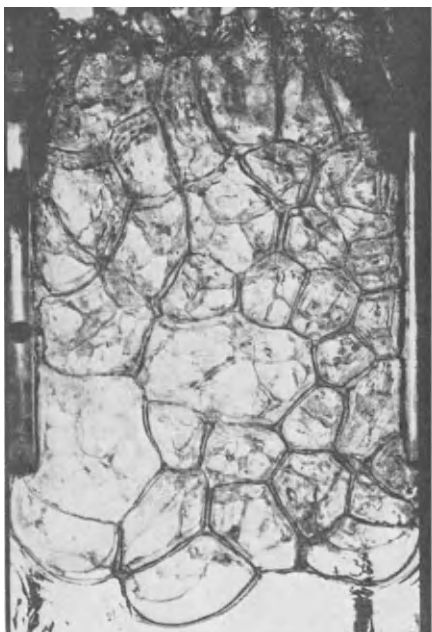


FIG. 8.4.2 A cellular foam; after Calderbank.³²

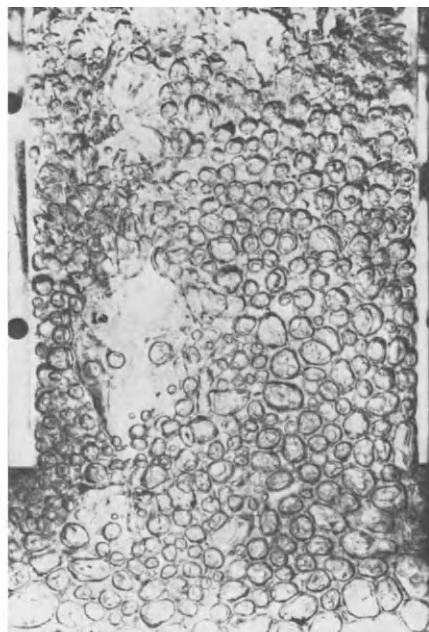


FIG. 8.4.3 A froth; after Calderbank.³²

to increase the gas holdup, until a certain limiting value is attained. For systems that form froths this limiting value is of the order of $\epsilon_B \simeq 0.5$, while for systems that form cellular foams this limiting value is of the order of 0.9–0.98.

The diversity of the findings reported by various authors is illustrated in Figs. 8.4.4 and 8.4.5.

Figure 8.4.4, taken from the work of Crozier,³⁸ was obtained for the countercurrent flow of water and air in a sieve plate column. The broken line corresponds to the equation proposed by Crozier:

$$\ln(1 - \epsilon_G)^{-1} = 0.586 U_{B,S}(\rho G)^{1/2} + 0.45 \quad (8.4.1)$$

which does represent the measurements in the frothing region, but not under foaming conditions.

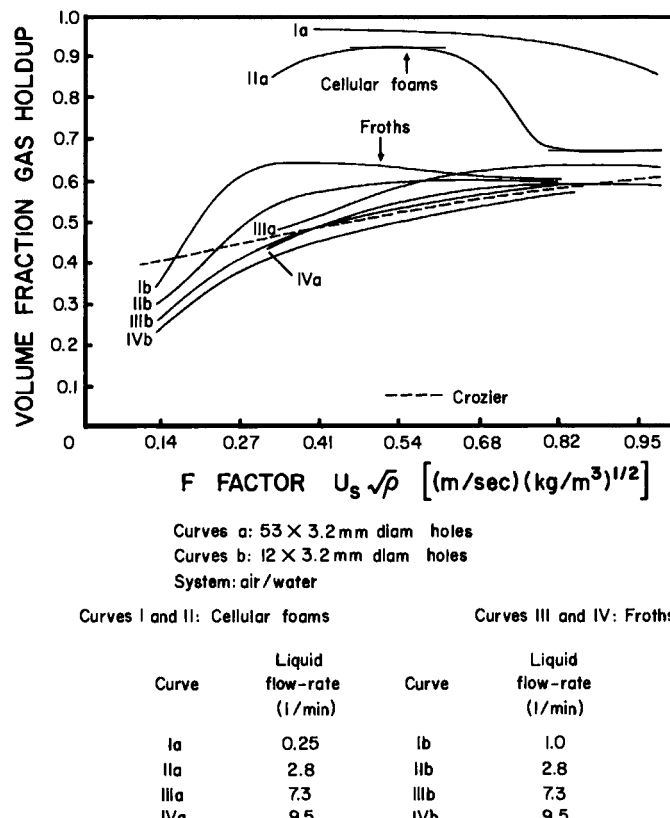


FIG. 8.4.4 Gas holdup in sieve plate columns; after Calderbank.³² The broken line denotes an expression put forward by Crozier.³⁸

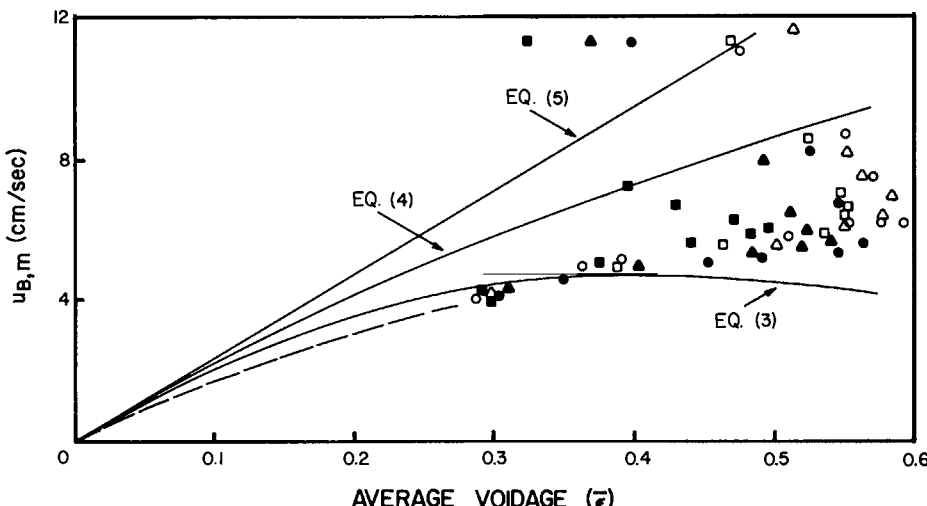


FIG 8.4.5 Plot of the void fraction against the superficial gas velocity, after Whalley *et al.*³⁹ The equations in the graph designate expressions in Davidson's article.

Figure 8.4.5 shows data reported by Whalley,³⁹ using aqueous solution of alcohols; the appreciable scatter of these data is readily apparent.

Interesting work on gas holdup in bubble columns was also reported by Yoshida and Akita,³⁶ who on the basis of extensive measurements proposed the following correlation:

$$\log(1 - \epsilon_G)^{-1} = 0.146 \log(1 + U_{B,S}) - 0.06 \quad (8.4.2)$$

The qualitative similarity between Eqs. (8.4.1) and (8.4.2) is readily apparent; both these expressions indicate that ϵ_G will tend to a limiting value of about 0.5–0.6 for high values of $U_{B,S}$.

MEAN BUBBLE SIZE

In work aimed at describing the interaction of dispersed bubble systems with melts in addition to holdup, the mean bubble size is of major interest because (through the interfacial area) this quantity will play a major role in determining the rate of mass transfer in these systems.

There are certain, semiquantitative techniques available for the estimation of the mean bubble size in dispersed bubble systems. Levich²⁰ suggested that in a turbulent fluid system the maximum stable bubble size may be estimated by the following equation:

$$d_{B,max} \approx \left(\frac{3}{C_D \rho_G \rho_L^2} \right)^{1/3} \frac{2\sigma}{U_B^2} \quad (8.4.3)$$

TABLE 8.4.2

The Maximum Bubble Size for Various Nitrogen-Melt Systems^a

Melt	Temperature (°C)	Pressure (atm)	σ (dyn/cm)	$d_{B,\max}$ (mm)
Steel	1600	1.5	1500	60
Blister copper	1300	1.5	900	45
Water	20	1.0	72	10.4

As calculated with the aid of Eq. (8.4.3); after Turkdogan.³⁵

where C_D is the drag coefficient and U_B is the rising velocity of the bubble. It may be more satisfactory to replace U_B with $U_{B,S}$ or some other characteristic velocity in the system.

Turkdogan³⁵ calculated the values of $d_{B,\max}$ using Eq. (8.4.3) for various systems of metallurgical interest, and the results in his calculations are summarized in Table 8.4.2.

The predictions based on Eq. (8.4.3) are at least in qualitative agreement with measurements reported for aqueous systems, where the mean bubble size observed was of the order of 5 mm.

An alternative means of estimating the mean bubble size in the frothing region is by using an expression proposed by Calderbank,³²

$$d_{B,m} = 2.25 \left[\frac{\sigma^{0.6}}{\rho_L^{0.2} \dot{\epsilon}^{0.4}} \right] \epsilon_G^{0.5} \left(\frac{\mu_G}{\mu_L} \right)^{0.25} \quad (8.4.4)$$

where $\dot{\epsilon}$ is the rate of energy dissipation in unit volume in the melt. While Eq. (8.4.4) was developed for mechanically agitated aqueous systems, it can be shown (see Example 8.4.1) that it gives predictions for the mean bubble size in the Q-BOP system that are comparable to those given by Levich's expression.

It has to be stressed that all the above equations and measurements were developed on the basis of data collected on aqueous or light organic systems. It is noted, however, that in a recent paper Fruehan⁴⁰ described measurements made on a 30-ton experimental Q-BOP system.

From his measurements, conducted on superficial velocities of the order of 0.7–2.5 m/s, he deduced that the holdup was of the order of 0.5; moreover, the mean bubble diameter calculated by him was of the order of 80 mm.

These measurements are in qualitative agreement with predictions based on Eqs. (8.4.2)–(8.4.4). We note, furthermore, that experimental observations on full-scale BOF vessels indicate that during peak decarburization, when the linear gas velocity in the system is of the order of 1–2 m/s, the actual expansion of the slag layer may amount to some 5–10 times its original

thickness. This would indicate the existence of cellular foams, with a very high void fraction. It has been suggested that these cellular foams may be stabilized by the presence of undissolved lime.

We may summarize the content of this section by stating that dispersed bubble systems behave very differently from single bubbles. In essence three regimes may be identified:

- (1) bubbling regime, $\epsilon_G < 0.4$,
- (2) froths, $\epsilon_G \simeq 0.4\text{--}0.6$,
- (3) cellular foams $\epsilon_G \simeq 0.9\text{--}0.98$.

There appears to be general agreement between numerous investigators that in the bubbling and frothing regime the gas holdup increases with the superficial gas velocity until a limiting value of about $\epsilon_G = 0.5$ is reached.

There is some tentative evidence that this relationship is obeyed by liquid metals also.

The interfacial area or mean bubble size in regimes (1) and (2) may be estimated with the aid of correlations, developed for aqueous or light organic systems; however, there is some evidence that these correlations apply, at least as an approximation, for certain metallic systems. Let us illustrate the use of these expressions by working two simple examples.

Example 8.4.1 If in a Q-BOP process the linear gas velocity is estimated as 2.0 m/s, use Eq. (8.4.1) to calculate the gas holdup. The gas density may be taken as 0.24 kg/m^3 (at temperature and pressure).

SOLUTION Upon substituting into Eq. (8.4.1) we have

$$\ln(1 - \epsilon_G)^{-1} = 0.586 \times 2\sqrt{0.24}$$

i.e.,

$$\epsilon_G = 0.43$$

This value is quite close to that found by Fruehan.⁴⁰

8.5 The Formation and Behavior of Droplets

The interaction of metal droplets with a gaseous or a liquid environment is of considerable practical importance in many metals processing operations. The atomization of metal streams into fine droplets of uniform size is gaining widespread application in powder metallurgy; the breakup of metal droplets is an important component of stream vacuum degassing, while the breakup of teemed metal streams may contribute to their re-oxidation.

Regarding metal-droplet-melt interactions, it is generally held that the large interfacial area caused by the dispersion (emulsion) of iron droplets in

the slag is responsible for the very fast rates of decarburization attained in the BOF process. Furthermore, the separation of finely divided copper particles from the slag is one of the more challenging problems encountered in the Noranda continuous copper smelting process.

8.5.1 Metal Droplet Formation by Atomization

As shown in Fig. 8.5.1,⁴¹ when a vertical jet of liquid is discharged from an orifice into a gaseous environment, eventually breakup will occur. In a classical analysis, Rayleigh⁴² has shown that a small disturbance, axially symmetrical about the jet, would cause breakup when the amplitude of the disturbance grew to one half of the diameter of the undisturbed jet. Rayleigh's work formed the basis of more refined mathematical representations that evolved for modeling jet breakup. A good discussion of these models is available in the text by Brodkey.

For most practical applications a simple nozzle is an inefficient producer of liquid droplets and the systems usually employed may be classified as:

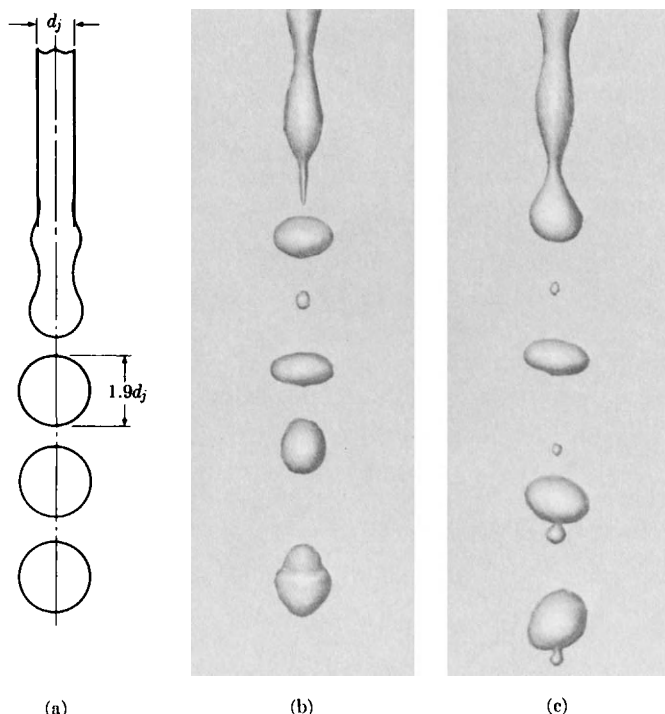


FIG. 8.5.1 The breakup of a liquid stream upon issuing from an orifice: (a) idealized behavior, suggesting uniform droplet diameter; (b,c) actual breakup as shown through high-speed photography; after Brodkey.⁴¹

(i) Swirl-type, or centrifugal pressure-type atomizers, impart a spinning or swirling motion to the liquid, before it is sprayed. These atomizers tend to produce a conical spray pattern.

(ii) The spinning disk, or rotating atomizers, produce a centrifugal acceleration on the fluid.

(iii) The pneumatic atomizers use the action of a high-velocity gas jet on the liquid stream in order to effect its breakup. The simplest arrangement is to spray the liquid (melt) into a high-velocity gas stream, as is done in the fuel injection through the tuyeres of the blast furnace.⁴³

A good review of atomization is available in the articles by Fraser and Eisenklam,⁴⁴ Lane and Green,⁴⁵ and Marshall.⁴⁶

Here we shall confine our attention to the discussion of a model proposed by Dombrowski and Johns⁴⁷ for the breakup of a nozzle spray and to a brief mention of some atomization work reported on liquid metal systems.

Figure 8.5.2a shows a photograph of a fan nozzle spray while 8.5.2b represents the idealization of the breakup process. As seen in the sketch, a liquid sheet of thickness h emerges from the nozzle. The subsequent breakup of this sheet may be considered to occur in three stages; namely,

- (1) Surface waves are formed, as a result of hydrodynamic instability.
- (2) The sheet is fragmented and ligaments are formed.
- (3) The ligaments are broken up into droplets.

Dombrowski and Johns⁴⁷ developed a model representing this process and the principal parameters that have to be considered include

- (i) the relative velocity of the liquid sheet and the surrounding gas;
- (ii) the surface tension, viscosity, and density of the liquid;
- (iii) the characteristics (wavelength and amplitude) of the disturbance.

By establishing a force balance, i.e., equating the force of the disturbances seeking to deform and break up the film and the surface tension forces resisting this deformation and upon evaluating the wave number which would cause the maximum disturbance, these authors developed the following expression for the mean droplet diameter \bar{d}_D :

$$\bar{d}_D = \left[\frac{3\pi}{\sqrt{2}} \right]^{1/3} d_L \left[1 + \frac{3\mu_L}{(\rho_L \sigma d_L)^{1/2}} \right]^{1/6} \quad (8.5.1)$$

where \bar{d}_D is the drop diameter and d_L the ligament diameter, defined as

$$d_L = 0.9614 \left[\frac{K^2 \sigma^2}{\rho_G \rho_L U^4} \right]^{1/6} \left[1 + 2.60 \mu^3 \left(\frac{K \rho^4 U^7}{72 \rho_L^2 \sigma^5} \right)^{1/2} \right]^{1/5} \quad (8.5.2)$$

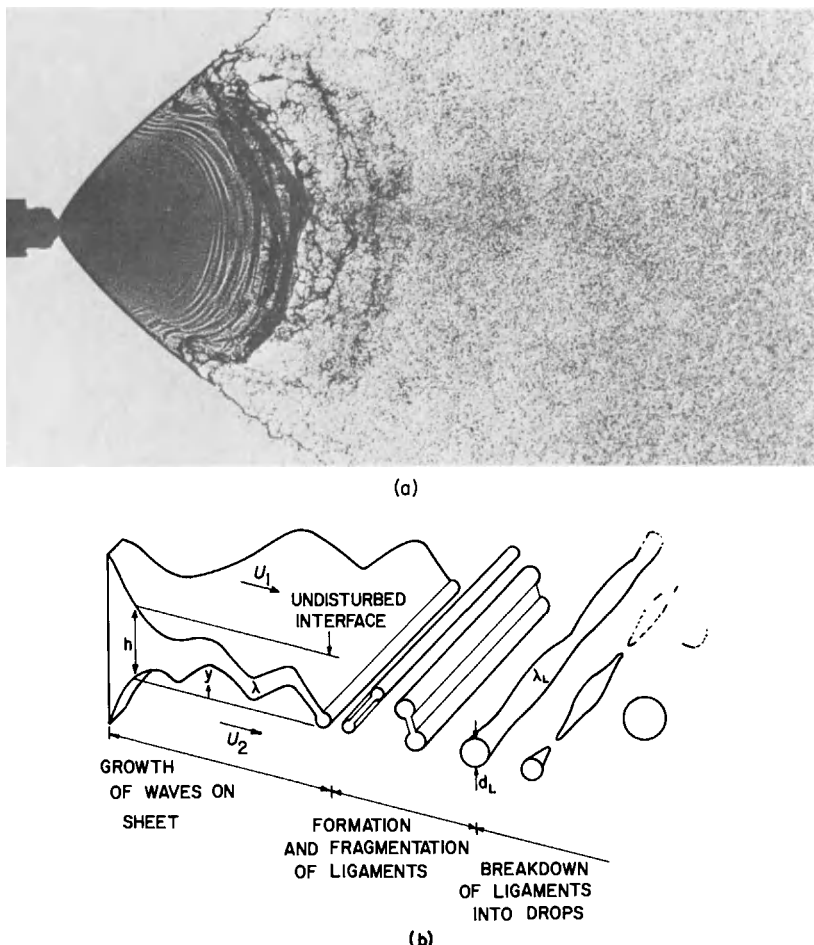


FIG. 8.5.2 Breakup of a fan-nozzle spray: (a) actual high-speed photograph, (b) idealization of the breakup process; after Dombrowski and Johns.⁴⁷

where ρ_G is the gas density, $K = hx$ is (sheet thickness) \times (distance in x direction), $U = (U_1^2 + U_2^2/2)^{1/2}$ is the "mean relative air-wave velocity," U_1 is the relative velocity parallel to upper surface, and U_2 is the relative velocity parallel to lower surface.

Dombrowski and Johns found that the predictions made on the basis of Eqs. (8.5.1) and (8.5.2) were in reasonable agreement with measurements, using liquid wax systems. In contrast, See *et al.*^{48,49} found that this equation was not able to predict quantitatively the atomization of lead or tin streams,

although the measurements were at least qualitatively consistent with the form of Eqs. (8.5.1) and (8.5.2). For obvious practical reasons, pneumatic atomization, that is, the breakup of liquid streams by impinging high-velocity gas streams, is the most suitable arrangement for the atomization of liquid metals.

Little detailed work has been reported on the atomization of liquid metals and in this regard the previously cited papers of See *et al.*^{48,49} constitute a notable exception. These authors studied the atomization of molten lead and tin steams. The experimental arrangement employed by them is sketched in Fig. 8.5.3 and a series of photographs depicting the breakup of a molten lead jet is shown in Fig. 8.5.4.

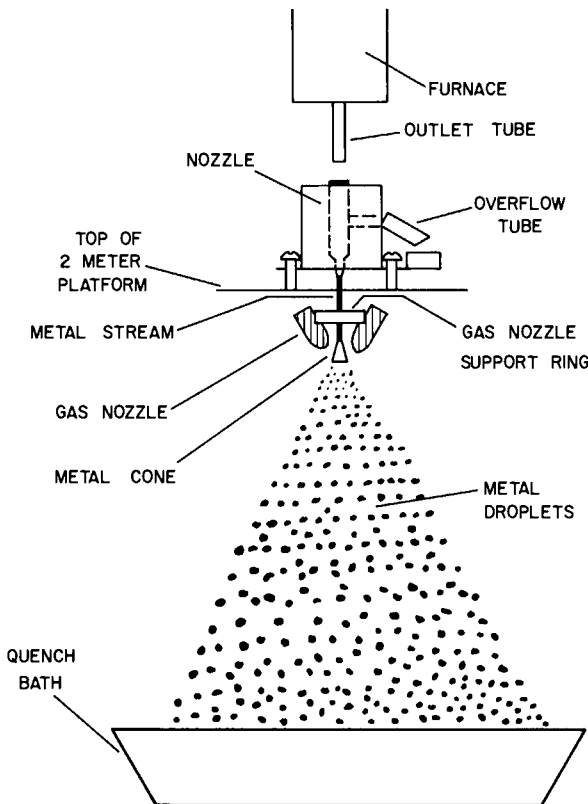


FIG. 8.5.3 Experimental arrangement for the study of the breakup of liquid tin jets; after See *et al.*⁴⁸

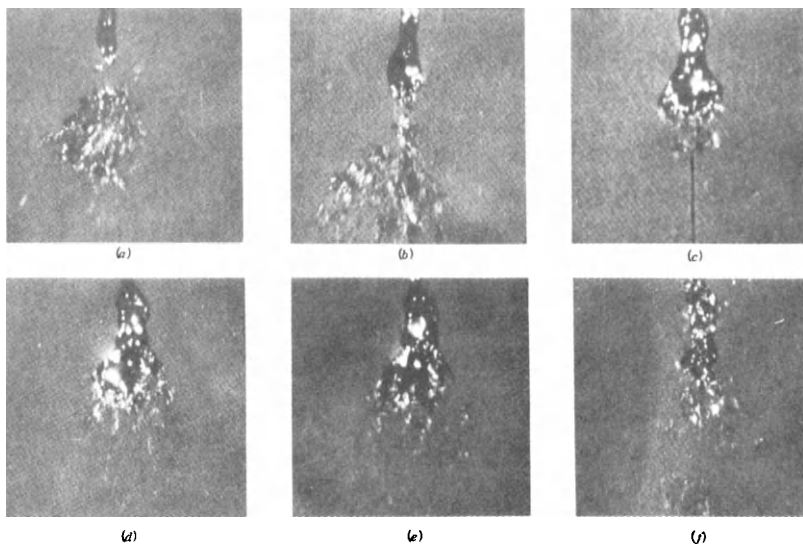


FIG. 8.5.4 (a-f) Selected frames of a high-speed motion picture depicting the disintegration of molten lead stream; after See *et al.*⁴⁸ Total lapsed time, 0.028 s.

A selection of the measured droplet size distribution is shown in Fig. 8.5.5, where it is seen that the higher the gas velocity the smaller the mean droplet diameter produced, which is at least in qualitative agreement with Eqs. (8.5.1) and (8.5.2).

8.5.2 Metal Droplet Formation in Pneumatic Steelmaking and Copper Refining Processes

As noted earlier, the formation of metal droplets, dispersed in slags, is a key ingredient in many steelmaking and metals refining operations, including open-hearth steelmaking, the BOF, and copper converting.

In these systems metal droplets are formed and dispersed in the slag by rising bubbles, impinging jets, and submerged jets. In the now obsolete open-hearth steelmaking process carbon monoxide bubbles are nucleated at the bottom of the bath, and upon detachment these bubbles rise through the liquid metal pool and the covering slag layer. When passing through the slag–metal interface, the bubbles carry with them a thin, covering metal sheet which is then dispersed in the slag. The sequence of events, on crossing the interface, is illustrated in Fig. 8.5.6, which shows an elegant series of photographs of a nitrogen bubble passing through a mercury pool, covered with water. It is seen that a bubble produced a finite number of small droplets. In open-hearth steelmaking, where the bubble frequency is quite low (say of the order of 1 s^{-1}), the dispersion thus produced is not very

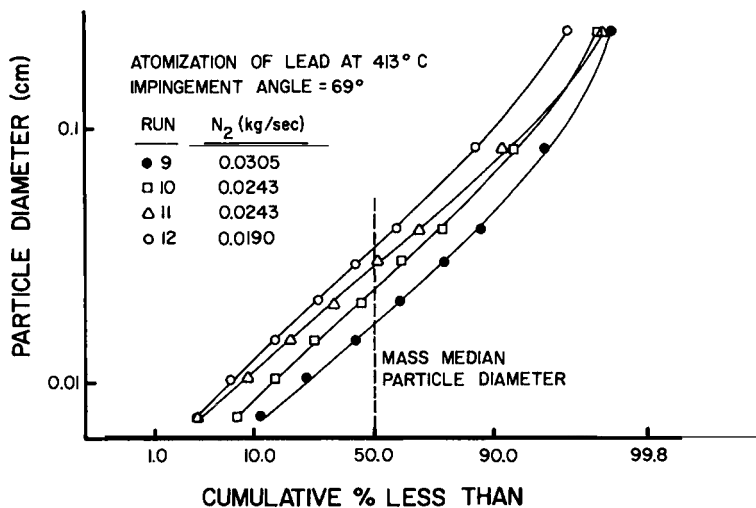


FIG. 8.5.5 Experimentally measured droplet size distribution; as reported by See *et al.*⁴⁸

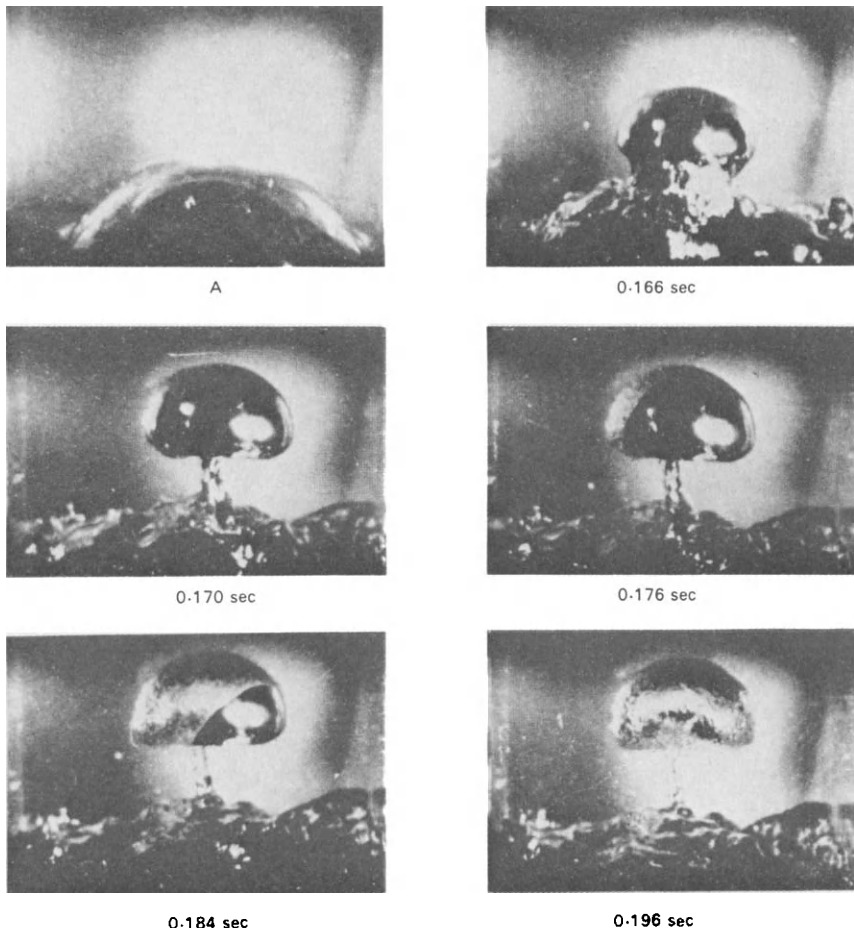


FIG. 8.5.6 Selected frames showing the passage of a spherical cap bubble from mercury into an acidified aqueous phase; after Davenport, cited by Richardson.²

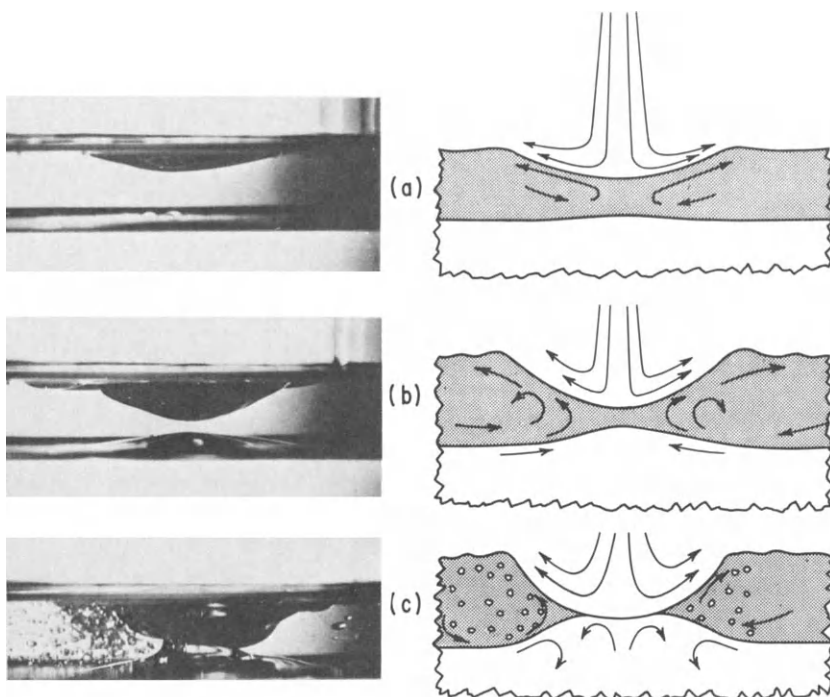


FIG. 8.5.7 Photographs and drawings showing the emulsification of an oil–water system, as caused by an impinging argon stream. Frames (a–c) depict a progressively increasing jet momentum; after Turkdogan.⁵⁰ Original photograph kindly supplied by Dr. E.T. Turkdogan of the U.S. Steel Corporation.

significant. In contrast, in BOF steelmaking the rate of CO evolution from the bath is very rapid, and here it is generally held that as much as 30–50% of the steel bath is being suspended in the slag during the peak decarburization period. This dispersion, sometimes called the slag–metal emulsion, is produced at least in part by the mechanism shown in Fig. 8.5.6.

Another mechanism for the formation of slag–metal emulsions (dispersions), due to the action of an impinging jet, is shown in Fig. 8.5.7. This figure, taken from a paper by Turkdogan,⁵⁰ depicts the behavior of a water pool, covered with an oil layer, upon which an argon jet is made to impinge. At low gas velocities no emulsification occurs, and the momentum of the jet is used up to cause circulation in both the oil and the aqueous phases. At higher gas velocities, when the jet momentum is sufficiently large to expose a bare water surface, emulsification does take place.

8.5.3 *The Rising (Sinking) Velocity of Droplets in Melts*

The movement of molten droplets in melts is of considerable interest in many processing applications. The rate at which nonmetallic inclusions rise

in molten steel may play an important role in the cleanliness of the product,⁵¹ moreover, the settling of metallic copper particles from slag (copper losses)⁵² and the separation of aluminum particles from aluminum bearing drosses, etc., are important in materials recovery.

Figure 8.5.8 taken from the work of Themelis and Subramanian⁵² clearly indicates the marked effect of particle size and the retention time on the efficiency of copper removal from slags. It is noted that these retention times are much longer predicted on the basis of Stokes' law.

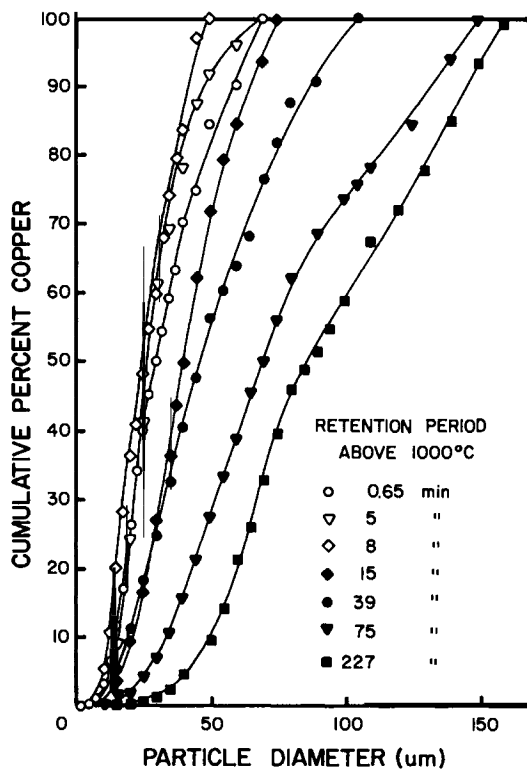


FIG. 8.5.8 The effect of particle size and retention time on copper recovery from converter slags; after Themelis and Subramanian.⁵²

In general, the behavior of liquid droplets in liquids (melts) parallels the previously discussed behavior of gas bubbles in liquids, in that rigid particle behavior is observed over a limited range of particle sizes.

Figure 8.5.9 shows measurements on the rising velocity of carbon tetrachloride droplets in water, in the presence and in the absence of surface active agents. The rising velocity of a rigid sphere is also indicated on this graph for the purpose of comparison.

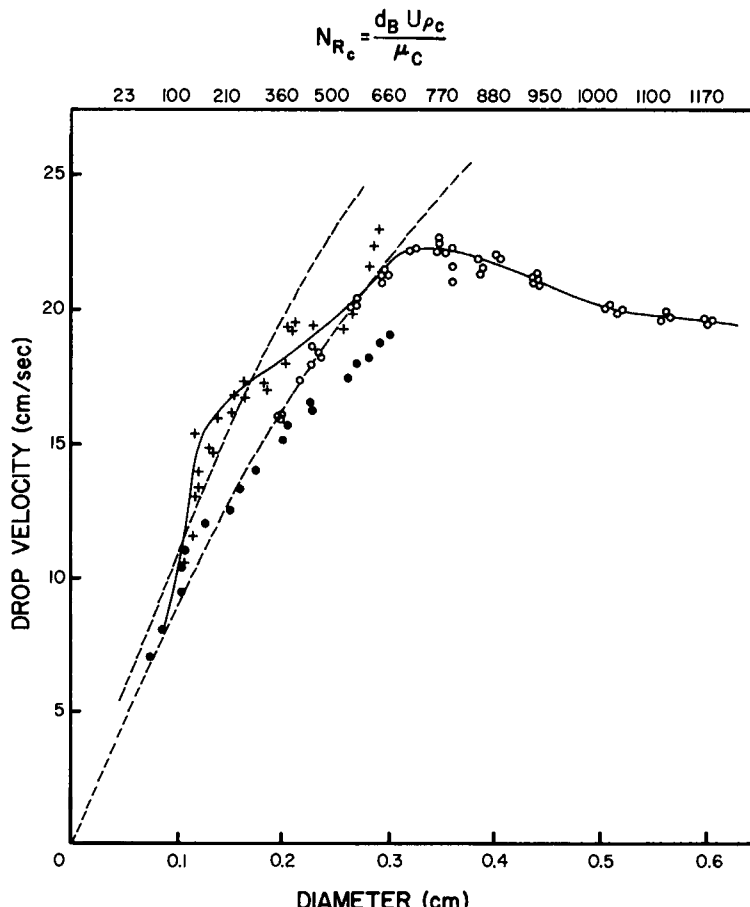


FIG. 8.5.9 Experimental measurements depicting the rising velocity of carbon tetrachloride droplets in water: +, pure system. ●, with surface active agents. Cited by Brodkey⁴¹.

The following observations should be made:

- (1) When the droplets are small, say $N_{Re,d} \ll 1$, the droplets behave like rigid spheres and the rising velocity is predicted by Stokes' law, i.e., the previously given Eq. (8.3.4).
- (2) For larger bubbles internal circulation will be set up and, because of the previously discussed Hadamard effect, these bubbles may rise faster than predicted on the basis of Stokes' law.

It has been suggested⁵³ that the onset of a departure from rigid sphere behavior occurs when

$$(\rho_{1L} - \rho_{2L}) d_D^2 g / \sigma \geq 0.4 \quad (8.5.3)$$

(3) When the size of the droplets is increased further, appreciable deformation in shape occurs which will cause a flattening or even a decrease in the rising velocity versus droplet size plot.

A more general correlation for the drag force of rising droplets has been proposed by Wasan and Knapik,⁵⁴ whose results are shown in Fig. 8.5.10 in graphical form. Here, C_D is the drag coefficient, N_{We} the Weber number, N_{Re} the Reynolds number, and $P = 3N_{Re}^4/4C_D N_{We}^3$. Figure 8.5.11, taken from the text of Richardson, shows calculated values of the terminal falling velocities of metal droplets in slag and mercury droplets in water, as a function of the droplet diameter.

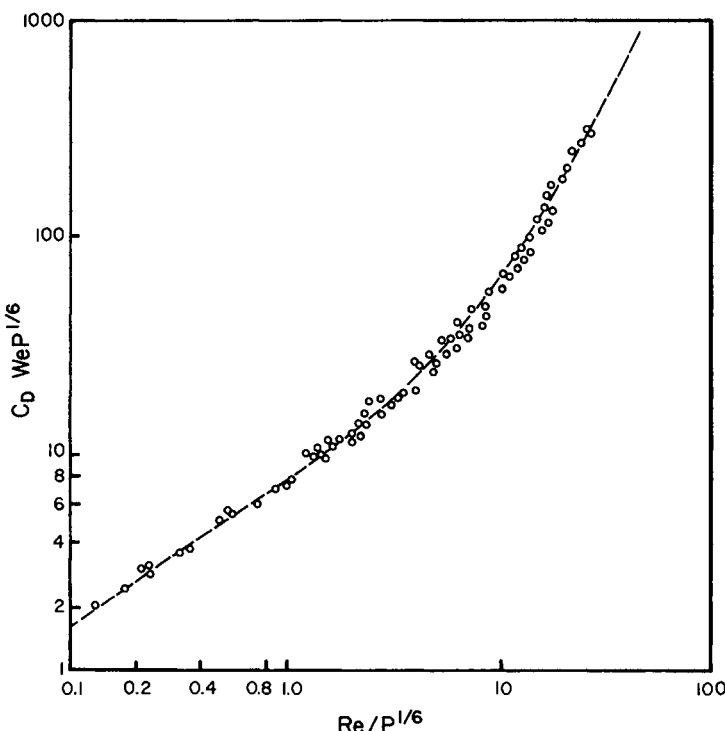


FIG. 8.5.10 Plot of the correlation proposed by Wasan and Knapik⁵⁴ for the rising velocity of liquid droplets in liquids: $Re = N_{Re}$, the Reynolds number; $We = N_{We}$, the Weber number; and P is defined in the text.

The continuous curves were obtained with the aid of the Wasan and Knapik correlation, while the broken lines show the values that would have been calculated with the aid of Stokes' law. The very wide discrepancy is

readily apparent. We note that Stokes' law would be inapplicable to these conditions for at least two reasons:

(1) The Reynolds number of the droplets would be too high, so that the assumption of a constant drag coefficient, namely $C_D = 0.44$, would have been much more appropriate.

(2) The rigid sphere assumption is incorrect in any case.

Furthermore, it is questionable as to what would be the maximum stable size of such droplets. The point that has to be made here is that liquid droplets, when moving in liquids, tend to have a substantially higher effective drag coefficient than predicted for rigid solid spheres.

This will be illustrated by the following example:

Example 8.5.1 Calculate the terminal falling velocity of a metal droplet in slag, for the following conditions:

$$\begin{array}{lll} \text{droplet diameter: } & 13 \text{ mm} & \text{slag viscosity: } & 0.1 \text{ g/cm s} \\ \text{metal density: } & 7200 \text{ kg/m}^3 & \text{interfacial tension: } & 900 \text{ dyn/cm} \\ \text{slag density: } & 2750 \text{ kg/m}^3 & & \end{array}$$

SOLUTION Let us work in the cgs system:

(a) *For a rigid sphere assumption:*

$$U_t = \left[\frac{\Delta\rho}{0.165} \times \left(\frac{g}{\rho_{si}} \right) \frac{dp}{2} \right]^{1/2} \quad (\text{i})$$

$$= \left[\frac{4.45 \times 980 \times 0.65}{2.75 \times 0.165} \right]^{1/2} = 79 \text{ cm/s}$$

$$N'_{Re} = d_p \rho_{si} U_t / \mu \sim 2820 \quad (\text{ii})$$

so that the use of Eq. (i) was justified.

(b) *Using the Knapik–Wasan correlation:*

$$P = \frac{3N_{Re}^4}{4C_d N_{we}^3} \quad \text{or} \quad P = \frac{9\rho_{si}\sigma^3}{16\mu_{si}^4 \Delta\rho g} \quad \text{or} \quad P^{1/6} \sim 43.5$$

and

$$C_d N_{we} \sim 10.2$$

so that $C_d N_{we} P^{1/6} \sim 446$. Then, using Fig. 8.5.9, we have $N_{Re}/P^{1/6} \sim 35$. Thus,

$$U_t \sim \frac{35 \times 43.5 \times 0.1}{2.75 \times 2 \times 0.65} \sim 43 \text{ cm/s}$$

which is close to the limiting value appearing in Fig. 8.5.11.

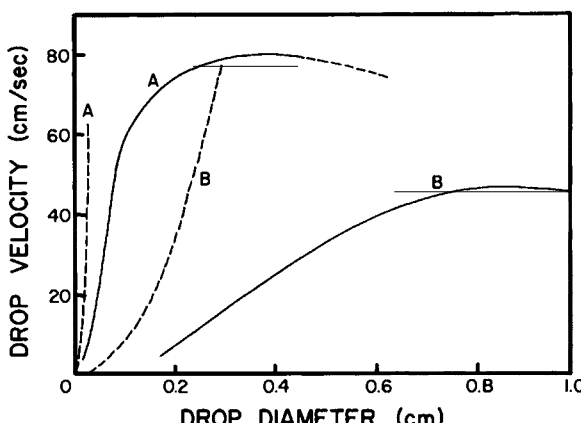


FIG. 8.5.11 Plot of the droplet velocity against the droplet diameter for (A) mercury drops falling through water and (B) iron drops falling through slag. The solid lines were calculated using the Wasan⁵⁴ and Knapik correlation, while the broken lines correspond to calculations based on Stokes' law; after Richardson.²

References

1. F. D. Richardson, Presidential Address. Inst. Min. Metall. London, 1974.
2. F. D. Richardson, "Physical Chemistry of Melts in Metallurgy," Vol. 2, Academic Press, New York, 1974.
3. L. E. Scriven, *Chem. Eng. Sci.* **10**, 1 New York, (1959).
4. J. Szekely and N. J. Themelis, "Rate Phenomena in Process Metallurgy," p. 451 Wiley, New York, 1971.
5. J. Szekely and G. P. Martins, *Chem. Eng. Sci.* **26**, 147 (1971).
6. J. Szekely and S.-D. Fang, *Chem. Eng. Sci.* **28**, 2028 (1973).
7. I. Leibson, E. G. Holcomb, A. G. Gacoso, and J. J. Jasmic, *AICHE J* **2**, 296 (1956).
8. R. Kumar and N. R. Kuloor, *Adv. Chem. Eng.* **8**, 256 (1970).
9. D. W. Van Krevelen and P. J. Hofstijzer, *Chem. Eng. Prog.* **46**, 29 (1950).
10. J. F. Davidson and D. Harrison, "Fluidized Particles." Cambridge Univ. Press, London New York, 1963. See also J. F. Davidson and B. O. G. Schnler, *Trans. Inst. Chem. Eng.* **38**, 144 (1960).
11. R. I. L. Guthrie and G. A. Irons, *Metall. Trans.* **9B** (in press).
12. R. J. Anderini and J. S. Foster, Department of Metallurgy Michigan Technological University, Houghton (unpublished research).
13. J. R. Grace, T. Wairegi, and T. H. Nguyen, *Trans Inst. Chem. Eng.* **54**, 167 (1976).
14. M. Sano and K. Mori, *Tetsu To Hagane* **60**, 348 (1974); also *Trans. Jpn. Inst. Met.* **17**, 344 (1976).
15. A. I. Johnson, A. E. Hamielec, and W. T. Houghton, *AICHE J.* **13**, 379 (1967).
16. F. N. Peebles and H. J. Garber, *Chem. Eng. Sci.* **3**, 1 (1954).
17. R. A. Hartunian and W. R. Sears, *J. Fluid Mech.* **3**, 27 (1957).
18. W. L. Haberman and R. K. Morton, "David Taylor Basin Model Report," No. 802. U.S. Dept. of Naval Research, Washington, D.C., 1953.
19. Hadamard and Rybczynsky, cited in R. A. Brodkey, "The Phenomena of Fluid Motions," pp. 582. Addison-Wesley, Reading, Massachusetts, 1957.

20. V. Levich, "Physicochemical Hydrodynamics." Prentice Hall, Englewood Cliffs, New Jersey, 1962.
21. J. R. Grace, T. Wairegi, and T. H. Nguyen, *Trans. Inst. Chem. Eng.* **51**, 116 (1973).
- 21a. R. M. Davies and G. I. Taylor, *Proc. R. Soc. London, Ser. A* **200**, 375 (1950).
22. W. G. Davenport, Ph.D. Thesis, University of London (1964).
23. W. G. Davenport, F. D. Richardson, and A. V. Bradshaw, *J. Iron Steel Inst., London* **92**, 24 (1965).
24. Proceedings on the Fifth International Conference on Vacuum Metallurgy and Electroslag Remelting Processes, M. Wahlster, ed., Leybold Heraeus, Hanau, Federal Republic of Germany, 1977.
25. Proceedings of the Fourth International Conference on Vacuum Metallurgy and Electroslag Remelting, Tokyo, Japan, 1974.
26. W. G. Davenport, *Can. Metall. Q.* **7**, 127 (1967).
27. A. V. Bradshaw and F. D. Richardson, *Iron Steel Inst., London. Spec. Rep.* **92**, 24 (1965).
28. J. Szekely, G. P. Martins, and S.-D. Fang, *VDI-Ber.* **182** (1972).
29. J. Szekely and S.-D. Fang, *Chem. Eng. Sci.* **28**, 2028 (1973).
30. J. Szekely and S.-D. Fang, *Metall. Trans.* **5**, 1429 (1974).
31. S.-D. Fang, Ph.D. Thesis, State University of New York at Buffalo (1973).
32. P. H. Calderbank, *Chem. Eng. (London)* CE209, October, (1967).
33. Symposium on Bubbles and Foams, Dusseldorf, *VDI-Ber.* **182** (1972).
34. "International Symposium on Distillation, Brighton, 1960." Inst. Chem. Eng., London, 1961.
35. E. T. Turkdogan, "Lecture Notes," Short course on Metallurgical Kinetics. M. Wadsworth and H. Y. Sohn, eds. University of Utah, Salt Lake City, 1975.
36. F. Yoshida and K. Akita, *AIChE J.* **11**, 9-3 (1965).
37. H. W. Meyer, F. W. Porter, G. C. Smith, and J. Szekely, *J. Metals* **20**, No. 7, 35 (1968).
38. R. D. Crozier, Ph.D. Thesis, University of Michigan, Ann Arbor (1956).
39. P. B. Whalley, B. D. Hedley, and J. F. Davidson, *VDI-Ber.* **182**, 57 (1972).
40. R. J. Fruehan, *Metall. Trans.* **7B**, 537 (1976).
41. R. S. Brodkey, "The Phenomena of Fluid Motions." Addison-Wesley, Reading, Massachusetts, 1967.
42. Lord Rayleigh, *Philos. Mag.* [] **34**, 177 (1892); **38**, 321 (1899), also cited by R. S. Brodkey,⁴³ p. 546.

longong, Australia.

44. R. P. Fraser and P. Eisenklam, *Trans. Inst. Chem. Eng.* **34**, 294 (1956).
45. W. R. Lane and H. L. Green, in "Surveys in Applied Mechanics" (G. K. Batchelor and R. M. Davies, eds.), Cambridge Univ. Press, London and New York, 1956.
46. W. R. Marshall, Jr., *Chem. Eng. Prog., Symp. Ser.* **50** (1954).
47. N. Dombrowski and W. R. Johns, *Chem. Eng. Sci.* **18**, 203 (1963).
48. J. B. See, J. C. Runkle, and T. B. King, *Metall. Trans.* **4**, 2669 (1973).
49. G. B. Johnston and J. B. See, private communication.
50. E. T. Turkdogan, in "Advances in Extractive Metallurgy" (M. Wadsworth and H. Y. Sohn, eds.), Plenum Press, 1979.
51. K. Nakanishi and J. Szekely, *Trans. Iron Steel Inst. Jpn.* 522 15, (1975).
52. N. J. Themelis and K. N. Subramanian, *J. Metals* **24**, 33-38 (1972).
53. W. N. Bond and D. A. Newfan, *Philos. Mag.* **5**, 794 (1928).
54. D. T. Wasan, Department of Chemical Engineering, Illinois Institute of Technology, Chicago, Illinois (private communication).

Gas and liquid jet systems play an important role in many metals processing operations. Some principal applications of jet systems are sketched in Fig. 9.0.1, and it is seen that these include basic oxygen steelmaking, copper converting, continuous casting, and the cooling of steel strip by impinging water jets.

In a physical sense the simplest form of jet motion may be visualized by considering the discharge of a fluid through a nozzle or an orifice into a medium, consisting of the same fluid at rest, as sketched in Fig. 9.0.2. It is seen that the jet, i.e., the moving region, broadens as we move downstream, because of the progressive entrainment of the medium by the moving fluid. Moreover, one may define, somewhat arbitrarily, as the diameter of the jet, the distance from the axis where the velocity falls to a sufficiently low level. In this regard jet phenomena are quite analogous to problems encountered in connection with *boundary layers* that were discussed in Chapters 3 and 4.

In the majority of practical situations our interest is in rather more complex problems than sketched in Fig. 9.0.2. In particular, one is interested in the *interaction* of a jet with a dissimilar fluid, e.g., in combustion, in the behavior of *confined* jets, where the rigid boundaries of a finite container modify the flow field (see Fig. 9.0.1c) in impinging jets (Fig. 9.0.1d) or submerged jets (Fig. 9.0.1b).

Nonetheless, the study of free jets, such as sketched in Fig. 9.0.2, is important because it allows us to define some of the key properties of jets systems.

Regarding the organization of the chapter, in Section 9.1 we shall discuss free jets, both laminar and turbulent, while Section 9.2 is devoted to confined jets. Impinging jet systems are treated in Section 9.3 and the chapter concludes

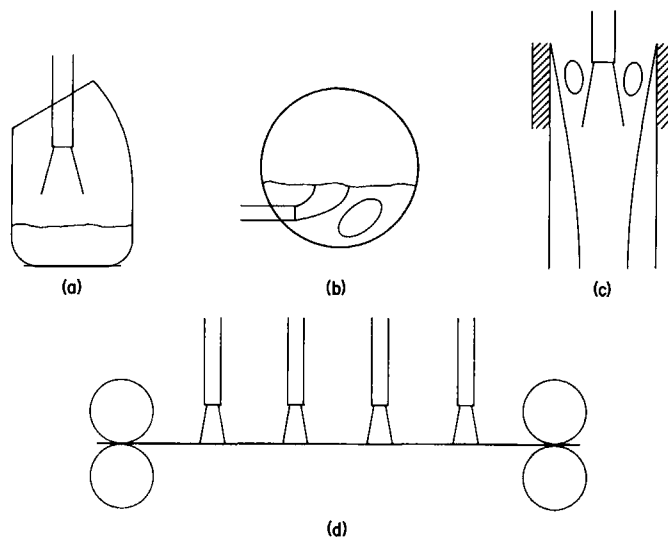


FIG. 9.0.1 Some applications of jet systems in process metallurgy: (a) BOF steelmaking, (b) copper converting, (c) continuous casting, (d) cooling of strip in rolling.

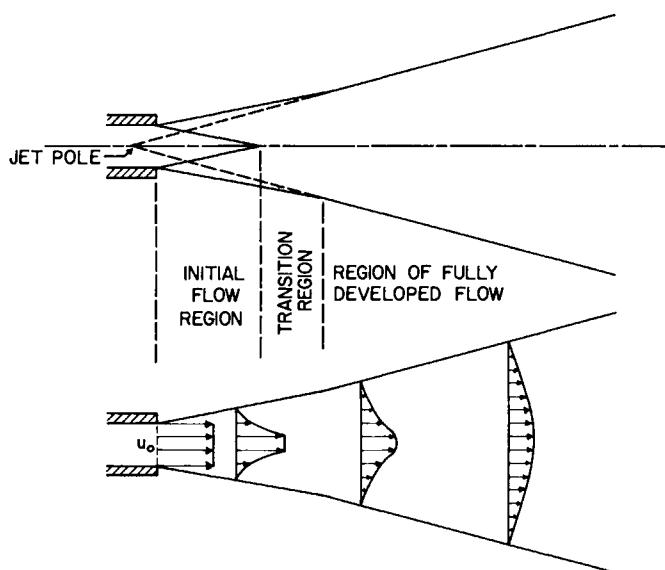


FIG. 9.0.2 Schematic flow diagram of a free jet, showing the potential core and the velocity profiles at various distances from the origin.

with a discussion of submerged gas jets, in Section 9.4. We draw the reader's attention to the fact that supersonic flow through nozzles has been discussed in Chapter 2.

9.1 Free Jets

A schematic sketch of a free jet has been given in Fig. 9.0.2; free jets designate systems where a fluid issues from a nozzle or from an orifice into a stagnant medium, which consists of the same material as the jet fluid. In describing the behavior of free jets our principal interest is to define the jet profile and the velocity profile within the jet. Free jets may be divided into *laminar* and *turbulent* systems. While most operations of practical interest involve turbulent flow, the treatment of the laminar system is instructive, because it illustrates some of the basic principles, without involving undue mathematical complexity.

9.1.1 Laminar, Cylindrical Free Jet

Let us consider a laminar, cylindrical jet issuing from an orifice, the streamline pattern of which is sketched in Fig. 9.1.1; this figure also shows the coordinate system to be adopted. Thus z denotes the axial distance from the origin of the jet, where r denotes the radial distance from the jet axis.

If we consider an incompressible fluid and constant viscosity, then the equations of continuity and motion in cylindrical coordinates may be

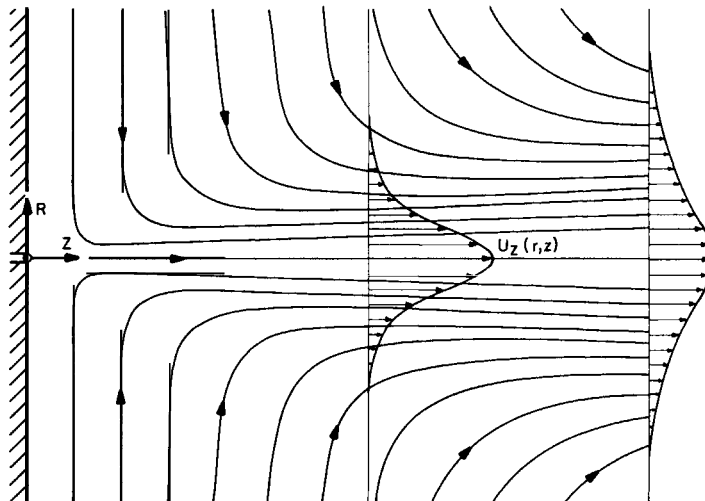


FIG. 9.1.1 The streamline pattern and the velocity profiles produced by a circular laminar jet.

written as

$$\frac{\partial u_z}{\partial z} + \frac{\partial u_r}{\partial r} + \frac{u_z}{r} = 0 \quad (\text{continuity}) \quad (9.1.1)$$

and

$$u_z \frac{\partial u_z}{\partial z} + u_r \frac{\partial u_z}{\partial r} = v \frac{1}{r} \frac{\partial}{\partial r} \left(r \frac{\partial u_z}{\partial r} \right) \quad (\text{motion}) \quad (9.1.2)$$

We note that in the statement of the equation of motion we neglected the axial pressure gradient. This step may be justified by arguments similar to those presented in Chapter 3 in connection with the development of the boundary layer equations. The boundary conditions have to express symmetry about the axis,

$$u_r = 0 \quad \text{at} \quad r = 0 \quad (9.1.3)$$

and

$$\frac{\partial u_z}{\partial r} = 0 \quad \text{at} \quad r = 0 \quad (9.1.4)$$

together with the stipulation that

$$u_z = 0 \quad \text{at} \quad r = \infty \quad (9.1.5)$$

Up to this point the system of Eqs. (9.1.1)–(9.1.5) would have been identical to that written for the formation of an axisymmetrical boundary layer on a thin cylinder.

However, for a boundary layer formed on a solid body the remaining boundary conditions would have to specify zero velocity at the solid surface.

In the present case there is no solid surface and no further boundary conditions may be invoked at the axis; however, one can specify that the total z momentum is conserved; that is,

$$J_z = \int_0^\infty u_z^2 \rho 2\pi r dr = \text{const} \quad (9.1.6)$$

Expressions analogous to Eq. (9.1.6) will be used frequently in the representation of free jet systems. The technique adopted for the solution of Eqs. (9.1.1)–(9.1.6) also parallels quite closely the methods used for tackling the boundary layer equations. We work in terms of the stream function, now defined as

$$u_z = \frac{1}{r} \frac{\partial \psi}{\partial r} \quad (9.1.7)$$

and

$$u_r = -\frac{1}{r} \frac{\partial \psi}{\partial z} \quad (9.1.8)$$

and seek the solution in the form[†]

$$\psi = F(\eta) \quad (9.1.9)$$

where $F(\eta)$ is an as yet unknown function of η and

$$\eta = r/z \quad (9.1.10)$$

The velocity components may be expressed in terms of these quantities as

$$u_z = vF'/z\eta \quad (9.1.11)$$

and

$$u_r = (v/z)(F' - F/\eta) \quad (9.1.12)$$

where $F' \equiv dF/d\eta$.

In terms of these new variables Eq. (9.1.2), the equation of motion, may be written as

$$\frac{FF'}{\eta^2} - \frac{(F')^2}{\eta} - \frac{FF''}{\eta} = \frac{d}{d\eta} \left(F'' - \frac{F'}{\eta} \right) \quad (9.1.13)$$

which can be integrated once to obtain

$$FF' = F' - \eta F'' \quad (9.1.14)$$

The boundary conditions are as given:

$$F = 0 \quad (9.1.15)$$

and

$$F' = 0 \quad \text{at } \eta = 0 \quad (9.1.16)$$

which readily follow from the previously given Eqs. (9.1.3) and (9.1.4).

At this stage it is convenient to define a new variable ξ as

$$\xi = \alpha\eta \quad (9.1.17)$$

where α is an as yet undetermined constant. Thus Eq. (9.1.14) becomes

$$F \frac{dF}{d\xi} = \frac{dF}{d\xi} - \xi \frac{d^2F}{d\xi^2} \quad (9.1.18)$$

A particular solution of (9.1.18) is given as

$$F = \xi^2/(1 + \frac{1}{4}\xi^2) \quad (9.1.19)$$

which also satisfies the boundary conditions contained in Eqs. (9.1.15) and (9.1.16).

[†] The considerations leading to this functional relationship are discussed in Schlichting.¹

The velocity components u_z and u_r are now readily obtained, using the definition of F :

$$u_z = \frac{v}{z} \alpha^2 \frac{1}{\xi} \frac{dF}{d\xi} = \frac{v}{z} \frac{2\alpha^2}{(1 + \frac{1}{4}\xi^2)^2} \quad (9.1.20)$$

and

$$u_r = \frac{v}{z} \alpha \left(\frac{dF}{d\xi} - \frac{F}{\xi} \right) = \frac{v}{z} \alpha \frac{\xi - \frac{1}{4}\xi^3}{(1 + \frac{1}{4}\xi^2)^2} \quad (9.1.21)$$

The constant α may be determined from an overall integral momentum balance:

$$J_z = \int_0^\infty 2\pi\rho u_z^2 r dr = \frac{16}{3} \pi \rho \alpha^2 v^2 \quad (9.1.22)$$

Thus finally we have

$$u_z = \frac{3}{8\pi} \frac{J_z}{\rho v z} \frac{1}{(1 - \frac{1}{4}\xi^2)^2} \quad (9.1.23)$$

$$u_r = \frac{1}{4z} \left(\frac{3J_z}{\rho\pi} \right)^{1/2} \frac{\xi - \frac{1}{4}\xi^3}{(1 + \frac{1}{4}\xi^2)^2} \quad (9.1.24)$$

where

$$\xi \equiv \alpha\eta = \left(\frac{3J_z}{16\rho\pi} \right)^{1/2} \times \frac{r}{vz} \quad (9.1.25)$$

The streamline pattern calculated from Eqs. (9.1.23) and (9.1.24) is shown in Fig. 9.1.1. The mass flow rate w at any axial position may be calculated from

$$w = \int_0^\infty u_z \rho 2\pi r dr \quad (9.1.26)$$

which, upon substitution from Eq. (9.1.24), is written as

$$w = 8\pi\rho\mu z \quad (9.1.27)$$

It is seen from Eq. (9.1.27) that the mass flow rate at any axial position is proportional to both the axial distance from the orifice and to the viscosity. The physical reason for this behavior is the entrainment of the medium by the jet; this phenomenon is rather similar to the entrainment or retardation of the fluid in boundary layers, discussed in Chapter 3, in connection with the displacement thickness. It is noted, however, that the actual functional relationships between the entrainment rate and axial distance are different in boundary layers and in jets.

The validity of the solutions presented here is restricted to laminar jets, that is, to conditions where $N_{Re,o} < 30$. Here, $N_{Re,o}$ refers to the conditions

at the orifice. While such laminar jets are not of great practical, industrial importance, the discussion of laminar jets is very useful because it illustrates, through a simple analytical solution, some of the basic characteristics of free jet systems, together with the boundary conditions employed in the formulation of free jet problems.

The boundary conditions and the use of an overall momentum balance is common to both laminar and to turbulent jets although, as will be shown subsequently, the entrainment characteristics of turbulent jets differ markedly from those encountered in laminar systems. In a qualitative sense this is to be expected, even from the form of Eq. (9.1.27), which shows that the mass flow rate is proportional to the viscosity.

9.1.2 Turbulent Jets

Let us consider a turbulent, circular jet, issuing from an orifice into a fluid at rest, which is identical to the jet fluid. In a qualitative sense the physical situation here is analogous to that sketched in Fig. 9.0.2, and the governing equations will be similar to those previously written for the laminar jet, but for the fact that we have to deal with *time-smoothed* quantities and that the effective viscosity is position dependent.

Again using the cylindrical coordinate system, and omitting the notation for time smoothing for the sake convenience, we have

$$\frac{\partial u_z}{\partial z} + \frac{\partial u_r}{\partial r} + \frac{u_z}{r} = 0 \quad (\text{continuity}) \quad (9.1.28)$$

and

$$u_z \frac{\partial u_z}{\partial z} + u_r \frac{\partial u_z}{\partial r} = \frac{1}{r\rho} \frac{\partial}{\partial r} \left(\mu_e r \frac{\partial u_r}{\partial r} \right) \quad (\text{equation of motion}) \quad (9.1.29)$$

Here, as before, μ_e is the effective viscosity:

$$\mu_e = \mu_t + \mu \quad (9.1.30)$$

For turbulent jets it is generally safe to assume that $\mu_t \gg \mu$.

The boundary conditions for Eq. (9.1.29) are identical to those previously given for laminar flow, specifying symmetry about the axis and the overall conservation of momentum, and are not reproduced here.

Before proceeding further, a realistic expression has to be found for μ_t . A detailed discussion of the considerations that would enter the selection of μ_t has been presented in Chapter 4, in connection with the various computational models for turbulence.

It has been suggested that, because of the symmetry of the flow field in turbulent circular jets (and due to the absence of solid boundaries), the Prandtl mixing length model would be adequate for the representation of

the turbulent viscosity. Thus we have

$$\mu_t = \rho l_m (\partial u_z / \partial r) \quad (9.1.31)$$

Spalding and Launder² recommended the following simple relationship for l_m :

$$l_m / \delta_j = 0.075 \quad (9.1.32)$$

where δ_j is the half-width of the jet, i.e., the distance from the centerline where the fluid velocity equals 1% of the maximum velocity difference across the jet. (This is a rather more general definition, which encompasses jets issuing into moving fluid streams; for a jet discharged into a stationary medium δ_j is the distance over which the velocity falls to 1% of the maximum at the centerline.)

On using the above definition of the mixing length, and hence the turbulent viscosity, the solution of the governing equations (9.1.28) and (9.1.29) is quite straightforward, although it requires the tackling of a two-point boundary value problem by a digital computer, as δ_j is, of course, a function of the axial distance and is given only implicitly in terms of the velocity profile.

The computational procedure employed is described by Spalding and Launder,² who found good agreement between predictions and measurements, both for stagnant fluids and for fluids moving with a uniform velocity.

A much simpler approximate approach was proposed by Tollmien³ in 1928 who postulated, after some arguments, that

$$\mu_t = \alpha' \rho \delta_j U_m \quad (9.1.33)$$

where α' is a constant and U_m is the centerline velocity, since $\delta \propto z$, while $U_m \propto (1/z)$.

The postulate in Eq. (9.1.33) is equivalent to suggesting that the turbulent viscosity is constant throughout the jet system. Under these conditions we may use the same analytical procedure that was employed for the integration of the laminar free jet, but noting that the viscosity term appearing in this equation is not a molecular property but a property of the system. Thus we have

$$u_z = 2.36 \left(\frac{J_z}{\rho} \right)^{1/2} \left[\frac{1}{z(1 + \frac{1}{4}\tilde{\eta}^2)^2} \right] \quad (9.1.34)$$

$$u_r = \left(\frac{3J_z}{\pi\rho} \right)^{1/2} \frac{\tilde{\eta} - \frac{1}{4}\tilde{\eta}^2}{z(1 + \frac{1}{4}\tilde{\eta}^2)^2} \quad (9.1.35)$$

where $\tilde{\eta} = 15.18r/z$.

The numerical constants appearing in Eqs. (3.1.34)–(3.1.36) reflect the empirically determined numerical value of the constant α . As illustrated in

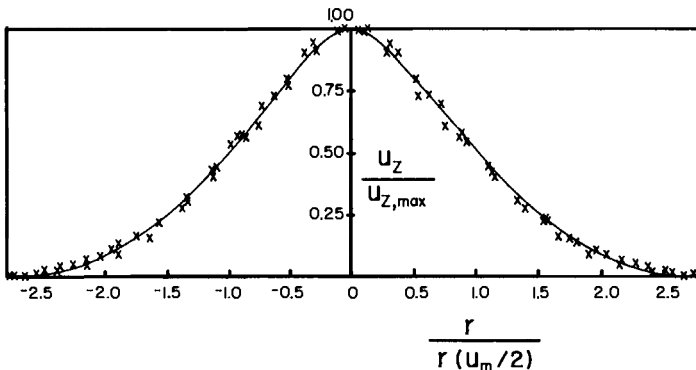


FIG. 9.1.2 Velocity distribution in a turbulent free jet; after Reichard.⁴

Fig. 9.1.2, taken from the work of Reichard,⁴ the simple model described above does provide a useful means for predicting experimental measurements. The streamline patterns corresponding to a turbulent free jet are sketched in Fig. 9.1.3. The mass rate of entrainment by a turbulent jet is given by the following relationship:

$$w = 0.404(J_z\rho)^{1/2}z \quad (9.1.36)$$

Let us illustrate the use of these formulas on a simple example.

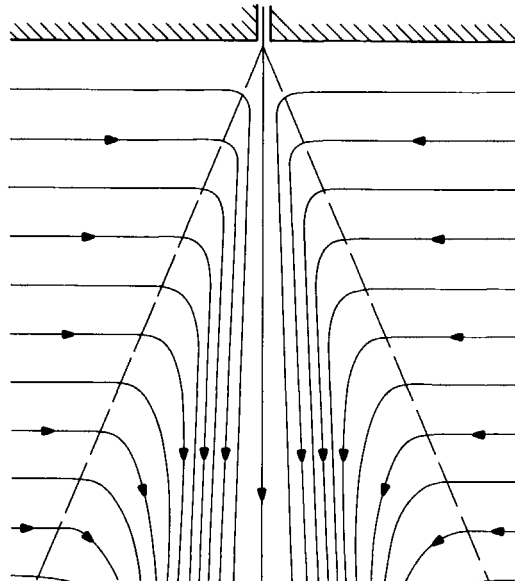


FIG. 9.1.3 Streamline patterns for a turbulent circular free jet.

Example 9.1.1 In a water treatment process a turbulent jet of water is discharged through an orifice, 0.05 m in diameter, at a mean velocity of 1.5 m/s, into a large tank, containing water, which may be regarded as an infinite medium. Calculate the centerline velocity and the total mass flow at a distance 1 m from the inlet.

SOLUTION

$$J_z = \frac{1}{4}(0.05)^2\pi(1.5)^2 \times 10^3 = 4.41 \text{ kg/s.}$$

Then the total mass flow is given, using Eq. (9.1.37):

$$w = 0.404(4.41 \times 10^3)^{1/2} \times 1 = 28.8 \text{ kg/s}$$

The centerline velocity is obtained from Eq. (9.1.34):

$$u_z = [2.36(4.41 \times 10^{-3})^{1/2}] \sim 0.156 \text{ m/s}$$

In closing this discussion of free jets, some comment should be made on heat and mass transfer in turbulent free jets, because experimental measurements in these systems have been helpful in assessing the mechanism of transfer. Moreover the principal application of jet systems in metals processing involves heat or mass transfer. Figure 9.1.4 shows the temperature and the velocity profiles, measured by Reichard,⁴ for a two-dimensional jet. It has been found that the profiles are similar, and Reichard suggested the following empirical expression for relating these two profiles:

$$T/T_{\max} = (U_z/U_{z,\max})^{1/2} \quad (9.1.37)$$

Simple physical reasoning would indicate that since the temperature profile is flatter than the velocity profiles, the ability of the system to transmit thermal energy is greater than its ability to transfer momentum. It is desirable,

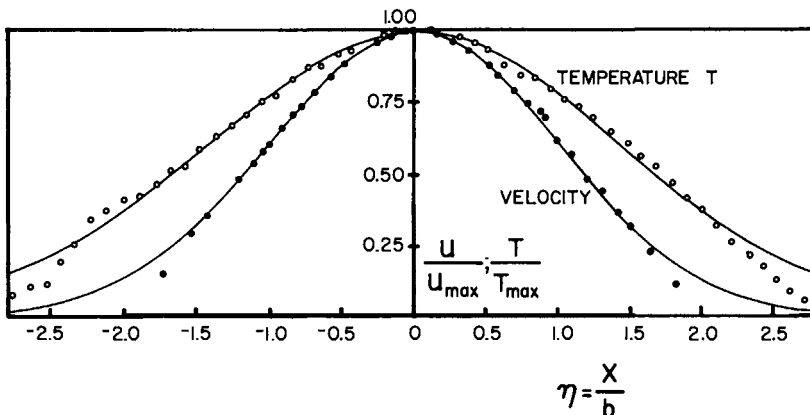


FIG. 9.1.4 Temperature and velocity profiles in a turbulent free jet; after Reichard.⁴

however, to develop this argument in a more quantitative manner. The expressions for heat transfer are remarkably similar to the momentum balance equation. Thus, upon assuming constant heat capacity and density and omitting the overbar designating time-smoothed quantities, we have

$$u_z \frac{\partial T}{\partial z} + u_r \frac{\partial T}{\partial r} = \frac{1}{r \rho C_p} \frac{\partial}{\partial r} \left(k_e r \frac{\partial T}{\partial r} \right) \quad (9.1.38)$$

for heat transfer and

$$u_z \frac{\partial C_A}{\partial z} + u_r \frac{\partial C_A}{\partial r} = \frac{1}{r} \frac{\partial}{\partial r} \left(D_e r \frac{\partial C_A}{\partial r} \right) \quad (9.1.39)$$

for mass transfer, where $k_e = k + k_t$ is the effective thermal conductivity, $D_e = D + D_t$ is the effective diffusivity, and C_A is the concentration of the transferred species.

If Eqs. (9.1.29), (9.1.38), and (9.1.39) were made dimensionless, e.g., through division by a reference velocity, temperature, and concentration, they would become identical, but for the following ratios:

$$N_{Pr}^t = C_p \mu_t / k_t \quad (\text{turbulent Prandtl number})$$

and

$$N_{Sc}^t = \mu_t / \rho D_t \quad (\text{turbulent Schmidt number})$$

If $N_{Pr}^t = N_{Sc}^t = 1$, then the velocity, concentration, and temperature profiles would coincide. In fact, as indicated by Fig. 9.1.4, $N_{Pr}^{(t)} < 1$. On the basis of extensive computation, Spalding and Launder² suggested that $N_{Pr}^{(t)} \approx 0.7 \approx N_{Sc}^t$ for round jets. These authors recommend slightly different values for the turbulent Prandtl and Schmidt numbers, depending on the jet geometry. The principal findings that should be remembered from this brief discussion are that the turbulent velocity, temperature and concentration profiles are similar, but not identical. The turbulent Prandtl and Schmidt numbers tend to be of the order of unity, but will vary with the geometry.

9.2 Confined Jets

In the majority of the practical applications of jet systems, jets are discharged into a confined space, rather than into an infinite medium. The streamline pattern for a simple confined jet is sketched in Fig. 9.2.1, where it is seen that the presence of the solid walls limits the extent to which jets may expand and the entrainment of the surrounding fluid may also be limited. A characteristic feature of confined jet systems is the establishment of a region where recirculation takes place.

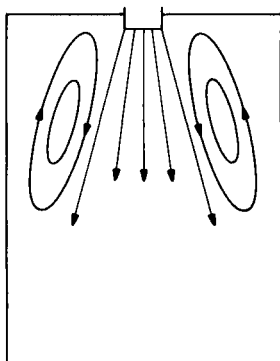


FIG. 9.2.1 The streamline pattern for a simple confined jet.

Flows of the type sketched in Fig. 9.2.1 are of considerable practical importance in the design of combustion chambers (in which the fuel discharged from the central orifice is made to react with the on-flowing air) in continuous casting; moreover, related phenomena also form an important component of flows through tanks, containers, and the like.

The complexity of the flow pattern, even for the relatively simple situation sketched in Fig. 9.2.1 (most recirculating flows tend to be rather more involved), precludes the availability of elegant analytical solutions of the type discussed in the preceding chapter for free jets.

Much of the work on confined jets has been motivated by their relevance to combustion chamber design. On the earlier work the experimental studies of Craya and Curtet⁵ should be cited, while a very good review of the patched, semianalytical techniques available for treating confined jet systems has been presented by Abramovich.⁶ However, in general, confined jets are probably best treated by using the formulation developed in Chapter 4 for the treatment of turbulent, recirculatory flow problems.

As discussed earlier, in general, this involves the statement of the turbulent Navier-Stokes equations; the boundary conditions have to express the fact that the velocity is zero at the solid surfaces ($\psi = \text{const}$); the velocity profile is specified at the inlet, together with the fact that symmetry is observed about the axis—if applicable. Numerous problems of this general type have been discussed in Chapter 4.

The only feature of the computational procedure, which is not straightforward, is the selection of an appropriate model or expression for the turbulent viscosity. Numerous problems of this type have been discussed by Spalding *et al.*,⁷ mainly in relation to the design of combustion chambers. Figure 9.2.2 shows a sketch of the streamline patterns computed by Spalding for a combustion chamber (in the presence of reactions) using a very simple algebraic expression for the turbulent diffusivity. The recirculatory flow

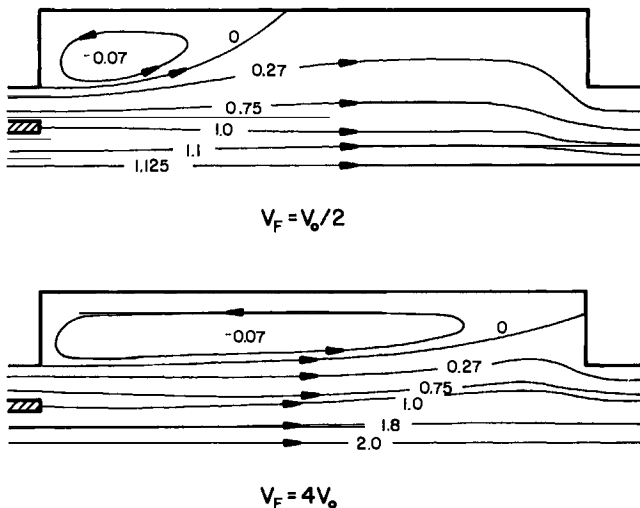


FIG. 9.2.2 Sketch of tech streamline pattern for a combustion chamber; after Gosman et al.⁷

pattern is readily observed. Figure 9.2.3 shows a sketch of the boundary conditions employed for the computation of the flow field in a "closed end" conical reactor. In a physical sense these boundary conditions express the fact that the walls are impervious, and that the flat velocity profile is specified at the inlet and that symmetry is observed about the centerline.

Of a perhaps more direct relevance to metals processing is the computation of the velocity field in the mold region of continuous casting

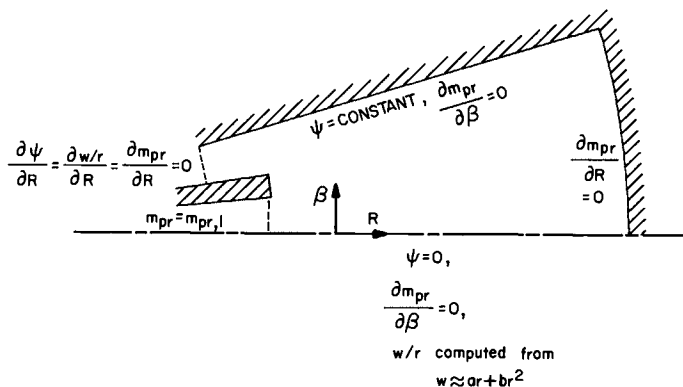


FIG. 9.2.3 Sketch of the boundary conditions employed for the computation of the flow field in a "closed-end" reactor.

systems.⁸ If we consider the casting of round billets, a schematic sketch of the system is shown in Fig. 9.2.4. In practice the proper statement of the problem requires an allowance for both the fluid flow phenomena and for the solidification process. This was in fact done in the article referenced. However, in the present instance we shall confine our attention to the fluid flow part of the problem.

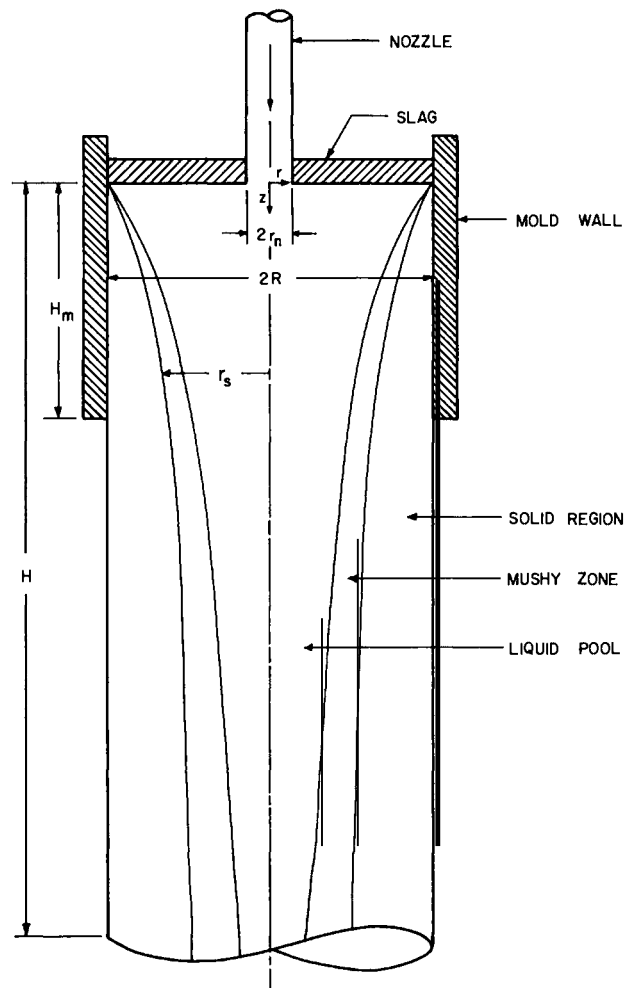


FIG. 9.2.4 A schematic sketch of the arrangement for the casting of round billets; after Asai and Szekely.⁸

In cylindrical coordinates the equation of motion may be written as

$$\begin{aligned} r^2 \rho \left[\frac{\partial}{\partial z} \left(\frac{\xi_\theta}{r} \frac{\partial \psi}{\partial r} \right) - \frac{\partial}{\partial r} \left(\frac{\xi_\theta}{r} \frac{\partial \psi}{\partial z} \right) \right] - \frac{\partial}{\partial z} \left(r^3 \frac{\partial}{\partial z} \mu_e \frac{\xi_\theta}{r} \right) \\ - \frac{\partial}{\partial r} \left[r^3 \frac{\partial}{\partial r} \left(\mu_e \frac{\xi_\theta}{r} \right) \right] = 0 \end{aligned} \quad (9.2.1)$$

where, as before,

$$\mu_e = \mu + \mu_t \quad (9.2.2)$$

and

$$\xi_\theta = \frac{\partial u_r}{\partial z} - \frac{\partial u_z}{\partial r} \quad (9.2.3)$$

$$u_r = \frac{1}{r} \frac{\partial \psi}{\partial z} \quad (9.2.4)$$

$$u_z = -\frac{1}{r} \frac{\partial \psi}{\partial r} \quad (9.2.5)$$

The one-equation model was used for specifying the turbulent viscosity,

$$\mu_t = \rho k^{1/2} l_m \quad (9.2.6)$$

in conjunction with the following formula for the mixing length:

$$l_m/R = 0.14 - 0.08(r/R)^2 - 0.06(r/R)^4 \quad (9.2.7)$$

The computational details and the numerical expressions used for the boundary conditions are discussed in the original article. Figure 9.2.5 shows the velocity field obtained for a straight nozzle of the type sketched in Fig. 9.2.4 and the corresponding map of the eddy diffusivity is shown in Fig. 9.2.6. The computed streamline patterns and turbulence energy distributions for an otherwise identical system, but on employing a radial flow nozzle, are shown in Figs. 9.2.7 and 9.2.8, respectively.

The intensive recirculation system in the upper mold region is readily seen in Fig. 9.2.7. Moreover, a comparison of Figs. 9.2.6 and 9.2.8 clearly indicates the much higher turbulence energy levels obtainable in the upper mold region with radial flow nozzles. These predictions for the flow patterns in the mold region of continuous casting systems have been confirmed, at least semiquantitatively, by both radio-active tracer tests and by velocity measurements on water models.⁹

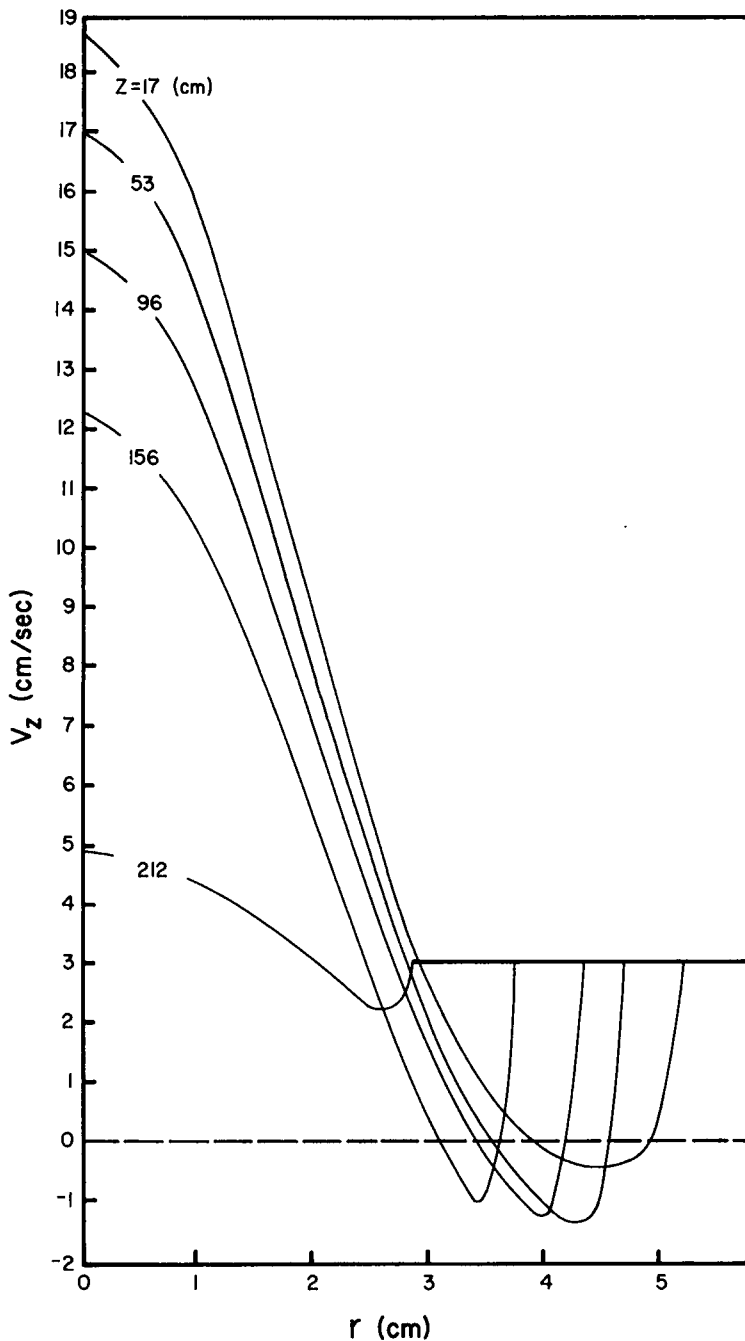


FIG. 9.2.5 The computed velocity profile in a continuous round billet casting system, for a straight nozzle. The numbers on the curves denote the distance from the inlet.⁸

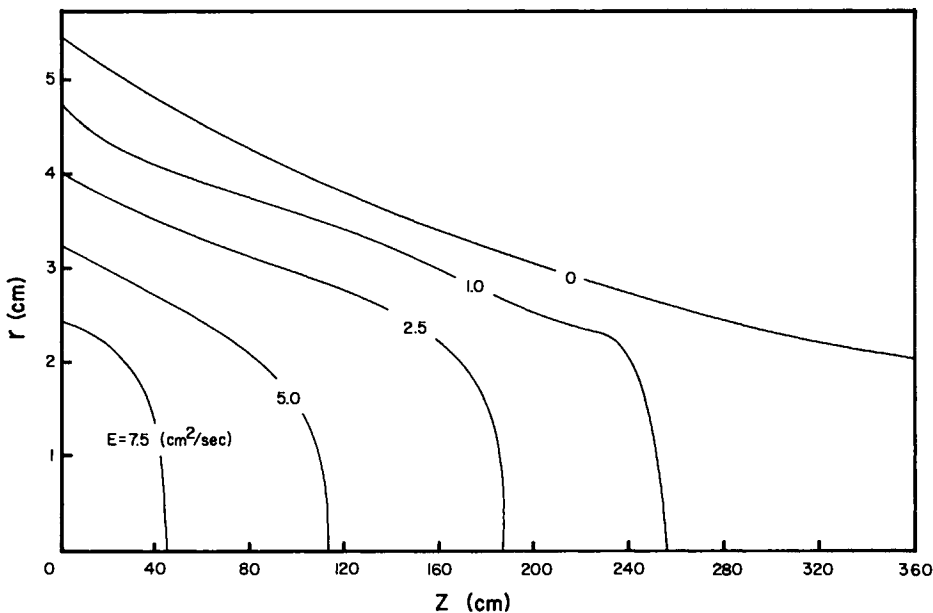


FIG. 9.2.6 The map of the eddy diffusivity for a straight nozzle, used in the casting of round billets.⁸

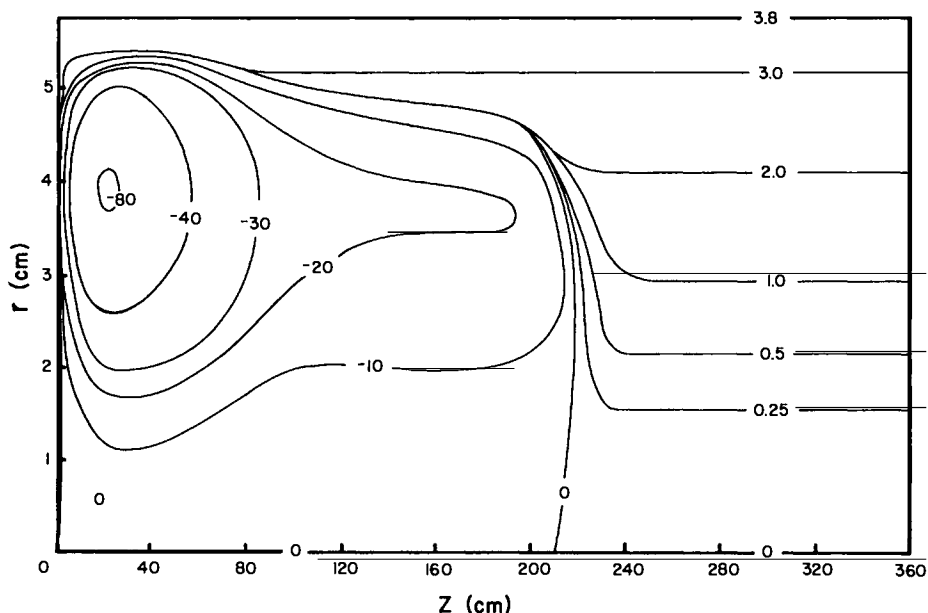


FIG. 9.2.7 The streamline pattern for a radial flow nozzle used for the continuous casting of round billets.⁸

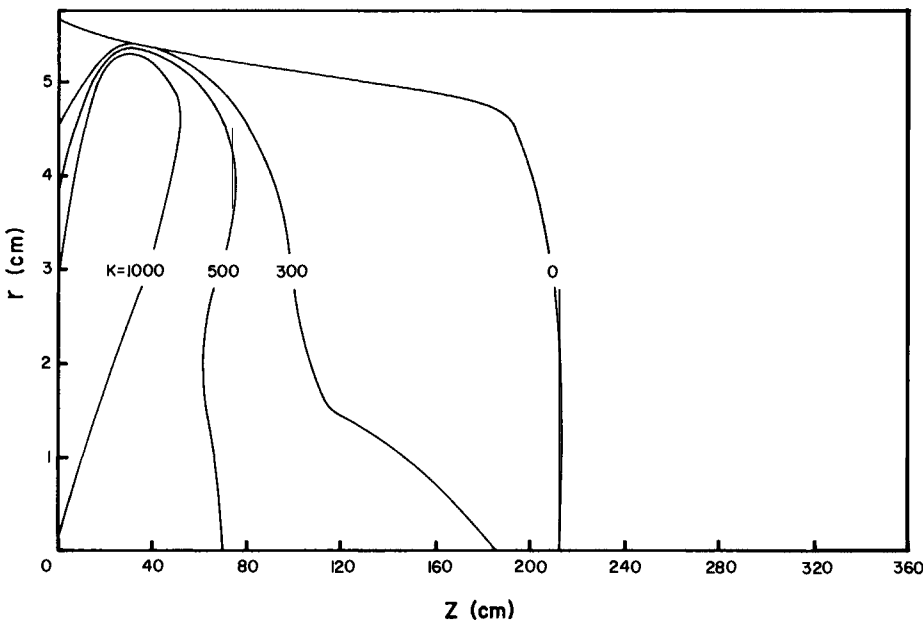


FIG. 9.2.8 The turbulent kinetic energy distribution.

9.3 Impinging Jet Systems

Impinging jets are of considerable practical importance in many metals processing operations. In classifying impinging jet problems it is convenient to draw the distinction between jets impinging on solid surfaces and jets impinging on deformable, liquid surfaces.

9.3.1 Jets Impinging on Solid Surfaces

Problems where gas jets impinge on solid surfaces are of importance mainly in connection with gas-solid heat transfer (cooling of strip, cooling of molds, etc.). Figure 9.3.1 shows a sketch of an impinging gas jet system. If our prime interest were to define the velocity field within the bulk of the gas stream, then, as the reader will recall, the simplest way to proceed is to postulate ideal flow behavior. As shown in Section 3.4, under these conditions the streamline pattern may be obtained readily by the conformal mapping. Thus, using the Cartesian coordinate system, with x' denoting the direction perpendicular to the plate, we have the following expressions for the velocity potential ϕ and the stream function ψ :

$$\phi = U_\infty(x'^2 - y'^2) \quad (9.3.1)$$

and

$$\psi = 2U_\infty x'y' \quad (9.3.2)$$

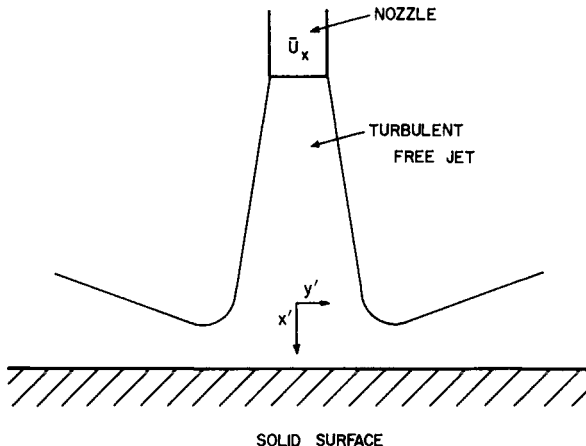


FIG. 9.3.1 Sketch of a turbulent impinging jet.

where, as before,

$$u_x = \frac{\partial \phi}{\partial x'} = \frac{\partial \psi}{\partial y'} \quad (9.3.3)$$

and

$$u_y = \frac{\partial \phi}{\partial y'} = -\frac{\partial \psi}{\partial x'} \quad (9.3.4)$$

The velocity field obtained through the combined use of Eqs. (9.3.1)–(9.3.4) is plotted in Fig. 9.3.2. This solution, while appealing because of its simplicity, is unlikely to be helpful for the majority of practical applications of impinging jet problems for two reasons:

- (a) The potential flow assumption precludes us from obtaining any information on the turbulence characteristics within the jet, so no account can be given of mixing phenomena.
- (b) The potential flow solution is inapplicable in the vicinity of the solid surface; if the objective is to estimate the heat transfer characteristics of the system, then this very region is of primary importance.

This problem may be tackled by employing the computational procedure outlined by Gosman *et al.*,⁷ who used Cartesian coordinates sketched in Fig. 9.3.1. For the jet system, if a one-equation model is used for computing the turbulent viscosity, the dependence of the mixing length has to be specified. Figure 9.3.3 shows the principal boundary conditions employed, together with the choice of the values for the mixing length l_m .

Figure 9.3.4 shows computed values of the stream function, the vorticity, and the turbulence energy. It is noted that the stream function plot is quite

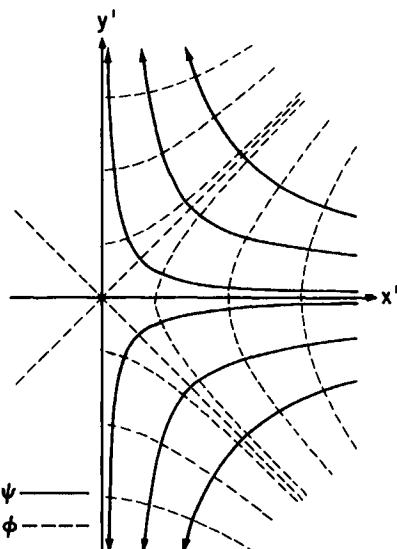


FIG. 9.3.2 Potential flow solution for an impinging jet onto a flat plate.

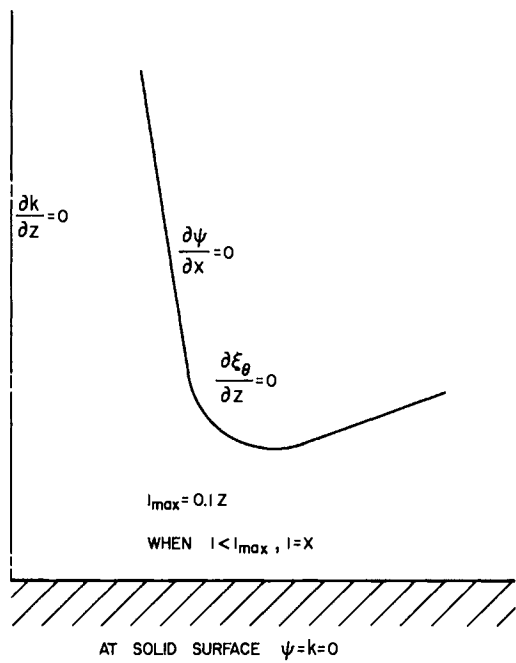
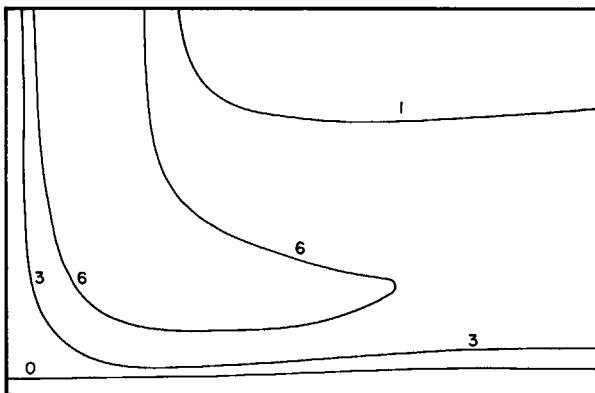
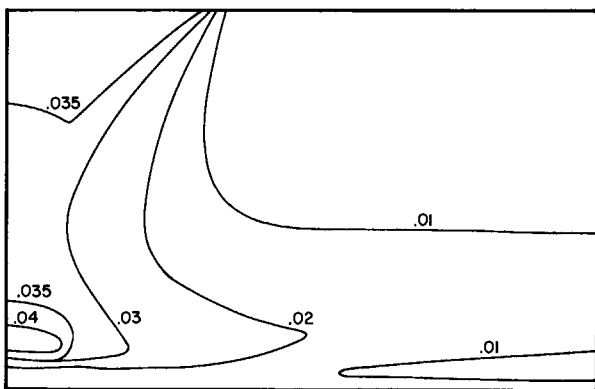


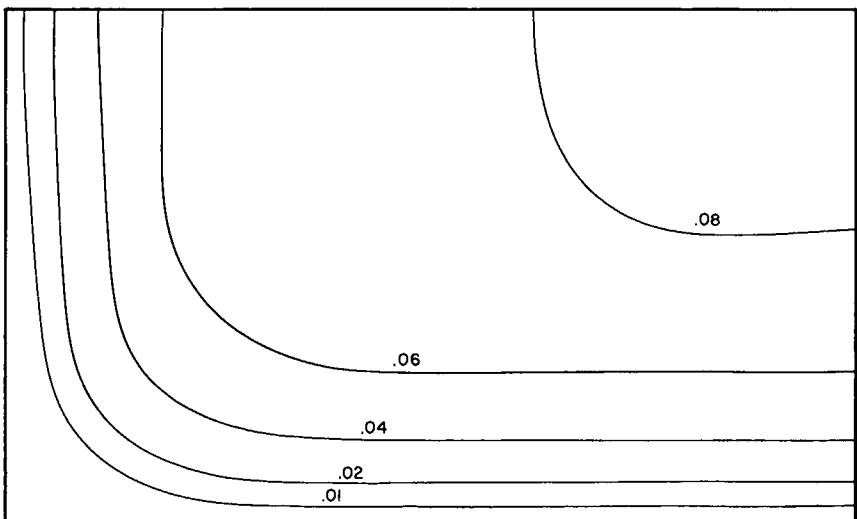
FIG. 9.3.3 Sketch of the boundary conditions used for formulating the turbulent impinging jet problem; after Gosman *et al.*⁷



(a)



(b)



(c)

FIG. 9.3.4 Sketch of the vorticity, turbulence energy profile, and the streamline pattern computed for an impinging turbulent jet: (a) vorticity, (b) turbulence energy, (c) stream function.

similar to that calculated for potential flow, although, as expected, the streamlines do get distorted in the vicinity of the solid wall. The vorticity plot is of interest because it is a clear indication of the differences between the potential flow solution and that computed for the turbulent flow system.

As discussed in the monograph by Gosman *et al.*⁷ the predictions based on the computed results were in reasonable agreement with measurements of both the fluid flow properties and (to a lesser extent) the heat transfer characteristics of the system. However by far the most important practical application of impinging jet systems in metals processing involves deformable liquid surfaces.

9.3.2 Jets Impinging on Liquid Surfaces

Figure 9.3.5 shows a sketch of the basic oxygen furnace (BOF, BOP), which is the principal application of impinging jet systems. In the basic

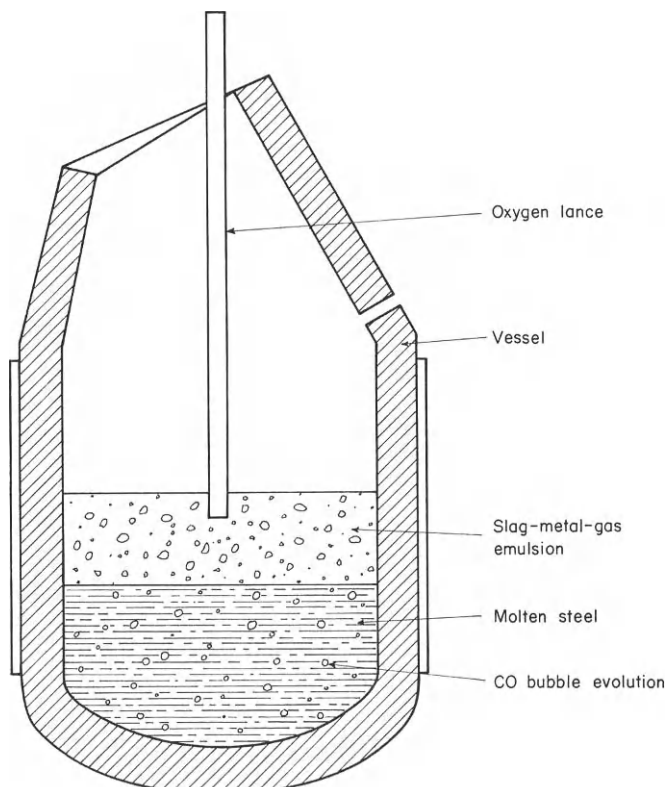


FIG. 9.3.5 Sketch of a basic oxygen furnace.

oxygen furnace a supersonic stream of oxygen is directed at the metal bath, which causes the oxidation of the undesirable impurities contained in the hot metal, such as carbon, silicon manganese, and phosphorous. The reaction mechanism is quite complex but is now reasonably well understood; the evolution of carbon monoxide (resulting from the oxidation of carbon) causes the formation of a frothy slag phase in which metal droplets are suspended. It is thought that the very large surface area of this slag–metal suspension is responsible for the very high rates of reaction attainable in the BOF.

While the fluid flow problem in the operation of the BOF is very complex, because of the three-phase nature of the system, interest in the reaction mechanism stimulated useful research into the interaction between gases and liquids. In this regard the early work of Bradshaw and Wakelin¹⁰ studied both the deformation of the liquid surface, as caused by an impinging jet, and the velocity field in the liquid thus produced.

A sketch of the system employed by these authors is shown in Fig. 9.3.6 and their experimental results, obtained using a range of systems plotted in Fig. 9.3.7. The symbols appearing in Fig. 9.3.7 have been largely defined in Fig. 9.3.6; thus, H_0 is the distance between the nozzle and the flat, undisturbed portion of the liquid surface, and H_c is the depth of the depression.

$$P_j = \frac{\pi}{4} d_0^2 \rho_G U_0^2 \quad (9.3.5)$$

is the momentum of the jet.

The measurements reported by Bradshaw and Wakelin¹⁰ were found to be in good agreement with the theoretical predictions of Banks and Chandrasekara¹¹ and the measurements of Mathieu.¹²

Perhaps of even greater interest is the recent work of Sharma *et al.*,¹³ who described measurements on jet penetration and liquid flow patterns obtained both in a water model of a BOF and in a 100-kg experimental BOF. By using a laboratory scale (100 kg) furnace equipped with a quartz window these authors were able to obtain direct photographic evidence of both the jet penetration and the bath circulation. Figure 9.3.8 is a photograph of the observed oxygen jet penetration at two different lance heights.

Sharma *et al.* found that their measurements were in very good agreement with the theoretical relationship

$$\frac{H_c}{H_0} \left(\frac{H_0 + H_c}{H_0} \right)^2 = \frac{154 P_j}{2\pi g \rho_1 H_0^3} \quad (9.3.6)$$

which has been plotted in Fig. 9.3.7.

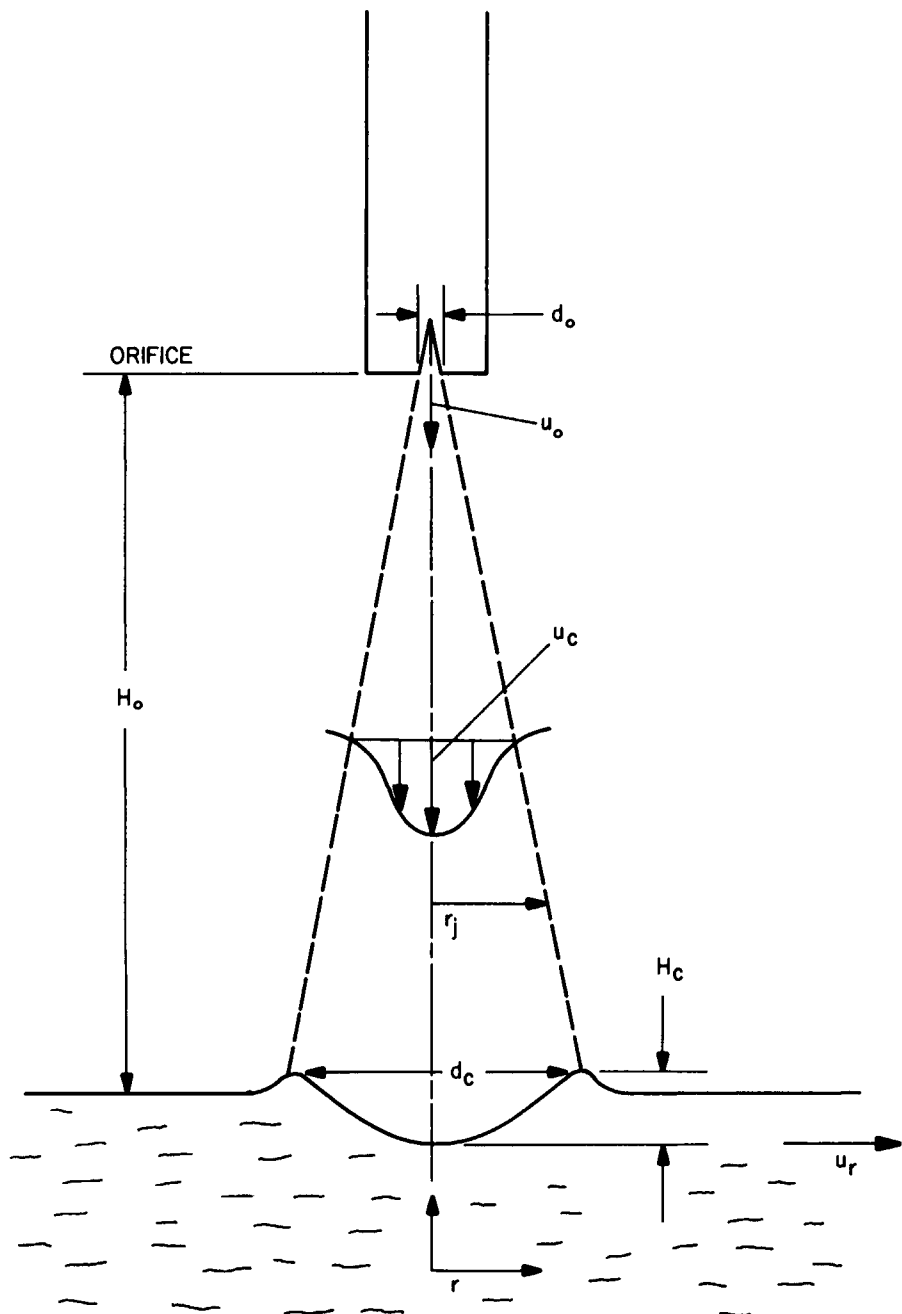


FIG. 9.3.6 The model of an impinging gas jet system used by Bradshaw and Wakelin.¹⁰

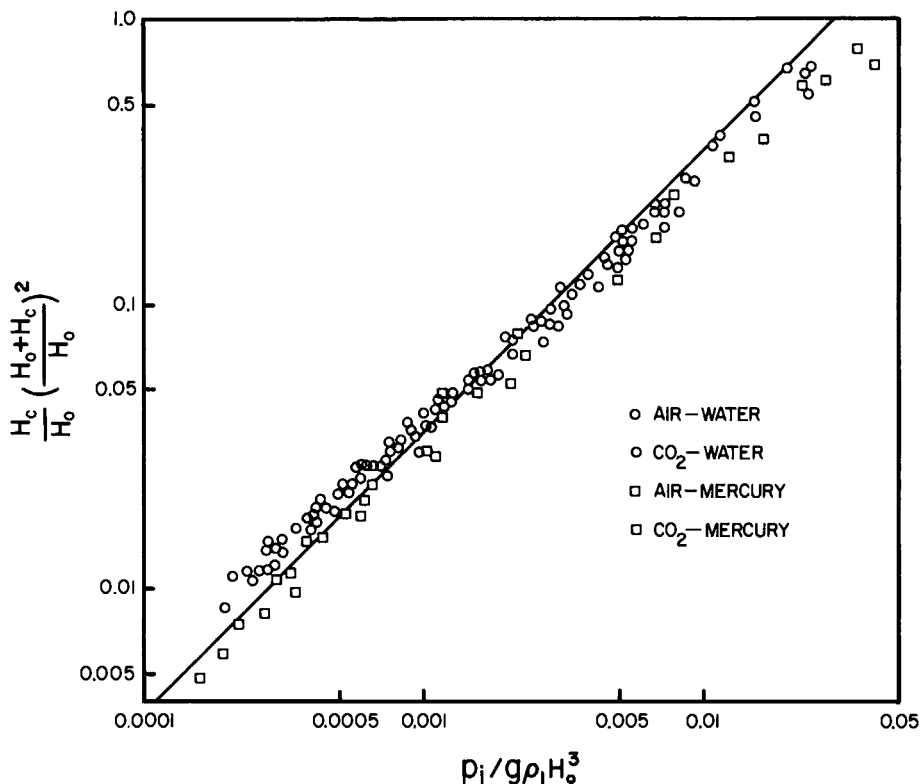


FIG. 9.3.7 The effect of the jet momentum and the nozzle height on the depth of the cavity, when a gas jet impinges on a liquid pool; after Bradshaw and Wakelin.¹⁰

Sharma *et al.* have noted that the jet momentum (P_j) appearing in Eq. (9.3.6) is of course uniquely related to the gas flow rate, for properly designed supersonic jets that are used in oxygen steelmaking practice.

Upon combining the relationships that were previously developed for supersonic flow through nozzles in Chapter 2, these authors developed a monogram for relating the jet penetration to the volumetric oxygen flow rate, the nozzle diameter, and the lance height. This monograph is reproduced in Fig. 9.3.9, where Q_0 is the oxygen flow rate in cubic meters per second, H_0 , the lance height in meters, d_0 , the internal diameter of the nozzle in meters, and H is the jet penetration in millimeters. Let us illustrate the use of this monograph by working the following simple example.

Example 9.3.1 In a basic oxygen furnace (BOF), employing a single nozzle, oxygen is being blown at a rate of $4.67 \text{ m}^3/\text{s}$ through a nozzle 0.057 m in diameter. If the lance height is 1.75 m , using Fig. 9.3.9, estimate the jet penetration.

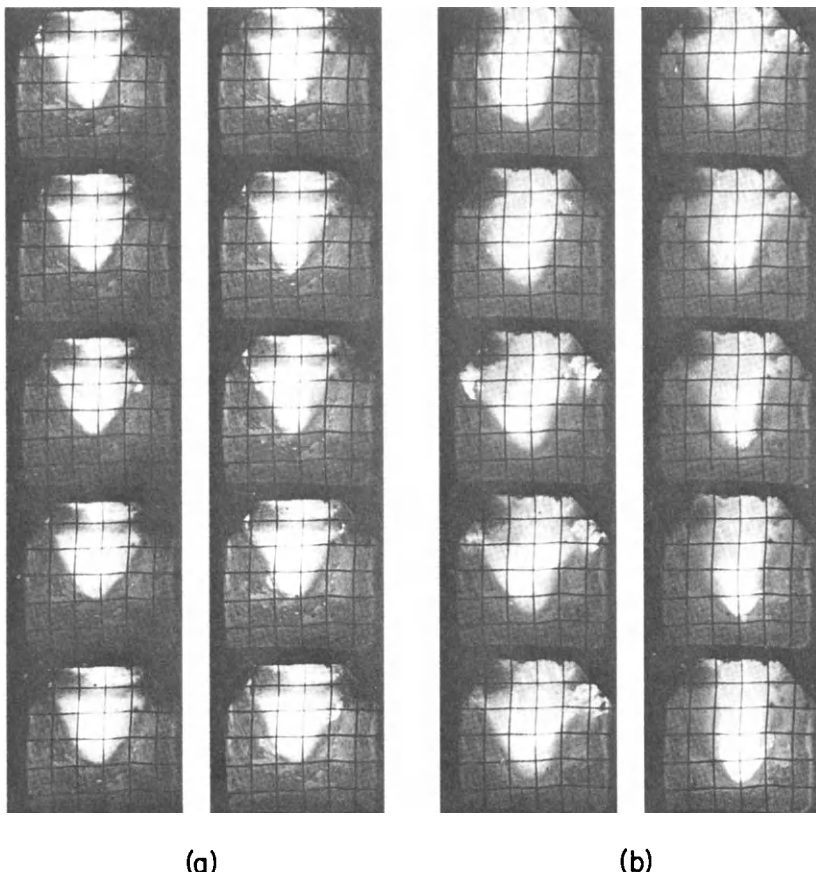


FIG. 9.3.8 Photograph of the observed penetration of an oxygen jet into a molten iron pool; as reported by Sharma *et al.*¹³: (a) lance height 3 $\frac{7}{8}$ in., (b) lance height 2 in.

SOLUTION Using Fig. 9.3.9,

$$Q_0/H_0^3 = 0.87$$

$$Q_0/D^2 = 1440.$$

Thus, using the monograph, the jet penetration is about 350 mm as indicated by the broken line.

This interesting paper by Sharma *et al.* has greatly improved our understanding of the BOF process; however, when it comes to the evaluation of the actual velocity fields, these measurements would be very difficult to make in molten metal systems, so that recourse has to be made to water modeling studies.

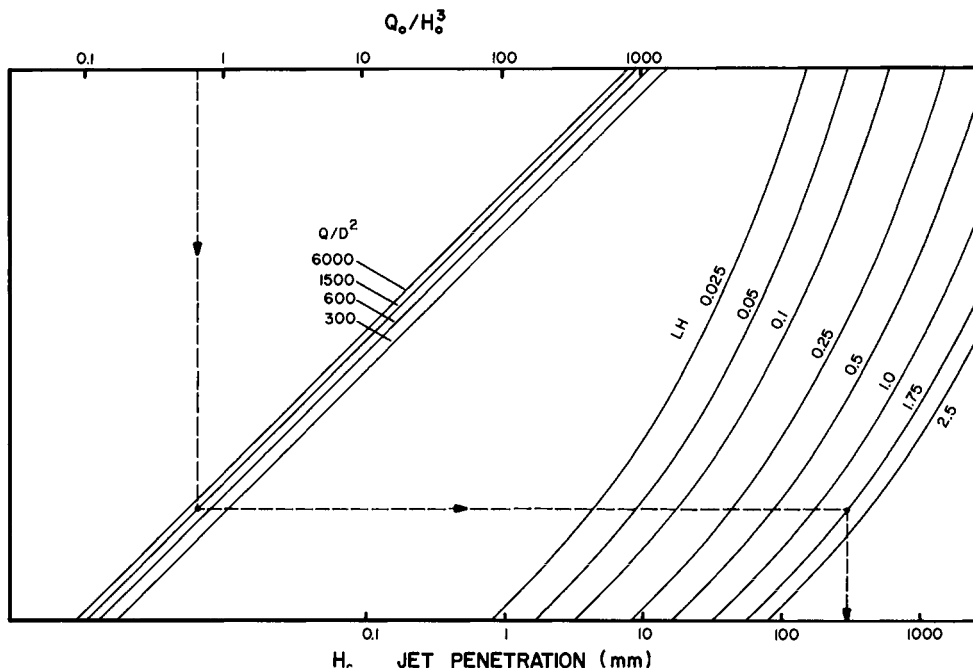


FIG. 9.3.9 Monograph for determining the jet penetration in molten steel; after Sharma *et al.*¹³ reworked in SI units. For English units, consult the original reference.

In this context, in the previously cited article Bradshaw and Wakelin¹⁰ also determined the velocity field in the liquid, caused by the impinging jet, using an air–water system. A typical set of their experimental results is shown in Fig. 9.3.10, which as expected indicates a recirculatory flow pattern which moves outwards from the impingement zone.

A simple mathematical representation of this recirculatory flow pattern has been developed by Szekely and Asai¹⁴ through the statement of the turbulent equation of motion in an axisymmetrical coordinate system and a one-equation model for the turbulent viscosity. The computed velocity field is sketched in Fig. 9.3.11, which is seen to be in good semiquantitative agreement with the measurements given in Fig. 9.3.10. The computed map of the turbulence energy is sketched in Fig. 9.3.12, from which it is seen that the turbulence energy of the system is very small, from which it could be inferred that turbulent mixing is almost nonexistent in such a system. This computed behavior is fully consistent with the experimental findings of Bradshaw and Wakelin, that a gas–liquid mass transfer process in these systems could be represented in terms of “surface renewal” type models based on the free surface, in the absence of turbulent transport between the bulk liquid and the

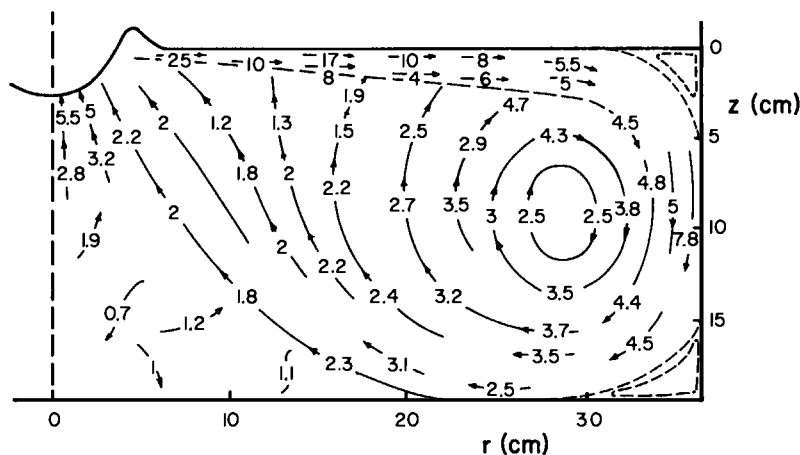


FIG. 9.3.10 Experimentally measured velocity field produced in water by an impinging air jet; after Bradshaw and Wakelin.¹⁰

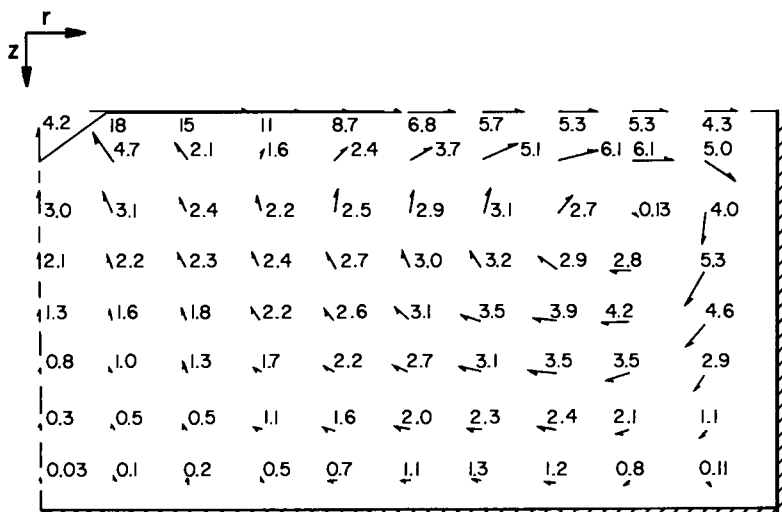


FIG. 9.3.11 Velocity profiles computed by Szekely and Asai¹⁴ to represent the measurements shown in Fig. 9.3.10.

free surface. These observations show that impinging jets would provide a very poor means of agitating liquid pools. Indeed, it is now quite well established that the intense agitation prevailing in the BOF is caused not by the impinging oxygen jet directly but rather by the rapid evolution of the product of carbon–oxygen reaction, namely carbon monoxide from the bath.

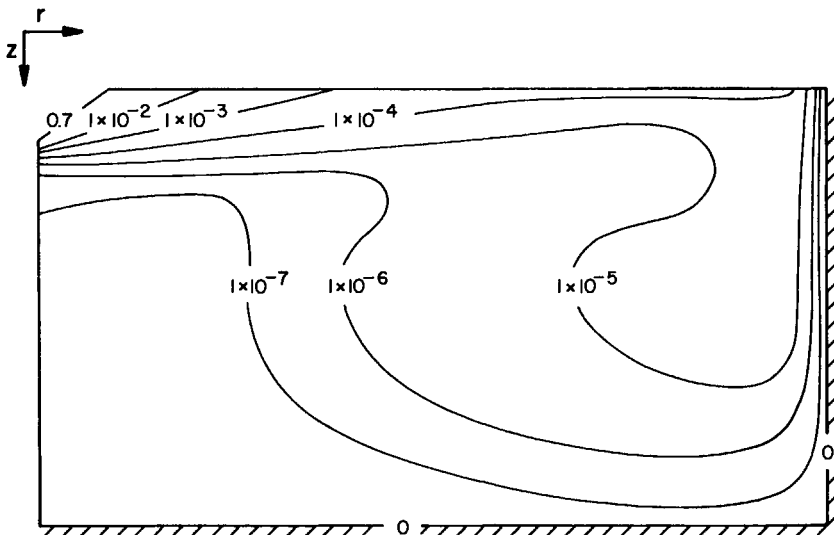


FIG. 9.3.12 The computed map of the turbulence energy in erg/cm^3 for the system depicted in Fig. 9.3.10.

Notwithstanding the impinging jet studies mentioned above, most of the practical application of jet theories to BOF steelmaking were in the area of supersonic, turbulent free jets. The concept of supersonic flow has been discussed in Chapter 2, which also contained worked examples, dealing with nozzle design. Moreover, the properties of turbulent-free jets were treated in the preceding section of this paper. Because of their important application to BOF steelmaking it may be appropriate to comment briefly on the behavior of turbulent, supersonic free jets.

It has been found that when a supersonic jet exits a nozzle, there is relatively little expansion of the jet until the velocity decreases to sonic levels. Beyond the supersonic portion the jet obeys the laws described in the preceding section. Anderson and Johns¹⁵ carried out extensive measurements on the expansion of supersonic jets. Their findings are summarized in Figs. 9.3.13 and 9.3.14.

Figure 9.3.13 shows the expansion of a supersonic jet on a plot of the ratio: (jet diameter where the velocity drops to half its maximum value)/(diameter of the nozzle) against the reduced axial distance from the nozzle.

Figure 9.3.14 shows the effect of the Mach number (at the exit from the nozzle) on the length of the supersonic core.

Smith used the information contained in Figs. 9.3.13 and 9.3.14 to calculate the expansion of a supersonic air jet in air and compared this with actual measurements, using a shadowgraph technique. As seen in Fig. 9.3.15 the agreement between measurements and predictions was quite reasonable.

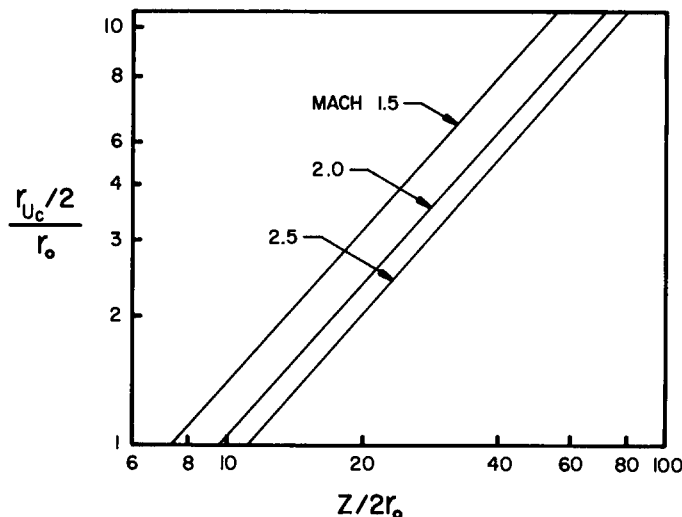


FIG. 9.3.13 Expansion of a supersonic jet with distance from the nozzle.

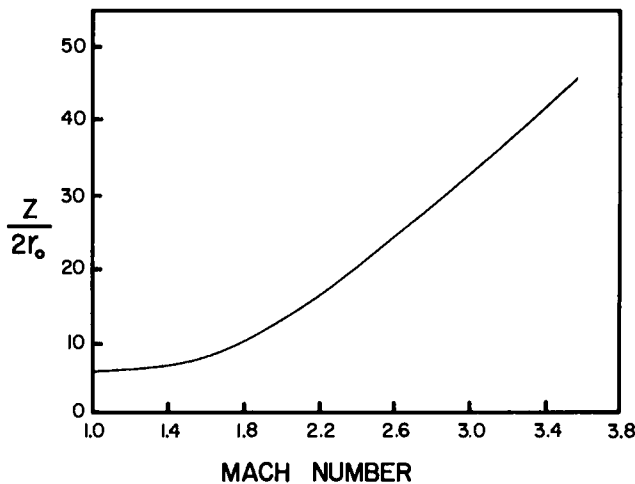


FIG. 9.3.14 The effect of the Mach number on the length of the supersonic core.

In current oxygen steelmaking practice multiple-hole lances, rather than single-hole lances, are used. For a full discussion of oxygen lance design criteria the readers are referred both to Smith's original article¹⁶ and to Volume 2 of the BOF monograph.

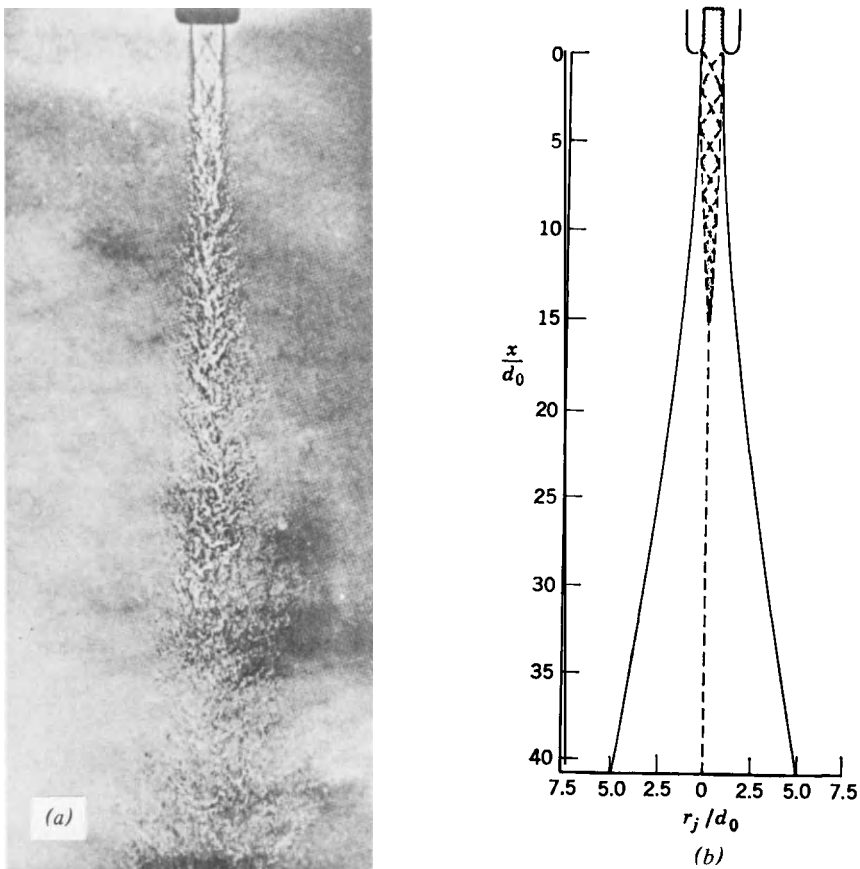
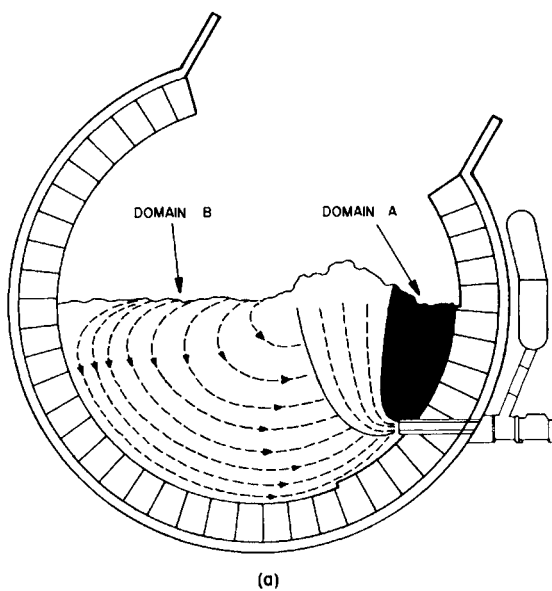


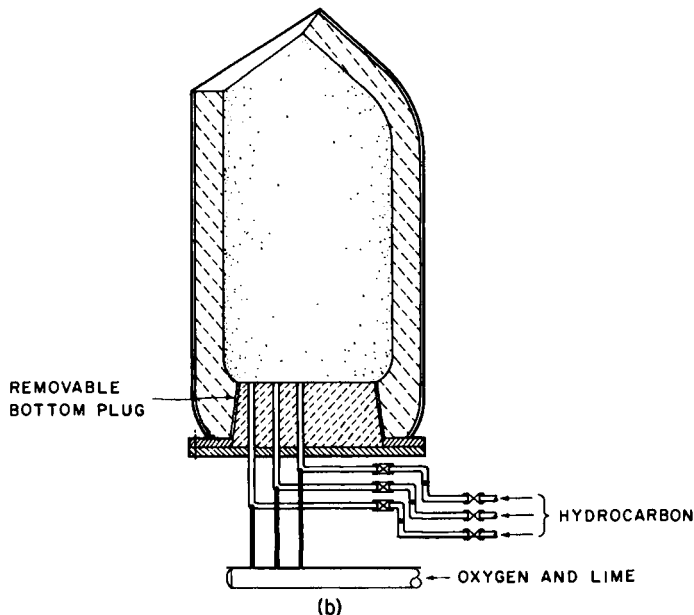
FIG. 9.3.15 (a) Shadowgraph of a supersonic jet in air, (b) jet profile computed by the technique described by Anderson and Johns.¹⁵

9.4 Submerged Jet Systems

We have seen in the preceding discussion that, while impinging jets may be attractive in metals processing operations because the jet nozzle does not have to be brought into direct contact with the metal or slag phase, the amount of direct agitation that may be provided through this arrangement is rather limited. Indeed, the basic oxygen process relies on the carbon monoxide evolved in the melt to provide the agitation. It follows that melts could be more effectively contacted with gases, if these were injected below the surface. The discussion of such submerged jets is the subject matter of this section.



(a)



(b)

FIG. 9.4.1 Sketch of (a) copper converter, (b) a Q-BOP vessel, and (c) an AOD vessel.
Kindly supplied by Dr. E. T. Turkdogan of U.S. Steel Corporation, Monroeville, Pa.

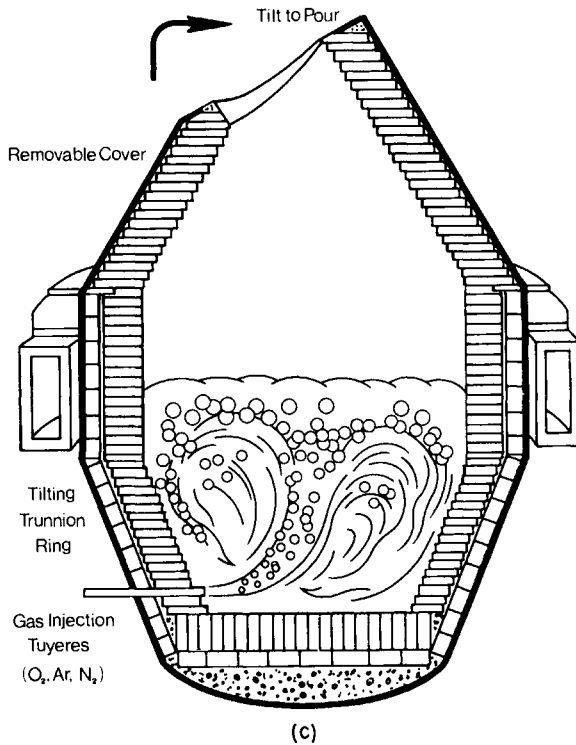


FIG. 9.4.1 (Continued).

Figure 9.4.1 shows a sketch of the three industrially most important applications of submerged jets in metals processing: (a) copper converting, the bottom-blown oxygen converter (Q-BOP or OBM), and (c) the AOD process. In copper converting, copper sulfide is reacted with oxygen, contained in air, to produce copper metal. In the bottom blown oxygen converter the oxidizable impurities contained in blast furnace hot metal (viz, carbon, silicon, manganese, etc.) are reacted with oxygen. In the AOD process, carbon is being oxidized selectively in a melt containing iron, chromium, and nickel. In copper converting (and also in the AOD process) the jets are horizontal or may be slightly inclined from the horizontal axis, while in the OBM process we have to deal with vertical jets. The reader will recall from the earlier discussion in Chapter 8 that when a gas is introduced into a liquid (melt) at volumetric flow rates corresponding to low values of the Reynolds number, discrete bubbles appear to form. At Reynolds numbers above about 2000 the coalescence of these bubbles becomes pronounced; the large bubbles thus formed, however, explode into smaller bubbles, the size of which

decreases with increasing values of the Reynolds number, until at $N_{Re} > 10,000$ the orifice velocity does not appear to have an effect on the mean bubble size.

In view of the predominant practical applications, namely horizontal subsonic jets (copper converting) and vertical supersonic jets (oxygen steel-making in the OBM), it is convenient to divide our discussion on these lines.

9.4.1 Horizontal Submerged Jets

Figure 9.4.2 shows two sets of photographs depicting the behavior of a horizontal air jet injected into water. Figure 9.4.2a, taken with a 0.6 ms exposure, shows the unsteady, unstable nature of the jet boundaries. It is also indicated that a gas-liquid mixture exists in the jet core, even at close

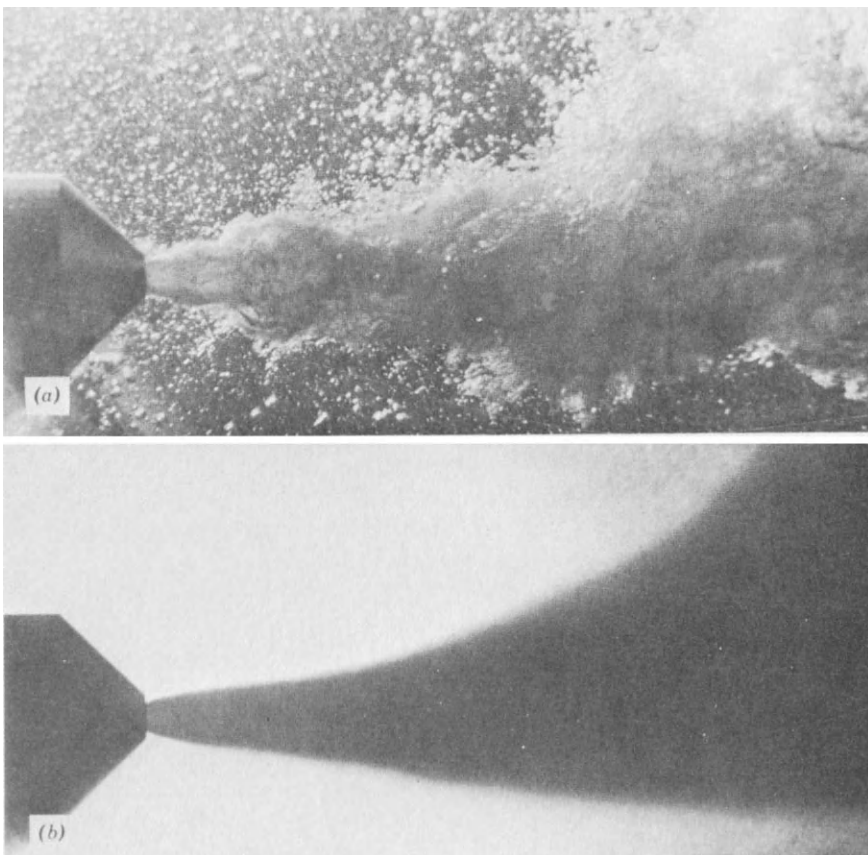


FIG. 9.4.2 Photograph of an air jet injected into water: (a) 0.6 ms exposure, (b) 5 s exposure, showing the characteristic jet cone.

proximity to the nozzle, rather than a pure continuous gas phase. This behavior is perhaps more readily seen in high-speed motion pictures¹⁷ and has been confirmed experimentally, through the use of conductivity probes on the mercury–nitrogen system.¹⁸

In contrast, Fig. 9.4.2b shows a picture of the identical system, taken with a 5-s exposure; such a representation may be regarded as a time averaging of the fluctuating motion so clearly shown in the upper photograph. Inspection of Fig. 9.4.2b shows that the system exhibits a characteristic jet cone angle, which is rather similar to that observed for gas jets, discussed in Section 9.2.

One of the important characteristics of submerged jets is their penetration into the melt, or more precisely their trajectory in the melt. It is readily seen from Fig. 9.4.2a that, after the jet has traveled some distance from the nozzle, it will tend to break up. This behavior may be explained by considering that the jet fluid is slowed down because it entrains liquid and, once the horizontal component reaches a value, which is comparable to the rising velocity of large bubbles in the liquid (say 0.3 m/s), the vertical velocity component will dominate and the jet will break up into bubbles.

In most practical applications deep penetration is desirable, because this will both maximize the contact between the melt and the gas and minimize the erosion of the containing walls, which would be aggravated by a rapidly rising gas stream. Themelis *et al.*¹⁹ considered the idealized system, sketched in Fig. 9.4.3, then, by making rather gross simplifying assumptions, these authors established a horizontal and a vertical momentum balance and developed the following differential equation for the trajectory of the center-line of the jet:

$$\frac{d^2 y_j}{dx_j^2} = 4N_{Fr}^{-1} \left[\frac{\tan^2(\theta_c/2)}{\cos \theta_0} \right] \left[1 + \left(\frac{dy_j}{dx_j} \right)^2 \right]^{1/2} \quad (9.4.1)$$

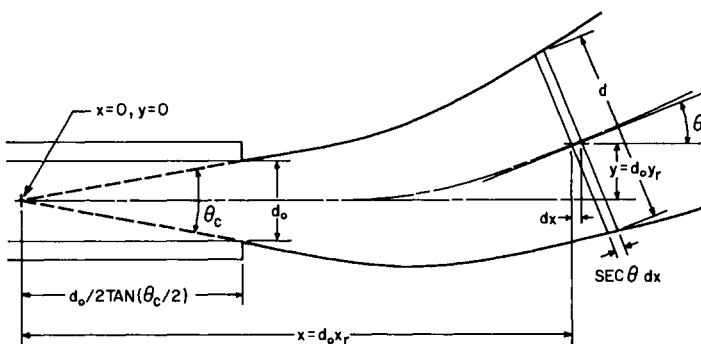


FIG. 9.4.3 Diagram showing the trajectory of an initially horizontal submerged jet.

where $y_j = y/d_o$ is the dimensionless vertical distance from the jet pole, $x_j = x/d_o$ the dimensionless horizontal distance from the jet pole, d_o the orifice diameter, $N'_{Fr} = \rho_G U_0^2/g (\rho_L - \rho_G) d_o$ the modified Froude number, ρ_G and ρ_L the gas and liquid densities, respectively, θ_c the jet core angle, θ the angle formed by the axis of the orifice with the horizontal coordinate, C the volume fraction of the gas in the jet at a distance x from the jet pole, and C may be obtained from a mass balance which, after some rearrangement, may be written as

$$C = \frac{1}{x_j} \left[C - \frac{\rho_L}{\rho_G} (1 - C) \right]^{1/2} \quad (9.4.2)$$

Figure 9.4.4 shows a plot of the computed values of C as a function of the dimensionless distance from the jet pole for the air-matte and the air-water systems. It is seen, as expected, that the volume of air decreases with increasing

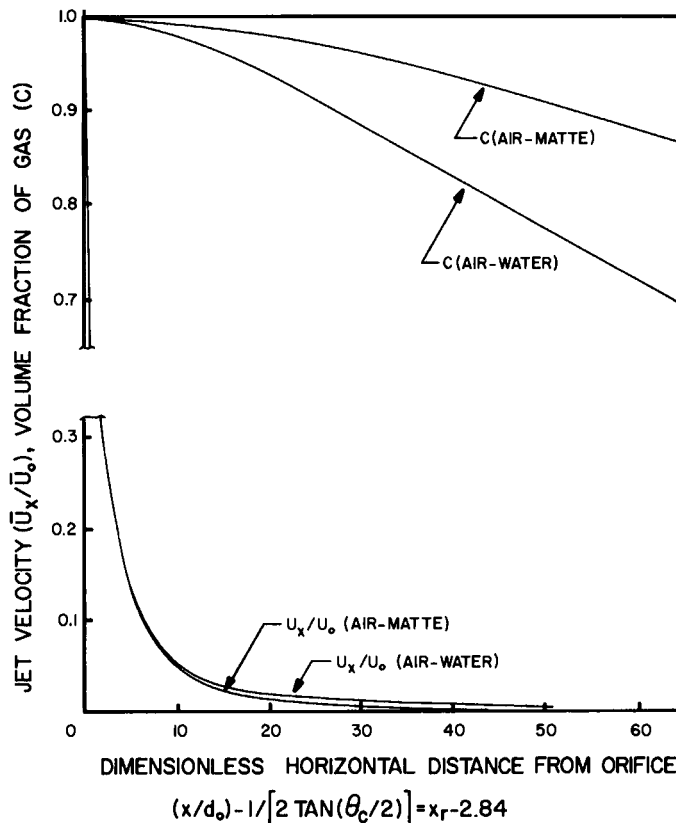


FIG. 9.4.4 Plot of the jet velocity and the volume fraction of the gas.

distance, because of the entrainment of the liquid (melt). The boundary conditions for Eq. (9.4.1) are written as

$$y_j = 0 \quad \text{at} \quad x_j = \frac{1}{2} \tan(\theta_c/2) \quad (9.4.3)$$

and

$$\frac{dy_j}{dx_j} = \tan \theta_0 \quad (9.4.4)$$

These boundary conditions are largely self-explanatory. Equation (9.4.3) specifies that the vertical position of the jet is zero at the jet pole, while Eq. (9.4.4) expresses the fact that the initial direction of the jet is specified.

The system of Eq. (9.4.1)–(9.4.4) is readily integrated numerically, using the Runge–Kutta procedure; Fig. 9.4.5 shows a comparison between the predicted jet trajectory computed for $\theta_c \approx 20^\circ$ of the centerline of the jet with actual experimental results obtained in a water model of a copper converter. These experimental results were deduced from long-exposure photographs, of the type shown in Fig. 9.4.2. It is seen that the agreement between measurements and predictions is quite reasonable, at least for the air–water system.

Figure 9.4.6 shows a more comprehensive set of the computed results, on a plot of the dimensionless trajectory of the centerline of the jet against the modified Froude number, for the air–matte system. It is seen, as perhaps

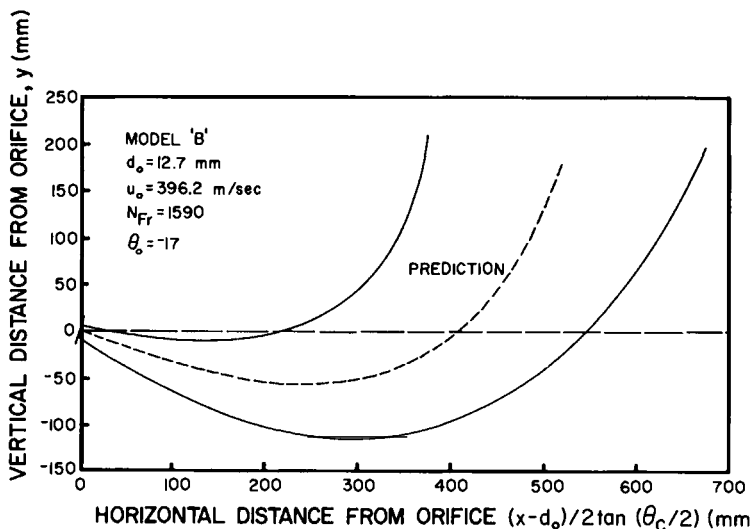


FIG. 9.4.5 Comparison of the theoretically predicted jet trajectory with measurements.

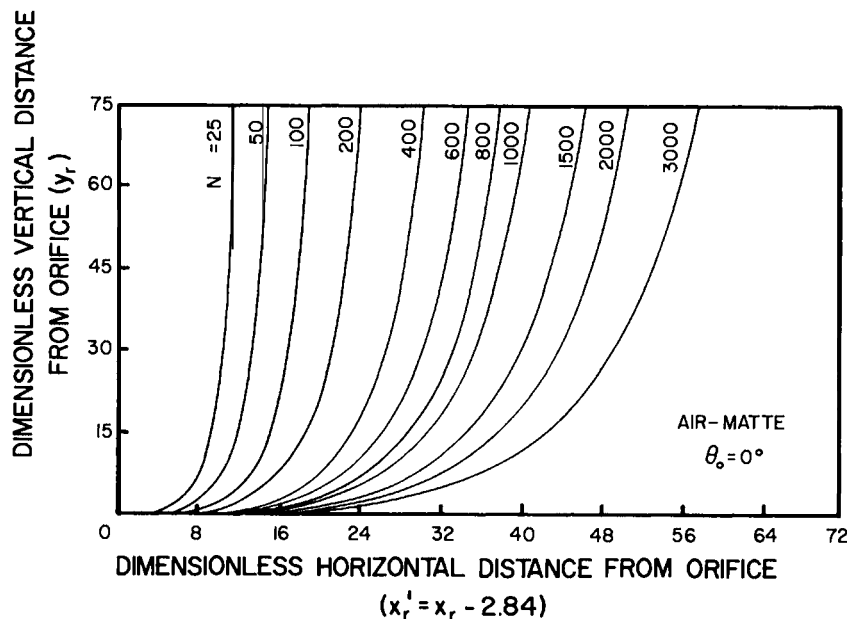


FIG. 9.4.6 The effect of the modified Froude number on the trajectory of an air jet injected into matter in copper converting.¹⁹

expected, that the larger the value of the modified Froude number the larger the jet penetration.

Let us illustrate the application of Fig. 9.4.6 by performing a simple calculation to estimate the jet trajectory in a copper conversion operation.

Example 9.4.1 Calculate the trajectory of the submerged horizontal air jet in a Pierce-Smith converter, for the following operating conditions: nozzle diameter, 0.04 m; linear air velocity, 150 m/s; density of air, 1.5 kg/m³; density of matte, 4.8×10^3 kg/m³.

SOLUTION The modified Froude number for this system is

$$N'_{Fr} = \frac{1.5 \times 2.25 \times 10^4}{9.81 \times (4.8 \times 10^3 - 1.5) \times 0.04} \approx 1.79$$

Thus using Fig. 9.4.6 we can plot the trajectory. Apart from the jet trajectory the other points of interest in the interaction between horizontal submerged gas jets and melts are the flow patterns induced in the melt, by the gas stream and the actual mass transfer between the jet and the melt. Nakanishi and Szekely²⁰ have reported computed results on the flow patterns in the liquid phase, caused by submerged jets, and, as seen in Fig. 9.4.7, these

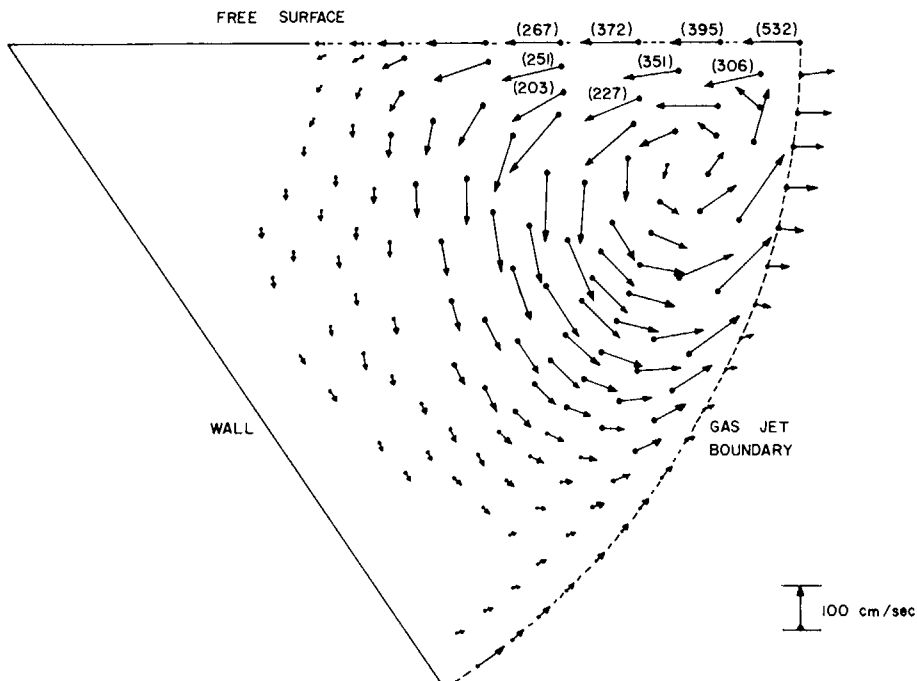


FIG. 9.4.7 Computed streamline pattern for the flow field in a copper converter; after Nakanishi and Szekely.²⁰

are at least in good qualitative agreement with experimental measurements.

Brimacombe and co-workers²¹ have reported on interesting work devoted to mass transfer between horizontal submerged jets and liquids using the SO₂-water system²¹; however, the mass transfer coefficients that could be deduced from their measurements were not consistent with analogous data reported by Themelis and Schmidt²² on the gas phase deoxidation of copper.

It is noted, moreover, that recent work by Brimacombe¹⁸ indicates that the results shown in Figs. 9.4.3-9.4.6 may have to be modified for liquid metal systems because the jet angle for molten metals may be rather larger than the value of 20° found for the air-water system.[†]

In view of the importance of submerged jets in metals processing, further work in this area would be highly desirable.

[†] A good discussion of submerged jet systems is available in the proceedings of a recently held symposium at the University of Newcastle upon Tyne, England; organizer: Dr. W. Wraight.

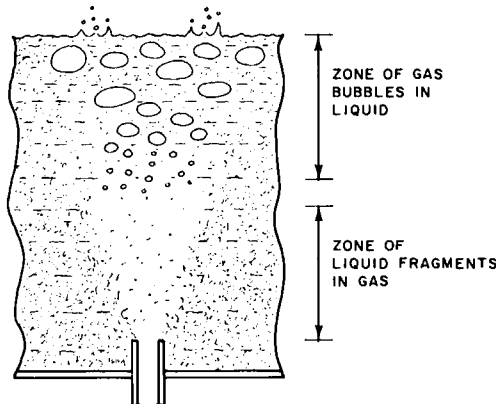


FIG. 9.4.8 The mechanism of jet breakup; after Turkdogan.²³

9.4.2 Submerged Vertical Jets

By far the greatest practical application of submerged vertical jets is the Q-BOP or the OBM process, which was sketched in Fig. 9.4.1. It is seen that the melt is bottom blown through tuyeres located in a removable plug. The tuyere consists of two co-axial pipes; oxygen is passed through the central pipe, while propane or natural gas is blown through the annular section. The decomposition of this natural gas is endothermic and the heat thus absorbed provides an effective coolant for the tuyere.

The fluid flow phenomena associated with the operation of the OBM process are even less well understood than the behavior of subsonic horizontal submerged jets, although some useful work is currently in progress.¹⁷

Turkdogan proposed the following qualitative picture for describing the behavior of vertical submerged jets, which is sketched schematically in Fig. 9.4.8.²³ He suggested that most of the kinetic energy of the gas introduced into the system was consumed in the lower zone (upon entry) by fragmenting liquid droplets and shearing off liquid layers from the unstable liquid-gas interface. The ejected liquid fragments are then thought to coalesce downstream, leading to a second zone of gas bubbles in the liquid. Since fragmentation of liquid droplets (i.e., work against surface tension forces) plays an important part in the mechanism proposed here, Turkdogan suggested, quite properly, that it may be misleading to model mass transfer processes involving liquid metals and gases through the use of aqueous systems, because of the large disparity in the interfacial tension in these two sets of systems.

Because of the obvious importance of the Q-BOP (OBM) system further work in this field would be very much justified.

References

1. H. Schlichting, "Boundary Layer Theory," 6th ed. McGraw-Hill, New York, 1968.
2. D. B. Spalding and B. E. Launder, "Mathematical Models of Turbulence," p. 27. Academic Press, New York, 1972.
3. W. Tollmien, Translation of 1928 German original, *NACA Tech Note TN 1085* (1945).
4. H. Reichard, *Z. Angew. Math. Mech.* **24**, 268 (1944), cited by Schlichting,¹ p. 600.
5. A. Craya and R. Curtet, *C. R. Hebd. Seances Acad. Sci.* **241**, 621 (1955).
6. G. N. Abramovich, "The Theory of Turbulent Jets." MIT Press, Cambridge, Massachusetts, 1963.
7. A. D. Gosman, W. M. Pun, A. K. Runchal, D. B. Spalding, and M. Wolfson, "Heat and Mass Transfer in Turbulent Recirculating Flows." Academic Press, New York, 1969.
8. S. Asai and J. Szekely, *Ironmaking Steelmaking* **3**, 205 (1975).
9. J. Szekely and R. T. Yadoya, *Metall. Trans.* **3**, 2673 (1972).
10. A. V. Bradshaw and D. Wakelin, in "Heat and Mass Transfer in Process Metallurgy." (A. W. D. Hills, ed.), The Institution of Mining and Metallurgy London, 1967.
11. R. B. Banks and D. V. Chandrasekara, *J. Fluid Mech.* **15**, 13 (1963).
12. F. Mathieu, *Rev. Univ. Mines, Metall., Mec.* **18**, 482 (1962).
13. S. K. Sharma, J. W. Hlinka, and D. W. Kern, *Iron Steelmaker* **4**, No. 7 (1977).
14. J. Szekely and S. Asai, *Metall. Trans.* **5**, 463 (1974).
15. A. R. Anderson and F. R. Johns, *Jet Propul.* **25**, 13 (1955).
16. G. C. Smith, *J. Metals* **18**, 846 (1966).
17. T. B. King, Photographs, private communication
18. G. N. Oryall and J. K. Brimacombe, *Metall. Trans. 7.B* 391 (1976).
19. N. J. Themelis, P. Tarasoff, and J. Szekely, *Trans. Metall. Soc. AIME* **242**, 5 (1969).
20. K. Nakanishi and Szekely, unpublished research, cited by Szekely in Scaninject Conference, Lulea, Sweden, Mefos Publ, 1977.
21. J. K. Brimacombe, E. S. Stratigakos, and P. Tarasoff, *Metall. Trans.* **5**, 763 (1974).
22. N. J. Themelis and P. R. Schmidt, *Trans. Metall. Soc. AIME* **239**, 1317 (1967).
23. E. T. Turkdogan, *Inst. Min. Metall., Trans.* **83**, C67 (1974).

10.1 Introduction

In the preceding chapter we examined various aspects of fluid flow phenomena in metals processing. The treatment was necessarily mathematical because quantitative description of these physical processes was our objective. Since in its practical applications fluid mechanics is not entirely an “exact science,” wherever possible the theoretical predictions made were compared with experimental measurements.

Our purpose in this chapter is to provide a brief introduction to the principal experimental techniques that are available for determining fluid flow rates and velocity fields together with a discussion of the elements of physical modeling. It is noted that the measurement of volumetric flow rates and velocities is quite straightforward for gases and liquids at room temperatures; however, substantial difficulties may arise when one attempts to measure velocities or flow rates in liquid metals, particularly at high temperatures (e.g., in molten steel). In many cases the techniques to be employed have to rely on indirect measurements; a discussion of these will be presented also. One alternative to actually measuring velocities in molten steel is the construction of room temperature physical models, where these measurements are much more easily made. The principles governing the construction of such models will be reviewed also. This chapter will also include a very brief discussion of the principles that govern the construction of these models.

Regarding the organization of the chapter, Section 10.2 will be devoted to volumetric flow rate measurements, while the techniques of velocity measurement will be discussed in Section 10.3. The chapter concludes with the principles of physical modeling.

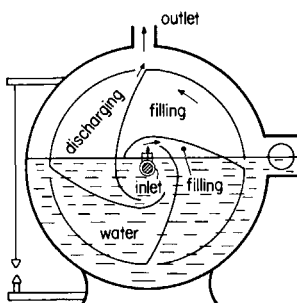
10.2 Measurement of Volumetric Flow Rates

10.2.1 Quantity Meters

In concept the simplest means for measuring volumetric flow rates is by determining the rate at which a known volume of fluid is displaced in a container.

In a wet-gas meter, sketched in Fig. 10.2.1, the gas fills a rotating segment and an equal volume of gas is expelled from another segment. The rotation of the shaft then directly corresponds to the displacement of a given volume, i.e., the passage of a given volume of gas through the meter. The dry-gas meters employ a pair of bellows; the gas enters one of the bellows and automatically expels from the other. The number of displacements, i.e., cycles, is then recorded on a dial. Since both these types are of a positive displacement, they do not require frequent calibration.

FIG. 10.2.1 A wet-gas meter.



Another simple device, used for the measurement of small gas flow rates (in particular, for the calibration of certain flow meters in the laboratory), is a "soap bubble flow meter," sketched in Fig. 10.2.2. In essence the soap bubble flow meter is a vertical burette through which a gas is passed. Provision is made for injecting a soap bubble into the burette and the flow rate is then determined by timing the passage of the bubble between two divisions which correspond to an accurately known volume.

The principle of quantity meters for measuring liquid flow rates is very similar to those discussed for gases. The so-called positive displacement types are like small pumps employing one or more pistons. These tend to be quite accurate and do not require frequent calibration, but are difficult to use for really high flow rates.

A more detailed discussion of quantity meters is available in Bean¹ and Coulson and Richardson.²

10.2.2 Orifice Plates, Nozzles, and Venture Meters

In all of these devices the fluid flowing through a pipe or duct is accelerated by causing it to pass through a constriction; the kinetic energy is thereby

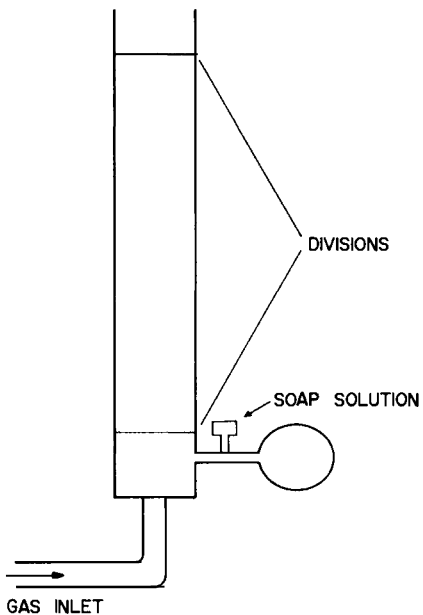


FIG. 10.2.2 Sketch of the soap bubble flow meter.

increased and the corresponding change in the pressure energy is then measured. The flow rate may then be obtained from the measured pressure difference through the application of the overall mass and energy balance, discussed in Chapter 2.

Figure 10.2.3 shows a sketch of an orifice plate indicating velocity profiles and the locations where the pressure differentials are measured. It is seen that at a given position, upstream from the orifice, the fluid passes

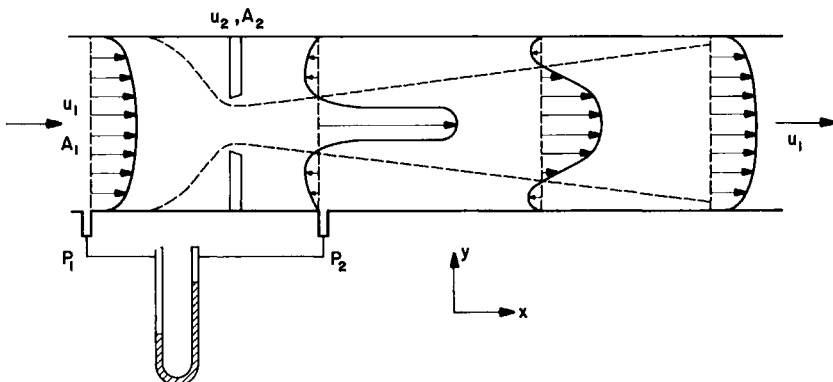


FIG. 10.2.3 Sketch of an orifice meter.

through a cross-sectional area A_1 , at a velocity u_1 , and at that stage has a pressure p_1 . At the orifice the fluid passes through a cross-sectional area A_2 , at a velocity u_2 , and its pressure has a value of p_2 .

In order to relate w , the mass flow rate of the fluid to the pressure difference $(p_1 - p_2)$, let us establish an overall mass balance and an overall energy balance on the system between points 1 and 2.

Thus we have

$$u_1 \rho_1 A_1 = u_2 \rho_2 A_2 \quad (\text{overall mass balance}) \quad (10.2.1)$$

Upon recalling Eq. (2.4.6), the overall energy balance takes the following form:

$$\begin{aligned} \frac{u_2^2}{2} - \frac{u_1^2}{2} &+ g(Z_2 - Z_1) + \int_1^2 v dp \\ \text{kinetic energy} &\quad \text{potential energy} \quad \text{pressure energy} \\ + W' &+ F' = 0 \\ \text{rate of work} &\quad \text{rate of work} \\ \text{done on the} &\quad \text{done against} \\ \text{surroundings} &\quad \text{frictional forces} \end{aligned} \quad (10.2.2)$$

Usually no work is done on the surroundings; moreover, for a short length of pipe the frictional effects are negligible. Furthermore, for an incompressible fluid

$$\int_1^2 v dp = (p_2 - p_1)/\rho \quad (10.2.3)$$

Thus Eq. (10.2.2) simplifies to

$$(u_2^2/2) - (u_1^2/2) = (p_1 - p_2)/\rho \quad (10.2.4)$$

On combining Eq. (10.2.4) with Eq. (10.2.1) and, after some arithmetic, we obtain the following:

$$u_2 = \left[\frac{2(p_1 - p_2)}{\rho(1 - A_2^2/A_1^2)} \right]^{1/2} \quad (10.2.5)$$

As sketched in Fig. 10.2.3, in practice the effective cross-sectional area available for flow of the orifice, A_2 , will be somewhat smaller than the actual cross-sectional area of the orifice, A_0 , because of the *formation of a vena contracta*.

In order to relate the flow to the measurable quantity A_0 , let us introduce a correction factor C_D termed the discharge coefficient. Thus Eq. (10.2.5) takes the following form:

$$u_2 = C_D \left[\frac{2(p_1 - p_2)}{\rho(1 - A_0^2/A_1^2)} \right]^{1/2} \quad (10.2.6)$$

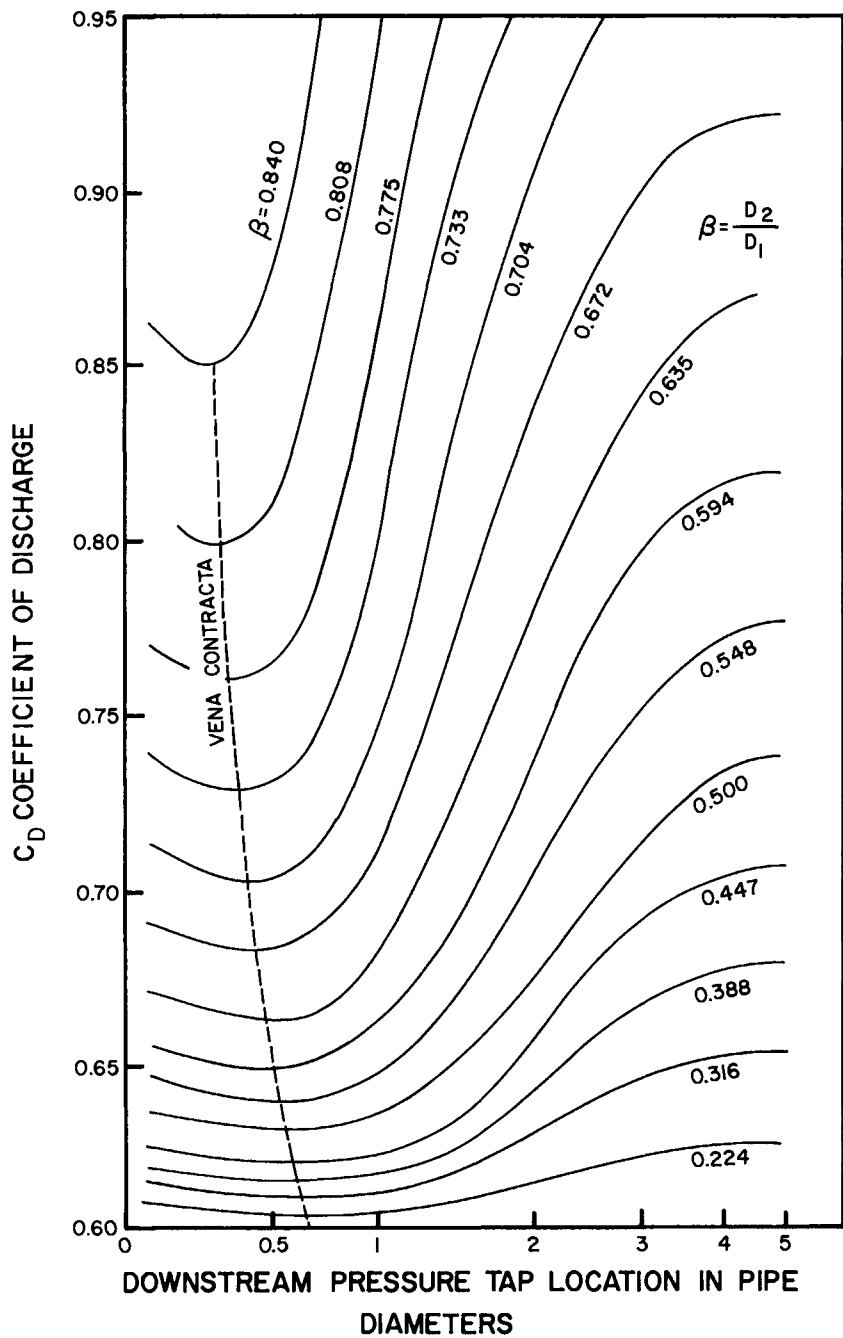


FIG. 10.2.4 Correlation for the discharge coefficient.

The quantity C_D cannot be readily predicted from first principles but numerous empirical correlations are available, an illustration of which is shown in Fig. 10.2.4.

Example 10.2.1 A sharp-edged orifice of diameter 0.03 m is installed in a water line of diameter 0.05 m to measure the water flow rate to an oxygen lance in a basic oxygen furnace. The pressure drop across the orifice is 20 N/m².

Calculate the linear velocity and the mass flow rate. Assume that $C_D \approx 0.8$.

SOLUTION On using Eq. (10.2.6) we have

$$u_2 = 0.8 \left[\frac{(2 \times 20)}{1 - (0.03)^4/(0.05)} \right]^{1/2} \approx 5.42 \text{ m/s}$$

The mass flow rate is

$$w = 5.42 \times 1000 \times \frac{1}{4}(3.14 \times (0.05)^2) = 10.6 \text{ kg/s}$$

Equation (10.2.6) is readily extended to compressible fluids. Here

$$\frac{1}{2}u_2^2 - \frac{1}{2}u_1^2 = \int_2^1 v dp \quad (10.2.7)$$

is the logical starting point.

For an ideal gas under isothermal conditions,

$$\int_2^1 v dp = P_1 v_1 \ln(p_1/p_2) \quad (10.2.8)$$

On recalling that the mass balance takes the following form,

$$u_1 A_1 / v_1 = u_2 A_2 / v_2 = w \quad (10.2.9)$$

we may combine Eqs. (10.2.7)–(10.2.9) to obtain the desired relationship between w and $(p_1 - p_2)$:

$$w = \frac{A_0}{v_2} C_D \left\{ 2P_1 v_1 \ln \frac{p_1}{p_2} \left/ \left[1 - \left(\frac{A_0}{A_1} \frac{\rho_2}{\rho_1} \right)^2 \right] \right\}^{1/2} \quad (10.2.10)$$

The orifice plate is compact in construction, but suffers from the drawback that there is irreversible energy loss inherently associated with it; the venturi meter is an alternative in which rather than placing a sharp constriction in the passage of the fluid the fluid is gradually accelerated by passing it through a converging cone and is then decelerated by passage through a gently diverging cone, as sketched in Fig. 10.2.5. As a result most of the kinetic energy is recovered, no *vena contracta* is formed, and the discharge coefficient is quite close to unity.

Clearly the pressure is at a minimum at the throat of the venturi; if the fluid velocity is high enough the pressure at the throat may fall below the pressure of the environment.

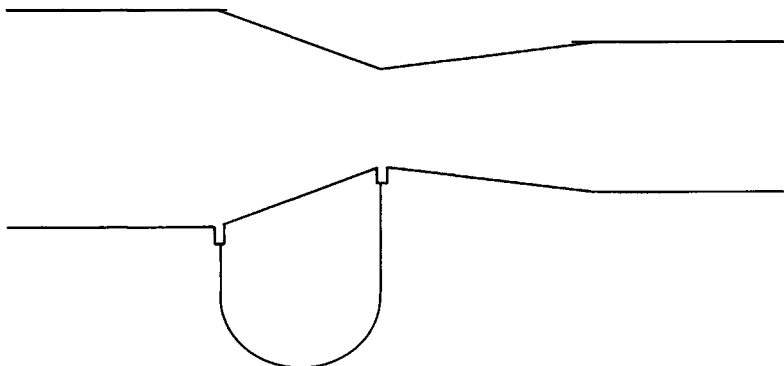


FIG. 10.2.5 Sketch of a venturi meter.

Such an arrangement has been used for mixing two fluids or for injecting water into gas streams. The venturi scrubber, for abating air pollution, in which water is injected into a gas stream at the throat of a venturi, in order to capture small particles, is based on this principle.

10.2.3 The Rotameter

Figure 10.2.6 shows a photograph of a rotameter, which is frequently used both in the laboratory and under industrial conditions for flow measurement.

In essence the rotameter is a vertical tube with a variable cross section which contains a float. When a fluid is passed through the rotameter the drag force acting on the float will cause it to take up a position in the tube, such that the drag force, which depends on the velocity, will balance the effective weight (less the buoyancy) of the float. The frictional force acting on the float may be calculated with the aid of the coefficient of discharge.

The pressure difference over the float is given by

$$-\Delta p = V_{\text{fl}}(\rho_{\text{fl}} - \rho_f)g/A_{\text{fl}} \quad (10.2.11)$$

where ρ_{fl} and ρ_f are the densities of the float and the fluid, respectively, V_{fl} the volume of the float, and A_{fl} is the minimum cross-sectional area of the float in the horizontal plane. If A_1 denotes the area of the tube just downstream of the float, and A_2 is the cross-sectional area of the annular space between the float and the tube walls, then upon applying the orifice plate equation we have the following relationship between the pressure drop across the float and the mass flow rate of the fluid:

$$w = C_D A_2 \{2\rho(\Delta p)/[1 - (A_2/A_1)^2]\}^{1/2} \quad (10.2.12)$$

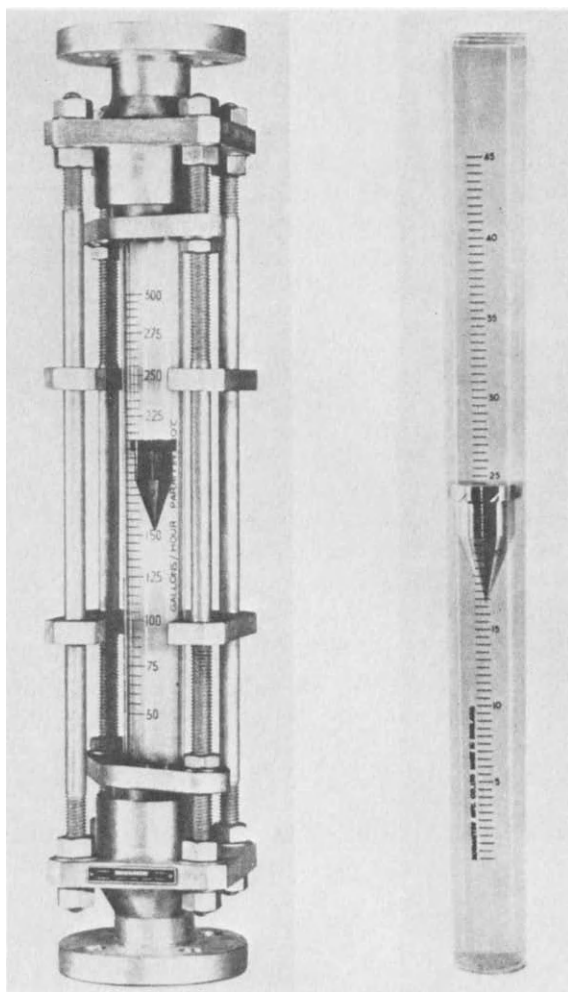


FIG. 10.2.6 Photograph of a rotameter.

using Eq. (10.2.6), the previously developed expression for the orifice plate. However, we may substitute from Eq. (10.2.11) for Δp and thus we have

$$w = C_D A_2 [2gV_{fl}(\rho_{fl} - \rho_f)/A_f(1 - A_2/A_1)^2]^{1/2} \quad (10.2.13)$$

The coefficient of discharge C_D , may vary widely depending on geometry and on the flow conditions. Suppliers of rotameters usually provide calibration curves; alternatively, rotameters have to be calibrated by the user.

10.3 Measurement of Fluid Velocity

In most of the industrial applications the principal objective is to determine the volumetric flow rate of a fluid through a given system.

There are, however, other circumstances when we wish to determine the velocity profile or the value of the fluid velocity at some particular location within the system. Numerous techniques are available for this purpose.

In this section we shall discuss the techniques available for the measurement of the fluid velocity; most of the devices to be described have been developed for the measurement of fluid velocities in air, water, or light organic materials; for this reason a special mention will be made at the end of the section of techniques that may be used in liquid metals or slags.

10.3.1 The Pitot Tube

The reader will recall from the discussion in Chapter 2 that the point in a moving fluid where the velocity is reduced to zero is termed the *stagnation point*. As an illustration, let us consider the symmetrical object, immersed in a moving fluid, as sketched in Fig. 10.3.1. On each side of the central streamline the fluid is deflected around the object; the divergence of the streamlines in the vicinity of the streamline Z-X indicates that the velocity along the central streamline decreases as the object is being approached. Clearly at point X the fluid must be stationary and hence the point X is a stagnation point.

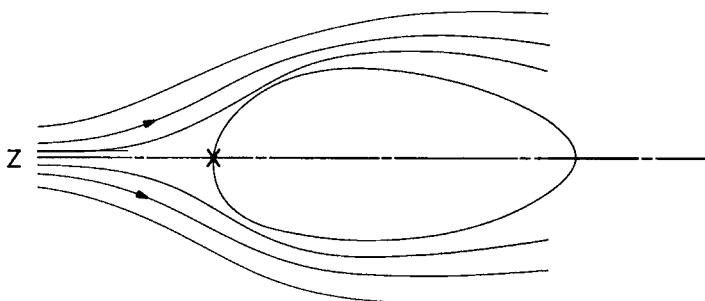


FIG. 10.3.1 Sketch, showing the position of a stagnation point, when a fluid flows past an immersed object. The stagnation point is marked X.

On writing Bernoulli's equation or the energy balance equation, we recall that this expresses the fact that the quantity

$$p + \frac{1}{2}\rho|u|^2 + \rho g Z = \text{const} \quad (10.3.1)$$

along a given streamline.

It follows that, if along a particular streamline the velocity is brought to zero (as was the case in Fig. 10.3.1), the pressure at this point is increased from p to $p + \frac{1}{2}\rho|u|^2$.

For a fluid of constant density the quantity $p + \frac{1}{2}\rho|u|^2$ is called *the stagnation pressure*, while the quantity p is termed the static pressure.

It follows that if a manometer were placed at point X in Fig. 10.3.1 to record the stagnation pressure and the static pressure were also measured at the same location, then from these two readings the velocity may be calculated directly at point X. This is the principle of the Pitot tube.

This technique was first employed by Pitot in 1732 to measure point velocities in the river Seine (France). More sophisticated designs have evolved since that time and Fig. 10.3.2 shows a sketch of a so-called Pitot-Prandtl tube, where the probe itself consists of two concentric pipes; the central pipe is used to measure the stagnation pressure while the holes drilled in the outer pipe are used for determining the static pressure. Provision is made to connect these pipes to the two arms of a manometer so that the difference between the static and the dynamic pressures may be measured directly. The Pitot tube is a very useful, accurate, and quite inexpensive device for the measurement of point velocities and has been frequently used. Its two principal drawbacks are that the Pitot tube interferes with the flow and that it cannot be readily used for measuring low velocities, e.g., below about 0.02–0.05 m/s. Moreover, Pitot tubes are useful only for the measurement of steady or slowly varying velocities because of the inertia necessarily associated with the manometers or other pressure-measuring devices.

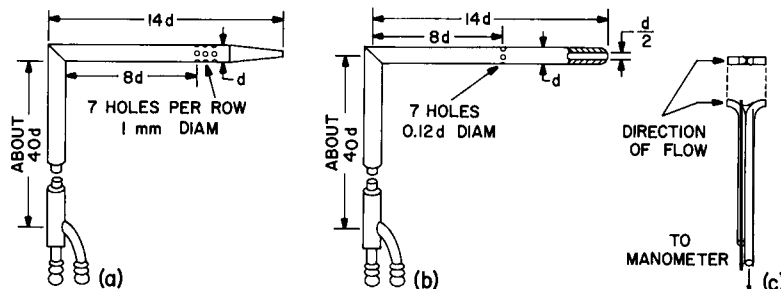


FIG. 10.3.2 A Pitot-Prandtl tube, also showing typical dimensions.

We note that, while Pitot tubes measure the point values of the fluid velocity within a system, the volumetric flow rates through a conduit may be determined by using Pitot tubes, through the establishment of the velocity profile. This technique is used in industrial systems that are too large for quantity meters and also for the testing of orifice plates.

10.3.2 The Hot-Film Anemometer

In essence, the hot-film or hot-wire anemometer (Fig. 10.3.3) consists of a small platinum or tungsten plate (or wire), mounted on a suitable support. This element is heated by passing a constant current through it. Under steady-state conditions, which are attained virtually instantaneously, because of the small size of the element, the rate at which heat is generated by the current must equal the rate at which heat is lost to the surrounding fluid. This rate of heat loss is a function of the difference between the temperature of the probe and that of the fluid and of the local fluid velocity.

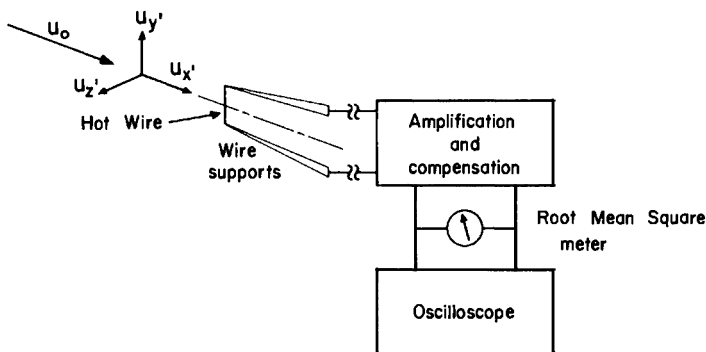


FIG. 10.3.3 Schematic sketch of a hot-wire anemometer assembly.

The following empirical equation has been suggested for relating q , the rate of heat loss, to the local fluid velocity:

$$q = [C_1 + C_2 u_{\text{loc}}^{1/2}] [T_{\text{probe}} - T_{\text{fluid}}] \quad (10.3.2)$$

where C_1 and C_2 are constants.

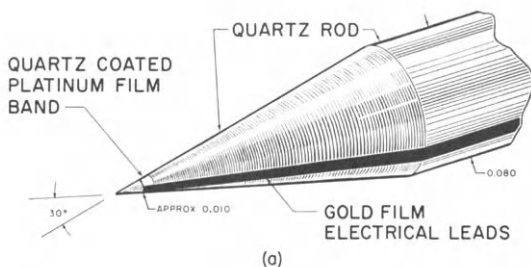
If by employing appropriate electronic circuitry the current passing through the probe is adjusted, such that the temperature of the probe is maintained constant (namely constant temperature anemometer), the corresponding variations in the voltage required to maintain this condition are related to the local velocity in the fluid in contact with the probe.

After calibration the hot-film probe may be used to measure the local velocity components. It is noted, furthermore, that because of the small size of the probe its inertia is also small, so that the probe can be used to determine the fluctuating velocity components, namely u_x' , u_y' , and u_z' . By the appropriate processing of these signals, through the use of anemometry, it is possible to determine the various statistical parameters that are used to characterize turbulent flow: namely turbulence intensity, the frequency spectrum, length scale of turbulence, etc. In fact, the availability of hot-film

anemometry as a sophisticated measuring tool has played a key role in motivating the growth of the statistical theory of turbulence.

Figures 10.3.4a and b show photographs of a hot-film probe and a typical collection of electronic measuring devices used in hot-film anemometry.

The hot-film anemometer is useful for measuring quite low fluid velocities, down to say 0.01 m/s, and may be used (with some modification) in liquid metals, provided the temperature is not unduly high (say below about



(a)



(b)

FIG. 10.3.4 (a) photograph of a conical hot-film probe; (b) photograph of a hot-film probe assembly, also showing the electronic components. Courtesy of Thermal Systems Inc., Minneapolis, Minn.

500°K). Until recent times the hot-film (or hot-wire) anemometer has been the principal measuring device in sophisticated turbulence studies. Its principal drawback is that, in spite of the small size of the probe, it still interferes with the flow field; moreover, its use is problematic in the vicinity of the walls. A full documentation on the use of hot-film anemometers is available.^{3,4}

A newer, potentially very attractive measurement technique is the use of Laser-Doppler anemometry.

10.3.3 Laser Anemometer

A schematic sketch of the principle on which the laser anemometry is based is shown in Fig. 10.3.5. It is seen that a laser beam is separated into two beams of equal length. Then, using an appropriate optical system, these two beams are made to cross at the spatial location where we wish to measure the flow.

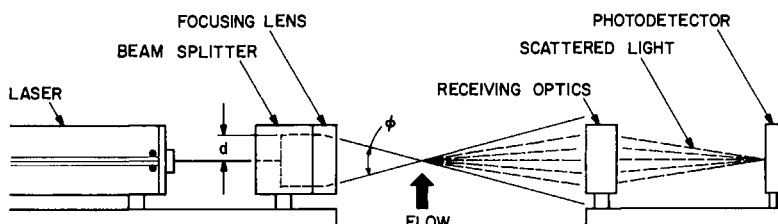


FIG. 10.3.5 Sketch illustrating the principle of a laser anemometry.

When the two beams cross, the wavefronts exhibit interference, thus forming regions of high- and low-intensity light. As the tracer particles (which must be added to the transparent fluid system) pass through these interference fringes, the light scattered from the particle alters these fringes. When this scattered light is picked up by a photodetector, it is converted into an electric signal, the frequency of which is proportional to the rate at which the tracer particle crosses the interference fringes. Thus, by the appropriate processing of this signal, it is possible to obtain both the mean and the fluctuating velocity. Figure 10.3.6 shows a photograph of the key components of a typical laser anemometer assembly, including the laser, the electronic processing system, and a selection of the lenses.

The laser anemometry system is attractive because it allows the measurement of velocities and turbulence characteristics in transparent fluids without any interference with the flow itself. The only necessary provision is that fine particles have to be added to the fluid in order to effect the scattering of the light. This technique cannot be used, however, for measuring the velocity within opaque fluids.

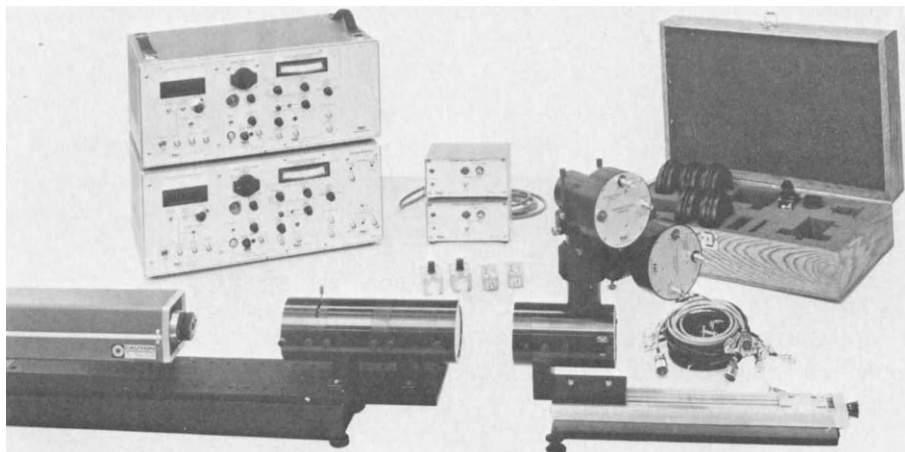


FIG. 10.3.6 Photograph showing a typical laser anemometer assembly. Courtesy of Thermal Systems Inc., Minneapolis, Minn.

A more detailed discussion of laser anemometry is available in Stevenson *et al.*⁵⁻⁷ and in the catalogs of the two major suppliers of this equipment, namely the Thermal Systems Corporation and DISA.

10.3.4 Other Flow Measurement Devices

In Sections 10.3.1–10.3.3 we discussed the principal techniques available for measuring volumetric flow rates and fluid velocities. This listing is far from exclusive. Other techniques frequently employed include the use of tracers in conjunction with time-lapse photography, interferometry, and Schlieren techniques.

The use of tracers is primarily for flow visualization. Thus if nontransparent particles are added to a transparent fluid, on taking photographs with a long exposure (say of the order of 0.1–2 s), the resultant photograph provides the *streaklines* which, as discussed in Chapter 3, become identical to the streamlines for steady-state conditions. Such a streamline pattern⁵ has been shown in Chapter 3.

If quantitative deductions are to be made regarding the velocity, considerable care has to be taken in the use of these techniques, especially if the flow field is multidimensional. A good description of such tracer techniques is available,⁸ particularly regarding the use of fine hydrogen bubbles for determining velocities in water under conditions when the use of hot-film techniques would have been problematic.

Fluid velocities may be deduced also from interferograms and from the use of Schlieren techniques, when fluid flow occurs simultaneously with heat transfer. Both of these techniques^{9,10} rely on the fact that the refractive

index of a transparent fluid depends on its temperature. From the distortion of the isotherms the fluid flow field may be deduced.

10.3.5 Flow Measurements in Liquid Metals

Liquid metals are opaque and have a high density, and most metals are liquid only at high temperatures; these factors render most of the standard flow measurement techniques inapplicable or at least very difficult to apply to liquid metal systems.

Here we may wish to draw a distinction between metals that have a relatively low melting point, say below about 300°C, such as mercury, Woods metal, lead, and the like, and metals which have a much higher melting temperature, say above 900°C, examples of which include copper, aluminum, and steel.

In measuring fluid velocities in mercury one may use Pitot-Prandtl tubes or hot-film anemometers,⁵ very much the same way as one would do in ordinary liquids, except that a special hot-film probe is required.

On going to higher-temperature systems, hot-film anemometry becomes rather more difficult to apply because of materials problems; however, one may still use the principle of the Pitot-Prandtl tube but employing pressure transducers rather than manometer connections. One such arrangement is sketched in Fig. 10.3.7 where it is seen that pressure transducer I measures the stagnation pressure while pressure transducer II measures the static pressure. From the difference of these two readings, and from the known orientation of the probe, the fluid velocity can be calculated. A variation of this technique, employing a spring-loaded pressure probe, has been used by Szekely *et al.*¹³ to measure the velocity fields in an induction-stirred Woods metal melt. (For induction-stirred systems the electric signals of the pressure transducers would have suffered major interference by the electromagnetic force field.)

Velocity measurement becomes rather more difficult at higher temperatures and one's choice of techniques is rather limited with the instruments available at present.

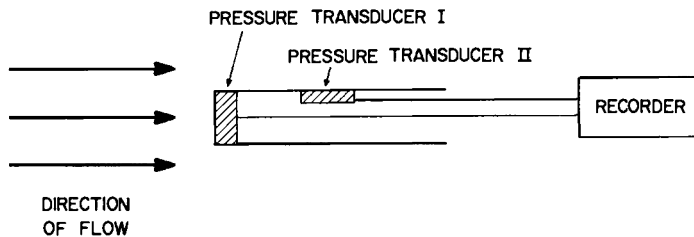


FIG. 10.3.7 A Pitot-Prandtl tube arrangement using pressure transducers.

One possibility is to measure, or rather estimate, the velocity at the surface of melts by taking motion pictures through an appropriately spaced grid. Such a technique has been employed by Evans,¹⁴ by Szekely *et al.*,¹⁵ and by others but the results can be regarded as only semiquantitative.

Yet another technique is the use of radioactive tracers, such as sketched in Fig. 10.3.8, where a radioactive tracer was added to an induction-stirred mold and the time required for the tracer pulse to pass between two detection points was recorded.¹⁶ This procedure does provide an estimate of some average velocity but for nonflat velocity profiles these results too are only semiquantitative.

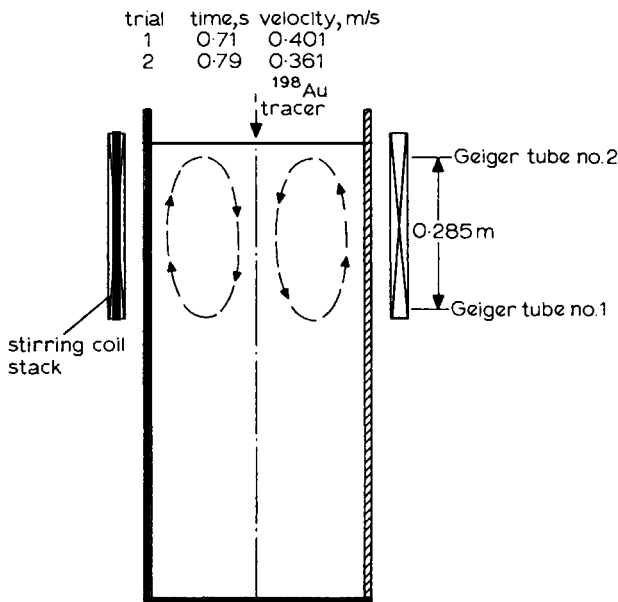


FIG. 10.3.8 Sketch of the arrangement used for estimating melt velocities in an induction-stirred mold, using a radioactive tracer and two Geiger counters.¹⁶

We may summarize our findings regarding velocity measurements in liquid metals by stating the following:

- (1) Velocity measurements are quite straightforward, using Pitot tubes, hot-film anemometers, and the like in liquid mercury.
- (2) Moreover, pressure transducers have been used to measure melt velocities, even at temperatures as high as 1000°C in molten aluminum.
- (3) It is very difficult to measure melt velocities directly in liquid iron or molten steel, and the results available up to the present tend to be only

semiquantitative. The fragmentary data that have become available have been obtained either by measuring the surface velocities using motion photography or by radioactive tracers.

Since our ability to predict melt velocities has improved considerably during the past five years, it is hoped that this in turn will stimulate the development of techniques for the measurement of velocities in ferrous melts.

10.4 The Physical Modeling of Fluid Flow Problems in Metals Processing

The majority of the fluid flow problems encountered in metals processing is too complex for one to rely solely on predictions based on mathematical modeling. For this reason it is desirable to compare theoretical predictions with direct measurements or to devise an overall strategy where experiments and theoretical analyses complement each other. As discussed in the preceding section, the student of metals processing operations is faced with difficulties in his attempts at measuring pressures, velocities, or forces in liquid metal systems, notwithstanding the fact that these are quite routine tasks when dealing with fluids at room temperature. These problems in carrying out direct measurements on liquid metal systems have made the physical modeling of these operations a very important tool in process metallurgy.

The physical modeling of flow systems, which forms the subject matter of this section, has been used extensively over the past decades: wind tunnel tests on airplanes, rockets, ships, and even on skis may be cited as representative examples.

In the order of descending rigor, these physical modeling approaches may be divided into the following categories:

(1) If a physical model is constructed according to certain strict rules, then quantitative measurements made on the model system may be translated directly through appropriate scaling to describe the behavior of the real system.

(2) A less rigorous approach would be to verify the applicability of certain mathematical models through measurements conducted on a physical system which shows some correspondence to a real situation.

(3) Finally, one may just conduct a few ad hoc experiments using a physical model in order to obtain a qualitative idea of the principal regimes that may characterize a system.

All three of these approaches have a definite place in research and development programs.

Thus properly scaled physical models, such as described in Johnstone and Thring,^{17,18} may be used to deduce melt velocities or flue-gas velocities in the prototype (the real industrial unit) while avoiding the need to construct elaborate mathematical models.

In the second category the elegant experiments on the rising velocity of spherical-cap gas bubbles in molten mercury and silver by Richardson and co-workers^{19,20} lead to the establishment of predictive relationships, generally valid for molten metal systems. These relationships were valid for molten steel, the system of particular interest, but where measurements would have been very difficult to conduct.

Finally, in the last category, tracer studies and photographs taken of water models of various metals processing operations did provide useful qualitative information on the behavior of the system.

In this section we shall confine our attention to some of the principles that govern physical modeling and the main tools used in this technique.

10.4.1 Dimensional Analysis

It is a self-explanatory restriction on equations representing a relationship between physical quantities that the dimensional homogeneity be observed. Or, in other words, the dimension of each term in the equation must be the same.

As an example we may consider the equation of motion for a laminar boundary layer, namely

$$\frac{\partial u_x}{\partial t} + u_x \frac{\partial u_x}{\partial x} + u_y \frac{\partial u_x}{\partial y} = -\frac{1}{\rho} \frac{\partial p}{\partial x} + \frac{\mu}{\rho} \left[\frac{\partial^2 u_x}{\partial x^2} + \frac{\partial^2 u_x}{\partial y^2} \right] + g_x \quad (10.4.1)$$

It is readily seen that all the terms have the dimension L/t^2 ; indeed, the quickest technique of checking whether an equation is correct is to ascertain that all the terms have the same dimension.[†] The requirement of dimensional homogeneity imposes constraints on the variables involved in representing a physical problem and provides useful ideas regarding the form that may be taken by a relationship between these variables.[‡]

A full discussion of this technique, termed dimensional analysis, is available.^{20,21} Here we shall confine our attention to the statement of Buckingham's π theorem, which expresses the following:

- (1) The solution of any dimensionally homogeneous equation representing physical quantities can be expressed in terms of a certain number of

[†] Clearly this is a necessary but not a sufficient condition.

[‡] There are certain empirical equations which are not dimensionally homogeneous; however, the constants appearing in these expressions have dimensions so as to satisfy the criterion of dimensional homogeneity.

dimensionless groups π , say

$$(\pi_1, \pi_2, \pi_3, \dots) = 0 \quad (10.4.2)$$

(2) If these quantities are independent then the number of dimensionless groups needed to define the problem equals the number of individual variables minus the number of fundamental magnitudes (mass, length, time, etc.) needed to express these variables.

Let us illustrate the use of the theorem using the following simple example:

Example 10.4.1 Let us consider that the force exerted on a body immersed in a flowing fluid F depends on the velocity u , density ρ , and viscosity μ of the fluid and on the characteristic dimension of the body L . Using Buckingham's theorem, define the number of dimensionless groups required for representing the problem. The number of variables is 5 and the number of basic dimensions is mass, length, and time, or mass, length, and velocity.

Thus we need $5 - 3 = 2$ dimensionless groups to represent the problem.

SOLUTION It may be shown that these two dimensionless groups are

$$uL\rho/\mu = \text{Reynolds number}$$

and

$$F/\rho u^2 L^2 = \text{Euler number}$$

On noting that F/L^2 is a force per unit area, say τ_w , $\tau_w/\rho u^2$ may also be regarded as the friction factor. Thus the solution to our problem is

$$F\left(\frac{uL\rho}{\mu}, \frac{F}{\rho u^2 L^2}\right) = 0 \quad (10.4.3)$$

We note that if we were to introduce another variable, say e/L , the relative roughness of the surface, then the fundamental dimensions remain unchanged, while the number of variables is increased to six. Under these conditions we need three dimensionless groups to represent the problem, namely

$$F\left(\frac{uL\rho}{\mu}, \frac{F}{\rho u^2 L^2}, \frac{e}{L}\right) = 0 \quad (10.4.4)$$

The form of Eq. (10.4.4) is, of course, consistent with the friction factor correlations that were presented in Chapter 2.

The preceding example illustrates both the strength and the weakness of the dimensional analysis approach. It was a very straightforward matter to organize the variables into (familiar) dimensionless groups; at the same time

the technique does not provide guidance as to the form of the relationship to be sought between these variables; furthermore, dimensional analysis cannot tell us whether a key parameter or key parameters have been omitted from consideration.

It should be stressed to the reader that, for most of the practical problems one is likely to encounter in metals processing operations, the appropriate dimensionless groups will have been established. A discussion of the principal dimensionless groups in fluid mechanics will be presented subsequently.

10.4.2 *The Concept of Similarity*

When we wish to develop a physical model of a real operating system, usually called the *prototype*, in order for the results to be obtained from the model experiments to be meaningful, the model and the prototype must be physically *similar*.

There exist many states of similarity; however, here we shall confine our attention to the following:

geometric similarity	dynamic similarity
kinematic similarity	thermal similarity

(i) *Geometric Similarity.* Geometric similarity is the similarity of shape. Systems are geometrically similar when the ratio of any length in one system to the corresponding length in the other system is everywhere the same. This ratio is usually termed the scale factor. While geometric similarity is one of the most obvious requirements in modeling, often it may not be possible to attain perfect geometric similarity. Under such conditions certain critical dimensions of the model are scaled to the prototype while other dimensions are not. This procedure is called the use of a distorted model. Examples where distorted models have to be used include studies where the surface roughness may not be appropriately represented or when the proper scaling of rivers, lakes, or processing equipment would result in too shallow a liquid level.

A special case of a distorted model is the use of a section model; e.g., in representing a kiln or a converter, the diameter and liquid (or solid) depth in the model may be appropriately scaled, but the model would have only a fraction of the (scaled) length of the prototype.

Figure 10.4.1 shows various types of geometric models representing the behavior of a liquid in a horizontal, cylindrical reactor.

(ii) *Kinematic Similarity.* Kinematic similarity represents the similarity of motion. In essence kinematic similarity is observed between two systems, if in addition to being geometrically similar the velocities at corresponding locations in the two systems are in the same fixed ratio.

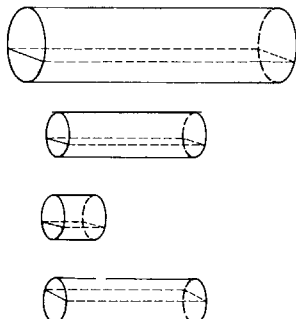


FIG. 10.4.1 Sketch of geometric similarity.

(iii) *Dynamic Similarity.* Dynamic similarity represents the similarity of forces. Dynamic similarity is observed between two systems when the magnitude of forces at corresponding locations in each system are in a fixed ratio.

In the modeling of fluid flow problems it is essential that both geometric and dynamic similarity be observed if quantitative deductions are to be made of the results.

The principal forces to be considered in obtaining dynamic similarity are listed in the following:

inertia forces	surface tension
pressure forces	elastic forces
viscous forces	electromagnetic forces
gravity	

Upon forming the ratios of some of these forces there result certain key dimensionless groups or dimensionless numbers. By ensuring that the numerical value of these dimensionless numbers is the same in the model and in the prototype, one can ascertain that dynamic similarity is observed.

Let us now proceed by defining these forces in terms of the principal variables.

The *inertial force* acting on a fluid element is the mass of the element, multiplied by its acceleration. Thus, on designating the characteristic length as L , the characteristic velocity as U , and the density as ρ , we may write

$$\text{inertial force} \underset{\text{mass}}{\propto} (\rho L^3) \times \underset{\text{acceleration}}{U^2/L} = \propto (\rho L^2 U^2)$$

The *viscous force* acting on the fluid may be characterized as (shear stress) \times (area), i.e., $(\mu du_x/dy)L^2$. On noting that $u_x \propto U$, $y \propto L$, we have viscous force $\propto (\mu UL)$.

By similar arguments we have that

$$\begin{aligned} \text{gravity force} &\propto \rho L^3 g \\ \text{surface tension force} &\propto \sigma L \\ \text{electromagnetic (Ponderomotive) force} &\propto \tilde{\sigma} U B^2 \end{aligned}$$

(Here $\tilde{\sigma}$ is the electric conductivity and B is the characteristic magnetic flux density.) From the combination of the ratios of these (and other) forces there results the following key dimensionless groups, listed in Table 10.4.1.

It is noted that the dimensionless groups listed in Table 10.4.1 could also be obtained from the differential equations describing these various processes. Upon making these differential equations dimensionless, through the introduction of the characteristic variables, these dimensionless groups would be readily formed.

Because of the many forces that may occur in a given metals processing operation, there are no hard and fast rules as to which of the criteria have to be satisfied. Some useful metallurgical examples are discussed in the text by Szekely and Themelis²¹ and in certain Symposium Proceedings.^{22,23} However, the following general comments should be appropriate:

- (1) In modeling a system consisting of just one continuous phase, e.g., a gas jet in a gas that results from forced flow, geometric similarity must be observed and the nozzle Reynolds numbers must be the same.
- (2) In modeling a system consisting of one continuous phase, results from gravity driven flow, e.g., a teemed stream, using a submerged nozzle in continuous casting, then in addition to geometric similarity, the Froude numbers must be the same.
- (3) In thermal natural convection-driven flows geometric similarity should be observed, in addition the (Grashof) (Prandtl) products, and the Froude numbers should be the same.
- (4) While in principle it should be possible to model dispersed systems, such as atomization processes, the breakup of gas jets in liquids (melts) through the simultaneous adjustment of the Froude and the Weber numbers, there are many practical difficulties, posed by the very high surface tension of liquid metals.

The application of these ideas are illustrated in the following simple examples:

Example 10.4.2 Molten steel is teemed into a billet caster 0.15×0.15 m square through a 0.05-m diam submerged nozzle at a mean linear velocity of 0.5 m/s.

If we wish to construct a water model for this process twice the size of the prototype, define the conditions in the model.

TABLE 10.4.1
Dimensionless Groups Useful in Process Metallurgy

Group	Formula	Nomenclature	Quantities represented	Application
Bond number, N_{Bo}	$\frac{u(\rho - \rho_f)d_p}{\sigma}$	d_p : drop diameter ρ : drop density ρ_f : density of surrounding fluid σ : surface tension	gravitational force surface tension force	Spraying
Drag coefficient, C_d	$\frac{u(\rho - \rho_f)L}{\rho u^2}$	L : characteristic length dimension of object ρ : density of object u : relative velocity	gravitational force inertial force	Free settling
$\frac{\mu}{L}$	$\frac{nL(\Delta P_f/\rho)}{2u^2}$	L : characteristic length dimension of conduit cross section $\Delta P_f/\rho$: friction head l : length of pipe	shear stress velocity head	Friction drop in conduits
Froude number, N_{Fr}	u^2/gL	L : characteristic length dimension of system	inertial force gravitational force	Wave and surface behavior pouring streams
Froude number, modified, N_F	$\frac{\rho_g u^2}{(\rho_g - \rho_f)gL}$	ρ_g : gas density ρ_f : liquid density	inertial force gravitational force	Fluid behavior of gas-liquid systems
Galileo number, N_{Ga}	$\frac{gP^2 L^3}{\mu^2}$	μ : viscosity	(inertial × gravitational)/(viscous force) ²	Flow in baths of viscous liquids

Mach number, N_M	$\frac{u}{u_s}$	u fluid velocity u_s velocity of sound in fluid		High-speed flow
Morton number, N_Mo	$\frac{g\mu_L^4}{\rho_L(\sigma)^3}$	μ_L liquid viscosity	$\frac{(\text{gravitational}) \times (\text{viscous}) \text{ forces}}{\text{surface tension force}}$	Velocity of bubbles in liquids
Power number, N_P	$\frac{P}{\rho n^3 L^5}$	P power input to agitator L characteristic dimension of agitator paddle n angular speed of rotation	$\frac{\text{drag force on paddle}}{\text{inertial force}}$	Power consumption in agitated vessels
Reynolds number, N_Re	$\frac{Lu\rho}{\mu}$	L characteristic length dimension of system ρ fluid density μ fluid viscosity	$\frac{\text{inertial force}}{\text{viscous force}}$	Fluid flow
Weber number, N_We	$\frac{\rho Lu^2}{\sigma}$	σ surface tension	$\frac{\text{inertial force}}{\text{surface tension force}}$	Bubble formation, atomization of liquid jet
Grashof number, N_{Gr}	$\frac{gp^2 L^3 \beta \Delta T}{\mu^2}$	L characteristic length dimension ρ density of fluid β coefficient of thermal volume expansion, - $(1/\rho)(\partial\rho/\partial T)_p$ ΔT temperature difference	$(N_{Re}) \left(\frac{\text{buoyancy force}}{\text{viscous force}} \right)$ $= (N_{Gr}) \beta \Delta T$	Free convection
Peclet Number, N_{Pe}	$\frac{Lu\rho C_p}{k} = \frac{Lu}{x}$	u fluid velocity C_p specific heat x thermal diffusivity	$\frac{\text{heat transfer by bulk motion}}{\text{conductive heat transfer}}$ $= N_{Re} N_{Pr}$	Forced convection
Prandtl number, N_{Pr}		C_p specific heat of fluid μ viscosity k thermal conductivity	$\frac{\text{momentum diffusivity}}{\text{thermal diffusivity}}$	Forced and free convection

TABLE 10.4.1 (Continued)

Group	Formula	Nomenclature	Quantities represented	Application
Rayleigh number, R^1	$\frac{\rho^2 L^3 C_f \beta \Delta T}{k}$	β : coefficient of thermal volume expansion ΔT : temperature difference across film L : characteristic length dimension	heat transfer by convection heat transfer by conduction	Free convection
Hartmann Number, N_{H^2}	$LB(\sigma_e \mu)^{1/2}$	L : characteristic length B : characteristic magnetic flux density σ_e : electric conductivity	(electromagnetic force) viscous force	
Grashof number, N_{Gr} (mass transfer)	$\frac{g \rho^2 L^3 \beta' \Delta X}{\mu^2}$	β' : coefficient of density change with concentration, $= (\partial \rho / \partial X)_T$ ΔX : concentration of driving force	$(N_{Re})^1 / \left(\frac{\text{buoyancy force}}{\text{viscous force}} \right)$ $= N_{Gr} \beta' \Delta T$	Free convection
Lewis number, N_{Le}	$\frac{\rho C_p D_{A-B}}{k}$	ρ : density of fluid C_p : specific D_{A-B} : molecular diffusivity k : thermal conductivity	molecular diffusivity thermal diffusivity	Combined mass and heat transfer
Peclet number (for mass transfer) N_{Pe}	$Lu D_{A-B}$	L : characteristic length D_{A-B} : characteristic diffusion coefficient	bulk mass transport mass transfer by diffusion	Mass transfer in reactors

SOLUTION Since the flow is gravity driven the only criteria to be considered are that:

- (i) the model and the prototype be geometrically similar,
- (ii) the Froude number must be the same for the model and the prototype, and
- (iii) conditions must be such that the flow is turbulent in the nozzle for both the model and the prototype.

Condition (i). Geometric similarity is readily observed. We note here that there are many occasions when the model is larger than the prototype, especially when the prototype itself is not very big and when one wishes to make precise measurements.

Condition (ii) may be written as

$$u_m^2/gL_m = u_p^2/gL_p$$

thus,

$$u_m/u_p = (L_m/L_p)^{1/2}$$

Thus the linear velocity exiting the nozzle in the model has to be $u_m = \sqrt{2} \times u_p \sim 0.71$ m/s.

Condition (iii). In the prototype

$$N_{Re} = \frac{0.5 \times 7.1 \times 10^3 \times 5 \times 10^{-2}}{5 \times 10^{-3}} \simeq 3.55 \times 10^4$$

i.e., turbulent. In the model

$$N_{Re} = \frac{0.71 \times 10^3 \times 0.1}{10^{-3}} \simeq 7.1 \times 10^4$$

i.e., turbulent.

References

1. H. S. Bean, ed., "Fluid Meters." Am. Soc. Mech. Eng., New York, 1971.
2. J. M. Coulson and J. F. Richardson, "Chemical Engineering," 2nd ed., Vol. 1, p. 19. Pergamon, Oxford.
3. S. G. Bankoff and R. S. Rosler, *Rev. Sci Instrum.*, **33**, 1209 (1967).
4. S. C. Ling, *J. Basic Eng. ASME*, Series D, **82**, 629 (1960).
5. E. B. Denison, W. H. Stevenson, and R. W. Fox, *AICHE J.* **17**, 781 (1971).
6. W. K. George and J. L. Lumley, *J. Fluid Mech.* **60**, 321 (1973) (excellent review).
7. H. D. Thompson and W. H. Stevenson, *Eng. Ext. Ser. (Purdue Univ)* **144** (1974).
8. Symposium on Flow Visualization, American Society of Mechanical Engineers, 1960, New York, N.Y.
9. R. W. Ladenburg, ed. "Physical Measurements in Gas Dynamics and in Combustion." Princeton University Press, New York, 1964.

10. J. Szekely and A. S. Jassal, *Metall. Trans.* **9B**, 389 (1978).
11. S. G. Bankoff and R. S. Rosler, *Rev. Sci. Instrum.*, **33**, 1209 (1967).
12. S. C. Ling, *J. Basic Eng. ASME*, Ser. D, **82**, 629 (1960).
13. J. Szekely, C. W. Chang, and R. E. Ryan, *Metall. Trans.* **8B**, 333 (1977).
14. E. D. Tarapore and J. W. Evans, *Metall. Trans.* **8B**, 343 (1976); *Ibid.* p. 179 (1977).
15. J. Szekely, C. W. Chang, and W. E. Johnson, *Metall. Trans.* **8B**, 514 (1977).
16. J. Szekely and C. W. Chang, *Ironmaking Steelmaking* **4** 190 and 196 (1977).
17. R. E. Johnstone and M. W. Thring, "Pilot Plants, Models and Scale-up Methods in Chemical Engineering," McGraw-Hill, New York, 1957.
18. M. W. Thring, "The Science of Flames and Furnaces," Wiley, New York, 1962.
19. W. G. Davenport, A. V. Bradshaw, and F. D. Richardson, *J. Iron Steel Inst.* **25**, 1034 (1967).
20. R. I. L. Guthrie and A. V. Bradshaw, *Trans. Metall. Soc. AIME* **245**, 2285 (1969).
21. J. Szekely and N. J. Themelis, "Rate Phenomena in Process Metallurgy," Wiley, New York, 1971.
22. J. W. Hlinka, in "Mathematical Modelling in the Iron and Steel Industries," Amsterdam, 1973.
23. Pilot Plants in the Iron and Steel Industry, *Iron Steel Inst. London, Spec. Rep.* **96** (1966).

The physical quantities that were used to represent fluid flow phenomena in the text may be classified as scalars, vectors, and tensors. Examples of scalar quantities are mass, pressure, and density. Examples of vectors include velocity, force, and acceleration, while the stress tensor is an example of a tensorial quantity. In this Appendix we shall present a very brief review of some of the vector and tensor operations that have been used in the text.

A1.1 Definition of a Vector and Vector Operations

A vector is defined as a quantity which is characterized by its magnitude and its direction. In the text the vectors were designated by boldface symbols, such as \mathbf{u} , \mathbf{F} , \mathbf{g} , \mathbf{B} .

Two vectors are equal when they have the same magnitude and when they point in the same direction.

Like the addition of scalar quantities, the addition of vectors is commutative, i.e.,

$$(\mathbf{u}_1 + \mathbf{u}_2) = (\mathbf{u}_2 + \mathbf{u}_1) \quad (\text{A1.1.1})$$

We may subtract one vector from another by reversing the sign and then performing the addition, viz

$$(\mathbf{u}_1 - \mathbf{u}_2) = \mathbf{u}_1 + (-\mathbf{u}_2) \quad (\text{A1.1.2})$$

When a *vector is multiplied by a scalar*, the result is a vector, the magnitude of which is altered, but which retains its original direction, viz

$$\mathbf{F} = m\mathbf{a} \quad (\text{A1.1.3})$$

where the force \mathbf{F} acts in the same direction as the acceleration \mathbf{a} .

The scalar product of two vectors is a scalar quantity, which is defined as

$$\mathbf{u}_1 \cdot \mathbf{u}_2 = \mathbf{u}_1 \mathbf{u}_2 \cos \phi_{u_1 u_2} \quad (\text{A1.1.4})$$

where $\phi_{u_1 u_2}$ is the angle formed between the two vectors.

Note that the scalar product of a vector with itself is the square of the absolute magnitude of the vector, viz

$$\mathbf{u}_1 \cdot \mathbf{u}_2 = u^2 \quad (\text{A1.1.5})$$

The scalar multiplication of a vector is commutative, viz

$$(\mathbf{u}_1 \cdot \mathbf{u}_2) = \mathbf{u}_2 \cdot \mathbf{u}_1 \quad (\text{A1.1.5'})$$

The vector or cross product of two vectors is defined as

$$\mathbf{u}_1 \times \mathbf{u}_2 = (u_1 u_2 \sin \phi_{u_1 u_2}) \mathbf{n}_{u_1 u_2} \quad (\text{A1.1.6})$$

Here \mathbf{n} is a unit vector normal to the plane containing \mathbf{u}_1 and \mathbf{u}_2 and pointing in the direction that a right handed screw would move if turned from \mathbf{u}_1 toward \mathbf{u}_2 by the shortest route.

It follows from the foregoing that

$$\mathbf{u}_1 \times \mathbf{u}_1 = 0 \quad \text{and} \quad (\mathbf{u}_1 \times \mathbf{u}_2) = -(\mathbf{u}_2 \times \mathbf{u}_1) \quad (\text{A1.1.6'})$$

Thus vectorial multiplication is not commutative.

A vector may be completely defined by giving the magnitudes of its projections on the coordinate axes, viz u_1 , u_2 , and u_3 or u_x , u_y , and u_z . It follows that a vector may be represented analytically by

$$\mathbf{u} = \mathbf{i}u_x + \mathbf{j}u_y + \mathbf{k}u_z$$

where \mathbf{i} , \mathbf{j} , and \mathbf{k} are the unit vectors in the x , y , and z directions.

A1.2 Differential Operations Involving Vectors

The differential vector operator ∇ usually termed “del” or “nabla” is defined in cartesian (rectangular) coordinates as follows:

$$\nabla = \mathbf{i} \frac{\partial}{\partial x} + \mathbf{j} \frac{\partial}{\partial y} + \mathbf{k} \frac{\partial}{\partial z} \quad (\text{A1.2.1})$$

In the following we shall summarize the results for the cases in which ∇ is made to operate on scalars and on vectors.

When ∇ is made to operate on a scalar field, the result is a vector which is called the gradient of the scalar field, i.e.,

$$\nabla P = \mathbf{i} \frac{\partial P}{\partial x} + \mathbf{j} \frac{\partial P}{\partial y} + \mathbf{k} \frac{\partial P}{\partial z} = \text{grad } P \quad (\text{A1.2.2})$$

Note that

$$\nabla P \neq P \nabla \quad (\text{A1.2.3})$$

Thus the operation is not commutative.

The divergence of a vector field is formed when a scalar product is formed between the ∇ operator and a vector. Thus

$$\nabla \cdot \mathbf{u} = \frac{\partial u_x}{\partial x} + \frac{\partial u_y}{\partial y} + \frac{\partial u_z}{\partial z} \quad (\text{A1.2.4})$$

for a compressible fluid; the equation of continuity is simply

$$-\nabla \cdot \rho \mathbf{U} = \frac{\partial \rho}{\partial t} \quad (\text{A1.2.5})$$

Note that the divergence operator is not commutative; thus

$$\nabla \cdot \mathbf{u} \neq \mathbf{u} \cdot \nabla \quad (\text{A1.2.6})$$

The curl of a vector field is obtained when cross or vectorial multiplication is performed between the ∇ operator and a vector. Thus

$$\text{curl } \mathbf{u} \quad \text{or} \quad \text{rot } \mathbf{u} = \nabla \times \mathbf{u} = \begin{vmatrix} \mathbf{i} & \mathbf{j} & \mathbf{k} \\ \frac{\partial}{\partial x} & \frac{\partial}{\partial y} & \frac{\partial}{\partial z} \\ u_x & u_y & u_z \end{vmatrix} \quad (\text{A1.2.7})$$

which is equivalent to

$$\nabla \times \mathbf{u} = \mathbf{i} \left(\frac{\partial u_z}{\partial y} - \frac{\partial u_y}{\partial z} \right) + \mathbf{j} \left(\frac{\partial u_x}{\partial z} - \frac{\partial u_z}{\partial x} \right) + \mathbf{k} \left(\frac{\partial u_y}{\partial x} - \frac{\partial u_x}{\partial y} \right) \quad (\text{A1.2.8})$$

The concept of curl or rot has been used in Chapter 3 in connection with the definition of irrotational flow and vorticity.

The Laplacian of a scalar field is a scalar quantity, viz

$$\nabla \cdot \nabla(\phi) \equiv \nabla^2 \phi \equiv \frac{\partial^2}{\partial x^2}(\phi) + \frac{\partial^2}{\partial y^2}(\phi) + \frac{\partial^2}{\partial z^2}(\phi) \quad (\text{A1.2.9})$$

The Laplacian of a vector field is formed as follows:

$$\nabla^2 \mathbf{u} = \nabla(\nabla \cdot \mathbf{u}) - [\nabla \times [\nabla \times \mathbf{u}]] \quad (\text{A1.2.10})$$

Equation (A1.2.10) has been used in the manipulation of Ergun's equation for multidimensional flows.

A1.3 Definition of Second-Order Tensors

A vector \mathbf{u} may be defined by specifying its three components u_x , u_y , and u_z .

A second-order tensor may be defined by specifying its nine components, viz

$$\boldsymbol{\tau} = \begin{pmatrix} \tau_{11} & \tau_{12} & \tau_{13} \\ \tau_{21} & \tau_{22} & \tau_{23} \\ \tau_{31} & \tau_{32} & \tau_{33} \end{pmatrix} \quad (\text{A1.3.1})$$

The quantities τ_{11} , τ_{22} , τ_{33} are called the diagonal elements, while the remainder of the terms are called the off-diagonal elements. When

$$\tau_{12} = \tau_{21}, \tau_{13} = \tau_{31}, \tau_{23} = \tau_{32}$$

then the tensor is said to be symmetric.

The *dyadic* product of two vectors is a special form of a tensor, viz

$$\mathbf{uv} = \begin{pmatrix} u_1 v_1 & u_1 v_2 & u_1 v_3 \\ u_2 v_1 & u_2 v_2 & u_2 v_3 \\ u_3 v_1 & u_3 v_2 & u_3 v_3 \end{pmatrix} \quad (\text{A1.3.2})$$

A dyadic vector product is formed when the $\rho \mathbf{u}\mathbf{u}$ term in the Navier–Stokes equations.

The unit tensor δ is defined as

$$\delta = \begin{pmatrix} 1 & 0 & 0 \\ 0 & 1 & 0 \\ 0 & 0 & 1 \end{pmatrix} \quad (\text{A1.3.3})$$

where all the diagonal elements are unity and all the off-diagonal elements are zero.

The ∇ operator may operate on a tensor as follows:

$$\nabla \cdot \boldsymbol{\tau} = \sum_k \delta_k \left[\sum_i \frac{\partial}{\partial x_i} \tau_{ik} \right] \quad (\text{A1.3.4})$$

which on changing the notation so that $x_1 = x$, $x_2 = y$, and $x_3 = z$ is equivalent to

$$\nabla \cdot \boldsymbol{\tau} = \begin{pmatrix} \tau_{xx} \tau_{xy} \tau_{xz} \\ \tau_{yx} \tau_{yy} \tau_{yz} \\ \tau_{zx} \tau_{zy} \tau_{zz} \end{pmatrix}$$

Appendix 2

Lennard-Jones Parameters for Selected Gases

Substance	Molecular weight <i>M</i>	Lennard-Jones parameters	
		σ (Å)	ε/k (°K)
H ₂	2.016	2.915	38
He	4.003	2.576	10.2
Ne	20.183	2.789	35.7
Ar	39.944	3.418	124
		3.498	225
		4.055	229
Air	28.97	3.617	97
N ₂	28.02	3.681	91.5
O ₂	32.00	3.433	113
CO	28.01	3.590	110
CO ₂	44.01	3.996	190
NO	30.01	3.470	119
		3.879	220
SO ₂	64.07	4.290	252
		3.653	112
Cl ₂	70.91	4.115	357
		4.268	520
		4.982	550

Postface

The purpose of this volume was to introduce the reader to the complex but exciting and growing field of fluid flow phenomena in metals processing. We sought to provide information on the fundamental principles that govern fluid flow phenomena, with emphasis on applications in metals processing (in Chapters 1, 3, 4, and 5), and then to illustrate the use of the concepts for tackling a broad range of practical problems in the remaining chapters.

While in recent years there has been enough accumulated experience with fluid flow applications in metals processing to make the compilation of this text feasible, there is little question that this whole area is a very fruitful field for research, and one in which major advances are quite likely within the next few years.

While the basic laws of fluid mechanics and of MHD are not likely to be changed in the near future, one can envision appreciable advances in the application of these ideas to practical problems.

Particular areas that are ripe for further development include the application of non-Newtonian fluid mechanics to problems in the casting of two phase mixtures (slurry casting), the more widespread application of turbulence models, in particular to two phase mixtures, and a more extensive use of MHD concepts in metals processing operations. It is hoped that this volume will contribute to stimulating these developments.

Index

A

Acceleration
effect on vertical drainage, 97
particle motion, 260, 261
Adiabatic flow, 49
Air entrainment in steel stream, example, 107, 108
Air jet, 377–380
submerged, 384, 385
Air velocity vs. friction factor, 295
Air–water interface, turbulent flow, 127
Alloy system, induction-stirred, low melting, 197, 199, 200
Aluminum
melt, induction-stirred, velocity, 198, 201
molten, surface tension, 237
thermal conductivity, 207
Anemometer, 130, *see also* specific type
Argon-stirred ladle, water model, 167–170
streamlines, 170
ASEA-SKF furnace, 191–197
body force component, 195
melt velocity, 194–197
operating parameters, 194, 195
property values, 199
tracer dispersion, 198
traveling wave, 194
turbulent kinetic energy, 197
velocity field, 196
Atomization, droplet formation, 338–342

B

Bearings, lubrication in, 114–116
Bed, *see* specific types
Bernoulli equation, 33, 35, 89, 400, *see also* Integral mechanical energy balance
Bessel function, 112
Binary diffusion coefficient
definition of, 208–210
for gases, 209, 210
for melt, 209, 210
Blast furnace
flooding, example, 279
flow resistance, 271, 272
Body force, 8, 68, 70, 73, 179, 184, *see also* Lorentz force
natural convection 204, 205
Bond number, 414
Boundary conditions, 91, 92, *see also* specific type
continuity of velocity, 91
electromagnetic, 180
no-slip, 91
shear stress, 91
Boussinesq's concept of eddy viscosity, 147
Boundary layer
displacement thickness, 106, 107
engineering problems, 101
jet system, 354
laminar, 100–108
leading edge, 106
stream function, 103, 104
thermal
laminar natural convection, 213–219
thickness, 218, 219
example, 219, 220
thickness, 102, 105
turbulent, 153, 154, 164–167
example, 167
laminar sublayer, 164
natural convection, 227
velocity profile, 228
velocity, 102, 103, 105
Brotz equation, film thickness, 162–164
Bubble, *see also* Gas bubble
detachment diameter, 308
dispersed systems, 331–337
dynamics, 90
effect of particle size on, 288
expansion, 325
in fluidized bed, 287–289
formation, 306–318
in aqueous and organic systems, 310–314
at nozzles, 309–318
example, 318
submerged in molten metals, 314–318

- Bubble (cont'd.)**
 at orifice, 309–318
 frequency, 312
 gas holdup, 334, 335
 example, 337
 mean size, 335–337
 motion in liquids, 318–331
 nucleation, 306
 example, 309
 heterogeneous, 306–309
 radius
 of curvature, 92
 drag coefficient, 305, 306
 estimation, 307
 rising
 growth of, 325, 326
 trajectory, 327–331
 size, nitrogen–melt systems, 336
 spherical-cap, 323–325
 velocity, 287
 superficial, 331, 332
 volume, 287
 very small, 320, 323
- Buckingham's π theorem**, 409, 410
- Buoyancy forces**, 307, 308, 312, 313, 318
- C**
- Capacitance number**, 317, 318
- Capillary number**, film flow, 99
- Casting**
 eddy diffusivity, 367
 machine, continuous, 1, 2
 schematic diagram, 364
 streamline pattern, 367
 velocity profile, 366
- Cauchy–Riemann equation**, 83, 84, 87
- Cavity**
 flow in, 224–226
 natural convection, 226
- Chapman–Enskog theory**, 20
- Charge unit**, 179
- Choking phenomena**, 290–294
- Choking velocity**, 294
- Coating of materials**, 97–100
- Collision diameter**, 20
- Combustion**, streamline patterns, 362, 363
- Composition**, effect on viscosity, 16, 18–20
- Compressible fluid**, 44–58
 example, 48, 49, 56
- flow in pipes**, 46–48
 mean density, 48
 overall energy balance, 47, 48
 thermodynamics, 45, 46
- Conduction current density**, 179
- Contact angle**, surface tension, 233, 234
- Continuity**, equation of, 64–67, 91, *see also*
 Differential mass balance
- boundary layer flow**, 101
- conservation of mass**, 65, 67
- cubical volume element**, 65
- cylindrical and spherical coordinates**, 66, 67
- expanding bubble**, 328
- ideal fluid**, 82
- jet system**, 354, 357
- laminar natural convection**, 214, 221
- laminar pipe flow**, 108
- lubrication**, 115
- turbulent flow**, 144, 145
- turbulent natural convection**, 227
- Control volume**, 23
- forces acting on**, 28
- fluid stream**, 25
- momentum**, 27, 28
- Convection**, 155
- boundary layer**, 103
- laminar natural**, 213–225
 boundary conditions, 215
 example, thermal energy, 219, 220
 general statement of, 220–225
 thermal boundary layer, 213–219
- momentum due to**, 69, 70, 73
- natural**
 interferogram, 226
 streamline pattern, 222, 223
 temperature profile, 222, 223
 velocity profiles, 216–218
- turbulent natural**, *see* Turbulent natural convection
- Convection driven flow**
 natural, 204–254
 streamline, 212, 213
 temperature profile, 211, 212, 217, 218
 velocity profile, 211, 212, 222
- Convective heat**, 205–210
- Convective heat transfer**, problems, 207, 208
- Convective mass transfer**, *see* Mass transfer, convective
- Conversion factors**, 7
- Conveyed systems**, 280–295
 choking velocity, 294

- pneumatically, 289–295
 pressure drop in, 295
 saltation velocity, 290–294
 vertical, 294
- Cooling tower, example, 58
- Copper converter
 example, jet trajectory, 388, 389
 fluid path lines, 80
 submerged jet, 382, 383
- Copper refining, droplet formation, 342–344
- Copper reverberatory furnace, slag flow, 91
- Copper slag, viscosity, effect of composition, 19
- Correlation coefficient, 135–138
 turbulent flow, 136
- Cube
 differential mass balance 65–67
 differential momentum balance, 67
 fluid flow through, 65, 67
- Curl operator, 273
- Current density, 183
- Cyclone separator, 264–267
- D**
- Degassing, vacuum, 48, 49
- Deoxidant, terminal falling velocity, 262, 263
- Differential equations
 fluid flow, 64–122
 turbulent flow, 144–158
- Differential mass balance, 64–67, *see also* Continuity, equation of
- Differential momentum balance, 64, 67–75, *see also* Motion, equation of
 forces acting on, 68–75
 isothermal system, cartesian coordinates, 74
 momentum transfer, 68
- Differential vector operator, 420, 421
- Diffusion, turbulence, 154, 155
- Diffusion coefficient, binary, 208–210
- Diffusive flux, 211
- Dimensions, 5–7
- Discharge coefficient, 37, 395, 396, 399
- Displacement thickness, 106, 107, 166
- Drag coefficient, 256–267, 414
 bubble radius, 305, 306
 expanding bubble, 329
 regions
 creeping flow, 256, 257, 259
 intermediate, 257
 Newton's law, 257–259
 Stokes' law, 256, 257, 259
- streamlines, 258
 terminal falling velocity, 259–264
- Drag force, 73, 256
 particle, 263, 264
- Drainage of liquid film, 95–97
- Droplet
 behavior, 337–349
 diameter, 339, 349
 formation of, 337–349
 by atomization, 338–342
 copper refining, 342–344
 fan nozzle spray, 339, 340
 steelmaking, 342–344
 velocity in melts
 example, 348, 349
 rising (sinking), 344–349
- Dynamic similarity, 412, 413, 417
- E**
- Eddy
 correlation of velocity components, 136
 effect of surface tension, 241–243
 energy degradation, 131
 energy dissipation, 138
 formation in turbulent flow, 126, 127
 macroscale, 138
 microscale, 140
 in turbulent flow, 131, 132
 types of, 131, 132
 velocity fluctuations, 138
 viscosity
 Boussinesq's concept, 147
 Prandtl's mixing length model, 147–149
- Elasticity, 412
- Electrical conductivity, 179
- Electric arc furnace, 176, 177
- Electric field, 179
- Electric flux density, 179
- Electrode, rotating disk, 116
- Electrodynamics
 laws of, 177
 parameters, principal, 178–185
 proportionality constants, 179
- Electromagnetic driving force, 183
- Electromagnetic force, 412, 413
- Electromagnetic force field, 187–191
 calculation of, 192, 193
 melts, 191–197
 velocity field in metals, 197–201

- Electromagnetic stirring, industrial processes, 175–177
- Electromagnetodynamics
Hartmann flow, *see* Hartmann flow
of melts, 175–202
- Electroslag refining, 175–177
- Elutriation constant, 285
- Elutriation of particles, 284–287
example, 286, 287
- Energy, 4, *see also* specific types
conservation, 45
- Energy balance
overall, 58–63
turbulent natural convection, 227
- Energy parameter, 20
- Enthalpy, 45
- Entrainment of particles, 284–287
- Entropy, 45
- Eotvos numbers, bubble, 320–322
- Ergun equation, 269, 270, 272, 273, 275, 280, 421
- Euler equation, 82, 83
pressure distribution, 89
- Euler number, 410
- F**
- Fick's law, 208
- Film
falling, 92–95
liquid, drainage of, 95–97
- Film flow
drainage of liquid film, 95–97
example, 95
falling, 92–95
laminar, 92
meniscus at vertical plate, 98
Navier–Stokes equation, 63
parallel, 99
problems involving, 92–100
turbulent falling, 159–164
withdrawal of solid bodies from liquids, 97–100
- Film thickness, 97
Brotz equation, 162, 163
effect of viscosity, 100
of withdrawal speed, 100
turbulent flow, 161, 162
- Filtration, 296, 300–302
design, 301
filter cake, 300
- filter cloth, 300
slurry, 300
- Fixed bed, 281
- Flooding, 277, 278
example, 279
- Flow, *see also* specific types
through noncircular conducts, 41
through open channels, 42–44
uniform, 42, 43
- Flow field
pipe entrance, 110, 111
turbulence, *see* Turbulent flow
- Flow maldistribution, 272
- Flow measurement, 392–408
in liquid metals, 406–408
- Flow meter
gas, 393
quantity, 393
soap bubble, 393, 394
- Flow pattern, 23
- Flow rate, volumetric, *see* Volumetric flow rate
- Fluid, 4, 5, *see also* specific types
entrance effect, 92
momentum, 27
- Fluid flow, 1
differential equations, 64–122
equations, 193, 194
irrotational, 76, 77
physical modeling in metal processing, 392, 408–417
types, vorticity, 76
- Fluidization curve, 282–284
- Fluidization velocity
example, 284
minimum, 28, 284
- Fluidized bed, 280–295
bubbles in, 287–289
diagram, 281
expansion, 280
fluidization curve, 282–284
general properties, 282–284
liquidlike properties, 281
- Fluid–solid separation processes, 255
- Fluid stream, 25
- Fluid velocity, 10
hot-wire anemometer, 402–404
Laser anemometer, 404, 405
measurement of, 400–408
Pitot tube, 400, 401
- Flux, 12
- Flux line corrosion, 244

- Foam, 332, 333
- Force, 5, 8, *see also* specific types
acting on, differential momentum, 68–75
- Force field, 68
electromagnetic, 68, 73
gravity, 68, 73, 75
- Fourier's law of heat conduction, 205, 206
- Friction, loss through pipe fittings, 41, 42
- Friction coefficient vs. Reynold numbers, 166
- Friction factor, 37–44, 74, 414
examples, 40–44
fluid velocity, 38
pneumatic conveying, 295
open channel flow, 42
overall balance, 59
pressure drop, 38
- Friction velocity, 141
- Fritz equation, bubble diameter, 308
- Froth, 332, 333
measurement of region, 334
- Froude number, 386, 388, 414
- G**
- Galileo number, 414
- Gas, *see also* Ideal gas
binary diffusion coefficient, 209, 210
countercurrent flow through packed bed,
276–280
critical pressure ratios, 54
Lennard–Jones parameters, 423
thermal conductivity, 206, 207
viscosity of, 20
of mixtures, 20, 21
- Gas bubble, *see also* Bubble
in fluidized bed, 287–289
motion in liquids, 318–331
radius, 239
surface tension, 229, 231
growth, 238–240
- Gas bubble–melt interaction, 305
- Gas flow
flooding, 277, 278
loading point, 276–278
- Gas jet, 351–390
metal processing, 127
- Gas–liquid interface, 92
- Gas–liquid system, 3
- Gas meter, 393
- Gas–solid cyclone separator, 264–267
- Gas–solid systems, 3
- Geometric similarity, 411, 412
- Glass tank, flow in, 91
- Grashof number, 218, 415, 416
- Gravity, 412, 413
- H**
- Hagen–Poiseuille equation, 109, 110
- Halides, surface tension, 236
- Hartmann flow, 187–191
channel geometry, 186, 187
example, liquid mercury, 190, 191
- Hartmann numbers, 181, 182, 189, 191, 416
- Hea, convective, *see* Convective heat
- Heat flux, 206
binary diffusion, 209
- Heat flux vector, 206
- Heat transfer, convective, 207, 208
- Hoch number, 55
- Hot film anemometer, 130
- Hot-wire anemometer, 402–404
- Hydrogen, thermal conductivity, 207
- I**
- Ideal flow, 64
sinks in, 84, 85
sources in, 84, 85
- Ideal fluid
behavior
example, 85, 86
Navier–Stokes equation, 81–90
irrotational flow field, 82, 83
- Ideal gas
behavior, 45, 46
internal energy, 46
isentropic flow, 55
isothermal expansion, 46
pressure ratio, 55
- Induction equation, 181
- Induction furnace, 175, 176
ASEA-SKF, *see* ASEA-SKF furnace
coil arrangement, 185
example, magnetic Reynolds number,
181–184
flow patterns, 185
melt velocity, 198, 201
surface velocity, 198, 200
traveling wave, 185
- Induction melting, principle of, 177
- Induction-stirred continuous casting, 176, 177

- Induction-stirred ladle, 175
 Induction stirring, principle of, 177
 Inertia, 412
 Inertial force, 42
 Integral mass balance, 23–27
 example, molten steel, 26, 27
 finite control volume, 24
 fluid stream, 25
 mass flow rate, 25
 mean velocity, 25
 rate of change of mass, 24
 surface integral, 24
 Integral mechanical energy balance, 23, 33–37
 energy forms, 33–35
 example, 37
 orifice meter, 35–37
 Integral momentum balance, 23, 27–32
 equation, 27, 28
 examples, 30–32
 forces acting on control volume, 28
 system for, 29
 Interfacial tension, *see* Surface tension
 Interfacial turbulence, surface tension, 248–253
 Interferograms, 226
 fluid velocity measurements, 405, 406
 Inviscid behavior, 82
 Iron, molten, surface tension, 237, 238
 Isopotential lines, ideal flow, 84, 85
 Isothermality, 33
- J**
- Jet
 confined, 361–368
 flow pattern, 362
 free, 353–361
 flow diagram, 351, 352
 laminar, cylindrical, 353–357
 turbulent, 357–361
 gas, *see* Gas jet
 impinging, 368–381
 flow patterns, 369, 370
 on liquid surface, 372–381
 on solid surface, 368–372
 interaction, 351
 liquid, *see* Liquid jet
 movement, 351
 penetration, 375–377
 submerged, 381–390
 break-up, 390
 horizontal, 384–389
 vertical, 389, 390
- supersonic, 379
 trajectory, 386–389
 velocity, 386
- K**
- Kelvin equation, 231
 Kinematic similarity, 411
 Kinetic energy, 33, 34
 Knapik–Wason correlation, 348
- L**
- Ladle
 argon-stirred, 167–170
 induction-stirred, 175
 Laminar boundary layer, 100–108
 Laminar flow, 40
 boundary layer, 106
 comparison with turbulent flow, 128–132
 viscous, Navier–Stokes equation, 90, 91
 Laplace’s equation, 83, 86, 89
 Laser–Doppler anemometer, 130
 Lead
 molten
 atomization, 341, 342
 example, friction factor, 40–44
 refining, example, film thickness, 163, 164
 thermal conductivity, 207
 Lennard–Jones parameter for gases, 423
 Lennard–Jones potential, 20
 Lewis numbers, 416
 Liquid
 countercurrent flow through packed bed, 276–280
 motion of gas bubbles in, 318–331
 solidification, 224, 225
 viscosity, 21, 22
 Liquid jet, 351–390
 submerged, surface tension, 241–243
 Liquid–liquid interface, 92
 Liquid–liquid systems, 4
 Liquid–solid systems, 4
 Loading point, gas flow, 276–278
 Lorentz force, 179, 180, 182, 184, *see also*
 Body force
 Lubrication, 92
 in bearing, 114–116
 hydrodynamic theory, 90, 113–116
 no-slip boundary conditions, 115
 slide-block-guide assembly, 114

M

- Mach number, 52, 54, 55, 380, 415
 Magnetic diffusivity, 181
 Magnetic field, 179, 183
 Magnetic flux density, 179, 183
 Magnetic flux intensity, 180, 184
 propagation of, 182
 Magnetic induction, 177
 Magnetic permeability, 179
Magnetohydrodynamics, see Electromagnetodynamics
 Manometer, pressure differential, 36
 Mapping, conformal
 ideal fluid, 83
 potential flow problems, 86–89
 Mass, 4
 conservation of, equation of continuity, 65
 Mass balance
 differential, *see* Differential mass balance
 integral, *see* Integral mass balance
 overall, 62, 63
 Mass flow rate, 25, 34
 convergent-divergent nozzle, 56
 jet system, 356
 streamlines, 80, 81
 Mass flux, 47
 Mass transfer, 205–210
 convective, problems, 210–228
 Maxwell's equation
 electrodynamics, 178–180, 182
 electromagnetic force field, 192, 193
 Mechanical energy
 conservation of, for steady state systems, 35
 rate of change, 33
 terms, 33
 Mechanical energy balance integral, *see* Integral mechanical energy balance
 Mechanical equilibrium, 230, 232
 Melt
 binary diffusion coefficient, 209, 210
 bubble size, 336
 droplets in, 305–349, *see also* Droplets
 electromagnetic force field, 191–197
 electromagnetodynamics, 175–202
 flow in mushy zone, 91
 gas bubble in, 305–349, *see also* Gas bubble
 Melt velocity
 in ASEA-SKF furnace, 194–197
 use of tracers, 407
 Mercury, liquid, fluid velocity, example, 190, 191
 Metal, *see also* specific metal
 droplet, *see* Droplet
 extraction, 1
 liquid
 flow measurements, 406–408
 surface tension, 235
 molten, *see also* Melt
 atomization, 341, 342
 bubble formation, 314–318
 open channel flow, 42–44
 example, 44
 refining, 1
 solidifying, 224, 225
 temperature dependence of viscosity, 16–18
 thermal conductivity, 206, 207
 velocity field, 197–201
 Metallurgy, *see also* Metal processing
 turbulent flow, 126
 Metals processing, 1–3, 175–177
 dimensionless groups in, 414–416
 jet systems, 351, 352
 MHD applications in, 186–201
 natural convection, 205
 physical modeling of fluid flow systems, 392, 408–417
 surface tension, 230
 turbulence in, 125
 turbulent recirculating flows, 172, 173
 MHD approximation, 178, 182
 applications in metal processing, 186–201
 Modeling, physical
 dimensional, example, 410, 411
 dimensional analysis, 409–411
 of fluid flow, in metals processing, 392, 408–417
 similarity, 411–413
 Molar flux, 208, 209
 Momentum, 4
 accumulation of, 70, 145
 control volume, 27, 28
 due to stress, 70
 rate of change, 28
 of outflow, 28
 per unit area and unit time, 12
 viscous transfer, 145
 Momentum balance
 differential, *see* Differential momentum balance

- Momentum balance (*cont'd.*)
 integral, *see* Integral momentum balance
 turbulent, 156
- Momentum flux, 146
- Momentum transfer, 68
- Morton number, 415
 bubble, 320, 322
- Motion, equation of, 23, 64, 67–75, *see also*
 Differential momentum balance, Navier–
 Stokes equation
- boundary conditions, 91, 92
- boundary layer flow, 101
- cylindrical coordinates, 71
- expanding bubble, 328
- fluid flow, 193, 194
- jet system, 354, 355, 357, 365
- laminar natural convection, 214–216, 221
- laminar pipe flow, 108
- lubrication, 114, 115
- Newtonian fluid, 69
- rectangular coordinates, 69
- rotating disk, 117
- spherical coordinates, 72
- turbulent flow, 145–147, 159–170
- turbulent natural convection, 227
- unsteady pipe flow, 112
- vorticity transport, 120
- Newtonian fluid, 12
- equation of motion
 cylindrical coordinates, 71
 rectangular coordinates, 69
 spherical coordinates, 72
- stress tensor, 14, 15
- Newton's law
 differential momentum balance, 68
 of viscosity, 12
 generalization of, 13, 14
- Nikuradse formula for turbulent flow, 149,
 150
- Nozzle
 bubble formation at, 309–318
 continuous casting system, 2
 convergent-divergent, 50–54
 example, mass flow rate, 56
 velocity profiles, 53
 density profile, 54
 diameter, 23, 26
 fan spray, droplet formation, 339, 340
 sonic velocity supersonic, 49–56
 supersonic, example, 57, 58
 total flow rate, 56
 velocity profile, 54
 volumetric flow rate, 393–397
- Nusselt film thickness, 161

N

- Navier–Stokes equation, 23, 75
 drainage of liquid film, 95–97
 electromagnetic force field, 188
 entrance effects in pipe flow, 110–112
 exact solutions, 91–121
 example, 85, 95, 107
 film flow, 92–95
 flow, rotating disk, 116–119
 ideal fluid behavior, 81–90
 laminar boundary layer, 100–108
 laminar flow
 through circular pipe, 108–110
 viscous, 90, 91
 lubrication, 113–116
 pipe flow, 108–113
 unsteady, 112, 113
 special solutions, 81–91
 as vorticity transport equation, 119–121
 withdrawal of solid bodies from liquids,
 97–100

O

- Ohm's law
 electromagnetic force field, 192, 193
 for moving fluid, 178, 183
- Orifice, bubble formation at, 309–318
- Orifice meter, 35–37
 examples, 58–63
 volumetric flow rate, 393–397
- Overall balance, *see also* specific types
 application of, 58–63
 examples, 58–63
- Oxides, surface tension, 236
- Oxygen
 mass flow rate, 56
 pressure, example, supersonic nozzle,
 57
 thermal conductivity, 207
- Oxygen furnace, 1, 2
 impinging jet system, 372–381
 jet penetration, 375, 376
- Oxygen lance for steelmaking, 380

P

- Packed bed
 countercurrent flow of gases and liquids, 276–280
 diagram, 268
 flow through, 267–280
 nonuniform, fluid flow through, 272–275
 outlet velocity, 274, 275
 particle shape, 268–271
 particle size, 268–271
 pressure drop, example, 269–272
 uniform, fluid flow through, 268–272
 void fraction, 268–271
- Particle
 elutriation, 284–287
 example, 286, 287
 entrainment, 284–287
 motion of, in fluids, 256–267
 in packed bed, 267–280
 shape, 268–271
 size, 268–271
 void fraction, 268–271
- terminal falling velocity, 259–264
 effect of motion in bulk of fluid, 263
 of solid surface, 263, 264
 spherical solid, 260
 unsteady motion, 260–263
- Path line, 78, 80
 copper converter, 80
- Peclet number, 415, 416
- Permittivity, 179
- Pierce-Smith converter, 388
- Pipe
 circular, laminar flow through, 108–110
 comparison of laminar and turbulent flow through, 128–132
 flow
 of compressible fluids, 46–48
 entrance effects, 110–112
 laminar, Hagen–Poiseuille equation, 109, 110
 momentum balance equation, 149, 150
 Navier–Stokes equation, 108–113
 problems in, 108–113
 turbulent, 149–153
 unsteady, 112, 113
 frictional loss through fittings, 41, 42
 geometry, 37, 38, 40
 hydraulic mean diameter, 41
 noncircular, 41
- velocity, average linear, 110
 volumetric flow rate, 109
- Pitot–Prandtl tube, 401, 406
- Pitot tube, fluid velocity, 400, 401
- Pneumatic conveying systems, 289–295
 pressure drop in, 295
- Potential energy, 33, 34
- Potential flow
 conformal mapping, 86–89
 diagram of field, 88
 high-speed digital computers, 90
 pressure field, 89, 90
- Power number, 415
- Prandtl number, 154, 361, 415
 for gases, 207
 magnetic, 181, 182
 natural convection, 217, 219
- Prandtl's mixing length model, 147–149
- Pressure, 412
 effect on viscosity, 15, 16
- Pressure differential, manometer, 36
- Pressure distribution, 23, 89
- Pressure drop
 example, 40
 friction factor, 38
- Pressure energy per unit mass, 34, 35
- Pressure field in potential flow, 89, 90
- Pressure gradient, 10, 11, 73
- Pressure ratio, critical, 53, 54
- Pressure transducer, 406
- Pressure wave, 49, 50
 propagation of, 51
- Proportionality constants, electrodynamics, 179
- Pumping
 example, 40
 power requirements, 41

R

- Rayleigh number, 416
 natural convection, 222
- Resistance parameter, 274
- Reynolds number, 38, 39, 383, 384, 410, 415
 bubble, 320–322
 compressible fluid, 48
 film, 94
 vs. friction coefficient, 166
 magnetic, 181
 example, 181–184
- nozzle, 311
- orifice, 312

- Reynolds number (*cont'd.*)
 particle, 256, 258, 273
 pipe flow, 128
- Reynolds stress, 134, 146, 154, 158
- Rotameter, volumetric flow rate, 398, 399
- Rotating disk
 boundary conditions, 117
 flow near, 116–119
 flow field, 115, 116
 geometry, 116
 streamlines, 119
- Rotation, vector, fluid element, 75
- S**
- Saltation velocity, 290–294
- Scalar, 419
 product, 420
- Scalar field, 420
 Laplacian, 421
- Schlieren techniques, flow measurements, 405, 406
- Schmidt number, 210, 361
- Sedimentation, 296–300
 of coarse suspensions, 298, 299
 of concentrated suspension, 297
 effect of solids concentration, 298
 of fine suspensions, 297
 suspension height, 298
- Settling, *see* Sedimentation
- Shear force, 8
- Shear stress, 5, 8, 12, 412
 boundary conditions, 91
 momentum due to, 70
 turbulent, 147
 turbulent flow, 134, 135
 on walls, 43
- Sherwood–Shipley–Holloway correlation, 278
- Shock wave, 50
- Silicates, surface tension, 236
- Similarity, in physical modeling, 411–413, 417
 dynamic, 412, 413, 417
 geometric, 411, 412
 kinematic, 411
- Single particle fluid systems, 256–267
- Slag
 droplet, surface tension, 234
 flow in copper reverberatory furnaces, 91
 surface tension, 235, 236
 thermal boundary layer, 219, 220
 viscosity, 21, 22
- Slag corrosion, 205
- Slag–metal emulsion, 1, 2
- Slag refining, 175
- Slide block–guide assembly, 114
- Solid, in packed bed, *see* Packed bed
- Solidification, 224, 225
- Solid particle fluid systems, 255–302
- Solid surface, effect on moving particle, 263, 264
- Solvent, surface tension, 244, 245
- Sound, velocity of, in fluid, 49
- Stack gas injection, 89
- Stagnation point, 400
- Stagnation pressure, 89, 401
- Steam jet ejector system, 3
- Steel
 droplet formation, 342–344
 molten
 example
 overall balance, 59–63
 surface tension damping, 243
 terminal rising velocity, 260
 integral mass balance, 26, 27
 stream, example, air entrapment, 107, 108
 thermal boundary layer, example, 219, 220
- Steel-making process, 57
- Stirring force, nature of, 184, 185
- Stokes' law, 90
- Streak line, 78, 80
- Stream, surface tension, 229
- Stream function, 64, 75, 77–81, 156
 boundary layer, 103, 104
 fluid flow, 193
 ideal fluid, 83
 impinging jet, 369
 jet system, 354
 laminar natural convection, 215, 221
 packed bed, nonuniform, 273
 physical significance, 78–81
 potential flow, 87, 89
 two-dimensional flow, 77
 vorticity, 121
- Streamline, 78
 argon–stirred ladle, 170
 circular, laminar jet, 353
 confined jet, 362
 convection driven flow, 212, 213
 experimental vs theoretical, 78
 gas bubble, 319
 ideal flow, 84, 85
 natural convection, 222, 223

- particle, 258
 potential flow, 87, 88
 rotating disk, 119
 surface tension, 247
 turbulent jet, 359
 in two-dimensional flow, 80, 81
 velocity map, 78, 79
- S**tress, 8–10
 bulk, 10
 dimension, 146
 momentum due to, 70
- S**tress tensor, 9, 10, 73
 differential momentum balance, 74
 for Newtonian fluids, 14, 15
 turbulent, 146
- S**ubstantial time derivative, 67, 73
- S**ulfides, surface tension, 236
- S**urface force, 8, 68, 70
- S**urface roughness, 43
- S**urface tension, 205, 412, 413
 boundary conditions, 245
 circulation patterns, 246
 contact angle, 233, 234
 definition of, 228–230
 deformation, 229
 dynamic system, 230, 238–253
 effect on bubble growth, 238–240
 on turbulence, 241–243
 example, 243
 interfacial turbulence, 248–253
 stationary system, 230–238
 arbitrary surface, 231–233
 mechanical equilibrium, shape of spherical cup, 230, 231
 uniform, 229
 values of, 235–238
- S**urface tension driven flow, 204, 228–253
 gas–solid–liquid interfaces, 244–248
- S**urfactant, accumulation of, 92
- S**ymmetry, statement of, 92
- T**
- T**emperature, effect on viscosity, 15–17
- T**ensor, second-order, definition, 422
- T**hermal conductivity
 definition of, 205–207
 of gases, 206, 207
 of metals, 206, 207
- T**hermal diffusivity, 206
- T**hermal energy, 33
Thermal energy balance equation, laminar
 natural convection, 214, 216, 221
- T**hickeners, industrial, 299, 300
- T**in, molten, atomization, 341
- T**oluene, turbulent flow, 138, 140
- T**racer
 flow measurements, 405
 melt velocity in induction–stirred mold, 407
- T**urbulence, *see also* Turbulent flow
 correlation coefficients, 135–138
 correlations, 135–138
 Eulerian viewpoint, 137
 homogeneous, 139
 intensity, 133
 interfacial tension, 248–253
 isotropic, 135, 139, 140
 length scale, 138
 microscale, example, 140, 141
 phenomena, 124–173
 statistical theory, 132–141
- T**urbulence energy, 365, 368
 convection, 155
 diffusion, 155
 dissipation, 155
 impinging jet, 369, 370
 mixing length, 153
 one-equation model, 153–157
 two-equation model, 157, 158
- T**urbulence energy balance equation, 155
- T**urbulent core, 141, 142
 laminar effects, 151
- T**urbulent flow, 40, 124–173, *see also*
 Turbulence
 air–water interface, 127
 buffer layer, 141, 142
 comparison of laminar flow and, through pipes, 128–132
 core, 141, 142
 correlation of velocity fluctuations, 136
 differential equations, 144–158
 eddy formation, 126, 127
 energy associated with, 138–140
 energy dissipation, 138, 139
 example, 140, 141
 equation of continuity, 144, 145
 of motion, 145–147
 film thickness, example, 163, 164
 fluctuating nature of, 129–131
 fluctuating velocity, 132–141
 laminar sublayer, 141, 142

- Turbulent flow (*cont'd.*)
 one-equation models, 153–157
 physical manifestations, 126–132
 through pipes, 149–153
 example, 150–153
 quantitative characterization, 132–144
 recirculating, 172, 173
 shear stress, 134, 135
 solutions of equation of motion, 159–170
 time-smoothed velocity, 132–141
 two-equation models, 157, 158
 universal velocity profiles, 141–144
 velocity fluctuations, frequency, 138–140
 velocity profile, 128, 129
 of vertical falling film, 159–164
 water model of argon-stirred ladle
- Turbulent jet, 357–361
 example, 360, 361
 streamline, 359
 velocity, 358, 359
- Turbulent mixing, extent of, 158
- Turbulent natural convection, 225–228
 physical manifestation of, 226–228
- Turbulent stress tensor, 146
- Turbulent transport, models of, 147–158
- Turbulent viscosity, 180, 227, 358
 confined jet, 365
 mixing length, 153
 one-equation models, 153–157
 two-equation models, 157, 158
- U**
- Unit, basic, 5–7
- Unit tensor, 422
- V**
- Vacuum degassing, 48, 49
- Vacuum pump, example, overall balance, 61–63
- Van Driest hypothesis, mixing length model, 151, 152
- Vector
 definition, 419, 420
 operation, 419, 420
- Vector differential operator, 66
- Vector field, 421
 Laplacian, 421
- Vector operator, differential, 420, 421
- Velocity
 angular, 76
 boundary layer, 102, 103, 105
 continuity of, 91
 dimensionless, 141
 of droplets in melts, 344–349
 fluctuating
 amplitude, 138
 frequency, 138–140
 fluctuations in turbulent flow, 129–131
 mean, 25
 mean linear, friction factor, 38
 overall balance, 59
 sonic, 50
 stagnation point, 400
 subsonic, 52
 supersonic, 52
 terminal falling, 259–264
 terminal rising, example, 260
 universal profiles for turbulent fields, 141–144
 water, example, 85, 86
- Velocity ceiling, 55
- Velocity field, 23, 197–201
 two-dimensional, 78
 uniform, 76
- Velocity gradient, differential momentum balance, 74
- Velocity potential, 64
 ideal fluid, 82
 mapping, 87
- Velocity vector, stream function, 78, 79
- Venturi meter, volumetric flow rate, 393–398
- Viscometry, Hagen–Poiseuille equation, 110
- Viscosity
 effect of composition, 16, 18–20
 of pressure, 15, 16
 of temperature, 15–17
 experimentally determined, 20
 factors affecting, 14–22
 gas, 20
 gas mixture, 20, 21
 example, 21
 liquid metals, 21
 Newtonian definition, 11–14
 prediction of, 20, 21
 slag, 21, 22
 units, 12, 13
 very slow motion, 90, 91
- Void fraction, packed bed, 268, 270, 271
- Volumetric flow rate, 43, 44
 measurement of, 393–399
 example, 397, 398
 nozzle, 393–397
 orifice plates, 393–397

quantity meters, 393
rotameter, 398, 399
venturi meter, 393–398
Vorticity, 64, 75–77, 120, 156
 conservation of, 121
 definition, 75
 fluid flow, 193
 impinging jet, 369, 370
 natural convection, 221
 stream function, 121
 types of flow, 76
Vorticity transport equation, 119–121
 boundary conditions, 120

W

Water
 air jet, interface, 127
 flow over vane, integral momentum balance,
 31, 32

flow behavior, 126
flow rate, integral mechanical energy balance,
 37
ideal fluid behavior, example, 85, 86
velocity, example, 85, 86
Water circuit, cooling, example, overall
 balance, 58, 59
Water jet, example of integral momentum
 balance, 30
Weber number, 415
 bubble, 320
Wind tunnel, velocity components, 134
Wire drawing, 116
Withdrawal speed, film thickness, 100
Work, rate of, 34

Z

Zinc-aluminum solution viscosity, 19